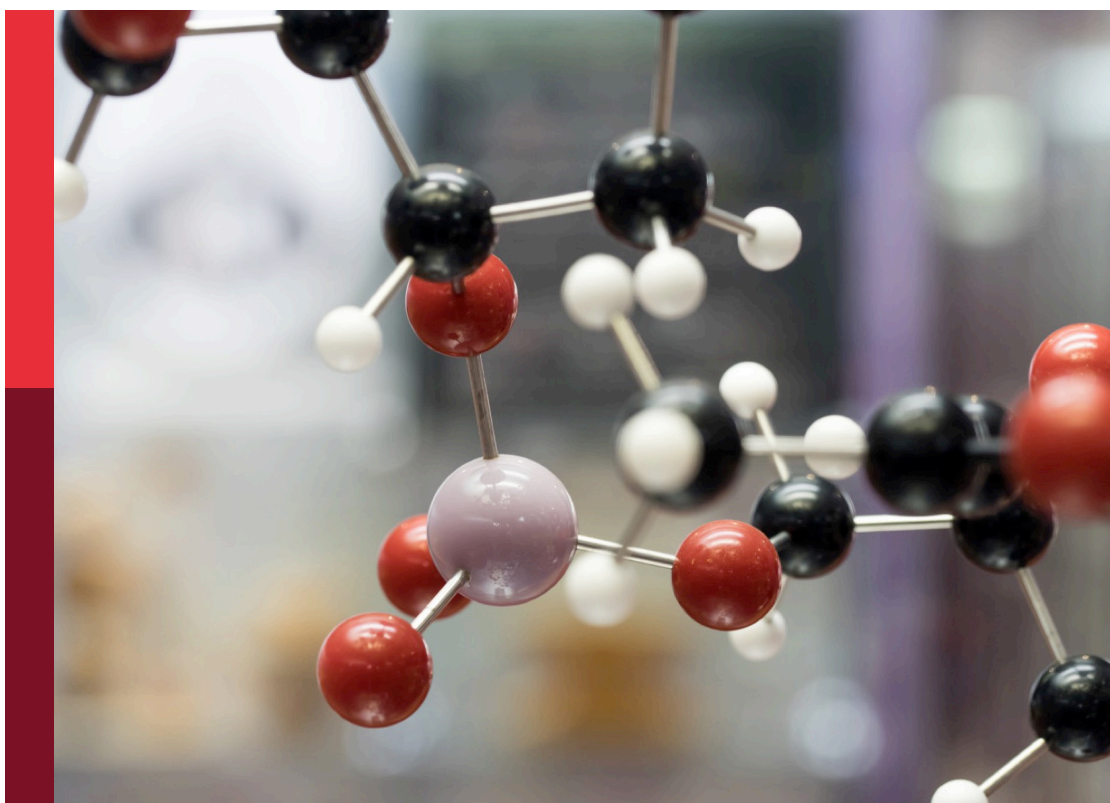# Medicinal chemistry for neglected tropical diseases using in-vitro, in-vivo and in silico approaches

Edited by
Jorddy Neves Cruz, Suraj N. Mali, Cleydson Breno Rodrigues dos Santos and Essa M. Saied

Published in
Frontiers in Chemistry

Generative AI statement
Any alternative text (Alt text) provided alongside figures in the articles in this ebook has been generated by Frontiers with the support of artificial intelligence and reasonable efforts have been made to ensure accuracy, including review by the authors wherever possible. If you identify any issues, please contact us.

About Frontiers

Frontiers is more than just an open access publisher of scholarly articles: it is a pioneering approach to the world of academia, radically improving the way scholarly research is managed. The grand vision of Frontiers is a world where all people have an equal opportunity to seek, share and generate knowledge. Frontiers provides immediate and permanent online open access to all its publications, but this alone is not enough to realize our grand goals.

Frontiers journal series

The Frontiers journal series is a multi-tier and interdisciplinary set of open-access, online journals, promising a paradigm shift from the current review, selection and dissemination processes in academic publishing. All Frontiers journals are driven by researchers for researchers; therefore, they constitute a service to the scholarly community. At the same time, the *Frontiers journal series* operates on a revolutionary invention, the tiered publishing system, initially addressing specific communities of scholars, and gradually climbing up to broader public understanding, thus serving the interests of the lay society, too.

Dedication to quality

Each Frontiers article is a landmark of the highest quality, thanks to genuinely collaborative interactions between authors and review editors, who include some of the world's best academicians. Research must be certified by peers before entering a stream of knowledge that may eventually reach the public - and shape society; therefore, Frontiers only applies the most rigorous and unbiased reviews. Frontiers revolutionizes research publishing by freely delivering the most outstanding research, evaluated with no bias from both the academic and social point of view. By applying the most advanced information technologies, Frontiers is catapulting scholarly publishing into a new generation.

What are Frontiers Research Topics?

Frontiers Research Topics are very popular trademarks of the *Frontiers journals series*: they are collections of at least ten articles, all centered on a particular subject. With their unique mix of varied contributions from Original Research to Review Articles, Frontiers Research Topics unify the most influential researchers, the latest key findings and historical advances in a hot research area.

Find out more on how to host your own Frontiers Research Topic or contribute to one as an author by contacting the Frontiers editorial office: frontiersin.org/about/contact

Medicinal chemistry for neglected tropical diseases using in-vitro, in-vivo and in silico approaches

Topic editors

Jorddy Neves Cruz — Federal University of Pará, Brazil

Suraj N. Mali — Padmashree Dr. D.Y. Patil University, India

Cleydson Breno Rodrigues dos Santos — Universidade Federal do Amapá, Brazil

Essa M. Saied — Humboldt University of Berlin, Germany

Table of contents

Editorial: Medicinal chemistry for neglected tropical diseases using *in-vitro*, *in-vivo* and *in silico* approaches

Suraj N. Mali[1], Essa M. Saied[2],
Cleydson Breno Rodrigues dos Santos[3] and Jorddy Neves Cruz[4]*

[1]School of Pharmacy, DY Patil University, Navi Mumbai, Maharashtra, India, [2]Humboldt University of Berlin, Berlin, Germany, [3]Federal University of Amapá, Macapá, Amapá, Brazil, [4]Federal University of Pará, Belém, Pará, Brazil

Editorial on the Research Topic
Medicinal chemistry for neglected tropical diseases using *in-vitro*, *in-vivo* and *in silico* approaches

Neglected tropical diseases continue to pose a major challenge to global health, disproportionately affecting resource-limited regions and vulnerable populations. Despite their epidemiological importance, the development of innovative therapies remains restricted due to limited investment and the biological complexity of the pathogens involved. In this context, medicinal chemistry plays a central role in the search for novel pharmacological solutions, as it enables the integration of *in vitro*, *in vivo*, and *in silico* approaches for drug discovery (Ferreira L. L. G. et al., 2022; Ferreira O. O. et al., 2022).

The study by Maliyakkal et al. presents a two-dimensional QSAR model based on machine learning to accelerate drug discovery against *Trypanosoma cruzi*, the etiological agent of Chagas disease, which still lacks effective therapies. Using a dataset of 1,183 inhibitors, predictive models were developed and validated, with the artificial neural network (ANN-QSAR) showing the highest accuracy. Virtual screening identified 12 promising compounds, with F6609-0134 emerging as the most relevant candidate, as further confirmed by molecular docking, molecular dynamics simulations, and free energy calculations Maliyakkal et al.

Zanthoxylum rhoifolium Lam., traditionally used in folk medicine as an antiparasitic agent, demonstrated promising results against *Leishmania amazonensis*. The ethanolic extract and its fractions, particularly the neutral fraction, revealed chromatographic profiles suggestive of alkaloids, with chelerythrine being isolated and identified. In biological assays, the extract and fractions exhibited dose-dependent leishmanicidal activity, with the neutral fraction showing high selectivity and low cytotoxicity in VERO cells. Moreover, this fraction enhanced cell proliferation and promoted wound-healing effects, reinforcing the therapeutic potential of this species both in parasite control and tissue regeneration (Correa-Barbosa et al.).

Tuberculosis remains a serious global health problem, further complicated by the emergence of drug-resistant *Mycobacterium tuberculosis* strains. In this context, one study

explored the therapeutic target PknG, a kinase essential for bacillary survival in macrophages, using multiple computational approaches to screen 460,000 molecules. Seven high-affinity compounds were identified, among which chromene glycoside (Hit 1) displayed the most favorable pharmacokinetic profile, low toxicity, and stability confirmed by molecular dynamics simulations. DFT analyses further supported its superior electronic properties compared to the reference ligand, consolidating it as a promising candidate for the development of new drugs against resistant TB strains (Alruwaili et al.).

The growing threat of resistant tuberculosis, including MDR-TB and XDR-TB, underscores the urgent need to identify new therapeutic targets against *M. tuberculosis*. In this *in silico* study, microbial natural products from the NPAtlas database were screened as potential inhibitors of DNA gyrase B, an enzyme essential for bacillary replication. Twelve initial compounds were identified and further refined through ADME-T evaluation, pharmacophore modeling, and molecular dynamics simulations. Among them, 1-Hydroxy-D-788-7, an anthracycline derivative, stood out for its higher affinity and binding stability, along with Erythrin and Pyrindolol K2. The findings highlight 1-Hydroxy-D-788-7 as the most promising candidate, reinforcing the potential of microbial natural products in the discovery of new agents against resistant TB strains, although further experimental studies are required to validate its therapeutic efficacy (Elsaman et al.).

Dengue continues to represent a global challenge due to the wide spread of its vectors and the limitations of available therapies and vaccines, emphasizing the need for new antiviral agents. Hanson et al. applied integrative approaches combining machine learning, molecular docking, and molecular dynamics simulations to identify potential inhibitors of the dengue virus NS2B/NS3 protease, an enzyme essential for viral replication. From over 21,000 compounds screened, the logistic regression model achieved 94% accuracy, highlighting four lead molecules (ZINC38628344, ZINC95485940, 2′,4′-dihydroxychalcone, and ZINC14441502), all showing high binding affinity and stable interactions with the catalytic triad of the enzyme. These compounds also exhibited favorable pharmacokinetic properties and low predicted toxicity, demonstrating their potential as safe and promising candidates for the development of novel anti-dengue therapeutics (Hanson et al.).

The study on *Ruta montana* L., a medicinal plant from the Middle Atlas region of Morocco, provided a detailed phytochemical characterization and a comprehensive evaluation of its biological properties. The essential oil, rich in 2-undecanone (81.16%), exhibited strong antimicrobial activity, particularly against fungi, along with analgesic and anti-inflammatory effects comparable to reference drugs. Phenolic extracts, especially those containing rosmarinic acid derivatives and quercitrin, showed pronounced antioxidant activity. Toxicological assays indicated relative safety at controlled doses, although mild biochemical alterations suggest caution at higher concentrations. These findings highlight the potential of this species as a natural source of antimicrobial, antioxidant, and anti-inflammatory agents (El Ouardi et al.).

The study by Zhang et al. investigated the phenolic compounds present in Bairui, a traditional preparation derived from *Thesium chinense* Turcz., identifying five major compounds: methyl-*p*-hydroxycinnamate, vanillin, kaempferol, isorhamnetin-3-*O*-glucoside, and astragalin. Notably, three of these compounds were reported for the first time in this formulation, expanding knowledge of its chemical composition. Co-culture assays demonstrated that isorhamnetin-3-*O*-glucoside promoted the proliferation of Chinese hamster ovary cells, human umbilical cord blood NK cells, and mesenchymal stem cells, while vanillin and astragalin also showed positive effects on immune cell expansion at specific concentrations. Conversely, some compounds displayed selective inhibitory effects on peripheral NK cells (Zhang et al.).

Research on hydroethanolic leaf extracts of *Ficus carica* L. from eastern Morocco, conducted by Tikent et al., revealed a rich profile of bioactive compounds, particularly polyphenols, flavonoids, vitamin C, and condensed tannins, associated with strong antioxidant activity confirmed by multiple assays (DPPH, β-carotene, ABTS, and TAC). Additionally, the extracts showed significant antimicrobial activity against both Gram-positive and Gram-negative bacteria, as well as *Candida albicans*. *In vitro* assays also revealed selective cytotoxicity against three breast cancer cell lines (MCF-7, MDA-MB-231, and MDA-MB-436), suggesting antitumor potential. *In silico* studies further indicated possible mechanisms of interaction between the metabolites and bacterial, fungal, and tumor targets, reinforcing their pharmacological versatility (Tikent et al.).

The study on *Aspidosperma nitidum* conducted by Brígido et al. provided important insights into its therapeutic potential against cutaneous leishmaniasis, demonstrating both antiparasitic activity and immunomodulatory effects in BALB/c mice infected with *L. amazonensis*. Ethanolic extracts and their alkaloid-rich fractions contained compounds such as corynantheol, yohimbine, and dihydrocorynantheol, identified by mass spectrometry, and confirmed *in silico* to interact stably with catalytic residues of trypanothione reductase, a validated leishmanicidal drug target. *In vivo*, treatment significantly reduced lesion progression and splenic parasite load in a dose-dependent manner, achieving up to 42.5% reduction. Furthermore, immune modulation was observed, with decreased IL-10 expression and increased IFN-γ production, promoting a protective host response (Brígido et al.).

Author contributions

SM: Conceptualization, Data curation, Formal Analysis, Funding acquisition, Investigation, Methodology, Project administration, Resources, Software, Supervision, Validation, Visualization, Writing – original draft, Writing – review and editing. ES: Conceptualization, Data curation, Formal Analysis, Funding acquisition, Investigation, Methodology, Project administration, Resources, Software, Supervision, Validation, Visualization, Writing – original draft, Writing – review and editing. CS: Conceptualization, Data curation, Formal Analysis, Funding acquisition, Investigation, Methodology, Project administration, Resources, Software, Supervision, Validation, Visualization, Writing – original draft, Writing – review and editing. JN: Conceptualization, Data curation, Formal Analysis,

Funding acquisition, Investigation, Methodology, Project administration, Resources, Software, Supervision, Validation, Visualization, Writing – original draft, Writing – review and editing.

Conflict of interest

The authors declare that the research was conducted in the absence of any commercial or financial relationships that could be construed as a potential conflict of interest.

The author(s) declared that they were an editorial board member of Frontiers, at the time of submission. This had no impact on the peer review process and the final decision.

Generative AI statement

The author(s) declare that no Generative AI was used in the creation of this manuscript.

Any alternative text (alt text) provided alongside figures in this article has been generated by Frontiers with the support of artificial intelligence and reasonable efforts have been made to ensure accuracy, including review by the authors wherever possible. If you identify any issues, please contact us.

Publisher's note

All claims expressed in this article are solely those of the authors and do not necessarily represent those of their affiliated organizations, or those of the publisher, the editors and the reviewers. Any product that may be evaluated in this article, or claim that may be made by its manufacturer, is not guaranteed or endorsed by the publisher.

References

Ferreira, O. O., Cruz, J. N., de Moraes, Â. A. B., Franco, C. de J. P., Lima, R. R., Dos Anjos, T. O., et al. (2022a). Essential oil of the plants growing in the Brazilian Amazon: Chemical composition, antioxidants, and biological applications. *Molecules* 27, 4373. doi:10.3390/molecules27144373

Ferreira, L. L. G., de Moraes, J., and Andricopulo, A. D. (2022b). Approaches to advance drug discovery for neglected tropical diseases. *Drug Discov. Today.* 27, 2278–2287. doi:10.1016/j.drudis.2022.04.004

Check for updates

Aspidosperma nitidum reduces parasite load and modulates cytokines in BALB/c mice infected with Leishmania (Leishmania) amazonensis

Heliton Patrick Cordovil Brígido[1,2], Everton Luiz Pompeu Varela[2,3],
Antônio Rafael Quadros Gomes[1,2,3,4], Jorddy Neves Cruz[5],
Juliana Correa-Barbosa[1], José Edson de Sousa Siqueira[6],
Cristian Kallahan Silva Chagas[7], Andrey Moacir do Rosário Marinho[6],
Liliane Almeida Carneiro[8], Márlia Regina Coelho-Ferreira[9],
Sandro Percário[2,3] and Maria Fâni Dolabela[1,2,7]*

[1]Postgraduate Pharmaceutical Innovation Program, Institute of Health Sciences, Federal University of
Pará, Belém, Brazil, [2]Post-Graduate Program in Biodiversity and Biotechnology, Belém, Brazil, [3]Oxidative
Stress Research Lab, Institute of Biological Sciences, Federal University of Pará, Belém, Brazil, [4]Center for
Biological and Health Sciences, State University of Pará, Tucuruí, Brazil, [5]Institute of Biological Sciences,
Federal University of Pará, Belém, Brazil, [6]Postgraduate Program in Chemistry, Institute of Exact and
Natural Sciences, Federal University of Pará, Belém, Brazil, [7]Postgraduate Program in Pharmaceutical
Ciences, Institute of Health Sciences, Federal University of Pará, Belém, Brazil, [8]National Primate Center,
Ananindeua, Brazil, [9]Emílio Goeldi Museum of Pará, Belém, Brazil

The lack of vaccines shows the need for alternative leishmaniasis treatments. *In
vitro* study previously demonstrated the leishmanicidal activity of *A. nitidum*
extracts. This study describes for the first time, the antileishmanial activity of
A. nitidum extracts in infected Balb/c mice and its immunomodulatory effect. The
extract (EE) was obtained by maceration of the peel powder with ethanol, which
was fractionated by acid-base partition, originating the alkaloid (FA) and neutral
(FN) fractions. EE and FA were analyzed using mass spectroscopy. Daily
intragastric treatment was performed with EE and FA, at doses of 200 mg/kg
and 400 mg/kg, in Balb/c mice with 28 days of infection by *Leishmania
amazonensis*. A thickness gauge was used to assess the progression of the
lesion and the MTT method to determine the parasite load in the spleen. The
quantification of IL-10 and IFN-γ was performed by ELISA. Analysis of the mass
spectrum of EE indicated the presence of the alkaloids corynantheol and
yohimbine, while in FA the alkaloid dihydrocorynantheol was identified. To
elucidate the mode of interaction of these alkaloids with the TR protein,
molecular target of antileishmanial drugs, we used molecular modeling
approaches such as docking, molecular dynamics simulations and free energy
affinity. Treatment with EE for 28 days at the highest dose tested, significantly
reduced the size of the lesion. EE and FA after 28 days of treatment showed dose-
dependent antileishmanial activity, which reduced the parasite load in the spleen
of infected mice by 42.5% and 22.1%, respectively. Both EE and FA presented
immunomodulatory effect, as they decreased IL-10 expression and increased
IFN-y levels. The effectiveness of *A. nitidum* in the treatment of cutaneous
leishmaniasis was proven in this study. The results obtained *in silico*
demonstrated that the compounds are capable of interacting with the

catalytic residues of the TR. The affinity energy results demonstrated that the complexes formed are favorable for enzymatic inhibition. The alkaloids present in the plant have demonstrated not only antileishmanial activity, but also the ability to modulate the host's immune response. These promising results open perspectives for developing more effective and comprehensive treatments against cutaneous leishmaniasis.

1 Introduction

Cutaneous leishmaniasis (CL) is an infectious, non-contagious disease caused by protozoan parasites of the *Leishmania* genus. In clinical terms, CL is characterized by the formation of skin lesions that can spontaneously heal or evolve into a chronic condition, which can spread and lead to massive tissue damage, being commonly caused by species of *Leishmania braziliensis*, *Leishmania major,* and *Leishmania amazonensis* (Silveira et al., 2004; Goto and Lauletta Lindoso, 2012).

Leishmaniasis is endemic in 98 countries across tropical and subtropical regions, affecting approximately 350 million people at risk of infection. Each year, around 2 million individuals are infected, with cutaneous leishmaniasis (CL) responsible for an estimated incidence of 700,000 to 1 million new cases. The disease is linked to poverty, malnutrition, displacement, inadequate housing, immunosuppression, and lack of financial resources. CL presents a wide geographic distribution, with the majority of cases reported in Brazil, Afghanistan, Algeria, Colombia, Iran, Syria, Ethiopia, Sudan, Costa Rica, and Peru (World Health Organization, 2023).

Few drugs are available for the treatment of the disease. The first-line treatment for leishmaniasis are the pentavalent antimonials (meglumine antimoniate), the second line includes miltefosine, pentamidine, and amphotericin B (Tiuman et al., 2011). All antileishmanial drugs present several limitations, including severe side effects, the need for higher doses to achieve the therapeutical effect, high treatment costs and toxicity, with consequent low adherence to treatment and the emergence of resistance in strains of circulating parasites (Ghorbani and Farhoudi, 2018; Uliana et al., 2018). Due to these problems, many studies are still been carried out to find new alternatives. A promising line lies upon medicinal plants, and some studies have proposed new therapies for this disease.

Aspidosperma nitidum, is a tree that can reach up to 40 m in height, being found in the American continent extending in an area that goes from Panama to Brazil, it is popularly known as *carapanaúba* (Brazil), *jaroro harinaros*, *apokuita* and *padapan* (Suriname), and *gabetillo* (Bourdy et al., 2004). Species from the *Aspidosperma* genus are used by folk medicine in parasitic diseases such as malaria and leishmaniasis. They are also used in various infections and wounds that are difficult to heal (Bourdy et al., 2004; do Socorro Silva da Veiga et al., 2022).

To demonstrate the antileishmanial activity of *A. nitidum*, our research group has previously used the bark extract for phytochemical studies and *in vitro* assays against promastigotes and amastigotes of *Leishmania* species. The ethanolic extract (EE) and the alkaloid fraction (FA) were active against Leishmania chagasi promastigotes ($IC_{50} < 100$ μg/mL) and moderate activity against *Leishmania amazonensis* promastigotes ($IC_{50=}$ 105–170 μg/mL; Veiga, 2013). Notwithstanding, against *L. amazonensis* amastigotes EE and FA) displayed high activity ($IC_{50} = 23.87 \pm 0.87$ μg/mL and 18.5 ± 0.94 μg/mL, respectively). Moreover, the cytotoxicity assay in peritoneal macrophages from Balb/c mice revealed that both EE and FA presented moderate toxicity ($CC_{50} = 491.8 \pm 1.86$ μg/mL and, respectively $209.1 + 1.7$ μg/mL), but with promising selectivity (SI = 21 and 11, respectively) (Veiga et al., 2021).

In addition to *in vitro* studies, our group evaluated the *in vivo* toxicological potential of *A. nitidum*. The study of acute and subacute toxicity of EE and FA obtained from *A. nitidum* was carried out orally in Balb/c mice. The results demonstrated that both the single dose and the repeated doses treatments did not cause mortality or signs of toxicity in mice. In this context, the 50% Lethal Dose (LD_{50}) of samples for mice was greater than 2.000 mg/kg in the acute test and greater than 1.000 mg/kg in the subacute test, suggesting a potential for safe use (Brígido et al., 2021).

Due to the limitations of current treatments for leishmaniasis, researchers are exploring plant-derived alkaloids as promising alternatives. Recent studies have highlighted the therapeutic potential of these compounds, demonstrating their efficacy in reducing parasite load and modulating immune responses (Sudarshan and Aidhen, 2013; Sudarshan et al., 2024). Thus, the ethanolic extract (EE) and alkaloid fraction (FA) from *A. nitidum* may serve as promising samples for efficacy studies in a murine experimental model with *Leishmania* infection, as they are selective and non-toxic for *in vivo* use. Based on these results, this study describes, for the first time, the antileishmanial activity of EE and FA obtained from *A. nitidum in vivo*, using Balb/c mice infected with *L. amazonensis*. Furthermore, it reports the immunomodulatory activity of these samples in infected animals.

2 Materials and methods

2.1 Plant material

Trunk bark of *A. nitidum* was collected on state highway PA-150 (coordinates S 02° 09′50.3″and W 048° 47′56.9″), in the state of Pará-Brazil, during August 2017. The plant material was identified by Dr. Márlia Regina Coelho-Ferreira and the exsiccate was

deposited at the João Murça Pires Herbarium of the Museu Paraense Emílio Goeldi, under no. MG206608.

In the present study, we used a wild plant collected in an Amazon virgin forest, and our work did not represent an extinction risk for the species. During collection, we took great care to remove the bark without damaging the species, in addition, only a small part of the bark was collected to guarantee the tree survival.

Our study complied with national and international guidelines and legislation. It is registered on the platform of the National System of Management and Genetic Heritage and Associated Traditional Knowledge (*Sistema Nacional de Gestão e Patrimônio Genético e Conhecimentos Tradicionais Associados* - SISGEN), with license under registration A2C3188 for the collection of the species. Furthermore, according to the 2019 IUCN Red List of Endangered Species, *Aspidosperma excelsum*, a synonym of *A. nitidum* is classified as a "least-concern" species (Botanic Gardens Conservation International (BGCI) and IUCN SSC Global Tree Specialist Group, 2019).

2.2 Extract preparation and alkaloid fraction obtaining

The barks of *A. nitidum* were washed in running water and dried in a circulated air oven (40°C, for 7 days). The dried material was submitted to milling in a knife mill. The plant powder was submitted to maceration with 96°GL ethanol (ratio 1:10). The ethanolic solution was filtered and concentrated in a rotary evaporator under reduced pressure until total evaporation of the alcohol, obtaining the dry ethanolic extract (EE).

The EE was subjected to acid:base extraction in order to obtain the alkaloid fraction (FA). For this purpose, 5 g of the extract was solubilized in ethanol and subjected to partitioning, in a separating funnel, with an aqueous solution of 1N hydrochloric acid (HCl). This solution was extracted with dichloromethane (250 mL for 3 times), then the neutral fraction (FN) was obtained. The acidic aqueous layer was alkalinized with 10% ammonium hydroxide (NH_4OH) to pH 9, followed by further extraction with dichloromethane (250 mL 3 times), obtaining an alkaline aqueous layer and an organic layer (FA), which was concentrated until residue.

2.3 Mass spectrum analysis

Mass spectra data were obtained by electrospray ionization (ESI) in positive ion mode using a Waters® Acquity® TQD instrument (Waters, Milford, MA, United States).

2.4 Animals

Seventy healthy adult male Balb/c mice (*Mus musculus*), aged between 6 and 8 weeks, weighing between 25 and 35 g, from the vivarium of Instituto Evandro Chagas (Ananindeua-Pará, Brazil) were used. The animals were housed in the Experimental Animal Facility of the Oxidative Stress Research Laboratory of the Institute of Biological Sciences of the Federal University of Pará (ICB/UFPA), on polypropylene cages (30 × 19 × 13 cm), covered with stainless

steel grids, containing a pine bed, with a maximum of 5 animals per cage kept at room temperature (24°C ± 2°C) and light/dark cycle of 12 h each. Before and during the study period, the animals were kept with food (Presença, São Paulo-SP, Brazil) and water *ad libitum*. Before any experimental procedure, the animals were acclimated to laboratory conditions for 15 days. The experimental procedures with mice were carried out at the Oxidative Stress Research Laboratory (LAPEO/ICB/UFPA) in accordance with the ethical standards for animal experimentation indicated by the Brazilian Society of Laboratory Animal Science (SBCAL) and international standards (NRC National Research Council, 1996).

2.5 Ethics declaration

All animal procedures were strictly in accordance with the National Institutes Guide for the Care and Use of Laboratory Animals (NRC National Research Council, 1996) and approved by the Animal Use Ethics Committee of the Evandro Chagas Institute (CEUA-IEC), under the number 38/2017. Furthermore, this study was conducted according to ARRIVE guidelines (du Sert et al., 2020).

2.6 Parasites

The parasite used was *Leishmania* (L.) *amazonensis*, isolated from a human case from Ulianópolis, PA, brazil (MHOM/BR/2009/M26361) obtained from Instituto Evandro Chagas, Ananindeua-PA, Brazil. *L. amazonensis* promastigotes were obtained after primary isolation on the slopes of NNN (Novy-MacNeil-Nicolle) blood. The strains were then grown and adapted to Roswell Park Memorial Institute 1640 medium (RPMI-1640). The parasites were cultured at 26°C in RPMI 1640 medium supplemented with 10% heat-inactivated fetal bovine serum (Gibco®, Grand Island, NY, United States), penicillin (100 U/mL) and streptomycin (100 μg/ML) (Mota et al., 2015; Brígido et al., 2020).

2.7 *In vivo* infection of the murine model

BALB/c mice were infected with *L. amazonensis* promastigotes gathered in stationary phase (1 × 10^6 cells in 50 μL PBS), intradermally injected in the right or left hind paw. The skin lesion measurement was performed from the 30th day after infection, and the size of the paw was evaluated weekly. For this purpose, a thickness gauge was used (Barão and Giorgio, 2003; Nakayama et al., 2005).

After infection, infected animals were randomly distributed into 7 groups (10 animals/group). Treatment started in the 8th week after infection and the arising of lesions. The extract and alkaloid fraction were administered in two water-diluted doses (200 mg/kg and 400 mg/kg), administered orally through an orogastric tube, once a day for 28 days. The negative control group was treated orally with water (sample vehicle; 1 mL/100 g). The positive control was treated with intraperitoneal injections of meglumine antimoniate (Glucantime®; 30 mg/kg/day) once a day for 28 days. The last group (control group) consisted of uninfected animals treated

with vehicle (water 1 mL/100 g). Lesion sizes were measured twice a week using a caliper.

2.8 Parasite load quantification

It is noteworthy that *L.* (L.) *amazonensis* infection is not limited to the skin, the parasite tends to spread to lymph nodes and reach the spleen and liver (De Oliveira Cardoso et al., 2010). Therefore, we used the spleen, which was removed on the 14th or 28th days after the beginning of the treatment, for parasite quantification by limiting dilution and the animals were euthanized. The spleens were aseptically removed.

The organs were macerated and homogenized in RPMI 1860 medium with 10% fetal bovine serum (FBS). The cells were centrifuged at 1500 rpm, for 10 min, in a refrigerated centrifuge, and were plated at a concentration of 2×10^5 cells/well in 96-well flat-bottom plates containing a final volume of 200 µL. Five serial dilutions (1:10) of the material were carried out. After 7 days incubated at 26°C, the plates were examined under an inverted microscope (Lima et al., 1997). The parasite load was quantified by the MTT method (3-(4,5-Dimethylthiazol-2-yl) 2,5 diphenyltetrazolium bromide), in which an aliquot of 100 µL of suspension from each well was homogenized with 10 µL of MTT (5 mg µg/mL diluted in PBS (Mosmann, 1983; Lima et al., 1997). The reaction was read at 490 nm (µQuant/Biotek Instruments INC. Winooski, United States).

2.9 Quantification of cytokines

The concentrations of the cytokines IL-10 and IFN-γ were evaluated in the animals' plasma according to the study period. Cytokines were quantified using commercial kits by the ELISA method (Enzyme-Linked Immunosorbent Assay) and used according to the procedures previously described by the manufacturers.

Cytokine quantification was detected by colorimetry in a microplate reader at a wavelength of 492 nm, and the concentration for each sample was calculated from the corresponding standard curve in pg/mg of protein.

2.10 Histopathology

The skin of the animals' paws was fixed in 10% buffered formalin and processed for inclusion in paraffin. Tissue sections (5 µm thick) were stained with Gomori's trichrome (Almeida-Souza et al., 2016). The analysis was conducted on samples from all animals in each group to ensure comprehensive evaluation.

For the selection of the lesion area for analysis, a standardized approach was employed. The area of interest was specifically chosen based on the most prominent lesions, ensuring consistency across samples. Criteria for selection included lesion size, visibility of tissue changes, and proximity to unaffected skin, allowing for a comparative assessment of pathological changes.

Slides were evaluated by an independent certified histopathologist, and the results were confirmed by a second

independent certified histopathologist. It is important to note that no statistical analysis was performed for this study, as the focus was primarily on qualitative histopathological evaluation.

2.11 Molecular docking

The molecular structures of yohimbine, corinanteol and dihydrocorinanteol were designed with the software GaussView 5.5 e optimized with Gaussian 09 (Frisch et al., 2024), using the Density Functional Theory (DFT) and B3LYP/6-31G* (Becke, 1993).

The molecular docking method was used to predict the binding mode of the molecules to the active site of Trypanothione reductase from *Leishmania infantum*. The docking was performed with the software Molegro Virtual Docker (MVD) 5.5 (Thomsen and Christensen, 2006), and the target crystal structure of Trypanothione reductase can be found in the Protein Data Bank with the following ID: 2JK6 (Baiocco et al., 2009).

The MolDock Score (GRID) scoring function was used with a grid resolution of 0.30 Å and radius of 10 Å, encompassing the entire connection cavity with its center at x, 17.85; y, 8.13; and z, −3.25. The MolDock SE algorithm was used with 50 runs, 3000 maximum interactions, and a maximum population size equal to 200. The maximum evaluation of 500 steps with a distance factor equal to 1 and an energy threshold of 100 was used in our protocol.

2.12 Molecular dynamics simulations

The molecular atomic charges were obtained with the Restrained Electrostatic Potential (RESP) protocol using the Hartree-Fock method with the 6-31G * base set (Cornell et al., 1993). The parameters for each molecule were constructed using the General Amber Force Field (GAFF) (Wang et al., 2004). Amber 16 package were used for the MD simulations (Case et al., 2005). The ff14SB force field (Maier et al., 2015) was used for all MD simulations. The absent hydrogens in the protein crystal were added by the tLEaP module during the process of building the complexes. The systems were solvated in an octahedron periodic box containing explicit water molecules described by the TIP3P model (Jorgensen et al., 1983). The distance chosen for the shear radius was 12 Å for all directions of the solvent from the solute.

The Particle Mesh Ewald method was used for the calculation of electrostatic interactions (Darden et al., 1993), and bonds involving hydrogen atoms were restricted with the SHAKE algorithm (Ryckaert et al., 1977). The simulation of MD was divided into stages of energy minimization, heating, equilibrium, and production. The sander module was used for both steps of energy minimization, where the steepest descent method and conjugate gradient algorithm were employed to perform 1500 cycles divided among the steps. In the first step, the solute was restricted with a constant harmonic force of 100 kcal/mol·Å-2, while the water and anti-ion molecules were free. In the second stage, the complexes were totally free to move.

Then, the systems were gradually heated for 600 ps until the temperature reached 300 K. The heating was divided into five stages, where the collision frequency was 3.0 ps^{-1} and the Langevin

thermostat was used for temperature control (Lzaguirre et al., 2001). The heavy atoms were restricted with a constant harmonic force of 50 kcal/mol·Å −2 during the initial four steps. In the last heating step, the constant harmonic force was removed. These simulations were performed at constant volume (NVT). In the equilibrium stage, the systems were submitted to a simulation of 5 nanoseconds (ns) with a temperature of 300 K and constant pressure. During the production stage, 100 ns of MD simulations were generated.

2.13 Free energy calculations using the MM/GBSA approach

The free energy of each complex was obtained from the last 5 ns of the trajectory corresponding to 500 snapshots. In the MM-GBSA approach, binding free energy is calculated from the free energy of a linker interacting with a receptor to form the complex (Sun et al., 2014). Equation 1 is related to this phenomenon:

$$\Delta G = \Delta G - \Delta G - \Delta G \qquad (1)$$

In each state, the free energy is calculated through the following expression, as shown in Equation 2:

$$\Delta G = \Delta G + \Delta G - T\Delta S \qquad (2)$$

ΔEMM is the energy of the total molecular mechanics in the gas phase, ΔGsolv is the free energy of solvation, and TΔS is the entropy of the system.

EMM represents the sum of the internal energy contributions (ΔEinternal, sum of the binding energies, angles and dihedrals), eletrostatic interactions (ΔEelectrostatic), and contributions of van der Waals (ΔEvdw), according to Equation 3:

$$\Delta E = \Delta E + \Delta E + \Delta E \qquad (3)$$

The free energy of solvation (ΔGsolv), as shown in Equation 4, is composed by polar (ΔGGB) and non-polar (ΔGSASA) contributions. Polar contributions are approximated by the Generalized Born (GB) method, and the non-polar contributions are determined from the calculation of the solvent-accessible surface area (SASA):

$$\Delta G = \Delta G + \Delta G \qquad (4)$$

2.14 Statistical analysis

Statistical analysis was carried out using the Graph pad Prisma 5 program. For each parameter analyzed, an analysis of possible discrepant points (outliers) was carried out, using the interquartile range in its calculation, with discrepant points not being considered in the statistical calculations. For each parameter analyzed, the homoscedasticity of the dispersion was assessed, applying the Analysis of Variance (ANOVA) test for homoscedastic dispersion and the Mann-Whitney test when homoscedasticity was not met. After the existence of significant differences, they were compared between the groups, using Tukey's *post hoc* test. In all tests, a significance level of 5% ($p \leq 0.05$) was considered.

3 Results

3.1 Composition of *A. nitidum* extract and fraction

Scanning using the Mass Spectrometer of the ethanolic extract indicated the presence of two main constituents with m/z of 297.20 [M + H]+ and 355.20 [M + H]+. Based on these data and checking the literature it can be proposed that these are the alkaloids corynantheol (MM: 296.4 g/mol) and yohimbine (MM: 354.4 g/mol; Figure 1).

As for the alkaloid fraction, a major constituent was identified with m/z equal to 299.21 [M + H]+, and based on the literature, it can be proposed that it is the alkaloid dihydrocorynantheol (MM: 298.43 g/mol; Figure 2).

3.2 Treatment with *A. nitidum* extract decreased lesion size

With the Glucantime® treatment we observed a regression in the size of the paw lesion by 32.97% after 14 days (11 weeks) of treatment when compared to the control group. After 28 days (12 weeks) of treatment the decrease in lesion size became more pronounced, with 55.08% of regression (Figures 3, 4).

In the evaluation of ulcer healing in infected animals treated with EE, we observed the response was dose dependent. On the 28th day of treatment (12 weeks) there was a regression of 37.42% at the dose of 400 mg/kg. When mice received the dose of 200 mg/kg/day, a deceleration of lesion growth was observed (Figures 3, 4).

Unlike expected, FA did not reduce the size of the lesion induced by *L. amazonensis* when compared to the group of uninfected animals (Control group), however, there was a slowdown in ulcer growth (Figures 3, 4).

3.3 Treatment with the extract and alkaloids fraction from *A. nitidum* reduced the parasite load and presented an immunomodulating action

For the EE, at a dose of 200 mg/kg/day, we observed a significant reduction ($p < 0.0001$) in parasitemia only after the 28th day of treatment (23.64%), when compared to the control group. At the dose of 400 mg/kg, we observed a significant reduction ($p < 0.0001$) of 11.4% in parasitemia on the 14th day of treatment and 42.56% on the 28th day. The reductions in parasitemia caused by EE were lower ($p < 0.0001$) than the reduction caused by Glucantime® (Figure 5).

In animals treated with FA, we observed reductions only at the 28th day of treatment. When the infected animals were treated with 200 mg/kg/28 days, the parasitemia reduced by 7.69%. At the highest dose (400 mg/kg/28 days) a greater reduction was observed: 22.1% (Figure 5).

In the serum of infected and untreated animals (negative control) there was an increase in IL-10 levels, and on the 28th day we observed a more significant increase in the level of this cytokine. On the other hand, the parasite decreases IFN-y level according to the days of treatment. On the 28th day, IL-10 showed
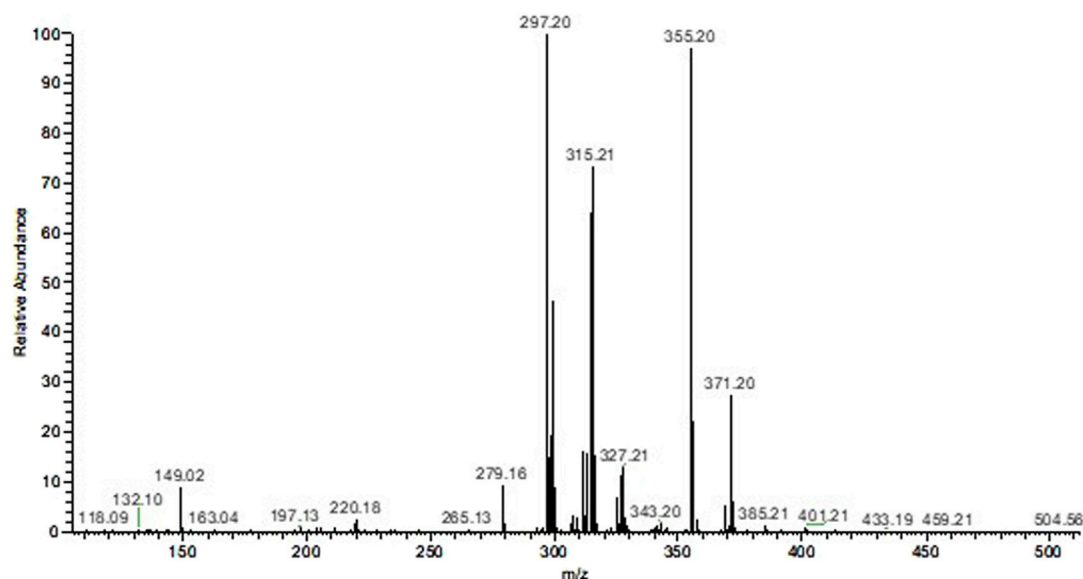
FIGURE 1
Mass spectrum of the ethanolic extract of *Aspidosperma nitidum*.
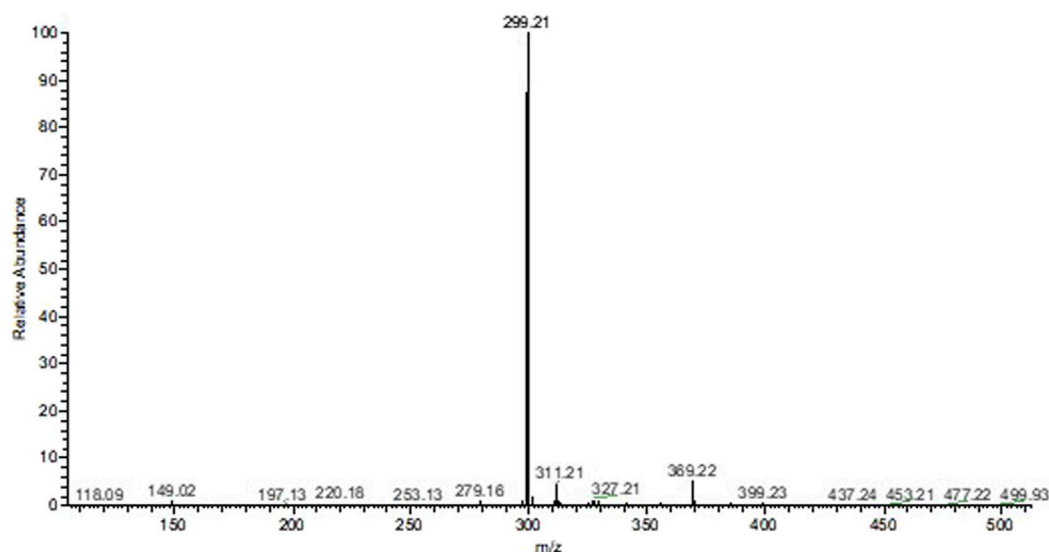
FIGURE 2
Mass spectrum of the alkaloid fraction of *Aspidosperma nitidum*.

the lowest level in the infected and treated groups (Glucantime®, EE, and FA), and treatment with EE at a dose of 400 mg/kg, after Glucantime®, presented the smallest decrease in the expression of this cytokine. Finally, treatment with Glucantime®, EE, or FA increased the production of IFN-γ after 28 days, and EE and FA at the dose of 400 mg/kg showed greater expression of the cytokine compared to Glucantime® (Figure 6).

The skin lesion site stained with Gomori's Trichomium showed a reduction in the normal structure of the dermis and a degradation of connective tissue in the foot pads of infected animals without any treatment when compared to the group of uninfected animals. In

addition, it was observed a reduction in the parasite load at the sites of injury in animals treated with Glucantime®, EE or FA, and an increase in collagen fibers when compared to the group of infected and untreated animals (Figure 7).

3.4 Molecular docking

To validate the docking methodology, we performed a redocking of the crystallographic ligand into the binding pocket of the Trypanothione reductase protein from the parasite *Leishmania*
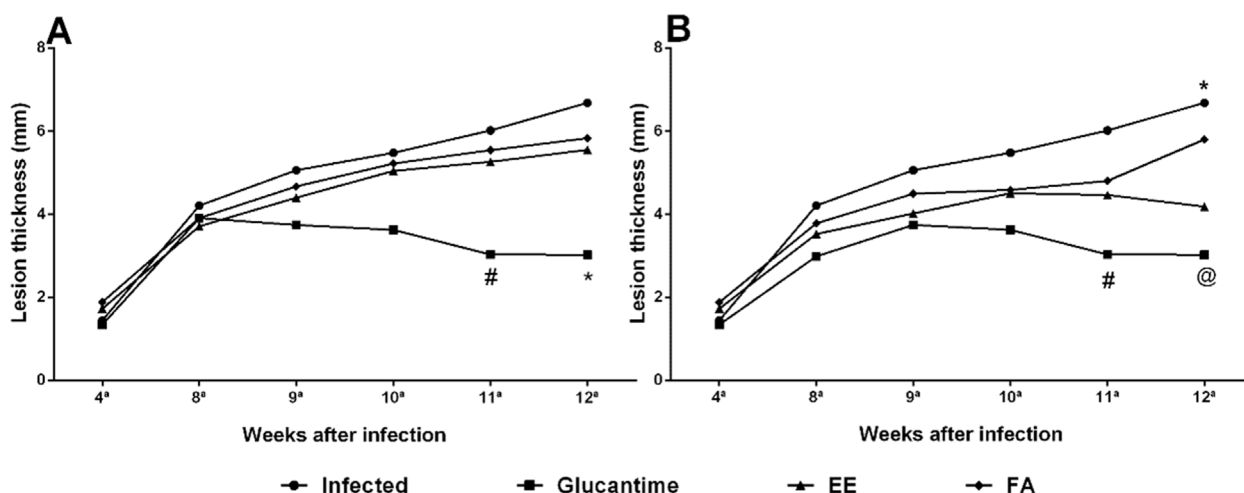
FIGURE 3
Evaluation of the cutaneous lesion in mice infected with *Leishmania amazonensis* treated with ethanolic extract (EE) and alkaloids fraction (FA) from *Aspidosperma nitidum*. Legend: **(A)** treatment with EE or FA 200 mg/kg; #p = 0.0213 versus Infected; *p = 0.0049 versus Infected and *p = 0.0313 versus FA; **(B)** treatment with EE or FA 400 mg/kg; #p = 0.0116 versus Infected and p = 0.0359 versus FA; *p = 0.0023 versus Glucantime and p = 0.0366 *versus* EE; @p = 0.0178 versus FA; EE: ethanolic extract; FA: alkaloids fraction; Glucantime®: 30 mg/kg/day intraperitoneally.

amazonensis. The fitness evaluation of the redocking was conducted using RMSD values and docking scores. The RMSD value between the crystallographic ligand and the redocked ligand was 1.3 Å. Docking experiments using known complexes with inhibitors that exhibit similar conformational complexity are typically performed to validate the docking protocol, following the recommendations of the Olson group. This process is crucial to ensure that the specified docking parameters in the input file are suitable and effective in accurately replicating the structure and interactions of a known complex (Forli et al., 2016; Silva et al., 2023).

The optimal conformation for the interaction of the compounds yohimbine, corinanteol, and dihydrocorinanteol was evaluated based on the Moldock score results. The most favorable conformation for each compound yielded Moldock scores of −65.37, −76.69, and −74.08, respectively (Table 1). The conformations obtained from molecular docking studies demonstrate that these molecules were able to interact with the catalytic residues of the molecular target, such as Cys52, Cys57, His461', and Glu466'. These residues are essential for the redox mechanism of the protein (Baiocco et al., 2009; Battista et al., 2020).

3.5 Molecular dynamics (MD) simulations

The complexes obtained from molecular docking were used as the initial coordinates for the molecular dynamics (MD) simulations. All complexes underwent energy minimization, heating, system equilibration, and production MD protocols, resulting in 100 ns trajectories.

The structural stability of the complexes was assessed using the RMSD values of the protein backbone and the ligands (Figure 8). The RMSD for yohimbine showed that the ligand experienced structural modifications between 0.5 and 1 Å, indicating minimal conformational changes throughout the simulation trajectory. The RMSD for corinanteol demonstrated structural shifts between 0.5 and 1 Å,

followed by an increase to 1–1.5 Å. However, in the last 30 ns, the ligand maintained a stable conformation with only minor structural modifications. The RMSD for dihydrocorinanteol remained around 0.5 Å throughout the trajectory, with no significant conformational changes. As illustrated in Figure 8, all ligands remained within the binding pocket of the molecular target during the entire 100 ns of MD simulations and continued to interact with the catalytic residues.

3.6 Affinity energy of complexes

We used the MM-GBSA approach to evaluate the interaction energy of the three complexes. MD simulations of 100 ns generate many conformational configurations, so we selected the simulation interval where the RMSD showed the most stability. Therefore, for these calculations, we used the last 10 ns of MD simulations for each complex.

The results are summarized in Table 2. According to the data, the interaction of yohimbine, corinanteol, and dihydrocorinanteol with the TR protein was favorable, with binding affinity energies of −21.72, −20.21, and −22.15 kcal/mol, respectively. The contributions from van der Waals interactions (ΔE_{vdW}), electrostatic energy (ΔE_{ele}), and nonpolar solvation energy (ΔG_{NP}) were favorable for the stability of the TR-ligand complexes. Among these contributions, van der Waals interactions were the most significant contributors to complex formation, with values of −26.85, −18.45, and −27.90 kcal/mol for yohimbine, corinanteol, and dihydrocorinanteol, respectively. Nonpolar contributions (ΔG_{NP}) were also favorable, though their impact was minimal.

4 Discussion

Phytochemical studies carried out on different parts of *A. nitidum* revealed the presence of several alkaloids. Among them, 10-methoxy-dihydro-corynantheol, corynantheol (Arndt et al.,
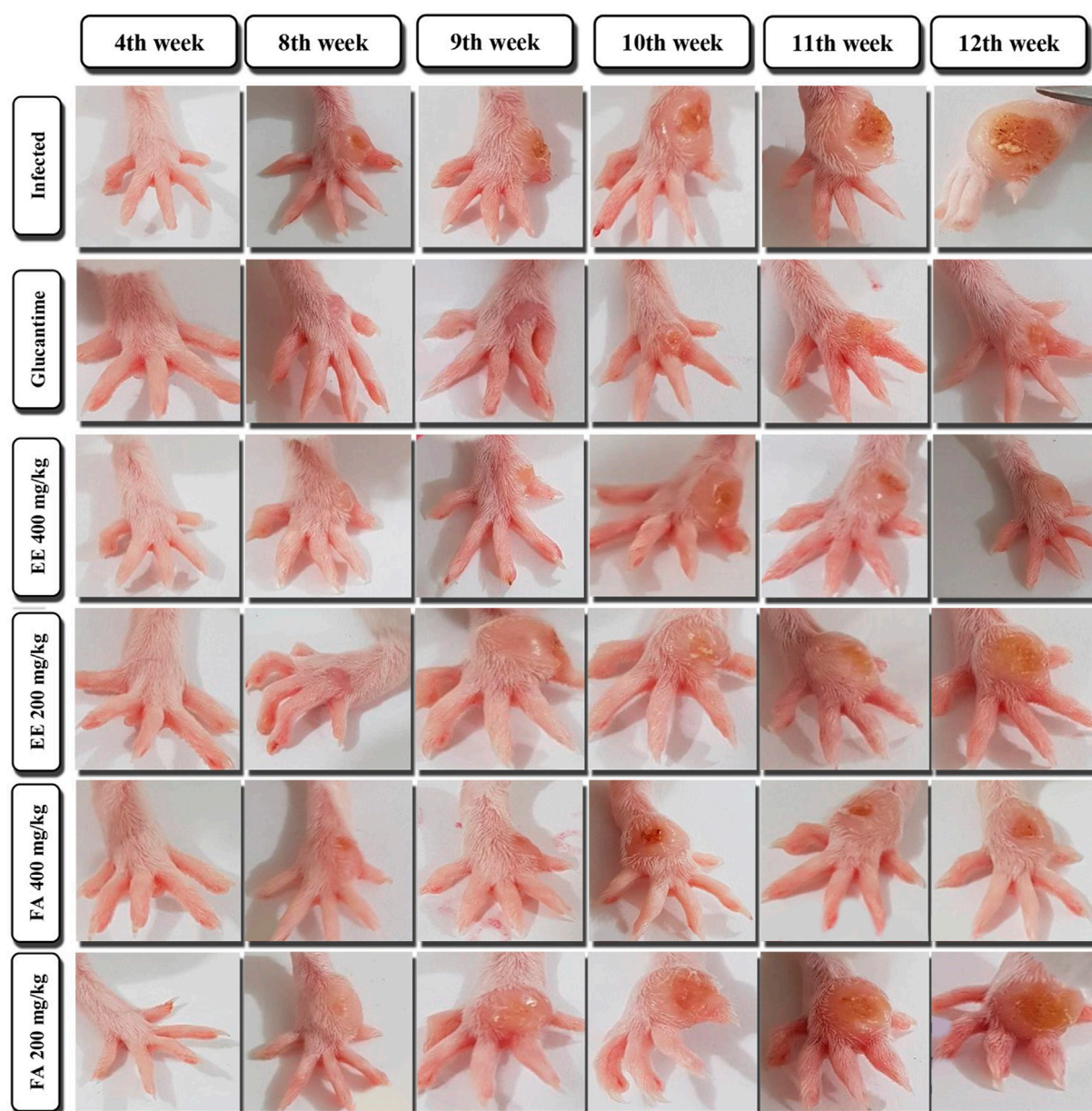
FIGURE 4
Evaluation of the cutaneous lesion of the paw in mice infected with *Leishmania amazonensis* treated with ethanolic extract (EE) and fraction of alkaloids (FA) obtained from *Aspidosperma nitidum*.

1967), aspidospermine, quebrachamine, yohimbine (Marques et al., 1996), harman carboxylic acid, 3-carboxylic ethylharman (Pereira et al., 2007), dihydrocorynantheol, dehydrositsiriquine and braznitidumine (Brandão et al., 2010). In a previous study carried out by our research group, both EE and FA obtained from *A. nitidum* were subjected to analysis by high-performance liquid chromatography (HPLC) (Brígido et al., 2021). In the EE chromatogram, indole alkaloids and β-carboline were identified, corroborating previous findings (Arndt et al., 1967; Bolzani et al., 1987). Indole alkaloids, with varying structure, are frequently isolated, many of which have a simple β-carboline skeleton (Wenkert, 1962; Allen and Holmstedt, 1980). On the other hand, in the FA chromatogram, only peaks suggestive of indole alkaloids

with an aspidospermine nucleus were observed (Pereira et al., 2007). It is worth mentioning that aspidospermine has been associated with antiplasmodial, antileishmanial and antitrypanosomal activities (Coatti et al., 2016).

Analysis of the mass spectrum of EE indicated the presence of the alkaloids corynantheol and yohimbine, while in FA the alkaloid dihydrocorynantheol was identified. Such compounds, such as yohimbine, corynantheol and dihydrocorynantheol, have already been identified in previous studies with *A. nitidum* (Arndt et al., 1967; De Oliveira Cardoso et al., 2010; do Socorro Silva da Veiga et al., 2022).

Indole alkaloids are recognized for their antileishmanial activity. Previous studies demonstrated that alkaloid fractions rich in this
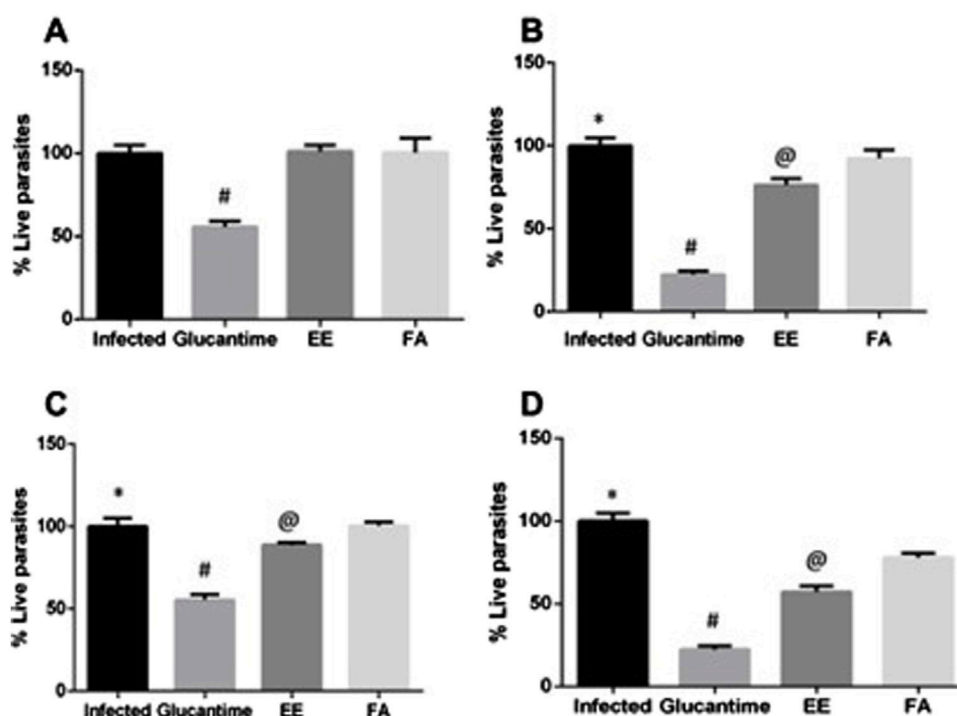
FIGURE 5
Parasite load in the spleen of mice infected with *Leishmania amazonensis* and treated with ethanolic extract (EE) or alkaloids fraction (FA) from *Aspidosperma nitidum*. Legend: **(A)** treatment with EE or FA 200 mg/kg for 14 days; #$p < 0.0001$ versus Infected, EE and FA; **(B)** treatment with EE or FA 200 mg/kg for 28 days; *$p < 0.0001$ versus Glucantime, EE and $p = 0.005$ versus FA; #$p < 0.0001$ versus EE and FA; @ $p < 0.0001$ versus FA. **(C)** treatment with 400 mg/kg for 14 days; *$p < 0.0001$ versus Glucantime and EE; #$p < 0.0001$ *versus* EE and FA; @ $p < 0.0001$ versus FA. **(D)** treatment with 400 mg/kg for 28 days *$p < 0.0001$ versus Glucantime, EE and FA; #$p < 0.0001$ versus EE and FA; @ $p < 0.0001$ versus FA. EE: ethanolic extract; FA: alkaloids fraction; Glucantime®: 30 mg/kg/day intraperitoneally.

class did not present acute toxicity at a dose of 2,000 mg/kg, nor subacute toxicity at a dose of 200 mg/kg for 28 days (Brígido et al., 2021). Furthermore, some of these compounds, such as dihydrocorynantheol, have been shown to cause changes in the flagellar pouch and cytoskeleton of *Leishmania*, leading to the death of the parasite and a consequent reduction in parasitemia (Veiga et al., 2021).

After the infection of Balb/c mice with *L. amazonensis*, the different experimental groups received the treatments from the 8th week, because the appearance of a small skin lesion in all groups inoculated with the parasites was only visible after this timeframe. Initially, the lesion was characterized by edema and a small erythema, with slow, but progressive growth. In fact, when treatment started, all lesions were about 2 mm thick.

The Glucantime® treatment significantly reduced lesion growth from the second week of treatment onwards, with lesion regression becoming more pronounced in the fourth week. In the treatment of human beings with american tegumentary leishmaniasis, the effect of this drug is also time dependent, requiring prolonged treatment (Moreira et al., 2017), which contributes to the emergence of adverse reactions and toxic events (Oliveira et al., 2011).

When seeking therapeutic alternatives for the treatment of leishmaniasis, it is expected to obtain drugs that promote ulcer healing faster than current use antimonials with less toxic potential. This therapeutic alternative also should be orally administered to enable high administration and to reduce the final treatment cost.

The ulcer healing and reduction of the parasite load of animals treated with EE from *A. nitidum* was dose and time dependent with better effect on the 28th. On the other hand, FA did not reduce the size of the lesion induced by *L. amazonensis*, however, there was a slowdown in ulcer growth, but there was a slight reduction in the parasite load on the 28th day.

When analyzing the chemical compositions of *A. nitidum*, previous phytochemical studies using HPLC-DAD indicated the likely presence of β-carboline and indole alkaloids in the extract, while an alkaloid fraction would be composed mainly of indole alkaloids (Brígido et al., 2021). In the present study, we identified the alkaloids corynatheol and yohimbine in the EE, while in the FA we found the alkaloid dihydrocorynatheol. Therefore, the antileishmanial activity of *A. nitidum* seems to be more related to these alkaloids (Brígido et al., 2020). An issue that needs to be better understood is the role of the immune response in this process, as a previous study demonstrated the *in vitro* antileishmanial activity of the β-carboline alkaloid flavopereirine with the results of molecular docking showed flavopereirin was able to inhibit oligopeptidase B (da Silva e Silva et al., 2019).

IFN-γ plays a crucial role in the control of *Leishmania* infection, the cytokine induces parasite clearance by activating the phagocyte oxidase (phox) and iNOS enzyme complex, which is the most effective mechanism to kill intracellular parasites mediated by macrophages (Murray and Nathan, 1999; Salaiza-Suazo et al., 1999; Murray et al., 2006). In the present study, an association of
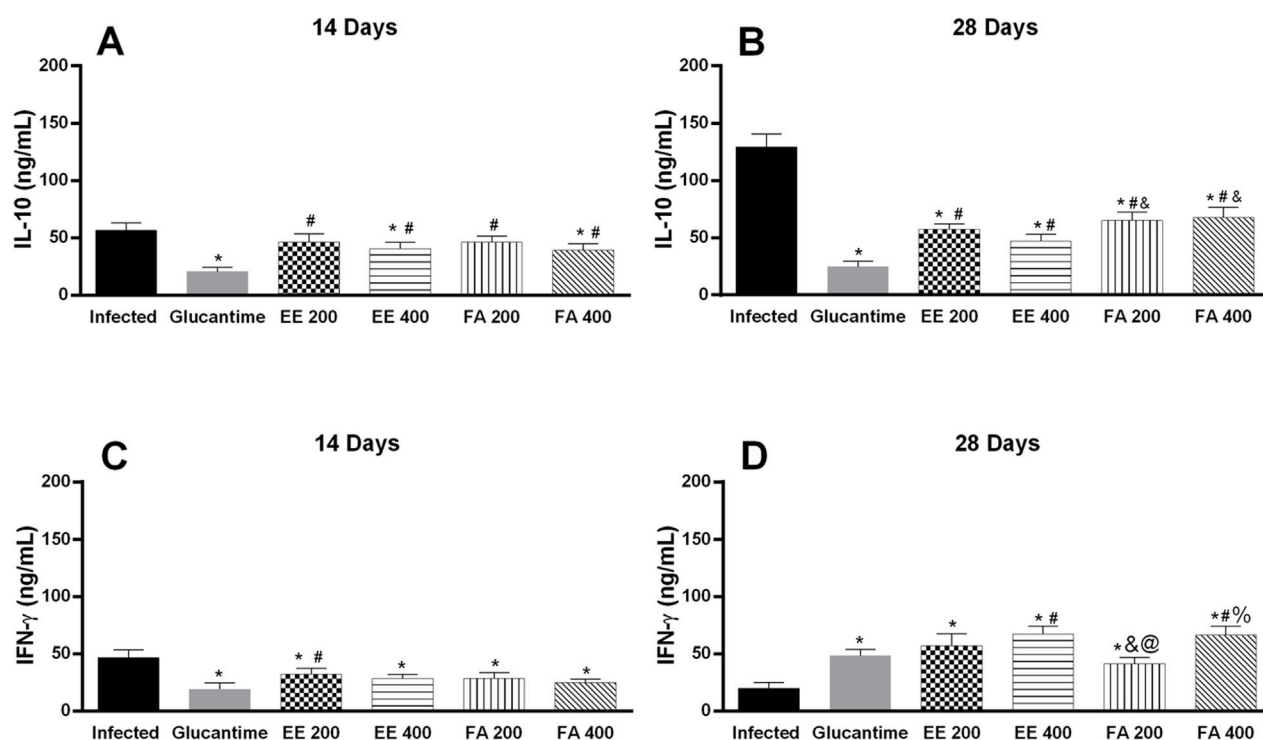
FIGURE 6
Quantification of cytokines in the serum of BALB/c mice infected with *Leishmania* (L.) *amazonensis* and treated with extract and alkaloids fraction from *Aspidosperma nitidum*. Legend: **(A)** IL-10 level in response to 14 days of treatment with 200 mg/kg; *$p < 0.001$ versus Infected; #$p < 00,003$ versus Glucantime. **(B)** IL-10 level in response to 28 days of treatment with 400 mg/kg; *$p < 00,001$ versus Infected; #$p < 0.001$ versus Glucantime; and $p < 0,01$ versus EE 400 mg/kg. **(C)** IFN-γ level in response to 14 days of treatment with 200 mg/kg; *$p < 0.001$ versus Infected; #$p = 0.004$ versus Glucantime. **(D)** IFN-γ level in response to 28 days of treatment with 400 mg/kg; *$p < 0.001$ versus Infected; #$p < 0.004$ versus Glucantime; and $p < 0,02$ versus EE 200 mg/kg; @ $p = 00,001$ versus EE 400 mg/kg; % $p = 00,002$ versus FA 200 mg/kg. EE: ethanolic extract; FA: alkaloids fraction. Glucantime®: 30 mg/kg/day intraperitoneally administered.

high levels of IFN-γ and increased parasite load after 28 days was observed with Glucantime®, as well as with EE or FA, especially at the highest dose tested, providing a possible mechanism for parasite death *in vivo*. However, we confirmed that other cytokines may be involved in this process, highlighting the need for more comprehensive investigations of the cytokine profile during infection and treatment.

The susceptibility phenotype of *L. amazonensis* infection is clearly associated with elevated IL-4 levels and the Th2 response (Kopf et al., 1996). IL-4 reduces iNOS expression and increases disease progression due to increased survival and parasite growth in infected cells (Hurdayal et al., 2013). Furthermore, high levels of IL-10 also participate in this process, as the cytokine causes inhibition of macrophage activation and contributes to the growth of parasites in lesions (Kane and Mosser, 2001).

Our results demonstrated that decreased IL-10 expression in groups treated with Glucantime®, EE or FA were associated with decreased parasite load, while high levels of IL-10 expression were associated with increased parasite load in mice with simulated treatment, confirming the role of IL-10 in maintaining the infection and the immunomodulatory activity of EE and FA.

Cytokines measured in serum revealed an IL-10 increase and a decrease in IFN-γ in untreated *L. amazonensis* infected animals, which were not observed after 28 days of treatment with EE, FA or Glucantime®. Decreased IL-10 and increased IFN-γ levels contributed to maintain a Th1 response in the treated groups. Furthermore, the increase in IFN-γ after 28 days of treatment with Glucantime® and with the extracts contribute to the effectiveness of macrophages by inducing iNOS in the skin and decreasing the parasite load. In fact, both extract and FA treatment decreased IL-10 and increased IFN-γ levels.

Together, these results support the immunomodulatory effects of *A. nitidum*. Studies demonstrate that immunochemotherapy is more effective than chemotherapy or immunotherapy alone (Joshi et al., 2014), and our results show that treatment with *A. nitidum* is an immunochemotherapy.

When the reduction of IL-10 is observed in the groups treated with *A. nitidum* and Glucantime®, there is a difference in the percentage of reduction. However, positive control needs to be parenterally injected, while EE can be orally administered, and this is very important in long-term treatment.

Furthermore, while our histopathological analysis of the skin suggested that both EE and FA helped control inflammatory infiltrates and initiate the remodeling process, it is important to consider that the lack of direct measurement of cytokines and inflammatory cells in the tissue of a mice future investigation including such direct analyzes would be crucial to a more complete understanding of the affected mechanisms involved in *Leishmania* infection and response to EE and FA treatment (Murray et al., 2006).
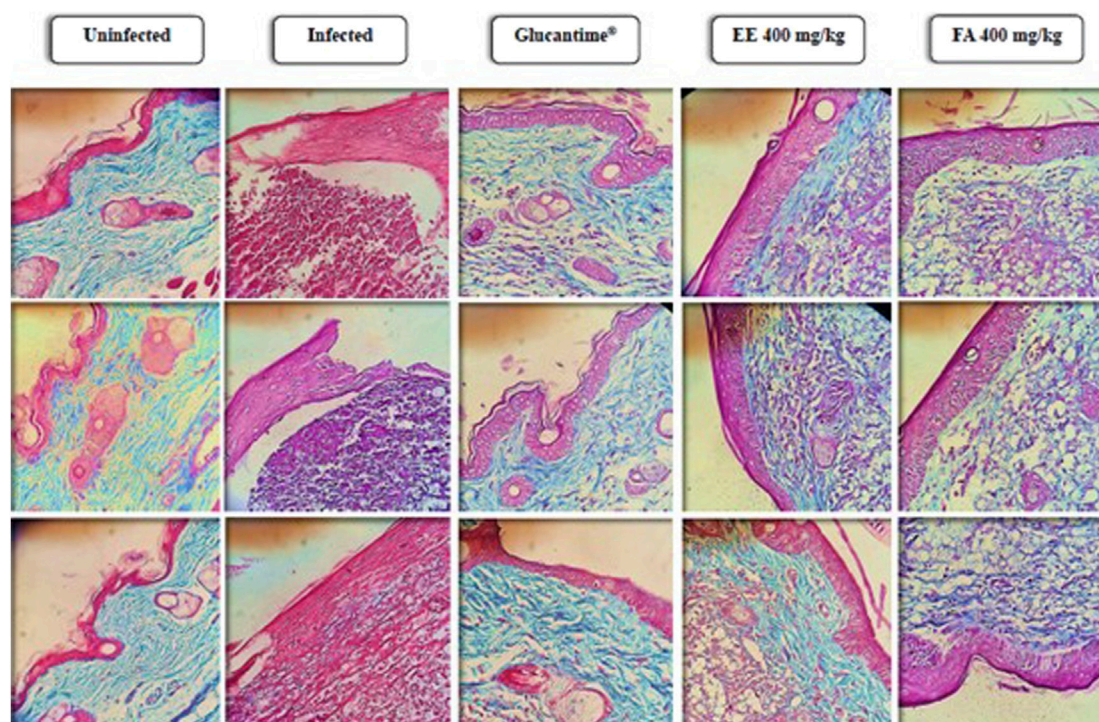
FIGURE 7
Histopathological analysis of the extracellular matrix of footpads from Balb/c mice infected with *Leishmania amazonensis* and treated for 28 days with ethanolic extract or alkaloid fraction obtained from *Aspidosperma nitidum* and matched controls. Legend: EE: ethanolic extract; FA: alkaloids fraction; Glucantime®: 30 mg/kg/day intraperitoneally administered.

TABLE 1 Moldock scores obtained from the docking protocol using MVD 5.5.

Molecule	Moldock score
Yohimbine	−65.37
Corinanteol	−76.69
Dihydrocorinanteol	−74.08

The tissue repair process is critically important for the rapid cure of cutaneous leishmaniasis (Sakthianandeswaren et al., 2005). Thus, the control of inflammatory process and tissue remodeling mediated by EE or FA should be associated with a reduction in IL-10 and an increase in IFN-γ (Corware et al., 2011) and TGF-β (Castellucci et al., 2012). In uninfected wounds, high levels of IL-10 decrease inflammation, normal collagen deposition, and restore the normal dermal architecture (Peranteau et al., 2008), while TGF-β and IFN-γ induce recruitment of immune cells and promotes matrix protein synthesis, while decreases matrix protein degradation, leading to fibrotic tissue formation (Goldberg et al., 2007).

To validate our docking methodology, we conducted a redocking of the crystallographic ligand into the binding pocket of the Trypanothione reductase (TR) protein from *Leishmania amazonensis*, achieving an RMSD value of 1.3 Å. This validation confirms that our docking protocol accurately replicates known interactions (Forli et al., 2016; Silva et al., 2023). The binding affinities of yohimbine, corinanteol, and dihydrocorinanteol were favorable, with Moldock scores of −65.37, −76.69, and −74.08, respectively. The interaction of these compounds with critical catalytic residues—Cys52, Cys57, His461', and Glu466'—highlights their potential as effective TR inhibitors, as these residues are essential for the protein's redox mechanism (Baiocco et al., 2009).

Furthermore, the molecular dynamics (MD) simulations demonstrated the structural stability of the TR-ligand complexes over a 100 ns trajectory, with minimal conformational changes observed in the ligands. The binding affinities were confirmed through the MM-GBSA method, showing interaction energies of −21.72, −20.21, and −22.15 kcal/mol. Given the importance of TR in *Leishmania* metabolism, our findings underscore its potential as a drug target for antileishmania therapies. Previous studies have indicated that targeting TR can lead to effective therapeutic interventions against leishmaniasis (Battista et al., 2020; Santiago-Silva et al., 2023). By integrating our *in silico* results with existing literature, we emphasize the therapeutic relevance of TR inhibitors in combating leishmaniasis and encourage further investigation into these promising compounds.

The mechanism of action of alkaloids on parasites seems to involve binding with the DNA topoisomerase complex (Brandão et al., 2010; Brígido et al., 2020) and inhibition of oligopeptidase B (Cahlíková et al., 2013; 2015), a cytosolic protein belonging to the prolyl oligopeptidase family of serine proteases, responsible for the regulation of the levels of enolase on the cell surface of *Leishmania* parasites, which contributes to parasite virulence (Barrett and Rawlings, 1995; Rawlings and Barrett, 1999). However, the
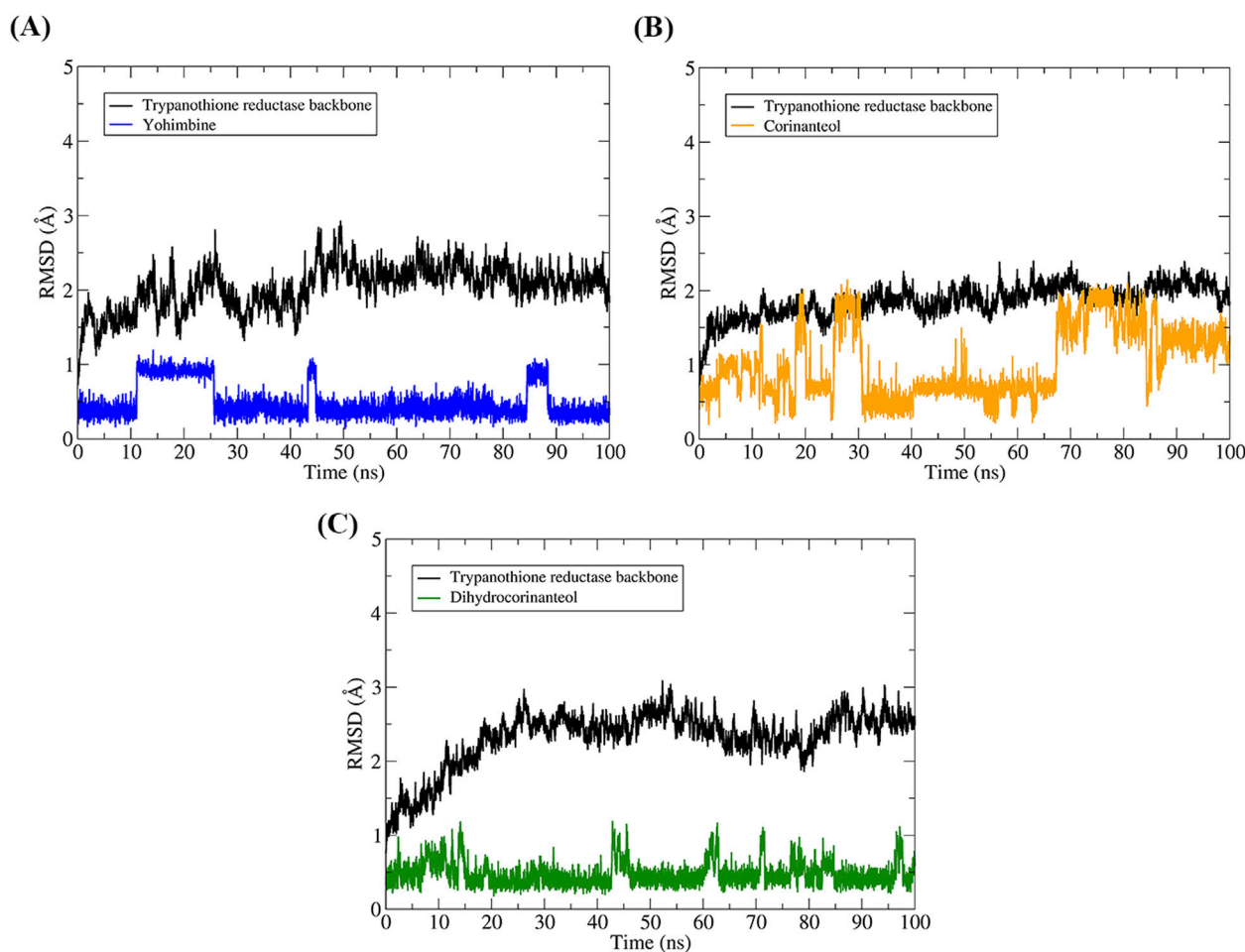
FIGURE 8
Analysis of the conformational stability of the systems over 100 ns of MD simulation. The protein backbone is represented in black in all graphs, while the colors representing the binders vary. The RMSD graphs were plotted in relation to the systems obtained after the steps of minimization, heating, and equilibrium. TR-yohimbine in blue **(A)**, TR-corinanteol in yellow **(B)**, TR-dihydrocorinanteol in green **(C)**.

TABLE 2 Affinity energy values (values in kcal/mol). ΔE_{vdW}, contributions by van der Waals interactions; ΔE_{ele}, electrostatic energy; ΔG_{GB}, polar solvation energy; ΔG_{NP}, nonpolar solvation energy; ΔG_{bind}, binding affinity.

Molecules	ΔEvdW	ΔEele	ΔGGB	ΔGNP	ΔGbinding
Yohimbine	−26.85	−4.42	13.14	−3.59	−21.72
Corinanteol	−18.45	−9.87	10.32	−2.21	−20.21
Dihydrocorinanteol	−27.90	−12.57	21.71	−3.38	−22.15

immunomodulator mechanism seems to involve the elevation of IFN-γ and IL-10, described for the first time in the present study.

Our study suggests that *A. nitidum* may have potential in reducing parasite load and lesion size in BALB/c mice infected with *L. amazonensis*. However, the effectiveness of the treatment has not yet been fully proven by the results presented. Furthermore, we observed immunomodulatory effects on cytokine expressions, which suggests a possible mechanism of action. These results highlight the importance of further investigations to fully understand the therapeutic potential of *A. nitidum* in cutaneous leishmaniasis.

Data availability statement

The raw data supporting the conclusions of this article will be made available by the authors, without undue reservation.

Ethics statement

The animal study was approved by the Comissão deÉtica no uso de Animais do Instituto Evandro Chagas. The study was conducted

in accordance with the local legislation and institutional requirements.

Author contributions

HB: Conceptualization, Data curation, Investigation, Methodology, Project administration, Software, Visualization, Writing–original draft, Writing–review and editing. EV: Investigation, Methodology, Writing–original draft. AQ: Investigation, Methodology, Writing–original draft, Writing–review and editing. JN: Investigation, Methodology, Software, Writing–original draft, Writing–review and editing. JC-B: Investigation, Writing–original draft. JS: Investigation, Methodology, Writing–review and editing. CC: Investigation, Methodology, Writing–original draft. AM: Methodology, Writing–original draft, Writing–review and editing. LA: Investigation, Methodology, Writing–original draft. MC-F: Methodology, Writing–original draft. SP: Data curation, Formal Analysis, Funding acquisition, Methodology, Resources, Writing–original draft, Writing–review and editing. MD: Conceptualization, Data curation, Formal Analysis, Funding acquisition, Methodology, Project administration, Resources, Supervision, Visualization, Writing–original draft, Writing–review and editing.

Funding

Conflict of interest

The authors declare that the research was conducted in the absence of any commercial or financial relationships that could be construed as a potential conflict of interest.

Publisher's note

All claims expressed in this article are solely those of the authors and do not necessarily represent those of their affiliated organizations, or those of the publisher, the editors and the reviewers. Any product that may be evaluated in this article, or claim that may be made by its manufacturer, is not guaranteed or endorsed by the publisher.

References

Allen, J. R. F., and Holmstedt, B. R. (1980). The simple β-carboline alkaloids. *Phytochemistry* 19, 1573–1582. doi:10.1016/S0031-9422(00)83773-5

Almeida-Souza, F., Cardoso, F. de O., Souza, B. V. da C., do Valle, T. Z., de Sá, J. C., Oliveira, I., et al. (2016). Morinda citrifolia Linn. Reduces parasite load and modulates cytokines and extracellular matrix proteins in C57bl/6 mice infected with leishmania (leishmania) amazonensis. *PLoS Negl. Trop. Dis.* 10, e0004900. doi:10.1371/journal. pntd.0004900

Arndt, R. R., Brown, S. H., Ling, N. C., Roller, P., Djerassi, C., Ferreira, J. M., et al. (1967). Alkaloid studies—LVIII. *Phytochemistry* 6, 1653–1658. doi:10.1016/S0031-9422(00)82898-8

Baiocco, P., Colotti, G., Franceschini, S., and Ilari, A. (2009). Molecular basis of antimony treatment in Leishmaniasis. *J. Med. Chem.* 52, 2603–2612. doi:10.1021/jm900185q

Barão, S. C., and Giorgio, S. (2003). Efficacy of 8-bromoguanosine against murine cutaneous leishmaniasis induced with Leishmania amazonensis. *Chemotherapy* 49, 159–162. doi:10.1159/000071138

Barrett, A. J., and Rawlings, N. D. (1995). Families and clans of serine peptidases. *Arch. Biochem. Biophys.* 318, 247–250. doi:10.1006/abbi.1995.1227

Battista, T., Colotti, G., Ilari, A., and Fiorillo, A. (2020). Targeting trypanothione reductase, a key enzyme in the redox trypanosomatid metabolism, to develop new drugs against leishmaniasis and trypanosomiases. *Molecules* 25 (8), 1924. doi:10.3390/molecules25081924

Becke, A. D. (1993). Density-functional thermochemistry. III. The role of exact exchange. *J. Chem. Phys.* 98, 5648–5652. doi:10.1063/1.464913

Bolzani, V. D. S., Serur, L. M., Francisco, F. J., and Golieb, O. R. (1987). Indole alkaloid evolution in Aspidosperma. *Biochem. Syst. Ecol.* 15, 187–200. doi:10.1016/0305-1978(87)90019-6

Botanic Gardens Conservation International (BGCI) and IUCN SSC Global Tree Specialist Group (2019). *"Aspidosperma excelsum" in The IUCN Red List of Threatened Species 2019: e.T145684962A145684964*. doi:10.2305/IUCN.UK.2019-2. RLTS.T145684962A145684964.en

Bourdy, G., Oporto, P., Gimenez, A., and Deharo, E. (2004). A search for natural bioactive compounds in Bolivia through a multidisciplinary approach: Part VI. Evaluation of the antimalarial activity of plants used by Isoceño-Guaraní Indians. *J. Ethnopharmacol.* 93, 269–277. doi:10.1016/j.jep.2004.03.045

Brandão, H. N., David, J. P., Couto, R. D., Nascimento, J. A. P., and David, J. M. (2010). Química e farmacologia de quimioterápicos antineoplásicos derivados de plantas. *Quim. Nova* 33, 1359–1369. doi:10.1590/s0100-40422010000600026

Brígido, H. P. C., Correa-Barbosa, J., da Silva-Silva, J. V., Costa, E. V. S., Percário, S., and Dolabela, M. F. (2020). Antileishmanial activity of annona species (annonaceae). *SN Appl. Sci.* 2, 1524. doi:10.1007/s42452-020-03340-7

Brígido, H. P. C., Varela, E. L. P., Gomes, A. R. Q., Bastos, M. L. C., de Oliveira Feitosa, A., do Rosário Marinho, A. M., et al. (2021). Evaluation of acute and subacute toxicity of ethanolic extract and fraction of alkaloids from bark of Aspidosperma nitidum in mice. *Sci. Rep.* 11, 18283. doi:10.1038/s41598-021-97637-1

Cahlíková, L., Hulová, L., Hrabinová, M., Chlebek, J., Hošťálková, A., Adamcová, M., et al. (2015). Isoquinoline alkaloids as prolyl oligopeptidase inhibitors. *Fitoterapia* 103, 192–196. doi:10.1016/j.fitote.2015.04.004

Cahlíková, L., Kulhánková, A., Benešová, N., Chlebek, J., Macáková, K., Opletal, L., et al. (2013). Alkaloids from cheiranthus fragrans and their acetylcholinesterase, butyrylcholinesterase and prolyl oligopeptidase activities. *Nat. Prod. Commun.* 8, 1541–1544. doi:10.1177/1934578x1300801110

Case, D. A., Cheatham, T. E., Darden, T., Gohlke, H., Luo, R., Merz, K. M., et al. (2005). The Amber biomolecular simulation programs. *J. Comput. Chem.* 26, 1668–1688. doi:10.1002/jcc.20290

Castellucci, L., Jamieson, S. E., Almeida, L., Oliveira, J., Guimarães, L. H., Lessa, M., et al. (2012). Wound healing genes and susceptibility to cutaneous leishmaniasis in Brazil. *Infect. Genet. Evol.* 12, 1102–1110. doi:10.1016/j.meegid.2012.03.017

Coatti, G. C., Marcarini, J. C., Sartori, D., Fidelis, Q. C., Ferreira, D. T., and Mantovani, M. S. (2016). Cytotoxicity, genotoxicity and mechanism of action (via gene expression analysis) of the indole alkaloid aspidospermine (antiparasitic) extracted from Aspidosperma polyneuron in HepG2 cells. *Cytotechnology* 68, 1161–1170. doi:10. 1007/s10616-015-9874-9

Cornell, W. D., Cieplak, P., Bayly, C. I., and Kollman, P. A. (1993). Application of RESP charges to calculate conformational energies, hydrogen bond energies, and free energies of solvation. *J. Am. Chem. Soc.* 115, 9620–9631. doi:10.1021/ja00074a030

Corware, K., Harris, D., Teo, I., Rogers, M., Naresh, K., Müller, I., et al. (2011). Accelerated healing of cutaneous leishmaniasis in non-healing BALB/c mice using

water soluble amphotericin B-polymethacrylic acid. *Biomaterials* 32, 8029–8039. doi:10. 1016/j.biomaterials.2011.07.021

Darden, T., York, D., and Pedersen, L. (1993). Particle mesh Ewald: an *N*·log(*N*) method for Ewald sums in large systems. *J. Chem. Phys.* 98, 10089–10092. doi:10.1063/1.464397

da Silva e Silva, J. V., Cordovil Brigido, H. P., Oliveira de Albuquerque, K. C., Carvalho, J. M., Reis, J. F., Faria, L. V., et al. (2019). Flavopereirine—an alkaloid derived from geissospermum vellosii—presents leishmanicidal activity *in vitro*. *Molecules* 24, 785. doi:10.3390/molecules24040785

De Oliveira Cardoso, F., Da Silva Freitas De Souza, C., Mendes, V. G., Abreu-Silva, A. L., Da Costa, S. C. G., and Da Silva Calabresa, K. (2010). Immunopathological studies of leishmania amazonensis infection in resistant and in susceptible mice. *J. Infect. Dis.* 201, 1933–1940. doi:10.1086/652870

do Socorro Silva da Veiga, A., Silveira, F. T., da Silva, E. O., Júnior, J. A. P. D., Araújo, S. C., Campos, M. B., et al. (2022). Activity of alkaloids from Aspidosperma nitidum against leishmania (leishmania) amazonensis. *Sci. Rep.* 12, 8662. doi:10.1038/s41598-022-12396-x

du Sert, N. P., Hurst, V., Ahluwalia, A., Alam, S., Avey, M. T., Baker, M., et al. (2020). The arrive guidelines 2.0: updated guidelines for reporting animal research. *PLoS Biol.* 18, e3000410. doi:10.1371/journal.pbio.3000410

Forli, S., Huey, R., Pique, M. E., Sanner, M. F., Goodsell, D. S., and Olson, A. J. (2016). Computational protein–ligand docking and virtual drug screening with the AutoDock suite. *Nat. Protoc.* 11, 905–919. doi:10.1038/nprot.2016.051

Frisch, M. J., Trucks, G. W., Schlegel, H. B., Scuseria, G. E., Robb, M. A., Cheeseman, J. R., et al. (2024). Gaussian~09 {R}evision {E}.01.

Ghorbani, M., and Farhoudi, R. (2018). Leishmaniasis in humans: drug or vaccine therapy? *Drug Des. devel. Ther.* 12, 25–40. doi:10.2147/DDDT.S146521

Goldberg, M. T., Han, Y. P., Yan, C., Shaw, M. C., and Garner, W. L. (2007). TNF-α suppresses α-smooth muscle actin expression in human dermal fibroblasts: an implication for abnormal wound healing. *J. Investig. Dermatol.* 127, 2645–2655. doi:10.1038/sj.jid.5700890

Goto, H., and Lauletta Lindoso, J. A. (2012). Cutaneous and mucocutaneous leishmaniasis. *Infect. Dis. Clin. North Am.* 26, 293–307. doi:10.1016/j.idc.2012.03.001

Hurdayal, R., Nieuwenhuizen, N. E., Revaz-Breton, M., Smith, L., Hoving, J. C., Parihar, S. P., et al. (2013). Deletion of IL-4 receptor alpha on dendritic cells renders BALB/c mice hypersusceptible to leishmania major infection. *PLoS Pathog.* 9, e1003699. doi:10.1371/journal.ppat.1003699

Jorgensen, W. L., Chandrasekhar, J., Madura, J. D., Impey, R. W., and Klein, M. L. (1983). Comparison of simple potential functions for simulating liquid water. *J. Chem. Phys.* 79, 926–935. doi:10.1063/1.445869

Joshi, J., Malla, N., and Kaur, S. (2014). A comparative evaluation of efficacy of chemotherapy, immunotherapy and immunochemotherapy in visceral leishmaniasis-an experimental study. *Parasitol. Int.* 63, 612–620. doi:10.1016/j.parint.2014.04.002

Kane, M. M., and Mosser, D. M. (2001). The role of IL-10 in promoting disease progression in leishmaniasis. *J. Immunol.* 166, 1141–1147. doi:10.4049/jimmunol.166.2.1141

Kopf, M., Brombacher, F., Köhler, G., Kienzle, G., Widmann, K. H., Lefrang, K., et al. (1996). IL-4-deficient Balb/c mice resist infection with Leishmania major. *J. Exp. Med.* 184, 1127–1136. doi:10.1084/jem.184.3.1127

Lima, H. C., Bleyenberg, J. A., and Titus, R. G. (1997). A simple method for quantifying Leishmania in tissues of infected animals. *Parasitol. Today* 13, 80–82. doi:10.1016/S0169-4758(96)40010-2

Lzaguirre, J. A., Catarello, D. P., Wozniak, J. M., and Skeel, R. D. (2001). Langevin stabilization of molecular dynamics. *J. Chem. Phys.* 114, 2090–2098. doi:10.1063/1.1332996

Maier, J. A., Martinez, C., Kasavajhala, K., Wickstrom, L., Hauser, K. E., and Simmerling, C. (2015). ff14SB: improving the accuracy of protein side chain and backbone parameters from ff99SB. *J. Chem. Theory Comput.* 11, 3696–3713. doi:10.1021/acs.jctc.5b00255

Marques, M. F. S., Kato, L., Leitáo Filho, H. F., and De Reis, F. A. M. (1996). Indole alkaloids from Aspidosperma ramiflorum. *Phytochemistry* 41, 963–967. doi:10.1016/0031-9422(95)00660-5

Moreira, V. R., De Jesus, L. C. L., Soares, R. E. P., Silva, L. D. M., Pinto, B. A. S., Melo, M. N., et al. (2017). Meglumine antimoniate (glucantime) causes oxidative stress-derived DNA damage in Balb/c mice infected by leishmania (leishmania) infantum Antimicrob. *Agents Chemother.* 61 (6), 10–1128. doi:10.1128/AAC.02360-16

Mosmann, T. (1983). Rapid colorimetric assay for cellular growth and survival: application to proliferation and cytotoxicity assays. *J. Immunol. Methods* 65, 55–63. doi:10.1016/0022-1759(83)90303-4

Mota, E. F., Rosario, D. M., Veiga, A. S. S., Do Socorro Barros Brasil, D., Silveira, F. T., and Dolabela, M. F. (2015). Biological activities of Croton palanostigma Klotzsch. *Pharmacogn. Mag.* 11, 601–606. doi:10.4103/0973-1296.160449

Murray, H. W., and Nathan, F. (1999). Macrophage microbicidal mechanisms *in vivo*: reactive nitrogen versus oxygen intermediates in the killing of intracellular visceral Leishmania donovani. *J. Exp. Med.* 189, 741–746. doi:10.1084/jem.189. 4.741

Murray, H. W., Xiang, Z., and Ma, X. (2006). Short report: responses to Leishmania donovani in mice deficient in both phagocyte oxidase and inducible nitric oxide synthase. *Am. J. Trop. Med. Hyg.* 74, 1013–1015. doi:10.4269/ajtmh. 2006.74.1013

Nakayama, H., Loiseau, P. M., Bories, C., Torres De Ortiz, S., Schinini, A., Serna, E., et al. (2005). Efficacy of orally administered 2-substituted quinolines in experimental murine cutaneous and visceral leishmaniases. *Antimicrob. Agents Chemother.* 49, 4950–4956. doi:10.1128/AAC.49.12.4950-4956.2005

NRC National Research Council (1996). Guide for the care and use of laboratory animals. National Academy Press. Available at: https://scholar.google.com/scholar_lookup?title= Guide.for.the.Care.and.Use.of.Laboratory.Animals&publication_year=1996&.

Oliveira, L. F., Schubach, A. O., Martins, M. M., Passos, S. L., Oliveira, R. V., Marzochi, M. C., et al. (2011). Systematic review of the adverse effects of cutaneous leishmaniasis treatment in the New World. *Acta Trop.* 118, 87–96. doi:10.1016/j.actatropica.2011.02.007

Peranteau, W. H., Zhang, L., Muvarak, N., Badillo, A. T., Radu, A., Zoltick, P. W., et al. (2008). IL-10 overexpression decreases inflammatory mediators and promotes regenerative healing in an adult model of scar formation. *J. Investig. Dermatol.* 128, 1852–1860. doi:10.1038/sj.jid.5701232

Pereira, M. D. M., Jácome, R. L. R. P., Alcântara, A. F. D. C., Alves, R. B., and Raslan, D. S. (2007). Alcalóides indólicos isolados de espécies do gênero Aspidosperma (Apocynaceae). *Quim. Nova* 30, 970–983. doi:10.1590/S0100-40422007000400037

Rawlings, N. D., and Barrett, A. J. (1999). MEROPS: the peptidase database. *Nucleic Acids Res.* 27, 325–331. doi:10.1093/nar/27.1.325

Ryckaert, J. P., Ciccotti, G., and Berendsen, H. J. C. (1977). Numerical integration of the cartesian equations of motion of a system with constraints: molecular dynamics of n-alkanes. *J. Comput. Phys.* 23, 327–341. doi:10.1016/0021-9991(77)90098-5

Sakthianandeswaren, A., Elso, C. M., Simpson, K., Curtis, J. M., Kumar, B., Speed, T. P., et al. (2005). The wound repair response controls outcome to cutaneous leishmaniasis. *Proc. Natl. Acad. Sci. U. S. A.* 102, 15551–15556. doi:10.1073/pnas.0505630102

Salaiza-Suazo, N., Volkow, P., Pérez Tamayo, R., Moll, H., Gillitzer, R., Pérez-Torres, A., et al. (1999). Treatment of two patients with diffuse cutaneous leishmaniasis caused by Leishmania mexicana modifies the immunohistological profile but not the disease outcome. *Trop. Med. Int. Heal.* 4, 801–811. doi:10.1046/j.1365-3156.1999.00491.x

Santiago-Silva, K. M., Camargo, P. G., and Bispo, M. L. (2023). Promising molecular targets related to polyamine biosynthesis in drug discovery against leishmaniasis. *Med. Chem.* 19 (1), 2–9. doi:10.2174/1573406418666220713145446

Silva, L. B., Ferreira, E. F. B., Maryam, Espejo-Román, J. M., Costa, G. V., Cruz, J. V., et al. (2023). Galantamine based novel acetylcholinesterase enzyme inhibitors: a molecular modeling design approach. *Molecules* 28, 1035. doi:10.3390/molecules28031035

Silveira, F. T., Lainson, R., and Corbett, C. E. P. (2004). Clinical and immunopathological spectrum of american cutaneous leishmaniasis with special reference to the disease in Amazonian Brazil - a review. *Mem. Inst. Oswaldo Cruz* 99, 239–251. doi:10.1590/S0074-02762004000300001

Sudarshan, K., and Aidhen, I. S. (2013). Synthesis of (+)-Centrolobine and its analogues by using acyl anion Chemistry. *Eur. J. Org. Chem.* 2013 (12), 2298–2302. doi:10.1002/ejoc.201300097

Sudarshan, K., Yarlagadda, S., and Sengupta, S. (2024). Recent advances in the synthesis of diarylheptanoids. *Chemistry–An Asian J.* 19 (15), e202400380. doi:10.1002/asia.202400380

Sun, H., Li, Y., Shen, M., Tian, S., Xu, L., Pan, P., et al. (2014). Assessing the performance of MM/PBSA and MM/GBSA methods. 5. Improved docking performance using high solute dielectric constant MM/GBSA and MM/PBSA rescoring. *Phys. Chem. Chem. Phys.* 16, 22035–22045. doi:10.1039/c4cp03179b

Thomsen, R., and Christensen, M. H. (2006). MolDock: a new technique for high-accuracy molecular docking. *J. Med. Chem.* 49, 3315–3321. doi:10.1021/jm051197e

Tiuman, T. S., Santos, A. O., Ueda-Nakamura, T., Filho, B. P. D., and Nakamura, C. V. (2011). Recent advances in leishmaniasis treatment. *Int. J. Infect. Dis.* 15, e525–e532. doi:10.1016/j.ijid.2011.03.021

Uliana, S. R. B., Trinconi, C. T., and Coelho, A. C. (2018). Chemotherapy of leishmaniasis: present challenges. *Parasitology* 145, 464–480. doi:10.1017/S0031182016002523

Veiga, A. do S. S. da, Silveira, F. T., Marinho, A. M. do R., Trindade, R. C., dos, S. da, Campos, M. B., et al. (2021). Atividade leishmanicida de Aspidosperma nitidum Benth. Ex Müll. *Arg. Res. Soc. Dev.* 10, e50210212646. doi:10.33448/rsd-v10i2.12646

Veiga, A. S. S. (2013). Antileishmania activity of amazon plants. Master's Dissertation. Belém, Brazil: University of Pará. Available online at: https://scholar.google.com/scholar?hl=pt-BR&as_sdt=0%2C5&q=Veiga%2C+ASS+%282013%29.+Atividade+Antileishmania+de+Plantas+da+Amaz%C3%B4nia+&btnG=.

Wang, J., Wolf, R. M., Caldwell, J. W., Kollman, P. A., and Case, D. A. (2004). Development and testing of a general Amber force field. *J. Comput. Chem.* 25, 1157–1174. doi:10.1002/jcc.20035

Wenkert, E. (1962). Biosynthesis of indole alkaloids. The Aspidosperma and iboga bases. *J. Am. Chem. Soc.* 84, 98–102. doi:10.1021/ja00860a023

World Health Organization (2023). Leishmaniasis. Available at: https://www.who.int/news-room/fact-sheets/detail/leishmaniasis.

Antioxidant potential, antimicrobial activity, polyphenol profile analysis, and cytotoxicity against breast cancer cell lines of hydro-ethanolic extracts of leaves of (*Ficus carica* L.) from Eastern Morocco

Aziz Tikent[1]*, Salah Laaraj[2,3], Toufik Bouddine[4], Mohamed Chebaibi[5,6], Mohamed Bouhrim[7], Kaoutar Elfazazi[2], Ali S. Alqahtani[8], Omar M. Noman[8], Lhoussain Hajji[4], Larbi Rhazi[9], Ahmed Elamrani[1] and Mohamed Addi[1]*

[1]Laboratoire d'Amélioration des Productions agricoles, Biotechnologie and Environnement (LAPABE), Faculté des Sciences, Université Mohammed Premier, Oujda, Morocco, [2]Regional Center of Agricultural Research of Tadla, National Institute of Agricultural Research (INRA), Rabat, Morocco, [3]Laboratory of Environmental, Ecological and Agro-Industrial Engineering (LGEEAI), Faculty of Science and Technology (FST), Beni Mellal, Morocco, [4]Bioactive and Environmental Health Laboratory, Moulay Ismail University of Meknes, Meknes, Morocco, [5]Ministry of Health and Social Protection, Higher Institute of Nursing Professions and Health Techniques, Fez, Morocco, [6]Biomedical and Translational Research Laboratory, Faculty of Medicine and Pharmacy of Fez, Sidi Mohamed Ben Abdellah University, Fez, Morocco, [7]Biological Engineering Laboratory, Faculty of Sciences and Techniques, Sultan Moulay Slimane University, Beni Mellal, Morocco, [8]Department of Pharmacognosy, College of Pharmacy, King Saud University, Riyadh, Saudi Arabia, [9]Institut Polytechnique UniLaSalle, Université d'Artois, Beauvais Cédex, France

Introduction: Many beneficial compounds found in fig leaves can be used in tea and medicine. These compounds aid with digestion, reduce inflammation, and treat diabetes and bronchitis. Chetoui, Malha, Ghoudane, and Onk Hmam fig leaf hydro-ethanol extracts from Eastern Morocco were analyzed for metabolites and biological activities.

Methods, results, and discussion: HPLC-UV examination revealed that the leaf extract included mainly caffeine, rutin, and ferrulic acid. Spectrophometric results show that Malha leaf is rich in polyphenols (62.6 $\pm$ 1.3 mg GAE/g) and flavonoids (26.2 $\pm$ 0.1 mg QE/g). Chetoui leaf contains the highest vitamin C content (8.2 $\pm$ 0.1 mg Asc A/100 g DW), while Onk Hmam leaf has the highest condensed tannin (4.9 $\pm$ 0.1 mg CatE/g). The investigations found that all leaf extracts were antioxidant-rich, with strong Pearson bivariate correlation between bioactive polyphenol levels and antioxidant tests for DPPH, β-carotene, ABTS, and TAC (values of −0.93, −0.94, −0.85, and 0.98, respectively). The coefficients for flavonoid content were −0.89, −0.89, −0.97, and 0.80, respectively. Disk diffusion and MIC results show that the hydro-ethanol fig leaf extracts eliminate fungi and bacteria. In addition, these fig leaf extracts showed promise cytotoxicity against the breast cancer cell lines MCF-7, MDA-MB-231, and MDA-MB-436 and an interesting selectivity index. In silico leaf bioactive component analysis revealed that myricitin inhibited NADPH oxidase the greatest

(gscore −6.59 Kcal/mol). Trans-ferulic acid inhibits Escherichia coli beta-ketoacyl-[acyl carrier protein] synthase (−6.55 kcal/mol), whereas quercetin inhibits *Staphylococcus aureus* nucleoside diphosphate kinase (−8.99). CYP51 from *Candida albicans* is best treated with kaempferol and myricitin. Both had a glide gscore of −7.84 kcal/mol. Rutin has the most potent Sespace 3 anticancer activity, with a glide gscore of −7.09 kcal/mol.

Conclusion: This research indicates that fig leaf extracts from the region can be used in medicine, food, natural cosmetics, and breast cancer prevention. To maximize the value of these leaves, their use must be carefully studied. Naturally, this fortunate tree's diversity must be preserved and enhanced.

1 Introduction

Oxidative stress occurs when a species' reactive and antioxidant defenses are not balanced. This condition is linked to numerous chronic diseases, including cancer, diabetes, neurodegenerative diseases, and cardiovascular diseases (McCord, 2000; Vladimir-Knežević et al., 2011). In addition to their physiological functions as typical secondary metabolites in plants, phenolic compounds possess advantageous health benefits as antioxidants (Çalişkan and Polat, 2011). Researchers have conducted thorough investigations on natural antioxidant molecules due to their potential in treating disorders associated with oxidative stress. Additionally, they are employed in the food industry due to their biological characteristics, particularly as antimicrobials (Taviano et al., 2013). Antioxidants can improve immune function and help prevent diseases such as cancer, cardiovascular disease, macular degeneration, cataracts, and asthma. They defend the body against the harmful effects of free radicals, which are produced as byproducts of regular metabolism (Sadia et al., 2014). The emergence of microbial resistance to existing antibiotics, along with the adverse effects caused by modern drugs and the scarcity of antibiotics in development, has underscored the importance of finding new antibacterial agents. Consequently, researchers have turned their attention to investigating the antimicrobial properties of medicinal plants (Mulat, Pandita and Khan, 2019; Reddy et al., 2022). One of the intriguing biological characteristics of polyphenols is their ability to prevent cancer. There is much epidemiological research indicating that consuming a diet abundant in fruits and vegetables may decrease the likelihood of developing specific types of malignancies. In part, the impact has been attributed to inherent polyphenols. Indeed, multiple laboratory experiments conducted both outside of and within a living organism have shown that natural compounds called polyphenols have the potential to be used in cancer prevention and treatment (Stagos et al., 2012; Zhou et al., 2016).

The fig tree, scientifically known as *Ficus carica* L., is a member of the Moraceae family (Nuri and Uddin, 2021). It is a fruit tree from classical antiquity that is associated with the origins of horticulture in the Mediterranean basin (Aradhya et al., 2010). In spite of the fact that it is a perennial plant, the fruit, leaf, and latex of the fig are the primary products that are developed and utilized in the market (Badgujar et al., 2014; Palmeira et al., 2019). The leaf has been utilized extensively for therapeutic purposes, and the decoction of the leaves is currently being taken as a beverage (Morovati et al.,

2022; Yang et al., 2023). Fig leaves, a by-product of fig fruit production, can serve as a vital source of bioactive chemicals for many industries. Potential uses include replacing synthetic chemicals with natural alternatives in the food sector, thus enhancing the physical and sensory properties of the foods in which they are incorporated (Chamorro et al., 2022). The fig leaf contains tocopherol and phenolic chemicals, which are powerful antioxidants (Konyalıoğlu et al., 2005). The fruits, roots, and leaves of the fig tree have been utilized in traditional medicine to address numerous illnesses such as diarrhea, indigestion, sore throats, coughs, bronchial problems, inflammatory and circulatory disorders, ulcerative illnesses, and malignancies (Gilani et al., 2008; Lee and Cha, 2010). The integration of chemical structures from various drugs into plant derivatives justifies the clear rebound in plant-based medicine utilization. Traditional medicine is the primary healthcare method used by 80% of the world's population. Most traditional medicines involve the use of plant extracts or their active components (Payyappallimana, 2010).

There are many bioactive compounds found in *F. carica*, such as phenolic compounds, phytosterols, organic acids, anthocyanin composition, triterpenoids, coumarins, and volatile compounds such as hydrocarbons, aliphatic alcohols, and a few other secondary metabolites that come from different parts of the plant (Kalefa and Al-Shawi, 2023; Tkachenko et al., 2017). The aqueous extract of *F. carica* leaves contained phenolic acids such as 3-O- and 5-O-caffeoylquinic acids, ferulic acid, quercetin-3-O-glucoside, quercetin-3-O-rutinoside, and organic acids (oxalic, citric, malic, quinic, shikimic, and fumaric acids) (Oliveira et al., 2009). Chunyan et al. (2008) (Chunyan et al., 2008) discovered that psoralen and bergapten are furocoumarins in F. *carica* leaves using countercurrent chromatography, 1H NMR proton magnetic and nuclear resonance, 13C NMR carbon, and mass spectrometry. Previous studies have identified other coumarins in F. *carica* leaves, such as bergapten, 4′, 5′dihydropsoralen (marmesin), and umbelliferone (Innocenti, Bettero and Caporale, 1982). Vaya and Mahmood (Vaya and Mahmood, 2006) used high-performance liquid chromatography and mass spectrometry to study *F. carica* leaves and found that the main flavonoids that were present were quercetin and luteolin. Both of these flavonoids are important in the body because they fight free radicals, prevent inflammation, keep the immune system in check, and help prevent cancer (Lansky et al., 2005; Zand et al., 2000). Teixeira et al. (2006) identified many phenolic compounds in F. *carica* leaves, including chlorogenic

acid and rutin. Rutin, also called rutoside, is a diglucoside of quercetin, a potent antioxidant. It is also the most widely studied flavonol in terms of pharmacology (Teixeira et al., 2006). Isocoumarins, isomers of flavonoid phenolic compounds, are recognized for their antioxidant, antimicrobial, and anticancer properties. For instance, 3-aryl isocoumarins are isomers of myricitin, kaempferol, and quercetin (Sudarshan et al., 2015). The same applies to the 3-glycosyl isocoumarins, which are isomers of rutin and naringin (Sudarshan and Aidhen, 2017). The number and content of bioactive chemicals vary by genotype, latitude, geographical region, and leaf collection period (Oliveira et al., 2010). It has been generally established that aqueous or acetone is suitable for extracting greater molecular weight flavanols, whereas methanol is more successful for extracting lower molecular weight polyphenols. Ethanol is selected due to its reputation as a safe substance for human consumption and its efficacy as a solvent for extracting polyphenols (Do et al., 2014).

In Morocco's Eastern region, the fig tree is a prominent fruit tree. This is exemplified by the annual Aghbal Fig Festival in Ahfir, the region's primary fig producer, which honors the fig fruit. This event recognizes the economic and socio-cultural importance of figs and their products. While fig fruits are well-known for their nutritional benefits and flavor, fig leaves are less so. As a result, it is critical to initially clarify the bioactive compound composition of hydro-ethanol fig leaf extracts. The purpose of this study is to demonstrate that fig leaves have the potential to be a valuable source of particular chemicals for application in food and phytopharmaceuticals. We want to increase the use and value of these leaves, while also boosting their reputation. To achieve the above, work was done to study the amounts of total polyphenols, flavonoids, condensed tannins, and vitamin C using spectroscopic methods. The extracts were also analyzed using high-performance liquid chromatography (HPLC) to determine the quality profile of the phenolic compounds that contribute to their bioactive activities. To test antioxidant capability, we used total antioxidant capacity, beta-carotene bleaching assay, DPPH scavenging, and ABTS scavenging. Furthermore, linear correlations are established to demonstrate the involvement of bioactive chemicals in antioxidant activity. Finally, we evaluate the extracts' antimicrobial activity against five specific strains and their cytotoxicity against three breast cancer cell lines. The *in silico* method was employed to validate and corroborate the involvement of the biologically active compound in the examined biological activities. By looking at specific examples, the study aims to explain how certain bioactive compounds in the fig leaf extract show anticancer, antimicrobial, and antioxidant properties.

2 Materials and methods

2.1 Materials sampling

In June 2023, the leaves of four different varieties of fig trees (*F. carica* L.) were gathered in three distinct locations in Ahfir province, Eastern Morocco. Three of the examined varieties are uniferous: Chetoui (CH), Malha (MA), and Onk Hmam (OH). Meanwhile, Ghoudane (GD) is biferous. The voucher specimen of the plant is deposited at the plant section of Herbarium University

Mohammed Premier Oujda Morocco (HUMPO 100). Leaf samples were collected at random, and an attempt was made to remove the influence of exposure by collecting the same number of leaves from all cardinal points: north, south, east, and west, as well as within the tree. For each variety, samples of 150 disease-free leaves (ten per tree and five trees per variety in each location) were picked, selected, and harvested. To safeguard the heat- and light-sensitive molecules, the leaves were dried for 20 days in an airy, dark, and room-temperature environment. To increase the contact surface between the sample and the extraction solvent, the dried leaves were ground into a fine, uniform powder that was then stored away from humidity.

2.2 Extraction process

A solid-liquid extraction technique was employed to extract antioxidant components from powdered fig leaves. A solvent containing 90% ethanol (v/v). The sample was extracted in the solvent using a fixed solid/liquid ratio of 1:10 (weight in grams/volume in milliliters). Subsequently, the concoction was agitated at a temperature of 50°C for duration of 90 min using a shaking water bath. For 20 min, the sample was centrifuged at 10,000 revolutions per minute at a temperature of 4°C. After centrifugation, it was filtered using a 0.45 μm polytetrafluoroethylene (PTFE) membrane filter. The aliquot extract was diluted to a final amount of 15 mL. The liquid extracts of fig leaves were promptly examined to determine the levels of the bioactive compounds being researched, as well as their antioxidant capabilities (Nakilcioğlu-Taş and Ötleş, 2021).

2.3 Bioactive compounds measurements

The Folin-Ciocalteu (FC) method was used to determine the total polyphenol content (TPC) (Tikent et al., 2023). 100 μL extract mixed with 500 μL FC reagent and 400 μL of 7.5% (w/v) Na_2CO_3. The mixture is stirred and incubated in the dark at room temperature for 10 minutes, and then the absorbance is measured at 760 nm. The results are reported in mg gallic acid equivalent (GAE) per gram of dry plant, with the gallic acid calibration curve as a reference. We used the $AlCl_3$ method (Dehpour et al., 2009), to find out the total flavonoid content (TFC). To do the test, we mixed 500 μL of each extract with 1,500 μL of 95% methanol, 100 μL of 10% (m/v) $AlCl_3$, 100 μL of 1 M sodium acetate, and 2.8 mL of distilled water. For 30 min, the mixture is mixed and incubated in the dark at room temperature. The blank is formed by replacing the extract with 95% methanol, and the absorbance at 415 nm is measured. With reference to the quercetin calibration curve, the results are presented in quercetin equivalent (QE) mg/g dry plant. The vanillin method was employed to determine the condensed tannin content (CTC) in an acidic medium (Mohti et al., 2020). The vanillin reagent was prepared by mixing equal volumes of: 8% (v/v) HCl, 37% (v/v) methanol, and 4% vanillin in methanol (m/v). Prior to the assay, the mixture was stored at 30°C. 200 μL of each extract to be analyzed was added to 1,000 μL of vanillin reagent; the mixture was shaken and then incubated in the dark for 20 min. Absorbance was measured at 500 nm against a blank consisting of a mixture of methanol (37%) and HCl (8%). The

results are expressed as mg catechol equivalent (Cat E)/g dry plant matter using the catechol calibration curve. The 2,6-dichlorophenolindophenol (DCPIP) spectrophotometric method (Hadini et al., 2022) was used to determine the vitamin C content. We add 1 g of dried leaf powder to 10 mL of oxalic acid (1%) and stir for 15 min. Then, we mix 3 mL of the filtrate with 1 mL of DCPIP (5 mM) and measure the absorbance at 515 nm after 15 s. The concentration of ascorbic acid (Asc A) is measured in milligrams (mg) per 100 g of dry matter.

2.4 Antioxidant activity assessment

The antioxidant activity of the hydro-ethanolic extracts of the examined fig leaves at a concentration of 0.1 g/mL was determined using four separate tests. All experiments were performed in triplicate.

2.4.1 2,2-diphenyl-1-picrylhydrazil (DPPH) free radical scavenging assay

The hydro-ethanol leaf extracts' free radical scavenging ability was measured using the procedures given in references (Tikent et al., 2023; Zrouri et al., 2021). DPPH solution was prepared by solubilizing 2 mg of DPPH in 100 mL of methanol. Different concentrations ranging from 5 to 500 μg/mL were prepared. Afterwards, each concentration was added to 2.5 mL of the prepared DPPH methanol solution to the final volume of 3 mL. After 30 min of incubation at room temperature, the absorbance was measured at 515 nm against a blank. The DPPH free radical scavenging activity was estimated in percentage (%) using the following formula:

$$\text{Radical scavenging activity (\%)} = \left[\left(\left([A]_{\text{blank}} - [A]_{\text{sample}} \right) \middle/ [A]_{\text{blank}} \right) \right] \times 100$$

A_{blank} is the absorbance of the control reaction and A_{sample} is the absorbance of the extract at different concentrations. IC_{50} values were determined graphically from the curve of antioxidant concentration (mg/mL) versus % inhibition, generated by GraphPad Prism 8. Ascorbic acid was employed as a positive control.

2.4.2 β-carotene bleaching assay

The antioxidant activity was performed using bleaching of a β-Carotene assay using the procedures given in the references (Elbouzidi et al., 2023; Rădulescu et al., 2021). First, 2 mg of β-carotene was dissolved in 10 mL of chloroform, and then mixed with 20 mg of linoleic acid and 200 mg of Tween-80. A vigorous stir was used to add 100 mL of distilled water to the flask after rotavapor at 40°C removed the chloroform mixture. A 96-well plate with triplicate samples was then incubated at 25°C for 30 min in the dark. Then, absorbance was measured spectrophotometrically at 470 nm immediately after hydro-ethanol fig leaf solution addition (t_0) and 2 h later (t_1) against a white reading containing all solution components but no-carotene. Butylated hydroxyanisole (BHA) was used as a standard reference.

$$\text{Residual color (\%)} = \left[\left(\left(OD\, t_0 - OD\, t_1 \right) \middle/ \left(OD t_0 \right) \right) \right] \times 100$$

where ODt_0 and ODt_1 are the absorbance at time zero (t_0) of Sample or Standard and ODt_1 after 2 h (t_1) respectively.

2.4.3 ABTS scavenging activity assay

The scavenging capacity to the 2,2-Azino-bis-(3-ethylbenzothiazoline-6-sulfonic acid) (ABTS) radical of the hydro-ethanol fig Leaf extracts were investigated, as described by Nakyai et al. (2021) (Nakyai et al., 2021),with certain modifications. In order to generate ABTS•+, the ABTS solution was mixed with 2.45 mM potassium persulfate and left to incubate at room temperature for a period of 16–18 h in the absence of light. The solution was subsequently mixed with ethanol until it reached an absorbance of 0.70 ± 0.02 at a wavelength of 750 nm. A concentrated solution of extract was prepared in ethanol. L-ascorbic acid was used as a positive control. The ABTS assay was conducted by mixing 200 μL of diluted ABTS•+ solution with 20 μL of the test material. The reaction mixture was kept in the absence of light at ambient temperature for duration of 10 min, after which it was quantified using a microplate reader at a wavelength of 734 nm. A percentage of ABTS radical cation decolorizing activity was determined, similar to the DPPH assay.

2.4.4 Total antioxidant capacity

The total antioxidant capacity was assessed using the phosphor-molybdenum method, as outlined in references (Chaudhary et al., 2015; Ouahabi et al., 2023; Taibi et al., 2023). The standard/extract solution, measuring 0.1 mL, was mixed with a reagent solution containing 0.6 M sulfuric acid, 28 mM sodium phosphate, and 4 mM ammonium molybdate. The mixture was then incubated at a temperature of 95°C for duration of 90 min. The solution was allowed to cool to the temperature of the surrounding environment, and the level of light absorption at a wavelength of 695 nm was determined. With the exception of the test sample, the blank solution included all of the reagents. A standard curve was generated utilizing ascorbic acid. The results were expressed in terms of ascorbic acid equivalents (Prieto et al., 1999).

2.5 HPLC-UV analysis

The phenolic composition of fig leaf extracts (0.1 g/mL) was analyzed chromatographically using an EC NUCLEOSIL column (5 μm, C18, 100–5,250 mm × 4.6 mm; Macherey-Nagel, Germany) in accordance with the procedures outlined in the protocol described by Kachmar et al. (2019), with minor adjustments. Water-phosphoric acid (0.01%) (A) and acetonitrile (B) comprised the mobile phase. A gradient was employed to obtain the following concentrations: 5% B after 3 min, 25% B after 13 min, 30% B at 25 min, 35% B at 35 min, 45% B at 39 min, 30% B at 25 min, 45% at 42 min, 55% B at 47 min, 75% at 56 min, 100% B at 60 min, 100% at 65 min, 5% at 73 min, and 5% at 80 min. UV detection at 280 nm was conducted. 20 μL was the volume of the injection, while the discharge rate was 0.9 mL/min. The apparatus for HPLC analysis is managed by the JASCO Chrom NAV2.0 HPLC software. The process of identification involved the comparison of the retention time of every pic to that of the corresponding standard.

2.6 Antimicrobial activities

For this experiment, a group of five microorganisms was used. There were two types of Gram-negative bacteria in the group, *Escherichia coli (ATCC 25922) and Pseudomonas aeruginosa (ATCC 27853)*, two types of Gram-positive bacteria, *Staphylococcus aureus (ATCC 25923) and Bacillus subtilis subsp. spizenii (ATCC 6633)*, and one type of pure fungus, *Candida albicans*. To support the growth of these bacteria, they were cultured on Biorad's Muller-Hinton agar (MH) at a temperature of +4°C. To facilitate growth, the cultures were periodically transferred every fortnight and scrutinized for purity. The samples were solubilized in dimethyl sulfoxide (DMSO). Twenty milliliters of aseptic Mueller Hinton agar (Sigma, Paris, France) were added to Petri dishes and subsequently inoculated with a 200 µL cell suspension. The concentration of the cell suspension was adjusted to 10^6 colony-forming units per milliliter (CFU/mL) using the McFarland 0.5 technique. Filter paper discs, devoid of bacteria or other microorganisms and with a diameter of 6 mm, were saturated with 20 µL of the extract solution (5 mg/disc). Subsequently, these discs were placed on the agar surface. The plates were incubated at a temperature of 37°C for a period of 24 h. The experimental group used gentamicin (15 µg/disc) and Fluconazole (60 µg/disc) as positive controls. The negative controls comprised paper discs holding 20 µL of DMSO or distilled water. The inhibitory zones were measured using digital calipers, and the measurements were repeated three times to minimize errors. A diameter of 14 mm or more for the inhibition zone, including the disc diameter, indicates a significant level of antibacterial activity (Philip et al., 2009). A serial dilution method was used in 96-well microtiter plates to find the minimum inhibitory concentration (MIC) for microbial growth. We found out how much extract to use in the test by letting the solvent evaporate from 1 mL of extract, mixing the dry extract with 20% v/v DMSO, and then adding 10 times as much Mueller-Hinton broth to it. After that, 100 µL of the bacterial or fungus solutions and dilutions were put into microtiter plates and left to grow at 37°C for 24 h. The positive control consisted of 100 µL of bacterium solution combined with 100 µL of Mueller Hinton broth. In contrast, the negative control consisted of 100 µL of diluent mixed with 100 µL of extract without bacteria. After 24 h, the positive and negative findings were assessed in relation to turbidity compared to the control well. The MIC values were determined as the minimum concentration of extract (from 16 to 1,000 µg/mL) that completely suppressed microbial development, as evidenced by a clear well,extracts were categorized as highly active when MICs were below 100 µg/mL, moderately active when values ranged from 100 to 625 µg/mL, and weakly active when values exceeded 625 µg/mL (Chusri et al., 2014). The validity of all extracts was assessed by conducting three separate tests (Tikent et al., 2023).

2.7 Cytotoxicity against breast cancer cell lines

2.7.1 Cell culture

The study used two types of breast cancer cells: MCF-7 cells, which are estrogen receptor-positive, and MDA-MB-231 and MDA-MB-436 cells, which are estrogen receptor-negative. To keep the cells alive, they were kept in Dulbecco's modified Eagle's medium (DMEM) with 10% Fetal bovine serum (FBS) and 50 µg/mL gentamicin at 37°C with 5% CO_2 in a humid room. The cells were cultured in 25-cm² tissue culture flasks to maintain continuous growth. To investigate cell viability, the study used cells in the rapid expansion phase.

2.7.2 Cell viability by MTT assay

To determine whether the studied extracts could inhibit the proliferation of cancer cells, we have used the 3-(4,5-dimethylthiazo-l-2-yl)-2,5-diphenyltetrazolium bromide (MTT) assay, following the method described in references (Chaudhary et al., 2015; Elbouzidi et al., 2023). MCF-7, MDA-MB-231, and MDA-MB-436 cells that were growing exponentially were put in 96-well plates at a density of 10^4 cells per well in 100 µL of medium and left there for 24 h. To obtain various concentrations, the studied extracts were solubilized in 0.1% DMSO and serially diluted with medium. Different concentrations of the studied extracts (from 6.25 to 300 µg/mL) were prepared by dissolving them in 0.1% DMSO and diluting them with medium and cisplatin was used as a positive control at various concentrations ranging from 0.39 to 50 µg/mL. The cells were then exposed to varying concentrations of the studied extracts for 72 h. The control group cells were only given medium containing 0.1% DMSO. 200 µL of culture medium was added to the medium, and then 20 µL of MTT reagent 5 mg/mL MTT in Phosphate Buffer Saline (PBS) was added. The mixture was then left to sit at 37°C for 4 h. After the medium was taken away, 100 µL of DMSO was added. An HT Multi-Detection Microplate Reader from Bio-Tek in Winooski, VT, United States, was used to measure the absorbance at 540 nm and find out what percentage of cells were still alive (Elbouzidi et al., 2023). The study evaluated the effect of the studied extracts on cell viability by measuring absorbance using the following equation:

$$\text{Cell viability (\%)} = 100 - \left[\left(\left(A_0 - A_t \right) / A_0 \right) \times 100 \right]$$

A_0 = absorbance of cells treated with 0.1% DMSO medium, and A_t = absorbance of cells treated with the studied extracts at various concentrations. As a negative control, 0.1% DMSO was added to the medium. The IC_{50} values were found using the software GraphPad Prism 8.01 and cisplatin was used as the standard. PBMCs were isolated from human blood samples using Ficollhypaque density centrifugation as per the manufacturer's instructions (Capricorn Scientific). The studies involving [human] participants were reviewed and approved by the Research Ethics Committee (03/22-LAPABE-10 and 4 March 2022) prior to the experiment. To assess the cytotoxic effects of fig leaf hydro-ethanol extracts on peripheral blood mononuclear cells (PBMCs), the same conditions and concentrations used for tumor cells were utilized.

2.8 Molecular docking study

The hydro-ethanol extracts of *F. carica* leaves were tested for their antioxidant, antimicrobial, and anticancer capabilities. The Schrodinger Suite's Maestro 11.5 software was used to perform

TABLE 1 Results of biological compounds analysis in hydro-ethanol leaf extracts from the four Eastern Moroccan fig trees (*Ficus carica* L.).

Extract Reference	Polyphenols (mg GAE/g DW)	Flavonoids (mg QE/g DW)	Condensed tannins (mg CatE/g DW)	Vitamin C (mg Asc A/100 g DW)
CHHEE	58.5 ± 1.6[b]	25.8 ± 0.0[a]	2.4 ± 0.0[d]	8.2 ± 0.1[a]
GDHEE	60.4 ± 1.0[ab]	25.3 ± 0.3[b]	4.7 ± 0.1[c]	7.8 ± 0.0[b]
MAHEE	62.6 ± 1.3[a]	26.2 ± 0.1[a]	4.8 ± 0.0[b]	2.3 ± 0.1[c]
OHHEE	58.1 ± 1.0[b]	24.5 ± 0.1[c]	4.9 ± 0.1[a]	2.3 ± 0.0[c]

MAHEE, Malha hydro-ethanol extract; GDHEE., Ghoudane hydro-ethanol extract; CHHEE, Chetoui hydro-ethanol extract; OHHEE, Onk Hmam hydro-ethanol extract; GAE, Gallic acid equivalent; QE, Quercetin equivalent; CatE, Catechol equivalent; Asc A, Ascorbic acid; DW, Dry weight. Values are expressed as mean ± Standard Error of Measurement "SEM" (n = 3). Ordinary one-way ANOVA using *post hoc* testing (Tukey's test) at the 5% threshold. Means followed by a different letter in the same column are significantly different (p < 0.05).

the molecular docking analysis. This study set out to discover how the compounds contained in the hydro-ethanol extracts from the *F. carica* leaves interact with the active sites of particular target proteins. These proteins include NADPH oxidase, beta-ketoacyl-[acyl carrier protein] synthase, nucleoside diphosphate kinase, sterol 14-alpha demethylase (CYP51), and caspase-3.

2.8.1 Protein preparation

The crystal structures of the target proteins, namely, NADPH oxidase (PDB ID: 2CDU), beta-ketoacyl-[acyl carrier protein] synthase from *E. coli* (PDB ID: 1FJ4), nucleoside diphosphate kinase from *S. aureus* (PDB ID: 3Q8U), sterol 14-alpha demethylase (CYP51) from *C. albicans* (PDB ID: 5FSA), and caspase-3 were obtained from the RCSB database. The process of protein preparation was carried out using the Protein Preparation Wizard of Maestro 11.5. This involved a series of phases, including preprocessing, refining, and reduction. Hydrogen atoms were introduced, and hydroxyl groups, water molecules, and amino acids were rearranged to correct structural defects such as atom overlap or absence. The proteins were subsequently modified in a delicate manner to enhance their structural characteristics (Kumar et al., 2022; Lafraxo et al., 2022; Tourabi et al., 2023).

2.8.2 Ligand preparation

For ligand generation, the Schrödinger suite's Ligprep wizard in Maestro 11.5 was used. This requires utilizing the OPLS3 force field to reduce structures, add hydrogen atoms, resolve bond length and angle issues, and transform 2D structures into 3D. The ionization states were fine-tuned while maintaining chirality (Aboul-Soud et al., 2022).

2.9 Statistical analysis

Microsoft Office Excel 2021 was utilized in order to determine the correlation coefficients (R^2) for the spectrophotometric experiments. Statistical analysis was performed using IBM SPSS Statistics V21.0 software for descriptive statistics, for comparing averages with ANOVA one-way of studied characteristics by *post hoc* (Tukey's test) at the 5% threshold, for bivariate Pearson correlation analysis with a significance level of P < 0.01 and for the Principal Component Analysis (PCA).

3 Results and discussions

3.1 Spectrophotometric analysis of bioactive components in hydro-ethanol leaf extracts

Total polyphenols, flavonoids, condensed tannins, and vitamin C were tested in hydro-ethanol extracts from the leaves of the fig plant that was being studied. Table 1 shows that these chemicals were present in the extracts in varying amounts. The synthesis and accumulation of phenolic compounds can be influenced by several internal and external stimuli, such as stress, damage, dryness, and the invasion of pathogens. Some plant species make phenylpropanoid chemicals when they are exposed to nutritional stressors like nitrogen, phosphate, potassium, sulfur, magnesium, boron, and iron, as well as when they are exposed to photo-inhibition. Furthermore, exposure to light stimulates the process of producing phenolic compounds in chloroplasts and storing them in vacuoles (Bhattacharya et al., 2010).

The average amount of polyphenols in Malha hydro-ethanol extract (MAHEE) is 62.6 ± 1.3 mg GAE/g DW. This is higher than Ghoudane hydro-ethanol extract (GDHEE), Chetoui hydro-ethanol extract (CHHEE), and Onk Hmam hydro-ethanol extract (OHHEE), which have 58.1 ± 1.0 mg GAE/g DW. When comparing the means of this leaf characteristic, the difference is only noticeable when MAHEE is compared to CHHEE or OHHEE, not when compared the other leaf types. Phenolic compounds are common secondary metabolites found in plants. They not only help plants work, but they are also good for people's health because they fight free radicals, quench singlet oxygen, and donate a hydrogen atom or electron to other compounds. Figs contain phenolic chemicals. Indeed, red wine and tea, two well-known sources of phenolic chemicals, have lower phenolic levels than figs (Oliveira et al., 2009; Vallejo et al., 2012).

The average amount of flavonoids in MAHEE was 26.2 ± 0.1 mg QE/g DW, followed by CHHEE, GDHEE, and OHHEE at 24.5 ± 0.1 mg QE/g DW. For this trait, there were also significant differences in the average amounts of flavonoids in fig leaves, except between MAHEE and CHHEE. Flavonoids are a distinct class of natural compounds that are the main active substances in many medicinal plants. They are used to treat a variety of diseases by inhibiting specific enzymes and hormones, as well as stimulating and reducing free radical activity. Flavonoids' antioxidant action is attributed to their phenolic groups and ability to form chelates with transitional metals (Trifunschi et al., 2015).

TABLE 2 Antioxidant and free radical scavenging results from the four studied hydro-ethanol leaf extracts.

Extract/ Reference	DPPH scavenging capacity IC50 (mg/mL)	β-Carotene bleaching assay (mg/mL)	ABTS scavenging assay (TE μmol/mL)	Total antioxidant capacity *
CHHEE	1.0 ± 0.2[bc]	4.4 ± 0.3[c]	97.5 ± 5.6[b]	113.0 ± 6.5[c]
GDHEE	0.9 ± 0.2[bc]	4.1 ± 0.1[c]	99.2 ± 2.5[b]	133.0 ± 9.2[b]
MAHEE	0.7 ± 0.2[b]	3.0 ± 0.1[b]	87.1 ± 6.2[b]	179.0 ± 2.1[a]
OHHEE	1.3 ± 0.1[c]	5.5 ± 0.1[d]	112.2 ± 5.6[c]	92.9 ± 9.7[d]
Ascorbic acid (Asc A)	0.3 ± 0.1[a]	-	07.2 ± 1.4[a]	-
Butylated hydroxytoluene (BHT)	-	0.1 ± 0.1[a]	-	-

DPPH: 2,2-diphényl 1-picrylhydrazyle; β-Carotene: Beta-Carotene; ABTS: 2,2'-Azinobis[3-éthyl-2,3-dihydrobenzothiazole-6-sulfonate; *: Total antioxidant capacity (TAC) expressed as μg ascorbic acid equivalents/mg extract; TE: Trolox equivalent; MAHEE, Malha hydro-ethanol extract; GDHEE, Ghoudane hydro-ethanol extract; CHHEE, Chetoui hydro-ethanol extract; OHHEE, Onk Hmam hydro-ethanol extract. Ordinary one-way ANOVA using *post hoc* testing (Tukey's test) at the 5% threshold. Means followed by a different letter in the same column are significantly different (p < 0.05).

The amounts of condensed tannins show that these molecules were not the main phenolic compounds in the different ethanol leaf extracts. Instead, the amounts in each extract were very different (ANOVA at p < 0.05). CHHEE 2.4 ± 0.0 mg Cat E/g DW was the lowest level, and OHHEE 4.9 ± 0.1 mg Cat E/g DW was the most significant amount. Condensed tannins are accountable for the astringency seen in fruits and beverages. Still, they are fundamentally different from hydrolysable tannins because they do not contain any sugars in their molecular structure and are more like flavonoids (Soares et al., 2020).

CHHEE had the greatest average vitamin C content, measuring 8.2 ± 0.1 mg Asc. A/100 g DW, followed by GDHEE, MAHEE, and OHHEE at 2.3 ± 0.1 mg Asc. A/100 g DW. Additionally, ANOVA analysis at a significance threshold of 5% revealed significant differences in vitamin C content among fig leaves, except for the comparison between MAHEE and OHHEE. Vitamin C, or ascorbic acid, is a vital nutrient that plays a crucial role in significant physiological processes within the human body. It operates as an antioxidant and enhances immune system functionality. It is responsive to variables such as the degree of ripeness, storage conditions, and heating conditions. *Ficus carica* figs are excellent natural sources of vitamin C (Nerdy et al., 2023).

3.2 Antioxidant activity of hydro-ethanol leaf extracts

Antioxidant activity is critical for the human body because it protects cells from free radicals, which are produced during many oxygen-dependent processes and are responsible for oxidative destruction (Havsteen, 2002). The antioxidant activity of fig leaf extracts was assessed using four distinct methodologies (Table 2). The analysis of the findings revealed that MAHEE has the most potent antioxidants when compared to other leaf extracts.

The analysis of variance (ANOVA) shows that there is only a significant difference between the highest mean antioxidant activity equivalent (MAHEE) value of 0.7 ± 0.2 and the lowest mean OHHEE value of 1.3 ± 0.1, which is measured in terms of DPPH IC$_{50}$ in mg Asc. A equivalence per milliliter, with a significance level of P < 0.05. In earlier work, Petruccelli et al. (2018) looked at ten

different types of Italian *F. carica* leaves and found that fig leaf extracts had antioxidant activity when tested using the DPPH method. The IC$_{50}$ value of the extracts ranged from 0.48 to 6.68 mg/mL, which is consistent with the values obtained in this study (Petruccelli et al., 2018). The results of the multiple comparisons of averages from the β-carotene bleaching experiment suggest that there is no significant difference observed only between GDHEE and CHHEE. The antioxidant potency of MAHEE is the strongest, measuring at 3.0 ± 0.1 mg BHT equivalents/mL. On the other hand, OHHEE has the weakest potency, measuring at 5.5 ± 0.1 mg BHT equivalents/mL.

We used a significance level of 5% to do an analysis of variance (ANOVA). The ABTS scavenging assay only showed significant differences between OHHEE and MAHEE. MAHEE demonstrated the most potent antioxidant activity, measuring 87.1 ± 6.2 TE μmol/mL, whereas OHHEE exhibited the least activity, measuring 112.2 ± 5.6 TE μmol/mL. Ergül et al. (2019) discovered that the IC$_{50}$ values for ABTS radical scavenging activity in methanol and water extracts of fig leaves were 559.39 μg BHT/mL and 428.51 μg BHT/mL, respectively (Ergül et al., 2019).

The differences in total antioxidant capacity (TAC) between the four fig leaf extracts that were looked at are statistically significant, as shown by an ANOVA test with a p-value of less than 0.05. It was found that MAHEE had the highest phosphomolybdenum reduction, at 179.0 ± 2.1 μg Asc. A equivalents/mg extract. This was followed by GDHEE, CHHEE, and OHHEE, which had a phosphomolybdenum reduction of 92.9 ± 9.7 μg Asc. A equivalents/mg extract. In a previous study, Raoufa et al. (2021) assessed the total antioxidant capacity of a fig leaf extract at room temperature after 24 h using a solution of 70% ethanol. The resulting value was 0.569 mg of vitamin C equivalents per gram of extract (Abdel-Rahman et al., 2021).

The spectrophotometric assessment of antioxidant efficacy is carried out by measuring the ability of the biological sample to scavenge the synthetic-colored radical. There are two types of tests that can be done. The first tests for hydrogen atom transfer, and the second, which is more interesting to us, tests for electron transfer. These include the DPPH (2.2-diphenyl-1-picrylhydrazy), ABTS (2.2′-Azinobis (3-Ethylbenzothiazoline-6-Sulphonic Acid), and FRAP (Ferric Reducing Antioxidant Potential) tests. These

TABLE 3 Bivariate Pearson correlation analysis results regarding relationship between antioxidants and their effectiveness in scavenging free radicals.

Correlation	DPPH	β-carotene	ABTS	TAC	TPC	TFC	TCT	Vit C
DPPH	1,00							
β-carotene	0,99	1,00						
ABTS	0,97	0,97	1,00					
TAC	−0,97	−0,97	−0,92	1,00				
TPC	−0,93	−0,94	−0,85	0,98	1,00			
TFC	−0,89	−0,89	−0,97	0,80	0,70	1,00		
TCT	−0,05	−0,06	0,14	0,25	0,40	−0,36	1,00	
Vit C	−0,01	0,014	−0,08	−0,19	−0,24	0,17	−0,65	1,00

Bivariate Pearson correlation analysis with a significance level of $P < 0.01$. DPPH., DPPH, Scavenging Capacity IC_{50}; β-carotene., β-Carotene Bleaching Assay; ABTS., ABTS, scavenging assay; TAC., total antioxidant capacity; TPC., total polyphenol content; TFC., total flavonoid content; TCT., total condensed tannins; Vit C., Vitamin C.

chemical assays are commonly used due to their simplicity, cost-effectiveness, easy accessibility, and independence from advanced laboratory equipment (Ulewicz-Magulska and Wesolowski, 2019). We can quickly, easily, and cheaply find out how antioxidant-rich food is by using a free radical called 2,2-Diphenyl-1-picrylhydrazyl (DPPH). It is commonly used to test substances for their ability to either scavenge free radicals or donate hydrogen and to check the antioxidant activity of foods. In recent years, it has been employed to quantify antioxidants in intricate biological systems. The DPPH method is applicable to both solid and liquid samples and is not limited to any specific antioxidant component; rather, it assesses the overall antioxidant capacity of the sample. An assessment of total antioxidant capacity aids in comprehending the functional attributes of foods (Shalaby and Shanab, 2013). The ABTS method offers additional versatility since it may be employed at various pH levels, in contrast to DPPH, which is sensitive to acidic conditions. This makes it advantageous for investigating the influence of pH on the antioxidant activity of different substances. It is also beneficial for quantifying the antioxidant activity of samples extracted using acidic solvents. Furthermore, ABTS is soluble in both aqueous and organic solvents, making it valuable for evaluating the antioxidant activity of materials across various media. Most of the time, it is used in a Phosphate Buffer Saline (PBS) with 150 mM NaCl to simulate a serum ionic potential solution. An additional benefit of the ABTS + method is that samples responded swiftly with ABTS in the phosphate-buffered saline (PBS), achieving a steady state within 30 min (Shalaby and Shanab, 2013). Antioxidant capacity detected by the ABTS assay was significantly higher for fruits, vegetables, and beverages compared to that by the DPPH assay. The high-pigmented and hydrophilic antioxidants were better reflected by the ABTS assay than the DPPH assay. The results suggest that the ABTS assay may be more useful than the DPPH assay for detecting antioxidant capacity in a variety of foods (Floegel et al., 2011).

Despite the numerous antioxidant activities of our hydro-ethanol extracts of the *Ficus carica* leaves, it is necessary to conduct a comparative study of extracts of varying polarity, as well as other antioxidant methods such as iron chelation and ferric reducing power, to the best of our knowledge.

A bivariate Pearson correlation analysis (Table 3) was performed to investigate the association between antioxidants and their effectiveness in eliminating free radicals. The findings demonstrated a notable and positive association between total polyphenol content (TPC) and total flavonoid content (TFC), with a correlation coefficient of 0.70. In addition, strong negative relationships were found between total condensed tannins (TCT) and vitamin C (Vit C) in the fig leaves that were studied, with a correlation coefficient of −0.65. Furthermore, there was a weak positive correlation observed between TPC and TCT, as well as between TFC and vit C, with correlation coefficients of 0.40 and 0.17, respectively. Conversely, there was a weak negative correlation observed between TPC and vit C, as well as between TFC and TCT, with correlation coefficients of −0.24 and −0.36, respectively. The findings suggest that the abundance of polyphenols in fig leaves is in line with flavonoids. However, the rise in vit C causes a lack of condensed tannin. Additionally, they suggest that the distribution of these bioactive substances within the leaves is dependent on the specific variety of fig tree.

The findings demonstrated a significant and positive association between the total polyphenol content (TPC) and the total antioxidant capacity (TAC), with a correlation coefficient of 0.98. Furthermore, there was a significant inverse relationship between TPC with β-carotene (−0.94), DPPH (−0.93), and ABTS (−0.85). Similarly, TFC demonstrates a strong and positive association with TAC (0.80), while showing significant negative correlation coefficients with β-carotene (−0.89), DPPH (−0.89), and ABTS (−0.97). It turns out that the polyphenolic and flavonoid parts in the hydro-ethanol extracts of the fig leaves that were studied are mainly responsible for antioxidants' ability to get rid of harmful free radicals. In contrast, we observe weak correlations between TCT or vit C and ABTS, β-carotene, DPPH, and TAC. This suggests that TCT's or vit C's role in neutralizing free radicals in these extracts is diminished.

Principal Component Analysis (PCA), as seen in Figure 1, accounts for 94.558% of the overall variance. Specifically, Component 1 explains 70.110% of the variance, while Component 2 explains 24.448%. Component 1 exhibits a very high positive correlation with β-carotene (0.999), DPPH (0.997), and ABTS (0.978). It also shows a substantial negative correlation with TAC (−0.981), TPC (−0.941), and finally TFC (−0.902). Component 2 exhibits a very significant positive correlation with TCT (0.945). Conversely, it shows a negative correlation with vitamin C (−0.859).
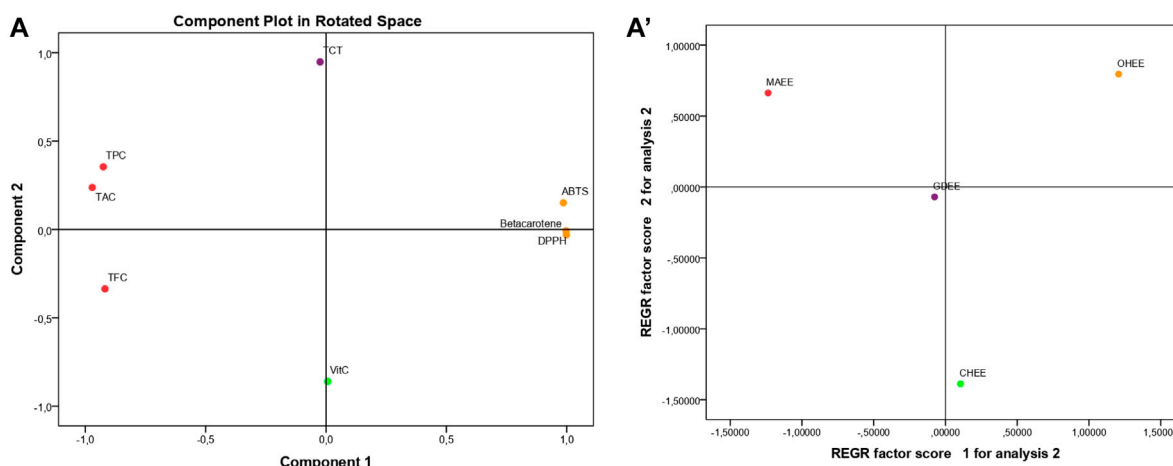
FIGURE 1
Principal component analysis (PCA); based on the different measurements of bioactive compounds and antioxidant activities in the hydro-ethanol leaf extracts of the four studied fig varieties TPC., Total polyphenol content; TFC., Total flavonoid content; TCT., Total condensed tannins; Vit C., Vitamin C; DPPH., DPPH Scavenging Capacity IC_{50}; Beta carotene., β-Carotene Bleaching Assay; ABTS., ABTS Scavenging Assay; TAC., Total Antioxidant Capacity; MAHEE., Malha hydro-ethanol extract; GDHEE., Ghoudane hydro-ethanol extract; CHHEE., Chetoui hydro-ethanol extract; OHHEE., Onk Hmam hydro-ethanol extract.

The regression (Figure 1) shows that the leaf extracts are spread out, which means that their bioactive components and antioxidant activity are very different from one another. MAHEE is notable for its high total antioxidant capacity (TAC), polyphenol content (TPC), and flavonoid content (TFC). These outstanding results can be attributed to the variety factor and/or the insufficient maintenance of the trees (due to the salty flavor, known as Malha in Arabic, of the figs they produce and their low market value), so they are vulnerable to stress. As a result of stress, the leaves produce a high concentration of polyphenols and flavonoids, increasing their resistance to cell and tissue damage as well as their antioxidant activity. CHHEE is distinguishable from the other leaf extracts studied by its high vitamin C content and low total condensed tannin content. In comparison to MAHEE, OHHEE has the lowest antioxidant strength (highest ABTS, β-carotene, and DPPH IC_{50}). However, unlike CHHEE, it is rich in total condensed tannins and low in vitamin C. GDHEE's pivotal location shows that the mix of its bioactive chemicals is unique. Its composition is more like any extract than the others analyzed. The findings amply illustrated the effect of the fig variety on the bioactive compounds and the antioxidant activities of their leaves.

3.3 HPLC-UV phytochemical analysis
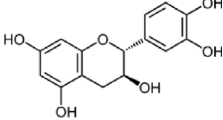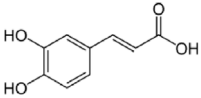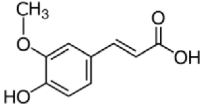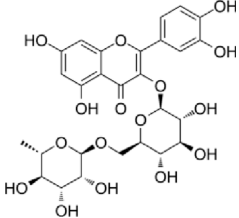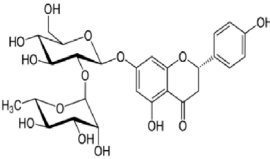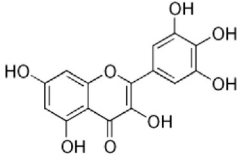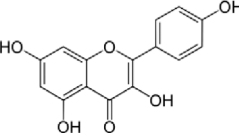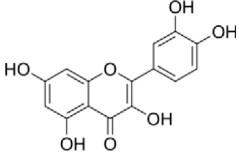
Table 4 shows that eight different phytochemicals, such as polyphenols and flavonoids, were found in the fourth hydro-ethanol leaf extract that was studied. The main parts of all the tested extracts were found to be caffeic acid, rutin, and trans ferulic. The active compounds cathechine for MAHEE, naringin for CHHEE, and kaempferol for GDHEE were only found in one of the fig leaf extracts. Myricitin is only present in CHHEE and OHHEE, whereas quercetin is completely absent in GDHEE.

Caffeic acid, a phenolic compound, is produced by plants and can be found in beverages including coffee, wine, tea, and propolis (Alam et al., 2022; Mirzaei et al., 2021). Furthermore, this phenolic acid and its derivatives possess antioxidant properties, in addition to their anti-carcinogenic and anti-inflammatory qualities. It has been shown to help fight hepatocarcinoma (HCC) in both *in vitro* and *in vivo* studies (Espíndola et al., 2019). It also contributes to the plant's defense against diseases and other destructive organisms by suppressing the growth of bacteria, fungus, and insects (Khan et al., 2021; Ramaroson et al., 2022; Riaz et al., 2019).

Rutin is the main compound of flavonoid glycosides found in Ficus (Vaya and Mahmood, 2006). It is possible to hydrolyze one terminal rhamnose into quercetin. Alternatively, it can be converted into isoquercitrin, which has higher bioavailability and stronger anti-proliferative properties compared to rutin and quercetin (Takahama et al., 2009). Rutin, an essential dietary component, influences the fragility and permeability of capillaries, hence enhancing human health (Kamalakkannan and Prince, 2006). It has various medical uses, such as being an antioxidant, an antiallergen, an antibacterial, an antiulcer, an anticarcinogenic, an anti-inflammatory, an anti-diabetic, and an antimutagenic substance (Caglayan et al., 2019; Li et al., 2010). When given orally to rats, its antioxidant activity and bioavailability were shown to be lower than those of quercetin. In humans, quercetin's bioavailability in capsule form is less than 1%, mainly due to its low absorption in the small intestine (Erlund, 2004).

Ferulic acid, a widely distributed phenolic acid found in plants, is a constituent of Chinese medicinal herbs. Usually, it combines with mono- and oligosaccharides, polyamines, lipids, and polysaccharides in plants and it demonstrates low toxicity and can be readily absorbed and digested. Scientific evidence has demonstrated that ferulic acid possesses antioxidant, antimicrobial, anti-inflammatory, anti-thrombotic, and anti-cancer properties. Furthermore, it offers defense against heart

TABLE 4 HPLC- UV phenolic profile of ethanol extracts from the studied fig leaves.

Compounds	Chemical formula	Structural formula	Classification	RT (min)	Area %			
					CH HEE	GD HEE	MA HEE	OH HEE
Catechin	$C_{15}H_{14}O_6$		Flavonoid flavonols	12.0	ND	ND	2.20	ND
Caffeic acid	$C_9H_8O_4$		Hydroxy cinnamic acid	13.9	38.79	40.58	33.34	32.92
Trans ferulic	$C_{10}H_{10}O_4$		Hydroxy cinnamic acid	14.8	12.86	9.35	13.21	7.61
Rutin	$C_{27}H_{30}O_{16}$		Flavonoid glycosides	18.4	24.37	21.82	31.04	16.74
Naringin	$C_{27}H_{32}O_{14}$		Flavanone glycosides	20.2	1.11	ND	ND	ND
Myricitin	$C_{15}H_{10}O_8$		Flavonoid flavonols	25.2	0.29	ND	ND	1.16
Kaempferol	$C_{15}H_{10}O_6$		Flavonoid flavonols	42.2	ND	3.37	ND	ND
Quercetin	$C_{15}H_{10}O_7$		Flavonoid flavonols	44.5	02.93	ND	1.47	3.55

RT., retention time; ND., Not detected; MAHEE., Malha hydro-ethanol extract; GDHEE., Ghoudane hydro-ethanol extract; CHHEE., Chetoui hydro-ethanol extract; OHHEE., Onk Hmam hydro-ethanol extract.

disease, lowers cholesterol levels, and improves sperm viability. It is extensively utilized in the food and cosmetic sectors due to its desirable qualities and minimal toxicity. It is the main component that is used in the production of vanillin and preservatives. Moreover, it serves as a cross-linking agent for the production of food gels and edible films. It is also used into sports foods and skin protection products. Ferulic acid can be chemically manufactured or created via biological transformation (Ou and Kwok, 2004).

3.4 Antimicrobial activity

The hydro-ethanol extracts derived from the leaves of the four fig varieties exhibited varying degrees of efficacy in eliminating the tested strains (Table 5). The reference medications exhibited the most potent inhibitory effect when compared to the four fig leaf extracts that were examined. This was demonstrated by an ANOVA study, utilizing Tukey's *post hoc* test, at a significance level of 5%.

TABLE 5 Disk diffusion assay results for the investigated leaf extracts and reference drugs.

Fig leaf extracts		Microbial strains tested				
		E. coli	*P. aeruginosa*	*S. aureus*	*B. subtilis*	*C. albicans*
CHHEE		12.6 ± 0.1[b]	11.8 ± 0.6[c]	10.5 ± 0.3[c]	12.6 ± 0.1[c]	18.65 ± 0.2[c]
GDHEE		12.85 ± 0.2[b]	13.9 ± 1.0[b]	11.5 ± 0.1[b]	12.8 ± 0.2[c]	18.9 ± 0.1[c]
MAHEE		12.9 ± 0.1[b]	13.95 ± 0.8[b]	11.6 ± 0.2[b]	14.0 ± 0.3[b]	20.4 ± 0.1[b]
OHHEE		12.5 ± 0.4[b]	11.7 ± 0.4[c]	10.4 ± 0.2[c]	12.5 ± 0.4[c]	18.6 ± 0.2[c]
Controls	Gentamicin	28.5 ± 0.1[a]	23.5 ± 0.4[a]	26.4 ± 0.2[a]	20.5 ± 0.2[a]	N.T
	Fluconazole	N.T	N.T	N.T	N.T	25.8 ± 0.2[a]
	DMSO	0	0	0	0	0

N.T, Not Tested; 0, No Activity; *E. coli*, *Escherichia coli* ATCC 25922; *P. aeruginosa*, *Pseudomonas aeruginosa* ATCC 27853; *S. aureus*, *Staphylococcus aureus* ATCC 25923; *B. subtilis*, *Bacillus subtilis* subsp. Spizizenii ATCC 6633; *C. albicans*, *Candida albicans* (Clinical isolated); MAHEE, Malha hydro-ethanol extract; GDHEE, Ghoudane hydro-ethanol extract; CHHEE, Chetoui hydro-ethanol extract; OHHEE, Onk Hmam hydro-ethanol extract; DMSO, Diméthyl Sulfoxide. Inhibition zones including the diameter of the paper disc (6 mm). Each value is represented as mean standard deviation, (n = 3), Means followed by a different letter in the same column are significantly different (ANOVA - by *post hoc* Tukey's test p < 0.05).

The increased antimicrobial efficacy of MAHEE and GDHEE, in comparison to CHHEE and OHHEE, can be attributed to their elevated levels of bioactive constituents, such as polyphenols and flavonoids.

It is noteworthy to highlight that the hydro-ethanol extracts from the examined fig leaves were quite effective against *C. albicans*. The ANOVA analysis revealed that the differences were only significant between MAHEE and the other leaf hydro-ethanol extracts. The OHHEE had the lowest effect (18.6 ± 0.2 mm), followed by CHHEE (18.65 ± 0.2 mm) and GDHEE (18.9 ± 0.2 mm), while MAHEE had the strongest effect (20.4 ± 0.1 mm). For gram-negative bacteria, there is no significant difference in inhibitory activity against Escherichia *coli* among the leaf extracts. MAHEE had the highest effect (12.9 ± 0.1 mm), followed by GDHEE (12.85 ± 0.2 mm) and CHHEE (12.6 ± 0.1 mm), while OHHEE had the lowest effect (12.5 ± 0.4 mm). MAHEE (13.95 ± 0.8 mm) and GDHEE (13.9 ± 1.0 mm) had the highest activity against *P. aeruginosa*, while CHHEE (11.8 ± 0.6 mm) and OHHEE (11.7 ± 0.4 mm) had smaller inhibition diameters. However, there was no significant difference in inhibitory activity between MAHEE and GDHEE or between CHHEE and OHHEE. In relation to Gram-positive bacteria, the OHHEE (10.4 ± 0.2 mm) and CHHEE (10.5 ± 0.3 mm) exhibited the least efficacy against *S. aureus*. Conversely, the GDHEE (11.5 ± 0.1 mm) and MAHEE (11.6 ± 0.2 mm) demonstrated the greatest diameters of inhibition. The inhibitory actions of OHHEE and CHHEE, as well as GDHEE and MAHEE, did not differ significantly. In addition, it was observed that leaf extracts exhibited inhibitory effects on *B. subtilis*. Among these, MAHEE demonstrated the most pronounced inhibitory effect (14.0 ± 0.3 mm), followed by GDHEE (12.85 ± 0.2 mm) and CHHEE (12.6 ± 0.1 mm). OHHEE exhibited the least effective effect (12.5 ± 0.4 mm). Furthermore, no statistically significant distinction in inhibitory action was found between GDHEE, CHHEE and OHHEE.

Resistance and sensitivity are not invariably associated with a singular substance or molecular class; they are intricate systems that involve multiple types of molecules (Coulibaly et al., 2020). The concentration and composition of bioactive chemicals and minerals may have influenced the extracts' antimicrobial effect against different strains. Certain minerals and bioactive compounds, such as polyphenols, can interact to enhance or reduce antimicrobial activity in plants and extracts, respectively (Cunningham et al., 2010). Many recent investigations have shown that medicinal mineral compounds serve as antimicrobials by interacting synergistically with bioactive components found in plant extracts such as polyphenols, flavonoids, terpenoids, and others, or by altering pH, These interactions can either augment or diminish the antimicrobial characteristics of the plant or the antibacterial efficacy of the extract, contingent upon the specific chemical elements present in minerals and bioactive chemicals (Divakar et al., 2018). Plants produce flavonoids and coumarins as a protective mechanism against microbial infections. The ability of these compounds to interact with extracellular and soluble proteins, as well as bacterial cell walls, may contribute to their claimed efficacy. Furthermore, lipophilic flavonoids have the ability to damage microbial membranes and act as bioactive molecules that interact with microorganisms in a variety of ways, impacting their development and survival (Tsuchiya et al., 1996). Several studies have found that *F. carica* leaf extracts exhibit antibacterial properties against oral bacteria, nosocomial infectious agents, food poisoning bacteria, fungi, and viruses (Jeong et al., 2009; Wang et al., 2004).

The minimum inhibitory concentrations (MIC) of the leaf extracts were analyzed (Table 6). All of the ethanol extracts from the varieties that were studied had the same MIC values for the two strains that were tested: 64 μg/mL against *E. coli* and 32 μg/mL against *C. albicans*. It also demonstrated that the ethanol extracts from both MA and GD varieties, as well as those from CH and OH, had equal MIC values against the other strains examined. However, MAHEE and GDHEE showed a MIC of 32 μg/mL against *P. aeruginosa*, whereas CHHEE and OHHEE showed a MIC of 64 μg/mL. The MAHEE and GDHEE showed a MIC of 128 μg/mL against *S. aureus*, while the CHHEE and OHHEE had a MIC of 256 μg/mL. *Bacillus subtilis* showed a higher sensitivity to MAHEE and GDHEE, with a MIC of 128 μg/mL. In contrast, it demonstrated lesser sensitivity to CHHEE and OHHEE, with a MIC of 256 μg/mL.

TABLE 6 Minimum inhibitory concentrations (MIC values) in µg/mL for the investigated leaf extracts.

Fig leaf extracts	E. coli	P. aeruginosa	S. aureus	B. subtilis	C. albicans
CHHEE	64 ± 0.0[a]	64 ± 0.0[b]	256 ± 0.0[b]	256 ± 0.0[b]	32 ± 0.0[a]
GDHEE	64 ± 0.0[a]	32 ± 0.0[a]	128 ± 0.0[a]	128 ± 0.0[a]	32 ± 0.0[a]
MAHEE	64 ± 0.0[a]	32 ± 0.0[a]	128 ± 0.0[a]	128 ± 0.0[a]	32 ± 0.0[a]
OHHEE	64 ± 0.0[a]	64 ± 0.0[b]	256 ± 0.0[b]	256 ± 0.0[b]	32 ± 0.0[a]

E. coli, Escherichia coli ATCC 25922; P. aeruginosa, Pseudomonas aeruginosa ATCC 27853; S. aureus, Staphylococcus aureus ATCC 25923; B. subtilis, Bacillus subtilis subsp. Spizizenii ATCC 6633; C. albicans, Candida albicans (Clinical isolated); MAHEE, Malha hydro-ethanol extract; GDHEE, Ghoudane hydro-ethanol extract; CHHEE, Chetoui hydro-ethanol extract; OHHEE, Onk Hmam hydro-ethanol extract. Each MIC value is represented as mean standard deviation, (n = 3), Means followed by a different letter in the same column are significantly different (ANOVA - by post-hoc Tukey's test p < 0.05).
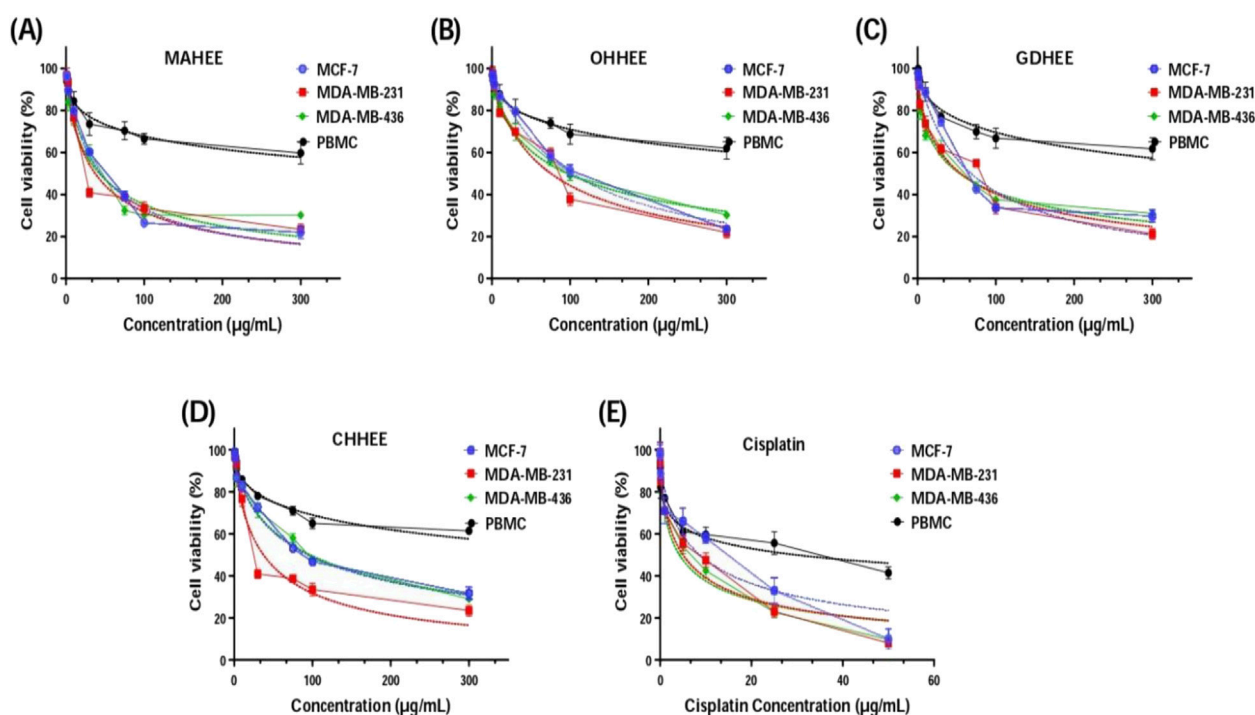
FIGURE 2
Cell viability of MCF-7, MDA-MB-231, MDA-MB-436 and PBMC cells after 72 h of treatment with F. carica hydro-ethanol extracts: **(A)** MAHEE, **(B)** OHHEE, **(C)** GDHEE, **(D)** CHHEE and **(E)** cisplatin as positive control, using MTT test. MAHEE., Malha hydro-ethanol extract; GDHEE., Ghoudane hydro-ethanol extract; CHHEE., Chetoui hydro-ethanol extract; OHHEE., Onk Hmam hydro-ethanol extract.

The minimum inhibitory concentration (MIC) is determined by several factors, including the botanical source and specific plant component used for extraction, the extraction process (including temperature and duration), the solvent used, the amount of active components extracted, and the specific microorganism that the extract is intended to inhibit (Tikent et al., 2023).

3.5 Anticancer activity against breast cancer cell lines

Cancer is one of the world's most serious health problems and the second-biggest cause of mortality after cardiovascular disease (Tayoub et al., 2018). Conventional clinic therapies such as chemotherapy, surgery, and radiotherapy have a number of

dangerous side effects and can damage noncancerous tissues (Birjandian et al., 2018). Furthermore, with rising medication resistance, particularly in cancer treatment, plants have become increasingly significant in the quest for novel chemotherapeutic agents. Many anticancer medicines originating from plants are used in clinics, including vincristine, vinblastine (Catharanthus sp.), paclitaxel (Taxus sp.), and epipodophyllotoxins (Podophyllum sp.) (Sengupta et al., 2017).

Upon analyzing the results presented in Figure 2 and Table 7, it is evident that the IC_{50} values, which indicate the concentration needed to inhibit 50% of cell growth, reveal that the most potent and distinguishable extracts are MAHEE and GDHEE for MCF-7 and MDA-MB-436. Similarly, for MDA-MB-231, the extracts MAHEE and CHHEE exhibit the strongest effects. The IC_{50} values of these extracts are the closest to the lowest IC_{50} values of cisplatin, the

TABLE 7 IC$_{50}$ and selectivity indexes of leaf hydro-ethanol extracts on the examined cancer cell lines.

	IC$_{50}$ value ± SD (µg/mL) *				Selectivity index**		
	MCF 7	MDA-MB 231	MDA-MB 436	PBMC	MCF 7	MDA-MB 231	MDA-MB 436
MAHEE	44.5 ± 4.3[b]	37.3 ± 1.4[b]	42.6 ± 2.3[b]	663.6 ± 11.2[b]	14.91	17.79	15.57
OHHEE	102.4 ± 2.2[d]	75.4 ± 3.2[d]	96.2 ± 5.5[d]	791.4 ± 5.8[a]	7.72	10.49	8.22
GDHEE	68.1 ± 5.4[c]	55.1 ± 1.9[c]	53.6 ± 1.8[c]	550.5 ± 9.1[d]	8.08	9.99	10.27
CHHEE	93.9 ± 7.3[d]	39.5 ± 2.6[b]	96.9 ± 4.7[d]	594.5 ± 4.1[c]	6.33	15.05	6.13
Cisplatin	8.6 ± 1.3[a]	5.0 ± 0.1[a]	4.2 ± 0.6[a]	29.6 ± 2.1[e]	3.44	5.92	7.04

IC, Inhibitory Concentration; MCF7, Michigan Cancer Foundation-7; MDA-MB 231, Monroe Dunaway Anderson -Metastasic Breast 231; MDA-MB 436, Monroe Dunaway Anderson -Metastasic Breast 436; PBMC, Peripheral Blood Mononuclear Cell MAHEE, Malha hydro-ethanol extract; GDHEE, Ghoudane hydro-ethanol extract; CHHEE, Chetoui hydro-ethanol extract; OHHEE, Onk Hmam hydro-ethanol extract. * Values are obtained from three independent experiments and expressed as means ± SD (standard deviation). ** Selectivity index = (IC$_{50}$ of PBMC/IC$_{50}$ of tumor cells), PBMCs are the first normal cell populations to come into contact with anticancer medicines employed in the conventional intravenous chemotherapy of patients.

FIGURE 3
The ligand "Myricitin" interacts with the active site of NADPH oxidase through the 2D viewer (A) and the 3D viewer (A').

conventional chemotherapeutic medication. In terms of selectivity index, cisplatin demonstrates the least selectivity when compared to all ethanol extracts of fig leaves that were tested. On the other hand, MAHEE exhibits the highest selectivity index among the three cancer cell lines examined, with values of 14.91 for MCF-7, 17.79 for MDA-MB-231, and 15.57 for MDA-MB-436. Polyphenols can halt or even reverse cancer progression by interacting with molecules in the intracellular signaling network that are involved in cancer initiation and promotion. By influencing a small number of critical components of cellular signaling, polyphenols can also induce apoptosis in cancer cells (Link et al., 2010).

To sum up, the data strongly support the good selectivity profile of the hydro-ethanol fig leaf extracts, especially MAHEE and GDHEE for MCF-7 and MDA-MB-436 and MAHEE and CHHEE for MDA-MB-231. The results indicate that fig leaf extracts possess promising anti-cancer effects, necessitating additional research, such as mechanistic studies and *in vivo* trials, to authenticate their efficacy. Further research into the potential application of these extracts in cancer therapy, combined with an in-depth understanding of their mechanisms of action, will significantly enhance their clinical applicability.

3.6 *In silico* analysis of the antioxidant, antimicrobial, and anticancer activity of the components found in the hydro-ethanol extract of leaves

NADPH oxidase (NOX) is a crucial enzyme involved in the generation of reactive oxygen species (ROS), and its function is closely regulated within cells. NADPH oxidase-generated reactive oxygen species (ROS) play a crucial role in protecting against pathogens and facilitating cellular communication. Many people think that oxidative stress, which is caused by NADPH oxidase making too many reactive oxygen species (ROS), is the main reason why tissues get damaged in a number of respiratory inflammatory diseases and injuries, such as asthma, cystic fibrosis, acute respiratory distress syndrome (ARDS), and chronic obstructive pulmonary disease (COPD). Suppressing the activity of NADPH oxidase is a highly effective method to enhance the antioxidant activity and provide protection against diseases associated with oxidative stress (Lee and Yang, 2012). NADPH oxidase inhibitors have the potential to preserve cellular wellbeing and restrain disease progression by reducing reactive oxygen

TABLE 8 Glide gscore based on targeted antioxidant protein and bioactive compounds of leaf extracts.

NADPH oxidase (PDB ID: 2CDU)	Leaf extracts bioactive compounds							
	Caffeic acid	Catechin	Kaempferol	Myricitin	Naringin	Rutin	Quercetin	Trans ferulic
Glide gscore (Kcal/mol)	−5.48	−5.55	−5.54	−6.59	−5.16	−5.97	−6.58	−5.40

TABLE 9 Glide gscore based on targeted microbial proteins and bioactive compounds of leaf extracts.

Microbial protein targeted	Leaf extracts bioactive compounds							
	Caffeic acid	Catechin	Kaempferol	Myricitin	Naringin	Rutin	Quercetin	Trans ferulic
Beta-ketoacyl-[acyl carrier protein] synthase (PDB ID: 1FJ4)	−6.42	−6.45	−5.95	−6.02	***	−4.83	−5.92	−6.55
Nucleoside diphosphate kinase (PDB ID: 3Q8U)	−7.93	−6.79	−8.98	−8.88	−4.67	−7.87	−8.99	−7.93
Sterol 14-alpha demethylase (CYP51) (PDB ID: 5FSA)	−5.39	−7.63	−7.84	−7.84	−5.57	−6.24	−7.62	−5.21

***, No interaction. Glide gscore mesure the interaction between the boactive compound and the protein targeted in (Kcal/mol).

species (ROS) generation, enhancing cellular antioxidant mechanisms, and mitigating chronic inflammation.

According to Figure 3 and Table 8, our *in silico* research revealed that the three most active compounds from leaf extracts against NADPH oxidase were myricitin, quercetin, and rutin. These compounds had glide gscores of −6.59, −6.58, and −5.97 kcal/mol, respectively. Myricitin has formed two hydrogen bonds with VAL 214 and ASP 179, and a single Pi cation bond with LYS 187 in the active region of NADPH oxidase.

Beta-ketoacyl-ACP synthase primarily functions to synthesize fatty acids of different lengths to be utilized by the organism. These applications encompass energy storage and the formation of cell membranes. Fatty acids have the ability to generate various compounds such as prostaglandins, phospholipids, and vitamins, among other substances (Witkowski et al., 2002). Beta-ketoacyl-ACP synthases are very important for making lipoproteins, phospholipids, and lipopolysaccharides. Because they do so many

important things in the body, they have become a focus for the development of antibacterial drugs. Bacteria modify the composition of their membranes by changing the phospholipids in order to adjust to their surroundings. Therefore, blocking this channel could serve as a strategic location for impeding the proliferation of bacteria (Zhang and Rock, 2008).

Trans ferulic, catechin, and caffeic acid had the highest antibacterial efficacy against beta-ketoacyl-[acyl carrier protein] synthase from *E. coli*, with glide gscores of −6.55, −6.45, and −6.42 kcal/mol, respectively (Table 9). Trans ferulic formed four hydrogen bonds with GLY 394, GLY 393, THR 302, and THR 300, and a solitary Pi-Pi stacking bond with PHE 392 in the active region of beta-ketoacyl-[acyl carrier protein] synthase from *E. coli* (Figure 4).

Bacterial diphosphate kinase (Ndk) controls the amount of nucleoside triphosphate (NTP) in cells by moving γ-phosphate from NTPs to NDPs and back again. In addition to its primary

FIGURE 4
The ligand "Trans ferulic" interacts with the active site of beta-ketoacyl-[acyl carrier protein] synthase through the 2D viewer **(A)** and the 3D viewer **(A′)**.
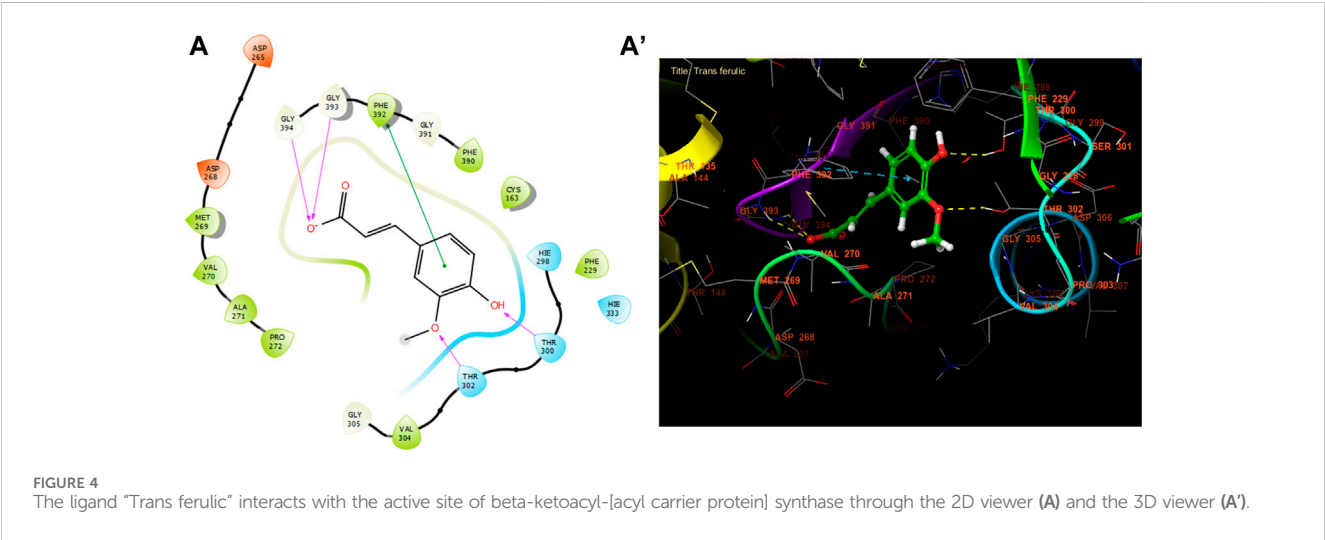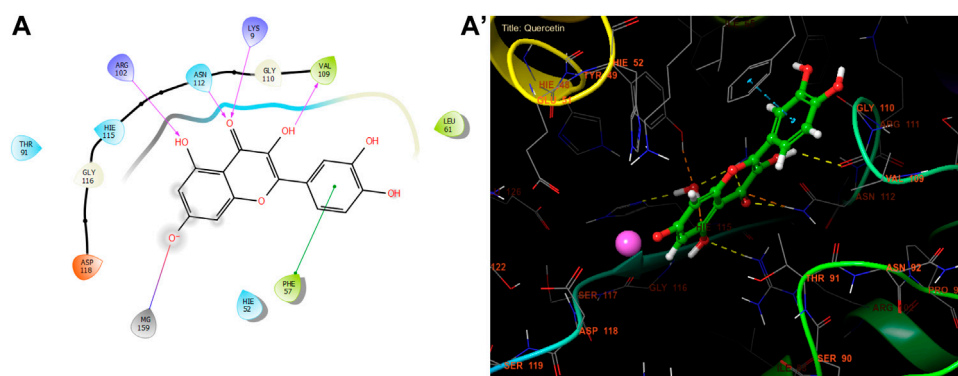
FIGURE 5
The ligand "Quercetin" interacts with the active site of nucleoside diphosphate kinase through the 2D viewer (A) and the 3D viewer (A').
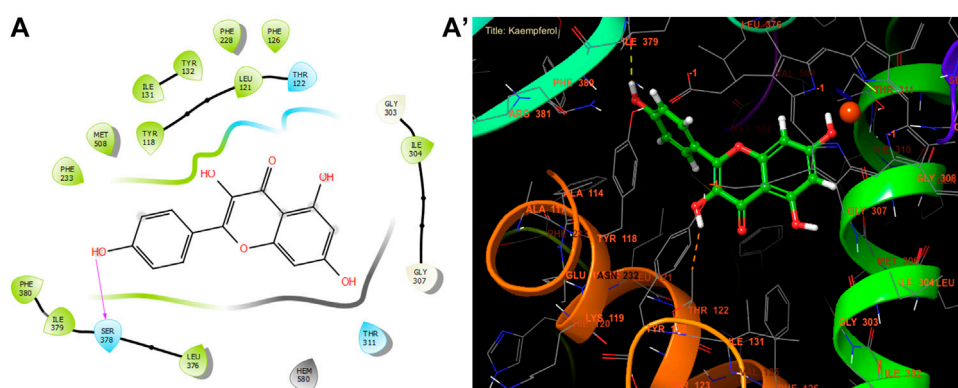
FIGURE 6
The ligand "Kaempferol" interacts with the active site of sterol 14-alpha demethylase (CYP51). Through the 2D viewer (A) and the 3D viewer (A').

function in nucleotide metabolism, Ndk is involved in protein histidine phosphorylation, DNA cleavage/repair, and gene regulation. Ndk also controls bacterial adaptive responses. Ndks made by bacteria inside cells stop many of the host's defense systems from working. These include phagocytosis, cell apoptosis/necrosis, ROS production, and inflammation. In contrast, extracellular bacteria-secreted Ndks exacerbate host cell cytotoxicity and the inflammatory response. Although Ndks from intra- and extracellular bacteria govern host cellular events in different ways, their basic function is the same, creating the host milieu conducive to colonization and dissemination (Yu et al., 2017). As a result, inhibiting Ndk is an effective strategy for preventing the emergence of bacteria.

Quercetin, kaempferol, and myricitin exhibited the highest level of activity against *S. aureus* nucleoside diphosphate kinase, with glide gscore values of −8.99, −8.98, and −8.88 kcal/mol respectively (Table 9). Quercetin formed four hydrogen bonds with residue LYS 9, ASN 112, ARG 102, and VAL 109, and a salt bridge with residue MG 159 at the active site of *S. aureus* nucleoside diphosphate kinase. Additionally, it established a Pi-Pi stacking bond with residue PHE, as seen in Figure 5.

The lanosterol or sterol 14α-demethylase is an enzyme belonging to the cytochrome P450 (CYP) superfamily. It is

linked to the CYP51 family, which is a crucial enzyme involved in sterol production in eukaryotes. This enzyme is also a primary target for antifungal azoles and has potential for antiprotozoan chemotherapy. While 14α-demethylase can be found in many different organisms, it is mainly investigated in fungi due to its crucial function in regulating membrane permeability (Daum et al., 1998). In fungi, the enzyme CYP51 helps break down lanosterol, which makes a key building block that is then changed into ergosterol (Lepesheva and Waterman, 2007). This steroid then spreads throughout the cell, modifying plasma membrane permeability and stiffness in a similar manner to cholesterol in animals (Becher and Wirsel, 2012). Due to the essential role of ergosterol in fungal membranes, numerous antifungal drugs have been developed to hinder the activity of 14α-demethylase and thus impede the synthesis of this crucial molecule (Becher and Wirsel, 2012).

With a glide gscore of −7.84, kaempferol and myricitin had the most powerful effect on sterol 14-alpha demethylase (CYP51) from the harmful fungus *C. albicans*. Catechin came in second, with a glide gscore of −7.63 kcal/mol (Table 9). Kaempferol exhibited antifungal action by forming a singular bond with SER 378 residue in the active region of sterol 14-alpha demethylase (CYP51) derived from the pathogenic *C. albicans* (Figure 6).

TABLE 10 Glide gscore based on targeted caspase-3 protein and bioactive compounds of leaf extracts.

Caspase-3 (PDB ID: 3GJQ)	Leaf extracts bioactive compounds							
	Caffeic acid	Catechin	Kaempferol	Myricitin	Naringin	Rutin	Quercetin	Trans ferulic
Glide gscore (Kcal/mol)	−6.00	−6.51	−5.75	−5.80	−6.54	−7.00	−5.91	−6.07
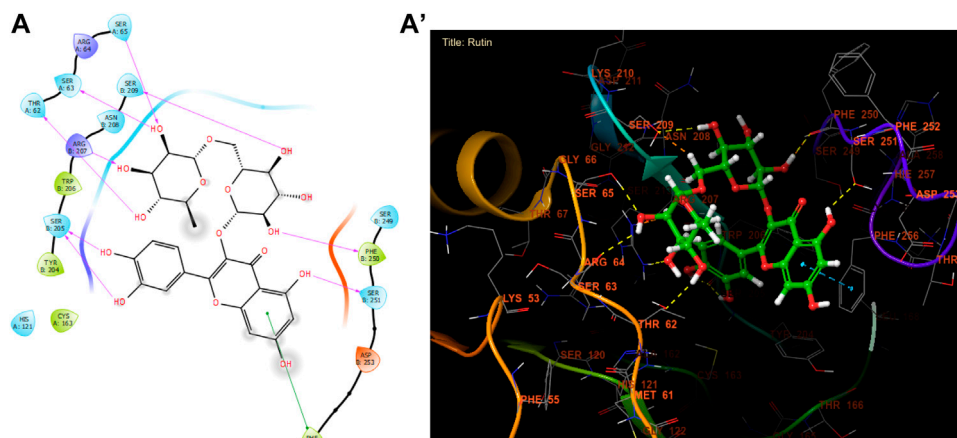
FIGURE 7
The ligand "Rutin" interacts with the active site of caspase-3 through the 2D viewer (A) and the 3D viewer (A').

Caspase-3 is crucial in the process of fighting cancer by acting as a key player in the pathway of programmed cell death, known as apoptosis, which is necessary for the controlled removal of cancer cells. Caspase-3 is activated by initiator caspases in both the internal and extrinsic pathways of apoptosis. This activation results in the breakdown of essential cellular components and ultimately leads to cell death. Inducing caspase-3 activation can initiate apoptosis in cancer cells, hence counteracting their survival mechanisms and resistance to traditional treatment. In addition, some anticancer strategies focus on enhancing caspase-3 activity using drugs that either increase pro-apoptotic signals or inhibit anti-apoptotic proteins inside the tumor microenvironment. Therefore, utilizing the activation of caspase-3 is a feasible approach in cancer treatment, aiming to induce cell death specifically in cancerous cells while minimizing harm to healthy organs (Asadi et al., 2022).

In our *in silico* study, Rutin, Naringin, and Catechin were the most active molecules in the active site of caspase-3 with a glide gscore of −7.00, −6.54, and −6.51 kcal/mol (Table 10). Furthermore, Rutin established nine hydrogen bonds with the residues, SER A 65, SER A 63, THR A 62, SER B 209, ARG B 207, SER B 205, PHE B 250, and SER B 251, and a single Pi-Pi stacking bond with the PHE B 256 residue in the active site of caspase-3 (Figure 7).

extracts from fig trees in Eastern Morocco revealed a diverse range of bioactive compounds, particularly polyphenols and flavonoids. These compounds contribute to the extracts' strong antioxidant capacity and antimicrobial activity against various bacterial and fungal strains. Specifically, the extracts demonstrated bactericidal effects against gram-positive strains (*S. aureus* and *B. subtilis subsp. spizenii*), gram-negative strains (*E. coli* and *P. aeruginosa*), and fungicidal effects against *C. albicans*. Additionally, the extracts exhibited significant cytotoxicity and a high selectivity index against three breast cancer cell lines: MCF-7, MDA-MB-231, and MDA-MB-436. Nevertheless, additional research, including *in vivo* tests, is necessary to validate these effects. Fig tree leaves have functional compounds and properties that make them suitable for use in the food industry, as they offer a variety of health benefits. Additionally, ongoing pharmaceutical research aims to identify new medications that exhibit improved efficacy and reduced adverse effects. *Ficus carica* is a plant with a variety of medicinal properties and potential therapeutic applications. Furthermore, their utilization could provide advantages to farmers by ensuring the sustainable administration of this waste. It is recommended to conduct further research on the incorporation of this leaf component and/or its extracts into food matrices for potential benefits.

4 Conclusion

According to the collected data, fig leaves are a sustainable source of industrially useful bioactive compounds with many potential applications. The analysis of hydro-ethanolic leaf

Data availability statement

The original contributions presented in the study are included in the article/supplementary material, further inquiries can be directed to the corresponding authors.

Ethics statement

The studies involving humans were approved by The Research Ethics Committee (03/22-LAPABE-10 and 4 March 2022). The studies were conducted in accordance with the local legislation and institutional requirements. The participants provided their written informed consent to participate in this study.

Author contributions

Funding

Acknowledgments

Conflict of interest

The authors declare that the research was conducted in the absence of any commercial or financial relationships that could be construed as a potential conflict of interest.

Generative AI statement

The author(s) declare that no Generative AI was used in the creation of this manuscript.

Publisher's note

All claims expressed in this article are solely those of the authors and do not necessarily represent those of their affiliated organizations, or those of the publisher, the editors and the reviewers. Any product that may be evaluated in this article, or claim that may be made by its manufacturer, is not guaranteed or endorsed by the publisher.

References

Abdel-Rahman, R., Ghoneimy, E., Abdel-Wahab, A., Eldeeb, N., Salem, M., Salama, E., et al. (2021). The therapeutic effects of Ficus carica extract as antioxidant and anticancer agent. *South Afr. J. Bot.* 141, 273–277. doi:10.1016/j.sajb.2021.04.019

Aboul-Soud, M. A., Ennaji, H., Kumar, A., Alfhili, M. A., Bari, A., Ahamed, M., et al. (2022). Antioxidant, anti-proliferative activity and chemical fingerprinting of centaurea calcitrapa against breast cancer cells and molecular docking of caspase-3. *Antioxidants* 11 (8), 1514. doi:10.3390/antiox11081514

Alam, M., Ahmed, S., Elasbali, A. M., Adnan, M., Alam, S., Hassan, M. I., et al. (2022). Therapeutic implications of caffeic acid in cancer and neurological diseases. *Front. Oncol.* 12, 860508. doi:10.3389/fonc.2022.860508

Aradhya, M. K., Stover, E., Velasco, D., and Koehmstedt, A. (2010). Genetic structure and differentiation in cultivated fig (Ficus carica L.). *Genetica* 138, 681–694. doi:10.1007/s10709-010-9442-3

Asadi, M., Taghizadeh, S., Kaviani, E., Vakili, O., Taheri-Anganeh, M., Tahamtan, M., et al. (2022). Caspase-3: structure, function, and biotechnological aspects. *Biotechnol. Appl. Biochem.* 69 (4), 1633–1645. doi:10.1002/bab.2233

Badgujar, S. B., Patel, V. V., Bandivdekar, A. H., and Mahajan, R. T. (2014). Traditional uses, phytochemistry and pharmacology of Ficus carica: a review. *Pharm. Biol.* 52 (11), 1487–1503. doi:10.3109/13880209.2014.892515

Becher, R., and Wirsel, S. G. (2012). Fungal cytochrome P450 sterol 14α-demethylase (CYP51) and azole resistance in plant and human pathogens. *Appl. Microbiol. Biotechnol.* 95, 825–840. doi:10.1007/s00253-012-4195-9

Bhattacharya, A., Sood, P., and Citovsky, V. (2010). The roles of plant phenolics in defence and communication during Agrobacterium and Rhizobium infection. *Mol. plant Pathol.* 11 (5), 705–719. doi:10.1111/j.1364-3703.2010.00625.x

Birjandian, E., Motamed, N., and Yassa, N. (2018). Crude methanol extract of Echinophora platyloba induces apoptosis and cell cycle arrest at S-phase in human breast cancer cells. *Iran. J. Pharm. Res. IJPR* 17 (1), 307–316.

Caglayan, C., Kandemir, F. M., Darendelioğlu, E., Yıldırım, S., Kucukler, S., and Dortbudak, M. B. (2019). Rutin ameliorates mercuric chloride-induced hepatotoxicity in rats via interfering with oxidative stress, inflammation and apoptosis. *J. Trace Elem. Med. Biol.* 56, 60–68. doi:10.1016/j.jtemb.2019.07.011

Çalişkan, O., and Polat, A. A. (2011). Phytochemical and antioxidant properties of selected fig (Ficus carica L.) accessions from the eastern Mediterranean region of Turkey. *Sci. Hortic.* 128 (4), 473–478. doi:10.1016/j.scienta.2011.02.023

Chamorro, F., Carpena, M., Fraga-Corral, M., Echave, J., Rajoka, M. S. R., Barba, F. J., et al. (2022). Valorization of kiwi agricultural waste and industry by-products by recovering bioactive compounds and applications as food additives: a circular economy model. *Food Chem.* 370, 131315. doi:10.1016/j.foodchem.2021.131315

Chaudhary, S., Chandrashekar, K. S., Pai, K. S., Setty, M. M., Devkar, R. A., Reddy, N. D., et al. (2015). Evaluation of antioxidant and anticancer activity of extract and fractions of Nardostachys jatamansi DC in breast carcinoma. *BMC Complement. Altern. Med.* 15, 50. doi:10.1186/s12906-015-0563-1

Chunyan, C., Bo, S., Ping, L., Jingmei, L., and Ito, Y. (2008). Isolation and purification of psoralen and bergapten from Ficus carica L. leaves by high-speed countercurrent chromatography. *J. Liq. Chromatogr. and Relat. Technol.* 32 (1), 136–143. doi:10.1080/10826070802548747

Chusri, S., Sinvaraphan, N., Chaipak, P., Luxsananuwong, A., and Voravuthikunchai, S. P. (2014). Evaluation of antibacterial activity, phytochemical constituents, and

cytotoxicity effects of Thai household ancient remedies. *J. Altern. Complementary Med.* 20 (12), 909–918. doi:10.1089/acm.2013.0173

Coulibaly, O., Yapo-Crezoit, C., Ira, B., Toure, A., and Soro, Y. (2020). Evaluation de l'activité antifongique des extraits totaux de Hugonia platysepala sur les pathogènes responsables de cryptococcoses et de candidoses chez les sujets infectés par le VIH. *J. Appl. Biosci.* 146 (1), 15046–15054. doi:10.35759/jabs.v146.7

Cunningham, T. M., Koehl, J. L., Summers, J. S., and Haydel, S. E. (2010). pH-dependent metal ion toxicity influences the antibacterial activity of two natural mineral mixtures. *PLoS One* 5 (3), e9456. doi:10.1371/journal.pone.0009456

Daum, G., Lees, N. D., Bard, M., and Dickson, R. (1998). Biochemistry, cell biology and molecular biology of lipids of *Saccharomyces cerevisiae*. *Yeast* 14 (16), 1471–1510. doi:10.1002/(sici)1097-0061(199812)14:16<1471::aid-yea353>3.0.co;2-y

Dehpour, A. A., Ebrahimzadeh, M. A., Fazel, N. S., and Mohammad, N. S. (2009). Antioxidant activity of the methanol extract of Ferula assafoetida and its essential oil composition. *Grasas aceites* 60 (4), 405–412. doi:10.3989/gya.010109

Divakar, D. D., Jastaniyah, N. T., Altamimi, H. G., Alnakhli, Y. O., Alkheraif, A. A., Haleem, S., et al. (2018). Enhanced antimicrobial activity of naturally derived bioactive molecule chitosan conjugated silver nanoparticle against dental implant pathogens. *Int. J. Biol. Macromol.* 108, 790–797. doi:10.1016/j.ijbiomac.2017.10.166

Do, Q. D., Angkawijaya, A. E., Tran-Nguyen, P. L., Huynh, L. H., Soetaredjo, F. E., Ismadji, S., et al. (2014). Effect of extraction solvent on total phenol content, total flavonoid content, and antioxidant activity of Limnophila aromatica. *J. food drug analysis* 22 (3), 296–302. doi:10.1016/j.jfda.2013.11.001

Elbouzidi, A., Taibi, M., Ouassou, H., Ouahhoud, S., Ou-Yahia, D., Loukili, E. H., et al. (2023). Exploring the multi-faceted potential of carob (ceratonia siliqua var. Rahma) leaves from Morocco: a comprehensive analysis of polyphenols profile, antimicrobial activity, cytotoxicity against breast cancer cell lines, and genotoxicity. *Pharmaceuticals* 16 (6), 840. doi:10.3390/ph16060840

Ergül, M., Ergül, M., Eruygur, N., Mehmet, A., and Esra, U. (2019). *In vitro* evaluation of the chemical composition and various biological activities of Ficus carica leaf extracts. *Turkish J. Pharm. Sci.* 16 (4), 401–409. doi:10.4274/tjps.galenos.2018.70037

Erlund, I. (2004). Review of the flavonoids quercetin, hesperetin, and naringenin. Dietary sources, bioactivities, bioavailability, and epidemiology. *Nutr. Res.* 24 (10), 851–874. doi:10.1016/j.nutres.2004.07.005

Espíndola, K. M. M., Ferreira, R. G., Narvaez, L. E. M., Silva Rosario, A. C. R., Da Silva, A. H. M., Silva, A. G. B., et al. (2019). Chemical and pharmacological aspects of caffeic acid and its activity in hepatocarcinoma. *Front. Oncol.* 9, 541. doi:10.3389/fonc.2019.00541

Floegel, A., Kim, D.-O., Chung, S.-J., Koo, S. I., and Chun, O. K. (2011). Comparison of ABTS/DPPH assays to measure antioxidant capacity in popular antioxidant-rich US foods. *J. food Compos. analysis* 24 (7), 1043–1048. doi:10.1016/j.jfca.2011.01.008

Gilani, A. H., Mehmood, M. H., Janbaz, K. H., Khan, A.-U., and Saeed, S. A. (2008). Ethnopharmacological studies on antispasmodic and antiplatelet activities of Ficus carica. *J. Ethnopharmacol.* 119 (1), 1–5. doi:10.1016/j.jep.2008.05.040

Hadini, A., Azdimousa, A., Khoulati, A., and Saalaoui, E. (2022). Valorization of Moroccan pistacia lentiscus L. Leaves: phytochemical and *in vitro* antioxidant activity evaluation compared to different altitudes. *Sci. World J.* 2022, 1–10. doi:10.1155/2022/6367663

Havsteen, B. H. (2002). The biochemistry and medical significance of the flavonoids. *Pharmacol. and Ther.* 96 (2-3), 67–202. doi:10.1016/s0163-7258(02)00298-x

Innocenti, G., Bettero, A., and Caporale, G. (1982). Determination of the coumarinic constituents of Ficus carica leaves by HPLC. *Il Farm. Ed. Sci.* 37 (7), 475–485.

Jeong, M.-R., Kim, H.-Y., and Cha, J.-D. (2009). Antimicrobial activity of methanol extract from Ficus carica leaves against oral bacteria. *J. Bacteriol. Virology* 39 (2), 97–102. doi:10.4167/jbv.2009.39.2.97

Kachmar, M. R., Oliveira, A. P., Valentão, P., Gil-Izquierdo, A., Domínguez-Perles, R., Ouahbi, A., et al. (2019). HPLC-DAD-ESI/MSn phenolic profile and *in vitro* biological potential of *Centaurium erythraea* Rafn aqueous extract. *Food Chem.* 278, 424–433. doi:10.1016/j.foodchem.2018.11.082

Kalefa, N. K., and Al-Shawi, A. A. (2023). The essential oils isolated from the fruit of Ficus carica induced reactive oxygen species and apoptosis of human liver cancer cells. *Egypt. J. Chem.* 66 (2), 257–265. doi:10.21608/ejchem.2022.136132.5995

Kamalakkannan, N., and Prince, P. S. M. (2006). Antihyperglycaemic and antioxidant effect of rutin, a polyphenolic flavonoid, in streptozotocin-induced diabetic wistar rats. *Basic and Clin. Pharmacol. and Toxicol.* 98 (1), 97–103. doi:10.1111/j.1742-7843.2006.pto_241.x

Khan, F., Bamunuarachchi, N. I., Tabassum, N., and Kim, Y.-M. (2021). Caffeic acid and its derivatives: antimicrobial drugs toward microbial pathogens. *J. Agric. Food Chem.* 69 (10), 2979–3004. doi:10.1021/acs.jafc.0c07579

Konyalıoğlu, S., Sağlam, H., and Kıvçak, B. (2005). α-tocopherol, flavonoid, and phenol contents and antioxidant activity of Ficus carica. leaves. *Pharm. Biol.* 43 (8), 683–686. doi:10.1080/13880200500383538

Kumar, A., Alfhili, M. A., Bari, A., Ennaji, H., Ahamed, M., Bourhia, M., et al. (2022). Apoptosis-mediated anti-proliferative activity of Calligonum comosum against human

breast cancer cells, and molecular docking of its major polyphenolics to Caspase-3. *Front. Cell Dev. Biol.* 10, 972111. doi:10.3389/fcell.2022.972111

Lafraxo, S., El Moussaoui, A., A Bin Jardan, Y., El Barnossi, A., Chebaibi, M., Baammi, S., et al. (2022). GC-MS profiling, *in vitro* antioxidant, antimicrobial, and *in silico* NADPH oxidase inhibition studies of essential oil of juniperus thurifera bark. *Evidence-Based Complementary Altern. Med.* 2022, 1–13. doi:10.1155/2022/6305672

Lansky, E. P., Harrison, G., Froom, P., and Jiang, W. G. (2005). Pomegranate (Punica granatum) pure chemicals show possible synergistic inhibition of human PC-3 prostate cancer cell invasion across Matrigel™. *Investig. new drugs* 23, 121–122. doi:10.1007/s10637-005-5856-7

Lee, I.-T., and Yang, C.-M. (2012). Role of NADPH oxidase/ROS in pro-inflammatory mediators-induced airway and pulmonary diseases. *Biochem. Pharmacol.* 84 (5), 581–590. doi:10.1016/j.bcp.2012.05.005

Lee, Y., and Cha, J. (2010). Synergistic antibacterial activity of fig (Ficus carica) leaves extract against clinical isolates of methicillin-resistant *Staphylococcus aureus*. 한국미생물· 생명공학회지 38 (4), 405–413.

Lepesheva, G. I., and Waterman, M. R. (2007). Sterol 14α-demethylase cytochrome P450 (CYP51), a P450 in all biological kingdoms. *Biochimica biophysica acta (BBA)-General Subj.* 1770 (3), 467–477. doi:10.1016/j.bbagen.2006.07.018

Li, X., Park, N. I., Xu, H., Woo, S.-H., Park, C. H., and Park, S. U. (2010). Differential expression of flavonoid biosynthesis genes and accumulation of phenolic compounds in common buckwheat (Fagopyrum esculentum). *J. Agric. Food Chem.* 58 (23), 12176–12181. doi:10.1021/jf103310g

Link, A., Balaguer, F., and Goel, A. (2010). Cancer chemoprevention by dietary polyphenols: promising role for epigenetics. *Biochem. Pharmacol.* 80 (12), 1771–1792. doi:10.1016/j.bcp.2010.06.036

McCord, J. M. (2000). The evolution of free radicals and oxidative stress. *Am. J. Med.* 108 (8), 652–659. doi:10.1016/s0002-9343(00)00412-5

Mirzaei, S., Gholami, M. H., Zabolian, A., Saleki, H., Farahani, M. V., Hamzehlou, S., et al. (2021). Caffeic acid and its derivatives as potential modulators of oncogenic molecular pathways: new hope in the fight against cancer. *Pharmacol. Res.* 171, 105759. doi:10.1016/j.phrs.2021.105759

Mohti, H., Taviano, M. F., Cacciola, F., Dugo, P., Mondello, L., Zaid, A., et al. (2020). Silene vulgaris subsp. macrocarpa leaves and roots from Morocco: assessment of the efficiency of different extraction techniques and solvents on their antioxidant capacity, brine shrimp toxicity and phenolic characterization. *Plant Biosystems-An Int. J. Deal. all Aspects Plant Biol.* 154 (5), 692–699. doi:10.1080/11263504.2019.1674404

Morovati, M. R., Ghanbari-Movahed, M., Barton, E. M., Farzaei, M. H., and Bishayee, A. (2022). A systematic review on potential anticancer activities of Ficus carica L. with focus on cellular and molecular mechanisms. *Phytomedicine* 105, 154333. doi:10.1016/j.phymed.2022.154333

Mulat, M., Pandita, A., and Khan, F. (2019). Medicinal plant compounds for combating the multi-drug resistant pathogenic bacteria: a review. *Curr. Pharm. Biotechnol.* 20 (3), 183–196. doi:10.2174/1872210513666190308133429

Nakilcioğlu-Taş, E., and Ötleş, S. (2021). Influence of extraction solvents on the polyphenol contents, compositions, and antioxidant capacities of fig (Ficus carica L.) seeds. *An. Acad. Bras. Ciências* 93 (1), e20190526. doi:10.1590/0001-3765202120190526

Nakyai, W., Pabuprapap, W., Sroimee, W., Ajavakom, V., Yingyongnarongkul, B.-E., and Suksamrarn, A. (2021). Anti-acne vulgaris potential of the ethanolic extract of Mesua ferrea L. flowers. *Cosmetics* 8 (4), 107. doi:10.3390/cosmetics8040107

Nerdy, N., Zebua, N. F., Xena, T., Kusuma, M., and Tanjung, R. F. B. (2023). The effect of ripeness level, storage and heating conditions on vitamin C in Fig (Ficus carica L.) fruit juice using bivoltammetry sensor. *J. Nat.* 23 (3), 162–173. doi:10.24815/jn.v23i3.32158

Nuri, Z., and Uddin, M. S. (2021). A review on nutritional values and pharmacological importance of Ficus carica. *J. Curr. Res. Food Sci.* 2 (1), 55–59. doi:10.33545/26631067.2020.v2.i1a.48

Oliveira, A. P., Silva, L. R., de Pinho, P. G., Gil-Izquierdo, A., Valentão, P., Silva, B. M., et al. (2010). Volatile profiling of Ficus carica varieties by HS-SPME and GC–IT-MS. *Food Chem.* 123 (2), 548–557. doi:10.1016/j.foodchem.2010.04.064

Oliveira, A. P., Valentão, P., Pereira, J. A., Silva, B. M., Tavares, F., and Andrade, P. B. (2009). Ficus carica L.: metabolic and biological screening. *Food Chem. Toxicol.* 47 (11), 2841–2846. doi:10.1016/j.fct.2009.09.004

Ou, S., and Kwok, K. C. (2004). Ferulic acid: pharmaceutical functions, preparation and applications in foods. *J. Sci. Food Agric.* 84 (11), 1261–1269. doi:10.1002/jsfa.1873

Ouahabi, S., Loukili, E. H., Elbouzidi, A., Taibi, M., Bouslamti, M., Nafidi, H.-A., et al. (2023). Pharmacological properties of chemically characterized extracts from mastic tree: *in vitro* and *in silico* assays. *Life* 13 (6), 1393. doi:10.3390/life13061393

Palmeira, L., Pereira, C., Dias, M. I., Abreu, R. M., Corrêa, R. C., Pires, T. C., et al. (2019). Nutritional, chemical and bioactive profiles of different parts of a Portuguese common fig (Ficus carica L.) variety. *Food Res. Int.* 126, 108572. doi:10.1016/j.foodres.2019.108572

Payyappallimana, U. (2010). Role of traditional medicine in primary health care: an overview of perspectives and challenging. 横浜国際社会科学研究= *Yokohama J. Soc. Sci.* 14 (6), 57–77.

Petruccelli, R., Ieri, F., Ciaccheri, L., and Bonetti, A. (2018). Polyphenolic profiling and chemometric analysis of leaves from Italian Ficus carica L. varieties. Polyphenol compounds in common fig. *Eur. J. Hortic. Sci.* 83 (2), 94–103. doi:10.17660/ejhs.2018/83.2.5

Philip, K., Malek, S. N., Sani, W., Shin, S. K., Kumar, S., Lai, H. S., et al. (2009). Antimicrobial activity of some medicinal plants from Malaysia. *Am. J. Appl. Sci.* 6 (8), 1613–1617. doi:10.3844/ajassp.2009.1613.1617

Prieto, P., Pineda, M., and Aguilar, M. (1999). Spectrophotometric quantitation of antioxidant capacity through the formation of a phosphomolybdenum complex: specific application to the determination of vitamin E. *Anal. Biochem.* 269 (2), 337–341. doi:10.1006/abio.1999.4019

Rădulescu, M., Jianu, C., Lukinich-Gruia, A. T., Mioc, M., Mioc, A., Șoica, C., et al. (2021). Chemical composition, *in vitro* and *in silico* antioxidant potential of Melissa officinalis subsp. officinalis essential oil. *Antioxidants* 10 (7), 1081. doi:10.3390/antiox10071081

Ramaroson, M.-L., Koutouan, C., Helesbeux, J.-J., Le Clerc, V., Hamama, L., Geoffriau, E., et al. (2022). Role of phenylpropanoids and flavonoids in plant resistance to pests and diseases. *Molecules* 27 (23), 8371. doi:10.3390/molecules27238371

Reddy, S., Barathe, P., Kaur, K., Anand, U., Shriram, V., and Kumar, V. (2022). Antimicrobial resistance and medicinal plant products as potential alternatives to antibiotics in animal husbandry. *Antimicrob. Resist. Underlying Mech. Ther. Approaches*, 357–384. doi:10.1007/978-981-16-3120-7_13

Riaz, U., Kharal, M. A., Murtaza, G., uz Zaman, Q., Javaid, S., Malik, H. A., et al. (2019). Prospective roles and mechanisms of caffeic acid in counter plant stress: a mini review. *Pak. J. Agric. Res.* 32 (1), 8. doi:10.17582/journal.pjar/2019/32.1.8.19

Sadia, H., Ahmad, M., Sultana, S., Abdullah, A. Z., Teong, L., Zafar, M., et al. (2014). Nutrient and mineral assessment of edible wild fig and mulberry fruits. *Fruits* 69 (2), 159–166. doi:10.1051/fruits/2014006

Sengupta, P., Raman, S., Chowdhury, R., Lohitesh, K., Saini, H., Mukherjee, S., et al. (2017). Evaluation of apoptosis and autophagy inducing potential of Berberis aristata, Azadirachta indica, and their synergistic combinations in parental and resistant human osteosarcoma cells. *Front. Oncol.* 7, 296. doi:10.3389/fonc.2017.00296

Shalaby, E. A., and Shanab, S. M. (2013). Antioxidant compounds, assays of determination and mode of action. *Afr. J. Pharm. Pharmacol.* 7 (10), 528–539. doi:10.5897/ajpp2013.3474

Soares, S., Brandão, E., Guerreiro, C., Soares, S., Mateus, N., and De Freitas, V. (2020). Tannins in food: insights into the molecular perception of astringency and bitter taste. *Molecules* 25 (11), 2590. doi:10.3390/molecules25112590

Stagos, D., Amoutzias, G. D., Matakos, A., Spyrou, A., Tsatsakis, A. M., and Kouretas, D. (2012). Chemoprevention of liver cancer by plant polyphenols. *Food Chem. Toxicol.* 50 (6), 2155–2170. doi:10.1016/j.fct.2012.04.002

Sudarshan, K., and Aidhen, I. S. (2017). Convenient synthesis of 3-glycosylated isocoumarins. *Eur. J. Org. Chem.* 2017 (1), 34–38. doi:10.1002/ejoc.201601264

Sudarshan, K., Manna, M. K., and Aidhen, I. S. (2015). Synthesis of 3-arylisocoumarins by using acyl anion chemistry and synthesis of thunberginol A and cajanolactone A. *Eur. J. Org. Chem.* 2015 (8), 1797–1803. doi:10.1002/ejoc.201403524

Taibi, M., Elbouzidi, A., Ouahhoud, S., Loukili, E. H., Ou-Yahya, D., Ouahabi, S., et al. (2023). Evaluation of antioxidant activity, cytotoxicity, and genotoxicity of ptychotis verticillata essential oil: towards novel breast cancer therapeutics. *Life* 13 (7), 1586. doi:10.3390/life13071586

Takahama, U., Tanaka, M., Hirota, S., and Yamauchi, R. (2009). Formation of an oxathiolone compound from rutin in acidic mixture of saliva and buckwheat dough: possibility of its occurrence in the stomach. *Food Chem.* 116 (1), 214–219. doi:10.1016/j.foodchem.2009.02.036

Taviano, M. F., Marino, A., Trovato, A., Bellinghieri, V., Melchini, A., Dugo, P., et al. (2013). Juniperus oxycedrus L. subsp. oxycedrus and Juniperus oxycedrus L. subsp. macrocarpa (Sibth. and Sm.) Ball."berries" from Turkey: comparative evaluation of phenolic profile, antioxidant, cytotoxic and antimicrobial activities. *Food Chem. Toxicol.* 58, 22–29. doi:10.1016/j.fct.2013.03.049

Tayoub, G., Al-Odat, M., Amer, A., Aljapawe, A., and Ekhtiar, A. (2018). Antiproliferative effects of Pancratium maritimum extracts on normal and cancerous cells. *Iran. J. Med. Sci.* 43 (1), 52–64.

Teixeira, D. M., Patão, R. F., Coelho, A. V., and da Costa, C. T. (2006). Comparison between sample disruption methods and solid–liquid extraction (SLE) to extract phenolic compounds from Ficus carica leaves. *J. Chromatogr. A* 1103 (1), 22–28. doi:10.1016/j.chroma.2005.11.047

Tikent, A., Laaraj, S., Marhri, A., Taibi, M., Elbouzidi, A., Khalid, I., et al. (2023). The antioxidant and antimicrobial activities of two sun-dried fig varieties (Ficus carica L.) produced in eastern Morocco and the investigation of pomological, colorimetric, and phytochemical characteristics for improved valorization. *Int. J. Plant Biol.* 14 (3), 845–863. doi:10.3390/ijpb14030063

Tkachenko, H., Buyun, L., Osadowski, Z., Honcharenko, V., and Prokopiv, A. (2017). Antimicrobial screening of the ethanolic leaves extract of Ficus carica L.(Moraceae)–an ancient fruit plant. *Plant Introd.* 73, 78–87. doi:10.5281/zenodo.2283589

Tourabi, M., Nouioura, G., Touijer, H., Baghouz, A., El Ghouizi, A., Chebaibi, M., et al. (2023). Antioxidant, antimicrobial, and insecticidal properties of chemically characterized essential oils extracted from mentha longifolia: *in vitro* and *in silico* analysis. *Plants* 12 (21), 3783. doi:10.3390/plants12213783

Trifunschi, S. I., Munteanu, M. F. F., Ardelean, D. G., Orodan, M., Osser, G. M., and Gligor, R. I. (2015). Flavonoids and polyphenols content and antioxidant activity of Ficus carica L. extracts from Romania. *Zb. Matice Srp. za Prir. nauke* 128, 57–65. doi:10.2298/zmspn1528057t

Tsuchiya, H., Sato, M., Miyazaki, T., Fujiwara, S., Tanigaki, S., Ohyama, M., et al. (1996). Comparative study on the antibacterial activity of phytochemical flavanones against methicillin-resistant *Staphylococcus aureus*. *J. Ethnopharmacol.* 50 (1), 27–34. doi:10.1016/0378-8741(96)85514-0

Ulewicz-Magulska, B., and Wesolowski, M. (2019). Total phenolic contents and antioxidant potential of herbs used for medical and culinary purposes. *Plant Foods Hum. Nutr.* 74, 61–67. doi:10.1007/s11130-018-0699-5

Vallejo, F., Marín, J., and Tomás-Barberán, F. A. (2012). Phenolic compound content of fresh and dried figs (Ficus carica L.). *Food Chem.* 130 (3), 485–492. doi:10.1016/j.foodchem.2011.07.032

Vaya, J., and Mahmood, S. (2006). Flavonoid content in leaf extracts of the fig (Ficus carica L.), carob (Ceratonia siliqua L.) and pistachio (Pistacia lentiscus L.). *Biofactors* 28 (3-4), 169–175. doi:10.1002/biof.5520280303

Vladimir-Knežević, S., Blažeković, B., Štefan, M. B., Alegro, A., Kőszegi, T., and Petrik, J. (2011). Antioxidant activities and polyphenolic contents of three selected Micromeria species from Croatia. *Molecules* 16 (2), 1454–1470. doi:10.3390/molecules16021454

Wang, G., Wang, H., Song, Y., Jia, C., Wang, Z., and Xu, H. (2004). Studies on anti-HSV effect of Ficus carica leaves. *Zhong yao cai= Zhongyaocai= J. Chin. Med. Mater.* 27 (10), 754–756.

Witkowski, A., Joshi, A. K., and Smith, S. (2002). Mechanism of the β-ketoacyl synthase reaction catalyzed by the animal fatty acid synthase. *Biochemistry* 41 (35), 10877–10887. doi:10.1021/bi0259047

Yang, Q., Liu, Y., Guo, Y., Jiang, Y., Wen, L., and Yang, B. (2023). New insights of fig (Ficus carica L.) as a potential function food. *Trends food Sci. and Technol.* 140, 104146. doi:10.1016/j.tifs.2023.104146

Yu, H., Rao, X., and Zhang, K. (2017). Nucleoside diphosphate kinase (Ndk): a pleiotropic effector manipulating bacterial virulence and adaptive responses. *Microbiol. Res.* 205, 125–134. doi:10.1016/j.micres.2017.09.001

Zand, R. S. R., Jenkins, D. J., and Diamandis, E. P. (2000). Steroid hormone activity of flavonoids and related compounds. *Breast cancer Res. Treat.* 62, 35–49. doi:10.1023/a:1006422302173

Zhang, Y.-M., and Rock, C. O. (2008). Membrane lipid homeostasis in bacteria. *Nat. Rev. Microbiol.* 6 (3), 222–233. doi:10.1038/nrmicro1839

Zhou, Y., Zheng, J., Li, Y., Xu, D.-P., Li, S., Chen, Y.-M., et al. (2016). Natural polyphenols for prevention and treatment of cancer. *Nutrients* 8 (8), 515. doi:10.3390/nu8080515

Zrouri, H., Elbouzidi, A., Bouhrim, M., Bencheikh, N., Kharchoufa, L., Ouahhoud, S., et al. (2021). Phytochemical analysis, antioxidant activity, and nephroprotective effect of the Raphanus sativus aqueous extract. *Mediterr. J. Chem.* 11 (1), 84–94. doi:10.13171/mjc02101211565lk

Check for updates

Cytotoxic activity of phenolic compounds in Bairui Granules obtained from the Chinese medicinal plant *Thesium chinense*

Shaobin Zhang, Hong Chen, Juan Hua* and Shihong Luo ⓘ *

Engineering Research Center of Protection and Utilization of Plant Resources, College of Bioscience and Biotechnology, Shenyang Agricultural University, Shenyang, Liaoning, China

The Chinese medicinal plant *Thesium chinense* Turcz. is the only plant used in the manufacture of Bairui Granules. However, to date, there has been very little research into the cytotoxic activity of active substances derived from Bairui Granules. Using chemical separation and spectroscopic methods, phenolic compounds 1–5 were identified as methyl-*p*-hydroxycinnamate, vanillin, kaempferol, isorhamnetin-3-*O*-glucoside, and astragalin, respectively. UPLC-MS/MS analyses revealed that compounds 1–5 were present at concentrations of 0.006 ± 0.002, 1.63 ± 0.87, 3.65 ± 0.83, 26.97 ± 11.41, and 27.67 ± 2.91 μg/g, respectively in Bairui Granules. Compounds 1, 2, and 4 were detected here for the first time in Bairui Granules. Using co-culture experiments, isorhamnetin-3-*O*-glucoside (4) was found to be beneficial to the proliferation Chinese hamster ovary (CHO) cells ($6.46\% \pm 0.86\%$ to $38.45\% \pm 9.04\%$), natural killer cells from human umbilical cord blood (UCB NK cells) ($25.68\% \pm 0.02\%$ to $70.81\% \pm 0.26\%$), and mesenchymal stem cells from human umbilical cord blood (UCB MSC cells) ($1.66\% \pm 0.05\%$ to $27.64\% \pm 0.51\%$) when the concentration was similar to that found in Bairui granules. Moreover, vanillin (2) was conducive to UCB NK cells proliferation ($28.21\% \pm 0.44\%$) at a concentration of 64 μg/mL, while maintaining cell viability. UCB NK cell proliferation was promoted at rates of $41.03\% \pm 0.48\%$ to $67.22\% \pm 0.68\%$ when astragalin (5) was present at low concentrations (8 and 16 μg/mL). Methyl-*p*-hydroxycinnamate (1) and vanillin (2) at different concentrations both had an inhibitory effect on the proliferation of natural killer cells from human peripheral blood (PB NK cells), but the inhibitory concentration ranges of these compounds were not equivalent to the concentration ranges of the compounds in Bairui Granules. These results provide a foundation for the safe use of *T. chinense* preparations.

GRAPHICAL ABSTRACT
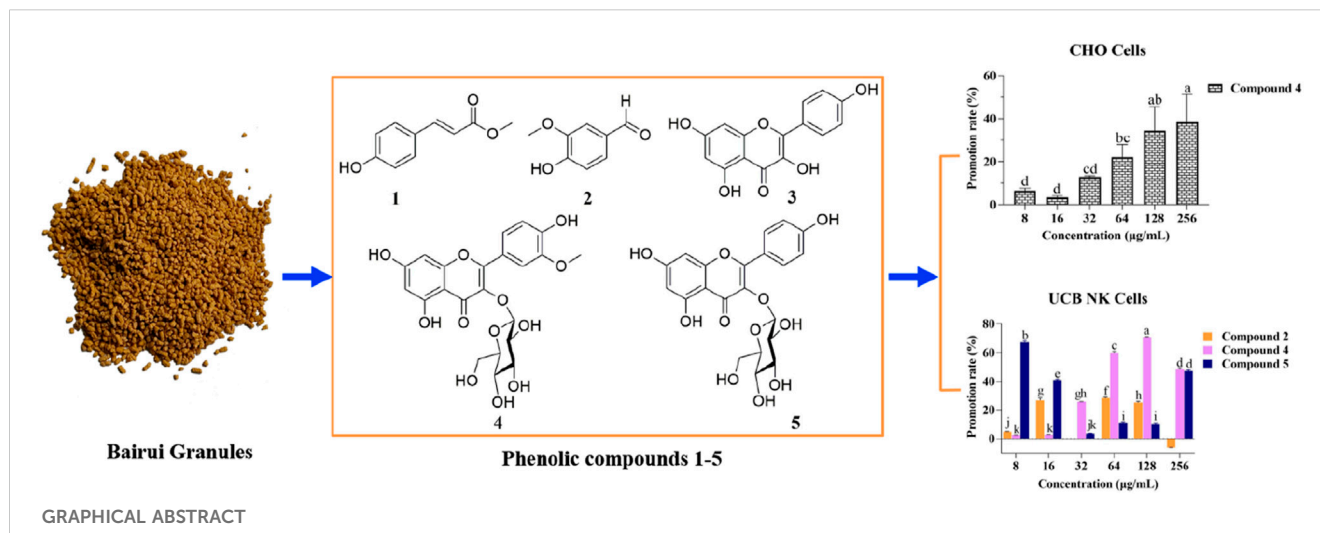
1 Introduction

Thesium chinense Turcz. Is a perennial herbaceous plant belonging to the Satalaceae family, and is widely distributed in eastern Asia (Shao et al., 2019). In China, *Thesium chinense* is used as a traditional Chinese medicine with many years of history, and described recorded in several Chinese ethnomedical monographs (Li G. H. et al., 2021). As early as the Song Dynasty, the Ben Cao Tu Jing described the usage and required dosage of *T. chinense* for clearing heat and detoxifying, tonifying the kidneys, and as an astringent essence (Liu et al., 2023). In 1950, other uses of *T. chinense*, including the treatment of head sores and cervical lymphadenitis, were recorded in the Guo Yao Ti Yao (Li G. H. et al., 2021). The decoction of the whole plant is used to treat mastopathy, headache resulting from pneumonia, stomach pain, and tuberculosis of cervical lymph nodes in Anhui and Fujian Provinces (Li G. H. et al., 2021; Parveen et al., 2007). Furthermore, *T. chinense* has also been made into modern pharmaceutical preparations, including Bairui Granules and Bairui Tablets, which are mainly used to treat tracheitis, rhinitis and colds. The Bairui Granules sales more than 400 million yuan in the last year. *T. chinense* has therefore played an important role as a Chinese herbal medicine at least since the Song Dynasty.

Because *T. chinense* has such widespread traditional uses, the active chemical substances in the plant have received widespread attention. *T. chinense* has been found to contain abundant secondary metabolites, including flavonoids, organic acids, alkaloids, and terpenoids (Liu et al., 2018; Lombard et al., 2020). The various biological activities of these chemical substances have been studied in *in vitro* and *in vivo* experiments (Li G. H. et al., 2021). The flavonoids are now considered to be the main functional substances in *T. chinense* (Cao et al., 2021), and total flavonoids and kaempferol are now taken to be the quality control standards for traditional medicinal preparations of *T. chinense* in China. These flavonoids not only exhibit anti-inflammatory and antioxidant activities, and inhibit the proliferation of cancer cells, but have also been found to play a certain role in protecting the liver and nerves (Khan et al., 2020; Soromou et al., 2012; Zhen et al., 2017). The phenolic

compounds isolated from *T. chinense* also exhibited certain anti-inflammatory effects (Liu et al., 2023). The positive therapeutic effects of *T. chinense* are therefore likely to be closely related to the chemical substances it contains. However, there is little research on the active substances present in Bairui Granules, which are prepared with *T. chinense* as their sole herbal ingredient.

The human body contains many types of immune cells and stem cells, including natural killer cells (NK cells) and mesenchymal stem cells (MSC cells) (Musina et al., 2005; Strowig et al., 2010). NK cells have the ability to clear leukemia and tumor cells, and MSC cells have strong hematopoietic support function and are able to differentiate into various different types of human cells as required (Steward and Kelly, 2014; Vyas et al., 2023). Chinese hamster ovary cells (CHO cells) are the most widely applied mammalian recombinant protein cell line in immunology (Róisín et al., 2020). However, it is not yet known whether the chemical substances present in *T. chinense* have an impact on human immune cells or stem cells. In this study, we focused on flavonoids and phenolic compounds present in Bairui Granules and investigated whether these have an impact on mammalian expression vectors, immune cells, and stem cells, further providing reference for the correct and safe dosage in preparations of *T. chinense*.

2 Materials and methods

2.1 Plant materials and test cell lines

Whole dried *T. chinense* plants were purchased from the Hebei Baoding Anguo Medicinal Material Wholesale Market, and were identified by Professor Bo Qu. Chinese hamster ovary cells (CHO cells), natural killer cells from human umbilical cord blood (UCB NK cells), natural killer cells from human peripheral blood (PB NK cells), and mesenchymal stem cells from human umbilical cord blood (UCB MSC cells) were provided by the Cell Preparation Center of Qinhuangdao Weiming Health City Development Co., Ltd. CHO cells were cultured in RPMI-1640 medium (Hyclone) containing 10% fetal bovine serum (Gibco). NK cells and MSC cells

were cultured with the corresponding cell culture kits. The NK and MSC cell culture kits were purchased from the Beijing Tongli Haoyuan Biotechnology Co., Ltd. FITC-conjugated anti-human CD3 antibody and APC-conjugated anti-human CD56 antibody were purchased from Meitianni Biotechnology Co., Ltd.

2.2 Isolation and identification of phenolic compounds from *Thesium chinense*

The entire dried *T. chinense* plants (15.0 Kg) were subjected to a methanol extraction. The resulting extract was then concentrated under a vacuum and was treated with an equal volume of ethyl acetate (1:1, v/v). The crude ethyl acetate fraction (204.0 g) was purified on a silica gel column using eluents (dichloromethane/methanol, 1:0–0:1), and resulting in five fractions (Fr.-1–Fr.-5). Fr.-2 (29.0 g) was passed through an MCI gel column chromatography column (methanol/water, 70:30–100:0) to get four parts (Fr.-2.1–Fr.-2.4). Fr-2.1 (19.4 g) was separated on a silica gel column with petroleum ether/acetone elution (15:1, v/v) to obtain six fractions (Fr.-2.1.1–Fr.-2.1.6). Fr.-2.1.5 (4.5 g) and Fr.-2.1.6 (6.5 g) were passed separately through a Sephadex LH-20 column to get four parts (Fr.-2.1.5.1–Fr.-2.1.5.4) and five parts (Fr.-2.1.6.1–Fr.-2.1.6.5), respectively. Fr.-2.1.5.2 (320.0 mg) was purified using semi-preparative HPLC with DAD detector (methanol/water, 45:55) to yield compound 1 (50.7 mg). Fr.-2.1.5.3 (452.2 mg) was purified using semi-preparative HPLC with DAD detector (methanol/water, 25:75) to yield compound 2 (90.4 mg). Fr.-2.1.5.4 (783.0 mg) was purified using semi-preparative HPLC with DAD detector (methanol/0.2% acid water, 58:42) to yield compound 3 (110.4 mg), and Fr.-2.1.6.3 (2.4 g) was purified using semi-preparative HPLC with DAD detector (methanol/0.2% acid water, 41:59) to yield compounds 4 (156.0 mg) and 5 (175.3 mg).

2.3 Qualitative and quantitative analysis of compounds one to five in Bairui Granules

Samples of Bairui Granules (Anhui Jiuhua Huayuan Pharmaceutical Co., Ltd.) were prepared for detection of the compounds. About 0.2 g sample was subjected three times in succession to a methanol extraction in an ultrasonic bath, each time for 45 min. The obtained methanol extract was then concentrated under vacuum until dry. Then, the dissolved liquid (500 μL chromatographic methanol) was filtered through 0.22 μm filter, and the prepared samples were finally analyzed on the UPLC-MS/MS (Shimadzu LCMS-8050). Briefly, 10 μL samples were injected into Shim-pack GIST C_{18} column (2 μm, 100 × 2.1 mm, 0.2 mL/min), and the column temperature was maintained at 40 °C. A (0.1% acid water) and B (acetonitrile) were selected as mobile phases, and the elution procedure was as follows: 0–12 min, from 5% B to 95% B; 12–13 min, 95% B; 13–14 min, from 95% B to 5% B; 14–17 min, 5% B. The ESI procedure was as follows: dry gas flow rate 10 L/min, heating block temperature 450 °C; interface temperature 300 °C; heating gas flow rate 10 L/min; atomizing gas flow rate 3 L/min; (Yang et al., 2022). Compounds one to five were monitored using multiple reaction monitoring (MRM) mode, and their related

parameters are given in Supplementary Table S1. The calibration curves for compounds one to five are shown in Supplementary Table S2.

2.4 *In vitro* cytotoxicity assay

The compounds to be assayed were dissolved in DMSO (0.5% of the total volume). Four cell suspensions (CHO cells, UCB NK cells, PB NK cells, and UCB MSC cells) were prepared in advance. Each of the compounds was diluted to the final concentrations: 8, 16, 32, 64, 128, and 256 μg/mL, and were added to a 24-well plate, in which compound 4 prepared for CHO cells, compounds 2, 4, and 5 prepared for UCB NK cells, compounds 1, 2, and 4 prepared for PB NK and UCB MSC cells. Each well included cell suspension, cell culture medium and compound solution, at the ratio of 100:99:1. 500 μL of cell culture medium/DMSO (99:1, v/v) was added to 500 μL of cell suspension as a control (Li et al., 2022). The number of cells in each well was approximately 1.0E+06, and each treatment included three biological replicates. The co-cultured cell suspensions were then cultured in a carbon dioxide incubator (5% CO_2, 37°C, saturated humidity) for 48 h. After the cultivation step was complete, 10 μL of co-cultured cell suspension was added to 0.4% trypan blue (10 μL) and a uniform mixture was prepared. Subsequently, 10 μL of this mixture was then injected into each cavity of the slide and maintained for 30 s. Finally, the cell morphology was observed using an inverted microscope (Nikon) and cells were counted using a cell counter (Thermo).

2.5 Detection of PB NK cell surface markers

PB NK cells were cultured for 48 h according to the method described above. The co-cultured cell suspension (about 1.0E+06) was moved to a EP tube (1.5 mL). The samples were centrifuged at 1,500 rpm for 3 min, an then the supernatant was removed and discarded. The remaining cells were re-suspended using 1,000 μL of phase buffer saline (PBS) and then centrifuged at 1,500 rpm for 3 min. The supernatant was then removed and discarded. This process was repeated twice. Finally, the obtained cells were re-suspended in 1,000 μL of PBS to obtain a new cell suspension. 100 μL of the new cell suspension was injected into each of three EP tubes, with one tube containing 5 μL of FITC-conjugated anti-human CD3 antibody, one containing 5 μL of APC-conjugated anti-human CD56 antibody, and with one tube serving as a blank control (5 μL PBS). Evenly mixed samples were incubated at 4 °C in the dark for 10 min. After incubation, each tube of cells was re-suspended using the above method, resulting in a new cell suspension with a final volume of 500 μL. Finally, the samples were analyzed using flow cytometry (MiltenyiBiotecB. V. and Co. KG).

2.6 Statistical analyses

Data were analyzed using PASW Statistics 19 and GraphPad. Prism 9. If the two groups of data conformed to a normal distribution, independent samples *t*-tests were used to investigate comparisons between two sets of data, and comparisons among
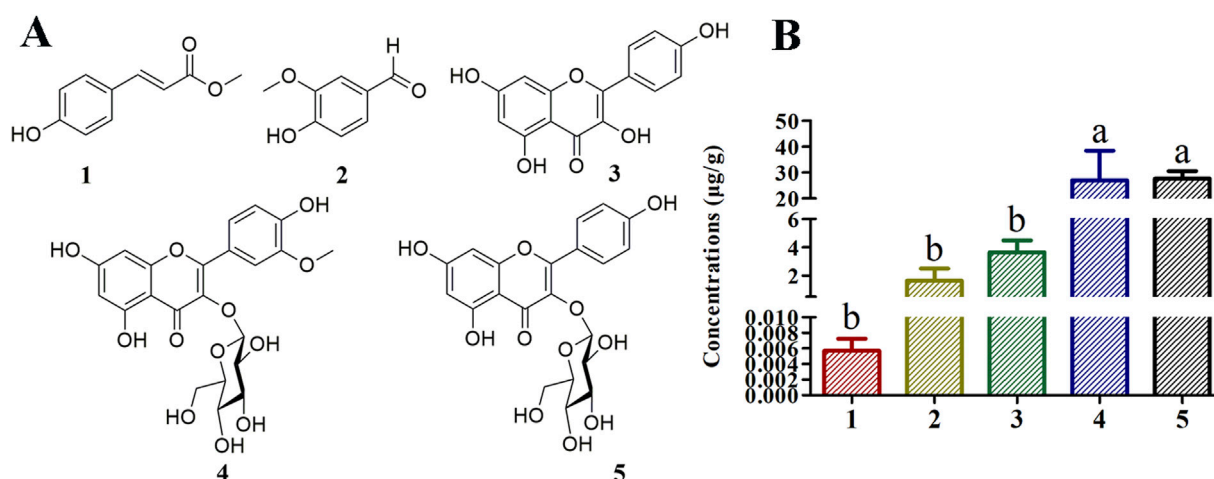
FIGURE 1
Structures of compounds isolated from *Thesium chinense* and quantitative analysis of their concentrations in Bairui Granules. **(A)** Chemical structures of flavonoid and phenolic compounds 1–5; **(B)** Concentrations of compounds one to five in Bairui Granules. Mean differences were compared using one-way ANOVA with Tukey's test. The different small letters **(A, B)** represent significant differences at the $p < 0.05$ level. The results shown represent the means $\pm$ standard deviation.

three or more groups were made using one-way ANOVAs with Tukey's tests. Differences were considered to be statistically significant if $p < 0.05$. The values given represent the mean $\pm$ standard deviation (SD).

3 Results

3.1 Structural identification of phenolic compounds one to five from *Thesium chinense*

Chemical separation and spectroscopic methods allowed the identification of compounds 1–5 as methyl-*p*-hydroxycinnamate (Kwon and Kim, 2003), vanillin (Pironti et al., 2021), kaempferol (Singh et al., 2008), isorhamnetin-3-*O*-glucoside (Fico et al., 2007), and astragalin (Wei et al., 2011), respectively (Supplementary Tables S3–S4; Figure 1A). Compounds 1 and 2 are phenolics, and compounds three to five are flavonoids. In this study compounds 2 and 4 have been isolated for the first time from *T. chinense*.

3.2 Qualitative and quantitative analyses of compounds one to five in Bairui Granules

To determine concentrations of compounds one to five present in Bairui Granules, an extract of Bairui Granules was assessed using an UPLC-MS/MS. Prepared samples were all analyzed using an external standard. The retention times of compounds one to five were found to be 7.864, 6.215, 8.112, 6.772, and 6.068 min (Figure 2), respectively, and compounds one to five were present in Bairui Granules at concentrations of 0.006 ± 0.002, 1.63 ± 0.87, 3.65 ± 0.83, 26.97 ± 11.41, and 27.67 ± 2.91 μg/g, respectively (Figure 1B, 2A–E). These results suggested that the concentrations of the flavonoid compounds three to five in Bairui Granules were higher than those

of the phenolic compounds 1 and 2. This study represents that compounds 1, 2, and 4 have been detected for the first time in Bairui Granules.

3.3 Effect of compound 4 on the proliferation of CHO cells

In order to determine the effect of compound 4 on the proliferation of CHO cells, different concentrations of compound 4 were co-cultured with CHO cells for 48 h. Examination with an inverted microscope revealed that after the CHO cells were treated with compound 4 at different concentrations, the cells remained round and bright, which was consistent with the morphology of the control group (Supplementary Figure S1). Treatment with compound 4 at concentrations of 8, 16, 32, 64, 128, and 256 μg/mL led to increases in CHO cell proliferation, with the promotion rates being 6.46 ± 0.86, 3.44 ± 0.43, 12.91 ± 0.43, 22.09 ± 4.16, 34.43 ± 7.89, and 38.45% ± 9.04%, respectively (Figure 3A). Treatment with compound 4 at concentrations of 8, 16, and 64 μg/mL had no obvious effect on CHO cells viability compared with the control. However, treatment with compound 4 at concentrations of 128 and 256 μg/mL significantly promoted the viability of CHO cells ($p < 0.01$) (Figure 3B). The above results indicated that at the concentrations present in Bairui Granules, compound 4 was beneficial to the proliferation of CHO cells.

3.4 Effects of compounds 2, 4, and 5 on the proliferation of UCB NK cells

In order to investigate the effects of compounds 2, 4, and 5 on the proliferation of UCB NK cells, compounds 2, 4, and 5 at different concentrations were separately co-cultured with UCB NK cells for 48 h. UCB NK cell morphology was not affected under any
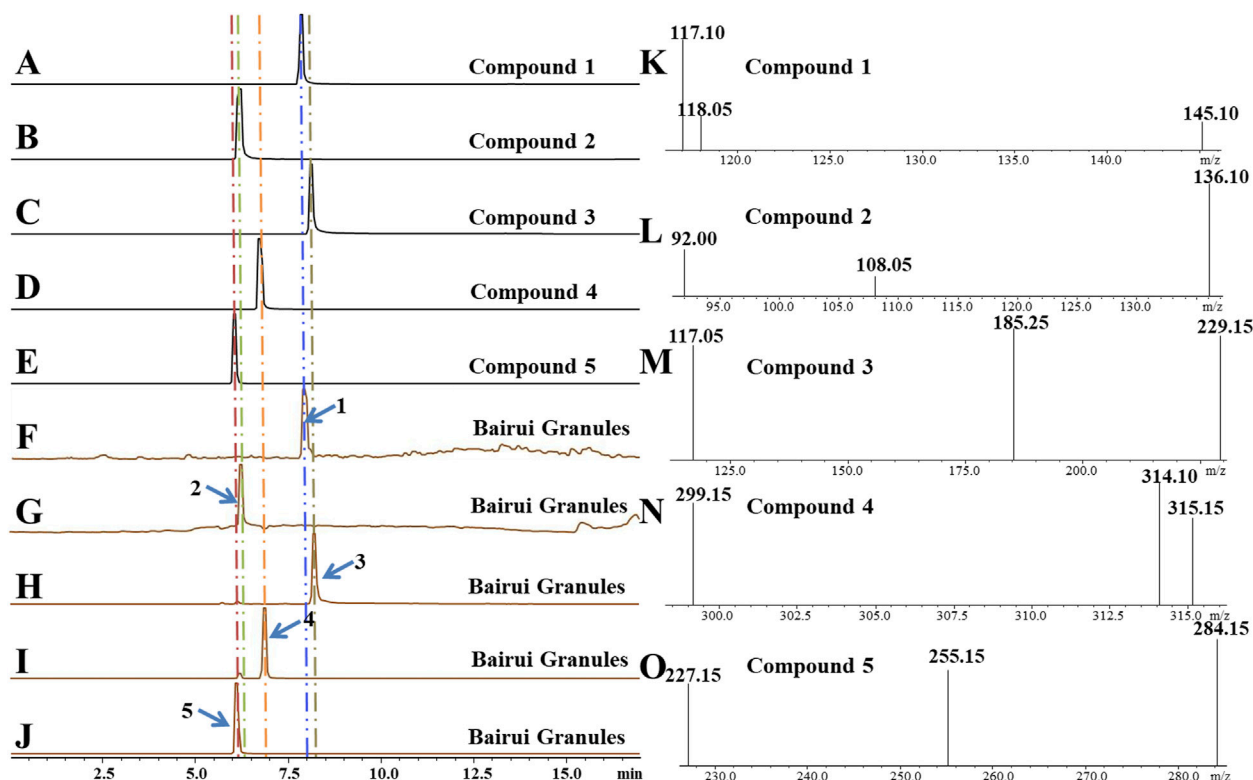
FIGURE 2
Qualitative analysis of in Bairui Granules using UPLC-MS/MS with an MRM-model. **(A-E)** Chromatogram of compounds 1–5; **(F-J)** Chromatograms of the Bairui Granules extracts; **(K-O)** Mass spectra of compounds one to five.
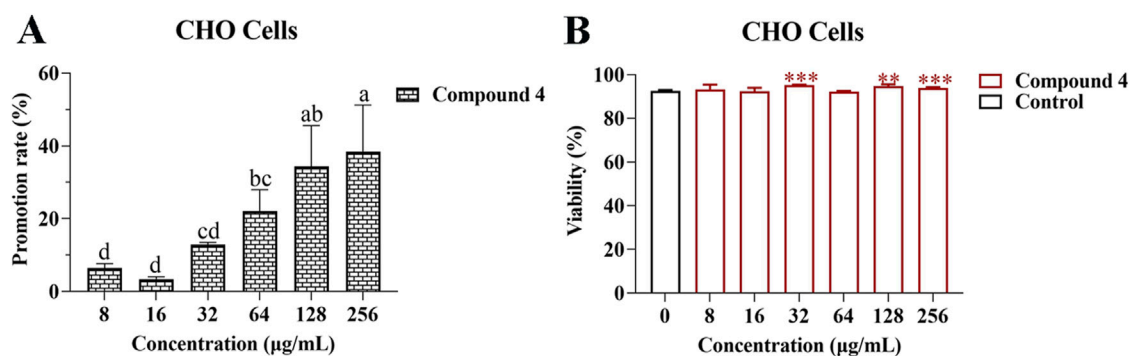
FIGURE 3
Effects of compound 4 on the proliferation and viability of CHO cells. **(A)** Promotion rate of compound 4 at different concentrations on the proliferation of CHO cells; **(B)** Effect of compound 4 at different concentrations on the viability of CHO cells. Mean differences were compared using one-way ANOVA with Tukey's test. The different small letters **(A, B)** represent significant differences at the $p < 0.05$ level. Double or triple asterisks (** or ***) indicate significant differences between the control group and other treatments. ** Indicates $p < 0.01$. ***$p < 0.001$.

concentrations of compounds 2, 4, or 5 (Supplementary Figures S2–S4).

When the concentrations of compound 2 were 16, 64, and 128 μg/mL, the rate of promotion of UCB NK cell proliferation remained within a certain range (25.09% ± 0.56% to 28.21% ± 0.44%). However, at a concentration of 64 μg/mL, compound 2 could significantly promote the viability of UCB NK cells

compared with the control, while at a concentration of 128 μg/mL, compound 2 exhibited a significant inhibitory effect.

At concentrations of 32, 64, 128, and 256 μg/mL, compound 4 was able to promote the proliferation of UCB NK cells, with promotion rates ranging from 25.68% ± 0.02% to 70.81% ± 0.26%. However, at the same concentrations, compound 4 exhibited an inhibitory effect on the viability of UCB NK cells.

FIGURE 4
Effects of compounds 2, 4, and 5 on the proliferation and viability of UCB NK cells. **(A)** Promotion rate of compounds 2, 4, and 5 at different concentrations on the proliferation of UCB NK cells; **(B)** The effects of compounds 2, 4, and 5 at different concentrations on the viability of UCB NK cells. Mean differences were compared using one-way ANOVA with Tukey's test. The different small letters (a, b, c, d, e, f, g, h, i, j, and k) represent significant differences at the $p < 0.05$ level. Double or triple asterisks (** or ***) indicate significant differences between the control group and other treatments. ** Indicates $p < 0.01$. ***$p < 0.001$.
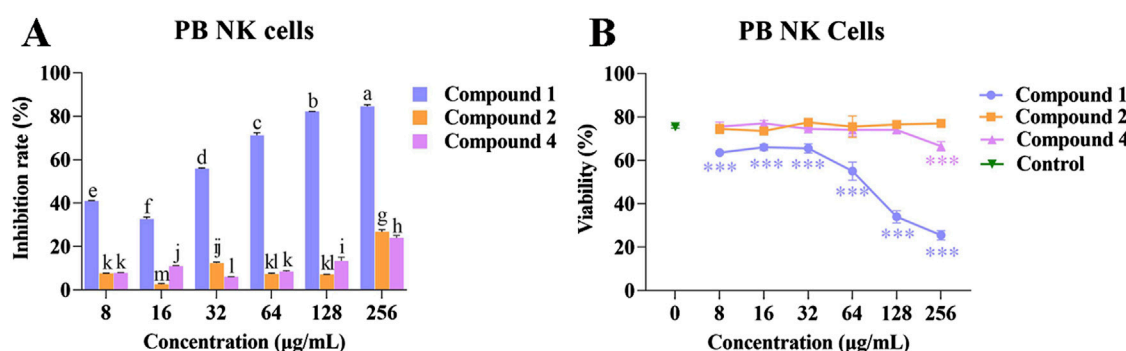
FIGURE 5
Effects of compounds 1, 2, and 4 on the proliferation and viability of PB NK cells. **(A)** Inhibition rate of compounds 1, 2, and 4 at different concentrations on the proliferation of PB NK cells; **(B)** The effects of compounds 1, 2, and 4 at different concentrations on the viability of PB NK cells. Mean differences were compared using one-way ANOVA with Tukey's test. The different small letters (a, b, c, d, e, f, g, h, i, j, k, and l) represent significant differences at the $p < 0.05$ level. Triple asterisks (***) indicate significant differences between the control group and other treatments. ***$p < 0.001$.

When compound 5 was present at low concentrations (8 and 16 μg/mL), the promotion rate of UCB NK cell proliferation ranged from 41.03% ± 0.48% to 67.22% ± 0.68%, but the compound exhibited an inhibitory effect on viability of the cells at these concentrations. At a concentration of 256 μg/mL, compound 5 promoted cell proliferation, but had no effect on cell viability (Figures 4A, B). These results showed that the phenolic compound 2 was conducive to the proliferation of UCB NK cells while maintaining normal cell morphology and viability at a concentration of 64 μg/mL.

3.5 The effects of compounds 1, 2, and 4 on the proliferation of PB NK cells

Compounds 1, 2, and 4 at different concentrations were co-cultured with PB NK cells to determine their effects on cell proliferation. Following co-culture for 48 h with compounds 1, 2, and 4 at different concentrations, no effect on PB NK cell morphology was observed (Supplementary Figures S5–S7).

However, when the concentration of compound 1 was increased, the inhibition rate of PB NK cells proliferation also gradually increased, and the cell viability gradually decreased.

The inhibitory rate of compound 2 on the proliferation of PB NK cells (2.70% ± 0.22% to 26.80% ± 0.68%) was comparable to that of compound 4 (6.08% ± 0.04% to 23.96% ± 0.80%). Compounds 2 and 4 at other concentrations had no effect on viability of PB NK cells compared with the control, although at a concentration of 256 μg/mL, compound 4 had an inhibitory effect on cell viability (Figures 5A, B). The above results suggested that compound 1 has a higher inhibitory effect on the proliferation of PB NK cells than compounds 2 and 4.

3.6 The effects of compounds 1, 2, and 4 on the proliferation of UCB MSC cells

Compounds 1, 2, and 4 at different concentrations were co-cultured with UCB MSC cells to investigate their effects on cell
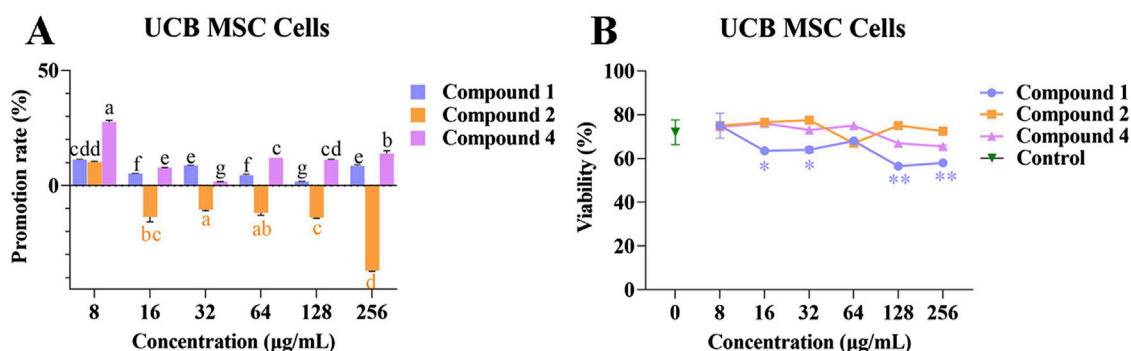
FIGURE 6
The effects of compounds 1, 2, and 4 on the proliferation and viability of UCB MSC cells. **(A)** Effect of compounds 1, 2, and 4 at different concentrations on the proliferation of UCB MSC cells; **(B)** The effects of compounds 1, 2, and 4 at different concentrations on the viability of UCB MSC cells. Mean differences were compared using one-way ANOVA with Tukey's test. The different small letters (a, b, c, d, e, f, and g) represent significant differences at the $p < 0.05$ level. Single or double asterisks (* or **) indicate significant differences between the control group and other treatments. *$p < 0.05$. ** Indicates $p < 0.01$.

proliferation. Following co-culture for 48 h with compounds 1, 2, and 4 at different concentrations, the UCB MSC cells were spindle shaped, which is consistent with normal MSC cell morphology (Supplementary F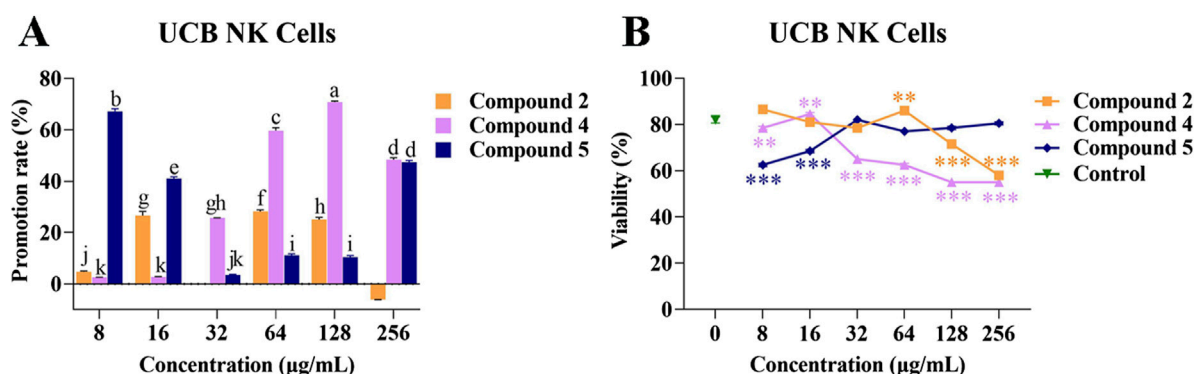igures S8–S10). The promotion rates of compounds 1 and 4 at different concentrations on UCB MSC cell proliferation range from 1.64% ± 0.19% to 11.28% ± 0.16% and from 1.66% ± 0.05% to 27.64% ± 0.51%, respectively.

Compound 2 inhibited UCB MSC cell proliferation at concentrations of 16, 32, 128, and 256 μg/mL, but had a promoting effect at a concentration of 8 μg/mL (Figure 6A). Compared with the control, compound 1 had a significant inhibitory effect on UCB MSC cell viability at concentrations of 16, 32, 128, and 256 μg/mL ($p < 0.05$), while compounds 2 and 4 had no significant effect on cell viability (Figure 6B). The above results indicate that compound 4 is able to promote UCB MSC cells proliferation without affecting cell viability.

3.7 The effects of compounds 1, 2, and 4 on the expression of PB NK cell markers

We next wanted to investigate the effects of low concentrations of compounds 1, 2, and 4 on the expression of NK cell markers. Low concentrations of compounds 1, 2, and 4 were co-cultured separately with PB NK cells. In human pathology, the proportion of CD3$^-$CD56$^+$ is commonly used as a proxy for NK cells in the diagnosis of certain diseases. The proportion of NK cells with a CD3$^-$CD56$^+$ cell phenotype when cultured in the presence of compound 1 at a concentration of 32 μg/mL was 54.46% (Figure 7A). Similarly, after 48 h of co-culture of PB NK cells with compound 2 at concentrations of 8 and 16 μg/mL, the proportion of cells with the CD3$^-$CD56$^+$ phenotype were 69.80% and 69.40%, respectively, while the proportions of cells co-cultured with this phenotype following co-culture with compound 4 under the same conditions were 70.94% and 70.32%, respectively (Figures 7B–E). These results suggest that compound 1 had an inhibitory effect on PB NK cell differentiation compared to the control (72.10%) at a concentration of 32 μg/mL.

4 Discussion

4.1 Bairui granules contain a high diversity of phenolic compounds

T. chinense is an important traditional Chinese medicine. When applied as a crude drug, *T. chinense* is able to significantly reduce ear swelling caused by xylene in mice (Yuan et al., 2006). Moreover, a concentration of the methanol extract of *T. chinense* is able to significantly reduce the edema in mouse paws induced by carrageenan, and reduces xylene-induced ear edema in mice (Parveen et al., 2007). The chemical substances present in this plant have been widely studied and identified. At present, most of the compounds isolated from *T. chinense* have been flavonoids and phenylpropanoids (Li G. H. et al., 2021; Liu et al., 2023). In this study, we isolated and identified two phenolic compounds and three flavonoids from *T. chinense*, with vanillin (2) and isorhamnetin-3-*O*-glucoside (4) isolated from this plant for the first time here. The concentrations of these compounds in Bairui Granules were further determined using UPLC-MS/MS.

4.2 Phenolic compounds exhibit diverse biological activities

Flavonoids in *T. chinense* have abundant biological activity. Previous research on the activities of kaempferol (3) and astragalin (5) mainly focused on their anti-inflammatory and analgesic properties (Ramanan et al., 2016; Sudarshan and Aidhen, 2016). Kaempferol (3) inhibited the writhing reaction following abdominal contraction tests induced by a certain concentration of acetic acid in mice (Parveen et al., 2007). Certain concentrations of astragalin (5) were able to inhibit the infiltration of inflammatory cells, reduce breast congestion and edema and inhibit the release of inflammatory cytokines in a mastitis mouse model (Li et al., 2013). Moreover, astragalin (5) was also able to block the NF-κB signaling pathway to combat colitis (Han et al., 2020). Diverse biological activities have also been observed in methyl-*p*-hydroxycinnamate (1), vanillin (2), and
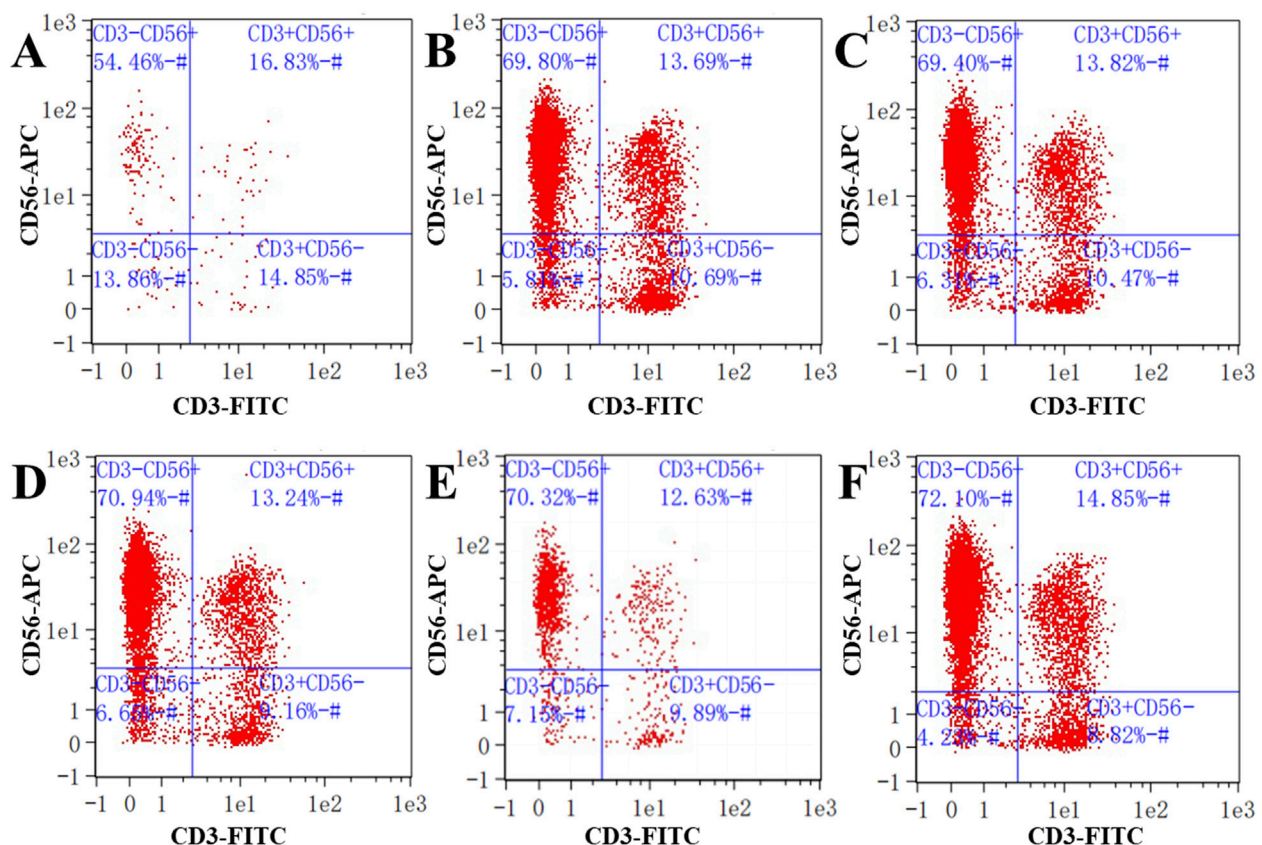
FIGURE 7
Detection of NK cell surface markers. **(A)** Expression of NK cell biomarkers in cells co-cultured with compound 1 at a concentration of 32 μg/mL; **(B, C)** Expression of NK cell biomarkers in cells co-cultured with compound 2 at concentrations of 8 and 16 μg/mL; **(D, E)** Expression of NK cell biomarkers in cells co-cultured with compound 4 at concentrations of 8 and 16 μg/mL; **(F)** Expression of NK cell biomarkers in the control. CD3⁻ represents CD3 negative; CD56⁺ represents CD56 positive.

isorhamnetin-3-*O*-glucoside (4). Methyl-*p*-hydroxycinnamate (1) was found to inhibit inflammation of RAW 264.7 macrophages under LSP induced stimulation (Vo et al., 2014). Vanillin (2) and isorhamnetin-3-*O*-glucoside (4) both had anticancer, anti-inflammatory, and antibacterial effects. Furthermore, vanillin (2) also has a protective effect on nerves and blood (Arya et al., 2021; Du et al., 2014). From this, it can be seen that research into *T. chinense* mainly focuses on how the component chemical substances exert their therapeutic effects. However, Bairui Granules are a medical preparation, whose only herbal ingredient is *T. chinense*, and to date there has been little research into the effects of the active substances on mammalian expression vectors, human immune cells, and stem cells.

4.3 Phenolics are the most biologically active substances in Bairui Granules

Flavonoids and phenolic compounds have certain effects on mammalian expression vectors, human immune cells, and stem cells (Burkard et al., 2017; Ozdal et al., 2018). Flavonoids from *Astragalus complanatus* R.Br. ex Bunge. seeds significantly promoted the proliferation of NK cells (Han et al., 2015), and the flavonoid quercetin has a close relationship with the

differentiation of MSC cells (Yu et al., 2010). In addition, phenolic compounds are able to increase NK cell activity significantly and can also serve as antioxidants to protect MSC cells (Kilani Jaziri et al., 2016; Li H. S. et al., 2021). In this study, the methyl-*p*-hydroxycinnamate (1), vanillin (2), and isorhamnetin-3-*O*-glucoside (4) present in Bairui Granules were qualitatively and quantitatively studied for the first time. Importantly, isorhamnetin-3-*O*-glucoside (4) was able to promote the proliferation of CHO cells, UCB NK cells, and UCB MSC cells when its concentration was close to that found in the Bairui Granules. Meanwhile, methyl-*p*-hydroxycinnamate (1) was conducive to the proliferation of UCB MSC cells, and vanillin (2) and astragalin (5) at different concentrations all promoted the proliferation of UCB NK cells. These results indicated that methyl-*p*-hydroxycinnamate (1), vanillin (2), isorhamnetin-3-*O*-glucoside (4), and astragalin (5) were potentially the active substances in Bairui Granules. However, not all flavonoids and phenolic compounds promote the activity of immune cells (Perche et al., 2014). Our results also demonstrated that methyl-*p*-hydroxycinnamate (1), vanillin (2), and isorhamnetin-3-*O*-glucoside (4) exhibited inhibitory effects on PB NK cells. The cytotoxicity tests of the phenolic compounds present in Bairui Granules could thus provide a scientific basis for the medicinal value of *T. chinense*.

5 Conclusion

Five phenolics were identified in Bairui Granules that obtained from the medicinal plant *T. chinense*. Moreover, methyl-*p*-hydroxycinnamate (1), vanillin (2), and isorhamnetin-3-*O*-glucoside (4) were found for the first time in Bairui Granules. These metabolites had a certain effect on mammalian expression vectors, human immune cells, and stem cells. The biological activity of those secondary metabolites from *T. chinense* justify the medicinal use of this plant.

Data availability statement

The data presented in the study are deposited in the figshare repository, accession number 10.6084/m9.figshare.27894771.

Author contributions

SZ: Conceptualization, Formal Analysis, Investigation, Validation, Writing–original draft. HC: Conceptualization, Data curation, Formal Analysis, Investigation, Methodology, Software, Supervision, Validation, Visualization, Writing–original draft. JH: Data curation, Funding acquisition, Investigation, Methodology, Project administration, Resources, Supervision, Validation, Visualization, Writing–original draft, Writing–review and editing. SL: Conceptualization, Data curation, Formal Analysis, Funding acquisition, Investigation, Methodology, Project administration, Resources, Software, Supervision, Validation, Visualization, Writing–original draft, Writing–review and editing.

Funding

Acknowledgments

Conflict of interest

The authors declare that the research was conducted in the absence of any commercial or financial relationships that could be construed as a potential conflict of interest.

Generative AI statement

The author(s) declare that no Generative AI was used in the creation of this manuscript.

Publisher's note

All claims expressed in this article are solely those of the authors and do not necessarily represent those of their affiliated organizations, or those of the publisher, the editors and the reviewers. Any product that may be evaluated in this article, or claim that may be made by its manufacturer, is not guaranteed or endorsed by the publisher.

Supplementary material

The Supplementary Material for this article can be found online at: https://www.frontiersin.org/articles/10.3389/fchem.2024.1506792/full#supplementary-material

References

Arya, S. S., Rookes, J. E., Cahill, D. M., and Lenka, S. K. (2021). Vanillin: a review on the therapeutic prospects of a popular flavouring molecule. *Adv. Tradit. Med.* 21, 1–17. doi:10.1007/s13596-020-00531-w

Burkard, M., Leischner, C., Lauer, U. M., Busch, C., Venturelli, S., and Frank, J. (2017). Dietary flavonoids and modulation of natural killer cells: implications in malignant and viral diseases. *J. Nutr. Biochem.* 46, 1–12. doi:10.1016/j.jnutbio.2017.01.006

Cao, J. F., Zhang, Y., Chen, P. Y., Wu, C., and Deng, Y. (2021). Analysis of transcriptome sequencing and related genes of flavonoid biosynthesis from *Thesium chinense* Turcz. *Med. Plant Res.* 11, 1–11. doi:10.5376/mpr.2021.11.0004

Du, L. Y., Zhao, M., Xu, J., Qian, D. W., Jiang, S., Shang, E. X., et al. (2014). Analysis of the metabolites of isorhamnetin 3-*O*-glucoside produced by human intestinal flora *in vitro* by applying ultraperformance liquid chromatography/quadrupole time-of-flight mass spectrometry. *J. Agric. Food Chem.* 62, 2489–2495. doi:10.1021/jf405261a

Fico, G., Rodondi, G., Flamini, G., Passarella, D., and Tome´, F. (2007). Comparative phytochemical and morphological analyses of three Italian *Primula* species. *Phytochemistry* 68, 1683–1691. doi:10.1016/j.phytochem.2007.04.019

Han, R., Wu, W. Q., Wu, X. P., and Liu, C. Y. (2015). Effect of total flavonoids from the seeds of *Astragali complanati* on natural killer cell function. *J. Ethnopharmacol.* 173, 157–165. doi:10.1016/j.jep.2015.07.017

Han, Y. M., Koh, J., Kim, J. H., Lee, J., Im, J. P., and Kim, J. S. (2020). Astragalin inhibits nuclear factor-κb signaling in human colonic epithelial cells and attenuates experimental colitis in mice. *Gut Liver* 15, 100–108. doi:10.5009/gnl19268

Khan, H., Tundis, R., Ullah, H., Aschner, M., Belwal, T., Mirzaei, H., et al. (2020). Flavonoids targeting NRF2 in neurodegenerative disorders. *Food Chem. Toxicol.* 146, 111817. doi:10.1016/j.fct.2020.111817

Kilani Jaziri, S., Mokdad Bzeouich, I., Krifa, M., Nasr, N., Ghedira, K., and Chekir-Ghedira, L. (2016). Immunomodulatory and cellular anti-oxidant activities of caffeic, ferulic, and *p*-coumaric phenolic acids: a structure-activity relationship study. *Drug Chem. Toxicol.* 40, 416–424. doi:10.1080/01480545.2016.1252919

Kwon, Y. S., and Kim, C. M. (2003). Antioxidant constituents from the stem of *Sorghum bicolor*. *Arch. Pharm. Res.* 26, 535–539. doi:10.1007/BF02976877

Li, F., Liang, D., Yang, Z., Wang, T., Wang, W., Song, X., et al. (2013). Astragalin suppresses inflammatory responses via down-regulation of NF-kappa B signaling pathway in lipopolysaccharide-induced mastitis in a murine model. *Int. Immunopharm.* 17, 478–482. doi:10.1016/j.intimp2013.07.010

Li, G. H., Fang, K. L., Yang, K., Cheng, X. P., Wang, X. N., Shen, T., et al. (2021a). *Thesium chinense* Turcz.: an ethnomedical, phytochemical and pharmacological review. *J. Ethnopharmacol.* 273, 113950. doi:10.1016/j.jep.2021.113950

Li, H. D., Kang, Z. L., Hua, J., Feng, Y. L., and Luo, S. H. (2022). Root exudate sesquiterpenoids from the invasive weed *Ambrosia trifida* regulate rhizospheric Proteobacteria. *Sci. Total Environ.* 834, 155263. doi:10.1016/j.scitotenv.2022.155263

Li, H. S., Zhu, H., Ge, T., Wang, Z. F., and Zhang, C. (2021b). Mesenchymal stem cell-based therapy for diabetes mellitus: enhancement strategies and future perspectives. *Stem Cell Rev. Rep.* 17, 1552–1569. doi:10.1007/s12015-021-10139-5

Liu, C., Li, X. T., Cheng, R. R., Han, Z. Z., Yang, L., Song, Z. C., et al. (2018). Anti-oral common pathogenic bacterial active acetylenic acids from *Thesium chinense* Turcz. *J. Nat. Med-Tokyo* 72, 433–438. doi:10.1007/s11418-018-1180-3

Liu, Z. Z., Ma, J. C., Deng, P., Ren, F. C., and Li, N. (2023). Chemical constituents of *Thesium chinense* Turcz. and their *in vitro* antioxidant, anti-Inflammatory and cytotoxic activities. *Molecules* 28, 2685. doi:10.3390/molecules28062685

Lombard, N., van Wyk, B. E., and le Roux, M. M. (2020). A review of the ethnobotany, contemporary uses, chemistry and pharmacology of the genus *Thesium* (Santalaceae). *J. Ethnopharmacol.* 256, 112745. doi:10.1016/j.jep.2020.112745

Musina, R. A., Bekchanova, E. S., and Sukhikh, G. T. (2005). Comparison of mesenchymal stem cells obtained from different human tissues. *Bull. Exp. Biol. Med.* 139, 504–509. doi:10.1007/s10517-005-0331-1

Ozdal, T., Sari-Kaplan, G., Mutlu-Altundag, E., Boyacioglu, E., and Capanoglu, E. (2018). Evaluation of *Turkish propolis* for its chemical composition, antioxidant capacity, anti-proliferative effect on several human breast cancer cell lines and proliferative effect on fibroblasts and mouse mesenchymal stem cell line. *J. Apic. Res.* 57, 627–638. doi:10.1080/00218839.2018.1494888

Parveen, Z., Deng, Y. L., Saeed, M. K., Dai, R. J., Ahamad, W., and Yu, Y. H. (2007). Antiinflammatory and analgesic activities of *Thesium chinense* Turcz extracts and its major flavonoids, kaempferol and kaempferol-3-*O*-glucoside. *J. Pharm. Soc. Jpn.* 127, 1275–1279. doi:10.1248/yakushi.127.1275

Perche, O., Vergnaud-Gauduchon, J., Morand, C., Dubray, C., Mazur, A., and Vasson, M. P. (2014). Orange juice and its major polyphenol hesperidin consumption do not induce immunomodulation in healthy well-nourished humans. *Clin. Nutr.* 33, 130–135. doi:10.1016/j.clnu.2013.03.012

Pironti, C., Ricciardi, M., Motta, O., Camin, F., Bontempo, L., and Proto, A. (2021). Application of ^{13}C quantitative NMR spectroscopy to isotopic analyses for vanillin authentication source. *Foods* 10, 2635. doi:10.3390/foods10112635

Ramanan, M., Sinha, S., Sudarshan, K., Aidhen, I. S., and Doble, M. (2016). Inhibition of the enzymes in the leukotriene and prostaglandin pathways in inflammation by 3-aryl isocoumarins. *Eur. J. Med. Chem.* 124, 428–434. doi:10.1016/j.ejmech.2016.08.066

Róisín, O. f., Bergin, A., Flampouri, E., Mota, L. M., Butler, M., Quigley, A., et al. (2020). Mammalian cell culture for production of recombinant proteins: a review of the critical steps in their biomanufacturing. *Biotechnol. Adv.* 43, 107552. doi:10.1016/j.biotechadv.2020.107552

Shao, L. J., Sun, Y., Liang, J., Li, M. Q., and Li, X. L. (2019). Decolorization affects the structural characteristics and antioxidant activity of polysaccharides from *Thesium chinense* Turcz.: comparison of activated carbon and hydrogen peroxide decolorization. *Int. J. Biol. Macromol.* 155, 1084–1091. doi:10.1016/j.ijbiomac.2019.11.074

Singh, R., Singh, B., Singh, S., Kumar, N., Kumar, S., and Arora, S. (2008). Anti-free radical activities of kaempferol isolated from *Acacia nilotica* (L.) Willd. Ex. Del. *Toxicol. Vitro* 22, 1965–1970. doi:10.1016/j.tiv.2008.08.007

Soromou, L. W., Chen, N., Jiang, L., Huo, M., Wei, M., Chu, X., et al. (2012). Astragalin attenuates lipopolysaccharideinduced inflammatory responses by down-regulating NF-kappa B signaling pathway. *Biochem. Biophys. Res. Commun.* 419, 256–261. doi:10.1016/j.bbrc.2012.02.005

Steward, A. J., and Kelly, D. J. (2014). Mechanical regulation of mesenchymal stem cell differentiation. *J. Anat.* 765, 717–731. doi:10.1111/joa.12243

Strowig, T., Chijioke, O., Carrega, P., Arrey, F., Meixlsperger, S., Rämer, P. C., et al. (2010). Human NK cells of mice with reconstituted human immune system components require preactivation to acquire functional competence. *Blood* 116, 4158–4167. doi:10.1182/blood-2010-02-270678

Sudarshan, K., and Aidhen, I. S. (2016). Convenient synthesis of 3-glycosylated isocoumarins. *Eur. J. Org. Chem.* 2017, 34–38. doi:10.1002/ejoc.201601264

Vo, V. A., Lee, J. W., Shin, S. Y., Kwon, J. H., Lee, H. J., Kim, S. S., et al. (2014). Methyl *p*-hdroxycinnamate suppresses lipopolysaccharide-induced inflammatory responses through Akt phosphorylation in RAW264.7 cells. *Biomol. Ther.* 22, 10–16. doi:10.4062/biomolther.2013.095

Vyas, M., Requesens, M., Nguyen, T. H., Peigney, D., Azin, M., and Demehri, S. (2023). Natural killer cells suppress cancer metastasis by eliminating circulating cancer cells. *Front. Immunol.* 13, 1098445. doi:10.3389/fimmu.2022.1098445

Wei, Y., Xie, Q. Q., Fisher, D., and Sutherland, I. A. (2011). Separation of patuletin-3-*O*-glucoside, astragalin, quercetin, kaempferol and isorhamnetin from *Flaveria bidentis* (L.) Kuntze by elution-pump-out high-performance counter-current chromatography. *J. Chromatogr. A* 1218, 6206–6211. doi:10.1016/j.chroma.2011.01.058

Yang, W., Li, H. D., Liu, J. Y., Shao, H., Hua, J., and Luo, S. (2022). Degraded metabolites of phlorizin promote germination of *Valsa mali* var. *Mali* in its host *Malus* spp. *J. Agric. Food Chem.* 70, 149–156. doi:10.1021/acs.jafc.1c06206

Yu, C. S., Lai, K. C., Yang, J. S., Chiang, J. H., Lu, C. C., Wu, C., et al. (2010). Quercetin inhibited murine leukemia WEHI-3 cells *in vivo* and promoted immune response. *Phytother. Res.* 24, 163–168. doi:10.1002/ptr.2841

Yuan, Y., Long, Z., Xu, X., Wang, L., and Ying, M. (2006). Comparison of wild and cultured *Thesium chinense* turcz. on bacteriostasis and anti-inflammation. *Chin. J. Pharm.* 13, 219–222. doi:10.1016/S0379-4172(06)60071-1

Zhen, Z. G., Ren, S. H., Ji, H. M., Ma, J. H., Ding, X. M., Feng, F. Q., et al. (2017). Linarin suppresses glioma through inhibition of NF-kappa B/p65 and up-regulating p53 expression *in vitro* and *in vivo. Biomed. Pharmacother.* 95, 363–374. doi:10.1016/j.biopha.2017.08.023

Machine learning and molecular docking prediction of potential inhibitors against dengue virus

George Hanson [1]*, Joseph Adams [1],
Daveson I. B. Kepgang [2], Luke S. Zondagh [3],
Lewis Tem Bueh [4], Andy Asante [5], Soham A. Shirolkar [6],
Maureen Kisaakye [7], Hem Bondarwad [8] and
Olaitan I. Awe [9]*

[1]Department of Parasitology, Noguchi Memorial Institute for Medical Research (NMIMR), College of
Health Sciences (CHS), University of Ghana, Accra, Ghana, [2]Department of Biochemistry, Faculty of
Sciences, University of Douala, Douala, Cameroon, [3]Pharmaceutical Chemistry, School of Pharmacy,
University of Western Cape Town, Cape Town, South Africa, [4]Department of Computer Engineering,
Faculty of Engineering and Technology, University of Buea, Buea, Cameroon, [5]Department of
Immunology, Noguchi Memorial Institute for Medical Research (NMIMR), College of Health Sciences
(CHS), University of Ghana, Accra, Ghana, [6]College of Engineering, University of South Florida, Florida,
United States, [7]Department of Immunology and Molecular Biology, College of Health Sciences,
Makerere University, Kampala, Uganda, [8]Department of Biotechnology and Bioinformatics, Deogiri
College, Dr. Babasaheb Ambedkar Marathwada University, Sambhajinagar, India, [9]African Society for
Bioinformatics and Computational Biology, Cape Town, South Africa

Introduction: Dengue Fever continues to pose a global threat due to the
widespread distribution of its vector mosquitoes, *Aedes aegypti* and *Aedes
albopictus*. While the WHO-approved vaccine, Dengvaxia, and antiviral
treatments like Balapiravir and Celgosivir are available, challenges such as drug
resistance, reduced efficacy, and high treatment costs persist. This study aims to
identify novel potential inhibitors of the Dengue virus (DENV) using an integrative
drug discovery approach encompassing machine learning and molecular
docking techniques.

Method: Utilizing a dataset of 21,250 bioactive compounds from PubChem (AID:
651640), alongside a total of 1,444 descriptors generated using PaDEL, we trained
various models such as Support Vector Machine, Random Forest, k-nearest
neighbors, Logistic Regression, and Gaussian Naïve Bayes. The top-performing
model was used to predict active compounds, followed by molecular docking
performed using AutoDock Vina. The detailed interactions, toxicity, stability, and

Abbreviations: 3D, Three-dimensional; ADMET, chemical Absorption, Distribution, Metabolism,
Excretion, and Toxicity; AI, Artificial Intelligence; AID, BioAssay Identification number; ANPDB, African
Natural Products Database; DENV, Dengue Virus; DF, Dengue Fever; DHF, Dengue Hemorrhagic Fever;
DSS, Dengue Shock Syndrome; EANPDB, Eastern Africa Natural Products Database; GaussianNB,
Gaussian Naïve Bayes; GBM, Gradient Boosting Machine; GROMACS, Groningen Machine for
Chemical Simulations; HTS, High Throughput Screen; KNN, K-Nearest Neighbors; LR, Logistic
Regression; MD, Molecular Dynamics; ML, Machine Learning; MMPBSA, Molecular Mechanics
Poisson-Boltzmann Surface Area; NB, Gaussian Naïve Bayes; PaDEL, Pharmaceutical Data
Exploration Laboratory; QSAR, Quantitative Structure-Activity Relationship; RF, Random Forest
classifier; RMSD, Root Mean Square Deviation; RMSF, Root Mean Square Fluctuation; SASA, Solvent-
Accessible Surface Area; SDF, Structure Data Format; SMILES, Simplified Molecular-Input Line-Entry
System; SVM, Support Vector Machine; UFF, Universal Force Field.

conformational changes of selected compounds were assessed through protein-ligand interaction studies, molecular dynamics (MD) simulations, and binding free energy calculations.

Results: We implemented a robust three-dataset splitting strategy, employing the Logistic Regression algorithm, which achieved an accuracy of 94%. The model successfully predicted 18 known DENV inhibitors, with 11 identified as active, paving the way for further exploration of 2683 new compounds from the ZINC and EANPDB databases. Subsequent molecular docking studies were performed on the NS2B/NS3 protease, an enzyme essential in viral replication. ZINC95485940, ZINC38628344, 2′,4′-dihydroxychalcone and ZINC14441502 demonstrated a high binding affinity of −8.1, −8.5, −8.6, and −8.0 kcal/mol, respectively, exhibiting stable interactions with His51, Ser135, Leu128, Pro132, Ser131, Tyr161, and Asp75 within the active site, which are critical residues involved in inhibition. Molecular dynamics simulations coupled with MMPBSA further elucidated the stability, making it a promising candidate for drug development.

Conclusion: Overall, this integrative approach, combining machine learning, molecular docking, and dynamics simulations, highlights the strength and utility of computational tools in drug discovery. It suggests a promising pathway for the rapid identification and development of novel antiviral drugs against DENV. These *in silico* findings provide a strong foundation for future experimental validations and *in-vitro* studies aimed at fighting DENV.

1 Introduction

Dengue Virus (DENV) is a positive-sense ssRNA virus belonging to the family *Flaviviridae*, responsible for the most prevalent viral hemorrhagic fever transmitted by mosquitoes (Chao et al., 2018). The disease is transmitted to humans by the mosquitoes *Aedes aegypti* and *Aedes albopictus*, especially in hyperendemic regions in Southeast Asia and the Pacific experience the cocirculation of multiple serotypes of the virus (Caminade et al., 2012; Cucunawangsih and Lugito, 2017). There are four unique DENV serotypes (DENV1, DENV2, DENV3, and DENV4); historically, these four serotypes circulated in different geographic areas (Jamal et al., 2024; Murray et al., 2013). The prevalence rates have been deemed 390 million cases as of 2024, with 96 million being symptomatic (Anasir and Ramanathan, 2020; Rachmawati et al., 2024) and annual death recorded at around 25,000 (Yadouleton et al., 2024). The impact of Dengue fever is at its peak in North and South America, the Southeastern part of Asia, and the Western Pacific (Gebhard et al., 2019). Its symptoms usually are myalgia, hemorrhagic features, arthralgia, headache, rash, and retro-orbital discomfort (Chikkaveeraiah et al., 2024; Drago et al., 2021). In severe cases, it may also lead to Dengue Hemorrhagic Fever (DHF) and Dengue Shock Syndrome (DSS), which is an acute vascular permeability syndrome (Chikkaveeraiah et al., 2024). The probability of the disease transitioning into DHF and DSS is considerably higher for patients who have developed secondary DENV infections, around 10 to 100-fold (Martina et al., 2009).

The DENV genome is 11 kb long, comprising 10,723 nucleotides, and encodes large polyprotein precursors of approximately 3,391 amino acid residues (Gautam et al., 2024).

After being cleaved by host and viral proteases, these DENV polyproteins form three structural proteins: C, prM, and E (where each stands for capsid, pre-membrane, and envelope, respectively) as well as seven non-structural proteins (NSPs): NS1, NS2A, NS2B, NS3, NS4A, NS4B, and NS5 (Dwivedi et al., 2017). The structural and non-structural proteins of the viral genome have all been identified as potential drug targets against Dengue infection (M. F. Lee et al., 2024). However, among these proteins, the envelope protein and the NSPs, NS3, and NS5 proteins have been identified as the proteins that play a vital role in viral replication (Chen et al., 2018; M. F. Lee et al., 2024). Due to mutations in specific proteins of the virus, emerging resistance to existing therapeutics has been reported (S. P. Lim, 2019) and thus calls for the urgent need to identify multiple vital drug targets that can effectively halt the replication of the virus in its host.

Significant efforts to contain the spread of Dengue fever can be seen in vaccine development, vector control mechanisms, and efforts to reduce viral load and preventive measures against severe forms of Dengue infection (M. F. Lee et al., 2024). Low et al. (2011) discovered that Narasin is a novel antiviral agent effective against all DENV serotypes with an IC50 of less than 1 μM (Gautam et al., 2024). Brefeldin is a promising antiviral compound with a 54.6–65.7 nM IC50 range for all DENV serotypes (Raekiansyah et al., 2017). There have been research efforts that aimed to model the evolution of viral pathogens like SARS-CoV-2 using genomic sequence data (Awe et al., 2023), HIV-1 evolution in sub-Saharan Africa (Obura et al., 2022) and Ebola Virus using comparative genomics (Oluwagbemi and Awe, 2018). Additionally, several experimental studies have evaluated the activity of repurposed drugs against DENV. Therefore,
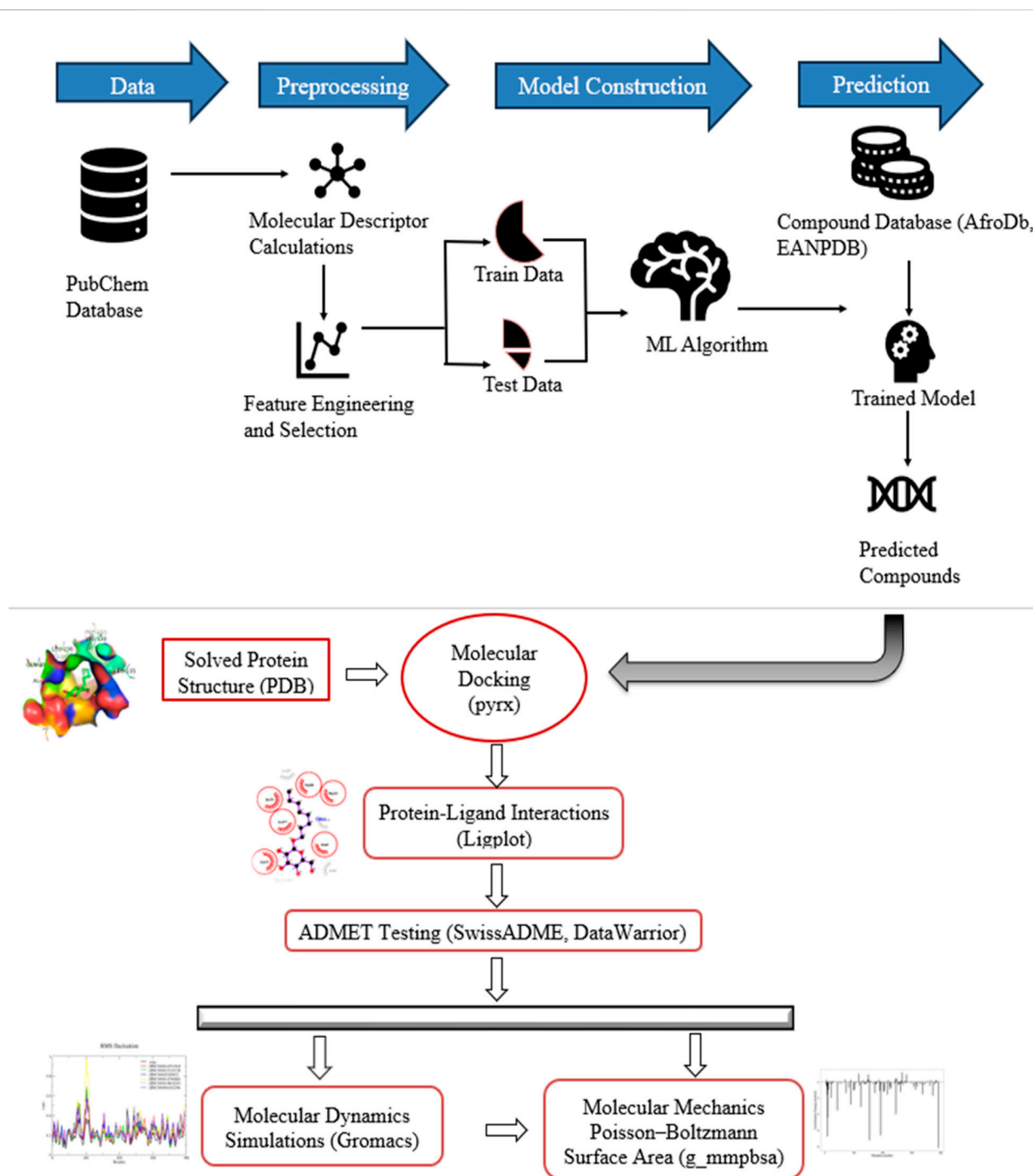
FIGURE 1
Graphical illustration of study workflow methods and instruments. The study developed five models on data from PubChem and used it for predicting new compounds. The predicted hits were screened through molecular docking, *in silico* pharmacological and toxicity tests, structural assessment using MD simulations, and estimation of binding free energies.

it is essential to continue exploring more elements and inhibitors to develop potent antivirals with high efficacy against DENV (Punekar et al., 2022). Despite decades of attempts to discover new drugs and vaccines, Dengvaxia is the sole vaccine accepted against DENV (marketed in several countries). Dengvaxia has been noted to be non-efficacious against certain dengue strains which dropped its efficacy rate to 61% (X.-N. Lim et al., 2019; Pintado Silva and

Fernandez-Sesma, 2023; Thomas, 2023). TAK-003 and Butantan-DV are newly developed live-attenuated vaccines against DENV that have completed their phase III clinical trials, but the data regarding their efficacy against DENV3 and DEN4 is still insufficient (Biswal et al., 2020; Durbin, 2020; Kallas et al., 2020). As effective prophylactic and therapeutic measures against DENV are not present, the focus of patient management diverts to supportive

therapy and controlling further transmission with drugs such as Chloroquine and Prednisolone (Lai et al., 2017).

Machine learning models like Support Vector Machine, Random Forest, Logistic Regression, and Naive Bayesian have been extensively applied in drug discovery, bioinformatics, and cheminformatics (Aniceto et al., 2023; Das et al., 2024; Niazi and Mariam, 2024). Advances in next-generation sequencing also enable the application of bioinformatics in diverse fields in the biomedical sciences and in applications like biomarker discovery (Chikwambi et al., 2023; Nyamari et al., 2023; El Abed et al., 2023; Ben et al., 2024; Alaya et al., 2024), co-infection biomarkers of parasites and viruses (Nzungize et al., 2022), analysis of RNA-seq, ChIP-seq data (Ather et al., 2018), genetics of complex diseases (Abolo et al., 2024) and in agriculture (Die et al., 2019; Omar et al., 2024), protein structure prediction (Pawar et al., 2024) and genomics applications in newborn screening (Wesonga and Awe, 2022). Various researchers used different ML techniques to study DENV, such as Gradient Boosting Machine (GBM), Random Forest (RF), and Support Vector Machine (SVM). Sanchez-Gendriz used an interesting technique (Sanchez-Gendriz et al., 2022) in which he developed a neural networking model with Long Short-Term Memory (LSTM) as the base for his studies in predicting future dengue cases in America. Another interesting study (Andersson et al., 2018) used a Convolution Neural Network to process street-level photos to predict DF and DHF rates in urban areas.

This study sought to build different machine learning models using the DENV2 CPE-Based HTS dataset from PubChem to distinguish between potential anti-dengue and non-anti-dengue compounds. The best-performing model based on the accuracy, specificity, Precision, and F1 score was used to predict active compounds solicited from the AfroDb (Ntie-kang et al., 2013), a catalog of ZINC15 database (Sterling and Irwin, 2015) and compounds present in the East African Natural Product Database (EANPDB) (Simoben et al., 2020). The predicted active compounds were further corroborated by employing molecular docking studies. The most promising drug candidates amongst the predicted compounds from our trained model were highlighted while also visualizing the intermolecular interactions between key residues in the active site and the compounds. The noxiousness of the compounds was estimated using SwissADME and DataWarrior. Molecular Dynamics (MD) simulations with Molecular Mechanics Poisson-Boltzmann Surface Area (MMPBSA) were utilized to evaluate predicted leads.

2 Methods

A visual representation of the methodology applied to this study is presented (Figure 1).

2.1 Dataset acquisition

This study proceeded in two phases as illustrated in the graphical depiction in Figure 1. First, a high throughput screen (HTS) measured in Cell-Based and Microorganism Combination System bioassay data of 343,305 compounds retrieved from PubChem was used for the study. The dataset with PubChem AID: 651640 was aimed to identify inhibitors of Dengue Virus by treating BHK-21 with various compounds before being infected with Dengue Virus serotype 2. The DENV2 strain New Guinea C, obtained from the American Type Culture Collection (ATCC) with catalog number VR-1584 was adapted (Che et al., 2009). Several viruses have been successfully studied using the cytopathic effect (CPE) assay to find new antiviral substances (Lin et al., 2023; McCormick et al., 2012).The expected outcome was that compounds increased ATP levels, indicating increased cell viability compared to the positive control (uninfected cells), and the neutral control was considered positive and otherwise negative. The dataset retrieved for this study comprised 5,946 active and 321,638 inactive compounds, a ratio of about 1:50 compounds. To compute molecular descriptors, the actives and inactives of the dataset were downloaded in the Structure Data Format (SDF).

2.2 Calculation of molecular descriptors and data preprocessing

Recent studies have demonstrated the utility of molecular descriptors in predicting compound activity, toxicity, and other properties from chemical structures (Comesana et al., 2022; Trinh et al., 2023). The active and inactive datasets were converted from SDF to Simplified Molecular-Input Line-Entry System (SMILES) formats for easier manipulation for machine learning. PaDEL-descriptor calculator (Yap, 2011) was used to compute 1440 molecular descriptors from the canonical SMILES of the compounds. Before descriptor calculations, compound standardization was performed, involving salt removal and nitro group normalization, to ensure uniformity and accuracy of the descriptor data (Viganò et al., 2024). The dataset used for training and testing the models comprised 4470 active compounds and 16780 inactive compounds, after reducing the ratio between the active and inactive compounds to 1:4 to enhance the computational efficiency.

The significant imbalance between active and inactive compounds was acknowledged, but oversampling techniques to balance the classes were not applied. A variance filter was employed to address the issue of dimensionality and enhance the relevance of features for predictive modeling (Velliangiri et al., 2019). Mean imputation was applied to handle any missing values within the dataset, ensuring a complete set of descriptors for each compound. Standardization of the dataset was done by removing the mean and scaling to unit variance using the Standard Scaler from the scikit-learn library. This transformation ensures that the features are centered around zero and have a standard deviation of one, which is crucial for many machine learning algorithms to perform optimally, as it ensures that the model is not biased towards features with larger numerical ranges. The was computed using the formula 1:

$$\text{Standard Scaler}(X) = \frac{X(i) - mean}{standard\ deviation} \quad (1)$$

Where i represent each value in the feature X.

2.3 Development of machine learning models

Five models were built from the training dataset using five machine learning algorithms and the model with superior performance in terms of classification metrics was chosen (Kee et al., 2023; Tougui et al., 2021). A 70%–30% split of the pre-processed data was used for training and testing the models, respectively. The classification models developed included Support Vector Machine (SVM), k-nearest neighbors (k-NN), Gaussian Naïve Bayes (GaussianNB) (Adams et al., 2022), Random Forest classifier (RF), and Logistic Regression (LR) (Khorshid et al., 2021). For the k-nearest neighbors (k-NN) model, k = 3 was used. The Gaussian Naïve Bayes model was implemented using default settings from the scikit-learn library (Pedregosa et al., 2011). The SVM model was optimized with the probability parameter set to True (Sandhu et al., 2022). The Random Forest model was built with a maximum depth of 8 and 100 estimators (J. Adams et al., 2022). Finally, the Logistic Regression model was constructed with a maximum iteration parameter of 1000.

2.4 Model validation

Prior to comparison with other optimized classifiers, each classifier underwent optimization to determine the optimal hyperparameters that yielded the maximum accuracy. The optimized models were evaluated using 10-fold cross-validation. This method splits the training data into kkk groups, trains the model on k-1k-1k-1 folds, and tests the model on the remaining fold to yield a trustworthy estimate of the model's performance on unseen data (Jung and Hu, 2015; Vabalas et al., 2019). It computes performance metrics such as accuracy, accuracy, precision, recall, and F1 score based on the confusion matrix, which includes true positives (TP), true negatives (TN), false positives (FP), and false negatives (FN) (Tharwat, 2021). These metrics (as shown in Equations 2–6) were used to compare and select the best-performing model for predicting Dengue Virus inhibitors (Adams et al., 2022; Orozco-arias et al., 2020)

$$\text{Accuracy} = \frac{TP + TN}{TP + FP + TN\ FN} \tag{2}$$

$$\text{Precision} = \frac{TP}{TP + FP} \tag{3}$$

$$\text{Recall} = \frac{TP}{TP + FN} \tag{4}$$

$$\text{F1} = 2\,x\,\frac{Precision * Recall}{Precision + Recall} \tag{5}$$

$$\text{Specificity} = \frac{TN}{TN + FP} \tag{6}$$

2.5 Prediction of compounds

The best-performing model was used to make predictions against 812 compounds from Afrodb, and 1871 EANPDB compounds. Prior to compound predictions, the model's predictive power was validated on known Dengue Virus inhibitors post-cross-validation. The molecular descriptors of these inhibitors were calculated and preprocessed similarly to the training and test data. This was done to reinforce the credibility of the cross-validation results for the best-performing model based on the metrics. The number of correct predictions made by the model on the submitted inhibitors defines the accuracy of the classification or prediction. A total of 18 known inhibitors curated from literature were submitted to the LR model as a result of their activity against the Dengue Virus shown in different studies.

2.6 Preparation of target protein and ligand libraries

The Crystal structure of the Dengue 2 Virus nonstructural protein NS2B/NS3 was obtained from the RCSB Protein Data Bank (http://www.rcsb.org/pdb) with PDB ID: 2FOM. Before selecting 2FOM, different suitable structures such as 4M9M, 4M9T, and 4M9I were retrieved, however, 2FOM was chosen based on its low resolution, low R values, and the number of missing residues. The selected protein structure was superimposed with the other suitable structure using PyMOL to measure their root mean square deviation (RMSD). The structure was cleaned using PyMOL (Yuan et al., 2017) to devoid the protein of ions, water molecules, and other structures like ligands before minimization was carried out by employing Groningen Machine for Chemical Simulations (GROMACS) (Abraham et al., 2015). The steepest descent minimization algorithm with a maximum number of 50,000 steps and a minimization step size of 0.01 was used to minimize the protein structure. The three-dimensional structures (.sdf) of the natural compounds predicted by the machine learning model were obtained for the molecular docking stage. Natural products were chosen for this investigation because of their structural and chemical variety, and the therapeutic effects of phytochemicals found in plants.

2.7 Molecular docking and mechanism of binding characterization

The molecular docking procedure for the predicted compounds was carried out using AutoDock Vina (Trott and Olson, 2010). All compounds were energy minimized in 200 steps using the Universal force field (UFF) before being translated to the Protein Data Bank partial charge and atom type (.pdbqt) format using Open Babel software (O'Boyle et al., 2011). Visualization of the resultant energy minimized protein structure and the removal of surrounding water molecules before the virtual screening was done in PyMOL v1.5.0.4. The prepared structure was then saved using PyMOL before applying the "make macromolecule" option in PyRx to prepare for the docking of selected hits. The library was screened against the NS2B/NS3 protease using a grid box dimension of center_x = −5.179Å center_y = −9.575Å center_z = 13.756Å size_x = 18.302Å size_y = 19.821Å size_z = 23.788Å.

All hit compounds that contributed binding affinities of at least −8.0 kcal/mol were considered. The output of AutoDock Vina is ranked in a decreasing order of binding affinity using a

FIGURE 2
3D plot showing the correlation between the active and inactive compounds based on ALogP, XLogP, and Zagreb. [Labels: Blue = Actives, Red = Inactives, Pink = Outliers].

TABLE 1 Comparison of model performance on withheld data sets; showing results for accuracy, precision, recall, and F1 scores.

Model	Accuracy	Precision	Recall	F1 score
LR	0.94	0.91	0.76	0.83
SVM	0.93	0.94	0.71	0.81
KNN	0.92	0.89	0.68	0.77
RF	0.91	0.94	0.6	0.73
NB	0.81	0.55	0.47	0.51

Dell EMC high-performance computing cluster at the WACCBIP, University of Ghana, Accra. The CHARMM36 all-atom force field produced the protein and ligand topology (July 2022). Utilizing a cubic box for all simulations, the systems were each solvated with water molecules, neutralized with ions, and energy-minimized to optimize the system. To equilibrate each system, NVT, and NPT ensemble were applied for 100 ps a piece before the production run. The parameters for the production run included 50,000,000 steps which translates into 100 ns and a step size of 0.002 (2 fs). Xmgrace (Turner, 2005) was used to visualize and analyze the root mean square deviation (RMSD), root mean square fluctuation (RMSF), and radius of gyration (Rg) obtained from the MD simulations.

negative function; a more negative binding affinity is preferred. The best mode for each compound was applied using the root mean squared deviation. The result was then examined with PyMOL to find the optimal-docked ligands. LigPlot + (v1.4.5) was used to analyze the interactions between key residues in the active site of the protein and the docked compounds (Laskowski and Swindells, 2011). The protein-ligand complexes generated in PyMOL were used as input for LigPlot. The resulting output provides a 2D depiction of intermolecular interactions, including hydrophobic interactions and hydrogen bonds.

2.8 ADMET screening of selected compounds

A pharmacokinetics profile, comprising an assessment of absorption, distribution, metabolism, and excretion (ADME), was applied to a subset of compounds using SwissADME (Daina et al., 2017). Along with Veber's rule, the ADMET testing also measured five properties: total average molecular weight in g/mol, the number of hydrogen bond donors, hydrogen bond acceptors, rotatable bonds, and partition coefficient—collectively referred to as Lipinski's rule of five (Devadasu et al., 2018; Jia et al., 2020). Using OSIRIS DataWarrior v06.02.05 (Sander et al., 2015), the toxicity characteristics, including mutagenicity and tumorigenicity, were predicted.

2.9 Molecular dynamics (MD) simulations

A 100 ns MD simulation was run on each protein-ligand complex and the unbound protein using GROMACS-2020.5 on a

2.10 Calculations of MMPBSA parameters

The binding free energies of the protein-ligand complexes and the individual energy contributions of the residues were calculated using the Molecular Mechanics Poisson-Boltzmann Surface Area (MMPBSA) method (Kumari et al., 2014). This is a corroboration technique used to verify the limitations of the existing scoring function utilizing the MD simulation output files (Wang C. et al., 2018). R programming software was utilized to plot the graphs from the MMPBSA computations.

3 Results

3.1 Data acquisition and processing

The bioactive dataset obtained from PubChem was an imbalanced set, with approximately one-third of its constituents being active compounds. As displayed in Figure 2, inactive compounds dominated the dataset. Using PaDEL, 1,444 molecular descriptors were generated, which provide a mathematical representation of the compounds for QSAR modeling by converting chemical information about the compounds into numerical values. The dataset underwent a three-dataset splitting strategy to be divided into training, validation, and test sets. The dataset of 21,250 compounds was split into 14,875 training data, 3,187 test data, and 3,188 externally held data. The first set is for training the algorithm, the validation set tunes hyperparameters, and the test set is used to test model performance and predicting ability. The application of a variance filter reduced the number of descriptors from 1,444 to 684, using a variance threshold of 0.1 to filter out descriptors with minimal

TABLE 2 Classification and mechanisms of action of known DENV inhibitors identified by the Logistic Regression model.

Number	Inhibitors	Prediction*	Mechanism of action	References
1	Pentoxifylline	1	Immune modulation	Salgado et al. (2012)
2	4-hydroxyphenyl retinamide	0	Inhibits viral replication	Carocci et al. (2015), Fraser et al. (2014)
3	Prochlorperazine	1	Inhibits viral binding and viral entry	Simanjuntak et al. (2015)
4	Balapiravir	1	Inhibits viral replication	Nguyen et al. (2013)
5	Bortezomib	1	Inhibits viral replication	Ci et al. (2023)
6	Leflunomide	1	Immunosuppressive effects	(W.-L. Wu et al., 2011)
7	SKI-417616	1	Inhibition of D4R suppressed DENV infection	Smith et al. (2014)
8	Celgosivir	1	Inhibits viral replication	Tian et al. (2018)
9	UV-4B	1	Inhibits viral replication	Franco et al. (2021)
10	2-C-methylcytidine	0	Inhibits viral replication	(J.-C. Lee et al., 2015)
11	Ketotifen	1	Vascular leakage	Lai et al. (2017)
12	Chloroquine	1	Inhibits viral replication	Lai et al. (2017)
13	Dasatinib	0	RNA replication inhibition	de Wispelaere et al. (2013)
14	Lovastatin	0	Inhibits viral replication	Whitehorn et al. (2016)
15	ST-148	0	Inhibits viral replication	Byrd et al. (2013)
16	Dexamethasone	0	Inhibits viral replication	Kularatne et al. (2009)
17	Prednisolone	1	Inhibits viral replication	Lai et al. (2017)
18	Ivermectin	0	Helicase inhibition	Xu et al. (2018)

*[0 = inactive; 1 = active].

variance. This step ensured that only the most informative features were retained for subsequent modeling, as low-variance features are often less useful in distinguishing between classes (Velliangiri et al., 2019).

3.2 Model development and evaluation

Five machine learning models were developed to predict Dengue Virus inhibitors: k-Nearest Neighbors (k-NN), Gaussian Naïve Bayes (NB), Support Vector Machine (SVM), Random Forest (RF), and Logistic Regression (LR). Each model was evaluated using statistical metrics such as accuracy, precision, recall, and F1 score, as displayed in Table 1 with the confusion matrix shown in Supplementary Table S1.

Among the models, Logistic Regression demonstrated the highest performance across most metrics, including an accuracy of 94%, a precision of 91%, and an F1 score of 0.83. This superior performance made Logistic Regression the most suitable model for predicting Dengue Virus inhibitors in this study. The SVM model followed closely, with an accuracy of 93%, a precision of 94%, and an F1 score of 0.81. Although the k-NN and Random Forest models performed well, they lagged behind the top two models in recall and F1 scores, indicating that they were less effective in identifying all active compounds.

Gaussian Naïve Bayes was the poorest-performing model, with an accuracy of 81% and an F1 score of 0.51. This model's low precision (0.55) and recall (0.47) indicate that it struggled to balance identifying true positives and minimizing false positives, particularly in the imbalanced dataset where inactive compounds were predominant. Overall, Logistic Regression emerged as the most reliable model for predicting potential inhibitors due to its robust performance across the different metrics.

3.3 Prediction of known inhibitors and new compounds

The study further validated the performance of the developed models by testing 18 known Dengue Virus inhibitors curated from literature. The prediction made by the Logistic Regression model for these compounds is listed in Table 2. The Logistic Regression model correctly predicted 11 of the 18 inhibitors as active, outperforming other models, including SVM and Random Forest.

Several inhibitors, such as Pentoxifylline, Prochlorperazine, and Balapiravir, were correctly classified as active by Logistic Regression, in line with their established mechanisms of action against the Dengue Virus. Notably, inhibitors like Celgosivir and Bortezomib, which inhibit viral replication, were also predicted accurately. This validation process of known inhibitors provided confidence in the model's predictive capability, suggesting it could effectively generalize to novel compounds with similar mechanisms of action.

Following this validation, the Logistic Regression model was applied to predict 2,683 new compounds, including 812 from the ZINC database and 1,871 from the EANPDB database. Out of these, 933 compounds were predicted to be active, representing a
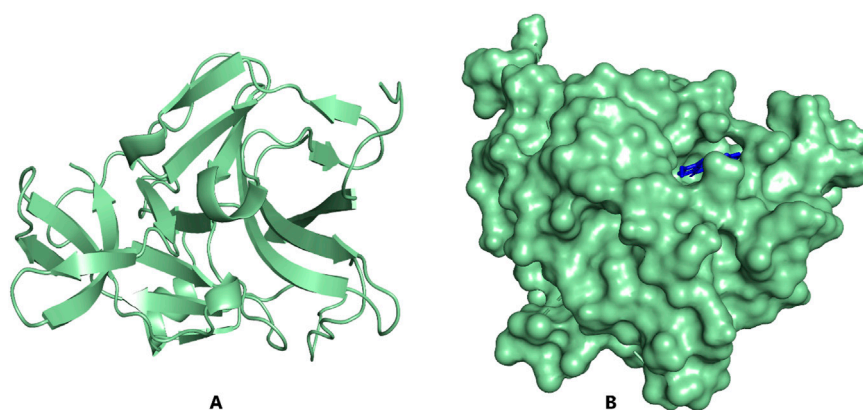
FIGURE 3
PyMOL visualization of NS2B/NS3 protease structure **(A)** Light-green cartoon structure representation; **(B)**. Light-green surface representation of the protein with ZINC000095486052 (blue) docked in the active site.

promising pool of potential Dengue Virus inhibitors for further experimental validation.

These predictions highlight the utility of the developed QSAR models, particularly the Logistic Regression model, in identifying novel drug candidates for Dengue Virus inhibition. The robust performance on known inhibitors and newly predicted compounds highlights its potential as a valuable tool in future drug discovery efforts targeting the Dengue Virus. The study's ability to handle imbalanced data effectively and generate accurate predictions underscores the importance of appropriate descriptor selection and data preprocessing in QSAR modeling.

3.4 Target selection and molecular docking of predicted compounds (PDB ID 2FOM)

In this study, the NS2B/NS3 protease was preferentially selected amongst the seven nonstructural proteins of the Dengue Virus as the target structure to corroborate the prediction by the logistic regression model. The NS2B/NS3 protease is an essential enzyme for viral replication and assembly, making it a principal antiviral target for developing therapeutics against the virus (Erbel et al., 2006; Norshidah et al., 2023). There are two potential locations for inhibiting DENV protease: the active site and the blocking attachment of protease (NS3) to its protein cofactor (NS2B). The active site on the NS3 which is the prime target is made up of a conserved catalytic triad like His51-Asp75-Ser135 (Noble et al., 2012; Zamri et al., 2019). A search via the Protein Data Bank repository for a solved structure of the NS2B/NS3 for the Dengue Virus serotype showed IDs such as 4M9T, 2FOM, 4M9M, and 4M9I with resolutions 1.74, 1.50, 1.53, and 2.40 Å respectively and R-value work of 0.215, 0.176, 0.203, and 0.215 respectively. The 2FOM, solved using x-ray diffraction, was selected for this study since it had the lowest resolution and R-value, both of which are a measure of the quality of the structure (Wlodawer et al., 2008). Additionally, the RMSD values after superimposing the selected protein structure to 4M9T, 4M9M, and 4M9I were 0.358, 0.151, and 0.276 Å, respectively, underlying their close structural similarity with the 2FOM. The three-dimensional structure of the 2FOM with a ligand

docked in the active site is shown Figure 3. The active site on the NS3 used in this study, besides consisting of the catalytic triad which is pivotal in inhibiting its activity, also consists of residues such as Leu128, Pro132, Ser131, and Tyr161 (Norshidah et al., 2023; Purohit et al., 2022).

A total of 853 compounds from the Logistic Regression prediction were docked into the active site of the target using Autodock. Anhydrophlegmacin showed the highest binding affinity of −9.2 kcal/mol towards the protease among all docked ligands. The docked compounds demonstrated binding affinities between −9.2 and −3.6 kcal/mol. This reinforces the prediction ability of the Logistic Regression model. Applying a threshold of −8.0 kcal, 59 ligands with affinities of −8.0 kcal/mol or better were considered for downstream analysis. A higher cutoff of −7.0 kcal/mol, taken as the standard threshold for a compound to be considered active against a particular target, was employed (Kwofie et al., 2019a). The higher the binding affinity, the stronger the bond between the ligands and the target protein. The protein in the complex with the ligands was visually inspected using PyMOL (Figure 4) to select the best-docked possess. In addition, inhibitors such as Leflunomide and Prednisolone were also incorporated into the docking to act as a control. They demonstrated affinities of −7.1 and −7.0 kcal/mol respectively. Table 3 shows the binding affinities of the top 20 of the selected compounds and the inhibitors.

3.5 Mechanism of binding characterization of selected compounds

In continuation of the structure-based molecular docking to further confirm the binding affinities of the predicted compounds, the interactions of the compounds within the predicted binding pocket were determined. The biomolecular interactions between the NS2B/NS3 protease and the compounds were generated using LigPlot. Studies into these interactions are crucial in determining promising lead compounds. Identification of crucial residues in the corresponding targets' active sites was made possible by characterizing the binding interactions. To find the suitable
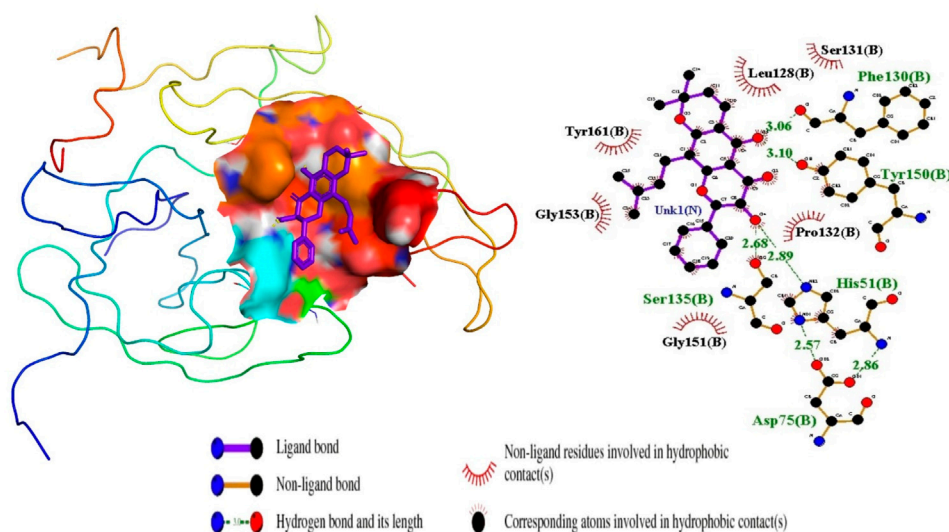
FIGURE 4
Ligand ZINC38628344 docked in NS2B/NS3 binding pocket; 3D pose and 2D protein-ligand interaction diagram generated using PyMOL and LigPlot, respectively.

compound that inhibits the activities of the NS2B/NS3 protease, hydrogen and hydrophobic interactions between the shortlisted compounds and the residues in the active site were elucidated.

For the interactions of the protease, the ligands docked to the active site were observed to interact with the proposed residues such as His51, Ser135, Leu128, Pro132, Ser131, Tyr161, and Asp75 as shown in Table 3 and Supplementary Table S2. Anhydrophlegmacin and anhydrophlegmacin-9,10-quinones_B2 which had the highest binding affinities interacted with similar residues such as His51, Asp75, Gly151, Leu128, Pro132, and Gly153. They interacted with conserved catalytic triad residues Asp75, Ser135, and His51 through hydrogen bonding with bond lengths of 2.57, 3.06, and 2.86 Å respectively. ZINC38628344, which had an affinity of −8.5 kcal/mol with the NS2B/NS3 protease formed hydrogen bond interaction with His51 (2.89 Å), Ser135 (2.68 Å), Asp75 (2.57 Å), Phe130 (3.06 Å), Tyr150 (3.10 Å) and hydrophobic interactions with residues Pro132, Ser131, Leu128, Tyr161, Gly153, Gly151 (Figure 4). The inhibitor Prednisolone interacted via hydrogen bonding with Gly151 (2.90 Å, 2.71 Å), Asp75 (2.95 Å), His51 (3.21 Å), and Gly153 (2.93 Å, 3.16 Å) as shown in Figure 5. In addition, ZINC14441502 formed hydrogen interactions with Gly151 and Ser135 with bond length 2.86 and 2.99 Å respectively; and hydrophobic bonding with Leu128, Gly153, Asn152, Val72, Asp75, His151 and Phe130 (Supplementary Table S2). 39 out of 56 hits docked firmly and interacted with critical residues in the active site, and these were selected for downstream analysis.

3.6 ADMET screening of selected compounds

Pharmacokinetics controls how medications are absorbed by the body and eventually eliminated (Wang G. Y. et al., 2018). Analyses were conducted on pharmacokinetic features, including

gastrointestinal (GI) absorption. Drugs taken orally can enter the bloodstream through a process known as gastrointestinal absorption (GI) (Suenderhauf et al., 2012). "High" compound absorption occurs in the GI tract. To select druglike compounds, Veber's criteria were also applied, and the selected hits that do not conform to Lipinski's rule of five (RO5) were eliminated (Ogbodo et al., 2023). Out of the 39 hits, 20 were in violation of the rule (see Supplementary Table S3). Twelve hits also broke one of the RO5s. The remaining 7 hits: 5,7′-physcion-fallacinol, ZINC000095485956, ZINC000085594516, amentoflavone, ZINC000095486111, voucapane-18,19-di-(4-methyl)-benzenesulphonate, ZINC000095485927 showed the least drug-likeness of two RO5 violations (Table 4). Veberr's rule, with TPSA ≤140 and rotatable bonds ≤10, was used as the main determinant (Veber et al., 2002). 26 out of the selected hits demonstrated 0 violations with the remaining showing only one violation of the rule. The solubility and pharmacological profiles such as GI absorption were also elucidated. Only ZINC000095485927 was predicted to be insoluble (Supplementary Table S3). Four of the 14 hits had a moderate solubility prediction and four had a soluble prediction. However, 19 of the selected hits were predicted to be poorly soluble (Supplementary Table S3). Compounds are considered to have met the GI absorption criteria if it is denoted as 'High' suggesting a high propensity of absorption into the intestinal tract for orally administered drugs. 21 and 18 of the selected hits were estimated to be high and low respectively. The mutagenicity and tumorigenicity levels of the hits were also predicted using DataWarrior (Table 4). From the results obtained, 26 out of the 39 hits tested were neither mutagenic nor tumorigenic.

3.7 Molecular dynamics simulations

Molecular dynamics simulations were carried out using GROMACS 2020.5 to further elucidate the stability of the

TABLE 3 Protein-ligand interactions of top 20 hits with NS2B/NS3 post-docking, including interactions of two known inhibitors.

Compounds names	Binding affinity (kcal/mol)	Hydrogen bonding with bond length (Å)	Hydrophobic contacts
anhydrophlegmacin	−9.2	Asn152 (2.76), Gly153 (2.88), Ser135 (3.06), Gly151 (2.86)	Val72, Asp75, His51, Pro132, Tyr150, Leu128
anhydrophlegmacin-9,10-quinones_B2	−9.2	Val72 (2.96), Asp75 (2.57), His51 (2.86), Lys73 (2.94)	Leu128, Pro132, Gly151, Gly153, Tyr161, Trp50
ZINC000035941652	−9.1	Leu149 (3.06)	Trp83, Asn152, Ala164, Ile165, Lys73, Asn167, Thr120, Ile123, Ala166, Lys74, Gly148, Leu76
chryslandicin	−9	Val72 (2.74)	Gly153, Trp50, His51, Tyr161, Leu128, Pro132, Gly151, Asn152, Asp75
ZINC000085594516	−8.8	Ser135 (3.09)	Leu128, Tyr150, Pro132, Phe130, Gly151, His51, Asn152, G1y153, Asp75
6a,12a-dehydromillettone	−8.7	None	His151, Asp75, Gly151, Gly153, Tyr150, Phe130, Pro132, Leu128
ZINC000028462577	−8.6	Ser135 (2.67), Val72 (2.94)	Trp50, Gly151, Leu128, Phe130, His51, Gly153, Pro132, Tyr150
anhydrophlegmacin-9′,10′-quinone	−8.6	Asn152 (2.88), Gly153 (2.84), Ser135 (2.94)	Asp75, Val154, Val72, Trp50, His51, Pro132, Leu128, Gly151
2′,4′-dihydroxychalcone-(4-O-5‴)-4″,2‴,4‴-trihydroxychalcone	−8.6	Leu149 (2.99), Thr120 (3.26)	Val154, Lys73, Val72, Asn152, His51, Asp75, Gly148, Leu76, Gly153. Trp83, Lys74, Ile165, Ala166, Ala164, Asn167, Ile123
ZINC000095485910	−8.6	Phe130 (2.71)	Ser135, Gly151, Leu128, His51, Asp75, Gly153, Pro132, Tyr150
ZINC000095485955	−8.6	Trp83 (2.84), Leu149 (3.20), Asn152 (2.80)	Gly87, Val146, Met149, Leu76, Ala164, Asn167, Ile165, Ala166, Gly148, Leu85, Val147
ZINC000095486025	−8.5	Leu128 (3.34) Gly153 (2.87)	Val72, His51, Asp75, Ser135, Gly151, Phe130, Pro132, Tyr150, Tyr161, Val54, Lys73, Asn152
ZINC000038628344	−8.5	His51 (2.89), Ser135 (2.68), Asp75 (2.57), Phe130 (3.06), Tyr150 (3.10)	Pro132, Ser131, Leu128, Tyr161, Gly153, Gly151
ZINC000095486053	−8.4	Gly151 (2.99)	His51, Pro132, Tyr150, Ser135, Phe130, Leu128
phaseollidin	−8.4	Gly87 (2.83), Val146 (2.98)	Leu85, Trp83, Gly148, Leu149, Ala164, Leu76, Asn167. Asn152, Lys74, Ile165, Trp89, Ala166, Glu88, Glu86, Val147
6-oxoisoiguesterin	−8.4	Tyr150 (2.80, Phe130 (3.16, 2.83)	Ser131, Leu128, Gly151, Gly153, His51, Pro132
ZINC000095486052	−8.4	Asn152 (3.20), Gly153 (3.14)	Pro132, Tyr150, Leu128, Tyr161, Gly151, His151, Asp75
ZINC000014444870	−8.4	Asn152 (3.01), Leu149 (3.19)	Leu85, Val147, Gly87, Val146, Asn167, Ile165, Val54, Ala164, Ile123, Lys74, Gly148, Leu76, Trp83
Leflunomide	−7.1	None	Asn152, Val54, Ala64, Asn167, Leu76, Lys74, Ile123, Ala166
Prednisolone	−7.0	Gly151 (2.90, 2.71), Asp75 (2.95), His51 (3.21), Gly153 (2.93, 3.16)	Leu128, Phe130, Asn152, Ser135, Pro132

predicted lead compounds within the active site of the NS2B/NS3 protein (Mazumder et al., 2017). Understanding the binding mechanisms of the various molecules in the active site is crucial for the design of efficacious drugs. To analyze the dynamic behavior of the unbound proteins and complexes, the root mean square deviation, the radius of gyration, and the root mean square fluctuation were plotted with the use of Xmgrace (Agyapong et al., 2021; Kwofie et al., 2019b; Musyoka et al., 2016). All simulations were carried out for 100 ns.

3.7.1 Root mean square deviation (RMSD)

A reliable indicator of a protein's stability is the RMSD, which assesses the stability of the complex from the original protein backbone atomic coordinates (Adinortey et al., 2022; Kwofie et al., 2022). From the RMSD plot, the unbound protein and the four lead compounds experienced stability throughout the 100 ns run except for the inhibitor Prednisolone which was observed to be unstable till 70 ns of the run. The unbound protein was observed to have the least fluctuations. The RMSD plot for the NS2B/NS3pro-Prednisolone complex rose sharply from 0 to 0.26 nm after which it

FIGURE 5
Inhibitor Prednisolone docked in the NS2B/NS3 binding pocket, showing the protein-ligand interactions visualized in LigPlot and the 3D pose in PyMOL.
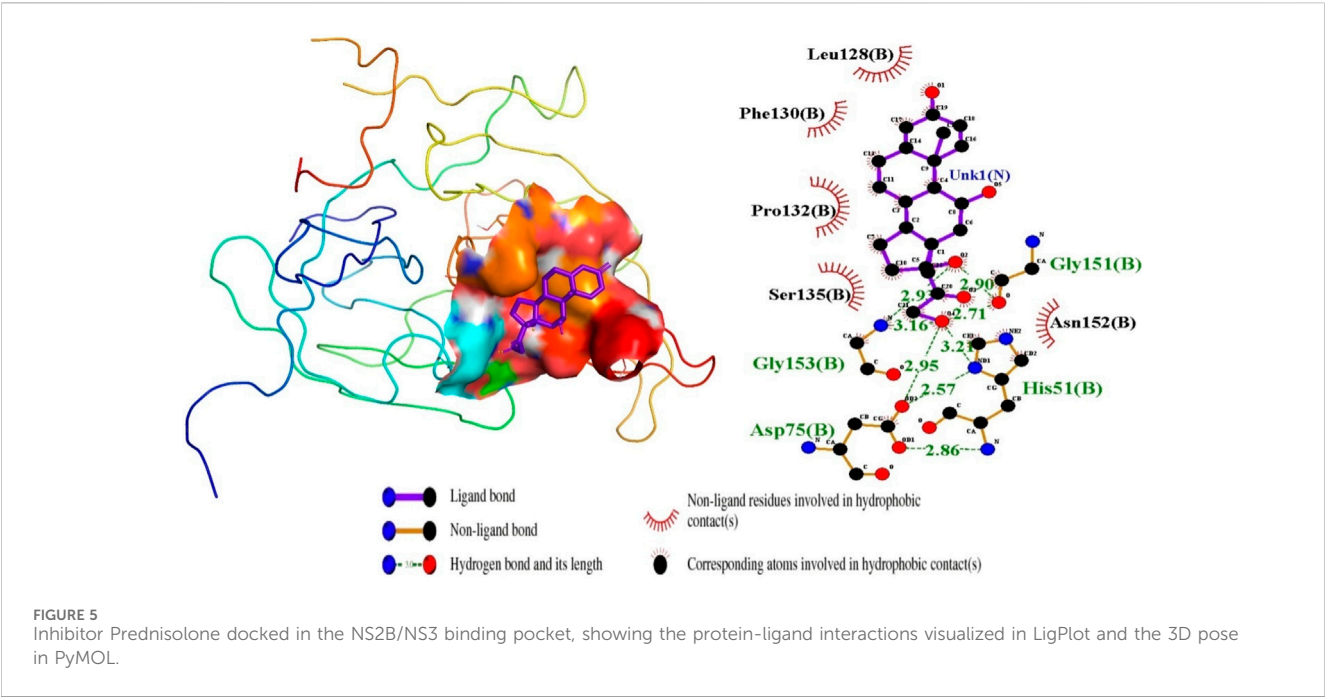
TABLE 4 Prediction of ADME and toxicity profiles of top 15 selected hits.

Ligands	ESOL solubility class	GI absorption	RO5 violation	Veber's rule violation	Mutagenicity	Tumorigenicity
ZINC000004095704	Soluble	Low	1	1	None	None
ZINC000095485958	Soluble	Low	1	1	None	None
ZINC000095485940	Soluble	High	0	0	None	None
ZINC000095485986	Soluble	Low	0	1	None	None
dihydrolanneaflavonol	Moderately soluble	High	0	0	None	None
lettowianthine	Moderately soluble	High	0	0	High	High
millettosine	Moderately soluble	High	0	0	None	None
ZINC000095486053	Moderately soluble	High	0	0	None	None
ZINC000031168265	Soluble	High	0	0	None	None
ZINC000095485910	Moderately soluble	High	0	0	High	High
ZINC000014780240	Moderately soluble	High	0	0	High	None
ZINC000085594516	Poorly soluble	Low	2	1	None	None
5,7′-physcion-fallacinol	Poorly soluble	Low	2	1	Low	None
ZINC000014441502	Moderately soluble	High	0	0	None	None
chryslandicin	Poorly soluble	Low	1	1	None	High

remained relatively unstable with large fluctuations until 70 ns where it demonstrated some stability (Figure 6). The RMSD of the NS2B/NS3pro-ZINC38628344 complex increased to 0.25 nm and stabilized, averaging 0.22 nm until the end. The complexes NS2B/NS3pro-ZINC95485940, NS2B/NS3pro-ZINC14441502, and NS2B/NS3pro-2′,4′-dihydroxychalcone showed similar fluctuations with the RMSD averaging around 0.17 nm (Figure 6).

3.7.2 Radius of gyration for 100 ns MD simulations

The compactness and folding of the five complexes and the unbound protein were examined in this work by charting the radius of gyration (Rg) throughout a 100 ns simulation duration (Liao et al., 2014). A stably folded protein maintains a reasonably steady Rg throughout the simulation. The Rg of the unbound NS2B/NS3 protease and protein-ligand complexes ranged from 1.51 to
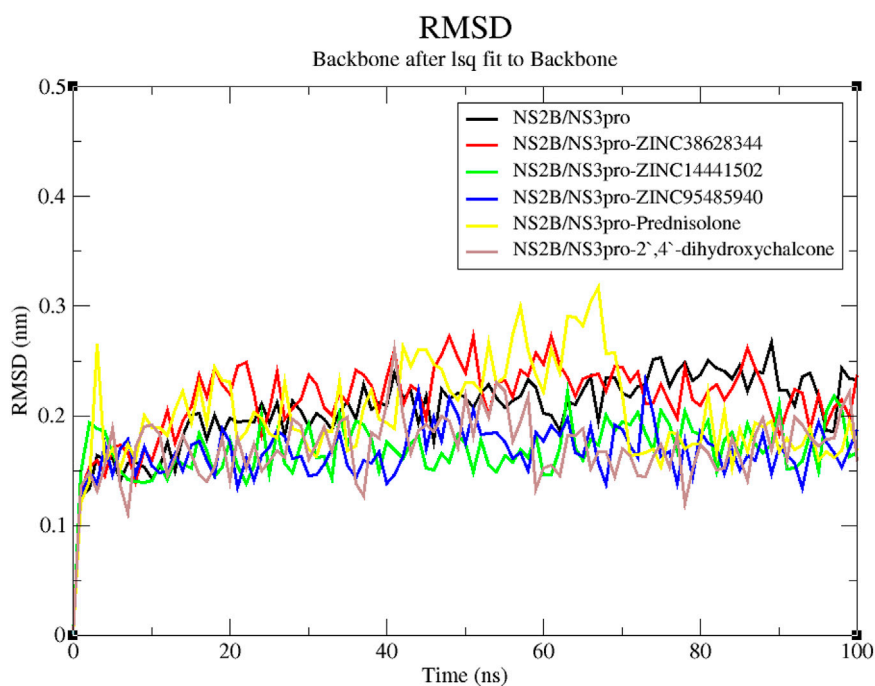
FIGURE 6
RMSD *versus* time graph of unbound protein and NS2B/NS3pro-ligand complexes generated over a 100 ns MD run.
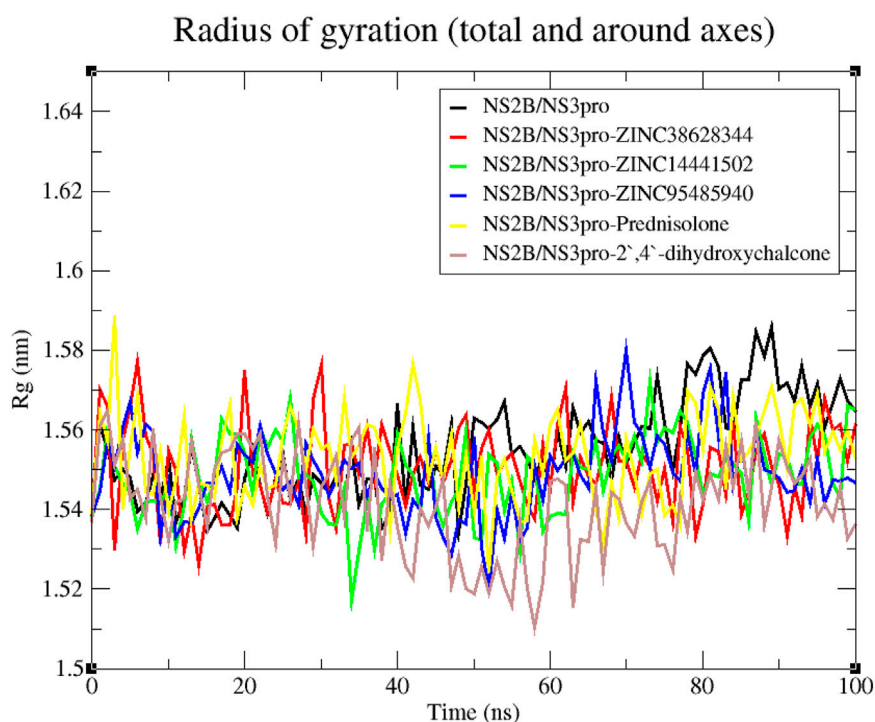
FIGURE 7
Rg graph of the NS2B/NS3pro-ligand complexes and unbound protein.

1.59 nm (Figure 7). Considering the unbound protease, it experienced relatively steady fluctuation till the 50 ns mark from which it rose sharply till the simulations ended. For the protein-ligand complexes, they demonstrated similar trends in fluctuation throughout the 100 ns run. The Rg for the NS2B/NS3pro-Prednisolone displayed fluctuations with the highest peak at
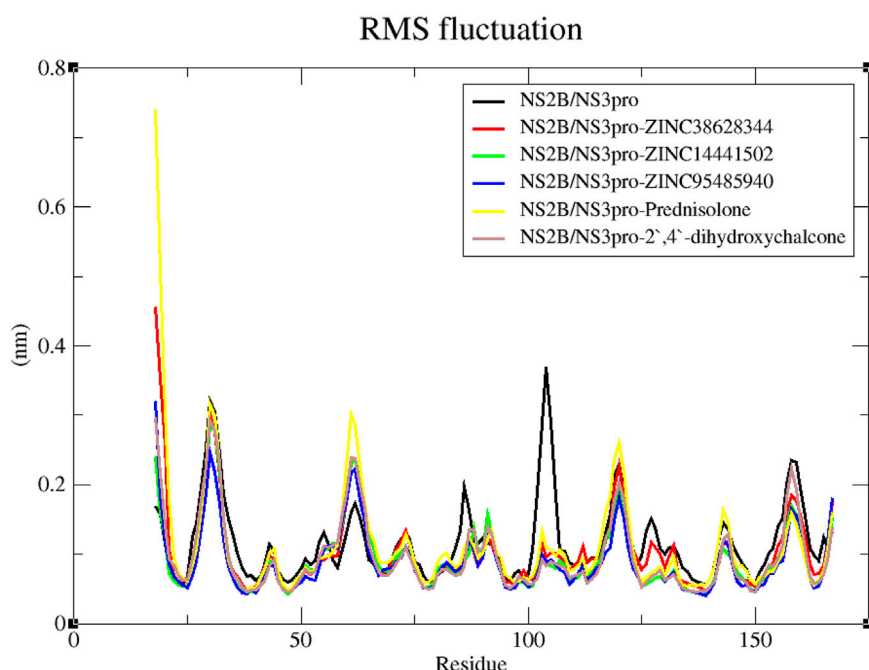
FIGURE 8
Examination of the RMSF trajectories of the NS2B/NS3pro-ligand complexes and the unbound protein residues.

1.59 nm (Figure 7). The complex NS2B/NS3pro-2′,4′-dihydroxychalcone had the largest fluctuations compared to their complexes, though most of the fluctuations occurred around 40–80 ns.

3.7.3 Root mean square fluctuations (RMSF) for 100 ns MD simulations

Additionally, the RMSF trajectories of the protein-ligand complexes and unbound NS2B/NS3pro were examined (L. Adams et al., 2023; Ashley et al., 2024). According to Cheng and Ivanov (2012), the RMSF reveals a protein's flexibility in several domains, some of which are connected to crystallographic B-factors. By using this stability profile analysis, residuals that contribute to the structural fluctuation can be evaluated. Greater variations are implied by higher RMSF values. Greater fluctuations occur in protein areas involved in catalysis and ligand binding (Dong et al., 2018). These protein sequence areas that influence the conformational changes of the complex are primarily responsible for adaptive variation in flexibility (Dong et al., 2018).

All the predicted lead compounds caused some degree of changes in comparable regions, according to the RMSF plot (Figure 8). Large fluctuations were observed from residue index 28–33 followed by some fluctuations between residue index 60–65 as well as 116–123. The RMSF graph also showed fluctuations in the unbound protein around residues 102–106 (Figure 8).

3.8 MMPBSA computations

3.8.1 Contributing energy terms

The binding free energies of the complexes were estimated using the Molecular Mechanics Poisson-Boltzmann Surface Area

(MMPBSA) calculation (Genheden and Ryde, 2015) (Table 5). Van der Waals energies, electrostatic, polar solvation, and solvent-accessible surface area energy are factors that contribute to the binding free energy (Asiedu et al., 2021; Boateng et al., 2020). The binding free energies were computed in terms of average and standard deviations. The leads ZIN38628344, ZINC95485940, and ZINC14441502 and 2′,4′-dihydroxychalcone had binding free energy of −44.957, −18.586, −25.881, and −55.805 kJ/mol respectively. 2′,4′-dihydroxychalcone demonstrated the lowest binding free energy while ZINC95485940 was observed to have the highest binding free energy among the four predicted lead compounds. The binding free energy of the known inhibitor Prednisolone was −17.682 kJ/mol. It has been found that compounds that have high polar energies and low electrostatic energies are active against receptors. (Gupta et al., 2018).

3.8.2 Per-residue energy decomposition

By employing per-residue decomposition, the binding energies of individual residues can be computed using the MMPBSA approach. This entails breaking down each residue by taking into account the interactions that each residue participates in. These offer helpful information on significant interactions between crucial residues in the free energy contribution. Critical residues for binding a ligand to a protein contribute binding free energy of at least ±5 kJ/mol (Kwofie et al., 2019a).

For every complex, the per-residue energy decomposition computation was carried out (Figure 9; Supplementary Figures S1A-D). For the NS2B/NS3-ZINC14441502 complex, only Tyr161 contributed energy of −6.4629 kJ/mol (Figure 9). For the NS2/NS3B-ZINC38628344 complex, Tyr161 and Leu128 contributed individual energies of −6.6957 and −3.4011 kJ/mol respectively (Supplementary

TABLE 5 MMPBSA contributing energy terms for NS2B/NS3-ligand complexes displayed as averages ± standard deviations in kJ/mol.

Compounds	van der waal energy (kJ/mol)	Electrostatic energy (kJ/mol)	Polar solvation energy (kJ/mol)	SASA energy (kJ/mol)	Binding energy (kJ/mol)
ZINC38628344	−73.805 ± 4.608	−10.304 ± 1.231	48.041 ± 3.817	−8.983 ± 0.555	−44.957 ± 3.383
ZINC95485940	−54.337 ± 3.716	−65.498 ± 5.335	65.388 ± 4.613	−7.682 ± 0.473	−18.586 ± 2.821
ZINC14441502	−52.459 ± 3.949	−22.090 ± 2.316	41.318 ± 3.042	−6.400 ± 0.476	−25.881 ± 3.519
Prednisolone	−39.913 ± 4.112	−9.190 ± 1.346	36.390 ± 3.989	−5.355 ± 0.527	−17.682 ± 3.583
2′,4′-dihydroxychalcone-(4-O-5‴)-4″,2‴,4‴-trihydroxychalcone	−160.105 ± 5.769	−41.801 ± 2.540	164.633 ± 6.076	−18.440 ± 0.639	−55.805 ± 3.467
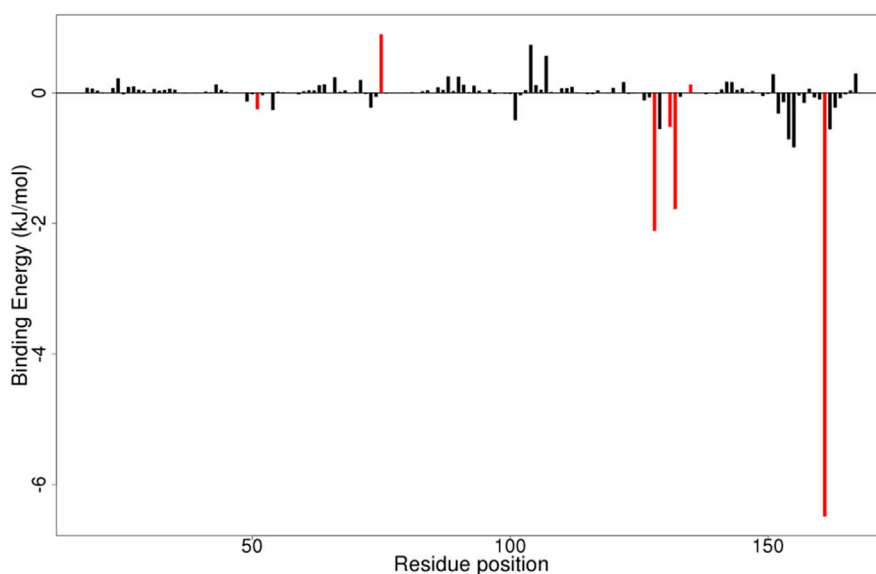
FIGURE 9
MMPBSA plot of binding free energy contributions per residue for NS2B/NS3–ZINC14441502 complex.

Figure S1A). Key residues interacting with ZINC95485940, 2′,4′-dihydroxychalcone, and Prednisolone contributed minor energies (Supplementary Figure 1).

4 Discussion

Despite being one of the leading causes of morbidity and mortality in different countries across the world, there is no approved efficacious drug for DENV infection (Palanichamy Kala et al., 2023; Bhatt et al., 2013). While there are currently no approved antiviral drugs or reliable vaccines, a vast number of plants have been tested against DENV through computational discovery (Malabadi et al., 2018; Powers and Setzer, 2016; Rasool et al., 2019; S et al., 2021). The effect of disrupting the function of NS2B/NS3 protease has already been established, particularly through interactions with critical residues His51, Asp75, and Ser135 (Purohit et al., 2022; Tian et al., 2018). In this study, we employed machine learning (ML) and molecular docking techniques to predict potential inhibitors against Dengue

Virus (DENV). The combination of machine learning models, molecular dynamics (MD) simulations, and molecular docking enables the exploration of drug candidates and accelerates the identification of lead compounds (Deo, 2015; Niazi and Mariam, 2023; Sarma et al., 2020).

The bioactive dataset from PubChem revealed a significant imbalance, with a ratio of 1:50 between the active and inactive compounds. This class imbalance phenomenon is commonly and largely observed in many bioinformatics and chemoinformatics studies (Japkowicz and Shah, 2011), which can lead to biased model training if not properly addressed. After processing, the dataset was refined to include 4,470 active compounds and 16,780 inactive compounds, achieving a ratio of approximately 1:4. This truncation was performed not merely due to computational constraints but as part of a deliberate effort to enhance the computational efficiency and balance the representation of active and inactive compounds. One key consideration was that excessively large and imbalanced datasets may introduce noise or over-represent the inactive class, thereby diminishing the model's ability to identify active compounds accurately.

The application of various machine learning algorithms, including k-NN, Gaussian Naïve Bayes, SVM, Random Forest, and Logistic Regression, highlights the diversity of approaches available for predictive modeling of active compounds in pharmacoinformatics (Leardi, 2001; W. Wu &Herath, 2016). The Logistic Regression model emerged as the most effective of the five tested, achieving the highest accuracy, recall, and F1 scores, which are critical metrics for evaluating classifier performance, particularly in imbalanced datasets (Davis and Goadrich, 2006; Mwanga et al., 2023). The performance of other antiviral ML classification models (Gawriljuk et al., 2021; Gupta and Mohanty, 2021; Sandhu et al., 2022), compared to our models though none of them were trained on the dataset used in this study. The recall of 0.76 shows the number of active compounds classified correctly as active while the F1 score of 0.83 illustrates the overall accuracy of the models by combining precision and recall metrics. The SVM closely followed the performance of the LR with a recall and F1 score of 0.71 and 0.81 respectively. In addition, the accuracy of the LR model at 0.94 was not far off from that of the SVM averaging an accuracy of 0.91. An SVM model (Sandhu et al., 2022) trained on 5692 molecules with inhibitory activity against acetylcholinesterase from the bindingDB database establishing accuracy and F1 score of 0.83 and 0.81, respectively. Validation of the model's predictive power involved testing against known DENV inhibitors, demonstrating the model's reliability in predicting active compounds. These predictions expand the pool of potential candidate Dengue Virus inhibitors for further validation.

The NS2B/NS3 protease complex, used in this study is composed of the NS3 protease, which carries out the catalytic activity, and the NS2B cofactor, which stabilizes the active conformation of NS3. A serine protease domain located at the N-terminal of NS3 is structurally responsible for cleaving the viral polyprotein into functional units required for viral replication (Low et al., 2011; Bhatt et al., 2013). Given its central role in viral replication, targeting the NS2B/NS3 complex disrupts a key step in the Dengue virus life cycle making NS2B/NS3 protease a key antiviral target for the development of therapeutic agents against the Dengue virus (Erbel et al., 2006; Norshidah et al., 2023; Bhatt et al., 2013). The selection of the PDB ID 2FOM for docking studies was based on structural quality metrics, underscoring the importance of selecting appropriate protein structures for virtual screening (Wlodaweret al., 2008). The results of the docking simulations indicated that anhydrophlegmacin exhibited superior binding affinity, reinforcing the predictive capabilities of the Logistic Regression model. Applying a high threshold of −8.0 kcal/mol improved selection conditions for further studies on active compounds (Kwofie et al., 2019b). Using a threshold of −8.0 kcal/mol, 56 hit compounds that docked firmly were selected for further analysis.

Characterization of ligand interactions using LigPlot provided insight into the binding mechanisms, which are vital for understanding how compounds can effectively inhibit the target protein (Laskowski and Swindells, 2011). This analysis is critical given that it helps identify key residues that contribute significantly to ligand binding, as a means of guiding future drug design efforts. Therefore, hydrogen and hydrophobic interactions between the shortlisted compounds and the residues in the active site helped to elucidate the top-hit compound that inhibits the activities of the NS2B/NS3 protease. Hydrophobic and hydrogen bonds between the selected compounds and catalytic triad His51-Asp75-Ser135 were the main determinants of good interaction and possible inhibition.

A structural similarity check between different NS2B/NS3pro confirms the conserved regions and residues (His51-Asp75-Ser135) on the NS3 protease sequence across all serotypes (Purohit et al., 2022; Wahaab et al., 2022), thus the lead compounds identified in this study can serve as cross-serotype inhibitors. The interactions such as His51, Tyr161, Pro132, Asp75, Gly153, and Ser135 by the compounds in this study are consistent with reported binding interactions through docking (Hariono et al., 2019; Purohit et al., 2022; Rasool et al., 2019). The four lead compounds were superimposed to compare their binding modes, revealing that key residues His51, Asp75, and Tyr161 were consistently present across all four complexes. Notably, the residue Ser135 was observed in three lead compounds, ZINC14441502, ZINC95485940, and ZINC38628344. These findings suggest that the four lead compounds share a similar mechanism of action. In addition, the ADMET helps to predict safe compounds by assessing the pharmacokinetic profiles and toxicity of compounds (Wang C. et al., 2018). The integration of Veber's rules and other drug-like filters serves to prioritize compounds that are more likely to succeed in preclinical and clinical phases denoted as "druglike compounds" (Veber et al., 2002).

Molecular dynamics simulations serve as a powerful tool to explore the stability of protein-ligand complexes over time (Maricarmen et al., 2016). The stability observed in the RMSD plots correlates with the low binding affinities observed during the molecular docking of the compounds. Lower fluctuations often indicate stronger and more stable interactions (Adinortey et al., 2022). However, the inhibitor Prednisolone was observed to be unstable, with its RMSD peaking at 0.3 nm. The predicted leads, ZINC14441502, $2',4'$-dihydroxychalcone, ZINC95485940, and ZINC38628344 demonstrated high fluctuations compared to the unbound state indicating that binding with compounds may have caused conformation changes in the structure. The Rg analysis further supported this by demonstrating the compactness of the complexes, a key indicator of structural integrity during simulations (Liao et al., 2014). A stable Rg between a range of 1.51–1.59 nm, shows a stably folded complex.

Molecular Mechanics Poisson-Boltzmann Surface Area (MMPBSA) calculations provided detailed insights into the energetic contributions of binding interactions, which are crucial for understanding the thermodynamic viability of the ligand-protein complexes (Genheden and Ryde, 2015). The findings indicate that the leads $2',4'$-dihydroxychalcone, ZINC14441502, ZINC95485940, and ZINC38628344 exhibited the most favorable binding free energies of -55.805, -25.881, and -44.957 kJ/mol, respectively, reinforcing their potential as lead compounds for further development (Abdullah et al., 2023; Saleh & Kamisah, 2021). The lead compounds demonstrated a more negative binding energy to the NS2B/NS3 protease than the inhibitor Prednisolone, which is suggestive of a stronger attraction.

Some limitations associated with the study include; the machine learning model was trained on a dataset heavily imbalanced toward inactive compounds, which could influence the model's ability to generalize well to external datasets. The results validate the logistic model in handling imbalanced datasets, a common issue in bioinformatics studies. While steps were taken to mitigate this, further work could involve data balancing techniques or increasing the number of active compounds to improve predictive accuracy. Additionally, while the molecular docking results are promising,

in vitro and *in vivo* validations of these compounds are essential to confirm their inhibitory effects against the Dengue virus. Furthermore, pharmacokinetic profiling, though performed *in silico*, would require experimental validation to ensure the predicted compounds meet safety and efficacy standards in a biological system.

5 Conclusion

Natural products used as a reservoir for novel therapeutic agents must be tapped and repurposed as effective DENV inhibitors. The significance of this study lies in applying a comprehensive approach to drug discovery, integrating Machine Learning, Molecular Docking, and Dynamics simulations to identify novel potential DENV inhibitors. From this study, five classification models were developed, from which the best-performing model based on accuracy, F1 score, precision, and specificity was employed to make predictions. With an accuracy and precision of 0.94 and 0.91 respectively, the Logistic Regression outperformed the other models and thus was used to predict potential inhibitors against the protease. Four lead compounds ZINC38628344, ZINC95485940, $2',4'$-dihydroxychalcone, and ZINC14441502 with high binding affinities of −0.85, −0.81, −8.6, and −0.81 kcal/mol respectively, and interactions with the conserved catalytic triad, His51-Asp75-Ser135 in the active site of the NS2B/NS3 protease were discovered. The successful prediction and characterization of binding interactions enhance our understanding of ligand-target dynamics based on natural compounds which can be biosynthesized, paving the way for further experimental validations and *in vitro* drug development. The compounds were predicted to possess pharmacokinetic properties and exhibit characteristics of non-tumorigenicity and non-mutagenicity, based on the physicochemical and toxicological characterization, adjourning them to be safe and drug-like. The probable inhibition of the activities of the NS2B/NS3pro of DENV by the leads was corroborated by 100 ns molecular dynamics simulation involving MMPBSA calculations. The study's approach provides a foundation for the continued use of computational tools in the fight against viral diseases, suggesting a promising path for rapid drug discovery in the future. In addition, the prospective compounds can be considered suitable anti-DENV scaffolds for fragment-based drug design and, thus, are worthy of further experimental validation.

Data availability statement

The dataset used in this study is available at the PubChem Database with AID 651640 (https://pubchem.ncbi.nlm.nih.gov/bioassay/651640) and the GitHub Repo (https://github.com/omicscodeathon/denguedrug/tree/main/data). The comprehensive pipelines and scripts utilized for the models' implementation as well as data and results for the Molecular Docking and Molecular Dynamics Simulations are available at the GitHub repository at https://github.com/omicscodeathon/denguedrug.

Author contributions

GH: Conceptualization, Data curation, Formal Analysis, Methodology, Project administration, Supervision, Visualization,

Writing–original draft, Writing–review and editing. JA: Formal Analysis, Methodology, Visualization, Writing–original draft, Writing–review and editing. DK: Formal Analysis, Validation, Visualization, Writing–original draft, Writing–review and editing. LZ: Formal Analysis, Methodology, Writing–original draft, Writing–review and editing. LT: Writing–original draft, Writing–review and editing. AA: Writing–original draft, Writing–review and editing. SS: Writing–original draft, Writing–review and editing. MK: Writing–original draft, Writing–review and editing. HB: Writing–original draft, Writing–review and editing. OA: Conceptualization, Project administration, Resources, Supervision, Validation, Writing–original draft, Writing–review and editing.

Conflict of interest

The authors declare that the research was conducted in the absence of any commercial or financial relationships that could be construed as a potential conflict of interest.

Generative AI statement

The author(s) declare that no Generative AI was used in the creation of this manuscript.

Publisher's note

All claims expressed in this article are solely those of the authors and do not necessarily represent those of their affiliated organizations, or those of the publisher, the editors and the reviewers. Any product that may be evaluated in this article, or claim that may be made by its manufacturer, is not guaranteed or endorsed by the publisher.

Supplementary material

The Supplementary Material for this article can be found online at: https://www.frontiersin.org/articles/10.3389/fchem.2024.1510029/full#supplementary-material

References

Abdullah, Z. L., Chee, H.-Y., Yusof, R., and &ohdFauzi, F. (2023). Finding lead compounds for dengue antivirals from a collection of old drugs through *in silico* target prediction and subsequent *in vitro* validation. *ACS Omega* 8 (36), 32483–32497. doi:10.1021/acsomega.3c02607

Abolo, L., Ssenkaali, J., Mulumba, O., and Awe, O. I. (2024). Exploring the causal effect of omega-3 polyunsaturated fatty acid levels on the risk of type 1 diabetes: a Mendelian randomization study. *Front. Genet.* 15, 1353081. doi:10.3389/fgene.2024.1353081

Abraham, M. J., Murtola, T., Schulz, R., Pall, S., Smith, J. C., Hess, B., et al. (2015). Gromacs: high performance molecular simulations through multi-level parallelism from laptops to supercomputers. *SoftwareX* 1–2, 19–25. doi:10.1016/j.softx.2015.06.001

Adams, J., Agyenkwa-mawuli, K., Agyapong, O., Wilson, M. D., and &Kwofie, S. K. (2022). EBOLApred: a machine learning-based web application for predicting cell entry inhibitors of the Ebola virus. *Comput. Biol. Chem.* 101 (March), 107766. doi:10.1016/j.compbiolchem.2022.107766

Adams, L., Afiadenyo, M., Kwofie, S. K., Wilson, M. D., Kusi, K. A., Obiri-Yeboah, D., et al. (2023). *In silico* screening of phytochemicals from dissotisrotundifolia against plasmodium falciparum dihydrofolate reductase. *Phytomedicine Plus* 3 (2), 100447. doi:10.1016/j.phyplu.2023.100447

Adinortey, C. A., Kwarko, G. B., Koranteng, R., Boison, D., Obuaba, I., Wilson, M. D., et al. (2022). Molecular structure-based screening of the constituents of calotropis procera identifies potential inhibitors of diabetes mellitus target alpha glucosidase. *Curr. Issues Mol. Biol.* 44 (2), 963–987. doi:10.3390/cimb44020064

Agyapong, O., Asiedu, S. O., Kwofie, S. K., Miller, W. A., Parry, C. S., Sowah, R. A., et al. (2021). Molecular modelling and *de novo* fragment-based design of potential inhibitors of beta-tubulin gene of Necatoramericanus from natural products. *Inf. Med. Unlocked* 26 (February), 100734. doi:10.1016/j.imu.2021.100734

Alaya, F., Baraket, G., Adediran, D. A., Cuttler, K., Ajiboye, I., Kivumbi, M. T., et al. (2024). Multiple sclerosis stages and their differentially expressed genes: a bioinformatics analysis. doi:10.1101/2024.01.20.576448

Anasir, M. I., and Ramanathan, B. (2020) *Structure-based design of antivirals against envelope glycoprotein of dengue virus*, 1–23.

Andersson, V. O., Ferreira Birck, M. A., and Araujo, R. M. (2018) "Towards predicting dengue fever rates using convolutional neural networks and street-level images," in *2018 international joint conference on neural networks (IJCNN)*, 1–8. doi:10.1109/IJCNN.2018.8489567

Aniceto, N., Albuquerque, T. S., Bonifácio, V. D. B., Guedes, R. C., and &rtinho, N. (2023). Using machine learning and molecular docking to leverage urease inhibition data for virtual screening. *Int. J. Mol. Sci.* 24 (9), 8180. doi:10.3390/ijms24098180

Ashley, C. N., Broni, E., Wood, C. M., Okuneye, T., Ojukwu, M. P. T., Dong, Q., et al. (2024). Identifying potential monkeypox virus inhibitors: an *in silico* study targeting the A42R protein. *Front. Cell. Infect. Microbiol.* 14 (March), 1351737–1351819. doi:10.3389/fcimb.2024.1351737

Asiedu, S. O., Kwofie, S. K., Broni, E., and Wilson, M. D. (2021). Computational identification of potential anti-inflammatory natural compounds targeting the p38 mitogen-activated protein kinase (Mapk): implications for Covid-19-induced cytokine storm. *Biomolecules* 11 (5), 653. doi:10.3390/biom11050653

Ather, S. H., Awe, O. I., Butler, T. J., Denka, T., Semick, S. A., Tang, W., et al. (2018). SeqAcademy: an educational pipeline for RNA-Seq and ChIP-Seq analysis. *F1000Research* 7, 628. doi:10.12688/f1000research.14880.4

Awe, O. I., EnNajih, N., Nyamari, M. N., and Mukanga, L. B. (2023). Comparative study between molecular and genetic evolutionary analysis tools using African SARS-CoV2 variants. *Inf. Med. Unlocked* 36, 101143. doi:10.1016/j.imu.2022.101143

Ben, A. H., Abassi, N., and Awe, O. I. (2024). NeuroVar: an open-source tool for the visualization of gene expression and variation data for biomarkers of neurological diseases. *Gigabyte* 2024, gigabyte143. doi:10.46471/gigabyte.143

Bhatt, P., Gething, P. W., Brady, O. J., Messina, J. P., Farlow, A. W., Moyes, C. L., et al. (2013). The global distribution and burden of dengue. *Nature* 496 (7446), 504–507. doi:10.1038/nature12060

Biswal, S., Borja-Tabora, C., Martinez Vargas, L., Velásquez, H., Theresa Alera, M., Sierra, V., et al. (2020). Efficacy of a tetravalent dengue vaccine in healthy children aged 4–16 years: a randomised, placebo-controlled, phase 3 trial. *Lancet*, 395(10234), 1423–1433. doi:10.1016/S0140-6736(20)30414-1

Boateng, R. A., Tastan Bishop, Ö., and &usyoka, T. M. (2020). Characterisation of plasmodial transketolases and identification of potential inhibitors: an *in silico* study. *Malar. J.* 19 (1), 442–519. doi:10.1186/s12936-020-03512-1

Byrd, C. M., Dai, D., Grosenbach, D. W., Berhanu, A., Jones, K. F., Cardwell, K. B., et al. (2013). A novel inhibitor of dengue virus replication that targets the capsid protein. *Antimicrob. Agents Chemother.* 57 (1), 15–25. doi:10.1128/AAC.01429-12

Caminade, C., Medlock, J. M., Ducheyne, E., Mcintyre, K. M., Leach, S., Baylis, M., et al. (2012). *Suitability of European climate for the Asian tiger mosquito* Aedes albopictus: *recent trends and future scenarios*, 2708–2717.

Carocci, M., Hinshaw, S. M., Rodgers, M. A., Villareal, V. A., Burri, D. J., Pilankatta, R., et al. (2015). The bioactive lipid 4-hydroxyphenyl retinamide inhibits Flavivirus replication. *Antimicrob. Agents Chemother.* 59 (1), 85–95. doi:10.1128/AAC.04177-14

Chao, L. H., Jang, J., Johnson, A., Nguyen, A., Gray, N. S., Yang, P. L., et al. (2018) *How small-molecule inhibitors of dengue-virus infection interfere with viral membrane fusion*, 1–11.

Che, P., Wang, L., and Li, Q. (2009). The development, optimization and validation of an assay for high throughput antiviral drug screening against dengue virus. *Int. J. Clin. Exp. Med.* 2 (4), 363–373.

Chen, H.-R., Lai, Y.-C., and Yeh, T.-M. (2018). Dengue virus non-structural protein 1: a pathogenic factor, therapeutic target, and vaccine candidate. *J. Biomed. Sci.* 25 (1), 58–11. doi:10.1186/S12929-018-0462-0

Cheng, X., and Ivanov, I. (2012). Molecular dynamics. *Methods Mol. Biol.* (Clifton, N.J.) 929, 243–285. doi:10.1007/978-1-62703-050-2_11

Chikkaveeraiah, S. K., Srinath, K. M., Hathur, B. V., Hari, V. S. A., and &Vanama, L. S. (2024). Study of dengue fever in an epidemic - a single centre observational study at tertiary care hospital. *APIK J. Intern. Med.* 12 (4), 205–209. doi:10.4103/ajim.ajim_45_23

Chikwambi, Z., Hidjo, M., Chikondowa, P., Afolabi, L., Aketch, V., Jayeoba, G., et al. (2023). Multi-omics data integration approach identifies potential biomarkers for Prostate cancer. *bioRxiv.* doi:10.1101/2023.01.26.522643

Ci, Y., Yao, B., Yue, K., Yang, Y., Xu, C., Li, D.-F., et al. (2023). Bortezomib inhibits ZIKV/DENV by interfering with viral polyprotein cleavage via the ERAD pathway. *Cell. Chem. Biol.* 30 (5), 527–539.e5. doi:10.1016/j.chembiol.2022.10.003

Comesana, A. E., Huntington, T. T., Scown, C. D., Niemeyer, K. E., and Rapp, V. H. (2022). A systematic method for selecting molecular descriptors as features when training models for predicting physiochemical properties. *Fuel*, 321, 123836. doi:10.1016/j.fuel.2022.123836

Cucunawangsih, L. N., and Lugito, N. P. H. (2017). Trends of dengue disease epidemiology. *Virology Res. Treat.* 8. doi:10.1177/1178122X17695836

Daina, A., Michielin, O., and &Zoete, V. (2017). SwissADME: a free web tool to evaluate pharmacokinetics, drug-likeness and medicinal chemistry friendliness of small molecules. *Sci. Rep.* 7 (January), 42717–42813. doi:10.1038/srep42717

Das, A. P., Mathur, P., and Agarwal, S. M. (2024). Machine learning, molecular docking, and dynamics-based computational identification of potential inhibitors against lung cancer. *Mach. Learn. Mol. Docking, Dynamics-Based Comput. Identif. Potential Inhibitors against Lung Cancer* 9, 4528–4539. doi:10.1021/acsomega.3c07338

Davis, J., and Goadrich, M. (2006) "The relationship between Precision-Recall and ROC curves," in *Proceedings of the 23rd international conference on machine learning*, 233–240. doi:10.1145/1143844.1143874

Deo, R. C. (2015). Machine learning in medicine. *Circulation* 132 (20), 1920–1930. doi:10.1161/CIRCULATIONAHA.115.001593

Devadasu, V. R., Deb, P. K., Maheshwari, R., Sharma, P., and &Tekade, R. K. (2018) "Physicochemical, pharmaceutical, and biological considerations in GIT absorption of drugs," in *Dosage form design considerations*, I. Elsevier Inc, 149–178. doi:10.1016/B978-0-12-814423-7.00005-8

de Wispelaere, M., LaCroix, A. J., and Yang, P. L. (2013). The small molecules AZD0530 and dasatinib inhibit dengue virus RNA replication via Fyn kinase. *J. Virology* 87 (13), 7367–7381. doi:10.1128/JVI.00632-13

Die, J. V., Elmassry, M. M., LeBlanc, K. H., Awe, O. I., Dillman, A., and Busby, B. (2019). geneHummus: an R package to define gene families and their expression in legumes and beyond. *BMC Genomics* 20, 591. doi:10.1186/s12864-019-5952-2

Dong, Y. W., Liao, M. L., Meng, X. L., and &Somero, G. N. (2018). Structural flexibility and protein adaptation to temperature: molecular dynamics analysis of malate dehydrogenases of marine molluscs. *Proc. Natl. Acad. Sci. U. S. A.* 115 (6), 1274–1279. doi:10.1073/pnas.1718910115

Drago, F., Ciccarese, G., Merlo, G., Trave, I., Javor, S., Rebora, A., et al. (2021). Oral and cutaneous manifestations of viral and bacterial infections: not only COVID-19 disease. *Clin. Dermatology* 39 (3), 384–404. doi:10.1016/j.clindermatol.2021.01.021

Durbin, A. P. (2020). Historical discourse on the development of the live attenuated tetravalent dengue vaccine candidate TV003/TV005. *Curr. Opin. Virology*, 43, 79–87. doi:10.1016/j.coviro.2020.09.005

Dwivedi, V. D., Tripathi, I. P., Tripathi, R. C., Bharadwaj, S., and Mishra, S. K. (2017). Genomics, proteomics and evolution of dengue virus. *Briefings Funct. Genomics* 16 (4), 217–227. doi:10.1093/bfgp/elw040

El Abed, F., Baraket, G., Nyamari, M. N., Naitore, C., and Awe, O. I. (2023). Differential expression analysis of miRNAs and mRNAs in epilepsy uncovers potential biomarkers. *bioRxiv.* doi:10.1101/2023.09.11.557132

Erbel, P., Schiering, N., D'Arcy, A., Renatus, M., Kroemer, M., Lim, S. P., et al. (2006). Structural basis for the activation of flaviviral NS3 proteases from dengue and West Nile virus. *Nat. Struct. Mol. Biol.* 13 (4), 372–373. doi:10.1038/nsmb1073

Franco, E. J., de Mello, C. P. P., and Brown, A. N. (2021). Antiviral evaluation of uv-4b and interferon-alpha combination regimens against dengue virus. *Viruses* 13 (5), 771. doi:10.3390/v13050771

Fraser, J. E., Watanabe, S., Wang, C., Chan, W. K. K., Maher, B., Lopez-Denman, A., et al. (2014). A nuclear transport inhibitor that modulates the unfolded protein response and provides *in vivo* protection against lethal dengue virus infection. *J. Infect. Dis.* 210 (11), 1780–1791. doi:10.1093/infdis/jiu319

Gautam, S., Thakur, A., Rajput, A., and Kumar, M. (2024). Anti-dengue: a machine learning-assisted prediction of small molecule antivirals against dengue virus and implications in drug repurposing. *Viruses* 16 (1), 45. doi:10.3390/v16010045

Gawriljuk, V. O., Zin, P. P. K., Puhl, A. C., Zorn, K. M., Foil, D. H., Lane, T. R., et al. (2021). Machine learning models identify inhibitors of SARS-CoV-2. *J. Chem. Inf. Model.* 61 (9), 4224–4235. doi:10.1021/acs.jcim.1c00683

Gebhard, L. G., Leal, E. S., Adler, N. S., Fern, G. A., Battini, L., Aucar, M. G., et al. (2019) *European Journal of Medicinal Chemistry De novo design approaches targeting an envelope protein pocket to identify small molecules against dengue virus*, 182. doi:10.1016/j.ejmech.2019.111628

Genheden, S., and Ryde, U. (2015). The MM/PBSA and MM/GBSA methods to estimate ligand-binding affinities. *Expert Opin. Drug Discov.* 10, 449–461. doi:10.1517/17460441.2015.1032936

Gupta, A., Chaudhary, N., and &roy, P. (2018). MM-PBSA and per-residue decomposition energy studies on 7-Phenyl-imidazoquinolin-4(5H)-one derivatives: identification of crucial site points at microsomal prostaglandin E synthase-1 (mPGES-1) active site. *Int. J. Biol. Macromol.* 119, 352–359. doi:10.1016/j.ijbiomac.2018.07.050

Gupta, P., and Mohanty, D. (2021). SMMPPI: a machine learning-based approach for prediction of modulators of protein-protein interactions and its application for identification of novel inhibitors for RBD:hACE2 interactions in SARS-CoV-2. *Briefings Bioinforma.* 22 (5), bbab111–15. doi:10.1093/bib/bbab111

Hariono, M., Choi, S. B., Roslim, R. F., Nawi, M. S., Tan, M. L., Kamarulzaman, E. E., et al. (2019). Thioguanine-based DENV-2 NS2B/NS3 protease inhibitors: virtual screening, synthesis, biological evaluation and molecular modelling. *PLoS ONE* 14 (1), 02108699–e210921. doi:10.1371/journal.pone.0210869

Jamal, Z., Haider, S. A., Hakim, R., Humayun, F., Umar, M., Muhammad, F., et al. (2024). Serotype and genomic diversity of dengue virus during the 2023 outbreak in Pakistan reveals the circulation of genotype III of DENV-1 and cosmopolitan genotype of DENV-2. *J. Med. Virol.* 96, 297277–e29813. doi:10.1002/jmv.29727

Japkowicz, N., and Shah, M. (2011). *Evaluating learning algorithms: a classification perspective*. Cambridge University Press.

Jia, C. Y., Li, J. Y., Hao, G. F., and Yang, G. F. (2020). A drug-likeness toolbox facilitates ADMET study in drug discovery. *Drug Discov. Today* 25 (1), 248–258. doi:10.1016/j.drudis.2019.10.014

Jung, Y., and Hu, J. (2015). A K-fold averaging cross-validation procedure. *J. Nonparametric Statistics* 27 (2), 167–179. doi:10.1080/10485252.2015.1010532

Kallas, E. G., Precioso, A. R., Palacios, R., Thomé, B., Braga, P. E., Vanni, T., et al. (2020). Safety and immunogenicity of the tetravalent, live-attenuated dengue vaccine Butantan-DV in adults in Brazil: a two-step, double-blind, randomised placebo-controlled phase 2 trial. *Lancet Infect. Dis.*, 20(7), 839–850. doi:10.1016/S1473-3099(20)30023-2

Kee, E., Chong, J. J., Choong, Z. J., and Lau, M. (2023). A comparative analysis of cross-validation techniques for a smart and lean pick-and-place solution with deep learning. *Electron. Switz.* 12 (11), 2371. doi:10.3390/electronics12112371

Khorshid, S. F., Abdulazeez, A. M., and Sallow, A. B. (2021). A comparative analysis and predicting for breast cancer detection based on data mining models. *Asian J. Res. Comput. Sci. May*, 45–59. doi:10.9734/ajrcos/2021/v8i430209

Kularatne, S. A. M., Walathara, C., Mahindawansa, S. I., Wijesinghe, S., Pathirage, M. M. K., Kumarasiri, P. V. R., et al. (2009). Efficacy of low dose dexamethasone in severe thrombocytopenia caused by dengue fever: a placebo controlled study. *Postgrad. Med. J.* 85 (1008), 525–529. doi:10.1136/pgmj.2008.078444

Kumari, R., Kumar, R., and Lynn, A. (2014). g_mmpbsa—a Gromacs Tool for High-Throughput MM-PBSA Calculations. *J. Chem. Inf. Model.* 54, 1951–1962. doi:10.1021/ci500020m

Kwofie, S. K., Broni, E., Teye, J., Quansah, E., Issah, I., Wilson, M. D., et al. (2019a). Pharmacoinformatics-based identification of potential bioactive compounds against Ebola virus protein VP24. *Comput. Biol. Med.* 113 (March), 103414. doi:10.1016/j.compbiomed.2019.103414

Kwofie, S. K., Dankwa, B., Enninful, K. S., Adobor, C., Broni, E., Ntiamoah, A., et al. (2019b). Molecular docking and dynamics simulation studies predict munc18b as a target of mycolactone: a plausible mechanism for granule exocytosis impairment in Buruli Ulcer Pathogenesis. *Toxins* 11 (3), 181. doi:10.3390/toxins11030181

Kwofie, S. K., Hanson, G., Sasu, H., Enninful, K. S., Mensah, F. A., Nortey, R. T., et al. (2022). Molecular modelling and atomistic insights into the binding mechanism of MmpL3 mtb. *Chem. Biodivers.* 19 (9), e202200160. doi:10.1002/cbdv.202200160

Lai, J.-H., Lin, Y.-L., and Hsieh, S.-L. (2017). Pharmacological intervention for dengue virus infection. *Biochem. Pharmacol.* 129, 14–25. doi:10.1016/j.bcp.2017.01.005

Laskowski, R. A., and Swindells, M. B. (2011). LigPlot+: multiple ligand–protein interaction diagrams for drug discovery. *J. Chem. Inf. Model.* 51 (10), 2778–2786. doi:10.1021/ci200227u

Leardi, R. (2001). Genetic algorithms in chemometrics and chemistry: a review. *J. Chemom.*, 15(7), 559–569. doi:10.1002/cem.651

Lee, J.-C., Tseng, C.-K., Wu, Y.-H., Kaushik-Basu, N., Lin, C.-K., Chen, W.-C., et al. (2015). Characterization of the activity of 2'-C-methylcytidine against dengue virus replication. *Antivir. Res.* 116, 1–9. doi:10.1016/j.antiviral.2015.01.002

Lee, M. F., Tan, S. L., Ahemad, N., Hamid, A. A. A., Hishamuddin, S. A. S. N., Batumalaie, K., et al. (2024). Molecular docking and dynamics simulation reveal withanolides as potent antivirals against dengue virus. *South Afr. J. Bot.*, 169, 426–434. doi:10.1016/j.sajb.2024.04.045

Liao, K. H., Chen, K. B., Lee, W. Y., Sun, M. F., Lee, C. C., and Chen, C. Y. C. (2014). Ligand-based and structure-based investigation for Alzheimer's disease from traditional Chinese medicine. *Evidence-Based Complementary Altern. Med.* 2014, 364819. doi:10.1155/2014/364819

Lim, S. P. (2019). Dengue drug discovery: progress, challenges and outlook. *Antivir. Res.* 163, 156–178. doi:10.1016/J.ANTIVIRAL.2018.12.016

Lim, X.-N., Shan, C., Marzinek, J. K., Dong, H., Ng, T. S., Ooi, J. S. G., et al. (2019). Molecular basis of dengue virus serotype 2 morphological switch from 29°C to 37°C. *PLoS Pathog.* 15 (9), e1007996. doi:10.1371/journal.ppat.1007996

Lin, C. L., Kiu, Y. T., Kan, J. Y., Chang, Y. J., Hung, P. Y., Lu, C. H., et al. (2023). The antiviral activity of varenicline against dengue virus replication during the post-entry stage. *Biomedicines* 11 (10), 2754–2814. doi:10.3390/biomedicines11102754

Low, J. S. Y., Wu, K. X., Chen, K. C., Ng, M. M. L., and Chu, J. J. H. (2011). Narasin, a novel antiviral compound that blocks dengue virus protein expression. *Antivir. Ther.* 16 (8), 1203–1218. doi:10.3851/IMP1884

Malabadi, R. B., Chalannavar, R. K., Supriya, S., Nityasree, B. R., Sowmyashree, K., and &Meti, N. T. (2018). Role of botanical drugs in controlling dengue virus disease. Available at: https://api.semanticscholar.org/CorpusID:212505980.

Maricarmen, H.-R., Martha, R.-H. C., Jessica, M.-W E., Marlet, M.-A., and José, B. C. (2016). Current tools and methods in molecular dynamics (MD) simulations for drug design. In *Curr. Med. Chem.* (Vol. 23, Issue 34, pp. 3909–3924). doi:10.2174/0929867323666160530144742

Martina, B. E. E., Koraka, P., and Osterhaus, A. D. M. E. (2009). Dengue virus pathogenesis: an integrated view. *Clin. Microbiol. Rev.* 22 (4), 564–581. doi:10.1128/CMR.00035-09

Mazumder, M., Ponnan, P., Das, U., Gourinath, S., Khan, H. A., Yang, J., et al. (2017). Investigations on binding pattern of kinase inhibitors with PPAR γ: molecular docking, molecular dynamic simulations, and free energy calculation studies. *PPAR Res.* 2017, 1–11. doi:10.1155/2017/6397836

McCormick, K. D., Liu, S., Jacobs, J. L., Marques, E. T. A., Sluis-Cremer, N., and Wang, T. (2012). Development of a robust cytopathic effect-based high-throughput screening assay to identify novel inhibitors of dengue virus. *Antimicrob. Agents Chemother.* 56 (6), 3399–3401. doi:10.1128/AAC.06425-11

Murray, N. E. A., Quam, M. B., and Wilder-Smith, A. (2013). Epidemiology of dengue: past, present and future prospects. *Clin. Epidemiol.* 5 (1), 299–309. doi:10.2147/CLEP.S34440

Musyoka, T. M., Kanzi, A. M., Lobb, K. A., and &Tastan Bishop, Ö. (2016). Structure based docking and molecular dynamic studies of plasmodial cysteine proteases against a South African natural compound and its analogs. *Sci. Rep.* 6 (December 2015), 23690–23712. doi:10.1038/srep23690

Mwanga, M. J., Obura, H., Evans, M., and Awe, O. I. (2023). Enhanced deep convolutional neural Network for SARS-CoV-2 variants classification. *BioRxiv*, 2023–2028. doi:10.1101/2023.08.09.552643

Nguyen, N. M., Tran, C. N. B., Phung, L. K., Duong, K. T. H., Huynh, H. le A., Farrar, J., et al. (2013). A randomized, double-blind placebo controlled trial of balapiravir, a polymerase inhibitor, in adult dengue patients. *J. Infect. Dis.* 207 (9), 1442–1450. doi:10.1093/infdis/jis470

Niazi, S. K., and Mariam, Z. (2023). Recent advances in machine-learning-based chemoinformatics: a comprehensive review. *Int. J. Mol. Sci.* 24 (14), 11488. doi:10.3390/ijms241411488

Niazi, S. K., and Mariam, Z. (2024) *Computer-aided drug design and drug discovery: a prospective analysis*, 1–22.

Noble, C. G., Seh, C. C., Chao, A. T., and Shi, P. Y. (2012). Ligand-bound structures of the dengue virus protease reveal the active conformation. *J. Virology* 86 (1), 438–446. doi:10.1128/JVI.06225-11

Norshidah, H., Leow, C. H., Ezleen, K. E., Wahab, H. A., Vignesh, R., Rasul, A., et al. (2023). Assessing the potential of NS2B/NS3 protease inhibitors biomarker in curbing dengue virus infections: *in silico* vs. *in vitro* approach. *Front. Cell. Infect. Microbiol.* 13 (February), 1061937–1062017. doi:10.3389/fcimb.2023.1061937

Ntie-kang, F., Zofou, D., Babiaka, S. B., Meudom, R., Scharfe, M., Lifongo, L. L., et al. (2013). AfroDb: a select highly potent and diverse natural product library from african medicinal plants. *PLoS One* 8 (10), 780855–e78115. doi:10.1371/journal.pone.0078085

Nyamari, M. N., Omar, K. M., Fayehun, A. F., Dachi, O., Bwana, B. K., and Awe, O. I. (2023). Expression level analysis of ACE2 receptor gene in african-American and non-african-American COVID-19 patients. *bioRxiv.* doi:10.1101/2023.09.11.557129

Nzungize, L., Kengne-Ouafo, J. A., Wesonga, M. R., Umuhoza, D., Murithi, K., Kimani, P., et al. (2022). Transcriptional profiles analysis of COVID-19 and malaria patients reveals potential biomarkers in children. *bioRxiv.* doi:10.1101/2022.06.30.498338

O'Boyle, N. M., Banck, M., James, C. A., Morley, C., Vandermeersch, T., and Hutchison, G. R. (2011). Open Babel: an open chemical toolbox. *J. Cheminformatics* 3, 33. doi:10.1186/1758-2946-3-33

Obura, H. O., Mlay, C. D., Moyo, L., Karumbo, B. M., Omar, K. M., Sinza, E. M., et al. (2022). Molecular phylogenetics of HIV-1 subtypes in african populations: a case study of sub-saharan african countries. *bioRxiv.* doi:10.1101/2022.05.18.492401

Ogbodo, U. C., Enejoh, O. A., Okonkwo, C. H., Gnanasekar, P., Gachanja, P. W., Osata, S., et al. (2023). Computational identification of potential inhibitors targeting cdk1 in colorectal cancer. *Front. Chem.* 11 (November), 1264808–1264817. doi:10.3389/fchem.2023.1264808

Oluwagbemi, O., and Awe, O. I. (2018). A comparative computational genomics of Ebola Virus Disease strains: in-silico Insight for Ebola control. *Inf. Med. Unlocked* 12, 106–119. doi:10.1016/j.imu.2018.07.004

Omar, K. M., Kitundu, G. L., Jimoh, A. O., Namikelwa, D. N., Lisso, F. M., Babajide, A. A., et al. (2024). Investigating antimicrobial resistance genes in Kenya, Uganda and Tanzania cattle using metagenomics. *PeerJ* 12, e17181. doi:10.7717/peerj.17181

Orozco-arias, S., Piña, J. S., Tabares-soto, R., Castillo-ossa, L. F., Guyot, R., and Isaza, G. (2020). Measuring performance metrics of machine learning algorithms for detecting and classifying transposable elements. *May* 8, 638. doi:10.3390/pr8060638

Palanichamy Kala, M., St. John, A. L., and Rathore, A. P. S. (2023). Dengue: update on clinically relevant therapeutic strategies and vaccines. *Curr. Treat. Options Infect. Dis.* 15 (2), 27–52. doi:10.1007/s40506-023-00263-w

Pawar, S. V., Banini, W. S. K., Shamsuddeen, M. M., Jumah, T. A., Dolling, N. N. O., Tiamiyu, A., et al. (2024). Proestrus: an open-source tool for 3D structure prediction using homology modeling. *Front. Chem.* 12, 1509407. doi:10.3389/fchem.2024.1509407

Pedregosa, F., Varoquaux, G., Gramfort, A., Michel, V., Thirion, B., Grisel, O., et al. (2011). Scikit-learn: machine learning in Python. *J. Mach. Learn. Res.* 12 (85), 2825–2830. Available at: http://jmlr.org/papers/v12/pedregosa11a.html.

Pintado Silva, J., and Fernandez-Sesma, A. (2023). Challenges on the development of a dengue vaccine: a comprehensive review of the state of the art. *J. General Virology* 104 (3), 001831. doi:10.1099/jgv.0.001831

Powers, C., and Setzer, N. (2016). An in-silico investigation of phytochemicals as antiviral agents against dengue fever. *Comb. Chem. and High Throughput Screen.* 19 (7), 516–536. doi:10.2174/1386207319666160506123715

Punekar, M., Kasabe, B., Patil, P., Kakade, M. B., Parashar, D., Alagarasu, K., et al. (2022). A transcriptomics-based bioinformatics approach for identification and *in vitro* screening of FDA-approved drugs for repurposing against dengue virus-2. *Viruses* 14 (10), 2150. doi:10.3390/v14102150

Purohit, P., Sahoo, S., Panda, M., Sahoo, P. S., and &eher, B. R. (2022). Targeting the DENV NS2B-NS3 protease with active antiviral phytocompounds: structure-based virtual screening, molecular docking and molecular dynamics simulation studies. *J. Mol. Model.* 28 (11), 365. doi:10.1007/s00894-022-05355-w

Rachmawati, Y., Ekawardhani, S., Fauziah, N., Faridah, L., and Watanabe, K. (2024). Potential way to develop dengue virus detection in Aedes larvae as an alternative for dengue active surveillance: a literature review. *Trop. Med. Infect. Dis.* 9 (3), 60. doi:10.3390/tropicalmed9030060

Raekiansyah, M., Mori, M., Nonaka, K., Agoh, M., Shiomi, K., Matsumoto, A., et al. (2017). Identification of novel antiviral of fungus-derived brefeldin A against dengue viruses. *Trop. Med. Health* 45 (1), 32–37. doi:10.1186/s41182-017-0072-7

Rasool, N., Ashraf, A., Waseem, M., Hussain, W., and Mahmood, S. (2019). Computational exploration of antiviral activity of phytochemicals against NS2B/NS3 proteases from dengue virus. , 44(3), 261–277. doi:10.1515/tjb-2018-0002

S, A. H., Pujar, G. V., Sethu, A. K., Bhagyalalitha, M., and Singh, M. (2021). Dengue structural proteins as antiviral drug targets: current status in the drug discovery and development. *Eur. J. Med. Chem.*, 221, 113527. doi:10.1016/j.ejmech.2021.113527

Saleh, M. S. M., and &Kamisah, Y. (2021). Potential medicinal plants for the treatment of dengue fever and severe acute respiratory syndrome-coronavirus. *Biomolecules* 11 (1), 42–25. doi:10.3390/biom11010042

Salgado, D., Zabaleta, T. E., Hatch, S., Vega, M. R., and Rodriguez, J. (2012). Use of pentoxifylline in treatment of children with dengue hemorrhagic fever. *Pediatr. Infect. Dis. J.* 31 (7), 771–773. doi:10.1097/INF.0b013e3182575e6a

Sanchez-Gendriz, I., de Souza, G. F., de Andrade, I. G. M., Neto, A. D. D., de Medeiros Tavares, A., Barros, D. M. S., et al. (2022). Data-driven computational intelligence applied to dengue outbreak forecasting: a case study at the scale of the city of Natal, RN-Brazil. *Sci. Rep.* 12 (1), 6550–6610. doi:10.1038/s41598-022-10512-5

Sander, T., Freyss, J., Von Korff, M., and &Rufener, C. (2015). DataWarrior: an open-source program for chemistry aware data visualization and analysis. *J. Chem. Inf. Model.* 55 (2), 460–473. doi:10.1021/ci500588j

Sandhu, H., Kumar, R. N., and Garg, P. (2022). Machine learning-based modeling to predict inhibitors of acetylcholinesterase. *Mol. Divers.* 26 (1), 331–340. doi:10.1007/s11030-021-10223-5

Sarma, D., Hossain, S., Mittra, T., Bhuiya, M. A. M., Saha, I., and Chakma, R. (2020) "Dengue prediction using machine learning algorithms," in *2020 IEEE 8th R10 humanitarian technology conference (R10-HTC)*, 1–6. doi:10.1109/R10-HTC49770.2020.9357035

Simanjuntak, Y., Liang, J.-J., Lee, Y.-L., and Lin, Y.-L. (2015). Repurposing of prochlorperazine for use against dengue virus infection. *J. Infect. Dis.* 211 (3), 394–404. doi:10.1093/infdis/jiu377

Simoben, C. V., Qaseem, A., Moumbock, A. F. A., Telukunta, K. K., Günther, S., Sippl, W., et al. (2020). Pharmacoinformatic investigation of medicinal plants from East Africa. *Mol. Inf.* 39 (11), 20001633–e2000215. doi:10.1002/minf.202000163

Smith, J. L., Stein, D. A., Shum, D., Fischer, M. A., Radu, C., Bhinder, B., et al. (2014). Inhibition of dengue virus replication by a class of small-molecule compounds that antagonize dopamine receptor d4 and downstream mitogen-activated protein kinase signaling. *J. Virology* 88 (10), 5533–5542. doi:10.1128/JVI.00365-14

Sterling, T., and Irwin, J. J. (2015). ZINC 15 - ligand discovery for everyone. *J. Chem. Inf. Model.* 55 (11), 2324–2337. doi:10.1021/acs.jcim.5b00559

Suenderhauf, C., Hammann, F., and &Huwyler, J. (2012). Computational prediction of blood-brain barrier permeability using decision tree induction. *Molecules* 17 (9), 10429–10445. doi:10.3390/molecules170910429

Tharwat, A. (2021). Classification assessment methods. *Appl. Comput. Inf.* 17 (1), 168–192. doi:10.1016/j.aci.2018.08.003

Thomas, S. J. (2023). Is new dengue vaccine efficacy data a relief or cause for concern? *Npj Vaccines* 8 (1), 55. doi:10.1038/s41541-023-00658-2

Tian, Y. S., Zhou, Y., Takagi, T., Kameoka, M., and &Kawashita, N. (2018). Dengue virus and its inhibitors: a brief review. *Chem. Pharm. Bull.* 66 (3), 191–206. doi:10.1248/cpb.c17-00794

Tougui, I., Jilbab, A., and &hamdi, J.El. (2021). Impact of the choice of cross-validation techniques on the results of machine learning-based diagnostic applications. *Healthc. Inf. Res.* 27 (3), 189–199. doi:10.4258/hir.2021.27.3.189

Trinh, C., Tbatou, Y., Lasala, S., Herbinet, O., and &eimaroglou, D. (2023). On the development of descriptor-based machine learning models for thermodynamic properties: Part 1—from data collection to model construction: understanding of the methods and their effects. *Processes* 11 (12), 3325–3340. doi:10.3390/pr11123325

Trott, O., and Olson, A. J. (2010). AutoDock Vina: improving the speed and accuracy of docking with a new scoring function, efficient optimization, and multithreading. *J. Comput. Chem.* 31 (2), 455–461. doi:10.1002/jcc.21334

Turner, P. (2005). *XMGRACE, version 5.1. 19.* Center for Coastal and land-margin research. Oregon Graduate Institute of Science and Technology, Beaverton. doi:10.1163/_q3_SIM_00374

Vabalas, A., Gowen, E., Poliakoff, E., and &Casson, A. J. (2019). Machine learning algorithm validation with a limited sample size. *PLOS ONE* 14 (11), e0224365. doi:10.1371/journal.pone.0224365

Veber, D. F., Johnson, S. R., Cheng, H., Smith, B. R., Ward, K. W., and Kopple, K. D. (2002). Molecular properties that influence the oral bioavailability of drug candidates. *J. Med. Chem.* 45, 2615–2623. doi:10.1021/jm020017n

Velliangiri, S., Alagumuthukrishnan, S., and &Thankumar joseph, S. I. (2019). A review of dimensionality reduction techniques for efficient computation. *Procedia Comput. Sci.*, 165, 104–111. doi:10.1016/j.procs.2020.01.079

Viganò, E. L., Ballabio, D., and &Roncaglioni, A. (2024). Artificial intelligence and machine learning methods to evaluate cardiotoxicity following the adverse outcome pathway frameworks. *Toxics* 12 (1), 87. doi:10.3390/toxics12010087

Wahaab, A., Mustafa, B. E., Hameed, M., Stevenson, N. J., Anwar, M. N., Liu, K., et al. (2022). Potential role of Flavivirus ns2b-ns3 proteases in viral pathogenesis and anti-Flavivirus drug discovery employing animal cells and models: a review. *Viruses* 14 (1), 44–27. doi:10.3390/v14010044

Wang, C., Greene, D., Xiao, L., Qi, R., and Luo, R. (2018a). Recent developments and applications of the MMPBSA method. *Front. Mol. Biosci.* 4 (JAN), 87. doi:10.3389/fmolb.2017.00087

Wang, G. Y., Zheng, H. H., Zhang, K. Y., Yang, F., Kong, T., Zhou, B., et al. (2018b). The roles of cytochrome P450 and P-glycoprotein in the pharmacokinetics of florfenicol in chickens. *Iran. J. Veterinary Res.* 19 (1), 9–14. doi:10.22099/ijvr.2018.4761

Wesonga, R. M., and Awe, O. I. (2022). An assessment of traditional and genomic screening in newborns and their applicability for Africa. *Inf. Med. Unlocked* 32, 101050. doi:10.1016/j.imu.2022.101050

Whitehorn, J., Nguyen, C. V. V., Khanh, L. P., Kien, D. T. H., Quyen, N. T. H., Tran, N. T. T., et al. (2016). Lovastatin for the treatment of adult patients with dengue: a randomized, double-blind, placebo-controlled trial. *Clin. Infect. Dis. Official Publ. Infect. Dis. Soc. Am.* 62 (4), 468–476. doi:10.1093/cid/civ949

Wlodawer, A., Minor, W., Dauter, Z., and &Jaskolski, M. (2008). Protein crystallography for non-crystallographers, or how to get the best (but not more) from published macromolecular structures. *FEBS J.* 275 (1), 1–21. doi:10.1111/j.1742-4658.2007.06178.x

Wu, W., and &Herath, A. (2016). "Chemometrics and predictive modelling," in *Nonclinical statistics for pharmaceutical and biotechnology industries*. Editor L. Zhang (Springer International Publishing), 653–673. doi:10.1007/978-3-319-23558-5_25

Wu, W.-L., Ho, L.-J., Chen, P.-C., Tsai, Y.-T., Hsu, S.-T., Chang, D.-M., et al. (2011). Immunosuppressive effects and mechanisms of leflunomide in dengue virus infection of human dendritic cells. *J. Clin. Immunol.* 31 (6), 1065–1078. doi:10.1007/s10875-011-9578-7

Xu, T.-L., Han, Y., Liu, W., Pang, X.-Y., Zheng, B., Zhang, Y., et al. (2018). Antivirus effectiveness of ivermectin on dengue virus type 2 in *Aedes albopictus*. *PLoS Neglected Trop. Dis.* 12 (11), e0006934. doi:10.1371/journal.pntd.0006934

Yadouleton, A., Nouatin, O., Kissira, I., Houngbegnon, P., Cottrell, G., Fievet, N., et al. (2024). Genomic surveillance of dengue virus in Benin. *Infect. Genet. Evol. J. Mol. Epidemiol. Evol. Genet. Infect. Dis.* 125, 105674. doi:10.1016/j.meegid.2024.105674

Yap, C. W. (2011). PaDEL-descriptor: an open source software to calculate molecular descriptors and fingerprints. *J. Comput. Chem.* 32 (7), 1466–1474. doi:10.1002/jcc.21707

Yuan, S., Chan, H. C. S., and Hu, Z. (2017). Using PyMOL as a platform for computational drug design. *Wiley Interdiscip. Rev. Comput. Mol. Sci.* 7 (2). doi:10.1002/wcms.1298

Zamri, A., Teruna, H. Y., Rahmawati, E. N., Frimayanti, N., and &Ikhtiarudin, I. (2019). Synthesis and *in silico* studies of a benzenesulfonyl curcumin analogue as a new anti dengue virus type 2 (DEN2) NS2B/NS3. *Indonesian J. Pharm.* 30 (2), 84–90. doi:10.14499/indonesianjpharm30iss2pp84-90

Microbial-based natural products as potential inhibitors targeting DNA gyrase B of *Mycobacterium tuberculosis*: an *in silico* study

Tilal Elsaman[1]*, Magdi Awadalla Mohamed[1]*, Malik Suliman Mohamed[2], Eyman Mohamed Eltayib[2] and Abualgasim Elgaili Abdalla[3]

[1]Department of Pharmaceutical Chemistry, College of Pharmacy, Jouf University, Sakaka, Saudi Arabia, [2]Department of Pharmaceutics, College of Pharmacy, Jouf University, Sakaka, Saudi Arabia, [3]Department of Clinical Laboratory Sciences, College of Applied Medical Sciences, Jouf University, Sakaka, Saudi Arabia

Introduction: Since the emergence of *Mycobacterium tuberculosis* (MBT) strains resistant to most currently used anti-tubercular drugs, there has been an urgent need to develop efficient drugs capable of modulating new therapeutic targets. Mycobacterial DNA gyrase is an enzyme that plays a crucial role in the replication and transcription of DNA in MBT. Consequently, targeting this enzyme is of particular interest in developing new drugs for the treatment of drug-resistant tuberculosis, including multidrug-resistant tuberculosis (MDR-TB) and extensively drug-resistant tuberculosis (XDR-TB).

Methods: In the present study, multiple computational tools were adopted to screen a microbial-based natural products database (NPAtlas) for potential inhibitors of the ATPase activity of MBT DNA gyrase.

Results and discussion: Twelve hits were initially identified as the top candidates based on their docking scores (ranging from −9.491 to −10.77 kcal/mol) and binding free energies (−60.37 to −73.21 kcal/mol). Following this, computational filters, including ADME-T profiling and pharmacophore modeling, were applied to further refine the selection. As a result, three compounds 1-Hydroxy-D-788-7, Erythrin, and Pyrindolol K2 emerged as the most promising, exhibiting favorable drug-like properties. Notably, 1-Hydroxy-D-788-7, an anthracycline derivative, demonstrated superior binding affinity in molecular dynamics simulations. The RMSD values, ranging from 1.7 to 2.5 Å, alongside RMSF analysis and a detailed evaluation of the established interaction forces, revealed that 1-Hydroxy-D-788-7 was the strongest binder to Mycobacterial DNA Gyrase B. The stable binding and favorable interaction profile highlighted 1-Hydroxy-D-788-7 as a top hit. These comprehensive computational findings strongly support the potential of 1-Hydroxy-D-788-7 as an effective anti-TB lead compound, warranting further experimental validation to confirm its therapeutic efficacy.
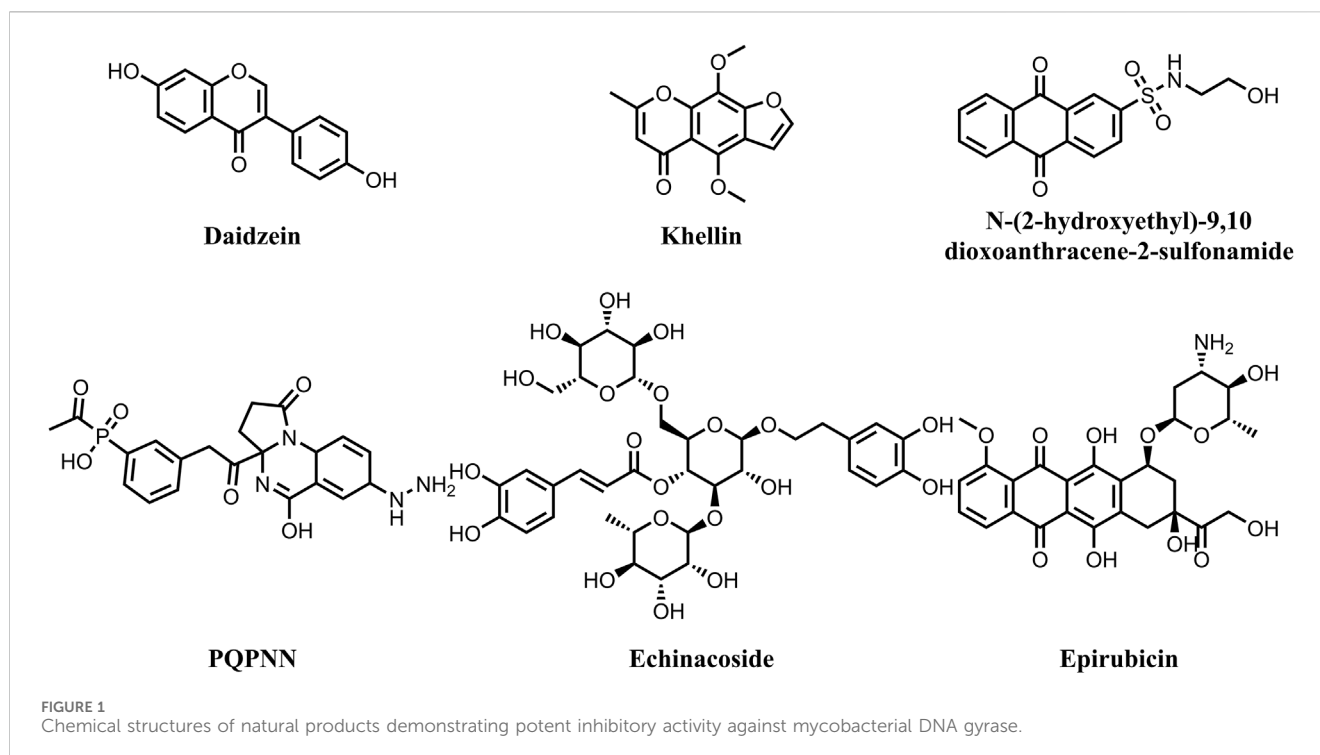
KEYWORDS

Mycobacterium tuberculosis, DNA gyrase B, natural products, virtual screening, resistance

1 Introduction

Mycobacterium tuberculosis (MBT) is the etiological agent of tuberculosis (TB) and affects one-third of world's population latently. Tuberculosis continues to be a longstanding global health problem, with 10.6 million new cases diagnosed and 1.6 million deaths attributed to TB worldwide in 2021 (Bagcchi, 2023). The recent surge in morbidity and mortality rates of tuberculosis is linked to the consistent rise of mycobacterial strains that are resistant to most of the currently used anti-TB medications (Seung et al., 2015; Miotto et al., 2018; Allue-Guardia et al., 2021). The global effort to end TB faces significant obstacles due to the increasing incidence of multidrug-resistant (MDR), extensively drug-resistant (XDR), and extremely drug-resistant (XXDR) TB (Dheda et al., 2017). Furthermore, the emergence of totally drug-resistant TB (TDR-TB) strains has severely compromised treatment options (Verma et al., 2021). Reports indicate that 75% of TB patients infected with XDR-MBT strains do not respond to the current anti-TB drugs (Dookie et al., 2018). Therefore, discovery and development of new effective anti-tuberculous therapies is urgently needed to replace the current medications, as the microorganism has developed multiple resistance mechanisms. DNA gyrase is an ATP-dependent enzyme that controls the transcription, replication and recombination processes by introducing transient breaks in both DNA strands. The DNA gyrase of MBT consists of four subunits, including two alpha (2α) and two beta (2β) subunits (Qiu et al., 2024). The α-subunits (gyrase A) are responsible for introducing negative supercoil (Germe et al., 2024), a process that requires energy from ATP hydrolysis by the β subunits (gyrase B) (Kashyap et al., 2018). Mycobacterial DNA gyrase A is the direct target for the fluoroquinolones, which are used as part of second-line treatment in combination with injectable drugs such as Amikacin, Capreomycin, and Streptomycin for treatment of MDR-TB (Miotto et al., 2018). They have proven effective against MBT and are considered the first anti-TB drugs developed since rifampin and are now a key part of treatment protocols for rifampin-resistant TB (Aubry et al., 2004). Studies have demonstrated that MBT's resistances to fluoroquinolone primarily results due to mutations in gyrase A rather than gyrase B (Avalos et al., 2015; Kashyap et al., 2018). The surge in resistance to fluoroquinolones has gathered the interest in focusing on the GyrB subunit. Targeting this subunit could offer similar phenotypic impacts on bacterial survival as fluoroquinolones, thereby extending the utility of DNA gyrase as a therapeutic target for tuberculosis (Chopra et al., 2012). In this context, the objective of this study was to investigate potential inhibitors of DNA gyrase B in MBT from natural products, with a particular focus on addressing the challenges posed by drug-resistant strains. The study aimed to enhance understanding of how natural compounds interact with DNA gyrase B, potentially paving the way for the development of new therapies targeting drug-resistant tuberculosis. For many years natural products have long been known as a valuable source of anti-TB drugs (Sudarshan et al., 2024). Many of the currently used anti-TB drugs, such as Streptomycin, Kanamycin, Amikacin, Rifampicin, Cycloserin, Capreomycin, originate from natural sources. Nonetheless, no natural product-derived anti-TB drug has advanced to the market since the 1970s (Han et al., 2022). This could be ascribed

to several challenges, including inefficient isolation, difficulties in chemical structures verification, and limited knowledge about potential targets (Atanasov et al., 2021; Han et al., 2022). Fortunately, recent technological advancements have overcome these obstacles, comprising the improved isolation and structure verification tools, microbial platforms for production enhancement, and modern methods for identifying and validating the targets of natural bioactive molecules (Atanasov et al., 2021; Thuan et al., 2022; Zhu et al., 2022). Consequently, natural products have once again received a great attention from the scientific community, particularly for addressing the problem of microbial drug resistance. Multiple studies revealed the potential of natural products for inhibiting the ATPase activity of mycobacterial DNA gyrase (Figure 1). Jagatab et al. reported the potent DNA gyrase inhibitory activity of daidzein (isofalvonoid) and khelline (furanochromone) with IC_{50} values of 0.042 and 0.822 μg/mL, respectively (Jagatap et al., 2023). In addition, Amorim et al. reported the potential of Anthraquinones, a class of naturally occurring organic compounds with a characteristic three-ring structure. Computational investigations identified 7122772 (N-(2-hydroxyethyl)-9,10 dioxoanthracene-2-sulfonamide) as the best-scored ligand (Amorim et al., 2022). Moreover, an independent study involved virtual screening of a dataset of 20,098 natural products reveled compound PQPNN as the best in terms of binding affinity towards mycobacterial DNA gyrase B (Arevalo and Amorim, 2022). Furthermore, Structure-based drug repurposing study identified Echinacoside and Epirubicin as potent inhibitors of the catalytic activity of mycobacterial DNA gyrase with IC_{50} values of 2.1–4.7 μM (Balasubramani et al., 2020).

Computer-aided drug design approach gain popularity in modern drug discovery and development field, guiding and expediting various phases of the drug design process. These approaches can be classified into (i) Structure based drug design (SBDD) and (ii) Ligand based drug design (LBDD) (Yu and MacKerell, 2017; Chang et al., 2022). The SBDD approach is used to predict the positioning of a small molecule into a target protein active site and to accurately estimate its binding free energetics (Wang et al., 2018). SBDD is regarded as a faster and more cost-effective approach for hit identification and optimization compared to conventional drug discovery approaches (Batool et al., 2019). SBDD comprises numerous methods, such as molecular docking, molecular dynamics (MD) simulations and *de novo* drug design (Chang et al., 2022). In this context, the aim of this study was to explore the potential of microbial-based natural products as inhibitors of DNA gyrase B in *M. tuberculosis* using various computational approaches. This study is the first to screen a library of natural products from microbial origins, which are known for their potent chemotherapeutic properties, with many of the most effective currently used antimycobacterial drugs having originated from microbes. In addition, multiple computational tools were efficiently integrated to extensively analyze and interpret the binding modes, affinities and interactions of the top hits, enhancing the reliability of our findings. To this end, in the present study, structure-based virtual screening was applied using 'Virtual Work Flow' to identify potential ATPase inhibitors from the microbial-based Natural Products Atlas (NPAtlas) database (https://www.npatlas.org). The MM-GBSA (molecular mechanics/Generalized-Boltzmann surface area) calculation was performed

FIGURE 1
Chemical structures of natural products demonstrating potent inhibitory activity against mycobacterial DNA gyrase.

to estimate the binding free energetics of the enzyme-ligand complexes. Following this, the identified potential inhibitors were filtered through *in silico* physicochemical and pharmacokinetic analyses. In addition, molecular dynamics (MD) simulation was carried out to assess the binding stability of the potential hits with the enzyme binding pocket.

2 Materials and methods

In this study, softwares implanted in Schrödinger suite were used including, Protein Preparation Wizard (Madhavi Sastry et al., 2013), LigPrep (Schrödinger, LLC, 2023a), Glide (Friesner et al., 2004; Halgren et al., 2004; Friesner et al., 2006), Prime (Jacobson et al., 2004; Klyshko et al., 2024), QikProp (Divyashri et al., 2020), Phase (Dixon et al., 2006a; Dixon et al., 2006b), Jaguar (Bochevarov et al., 2013) and Desmond (Ivanczi et al., 2023). Maestro graphical interface (Schrödinger, LLC, 2023b) was used to access these softwares. Additionally, ADMETlab 2.0 (Xiong et al., 2021), an integrated free web-based platform was employed in ADMET properties predictions.

2.1 Target selection and validation

The protein reliability report was generated using the PDB structures (**4B6C**, **4BAE**, **3ZKB**, and **3ZM7**) and their corresponding reflection data. The structures were refined using the Protein Preparation Wizard in Schrödinger, and the reliability of the models was assessed through both pre- and post-refinement reports. During the refinement process, missing atoms, steric clashes, and unsatisfied buried donors were manually addressed using PyMOL and Swiss PDB Viewer (SPDBV) (Guex et al., 2009).

The best crystal structure was selected based on the overall quality of the refinement, the results of the reliability assessments, and the stability of the model, ensuring that it would provide an accurate basis for subsequent analysis.

2.2 Receptor based virtual screening

Virtual screening analysis of the microbial-based Natural Products Atlas (NPAtlas) database was carried out using Virtual screening workflow of Schrödinger software suite. This database was selected to perform the screening based on several factors including: (i) its relevancy to our study aimed at identifying microbial-derived natural products which are known for their potential in developing new medicines for treating infectious diseases (Almansour et al., 2023). In addition, it comprehensively covers microbial-derived natural products comprising curated data on microbial metabolites, making it a valuable resource for identifying bioactive compounds. Furthermore, its user-friendly web interface and updated repository of microbial metabolites were key factors in our selection. For docking studies the downloaded compounds library in 2D SDF formats were converted to 3D formats and then were optimized using OPLS4 force field. The LigPrep module of Schrödinger was used to prepare the structures for docking, providing that the original chirality of the ligands were maintained. The SDF files, containing 2D structures of the investigated library, were imported into Maestro and processed using the LigPrep module. This module converted the 2D structures into 3D formats, optimizing their geometry, generating appropriate ionization states, and ensuring stereochemical accuracy. The resulting output was saved in the MAE (Maestro) file format. The possible ionization states were generated at pH 7.00 ± 2 units

using Epik, and we obtained one low energy conformer for each ligand. In the present work, the 3D crystal structure of the target MBT DNA Gyrase B (PDB code: 4B6C) with co-crystal ligand was downloaded from the protein data bank website (http://www.rcsb.org) (Agrawal et al., 2013). Subsequently, the multi-step Protein Preparation Wizard (PrepWizard) from Maestro Task was employed to prepare the target protein structure. All water molecules beyond 5 Å were removed and the co-crystal ligand was kept in the binding site. Furthermore, OPLS4 force field was employed for optimization and energy minimization. Following this, receptor grid generation tool embedded within the Schrödinger suite was utilized for the 3D cubic grid box generation around the co-crystal ligand. Molecular docking was performed with constraints applied to the critical residue ASP79 (Supplementary Figure S1) to ensure accurate and focused interaction analysis. This approach emphasized the role of ASP79 in stabilizing ligand binding and allowed for the identification of compounds with strong and specific interactions at this key site. Next, Glide program was used to screen the prepared ligands against the refined target protein following multistep screening approach. This approach is an advanced technique that refines the docking process, enhancing both accuracy and reliability, which results in more precise predictions of ligand binding (Owoloye et al., 2022). It is designed to efficiently run a full sequence of tasks that facilitate the screening of large compound libraries. These libraries are tested against one or more target proteins to identify potential inhibitors. This process helps in rapidly narrowing down promising hits for further analysis and testing (Perez-Regidor et al., 2022). Several studies in the literature have used multistep molecular docking to identify inhibitors from large compound libraries targeting MBT (Mustyala et al., 2015; Naz et al., 2019; Kumar et al., 2023). Initially, Glide high-throughput virtual screening (HTVS) mode was utilized for filtering the compounds library, then for further screening the standard precision (SP) mode was used and finally more accurate docking calculations results were obtained using extra precision (XP) mode. For each input molecule, one best pose was generated, and the molecules were ranked based on their Glide XP docking score. Additionally, enrichment calculations were performed to validate the docking results and evaluate the effectiveness of the virtual screening process in distinguishing between active compounds and decoys for the potential inhibition of MBT GyrB. The enrichment process assessed the screening workflow's ability to prioritize active compounds from a dataset of 1,466 ligands. Key metrics, including EF, AUC, BEDROC, and ROC curve analysis, were calculated, resulting in the identification of 18 active compounds. These findings demonstrated the reliability and robustness of the virtual screening methodology in identifying potential GyrB inhibitors.

2.3 MM-GBSA calculations

Estimation of the binding free energies of receptors and docked ligands was done using Prime module interfaced with Schrödinger. Post docking generated Pose Viewer Files (PVF) of the top hits were used as input files for energy computation for each hit. VSGB 2.0 solvation model and OPLS4 force field were used to calculate the binding free energy descriptors following the protocol that was previously reported in the literature (Azam

et al., 2021). MMGBSA ΔG binding free energy score was employed to rank the ligands.

2.4 *In silico* ADMET profiling

In this study, the computational tool QikProp (Schrodinger Release 2023-1) was used to evaluate the ADMET profiles and drug-likeness descriptors of the top hits with high binding free energy scores along with the reference drug candidate SPR720. Ligand structures were prepared using the LigPrep tool to optimize 3D geometries and assign protonation states at a physiological pH of 7.4. Predictions were generated using the default settings of QikProp, which include evaluations of key parameters such as LogP, solubility (LogS), CNS permeability, human oral absorption, and toxicological risks. All calculations were conducted in standalone mode within the Schrödinger software environment. The program offers a set of recommended ranges for various properties and descriptors of small molecules, based on an analysis of 95% of known drugs. The results were exported in an MS Excel file, displaying the number of principal descriptors and ADME predictions in MS Excel file format. Additional toxicity parameters were estimated using the web-based tool ADMETlab 2.0 freely available at (https://admetmesh.scbdd.com). The molecules were drawn in Schrödinger, and its canonical SMILES representation was then submitted to the ADMETlab 2.0 webserver for evaluation using default parameters. All of the calculated parameters were evaluated for compliance with their respective specified limits.

2.5 Pharmacophore modeling

Pharmacophore modeling was carried out using the Phase module implanted in Schrödinger suite. The ligands obtained from the literature (67 compounds) were considered active when the IC_{50} for the inhibition of MBT DNA Gyrase B was <20 μM. These ligands were prepared via retention of the original chirality, generation of the ionization states at pH 7.00 ± 2 using OPLS4 force fields. Fifty conformers were generated for each active ligand and the hypothesis requirement was set to match 50% of the active ligands. The pharmacophore model was developed based on the six chemical features, namely, hydrogen bond donor (D), hydrogen bond acceptor (A), hydrophobic group (H), aromatic ring (R), negative ionizable group (N), and positive ionizable group (P). The resultant hypotheses were ranked according to their phaseHypoScores. Following the generation of the hypotheses, the top hits were screened against the high-ranking hypothesis and they were required to match all four pharmacophore features of the model to be selected for MD simulations study.

2.6 Quantum computational calculations

DFT method in the Jaguar module of Schrödinger suite was used to perform quantum chemical calculations of the top three hits 1-Hydroxy-D-788-7, Erythrin, and Pyrindolol K2 electronic molecular properties such as Electron density, MESP and energies of both HOMO and LUMO molecular orbitals (Khan and Singh, 2023).
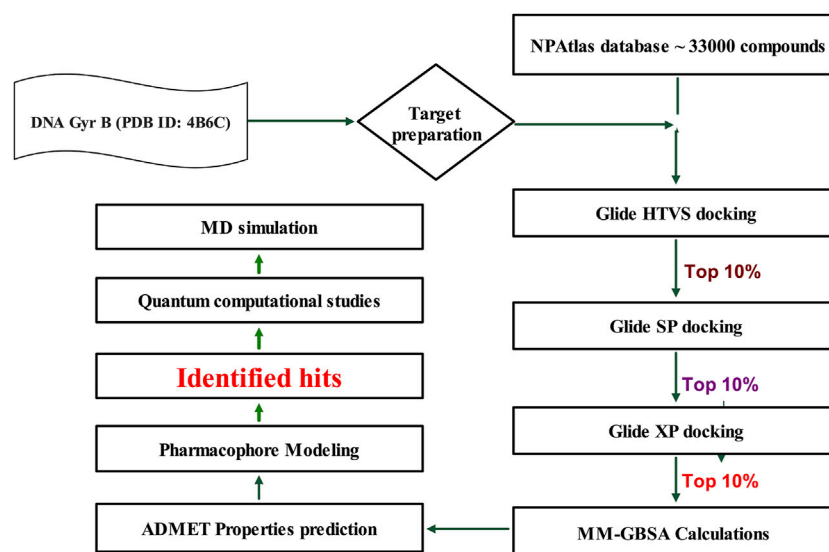
FIGURE 2
Work Flow for Virtual Screening. Generated using Microsoft PowerPoint.

These energies were then utilized to compute various quantum chemical parameters, including the energy gap (HLG), chemical hardness, chemical softness, electronegativity, and the global electrophilicity index, following equations reported in the literature (Srivastava and Misra, 2021; Guezane-Lakoud et al., 2023). The electron-deficient surfaces are marked by the blue color, whereas the electron-rich ones are indicated by the red color.

2.7 MD simulations

MD simulation study was performed using Desmond for the best ligand-target complexes of the co-crystal ligand and the top three hits 1-Hydroxy-D-788-7, Erythrin, and Pyrindolol K2 taken from the docking experiments. In the first step, SPC solvation model was employed and the system was placed within orthorhombic water box of 10 Å × 10 Å × 10 Å coordinates to ensure complete coverage of the surface of each complex with solvent model (Alghamdi et al., 2023). Next, Na$^+$ counter ions were added to the built systems to balance the net charges, and 0.15 M NaCl was further included to neutralize the systems. Finally, minimization and pre-equilibration of these systems were done before the simulation run using the default relaxation protocol. The system's temperature was fixed at 300 K, and the atmospheric pressure at 1 bar, using the isothermal-isobaric (NPT) ensemble (Lazim et al., 2020). A 100 ns simulation was carried out to strike a balance between computational cost and the ability to observe important dynamic behaviors. Data from 1,000 frames were generated, with a recording interval of 100 ps. The average RMSD and RMSF were calculated for each protein region as well as for the entire protein. This time frame effectively captures key stability metrics such as RMSD, hydrogen bond stability, the maintenance of critical interactions, and the overall structural integrity of the system (De Vivo et al., 2016). Further, multiple studies have used MD simulations lasting 50–200 ns to investigate protein-ligand interactions with MBT

targets, including DNA gyrase B (Amorim et al., 2022; Arevalo and Amorim, 2022; Pakamwong et al., 2024).

3 Results and discussion

Mycobacterial DNA gyrase is crucial for processes such as DNA replication, transcription, and recombination (Aubry et al., 2004). Fluoroquinolones act on GyrA, a component of the functional gyrase complex. Resistance to fluoroquinolones commonly arises from point mutations in the *gyrA* gene, leading to class-wide resistance against fluoroquinolones. In contrast, targeting GyrB produces similar effects on bacterial viability, preserving the potential of DNA gyrase as a viable drug target (Aubry et al., 2004). In this context, a library of microbial-based natural products (33000 compounds) was virtually screened to identify potential inhibitors of DNA Gyrase B of MBT, following the work flow illustrated in Figure 2.

3.1 Target selection and validation

Choosing the appropriate protein structure is a crucial step in ensuring the success of drug discovery efforts that rely on structure-based design approaches. Since multiple crystal structures for the same protein are often available in the Protein Data Bank (PDB), selecting the most suitable structure is essential for achieving accurate and reliable results (Murumkar et al., 2023). The protein structures were refined using the Protein Preparation Wizard, and their reliability was assessed through reports generated before and after refinement (Supplementary Figure S2) using the protein reliability report in Schrödinger. Among the analyzed structures, **4B6C** (Shirude et al., 2013) from *Mycobacterium smegmatis* emerged as the most reliable due to its high resolution, relevance to the target, and superior experimental validation. In comparison,
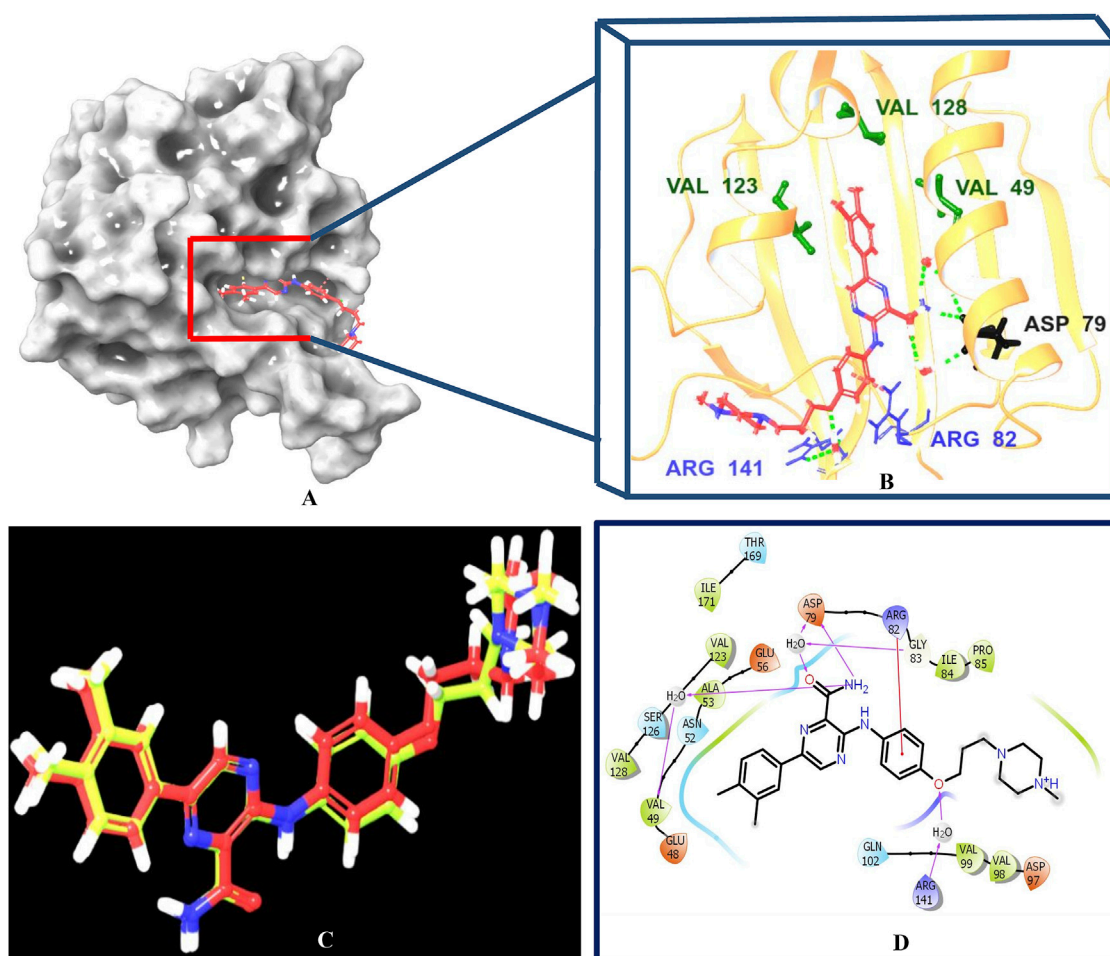
FIGURE 3
Post-docking analysis of the co-crystal ligand with the ATP-binding site of the GyrB subunit of MBT DNA gyrase. **(A, B)** representing 3D crystal structure of the enzyme bound to the co-crystal ligand. **(C)** represents the superposition of the docked ligand pose (yellow) into the original ligand pose (red) (RMSD < 2 Å. **(D)** represents 2D enzyme-ligand interaction of the co-crystal ligand. The interacting residues of the binding site are VAL49, ASP79, ARG82, VAL123, VAL128, ARG141 are represented by three-letter codes. In **(B)** the HB and the Pi–cation interactions are shown by green and red dotted lines, respectively. In **(D)**, the HB and Pi-cation interactions are shown by magenta, and red lines, respectively. Created using Maestro interface of Schrödinger suite version 2023-1.

4BAE showed minor deviations and improvements, while **3ZKB** and **3ZM7** exhibited persistent issues, including low resolution and structural instability, reducing their suitability for accurate modeling. Based on these qualities, **4B6C** was selected for virtual screening of 33,000 microbial-based products, while the other structures require further optimization.

3.2 Receptor based virtual screening

Multistep molecular docking study was performed using the Glide program as filtering protocol to investigate the binding modes of the tested library with the target protein. The crystal structure of the target protein, DNA gyrase B of MBT (PDB code: 4B6C) was downloaded from protein data bank (PDB) (https://www.rcsb.org). A microbial-based library of approximately 33000 compounds was docked into the ATP binding site of DNA gyrase B of MBT. Such compounds are expected to competitively inhibit ATP from binding to the enzyme's catalytic region, thereby preventing its hydrolysis.

Re-docking of the bound co-crystal ligand in the same binding site was performed in triplicates to validate the docking protocol (Figure 3). Root mean square deviation (RMSD) was calculated, and the obtained value of 1.757 ± 0.05 Å between the docked conformation and the original conformation validated the accuracy of the docking protocol. Initially, High Throughput Virtual Screening (HTVS) was adopted, and the top 10% hits were subsequently docked with Glide standard precision (SP). Finally, the top 10% from the previous step were subjected to Glide extra precision (XP) mode docking, which is associated with higher accuracy than the other docking modes. This filtering protocol ultimately afforded 12 hits, as shown in Table 1; Figure 4, with Glide XP scores ranging from −9.491 to −10.77 kcal/mol. Moreover, a step of enrichment calculations was undertaken to validate the docking results and assess the ability of the virtual screening process to effectively distinguish between active compounds and decoys for the potential inhibition of GyrB in MBT (Pandey et al., 2017). The virtual screening results demonstrated promising performance in

TABLE 1 Docking scores and the ligand-target interactions forces of the top 12 hits.

No	NPAtlas ID	Name	Binding free energy (kcal/mol)	Docking score (kcal/mol)	Key interactions
	Co-crystal ligand		**−81.05**	**−10.523**	1. Pi-cation with ARG82 (3.46 Å) 2. Water mediated H-bonds with the following residues: i. VAL49 (2.09 Å and 1.90 Å) ii. ASP79 (1.83 Å and 1.92 Å) iii. GLY83 (1.83 Å and 1.98 Å) iv. ARG141 (1.6 Å and 2.33 Å) 3. Direct H-bonds i. ASP79 (2.33 Å)
1	NPA029673	Dipleosporalone B	−64.93	−10.77	1. Water mediated H-bonds with the following residues: i. ASP79 (2.05 Å and 1.92 Å) ii. ARG82 (1.94 Å and 2.2 Å) iii. GLY83 (2.05 Å and 1.98 Å) 2. Direct H-bonds i. ARG141 (2.5 Å) ii. ASP79 (2.69 Å)
2	NPA021035	Glysperin B	−64.80	−10.690	1. Pi-cation with ARG82 (3.67 Å) 2. Water mediated H-bonds with the following residues: i. ASP79 (2.05 Å and 1.92 Å) ii. GLY83 (2.05 Å and 1.98 Å) iii. ARG141 (2.15 Å and 2.33 Å)
3	NPA028815	Dihydrospumigin N	−62.10	−10.497	1. Water mediated H-bonds with the following residues: i. ASP79 (2.12 Å and 1.99 Å) ii. GLY83 (2.12 Å and 1.98 Å) 2. Direct H-bonds GLY83 (1.89 Å)
4	NPA020353	Fuscachelin A	−73.21	−10.476	1. Water mediated H-bonds with the following residues: i. ASP79 (1.92 Å and 1.99 Å) ii. ARG82 (1.98 Å and 2.20 Å) iii. ARG141 (2.69 Å and 2.33 Å) iv. GLY83 (1.99 Å and 1.98 Å)
5	NPA019546	1-Hydroxy-D-788-7	−60.37	−10.253	1. Water mediated H-bonds with the following residues: i. VAL49 (1.8 Å and 1.90 Å) ii. ASP79 (2.27 Å and 1.92 Å) iii. GLY83 (2.27 Å and 1.98 Å)
6	NPA002954	Pyridindolol K2	−64.51	−9.590	1. Water mediated H-bonds with the following residues: i. VAL49 (1.8 Å, 1.86 Å and 1.85 Å) ii. ASP79 (1.77 Å and 1.99 Å) iii. GLY83 (1.77 Å and 1.98 Å)
7	NPA032921	Wexrubicin	−60.41	−9.553	1. Water mediated H-bonds with the following residues: i. VAL49 (1.91 Å and 1.90 Å)
8	NPA005438	Lampteroflavin	−63.44	−9.544	1. Water mediated H-bonds with the following residues: i. ASP79 (1.63 Å and 1.99 Å) ii. GLY83 (1.63 Å and 1.98 Å)
9	NPA007770	Not named	−62.67	−9.544	1. Water mediated H-bonds with the following residues: iii. ASP79 (1.70 Å and 1.99 Å) iv. GLY83 (1.70 Å and 1.98 Å) 2. Direct H-bonds i. GLY83 (1.89 Å)
10	NPA007224	Pyrronamycin B	−60.54	−9.525	1. Pi-cation with ARG82 (3.64 Å) 2. Water mediated H-bonds with the following residues:

(Continued on following page)

TABLE 1 (*Continued*) Docking scores and the ligand-target interactions forces of the top 12 hits.

No	NPAtlas ID	Name	Binding free energy (kcal/mol)	Docking score (kcal/mol)	Key interactions
					i. VAL49 (1.72 Å and 1.90 Å) ii. ASP79 (2.31 Å and 1.92 Å) iii. GLY83 (2.18 Å and 1.98 Å) iv. ARG141 (1.96 Å and 2.33 Å)
11	NPA000223	Erythrin	−65.68	−9.492	1. Water mediated H-bonds with the following residues: i. VAL49 (1.64 Å and 1.90 Å) ii. ASP79 (1.70 Å and 1.99 Å) iii. GLY83 (1.70 Å and 1.98 Å) 2. Direct H-bonds i. GLY83 (1.89 Å)
12	NPA016415	Closthioamide	−66.26	−9.491	1. Water mediated H-bonds with the following residues: i. ASP79 (1.85 Å and 1.99 Å) ii. ARG82 (2.79 Å and 2.33 Å) iii. GLY83 (1.85 Å and 1.98 Å)

Bold values represent the binding free energy and docking score of the co-crystal ligand, serving as a reference for comparison with the test compounds.

identifying actives. A total of 18 active compounds were identified out of 1,466 ligands. The Boltzmann-Enhanced Discrimination of Relevance of Compounds (BEDROC values), with the highest at 0. 890 (alpha = 8.0), indicated strong early enrichment of actives in the ranked list. The Receiver Operating Characteristic Curve (ROC) score of 0.97 further supported the efficacy of the screening in correctly discriminating actives from decoys, as shown in Figure 5. With Rank-Order Enrichment (RIE) of 14.92, the screening successfully outranked a significant number of decoys. The Area Under Accumulation Curve (AUAC) of 0.97 highlighted the ability to prioritize relevant compounds throughout the screening process. On average, 40 decoys were outranked by each active compound, suggesting good compound ranking. These metrics confirmed the validity of the docking procedure and its effectiveness in identifying GyrB inhibitors. The multistep docking protocol commenced with the screening of 33,000 compounds using High-Throughput Virtual Screening (HTVS), narrowing down the selection to 2,434 compounds. These were then subjected to Standard Precision (SP) docking, resulting in 440 compounds. Finally, Extra Precision (XP) docking was performed, identifying 50 top-ranking compounds. It is worth mentioning that, constraints were applied during the docking protocol based on interactions with key residue ASP79, through H-bonds (Shirude et al., 2013; Amorim et al. , 2022). These interactions were critical in refining the selection, ensuring that the compounds aligned properly with the enzyme's active site to maximize binding affinity and potential for inhibition. The identified compounds exhibited docking scores ranging from −9.27 to −12.61 kcal/mole, with 18 showed scores better than that of the co-crystal ligand (−10.523 kcal/mole). Following XP docking, MM-GBSA calculations were performed, and 12 compounds (Table 1) were selected based on their high binding affinity as well as their interactions with key residues in the enzyme binding pocket. These compounds demonstrated strong potential for further investigation due to their favorable binding free energies and critical residue interactions. The docking analysis of the selected 12 compounds (Table 1) revealed that Dipleosporalone B (−10.77 kcal/mol) and Glysperin B (−10.690 kcal/mol) had the best score, exceeding that of the co-crystal ligand (−10.523 kcal/mol).

Dihydrospumigin N (−10.497 kcal/mol), and Fuscachelin A (−10. 476 kcal/mol) closely approached the co-crystal ligand's binding affinity. The remaining compounds exhibited relatively lower scores, ranging from −9.553 to −9.491 kcal/mol. The comparative analysis of binding free energies (Table 1) indicated that the co-crystal ligand had the strongest binding affinity (−81.05 kcal/mol), followed by Fuscachelin A (−73.21 kcal/mol). Other notable hits include Closthioamide (−66.26 kcal/mol), Erythrin (−65.68 kcal/mol), Dipleosporalone B (−64.93) and Glysperin B (−64.80 kcal/mol). The top-ranked hit Fuscachelin A is a cyclic peptide iron-sequestering siderophore synthesized by filamentous fungus (Dimise et al., 2008; Miethke and Marahiel, 2007). Siderophores have been described as having the potential for treatment of microbial infection. The second-ranked hit, Closthioamide is a unique polythioamide, isolated from the bacterium *Ruminiclostridium cellulolyticum*. Significant antibacterial activity has been reported for this hit specifically against multi-drug resistant strains such as MRSA (Methicillin-resistant *Staphylococcus aureus*) and VRE (Vancomycin-resistant enterococci) (Barth et al., 2024). This potent activity is believed to be mediated via the inhibition of ATPase function of DNA gyrase. Studies revealed its potential to allosterically modulate the ATPase activity of bacterial DNA gyrase, however, in our study it showed high affinity towards mycobacterial DNA gyrase B, suggesting potential direct inhibition mechanism (Chiriac et al., 2015). Such finding suggests Closthioamide's potential as a promising new agent for both bacterial and mycobacterial infections. Further, the phenolic metabolite Erythrin derived from different plants belong to the genus Erythrina, displayed high affinity towards the enzyme binding pocket. Studies have reported the potent antimycobacterial activity of compounds isolated from these plants with structural similarity to Erythrin (Rukachaisirikul et al., 2007). This combination of evidence points to GyrB inhibition as a potential mode of action for compounds like Erythrin. Dipleosporalone B is a dimeric azaphilone compound marine-derived *Pleosporales* sp. fungus. Dimeric natural products are known for their potent biodynamic activities (Cao et al., 2020; Wang et al., 2023). Glysperin B which exhibited the highest docking score among
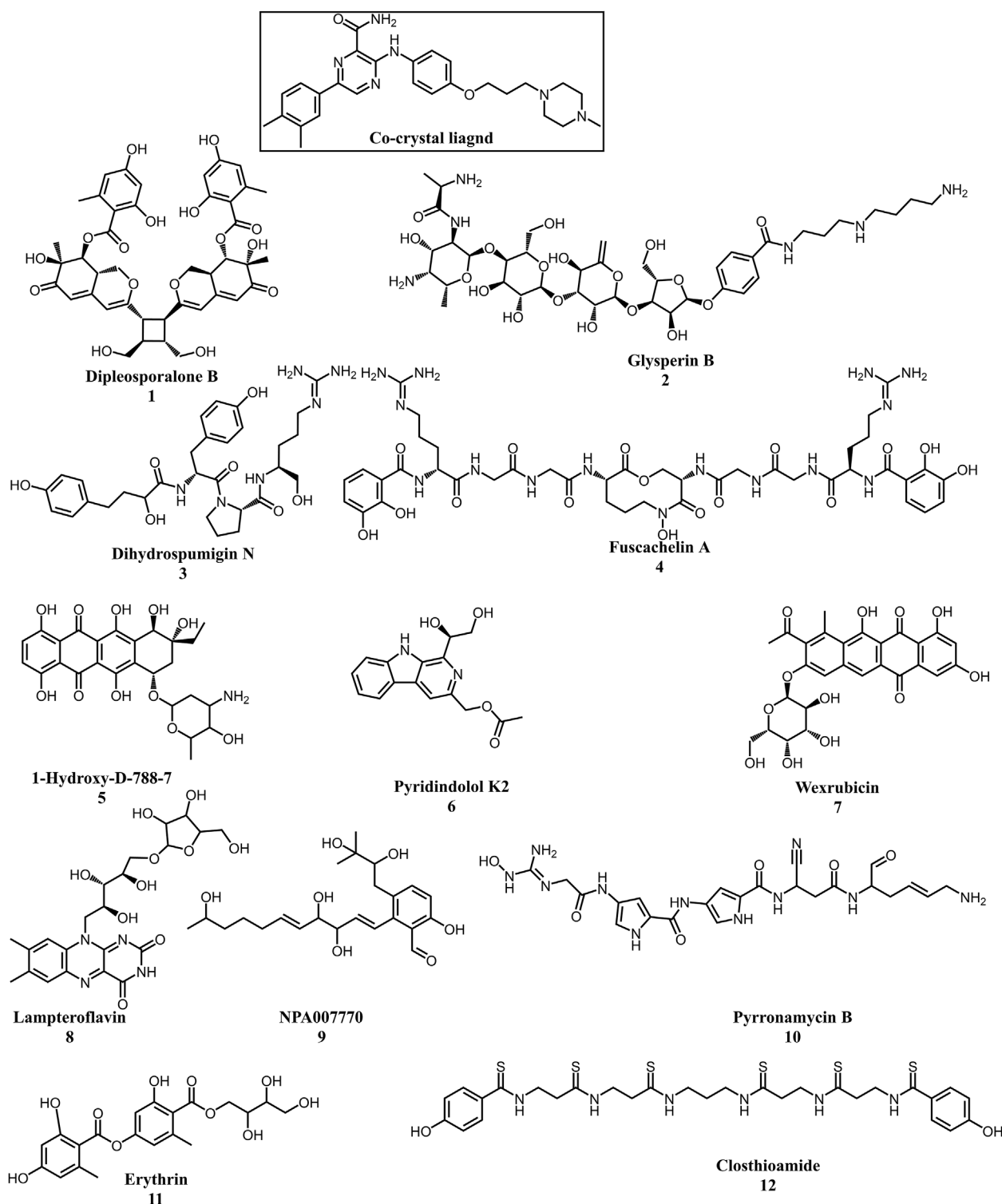
FIGURE 4
Chemical structures of the top 12 hits and the co-crystal ligand. Created using ChemDraw office version 20.1.1.

the investigated compounds is a glycosylated benzamide derivative, part of a class of molecules recognized for their potent antibacterial activity (Kawaguchi et al., 1977). Furthermore, the virtual screening process identified two anthracycline derivatives, namely 1-Hydroxy-D-788-7 and Wexrubicin, which displayed similar binding affinity

towards the enzyme. Interestingly, those hits are structurally related to the previously reported mycobacterial Gyr B inhibitor Epirubicin (Pakamwong et al., 2022). Further, several anthracyclines have demonstrated potent antibacterial activity against both Gram-positive and Gram-negative organisms, as well as significant

FIGURE 5
ROC Curve for the virtual screening of GyrB inhibitors showing a strong ability to distinguish actives from decoys (ROC = 0.97).

FIGURE 6
Superposition of the best poses of the top 12 hits relative to the original pose of the co-crystal ligand in the GyrB catalytic site showing the key interacting residues. The co-crystal ligand shown in red color, and the 12 hits in blue color. Created using Maestro interface of Schrödinger suite version 2023-1.

antimycobacterial activity (Trenado-Uribe et al., 2018; Qun et al., 2023). Pyridindolol K2 is a β-carboline alkaloid, isolated from the culture broth of *Streptomyces* sp (Kim et al., 1997). Literature revealed several β-carboline derivatives as antimicrobial drug candidates (Szabo et al., 2021). Further, carbazole derivatives have been reported as potent inhibitors of MBT gyrase B, offering significant promise for the development of novel anti-TB agents (Pakamwong et al., 2024). Pyrronamycin B is an antibiotic that comprises a pyrrole-amide repeating unit in its structure, contributing to its potent antibacterial activity against both Gram-positive and Gram-negative bacteria. Research has shown that its antimicrobial properties are primarily mediated through the inhibition of DNA gyrase (Asai et al., 2000). Lampteroflavin is a flavin derivative, structurally related to Riboflavin, commonly known as vitamin B2. It is isolated from the luminous mushroom, *Lampteromyces japomcus* (Takahashi et al., 1991). Research reveals that bacteria are likely to develop resistance to antimicrobial flavins at a significantly lower rate (Pedrolli et al., 2014). Dihydrospumigin N is a polycyclic natural product isolated from Cyanobacteria. It is a member of the spumigin family of secondary metabolites, known for their bioactive properties (Sanz et al., 2017). Overall, most of the hits we identified have been previously reported to exhibit antimicrobial properties, with some also demonstrating gyrase inhibitory activity against both Gram-positive and Gram-negative bacteria. Nevertheless, this study is the first to identify these compounds as potential candidates targeting the ATPase activity of MBT DNA gyrase. Furthermore, the retrieved hits in the present study demonstrate gyrase inhibitory properties, further validating our docking protocol. Moreover, to the best of our knowledge, this study is the first to utilize the high-resolution crystal structure of mycobacterial GyrB to screen natural products library, further strengthening the reliability of the findings (Shirude et al., 2013). Additionally, as explained in the following paragraph, the identified hits demonstrated superior binding affinity compared to most previously reported natural products or repurposed drugs, exhibiting enhanced interaction with the enzyme. As a result, they are expected to represent novel candidates with higher efficacy and
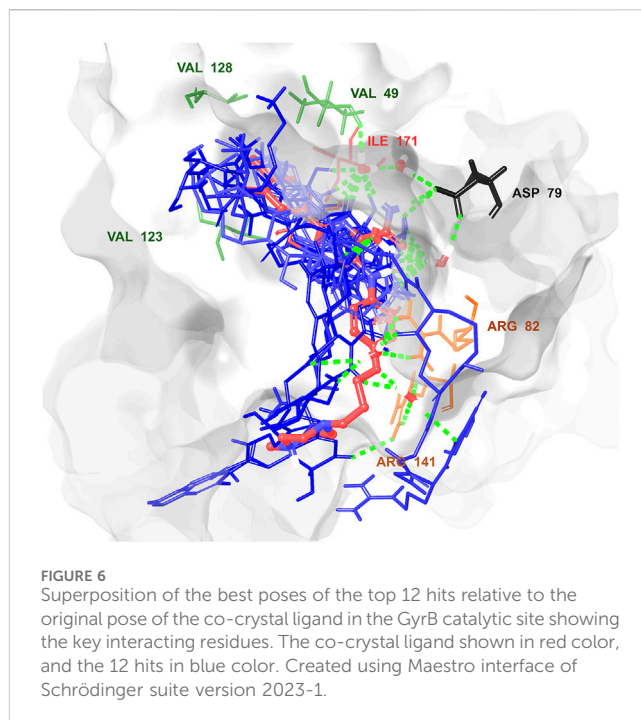
lower resistance potential. Notably, The DNA gyrase enzyme pocket, particularly the GyrB subunit, is highly conserved among *Mycobacterium* species. This conservation implies that the identified hits could potentially inhibit GyrB across different *Mycobacterium* species, including MBT making them valuable candidates for developing broad-spectrum anti-mycobacterial agents (Fu et al., 2009). All 12 hits were properly docked into the ATP-binding site of the GyrB subunit of MBT DNA gyrase and exhibited binding interactions similar to those of the co-crystal ligand (Table 1; Supplementary Figure S3). A variety of molecular interactions were identified as characterizing the binding of the hits to the enzyme's active site. These interactions included ionic bonds, direct and water-mediated hydrogen bonding, Pi-cation interactions, and Van der Waals (VdW) forces. As reported by several studies (Shirude et al., 2013; Hameed et al., 2014; Tomasic et al., 2021), two key sites in the enzyme pocket are essential for high-potency inhibitors, complemented by hydrophobic interactions within the hydrophobic loop. Site 1 involves interactions with ASP79, which may occur via direct hydrogen bonds or water-mediated hydrogen bonds. Site 2 includes interactions with GLY83 alongside ARG141 (via direct or water-mediated hydrogen bonds) and ARG82 (via pi-cation interactions). Additionally, hydrophobic interactions with residues in the hydrophobic pocket—VAL149, VAL123, VAL125, VAL128, and ILE171 are critical for enhancing inhibitor potency. These interactions collectively contribute to binding affinity and specificity. Importantly, the identified hits, similar to the co-crystal ligand (Figure 6; Supplementary Figure S3), engaged in multiple interactions with residues located in the two key sites (ASP79, ARG82, and ARG141). Additionally, they form interactions with nearby residues such as GLU48, GLU56, ASN52, and HIS89, which considered essential for enhanced binding, as reported by Tambe et al. (2020). These

TABLE 2 Docking scores and binding free energies in kcal/mol of the reported mycobacterial DNA gyrase B inhibitors.

No.	Name of the reported inhibitor	Docking score (kcal/mol)	Binding energy (kcal/mol)	References
1	Epirubicin	−10.500	−71.97	Balasubramani et al. (2020)
2	Echinacoside	−7.849	−46.43	Balasubramani et al. (2020)
3	Daidzein	−5.571	−32.49	Jagatap et al. (2023)
4	N-(2-hydroxyethyl)-9,10 dioxoanthracene-2-sulfonamide	−4.782	−47.91	Amorim et al. (2022)
5	Aminotriazole Anthraquinone Derivative (ATD)	−5.123	−35.19	Amorim et al. (2022)
6	Khelline	−4.770	−37.57	Jagatap et al. (2023)
7	PQPNN	−3.891	−20.74	Arevalo and Amorim (2022)

supplementary interactions further enhanced their binding stability and strengthened the overall interaction network within the enzyme pocket. Overall, the nature of the interactions consistently contributed to ligand stability across the identified hits, emphasizing their critical role in achieving high binding affinity. Taken together, these interactions provided a robust foundation for ligand binding and represent crucial targets for the future optimization of the hits identified in this study. Considering the higher docking scores and binding affinity of Fuscachelin A, it was selected as representative example for further analysis to gain more insight into its binding characteristics. The best docking pose of Fuscachelin A obtained at Glide XP-docking level was displayed in Supplementary Figure S3. Fuscachelin A formed crucial interactions within the enzyme pocket. It engaged with ASP79 and ARG141 through water-mediated H-bonds and formed an H-bond with ARG82 instead of a pi-cation interaction observed for the co-crystal ligand. Additionally, it established a salt bridge with ASP142 in site 1 and formed four hydrogen bonds, significantly stabilizing the complex. The decacyclic ring protruded to the solvent exposed area. The top 12 ranked hits positioned perfectly and similarly to the co-crystal ligand (Figure 6), with larger compounds showing their polar parts exposed to the solvent. This orientation suggests that the polar regions of the ligands interact with the surrounding aqueous environment, potentially enhancing solubility and binding efficiency.

To contextualize our findings, a comparative assessment was performed focusing on the identified microbial natural products in relation to previously reported natural product inhibitors and repurposed drugs (Balasubramani et al., 2020; Amorim et al., 2022; Arevalo and Amorim, 2022; Jagatap et al., 2023). As depicted in Table 2, all reported inhibitors (except Epirubicin) had higher docking scores compared to our identified hits 1–12. Moreover, except for Epirubicin (binding free energy −71.97 kcal/mol), the binding affinities of our identified hits (−60.37 to −73.21 kcal/mol) were superior to those of the reported inhibitors (−20.74 to −46.43 kcal/mol). In addition, hits 3, Fuscachelin A, the top hit in our study, displayed binding affinity exceeded that of Epirubicin. Epirubicin, is a known intercalating agent, demonstrated a high binding affinity (−71.97 kcal/mol) and docking score (−10.5 kcal/mol) with mycobacterial Gyr B. Epirubicin features planar aromatic structures allowing it to

establish hydrophobic as well as Pi-Pi stacking interactions with amino acid residues residing in the ATP binding site such as VAL123, VAL125, VAL128, and ILE171 of Gyr B. Moreover, other interactions including water-mediated H-bond with VAL49 and two direct H-bonds and one ionic bond with GLU48 further strengthening its binding affinity. However, Epirubicin is not suitable for DNA gyrase inhibition or tuberculosis treatment due to its potential for immunosuppression and cardiotoxic effects (Banke et al., 2018). Additionally, unlike our identified hits, most reported natural product inhibitors failed to establish significant interaction forces with key residues in the enzyme binding pocket (VAL49, ASP79, ARG82, GLY83, and ARG141) (Figure 7), suggesting a potentially lower inhibitory effect compared to our identified compounds (Shirude et al., 2013). Furthermore, virtual screening conducted by Amorim et al. (2022) identified N-(2-hydroxyethyl)-9,10-dioxoanthracene-2-sulfonamide as the best-scored hit. However, this compound failed to establish meaningful interactions with crucial residues in the binding pocket, such as ASP79, VAL49, and ARG82, which are essential for effective enzyme inhibition. To overcome this limitation, they designed the Aminotriazole Anthraquinone Derivative (ATD) (Figure 7), incorporating structural modifications to improve interactions within the binding site. As a result, ATD successfully formed an interaction with ASP79, but the overall binding affinity and binding free energy were suboptimal compared to our identified compounds. Similarly, Arevalo and Amorim (2022) identified a pyrrolo [1,2-a]quinazoline derivative (PQN) via virtual screening of a natural product database. However, PQN also lacked interactions with key residues, such as ASP79 and ARG141. To enhance its binding properties, they synthesized the PQPNN derivative (Figure 7), specifically designed to optimize interactions with the critical residues. Although PQPNN established interaction with ASP79, its binding free energy and affinity were inferior, remaining two-fold less effective than the hits identified in our study (binding free energy >−35 kcal/mol). In contrast, our study identified naturally occurring compounds that inherently interact with multiple key residues in the enzyme's binding pocket, including ASP79, VAL49, ARG82, GLY83, and ARG141. These strong and meaningful interactions suggest a higher inhibitory potential, surpassing the modified derivatives reported by Amorim et al. (2022), Arevalo and
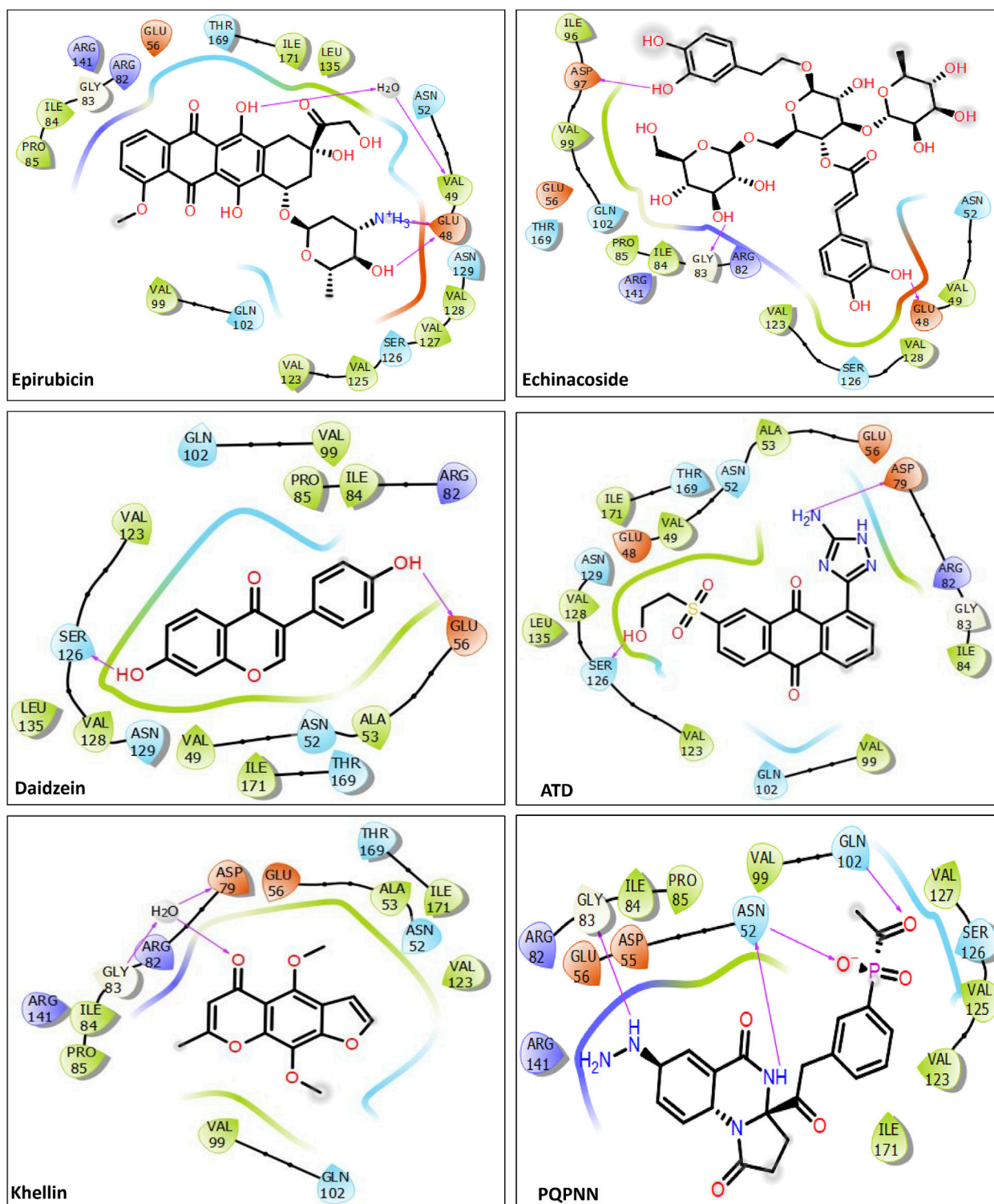
FIGURE 7
2D interactions of the previously reported inhibitors with MBT Gyr B (PDB ID: 4B6C).

Amorim (2022). Notably, our compounds did not require any structural modifications to achieve these superior binding affinities, making them more viable as lead compounds for further development. Additionally, the computational expense and time required for designing and testing derivatives, as seen in ATD and PQPNN, highlight another advantage of our hits. The natural origin of our compounds also aligns with the broader trend of utilizing microbial natural products for their inherent diversity,
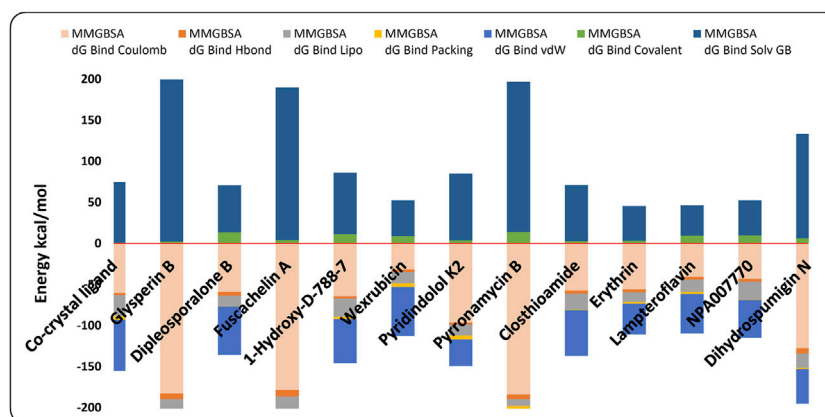
FIGURE 8
Contribution of various energy terms to the binding free energy of the co-crystal ligand and the top 12 hits. The analysis highlights how different energy components, such as van der Waals, electrostatic, and solvation energies, influence the overall binding affinity.

potency, and lower resistance potential. This further substantiate the significance of our findings and their potential impact on developing novel inhibitors targeting *M. tuberculosis* DNA gyrase B.

3.3 MM-GBSA calculations

Following the multistage docking simulations, the docked poses of the top 12 hits and the co-crystal ligand were rescored by MM-GBSA method. In Prime to support the docking study and obtain more accurate predictive binding free energy (ΔG_{bind}). The energy was calculated and the more negative value indicates a stronger binding affinity. It has been observed that the identified hits demonstrated binding free energies ranging from −60.37 to −73.21 kcal/mole (Table 1; Figure 8) signifying their high affinities towards the GyrB active site. Fuscachelin A displayed the highest affinities among the top 12 hits with binding free energies of −73.21 kcal/mole. An analysis of the energy terms contributing to the overall binding free energy of the top 12 hits is provided. As shown in Figure 8, the energy breakdown highlights the interaction profile of each compound compared to the co-crystal ligand, emphasizing specific binding contributions. The co-crystal ligand showed moderate MMGBSA dG Bind Coulomb (−60.35) and dG Bind Lipo (−25.19), indicating balanced electrostatic and hydrophobic interactions. As illustrated in Figure 8, hit compounds such as Pyrromycin B and Glyperin B outperformed the co-crystal ligand in Coulombic (−184.2 and −182.86, respectively), suggesting stronger electrostatic contributions. However, these hits had weaker dG Bind Lipo values, hinting at a potential gap in hydrophobic interactions. Comparatively, Fusachelin A had favorable Coulomb (−178.64) and dG Bind Covalent (−56.84) terms, indicating strong polar and covalent contributions. In contrast, weaker hits like Lampteroflavin had lower energy values across all categories, indicating overall reduced binding affinity. The van der Waals (vdW) and covalent terms vary significantly. Hits such as Glyperin B and Pyrromycin B excel in vdW (−59.37 and −55.63, respectively) (Figure 8) but showed limitations in dG Bind Solv GB, suggesting room for

optimization of solvation effects. To improve binding affinities, enhancing hydrophobic interactions (dG Bind Lipo) and fine-tuning solvation energies (dG Solv GB) could provide more balanced binding profiles. For hits with strong electrostatics, such as Pyrromycin B, improving lipophilic interactions may further strengthen the binding. Optimization of hydrogen bonding networks could also enhance specific contributions seen in weaker terms like dG Bind Hbond (Figure 8). In addition, detailed analysis was performed to evaluate the energy terms of each compound based on its structure, with the goal of guiding potential optimization strategies. The energy breakdowns of the compounds analyzed (Figure 8) showed strong Coulombic interactions driven by hydroxyl, amide, and amino groups, which supported extensive electrostatic and hydrogen-bonding interactions. These interactions were significant in Glyperin B, Dipleosporalone B, Fuscachelin A, and several others, with large sugar frameworks or polar groups contributing to van der Waals interactions. However, the high polarity in many of these compounds, such as in Glyperin B and Wexrubicin, led to considerable solvation penalties. Lipophilic contributions were moderate, with hydrophobic regions like the aromatic cores or methyl groups balancing polarity. The co-crystal ligand exhibited similar Coulombic interactions but also demonstrated notable hydrophobic and basicity contributions from the 4-methylpiperazine group, enhancing binding stability. Further, Figure 8 indicated that, compared to the other compounds, the co-crystal ligand exhibited a better balance between hydrophobicity and polarity, which could potentially result in improved binding efficiency if optimized. Some compounds, like NPA007770 and Closthioamide, exhibited higher polarity and solvation penalties, suggesting the need for further structural refinement to optimize their binding properties. Dihydrospumigin N exhibited strong Coulombic (−127.88 kcal/mol) and van der Waals (−42.24 kcal/mol) contributions (Figure 8), driven by polar groups and hydrophobic regions, but faces high solvation penalties (127.42 kcal/mol). Its moderate hydrophobicity and weak packing suggest room for optimization. Enhancing hydrophobic interactions and reducing desolvation costs could improve binding affinity.

Overall, optimizing both polar and nonpolar interactions while mitigating solvation penalties is crucial for enhancing hit potential in the development of antimycobacterial drugs targeting the ATPase activity of Gyr B. By refining structural features to balance electrostatic, van der Waals, and lipophilic contributions, we can improve binding efficiency. These efforts are essential for advancing the design of effective anti-TB hits targeting MBT.

3.4 *In silico* ADMET profiling

In the past five decades, the evaluation of the physicochemical and pharmacokinetics profiles of drug candidates in the early phases has become an integral component of the drug design and development processes (Caldwell et al., 2003). It involves initial assessments of Absorption, Distribution, Metabolism, Excretion, and Toxicity (ADMET) parameters in order to exclude hits associated with suboptimal or inadequate ADMET profiles from further consideration as potential drug candidates and are thus represent an ideal filtration approach. In the present work, computer-based methods were utilized to predict the ADMET and physicochemical profiles of the top 12 hits identified for their potential to inhibit MBT DNA Gyrase B. The QikProp analysis revealed the physicochemical and pharmacokinetic properties of the compounds (Supplementary Table S1), offering insights into their drug-likeness and ADME profiles. In this context, an overall ADME-compliance score (drug likeness parameter #stars) was used to calculate the number of descriptors for the top 12 hits that fall outside the permissible range of values for 95% of known drugs (Mohamed et al., 2024). Glysperin B and Fuscachelin A had the highest #stars values (18 each), suggesting significant deviations from drug-likeness criteria. In contrast, compounds like Wexrubicin (3), Erythrin (1), and Lampteroflavin (6) showed values within or near the acceptable range, suggesting fewer property violations. Molecular weight (mol_MW), an important factor influencing bioavailability, was recommended to be within 130–725. Several compounds, such as Glysperin B (919) and Fuscachelin A (1,030), exceeded this range, indicating potential absorption challenges due to their large size. Similarly, the solvent-accessible surface area (SASA), ideally between 300 and 1,000, was significantly higher for Fuscachelin A (1,547), suggesting potential issues with solubility and permeability. The SASA components—FOSA (hydrophobic surface area), FISA (polar surface area), and PISA (pi surface area)—varied widely across the compounds. Fuscachelin A, in particular, exhibited an exceptionally high FISA value (799.9), reflecting excessive polarity, which likely hindered its membrane permeability. Hydrogen bond donor (DonorHB) and acceptor (AccptHB) values, critical for solubility and target binding, revealed that Glysperin B had excessively high values (DonorHB: 17, AccptHB: 34), which may have increased its hydrophilicity and reduced its permeability. LogP (QPlogPo/w) and solubility (CIQPlogS) values, crucial for absorption and distribution, indicated limitations for several compounds. For example, Glysperin B displayed excessive hydrophilicity with a QPlogPo/w of −7.01, while Dipleosporalone B exhibited very poor solubility with a CIQPlogS of −10.0. Permeability metrics such as QPPCaco and QPPMDCK, which assessed intestinal permeability and drug transport potential, showed poor results for most compounds.

However, Pyridindolol K2 and Closthioamide demonstrated relatively better permeability profiles. Evaluating drug bioavailability is critical for analyzing how drugs are absorbed, distributed, metabolized, and excreted, as well as for establishing suitable therapeutic dosages. This assessment is also fundamental in drug development processes and in comparing the effectiveness of different delivery methods (Stielow et al., 2023). The human oral absorption metrics (%Oral Absorption and Human Oral Absorption categories) highlighted additional challenges. Only Pyridindolol K2 achieved high oral absorption (81%), while the other hits were classified as having low or poor absorption potential. The therapeutic efficacy of any drug is greatly affected by its binding to the plasma proteins, as this determines the amount of the free drug that can traverse the cellular membranes (Ntie-Kang, 2013). In this regard, the logKHSA parameter was utilized to assess the potential of the screened hits to bind to human albumin. The logKHSA parameter assesses plasma protein binding, which influences drug distribution and pharmacokinetics. Compounds like Dipleosporalone B, Wexrubicin, Pyridindolol K2, and Closthioamide demonstrated optimal binding (logKHSA within −1.5 to 1.5), ensuring balanced bioavailability and retention. In contrast, Glysperin B (−3.265) and Fuscachelin A (−2.8) exhibited very weak binding, potentially leading to rapid clearance or toxicity due to high free drug concentrations. While most top 12 hits fell within the permissible range, weak-binding ones may require structural optimization. In drug development, blocking the human ether-a-go-go-related gene (hERG) channel by small molecules is a significant concern. Inhibition or disruption of hERG channel activity by drug compounds can prolong the QT interval, potentially leading to severe cardiotoxicity (Lamothe et al., 2016). Toxicity concerns were apparent in QPlogHERG values, where compounds such as Glysperin B and Closthioamide (both −8.2) raised significant cardiotoxicity risks by exceeding the threshold of −5. Assessment of on drug metabolism at early stages of drug discovery is a crucial step in optimizing lead compounds to achieve ideal pharmacokinetic and pharmacodynamic profiles (Zhang and Tang, 2018). The #metab parameter, which predicts the number of metabolic reactions a compound is likely to undergo, was another critical factor. The acceptable range is 1–8, and most compounds exceeded this limit, with Fuscachelin A (16) and Glysperin B (15) showing particularly high values. These results indicated that these compounds were highly prone to metabolism, potentially leading to rapid clearance or the production of undesirable metabolites. Conversely, compounds such as Pyridindolol K2 (3) and Closthioamide (6) had values closer to the acceptable range, indicating better metabolic stability. Most compounds adhered to the Rule of Five (maximum four violations) and the Rule of Three (maximum three violations), demonstrating general drug-likeness. Among the tested compounds, Pyridindolol K2 stood out with favorable absorption, permeability, and metabolic stability, making it a promising hit. However, most compounds, particularly Glysperin B and Fuscachelin A, required structural modifications to address solubility, permeability, metabolism, and toxicity issues identified in the analysis. This assessment emphasized the importance of optimizing these parameters to improve the pharmacokinetic profiles of the identified hits. Further, parameters verified by ADMETlab webserver were evaluated for the top 12 hits, and the results are tabulated on Supplementary Table

S2. These parameters comprise, human hepatotoxicity, drug-induced liver injury, AMES toxicity, rat oral acute toxicity, FDA maximum daily dose, carcinogenicity, mutagenicity, skin sensitization, eye corrosion, eye irritation, and respiratory toxicity. The toxicity profiles of the compounds revealed significant variations in their safety and potential risks. Glysperin B and Fuscachelin A consistently showed high toxicity across multiple parameters, including hepatotoxicity (0.97 and 0.95), mutagenicity (0.99), and skin sensitization (1), indicating a high risk for both human liver damage and genetic mutations. In contrast, NPA007770 and Dihydrospumigin N exhibited lower toxicity values, particularly for drug-induced liver injury (0.01) and carcinogenicity (0.02), making them relatively safer. Wexrubicin and Pyridindolol K2 had moderate toxicity risks in liver injury (0.99 and 0.53) and mutagenicity (0.99 and 0.92), but they also showed higher carcinogenic potential. Closthioamide and Pyrronamycin B showed a mixed toxicity profile with moderate skin sensitization and irritation risks, with Closthioamide also having a notable potential for eye irritation (0.65). Overall, NPA007770 and Dihydrospumigin N appeared to be safer, while Glysperin B and Fuscachelin A presented significant toxicity challenges that required careful consideration in drug development. Pyridindolol K2 exhibited moderate toxicity risks, particularly in liver injury (0.53) and mutagenicity (0.92), with a higher potential for carcinogenicity (0.92). It also showed moderate skin sensitization (0.67) and eye irritation (0.17). While not as toxic as Glysperin B or Fuscachelin A, it still posed notable concerns, particularly in terms of carcinogenicity and mutagenicity, which would require careful assessment during further development. In conclusion, while NPA007770 and Dihydrospumigin N demonstrated relatively safer toxicity profiles, compounds like Glysperin B and Fuscachelin A posed significant risks, highlighting the need for further optimization and careful evaluation in the drug development process. Pyridindolol K2 on the other hand demonstrated a more balanced toxicity profile compared to the highest-risk compounds but still warranted attention in safety evaluations. In conclusion, among the 12 hits, Pyridindolol K2 demonstrated the best drug-likeness, exhibiting no ADME deviations, which indicated optimal pharmacokinetic properties. Erythrin and NPA007770 displayed minimal ADME issues, suggesting they also have strong potential, though some minor refinements were necessary. In contrast, Wexrubicin and 1-Hydroxy-D-788-7 showed moderate drug-likeness, with noticeable deviations in ADME properties that would require optimization to improve their pharmacokinetic profiles. Regarding toxicity, Pyridindolol K2 and Erythrin exhibited favorable toxicity profiles, with low risks for hepatotoxicity and mutagenicity, making them safer hit for development. NPA007770 also showed promising toxicity data, while Wexrubicin and 1-Hydroxy-D-788-7 exhibited moderate toxicity concerns, particularly regarding liver injury and mutagenicity, indicating a need for further optimization to reduce potential harmful effects. To obtain meaningful insights, we conducted a comprehensive comparison of the ADMET properties of our identified hits with those of SPR720 (Supplementary Table S1). This approach was necessitated by the fact that, to date, no approved drug existed for the treatment of tuberculosis targeting MBT gyrase B, with SPR720, a benzimidazole derivative, being the sole candidate

under clinical development in this context (Talley et al., 2021). Pyridindolol K2 demonstrated the most favorable properties compared to SPR720 in QikProp analysis, emerging as the leading hit. It exhibited high human oral absorption (81%), excellent compliance with the Rule of Five (0 violations), and favorable solubility and lipophilicity (QPlogPo/w: 1.5). Its blood-brain barrier penetration (QPlogBB: −1.3) further supported its potential. SPR720 served as the reference with reasonable drug-likeness and low HERG inhibition risk, but its lower oral absorption (24.9%) and higher molecular weight limited its efficiency. In contrast, 1-Hydroxy-D-788-7 and Erythrin displayed significant limitations, such as poor absorption and excessive rotatable bonds, which impacted bioavailability. Erythrin also showed a high risk of HERG inhibition, raising safety concerns. Furthermore, we also made a comparative analysis of the ADMETLab results, which are presented in Supplementary Table S2, to evaluate the safety profiles of the hits alongside SPR720. Pyridindolol K2 demonstrated a balanced safety profile with moderate risks in hepatotoxicity (0.48) and mutagenicity (0.92), and concerns in carcinogenicity (0.92) and skin sensitization (0.67), making it a promising hit compared to SPR720. Erythrin showed low hepatotoxicity (0.09) and excellent respiratory safety (0.07), but posed risks in eye irritation (0.65) and moderate mutagenicity (0.22), making it safer than SPR720 in liver and respiratory safety but requiring refinement. In contrast, 1-Hydroxy-D-788-7 exhibited significant risks, with high hepatotoxicity (0.93), mutagenicity (0.98), and respiratory toxicity (0.93), making it less favorable than SPR720. Overall, Pyridindolol K2 emerged as the most promising hit, while the others demonstrated potential but required further refinement for both pharmacokinetic optimization and toxicity mitigation.

3.5 Pharmacophore modeling

Amongst the diverse computer-aided drug design approaches, pharmacophore-based drug design is considered an efficient approach for the rational design of novel bioactive molecules. Pharmacophore modeling is most commonly applied to virtually screen small molecule libraries for potential modulators of specific biological effects (Voet et al., 2014). Herein, we conducted pharmacophore modeling to identify hits that match the essential features required for potent MBT DNA Gyrase B inhibitors. The Phase software in the Schrödinger Drug Discovery Suite was used to generate the 3D pharmacophore model. For this purpose, a training set composed of 67 previously reported inhibitors of DNA gyrase B were selected based on their known inhibitory activity of MBT DNA Gyrase B (Jeankumar et al., 2013; Kale et al., 2013; Shirude et al., 2013; Jeankumar et al., 2014; Kale et al., 2014; Reddy et al., 2014; Renuka et al., 2014; Jeankumar et al., 2015; Locher et al., 2015; Medapi et al., 2015a; Medapi et al., 2015b; Saxena et al., 2015) (Supplementary Table S3). They were employed to generate several pharmacophore hypotheses (Table 3) with diverse combinations of chemical features. Then, Phase HypoScore was used to rank them using an internal validation method. As illustrated in Figure 9, the best-fitted four-point pharmacophore hypothesis (ADRR_1) was elected as the best from the generated hypotheses to perform virtual screening. It consists of two aromatic rings features (R), one

TABLE 3 Parameters scores of the generated hypotheses.

No.	Hypothesis	PhaseHypoScore	Num matched	Selectivity score	Volume score	Vector score	Site score	Survival score
1	ADRR_1	0.956472	51	1.136750	0.561684	0.947172	0.898032	5.251209
2	ADRR_2	0.955290	51	1.136941	0.564364	0.945307	0.887346	5.241529
3	ADDRR_3	0.934114	44	1.506127	0.515424	0.985061	0.761866	5.411932
4	ADDDRR_6	0.932594	44	2.003748	0.480918	0.902195	0.599589	5.629902
5	ADDDRR_1	0.931054	37	1.987496	0.579493	0.918213	0.752505	5.805910
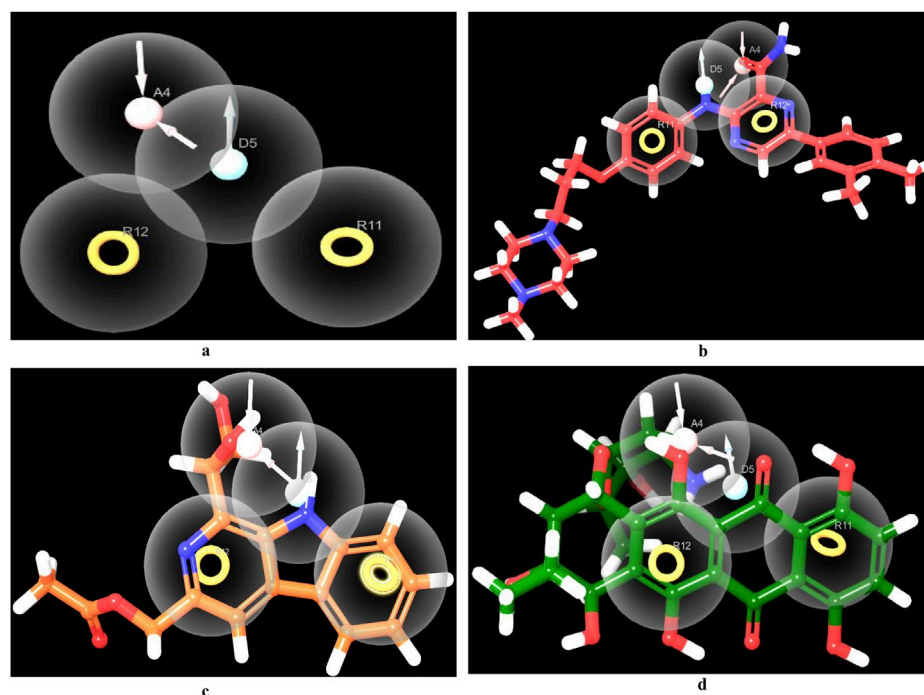
FIGURE 9
Pharmacophore screening. Created using the Maestro interface of Schrödinger Suite version 2023-1. **(A)** The best-fitted four-point pharmacophore model generated using known actives. The pharmacophoric features are represented as spheres, including two aromatic ring systems (R), one hydrogen bond donor (D), and two hydrogen bond acceptors (A). **(B)** 3D feature alignment of the co-crystal ligand (red), showing the alignment of the compound to the pharmacophore model. **(C)** 3D feature alignment of Pyridindolol K2 (Orange), showing the alignment of the compound to the pharmacophore model. **(D)** 3D feature alignment of 1-Hydroxy-D-788-7 (green), showing the alignment of the compound to the pharmacophore model.

hydrogen bond acceptor feature (A) and one hydrogen bond donor feature (D). Subsequently, the 12 hits were screened against the best-fitted hypothesis, and the results (Table 4; Figure 9) led to the identification of 6 hits as the best (PhaseScreenScores ranged from 0.94 to 2.03), matching all four chemical features of the pharmacophore model. The co-crystal ligand, as shown in Figure 9, aligned well with the pharmacophoric features, achieving a PhaseScreenScore of 2.3, reflecting strong compatibility with the binding site. Key interactions observed in the ligand binding included the donor feature at Site-1, which likely formed a water-mediated hydrogen bond with ASP79, and the aryl or heteroaryl groups at Site-2, which engaged in Pi-cation interactions with ARG82. Hydrophobic contacts with residues VAL123, VAL125, VAL128, and ILE171 further stabilized the ligand. Among the identified hits, Pyridindolol K2 emerged as

the top candidate, with the highest PhaseScreenScore and Fitness Scores (2.03), although its moderate Align Score (0.562) suggested room for spatial optimization. Pyrronamycin B exhibited excellent spatial alignment (Align Score: 0.949) despite moderate PhaseScreenScore and Fitness Scores (1.32), suggesting its potential as a promising hit. 1-Hydroxy-D-788-7 achieved the highest Align Score (1.12) but recorded the lowest PhaseScreenScore and Fitness Scores (0.95), warranting further investigation for potential activity. Erythrin displayed balanced scores (PhaseScreen/Fitness: 1.42, Align: 0.783), indicating good feature matching and spatial alignment. Closthioamide demonstrated strong spatial alignment (Align Score: 0.915) but lower PhaseScreenScore and Fitness Scores (0.94), while Lampteroflavin showed moderate performance across all metrics, with a low Align Score (0.540), indicating weaker spatial

TABLE 4 Phase screen parameters for screening the 6 hits that fit the ADRR_1 hypothesis out of the 12 identified hits.

Name	PhaseScreenScore	Fitness score	Align score
Co-crystal ligand	2.30	2.31	0.25
Pyridindolol K2	2.03	2.03	0.56
Erythrin	1.42	1.42	0.78
Pyrronamycin B	1.32	1.32	0.94
Lampteroflavin	1.20	1.20	0.53
1-Hydroxy-D-788-7	0.95	0.95	1.11
Closthioamide	0.94	0.94	0.91

compatibility. These results reinforce the importance of balancing spatial alignment and pharmacophoric feature matching for optimal ligand binding. The pharmacophoric features align closely with the binding pockets described by Shirude et al. (2013). The co-crystal ligand and identified hits reflect critical interactions at Site-1, Site-2, and the hydrophobic pocket, confirming the validity of the pharmacophore model and the strength of the screening approach. The docking study revealed that replacing the ethyl group on 1-Hydroxy-D-788-7 with a propyl group significantly improved the docking score from −10.2 kcal/mol to −11.25 kcal/mol, due to enhanced hydrophobic interactions with residues VAL128, VAL125, and VAL127. R-group enumeration using monocyclic, aromatic, and alkyl groups indicated that only small hydrophobic groups, such as an additional methyl, were tolerated within the hydrophobic pocket. The propyl analog maximized van der Waals contacts while avoiding steric clashes, highlighting the strict spatial constraints of the pocket. These findings suggested that future optimization could explore small alkyl or compact aromatic groups to further enhance binding affinity. Refer to Supplementary Figure S4 for a visual comparison of the parent compound and the designed analog, showing the R-group modifications.

3.6 Quantum computational calculations

Over the last decade, Quantum mechanics (QM)-based methods have gathered an immense attention in the field of drug discovery as powerful and highly accurate tools for describing ligand-target interactions (Cavasotto et al., 2018). Among the most commonly used methods is the Density Functional Theory (DFT) method which has been proven to be useful, efficient, and sufficiently rigorous in various branches of Computer-aided Drug Design (CADD) (LaPointe and Weaver, 2007; Manathunga et al., 2022). In this study, we performed DFT at the B3LYP level to correlate the predicted affinity with the structural features, focusing mainly on the top three hits, which demonstrated high affinity, good ADMET properties, and matching to all chemical features of the generated pharmacophore model. The studied structural features included localization energies of lowest unoccupied molecular orbital (LUMO) and highest occupied molecular orbital (HOMO), along with the molecular electrostatic potential (MESP). These localization energies are known as frontier molecular orbitals (FMOs), and they play an important role in chemical stability, serving as an efficient tool for studying donor-acceptor interactions (Yele et al., 2021). The

HOMO energy can determine the molecule's tendency to contribute electrons to electrophilic centers, whereas LUMO can determine the capacity of a molecule to accept electrons from nucleophilic centers (Guezane-Lakoud et al., 2023). As shown in Table 5, the electronic properties of the three compounds, Pyridindolol K2, Erythrin, and 1-Hydroxy-D-788-7, revealed distinct differences in their reactivity and stability. 1-Hydroxy-D-788-7 features a complex framework, including a tetrahydrotetracene backbone with multiple hydroxyl groups and an ether linkage. The presence of multiple hydroxyl groups suggests the compound has a high potential for hydrogen bonding, which likely contributes to its high electronegativity (4.30 eV) and global electrophilicity index (2.80 eV). The smaller HOMO-LUMO gap (3.19 eV) and chemical softness (0.30 eV^{-1}) indicate it is highly reactive, making it prone to electron donation or acceptance (Bouback et al., 2021; Ahmad et al., 2023). Its electron affinity (2.71 eV) aligns with its electrophilic nature, suggesting that 1-Hydroxy-D-788-7 is the most chemically reactive and capable of forming strong interactions with biological targets, especially through hydrogen bonds and electron interactions. On the other hand, Pyridindolol K2 contains an indole ring system, which is substituted with an amino group and a methoxy group. The relatively simple structure, with fewer hydroxyl groups compared to 1-Hydroxy-D-788-7, correlates with its more moderate HOMO-LUMO gap (4.4 eV) and chemical hardness (2.2 eV). This suggests that Pyridindolol K2 is more stable and less reactive than 1-Hydroxy-D-788-7, which is consistent with its moderate chemical softness (0.23 eV^{-1}). The compound's ability to accept electrons may be somewhat limited due to the absence of highly reactive functional groups like hydroxyl groups, but its electronegativity (3.5 eV) still indicates a potential for electron attraction in binding interactions. Further, Erythrin features a phenolic core with a trihydroxybutoxy side chain. The molecule's high HOMO-LUMO gap (5.12 eV) and moderate chemical hardness (2.56 eV) suggest that it is relatively stable with limited reactivity, though it has the potential for moderate electron acceptance or donation. The compound's electronegativity (3.64 eV) and chemical softness (0.20 eV) further indicate a moderate ability to interact with biological targets through hydrogen bonding or hydrophobic interactions. The structure's hydroxyl groups suggest that Erythrin may interact with biological molecules through hydrogen bonding, but its stability and lower reactivity make it less prone to undergo significant electron transfer reactions compared to 1-Hydroxy-D-788-7. The distributions of HOMO and LUMO plots for three hits are shown in Figures 10A–F. It was observed that Pyridindolol

TABLE 5 Quantum chemical reactivity descriptors of the top three hits.

Property	HOMO	LUMO	HLG	Electron affinity	Ionization potential	Chemical hardness	Chemical softness	Electronegativity	Global electrophilicity index
Pyridindolol K2	−5.7	−1.30	4.4	1.30	5.7	2.2	0.23	3.5	2.78
Erythrin	−6.2	−1.08	5.12	1.08	6.2	2.56	0.20	3.64	2.58
1-Hydroxy-D-788-7	−5.9	−2.71	3.19	2.71	5.9	1.65	0.30	4.30	2.80

K2 demonstrated a compact and rigid Pyridoindole core, which served as the primary structural motif for both its HOMO and LUMO orbitals (Figures 10A, B, respectively). The HOMO was distributed across the core, highlighting its electron-donating potential, while the LUMO was similarly localized, emphasizing the core's role in electron acceptance. This dual functionality, combined with its ability to form H-bonds, makes Pyridindolol K2 a highly stable and strong binder to DNA gyrase B. Erythrin exhibited distinct separation in the structural motifs for its orbitals. The HOMO (Figure 10C) was localized on the resorcinol ring, reflecting its role as an electron donor due to its hydroxyl substituents, while the LUMO (Figure 10D) was concentrated on the phenolic ester ring, indicating its electron-accepting functionality. This separation of orbital distribution enabled Erythrin to effectively engage in donor-acceptor interactions and H-bonding with DNA gyrase B residues, enhancing its binding efficiency. Regarding 1-Hydroxy-D-788-7 presented a more complex structural motif for its orbitals. The HOMO (Figure 10E) was distributed across the dihydroxybenzene ring and dihydroxyhexane chain, highlighting its strong electron-donating capacity. In contrast, the LUMO (Figure 10F) was concentrated on the dioxocyclohexane ring, particularly around the two carbonyl groups, showcasing its electron-accepting role. This spatial separation between electron-dense and electron-deficient regions allowed 1-Hydroxy-D-788-7 to form multiple interaction types, including H-bonding, making it highly reactive and adaptable within the binding pocket.

3.7 MD simulations

With increased computer power and the development of novel force fields, MD simulations have proven increasingly valuable in providing vital insights into real-life molecular interactions events. In this regard, MD simulations can be a valuable tool in facilitating the early stages of modern drug discovery and development processes (Salo-Ahen et al., 2020). In the present study, MD simulations were performed to evaluate the stability and intermolecular interactions of Pyridindolol K2, Erythrin, and 1-Hydroxy-D-788-7, which demonstrated favorable binding affinity and a druggable ADMET profile. The enzyme-ligand complexes of those hits, the co-crystal ligand complex, alongside the unbound protein, were simulated over 100 ns using the Desmond package with the SPC solvation model. Certain parameters such as RMSD, root mean square fluctuation (RMSF), and intermolecular interactions were utilized to reveal the molecular details of ligand-protein simulations (Mohankumar et al., 2020). RMSD is a key measure used to evaluate the overall stability of the ligand-protein complex during the simulation. As shown in Table 6; Figure 11, the RMSD trajectories for each system revealed key insights into the stability of the ligand binding throughout the 100 ns simulation. The RMSD of the co-crystal ligand remained steady at approximately 2.1 Å after an initial stabilization phase within the first 10 ns, demonstrating its strong and stable interaction with the protein. This suggests that the co-crystal ligand maintained consistent binding throughout the simulation, confirming that it forms a stable complex with the protein. The co-crystal ligand's RMSD remained unchanged for the remainder of the simulation,
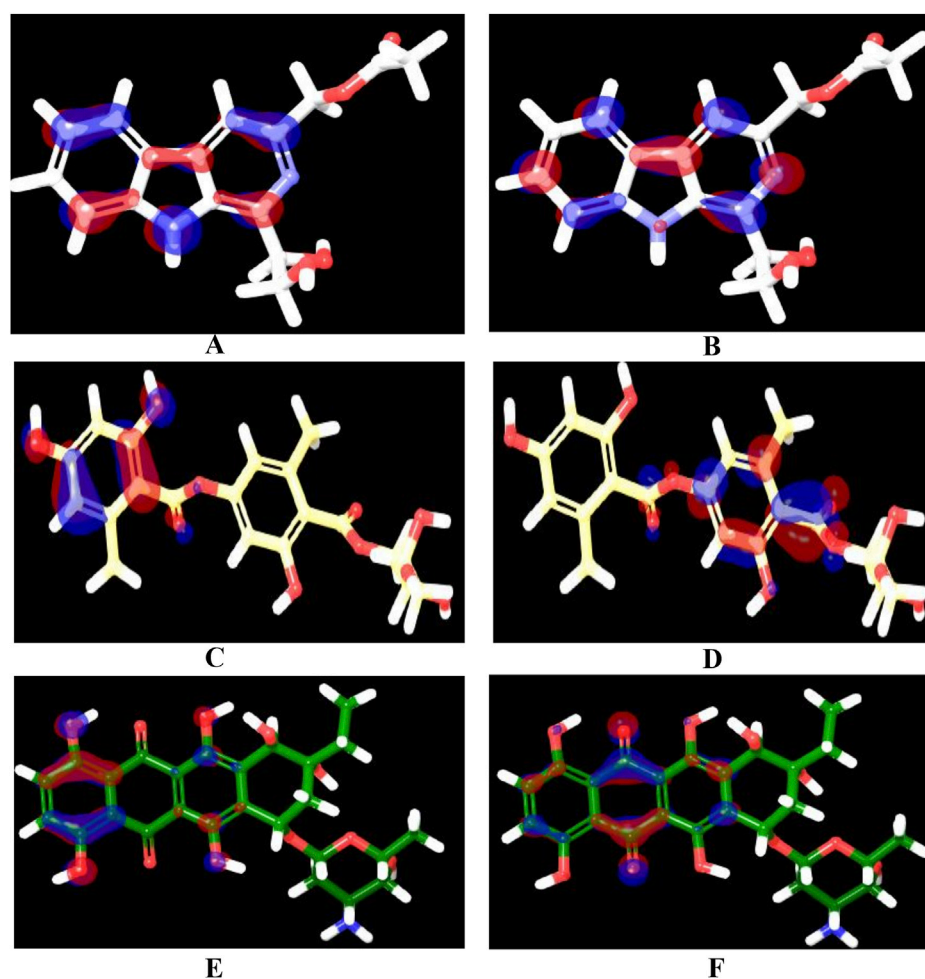
FIGURE 10
HOMO and LUMO orbitals of the three identified hits: Pyridindolol K2 [**(A)**: HOMO, **(B)** LUMO], Erythrin [**(C)**: HOMO, **(D)** LUMO], and 1-Hydroxy-D-788-7 [**(E)**: HOMO, **(F)** LUMO]. The orbitals were calculated using the B3LYP/6-31G**++ basis set with hybrid DFT. The red regions represent electron-dense areas, while the blue regions indicate electron-deficient areas. Created using the Maestro interface of Schrödinger Suite version 2023-1.

indicating no significant conformational changes or instability. Among the hits, 1-Hydroxy-D-788-7 displayed the most stable binding, with an RMSD of 1.7 Å, which quickly stabilized after the first 10 ns. The RMSD profile for 1-Hydroxy-D-788-7 remained consistent over the entire simulation, with only minor fluctuations in the initial phase. Importantly, after 30 ns, this ligand showed superior stability compared to the co-crystal ligand, maintaining a more stable RMSD trajectory, indicating more reliable binding interactions with the protein. The low RMSD values indicate that 1-Hydroxy-D-788-7 interacts with the protein in a highly stable manner, providing strong evidence of its potential as a promising hit. The stability of 1-Hydroxy-D-788-7, indicated by its low RMSD (1.7 Å), strongly correlated with its consistent intermolecular interactions with the protein. The low RMSD value suggested that the ligand maintained a stable binding conformation, with minimal structural deviations throughout the simulation. This stability was further supported by the ligand's favorable hydrogen bonding and water-bridge contacts, which likely contributed to the rigid binding at the active site. The consistent interactions, especially in the later stages of the simulation, indicated that 1-Hydroxy-D-788-7 formed strong, reliable interactions with key residues, reducing protein flexibility and enhancing its stability. This stable binding profile reinforced its potential as a promising drug candidate. The strong binding interactions, coupled with minimal fluctuation, implied that 1-Hydroxy-D-788-7 could effectively inhibit the target protein. Both Pyrindolol K2 and Erythrin exhibited slightly higher RMSD values (around 2.0 Å) compared to 1-Hydroxy-D-788-7. Although these ligands remained relatively stable throughout the simulation, their higher RMSD values indicated that they may experience slightly more conformational flexibility or weaker interactions with the protein, suggesting they are somewhat less stable than 1-Hydroxy-D-788-7. However, both ligands still displayed acceptable stability and could be considered as secondary candidates for further evaluation. In comparison to Amorim et al. (2022) and Arevalo and Amorim (2022), who reported that the Gyr B-ATD complex, involving an anthraquinone-like ligand similar to 1-Hydroxy-D-788-7, showed lower RMSD values (around 2 Å) than the apo form, the results in this study demonstrated that 1-Hydroxy-D-788-7 formed a more stable complex with the protein, with an RMSD value of 1.7 Å,

TABLE 6 RMSD, RMSF, and ligand-protein contacts (H-bonds, water bridges, hydrophobic, and Pi-cation interactions) for apo form, Co-crystal ligand, and Top 3 hits (1-Hydroxy-D-788-7, Erythrin, and Pyrindolol K2) over a 100 ns MD simulation.

Gyr B complex	Apo	Co-crystal ligand	1-Hydroxy-D-788-7	Erythrin	Pyrindolol K2
PL-RMSD (Å)					
Average	2.4	2.1	1.7	2.1	2.2
Maximum	3.2	2.7	2.5	2.9	3.2
Minimum	1.1	1.1	1.1	1.0	1.0
P-RMSF (Å)					
Average	1.1	0.9	0.9	1.0	1.0
Maximum	8.3	4.8	3.2	7.8	6.4
Minimum	0.4	0.4	0.4	0.4	0.4
H-bond contacts					
Average	-	1.4	2.0	2.5	2.0
Maximum	-	3.0	6.0	7.0	5.0
Minimum	-	0.0	0.0	0.0	1.0
Hydrophobic contacts					
Average	-	1.7	1.1	1.0	0.6
Maximum	-	5.0	4.0	3.0	4.0
Minimum	-	0.0	0.0	0.0	0.0
Pi-cation contacts					
Average	-	0.6	0.3	0.5	0.0
Maximum	-	1.0	1.0	1.0	0.0
Minimum	-	0.0	0.0	0.0	0.0
Water-bridge contacts					
Average	-	3.7	4.8	2.7	1.6
Maximum	-	8.0	14.0	11.0	6.0
Minimum	-	1.0	0.0	0.0	0.0

FIGURE 11
RMSD plot of the apoprotein, co-crystal ligand-protein complex, and the top three hits-protein complexes (1-Hydroxy-D-788-7, Erythrin, and Pyrindolol K2) over the 100 ns molecular dynamics simulation. Generated using Microsoft Excel.

TABLE 7 Comparative analysis of study compounds vs literature-reported compounds.

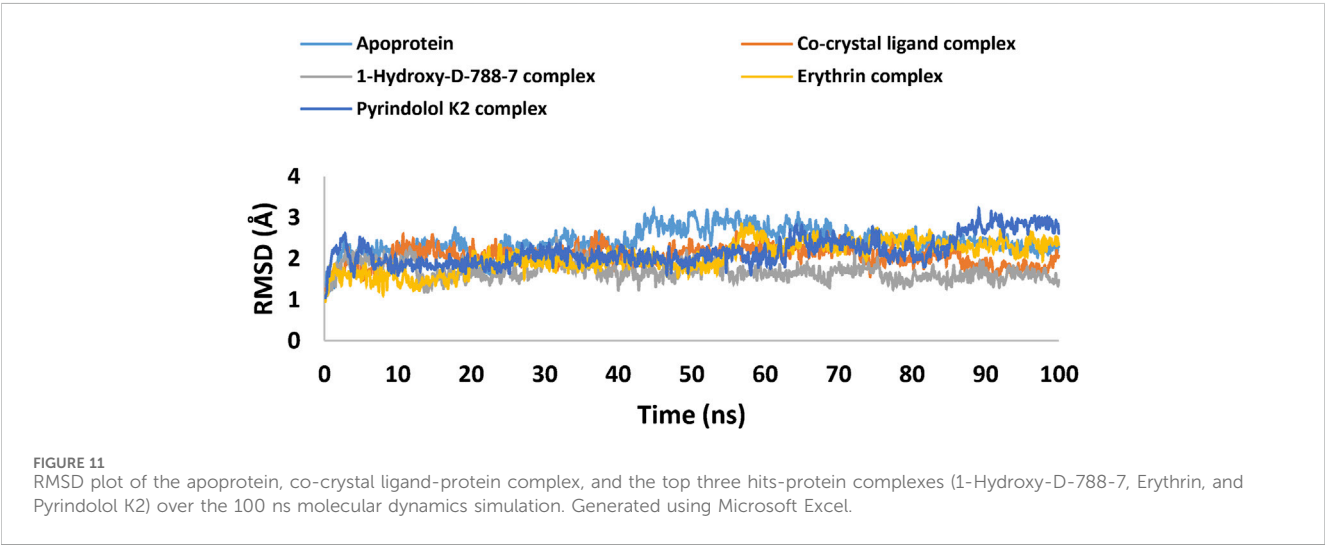| Hits	Virtual screening parameters		Average MD parameters		References
	Docking score	Binding free energy	RMSD (Å)	RMSF (Å)	
1-Hydroxy-D-788-7	−10.253	−60.37	1.7	0.9	Hits identified from the present study
Erythrin	−9.492	−65.68	2.1	1.0	
Pyrindolol K2	−9.590	−64.51	2.2	1.0	
Literature reported compounds					
ATD	−5.123	−35.19	2	4	Amorim et al. (2022)
PQPNN	−3.891	−20.74	3.1	>1	Arevalo and Amorim (2022)
D5	−4.225	−44.59	2.02 to 3.27	3.8	Islam and Pillay (2017)

outperforming the anthraquinone-like ligand in Amorim et al.'s study and PQNN in Amorim and Arévalo study. On the other hand, Erythrin and Pyrindolol K2 exhibited similar RMSD values (around 2.1 Å and 2.2 Å, respectively), indicating comparable stability but with slightly more fluctuation than 1-Hydroxy-D-788-7. Furthermore, the RMSD values for the top three hits are comparable to or better than those reported in the Islam and Pillay study (Islam and Pillay, 2017), which also used the same PDB ID (4B6C) for DNA Gyrase B. With RMSD values ranging from 1.70 to 2.1 Å, the identified hits in this study demonstrate slightly more stable binding compared to the study's range of 2.02–3.27 Å, suggesting an enhanced binding affinity for our selected compounds. The apoprotein demonstrated significant instability throughout the simulation, with RMSD values fluctuating widely and averaging 2.4 Å, underscoring the dynamic and flexible nature of the protein in the absence of a stabilizing ligand. The higher RMSD value for the apoprotein further highlighted the critical role of ligand binding in maintaining protein structure stability, with the absence of a ligand leading to greater conformational variability. Thus, the top three hits from the virtual screening, as shown in Table 7, demonstrated superior performance metrics compared to literature-reported compounds. Specifically, 1-Hydroxy-D-788-7, Erythrin, and Pyrindolol K2 achieved docking scores ranging from −9.492 to −10.253, reflecting stronger binding affinities to the target protein when compared to literature compounds, which exhibited significantly weaker scores (−3.891 to −5.123). Their binding free energies, calculated between −60.37 and −65.68 kcal/mol, suggested greater thermodynamic stability, highlighting their ability to form energetically favorable interactions with the binding pocket. Furthermore, the top hits showed lower RMSD values (1.7–2.2 Å), indicating better alignment of their conformations with the reference structure during molecular dynamics simulations. In addition, the lower RMSF values (0.9–1.0 Å) demonstrated reduced atomic fluctuations, suggesting enhanced stability of these compounds within the dynamic protein-ligand complex. In contrast, literature-reported compounds displayed higher RMSD and RMSF values, signifying weaker structural stability and flexibility during simulation. These findings collectively underscore the superior binding affinity, stability, and structural alignment of the identified top hits, making them highly promising candidates for further optimization and experimental

validation in the context of targeting *M. tuberculosis* gyrase B. Overall, the RMSD data revealed that 1-Hydroxy-D-788-7 provided the most stable binding interactions with the protein, outperforming the co-crystal ligand and the anthraquinone-like ligand from Amorim et al. (2022). Erythrin and Pyrindolol K2 demonstrated relatively less stability compared to 1-Hydroxy-D-788-7, but still showed consistent binding interactions, suggesting that both ligands may require further optimization for more robust interactions. The RMSD graph of the unbound protein, the co-crystallized ligand, and the top three hits (Table 6; Figure 11) demonstrated that the 1-Hydroxy-D-788-7 complex achieved greater stability and equilibration compared to the co-crystal ligand complex throughout the simulation period. The C-alpha atoms of the protein-1-Hydroxy-D-788-7 complex exhibited fluctuations ranging from 1.1 Å to 2.5 Å during the entire simulation, whereas the protein-co-crystal ligand complex fluctuated between 1.1 Å and 2.7 Å over the 100 ns run. In contrast, the unbound protein displayed more pronounced fluctuations, ranging from 1.1 Å to 3.2 Å throughout the simulation. Figure 11 highlighted that the top three hits binding to the mycobacterial DNA gyrase B conferred dynamic equilibration and maintained a steady interaction profile with the protein over the 100 ns simulation. For gain more insights into the dynamic behaviors of each amino acid residue during the simulation run, the RMSF was monitored. It is defined as the displacement of a specific atom or group of atoms relative to the reference structure, averaged across the number of atoms (Ravikumar et al., 2023). As depicted in Table 6 and The RMSF graph (Figure 12), the co-crystal ligand and 1-Hydroxy-D-788-7 induced the least residue flexibility, with average P-RMSF values of 0.9 Å, indicating strong interactions that minimized protein flexibility. Erythrin and Pyrindolol K2 caused slightly higher residue fluctuations (1.0 Å), suggesting comparable binding strength. The apoprotein displayed relatively higher flexibility, with an average RMSF of 1.1 Å and peaks reaching 8.3 Å, reflecting substantial conformational changes without ligand stabilization. Interestingly, the loop containing the residues responsible for ligand interactions showed less flexibility (below 1 Å) for the 3 hits and the co-crystal ligand, as indicated by the RMSF data. This suggested that these ligands stabilized the protein and reduced the flexibility of the binding site residues, in contrast to the apo form, which showed greater flexibility. This further emphasized the stabilizing role of ligand binding in maintaining
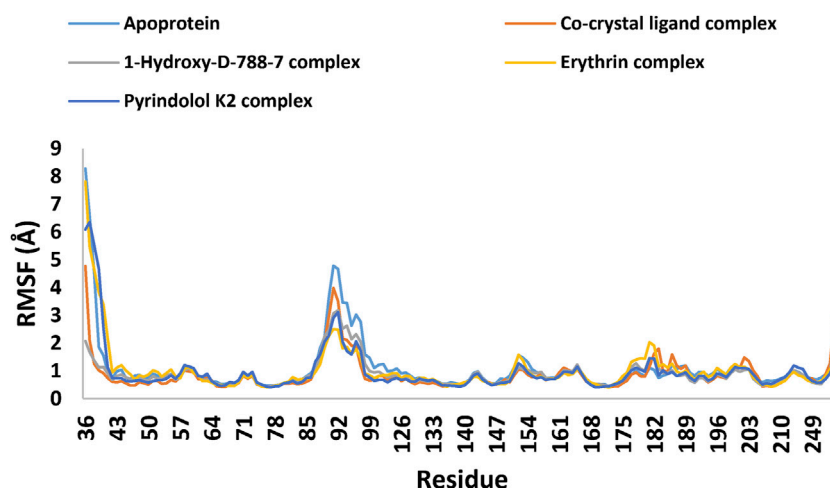
FIGURE 12
RMSF Plot generated through MDS trajectories, showing the Root Mean Square Fluctuation (RMSF) of the apoprotein, co-crystal ligand-protein complex, and the top three hits-protein complexes (1-Hydroxy-D-788-7, Erythrin, and Pyrindolol K2) over the 100 ns molecular dynamics simulation. Generated using Microsoft Excel.

a more rigid protein conformation. This is further substantiated by the fact that the RMSF values for the top three hits ranged from 0.9 to 1.0 Å, indicating significantly lower fluctuations in the protein backbone compared to the study by Islam and Pillay (Islam and Pillay, 2017), where the RMSF values ranged from 2.3 to 3.8 Å. Further, the individual RMSF values for residues in the active site were examined, with a particular focus on the critical residues Val49, Glu56, Asp79, Arg82, Gly83, Val123, Val125, Val128, and Arg141. These residues demonstrated reduced flexibility when bound to the top three hits, showcasing stability that was either comparable to or better than that observed for the co-crystallized ligand. Notably, the most critical residue, Asp79, was stabilized by Pyrindolol K2 with an RMSF value of 0.45 Å, which was superior to the stabilization observed for the co-crystallized ligand (0.47 Å) and the unbound protein (0.49 Å). This finding underscores the significant role of the top three hits in conferring enhanced stability to the active site residues, thereby highlighting their potential effectiveness in binding and stabilizing the protein's active site. These results suggested that the top three hits in the present study induced more stable conformations of DNA Gyrase B, with reduced flexibility, thereby further supporting their enhanced binding affinity and potential as promising inhibitors. The RMSF analysis of 1-Hydroxy-D-788-7 revealed a significant reduction in flexibility, particularly at the active site, where the RMSF was lower than the apo-protein. This suggested that the ligand binding effectively stabilized the protein, limiting fluctuations in key residues involved in catalysis. Compared to the unbound protein, the ligand-bound system exhibited a more rigid structure, with minimal changes in the active site residues, indicating stronger interactions. The RMSF values for the ligand-protein complex were consistent, showing that 1-Hydroxy-D-788-7 maintained stable interactions throughout the simulation. Furthermore, Table 8 presents a comprehensive analysis of the average protein RMSF (P-RMSF) values across different regions of the GyrB complex, evaluated in both Apo and ligand-bound forms. Three primary regions were analyzed: the Active Site Region, the ATPase Domain, and the Toprim Domain. Each of these regions

is essential for the protein's functionality. The Active Site Region is primarily responsible for DNA binding and catalysis, the ATPase Domain plays a key role in energy hydrolysis, and the Toprim Domain aids in the interaction between the protein and DNA. Together, these regions ensure the proper function and stability of the GyrB complex (Papillon et al., 2013). In the Active Site region, the Apo form exhibited the highest flexibility (P-RMSF = 0.99 Å), indicating greater structural mobility in the unbound state. However, upon ligand binding, particularly with the co-crystal ligand, this flexibility was notably reduced, with the lowest P-RMSF value observed (0.67 Å), suggesting enhanced stability in the region when the ligand is bound. In contrast, the ATPase domain exhibited consistent flexibility between the Apo form and the co-crystal ligand (P-RMSF = 1.42 Å), reflecting a relatively stable structural conformation in both conditions. Ligands such as 1-Hydroxy-D-788-7, Erythrin, and Pyrindolol K2 led to a reduction in flexibility within this domain, with 1-Hydroxy-D-788-7 providing the most substantial stabilization (P-RMSF = 0.96 Å). This decrease in flexibility underscores the potential for these ligands to induce more rigid, functionally relevant conformations. The Toprim domain displayed consistent stability across all conditions, with P-RMSF values ranging from 0.78 Å to 0.85 Å, highlighting its inherent stability regardless of the presence of ligands. Notably, the Apo form exhibited the highest flexibility in this region, whereas Pyrindolol K2 induced the greatest stabilization (P-RMSF = 0.78 Å), demonstrating its ability to stabilize this domain effectively. Overall, ligand binding was shown to generally stabilize the protein, particularly within the Active Site region, where the co-crystal ligand had the most pronounced effect. These results indicate that 1-Hydroxy-D-788-7 and Pyrindolol K2 played critical roles in stabilizing the ATPase and Toprim domains, respectively. These findings offer valuable insights into the molecular interactions of ligands with the GyrB complex and provide a foundation for prioritizing potential ligands for future hits identification, particularly those with the capacity to reduce flexibility and enhance protein stability. To gain deeper insights into the

TABLE 8 Protein flexibility analysis of GyrB complex in Apo and ligand-bound states across active site, ATPase, and Toprim regions.

Gyr B complex	Average P-RMSF (Å) per protein region		
	Active site region	ATPase domain	Toprim domain
Apo	0.99	1.42	0.85
Co-crystal ligand	0.67	1.42	0.82
1-Hydroxy-D-788-7	0.82	0.96	0.80
Erythrin	0.79	1.02	0.84
Pyrindolol K2	0.72	1.2	0.78

binding interactions of the top three compounds with mycobacterial DNA Gyrase B during the simulation, an extensive analysis of ligand-residue interactions was performed. The results are illustrated in Figure 13. As summarized in Table 6; Figure 13A, hydrogen bond analysis highlighted that 1-Hydroxy-D-788-7 exhibited the strongest interactions, averaging 2.5 hydrogen bonds and reaching a maximum of 7, outperforming the co-crystal ligand (average: 2.0; maximum: 6). Erythrin demonstrated comparable average hydrogen bonding to the co-crystal ligand (2.0) but showed fewer maxima (5). In contrast, Pyrindolol K2 displayed weaker and less consistent interactions (average: 1.4; maximum: 3). Notably, Pyrindolol K2 retained a hydrogen bond with the critical residue ASP79 for 98% of the simulation duration, closely mirroring the behavior of the co-crystal ligand. Hydrophobic contact analysis (Table 6; Figure 13B) revealed that the co-crystal ligand had the strongest interactions (average: 1.7), followed by 1-Hydroxy-D-788-7 (1.1) and Erythrin (1.0), while Pyrindolol K2 contributed minimally (0.6). Regarding Pi-cation interactions (Table 6), the co-crystal ligand exhibited the most significant contacts (average: 0.6), marginally exceeding Erythrin (average: 0.5). 1-Hydroxy-D-788-7 showed moderate interactions (average: 0.3; maximum: 1.0), whereas Pyrindolol K2 lacked notable Pi-cation interactions (average: 0.0). Analysis of water-bridge contacts (Table 6; Figure 13C) indicated that 1-Hydroxy-D-788-7 exhibited the highest levels of interaction, with an average of 4.8 and a peak of 14, surpassing the co-crystal ligand (average: 3.7; maximum: 8.0). Erythrin and Pyrindolol K2 displayed lower water-bridge interactions, reflecting reduced stability in their binding modes. Supplementary Figure S5 detailed protein-ligand contact histograms for a comprehensive view of the interactions. Overall, 1-Hydroxy-D-788-7 emerged as the most promising candidate, demonstrating superior or comparable performance to the co-crystal ligand across key metrics, including binding interactions, stability, and flexibility, thus establishing itself as a robust hit. Erythrin also showed significant promise as an alternative candidate, with consistent binding interactions and stability throughout the simulation. While Pyrindolol K2 exhibited relatively weaker interactions, its sustained binding to the critical residue ASP79 underscores its potential for further exploration. Importantly, all three compounds require chemical optimization to enhance pharmacokinetic properties and strengthen interactions within the enzyme's hydrophobic pocket, a crucial step to improving their binding efficacy and therapeutic potential. Such advancements would address current limitations and foster the development of highly potent enzyme inhibitors.

3.8 Study limitations and future perspective

In the present study an innovative approach was explored to identify new mycobacterial DNA gyrase B inhibitors from microbial-derived natural products database. These products have long been known for their potential bioactivity against infectious diseases. Implementation of multiple computational tools such as, target-based virtual screening, XP molecular docking, binding free energy calculations, ADMET profiling, pharmacophore modeling, quantum mechanical calculations and MD simulations, the identified hits (1-Hydroxy-D-788-7, Erythrin, and Pyrindolol K2) demonstrated properties that were better than those of the existing natural inhibitors of the catalytic activity of mycobacterial DNA gyrase. Despite these promising computational findings, significant limitations need to be addressed. Of particular importance is the accuracy of the computational methods which heavily dependent on the availability of the structural data which may not fully reflect the intricacies of the biological systems. For instance, computer-based simulations could not predict the potential *in vivo* metabolic reactions and off-target effects resulting in uncertainty regarding the therapeutic efficacy and safety of the investigated hits. Further, molecular docking simulations involves assumptions about the flexibility of both proteins and ligands. Instead, it assumes a static active site, which may not precisely capture the dynamic behavior of proteins that can adopt several conformations, potentially affecting the reliability of the results. Accordingly, the calculated docking scores which predict the binding potential of the investigated hits do not consistently correlate with the experimental binding affinity values. To tackle this issue, binding free energy calculations were employed to enhance the accuracy of estimating the affinity of our investigated hits. In this regard, two main factors were incorporated, the solvent effects and the structural flexibility of both protein and the investigated hits. Furthermore, MD simulations, which provide a dynamic view, were conducted to assess the stability of the identified hits complexes as potent mycobacterial DNA gyrase inhibitors. Nevertheless, MD studies are also constrained by the relatively short time scales commonly simulated. To accurately reproduce thermodynamic properties and fully elucidate all binding site configurations important for drug design, it is necessary to explore all potential conformational states of the protein within the simulation. Unfortunately, several biological processes, such as receptor conformational changes relevant to drug binding, occur over much longer time scales exceeding those suitable for simulation. Given the above-mentioned shortcomings, wet-lab validation is essential to
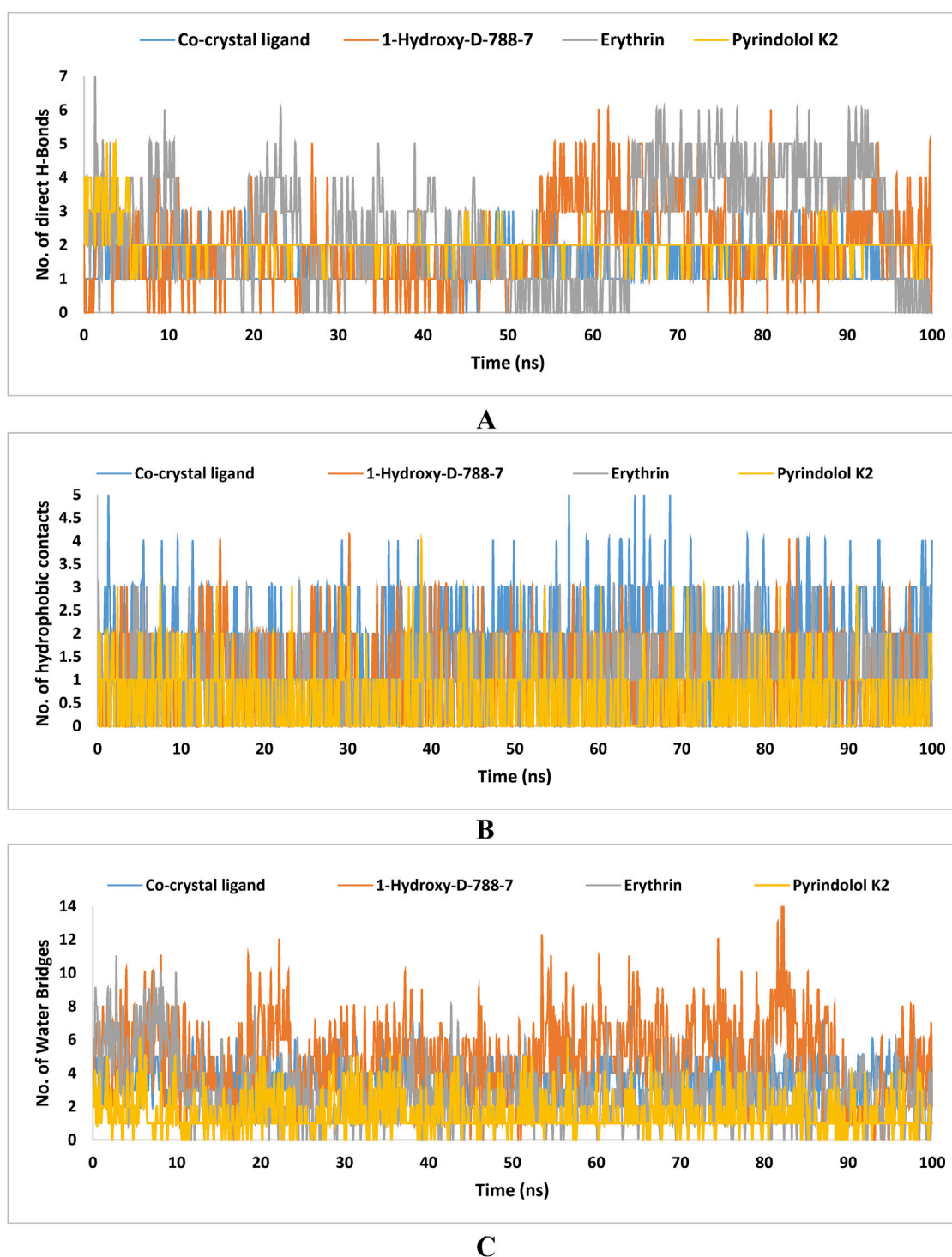
FIGURE 13
Number of **(A)** hydrogen bonds, **(B)** hydrophobic interactions, and **(C)** water-bridge interactions formed during the 100 ns MD simulation of the co-crystal ligand and the top three hits (1-Hydroxy-D-788-7, Erythrin, and Pyrindolol K2) with Mycobacterial DNA Gyrase B (PDB: 4B6C). The data were generated using Microsoft Excel.

confirm the potential of our identified hits, as effective inhibitors targeting mycobacterial DNA gyrase B. Experimental validation in the process of drug discovery comprises both *in vitro* and *in vivo* assays. In this context, *in vitro* testing involving enzyme inhibition assays and cell-based tests, are highly recommended to validate the

potential of the identified hits as effective inhibitors of mycobacterial DNA gyrase B. Further, *in vivo* studies will be crucial for evaluating its ADMET properties as well as its therapeutic potential. Overall, the computational approach used in this study provides valuable insights, but its limitations include the absence of experimental

validation for the identified hits. Future research should focus on conducting thorough *in vitro* and *in vivo* evaluations of these compounds to improve their practical application and translational potential.

4 Conclusion

This study identified 1-Hydroxy-D-788-7, an anthracycline derivative, as a promising hit compound for targeting Mycobacterial DNA gyrase, a key enzyme in *M. tuberculosis*. Using computational tools like docking, ADME-T profiling, and molecular dynamics simulations, 12 potential inhibitors were screened, with 1-Hydroxy-D-788-7, Erythrin, and Pyrindolol K2 emerging as top candidates. 1-Hydroxy-D-788-7 showed the strongest binding affinity and stable interactions with DNA gyrase B. The results highlight its potential as an anti-tuberculosis agent, particularly against drug-resistant strains. Further experimental validation is needed to confirm its efficacy as a novel treatment for MDR-TB and XDR-TB.

Data availability statement

The original contributions presented in the study are included in the article/Supplementary Material, further inquiries can be directed to the corresponding authors.

Author contributions

TE: Conceptualization, Funding acquisition, Methodology, Project administration, Software, Writing–original draft. MgM: Conceptualization, Formal Analysis, Methodology, Writing–original draft. MlM: Investigation, Methodology, Validation, Writing–review and editing. EE: Formal Analysis, Validation, Writing–review and editing, Investigation. AA: Formal Analysis, Investigation, Writing–original draft, Validation.

Conflict of interest

The authors declare that the research was conducted in the absence of any commercial or financial relationships that could be construed as a potential conflict of interest.

Generative AI statement

The author(s) declare that Generative AI was used in the creation of this manuscript. Generative artificial intelligence (AI) was used for language editing and punctuation correction.

Publisher's note

All claims expressed in this article are solely those of the authors and do not necessarily represent those of their affiliated organizations, or those of the publisher, the editors and the reviewers. Any product that may be evaluated in this article, or claim that may be made by its manufacturer, is not guaranteed or endorsed by the publisher.

Supplementary material

The Supplementary Material for this article can be found online at: https://www.frontiersin.org/articles/10.3389/fchem.2025.1524607/full#supplementary-material

References

Agrawal, A., Roué, M., Spitzfaden, C., Petrella, S., Aubry, A., Hann, M., et al. (2013). *Mycobacterium tuberculosis* DNA gyrase ATPase domain structures suggest a dissociative mechanism that explains how ATP hydrolysis is coupled to domain motion. *Biochem. J.* 456 (2), 263–273. doi:10.1042/bj20130538

Ahmad, S., Gupta, D., Ahmed, T., and Islam, A. (2023). Designing of new tetrahydro-β-carboline-based ABCG2 inhibitors using 3D-QSAR, molecular docking, and DFT tools. *J. Biomol. Struct. Dyn.* 41, 14016–14027. doi:10.1080/07391102.2023.2176361

Alghamdi, A., Abouzied, A. S., Alamri, A., Anwar, S., Ansari, M., Khadra, I., et al. (2023). Synthesis, molecular docking, and dynamic simulation targeting main protease (mpro) of new, thiazole clubbed pyridine scaffolds as potential COVID-19 inhibitors. *Curr. Issues Mol. Biol.* 45 (2), 1422–1442. doi:10.3390/cimb45020093

Allue-Guardia, A., Garcia, J. I., and Torrelles, J. B. (2021). Evolution of drug-resistant *Mycobacterium tuberculosis* strains and their adaptation to the human lung environment. *Front. Microbiol.* 12, 612675. doi:10.3389/fmicb.2021.612675

Almansour, N. M., Allemailem, K. S., Abd El Aty, A. A., Ismail, E. I. F., and Ibrahim, M. A. A. (2023). *In silico* mining of natural products Atlas (NPAtlas) database for identifying effective bcl-2 inhibitors: molecular docking, molecular dynamics, and pharmacokinetics characteristics. *Molecules* 28 (2), 783. doi:10.3390/molecules28020783

Amorim, J. C., Cabrera Bermeo, A. E., Vasquez Urgiles, V. E., Martinez Leon, M. R., and Carpio Arevalo, J. M. (2022). An in-silico evaluation of anthraquinones as potential

inhibitors of DNA gyrase B of *Mycobacterium tuberculosis*. *Microorganisms* 10 (12), 2434. doi:10.3390/microorganisms10122434

Arevalo, J. M. C., and Amorim, J. C. (2022). Virtual screening, optimization and molecular dynamics analyses highlighting a pyrrolo[1,2-a]quinazoline derivative as a potential inhibitor of DNA gyrase B of *Mycobacterium tuberculosis*. *Sci. Rep.* 12 (1), 4742. doi:10.1038/s41598-022-08359-x

Asai, A., Sakai, Y., Ogawa, H., Yamashita, Y., Kakita, S., Ochiai, K., et al. (2000). Pyrronamycin A and B, novel antitumor antibiotics containing pyrrole-amide repeating unit, produced by Streptomyces sp. *J. Antibiotics* 53 (1), 66–69. doi:10.7164/antibiotics.53.66

Atanasov, A. G., Zotchev, S. B., Dirsch, V. M., International Natural Product Sciences, T., Supuran, C. T., Rollinger, J. M., et al. (2021). Natural products in drug discovery: advances and opportunities. *Nat. Rev. Drug Discov.* 20 (3), 200–216. doi:10.1038/s41573-020-00114-z

Aubry, A., Pan, X. S., Fisher, L. M., Jarlier, V., and Cambau, E. (2004). *Mycobacterium tuberculosis* DNA gyrase: interaction with quinolones and correlation with antimycobacterial drug activity. *Antimicrob. Agents Chemother.* 48 (4), 1281–1288. doi:10.1128/AAC.48.4.1281-1288.2004

Avalos, E., Catanzaro, D., Catanzaro, A., Ganiats, T., Brodine, S., Alcaraz, J., et al. (2015). Frequency and geographic distribution of gyrA and gyrB mutations associated with fluoroquinolone resistance in clinical *Mycobacterium tuberculosis* isolates: a systematic review. *PLoS One* 10 (3), e0120470. doi:10.1371/journal.pone.0120470

Azam, F., Eid, E. E., and Almutairi, A. (2021). Targeting SARS-CoV-2 main protease by teicoplanin: a mechanistic insight by docking, MM/GBSA and molecular dynamics simulation. *J. Mol. Struct.* 1246, 131124. doi:10.1016/j.molstruc.2021.131124

Bagcchi, S. (2023). WHO's global tuberculosis report 2022. *Lancet Microbe* 4 (1), e20. doi:10.1016/S2666-5247(22)00359-7

Balasubramani, G. L., Rajput, R., Gupta, M., Dahiya, P., Thakur, J. K., Bhatnagar, R., et al. (2020). Structure-based drug repurposing to inhibit the DNA gyrase of *Mycobacterium tuberculosis*. *Biochem. J.* 477 (21), 4167–4190. doi:10.1042/bcj20200462

Banke, A., Fosbol, E. L., Moller, J. E., Gislason, G. H., Andersen, M., Bernsdorf, M., et al. (2018). Long-term effect of epirubicin on incidence of heart failure in women with breast cancer: insight from a randomized clinical trial. *Eur. J. Heart Fail* 20 (10), 1447–1453. doi:10.1002/ejhf.1168

Barth, S. A., Preussger, D., Pietschmann, J., Fessler, A. T., Heller, M., Herbst, W., et al. (2024). *In vitro* antibacterial activity of microbial natural products against bacterial pathogens of veterinary and zoonotic relevance. *Antibiot. (Basel)* 13 (2), 135. doi:10.3390/antibiotics13020135

Batool, M., Ahmad, B., and Choi, S. (2019). A structure-based drug discovery paradigm. *Int. J. Mol. Sci.* 20 (11), 2783. doi:10.3390/ijms20112783

Bochevarov, A. D., Harder, E., Hughes, T. F., Greenwood, J. R., Braden, D. A., Philipp, D. M., et al. (2013). Jaguar: a high-performance quantum chemistry software program with strengths in life and materials sciences. *Int. J. Quantum Chem.* 113 (18), 2110–2142. doi:10.1002/qua.24481

Bouback, T. A., Pokhrel, S., Albeshri, A., Aljohani, A. M., Samad, A., Alam, R., et al. (2021). Pharmacophore-based virtual screening, quantum mechanics calculations, and molecular dynamics simulation approaches identified potential natural antiviral drug candidates against MERS-CoV S1-NTD. *Molecules* 26 (16), 4961. doi:10.3390/molecules26164961

Caldwell, G. W., Yan, Z., Masucci, J. A., Hageman, W., Leo, G., and Ritchie, D. M. (2003). Applied pharmacokinetics in drug development: an overview of drug discovery. *Pharm. Dev. Regul.* 1, 117–132. doi:10.1007/bf03257371

Cao, F., Meng, Z. H., Wang, P., Luo, D. Q., and Zhu, H. J. (2020). Dipleosporalones A and B, dimeric azaphilones from a marine-derived Pleosporales sp. fungus. *J. Nat. Prod.* 83 (4), 1283–1287. doi:10.1021/acs.jnatprod.0c00132

Cavasotto, C. N., Adler, N. S., and Aucar, M. G. (2018). Quantum chemical approaches in structure-based virtual screening and lead optimization. *Front. Chem.* 6, 188. doi:10.3389/fchem.2018.00188

Chang, Y., Hawkins, B. A., Du, J. J., Groundwater, P. W., Hibbs, D. E., and Lai, F. (2022). A guide to *in silico* drug design. *Pharmaceutics* 15 (1), 49. doi:10.3390/pharmaceutics15010049

Chiriac, A. I., Kloss, F., Kramer, J., Vuong, C., Hertweck, C., and Sahl, H. G. (2015). Mode of action of closthioamide: the first member of the polythioamide class of bacterial DNA gyrase inhibitors. *J. Antimicrob. Chemother.* 70 (9), 2576–2588. doi:10.1093/jac/dkv161

Chopra, S., Matsuyama, K., Tran, T., Malerich, J. P., Wan, B., Franzblau, S. G., et al. (2012). Evaluation of gyrase B as a drug target in *Mycobacterium tuberculosis*. *J. Antimicrob. Chemother.* 67 (2), 415–421. doi:10.1093/jac/dkr449

De Vivo, M., Masetti, M., Bottegoni, G., and Cavalli, A. (2016). Role of molecular dynamics and related methods in drug discovery. *J. Med. Chem.* 59 (9), 4035–4061. doi:10.1021/acs.jmedchem.5b01684

Dheda, K., Gumbo, T., Maartens, G., Dooley, K. E., McNerney, R., Murray, M., et al. (2017). The epidemiology, pathogenesis, transmission, diagnosis, and management of multidrug-resistant, extensively drug-resistant, and incurable tuberculosis. *Lancet Respir. Med.* 5, 291–360. doi:10.1016/s2213-2600(17)30079-6

Dimise, E. J., Widboom, P. F., and Bruner, S. D. (2008). Structure elucidation and biosynthesis of fuscachelins, peptide siderophores from the moderate thermophile Thermobifida fusca. *Proc. Natl. Acad. Sci. U. S. A.* 105 (40), 15311–15316. doi:10.1073/pnas.0805451105

Divyashri, G., Krishna Murthy, T. P., Sundareshan, S., Kamath, P., Murahari, M., Saraswathy, G. R., et al. (2020). *In silico* approach towards the identification of potential inhibitors from Curcuma amada Roxb against *H. pylori*: ADMET screening and molecular docking studies. *BioImpacts* 11 (2), 119–127. doi:10.34172/bi.2021.19

Dixon, S. L., Smondyrev, A. M., Knoll, E. H., Rao, S. N., Shaw, D. E., and Friesner, R. A. (2006a). PHASE: a new engine for pharmacophore perception, 3D QSAR model development, and 3D database screening: 1. Methodology and preliminary results. *J. computer-aided Mol. Des.* 20, 647–671. doi:10.1007/s10822-006-9087-6

Dixon, S. L., Smondyrev, A. M., and Rao, S. N. (2006b). PHASE: a novel approach to pharmacophore modeling and 3D database searching. *Chem. Biol. and drug Des.* 67 (5), 370–372. doi:10.1111/j.1747-0285.2006.00384.x

Dookie, N., Rambaran, S., Padayatchi, N., Mahomed, S., and Naidoo, K. (2018). Evolution of drug resistance in *Mycobacterium tuberculosis*: a review on the molecular determinants of resistance and implications for personalized care. *J. Antimicrob. Chemother.* 73 (5), 1138–1151. doi:10.1093/jac/dkx506

Friesner, R. A., Banks, J. L., Murphy, R. B., Halgren, T. A., Klicic, J. J., Mainz, D. T., et al. (2004). Glide: a new approach for rapid, accurate docking and scoring. 1. Method and assessment of docking accuracy. *J. Med. Chem.* 47 (7), 1739–1749. doi:10.1021/jm0306430

Friesner, R. A., Murphy, R. B., Repasky, M. P., Frye, L. L., Greenwood, J. R., Halgren, T. A., et al. (2006). Extra precision glide: docking and scoring incorporating a model of hydrophobic enclosure for protein– ligand complexes. *J. Med. Chem.* 49 (21), 6177–6196. doi:10.1021/jm051256o

Fu, G., Wu, J., Liu, W., Zhu, D., Hu, Y., Deng, J., et al. (2009). Crystal structure of DNA gyrase B' domain sheds lights on the mechanism for T-segment navigation. *Nucleic Acids Res.* 37 (17), 5908–5916. doi:10.1093/nar/gkp586

Germe, T. R., Bush, N. G., Baskerville, V. M., Saman, D., Benesch, J. L., and Maxwell, A. (2024). Rapid, DNA-induced interface swapping by DNA gyrase. *Elife* 12, RP86722. doi:10.7554/eLife.86722

Guex, N., Peitsch, M. C., and Schwede, T. (2009). Automated comparative protein structure modeling with SWISS-MODEL and Swiss-PdbViewer: a historical perspective. *Electrophoresis* 30 (Suppl. 1), S162–S173. doi:10.1002/elps.200900140

Guezane-Lakoud, S., Ferrah, M., Merabet-Khelassi, M., Touil, N., Toffano, M., and Aribi-Zouioueche, L. (2023). 2-Hydroxymethyl-18-crown-6 as an efficient organocatalyst for alpha-aminophosphonates synthesized under eco-friendly conditions, DFT, molecular docking and ADME/T studies. *J. Biomol. Struct. Dyn.*, 1–17. doi:10.1080/07391102.2023.2213336

Halgren, T. A., Murphy, R. B., Friesner, R. A., Beard, H. S., Frye, L. L., Pollard, W. T., et al. (2004). Glide: a new approach for rapid, accurate docking and scoring. 2. Enrichment factors in database screening. *J. Med. Chem.* 47 (7), 1750–1759. doi:10.1021/jm030644s

Hameed, P. S., Raichurkar, A., Madhavapeddi, P., Menasinakai, S., Sharma, S., Kaur, P., et al. (2014). Benzimidazoles: novel mycobacterial gyrase inhibitors from scaffold morphing. *ACS Med. Chem. Lett.* 5 (7), 820–825. doi:10.1021/ml5001728

Han, J., Liu, X., Zhang, L., Quinn, R. J., and Feng, Y. (2022). Anti-mycobacterial natural products and mechanisms of action. *Nat. Prod. Rep.* 39 (1), 77–89. doi:10.1039/d1np00011j

Islam, M. A., and Pillay, T. S. (2017). Identification of promising DNA GyrB inhibitors for Tuberculosis using pharmacophore-based virtual screening, molecular docking and molecular dynamics studies. *Chem. Biol. Drug Des.* 90 (2), 282–296. doi:10.1111/cbdd.12949

Ivanczi, M., Balogh, B., Kis, L., and Mandity, I. (2023). Molecular dynamics simulations of drug-conjugated cell-penetrating peptides. *Pharm. (Basel)* 16 (9), 1251. doi:10.3390/ph16091251

Jacobson, M. P., Pincus, D. L., Rapp, C. S., Day, T. J., Honig, B., Shaw, D. E., et al. (2004). A hierarchical approach to all-atom protein loop prediction. *Proteins Struct. Funct. Bioinforma.* 55 (2), 351–367. doi:10.1002/prot.10613

Jagatap, V. R., Ahmad, I., Sriram, D., Kumari, J., Adu, D. K., Ike, B. W., et al. (2023). Isoflavonoid and furanochromone natural products as potential DNA gyrase inhibitors: computational, spectral, and antimycobacterial studies. *ACS omega* 8 (18), 16228–16240. doi:10.1021/acsomega.3c00684

Jeankumar, V. U., Kotagiri, S., Janupally, R., Suryadevara, P., Sridevi, J. P., Medishetti, R., et al. (2015). Exploring the gyrase ATPase domain for tailoring newer anti-tubercular drugs: hit to lead optimization of a novel class of thiazole inhibitors. *Bioorg Med. Chem.* 23 (3), 588–601. doi:10.1016/j.bmc.2014.12.001

Jeankumar, V. U., Renuka, J., Pulla, V. K., Soni, V., Sridevi, J. P., Suryadevara, P., et al. (2014). Development of novel N-linked aminopiperidine-based mycobacterial DNA gyrase B inhibitors: scaffold hopping from known antibacterial leads. *Int. J. Antimicrob. Agents* 43 (3), 269–278. doi:10.1016/j.ijantimicag.2013.12.006

Jeankumar, V. U., Renuka, J., Santosh, P., Soni, V., Sridevi, J. P., Suryadevara, P., et al. (2013). Thiazole-aminopiperidine hybrid analogues: design and synthesis of novel *Mycobacterium tuberculosis* GyrB inhibitors. *Eur. J. Med. Chem.* 70, 143–153. doi:10.1016/j.ejmech.2013.09.025

Kale, M. G., Raichurkar, A., P, S. H., Waterson, D., McKinney, D., Manjunatha, M. R., et al. (2013). Thiazolopyridine ureas as novel antitubercular agents acting through inhibition of DNA Gyrase B. *J. Med. Chem.* 56 (21), 8834–8848. doi:10.1021/jm401268f

Kale, R. R., Kale, M. G., Waterson, D., Raichurkar, A., Hameed, S. P., Manjunatha, M. R., et al. (2014). Thiazolopyridone ureas as DNA gyrase B inhibitors: optimization of antitubercular activity and efficacy. *Bioorg Med. Chem. Lett.* 24 (3), 870–879. doi:10.1016/j.bmcl.2013.12.080

Kashyap, A., Singh, P. K., and Silakari, O. (2018). Chemical classes targeting energy supplying GyrB domain of *Mycobacterium tuberculosis*. *Tuberc. (Edinb)* 113, 43–54. doi:10.1016/j.tube.2018.09.001

Kawaguchi, H., Tsukiura, H., Tomita, K., Konishi, M., and Saito, K. (1977). Tallysomycin, a new antitumor antibiotic complex related to bleomycin. I. Production, isolation and properties. *J Antibiot (Tokyo).* 30(10):779–88. doi:10.7164/antibiotics.30.779

Khan, M. A., and Singh, S. K. (2023). Atom-based 3D-QSAR and DFT analysis of 5-substituted 2-acylaminothiazole derivatives as HIV-1 latency-reversing agents. *J. Biomol. Struct. Dyn.* 41 (14), 6759–6774. doi:10.1080/07391102.2022.2112078

Kim, Y.-P., Takamatsu, S., Hayashi, M., Komiyama, K., and Omura, S. (1997). Pyridindolols K1 and K2, new alkaloids from Streptomyces sp. K93-0711. *J. antibiotics* 50 (3), 189–193. doi:10.7164/antibiotics.50.189

Klyshko, E., Kim, J. S., McGough, L., Valeeva, V., Lee, E., Ranganathan, R., et al. (2024). Functional protein dynamics in a crystal. *Nat. Commun.* 15 (1), 3244. doi:10.1038/s41467-024-47473-4

Kumar, A., Prasun, C., Rathi, E., Nair, M. S., and Kini, S. G. (2023). Identification of potential DNA gyrase inhibitors: virtual screening, extra-precision docking and molecular dynamics simulation study. *Chem. Pap.* 77 (11), 6717–6727. doi:10.1007/s11696-023-02971-5

Lamothe, S. M., Guo, J., Li, W., Yang, T., and Zhang, S. (2016). The human ether-a-go-go-related gene (hERG) potassium channel represents an unusual target for protease-mediated damage. *J. Biol. Chem.* 291 (39), 20387–20401. doi:10.1074/jbc.M116.743138

LaPointe, S. M., and Weaver, D. F. (2007). A review of density functional theory quantum mechanics as applied to pharmaceutically relevant systems. *Curr. Computer-Aided Drug Des.* 3 (4), 290–296. doi:10.2174/157340907782799390

Lazim, R., Suh, D., and Choi, S. (2020). Advances in molecular dynamics simulations and enhanced sampling methods for the study of protein systems. *Int. J. Mol. Sci.* 21 (17), 6339. doi:10.3390/ijms21176339

Locher, C. P., Jones, S. M., Hanzelka, B. L., Perola, E., Shoen, C. M., Cynamon, M. H., et al. (2015). A novel inhibitor of gyrase B is a potent drug candidate for treatment of tuberculosis and nontuberculosis mycobacterial infections. *Antimicrob. Agents Chemother.* 59 (3), 1455–1465. doi:10.1128/AAC.04347-14

Madhavi Sastry, G., Adzhigirey, M., Day, T., Annabhimoju, R., and Sherman, W. (2013). Protein and ligand preparation: parameters, protocols, and influence on virtual screening enrichments. *J. computer-aided Mol. Des.* 27, 221–234. doi:10.1007/s10822-013-9644-8

Manathunga, M., Götz, A. W., and Merz Jr, K. M. (2022). Computer-aided drug design, quantum-mechanical methods for biological problems. *Curr. Opin. Struct. Biol.* 75, 102417. doi:10.1016/j.sbi.2022.102417

Medapi, B., Renuka, J., Saxena, S., Sridevi, J. P., Medishetti, R., Kulkarni, P., et al. (2015a). Design and synthesis of novel quinoline-aminopiperidine hybrid analogues as *Mycobacterium tuberculosis* DNA gyraseB inhibitors. *Bioorg Med. Chem.* 23 (9), 2062–2078. doi:10.1016/j.bmc.2015.03.004

Medapi, B., Suryadevara, P., Renuka, J., Sridevi, J. P., Yogeeswari, P., and Sriram, D. (2015b). 4-Aminoquinoline derivatives as novel *Mycobacterium tuberculosis* GyrB inhibitors: structural optimization, synthesis and biological evaluation. *Eur. J. Med. Chem.* 103, 1–16. doi:10.1016/j.ejmech.2015.06.032

Miethke, M., and Marahiel, M. A. (2007). Siderophore-based iron acquisition and pathogen control. *Microbiol. Mol. Biol. Rev.* 71 (3), 413–451. doi:10.1128/MMBR.00012-07

Miotto, P., Zhang, Y., Cirillo, D. M., and Yam, W. C. (2018). Drug resistance mechanisms and drug susceptibility testing for tuberculosis. *Respirology* 23 (12), 1098–1113. doi:10.1111/resp.13393

Mohamed, M. A., Elsaman, T., Elderdery, A. Y., Alsrhani, A., Ghanem, H. B., Alruwaili, M. M., et al. (2024). Unveiling the anticancer potential: computational exploration of nitrogenated derivatives of (+)-Pancratistatin as topoisomerase I inhibitors. *Int. J. Mol. Sci.* 25 (19), 10779. doi:10.3390/ijms251910779

Mohankumar, T., Chandramohan, V., Lalithamba, H. S., Jayaraj, R. L., Kumaradhas, P., Sivanandam, M., et al. (2020). Design and molecular dynamic investigations of 7,8-dihydroxyflavone derivatives as potential neuroprotective agents against alpha-synuclein. *Sci. Rep.* 10 (1), 599. doi:10.1038/s41598-020-57417-9

Murumkar, P. R., Sharma, M. K., Gupta, P., Patel, N. M., and Yadav, M. R. (2023). Selection of suitable protein structure from protein Data Bank: an important step in structure-based drug design studies. *Mini Rev. Med. Chem.* 23 (3), 246–264. doi:10.2174/1389557522666220512151454

Mustyala, K. K., Malkhed, V., Chittireddy, V. R., and Vuruputuri, U. (2015). Virtual screening studies to identify novel inhibitors for Sigma F protein of *Mycobacterium tuberculosis*. *Int. J. Mycobacteriol* 4 (4), 330–336. doi:10.1016/j.ijmyco.2015.05.013

Naz, S., Farooq, U., Ali, S., Sarwar, R., Khan, S., and Abagyan, R. (2019). Identification of new benzamide inhibitor against α-subunit of tryptophan synthase from *Mycobacterium tuberculosis* through structure-based virtual screening, anti-tuberculosis activity and molecular dynamics simulations. *J. Biomol. Struct. Dyn.* 37 (4), 1043–1053. doi:10.1080/07391102.2018.1448303

Ntie-Kang, F. (2013). An *in silico* evaluation of the ADMET profile of the StreptomeDB database. *Springerplus* 2, 353. doi:10.1186/2193-1801-2-353

Owoloye, A. J., Ligali, F. C., Enejoh, O. A., Musa, A. Z., Aina, O., Idowu, E. T., et al. (2022). Molecular docking, simulation and binding free energy analysis of small molecules as Pf HT1 inhibitors. *PloS one* 17 (8), e0268269. doi:10.1371/journal.pone.0268269

Pakamwong, B., Thongdee, P., Kamsri, B., Phusi, N., Kamsri, P., Punkvang, A., et al. (2022). Identification of potent DNA gyrase inhibitors active against *Mycobacterium tuberculosis*. *J. Chem. Inf. Model* 62 (7), 1680–1690. doi:10.1021/acs.jcim.1c01390

Pakamwong, B., Thongdee, P., Kamsri, B., Phusi, N., Taveepanich, S., Chayajarus, K., et al. (2024). Ligand-based virtual screening for discovery of indole derivatives as potent DNA gyrase ATPase inhibitors active against *Mycobacterium tuberculosis* and hit validation by biological assays. *J. Chem. Inf. Model* 64 (15), 5991–6002. doi:10.1021/acs.jcim.4c00511

Pandey, R. K., Kumbhar, B. V., Srivastava, S., Malik, R., Sundar, S., Kunwar, A., et al. (2017). Febrifugine analogues as Leishmania donovani trypanothione reductase inhibitors: binding energy analysis assisted by molecular docking, ADMET and

molecular dynamics simulation. *J. Biomol. Struct. Dyn.* 35 (1), 141–158. doi:10.1080/07391102.2015.1135298

Papillon, J., Menetret, J. F., Batisse, C., Helye, R., Schultz, P., Potier, N., et al. (2013). Structural insight into negative DNA supercoiling by DNA gyrase, a bacterial type 2A DNA topoisomerase. *Nucleic Acids Res.* 41 (16), 7815–7827. doi:10.1093/nar/gkt560

Pedrolli, D. B., Jankowitsch, F., Schwarz, J., Langer, S., Nakanishi, S., and Mack, M. (2014). "Natural Riboflavin analogs," in *Flavins and flavoproteins: methods and protocols*. Editors S. Weber and E. Schleicher (New York, NY: Springer New York), 41–63.

Perez-Regidor, L., Guzman-Caldentey, J., Oberhauser, N., Punzon, C., Balogh, B., Pedro, J. R., et al. (2022). Small molecules as toll-like receptor 4 modulators drug and in-house computational repurposing. *Biomedicines* 10 (9), 2326. doi:10.3390/biomedicines10092326

Qiu, X., Zhang, Q., Li, Z., Zhang, J., and Liu, H. (2024). Revealing the interaction mechanism between *Mycobacterium tuberculosis* GyrB and novobiocin, SPR719 through binding thermodynamics and dissociation kinetics analysis. *Int. J. Mol. Sci.* 25 (7), 3764. doi:10.3390/ijms25073764

Qun, T., Zhou, T., Hao, J., Wang, C., Zhang, K., Xu, J., et al. (2023). Antibacterial activities of anthraquinones: structure-activity relationships and action mechanisms. *RSC Med. Chem.* 14 (8), 1446–1471. doi:10.1039/d3md00116d

Ravikumar, Y., Koonyosying, P., Srichairatanakool, S., Ponpandian, L. N., Kumaravelu, J., and Srichairatanakool, S. (2023). *In silico* molecular docking and dynamics simulation analysis of potential histone lysine methyl transferase inhibitors for managing β-thalassemia. *Molecules* 28 (21), 7266. doi:10.3390/molecules28217266

Reddy, K. I., Srihari, K., Renuka, J., Sree, K. S., Chuppala, A., Jeankumar, V. U., et al. (2014). An efficient synthesis and biological screening of benzofuran and benzo[d]isothiazole derivatives for *Mycobacterium tuberculosis* DNA GyrB inhibition. *Bioorg Med. Chem.* 22 (23), 6552–6563. doi:10.1016/j.bmc.2014.10.016

Renuka, J., Reddy, K. I., Srihari, K., Jeankumar, V. U., Shravan, M., Sridevi, J. P., et al. (2014). Design, synthesis, biological evaluation of substituted benzofurans as DNA gyraseB inhibitors of *Mycobacterium tuberculosis*. *Bioorg Med. Chem.* 22 (17), 4924–4934. doi:10.1016/j.bmc.2014.06.041

Rukachaisirikul, T., Saekee, A., Tharibun, C., Watkuolham, S., Watkuolham, S., and Suksamrarn, A. (2007). Biological activities of the chemical constituents of Erythrina stricta and Erythrina subumbrans. *Arch. Pharm. Res.* 30 (11), 1398–1403. doi:10.1007/BF02977363

Salo-Ahen, O. M. H., Alanko, I., Bhadane, R., Bonvin, A. M. J. J., Honorato, R. V., Hossain, S., et al. (2020). Molecular dynamics simulations in drug discovery and pharmaceutical development. *Processes* 9 (1), 71. doi:10.3390/pr9010071

Sanz, M., Salinas, R. K., and Pinto, E. (2017). Namalides B and C and spumigins K-N from the cultured freshwater cyanobacterium sphaerospermopsis torques-reginae. *J. Nat. Prod.* 80 (9), 2492–2501. doi:10.1021/acs.jnatprod.7b00370

Saxena, S., Samala, G., Renuka, J., Sridevi, J. P., Yogeeswari, P., and Sriram, D. (2015). Development of 2-amino-5-phenylthiophene-3-carboxamide derivatives as novel inhibitors of *Mycobacterium tuberculosis* DNA GyrB domain. *Bioorg Med. Chem.* 23 (7), 1402–1412. doi:10.1016/j.bmc.2015.02.032

Schrödinger, LLC. (2023a). *LigPrep (Release 2023-1)*. New York, NY: Schrödinger, LLC.

Schrödinger, LLC. (2023b). *Maestro (Release 2023-1)*. New York, NY: Schrödinger, LLC.

Seung, K. J., Keshavjee, S., and Rich, M. L. (2015). Multidrug-resistant tuberculosis and extensively drug-resistant tuberculosis. *Cold Spring Harb. Perspect. Med.* 5 (9), a017863. doi:10.1101/cshperspect.a017863

Shirude, P. S., Madhavapeddi, P., Tucker, J. A., Murugan, K., Patil, V., Basavarajappa, H., et al. (2013). Aminopyrazinamides: novel and specific GyrB inhibitors that kill replicating and nonreplicating *Mycobacterium tuberculosis*. *ACS Chem. Biol.* 8 (3), 519–523. doi:10.1021/cb300510w

Srivastava, A. K., and Misra, N. (2021). *DFT-based studies on bioactive molecules*. Sharjah, United Arab Emirates: Bentham Science Publishers.

Stielow, M., Witczynska, A., Kubryn, N., Fijalkowski, L., Nowaczyk, J., and Nowaczyk, A. (2023). The bioavailability of drugs-the current state of knowledge. *Molecules* 28 (24), 8038. doi:10.3390/molecules28248038

Sudarshan, K., Yarlagadda, S., and Sengupta, S. (2024). Recent advances in the synthesis of diarylheptanoids. *Chem. Asian J.* 19 (15), e202400380. doi:10.1002/asia.202400380

Szabo, T., Volk, B., and Milen, M. (2021). Recent advances in the synthesis of β-carboline alkaloids. *Molecules* 26 (3), 663. doi:10.3390/molecules26030663

Takahashi, H., Isobe, M., and Goto, T. (1991). Chemical synthesis of lampteroflavin as light emitter in the luminous mushroom, Lampteromyces japonicus. *Tetrahedron* 47 (32), 6215–6222. doi:10.1016/s0040-4020(01)86553-4

Talley, A. K., Thurston, A., Moore, G., Gupta, V. K., Satterfield, M., Manyak, E., et al. (2021). First-in-human evaluation of the safety, tolerability, and pharmacokinetics of

SPR720, a novel oral bacterial DNA gyrase (GyrB) inhibitor for mycobacterial infections. *Antimicrob. Agents Chemother.* 65 (11), e0120821. doi:10.1128/aac.01208-21

Tambe, P. M., Bhowmick, S., Chaudhary, S. K., Khan, M. R., Wabaidur, S. M., Muddassir, M., et al. (2020). Structure-based screening of DNA GyraseB inhibitors for therapeutic applications in tuberculosis: a pharmacoinformatics study. *Appl. Biochem. Biotechnol.* 192 (4), 1107–1123. doi:10.1007/s12010-020-03374-y

Thuan, N. H., Tatipamula, V. B., Canh, N. X., and Van Giang, N. (2022). Recent advances in microbial co-culture for production of value-added compounds. *3 Biotech.* 12 (5), 115. doi:10.1007/s13205-022-03177-4

Tomasic, T., Zubriene, A., Skok, Z., Martini, R., Pajk, S., Sosic, I., et al. (2021). Selective DNA gyrase inhibitors: multi-target *in silico* profiling with 3D-pharmacophores. *Pharm. (Basel)* 14 (8), 789. doi:10.3390/ph14080789

Trenado-Uribe, M., Silva-Miranda, M., Rivero-Cruz, J. F., Rodríguez-Peña, K., Espitia-Pinzón, C. I., Rodríguez-Sanoja, R., et al. (2018). Antimycobacterial activity of an anthracycline produced by an endophyte isolated from Amphipterygium adstringens. *Mol. Biol. Rep.* 45 (6), 2563–2570. doi:10.1007/s11033-018-4424-0

Verma, H., Nagar, S., Vohra, S., Pandey, S., Lal, D., Negi, R. K., et al. (2021). Genome analyses of 174 strains of *Mycobacterium tuberculosis* provide insight into the evolution of drug resistance and reveal potential drug targets. *Microb. Genom* 7 (3), mgen000542. doi:10.1099/mgen.0.000542

Voet, A., Qing, X., Lee, X. Y., De Raeymaecker, J., Tame, J., Zhang, K., et al. (2014). Pharmacophore modeling: advances, limitations, and current utility in drug discovery. *J. Recept. Ligand Channel Res.*, 81. doi:10.2147/jrlcr.S46843

Wang, J.-L., Sang, C.-Y., Wang, J., Li, P.-L., Chai, T., Naghavi, M. R., et al. (2023). Sesquiterpene coumarins from Ferula sinkiangensis and their anti-pancreatic cancer effects. *Phytochemistry* 214, 113824. doi:10.1016/j.phytochem.2023.113824

Wang, X., Song, K., Li, L., and Chen, L. (2018). Structure-based drug design strategies and challenges. *Curr. Top. Med. Chem.* 18 (12), 998–1006. doi:10.2174/1568026618666180813152921

Xiong, G., Wu, Z., Yi, J., Fu, L., Yang, Z., Hsieh, C., et al. (2021). ADMETlab 2.0: an integrated online platform for accurate and comprehensive predictions of ADMET properties. *Nucleic Acids Res.* 49 (W1), W5–W14. doi:10.1093/nar/gkab255

Yele, V., Sigalapalli, D. K., Jupudi, S., and Mohammed, A. A. (2021). DFT calculation, molecular docking, and molecular dynamics simulation study on substituted phenylacetamide and benzohydrazide derivatives. *J. Mol. Model* 27 (12), 359. doi:10.1007/s00894-021-04987-8

Yu, W., and MacKerell, A. D., Jr. (2017). Computer-aided drug design methods. *Methods Mol. Biol.* 1520, 85–106. doi:10.1007/978-1-4939-6634-9_5

Zhang, Z., and Tang, W. (2018). Drug metabolism in drug discovery and development. *Acta Pharm. Sin. B* 8 (5), 721–732. doi:10.1016/j.apsb.2018.04.003

Zhu, Y., Ouyang, Z., Du, H., Wang, M., Wang, J., Sun, H., et al. (2022). New opportunities and challenges of natural products research: when target identification meets single-cell multiomics. *Acta Pharm. Sin. B* 12 (11), 4011–4039. doi:10.1016/j.apsb.2022.08.022

Frontiers in Chemistry

Molecular docking, free energy calculations, ADMETox studies, DFT analysis, and dynamic simulations highlighting a chromene glycoside as a potential inhibitor of PknG in *Mycobacterium tuberculosis*

Muharib Alruwaili[1]*, Tilal Elsaman[2]*, Magdi Awadalla Mohamed[2],
Abozer Y. Elderdery[1], Jeremy Mills[3], Yasir Alruwaili[1],
Siddiqa M. A. Hamza[4], Salma Elhadi Ibrahim Mekki[5],
Hazim Abdullah Alotaibi[6], Maily J. Alrowily[7] and
Maryam Musleh Althobiti[8]

[1]Department of Clinical Laboratory Sciences, College of Applied Medical Sciences, Jouf University,
Sakaka, Saudi Arabia, [2]Department of Pharmaceutical Chemistry, College of Pharmacy, Jouf University,
Sakaka, Saudi Arabia, [3]School of Pharmacy and Biomedical Sciences, University of Portsmouth,
Portsmouth, United Kingdom, [4]Department of Pathology, College of Medicine in Alqunfudah, Umm
Alqura University, Algunfuda, Saudi Arabia, [5]Department of Physiology, College of Medicine in
Alqunfudah, Umm Alqura University, Alqunfudah, Saudi Arabia, [6]Department of Internal Medicine and
Oncology, Prince Mohammed Medical City, Hail, Saudi Arabia, [7]Consultant -Research Center, Aljouf
Health Cluster, Aljouf, Saudi Arabia, [8]Department of Clinical Laboratory Sciences, College of Applied
Medical Sciences, Shaqra University, Shaqra, Saudi Arabia

Introduction: Tuberculosis (TB), caused by the *Mycobacterium tuberculosis* (M.tb), remains a serious medical concern globally. Resistant M.tb strains are emerging, partly because M.tb can survive within alveolar macrophages, resulting in persistent infection. Protein kinase G (PknG) is a mycobacterial virulence factor that promotes the survival of M.tb in macrophages. Targeting PknG could offer an opportunity to suppress the resistant M.tb strains.

Methods: In the present study, multiple computational tools were adopted to screen a library of 460,000 molecules for potential inhibitors of PknG of M.tb.

Results and discussions: Seven Hits (**1−7**) were identified with binding affinities exceeding that of the reference compound (AX20017) towards the PknG catalytic domain. Next, the ADMETox studies were performed to identify the best hit with appropriate drug-like properties. The chromene glycoside (Hit **1**) was identified as a potential PknG inhibitor with better pharmacokinetic and toxicity profiles rendering it a potential drug candidate. Furthermore, quantum computational analysis was conducted to assess the mechanical and electronic properties of Hit **1,** providing guidance for further studies. Molecular dynamics simulations were

also performed for Hit **1** against PknG, confirming the stability of its complex. In sum, the findings in the current study highlight Hit **1** as a lead with potential for development of drugs capable of treating resistant TB.

1 Introduction

Tuberculosis (TB) is a contagious illness caused by the airborne bacilli *Mycobacterium tuberculosis* (M.tb). Its primary site of infection is the lung, but it can involve other organs in the human body. Some studies reported that TB is still a serious global health concern, particularly in the global south (Fernandes et al., 2022; Bloom, 2023). In 2020, the estimated number of symptomatic new TB cases was 9.9 million, with over 1.5 million deaths (Bagcchi, 2023). Fernandes, G.F.S and co-workers reported high morbidity and mortality rates in TB patients around the globe (Fernandes et al., 2022). In fact, from 2012 to 2019, TB was the leading cause of death from a single infectious agent (Friedrich, 2017; WHO, 2020). Since 1960, successful efforts have been made to develop a variety of antibiotics (Figure 1) which have contributed to the saving of millions of human lives. However, the number of currently used drugs in clinical practice is very limited and this has been further exacerbated by the emergence of resistant strains of TB, such as multidrug resistant TB (MDR-TB) and extensive drug resistant TB (XDR-TB) (Dartois and Rubin, 2022). Moreover,

FIGURE 1
Chemical structures of the front-line anti-TB drugs (Pyrazinamide, Ethambutol, Isoniazid, Rifampicin, and Streptomycin). In addition, the chemical structures of the recently approved anti-TB drugs Delamanid and Bedaquiline are also depicted.

resistant strains to newly approved anti-TB medications, including Delamanid and Bedaquiline (Figure 1) have been detected in clinical settings (Yoshiyama et al., 2021).

This troubling condition is due, to some extent, to a nearly 5 decade long gap in anti-TB medication discovery research and development (Teneva et al., 2023). In general, the current TB chemotherapy is often inadequate due to multiple factors including (i) the prolonged treatment regiments; (ii) serious adverse effects, (iii) the continued evolution of drug resistance, and (iv) the slow development of new therapeutics (Rock, 2019; Akinnuwesi et al., 2023; Capela et al., 2023). To this end, mycobacterial resistance to the currently used anti-TB drugs has been attributed, in part, to the ability of the M.tb to survive within macrophages resulting in persistent infection (latent TB) (Simmons et al., 2018). Multiple research studies have demonstrated that the virulence factor protein kinase G (PknG), which contains a thioredoxin motif, aids in the survival of M.tb inside macrophages through several different mechanisms (Figure 2) (Koul et al., 2001; Cowley et al., 2004; O'Hare et al., 2008; Forrellad et al., 2013; Khan et al., 2017; Swain et al., 2022). Therefore, PknG could be considered as a crucial druggable macromolecule for the development of new therapeutics with potential to both, inhibit non-proliferating mycobacteria and suppress the evolution of M.tb resistant strains (Khan et al., 2018). Recently, several molecules belonging to secondary plant metabolites have been investigated as potential anti-tubercular agents, including diarylheptanoids, 3-glycosyl isocoumarins, biphenyl and diaryl ether diarylheptanoids, tetrahydropyran-based diarylheptanoids such as engelheptanoxides, and various 3-aryl isocoumarins (Sudarshan and Aidhen, 2017; Sudarshan et al., 2024).

Computational methods accelerate drug discovery by identifying and optimizing therapeutic agents while reducing time, cost, and experimental efforts. They provide key insights into molecular interactions and target validation (Athar et al., 2016). Exploring the structural targets of M.tb through *in silico* approaches aids in identifying promising therapeutic candidates. This method enhances the understanding of protein structures and interactions, streamlining the process of tuberculosis drug discovery (Lone et al., 2018).

In this study, we screened the NCI library (https://cactus.nci.nih.gov/download/roadmap/) of 460,000 molecules using the CADD approach (Figure 3) [20] against the PknG ATP binding pocket, aiming to identify novel inhibitors as potential leads against TB.

2 Materials and methods

In this work various computational tools interfaced in Schrödinger suite were used, including Protein Preparation

FIGURE 2
Mechanisms by which PknG enhances the *in vivo* survival and persistence of M.tb.

FIGURE 3
Multistep virtual screening workflow for the identification of potential PknG inhibitors.
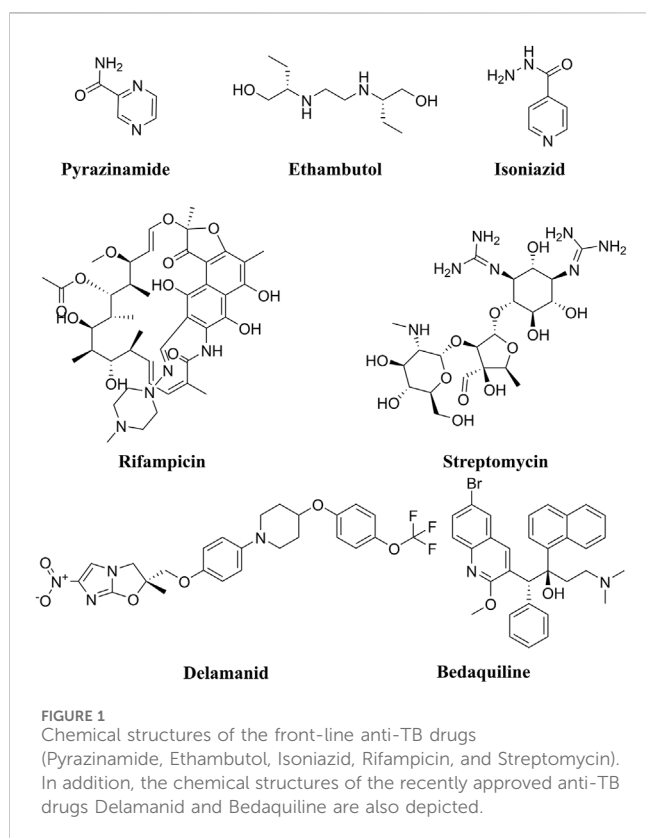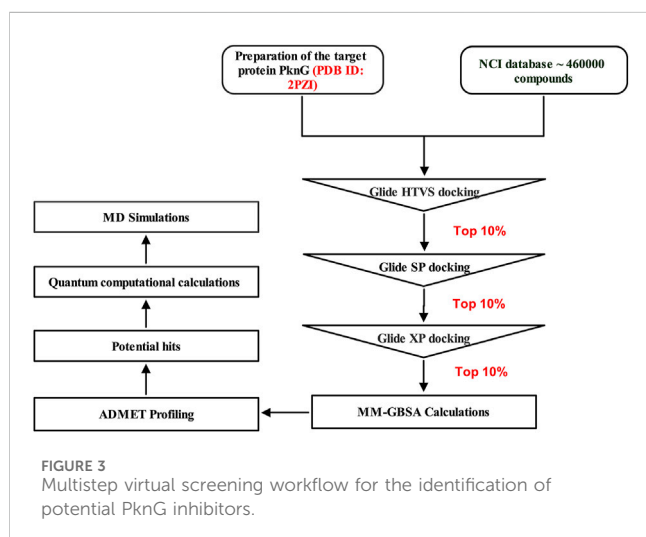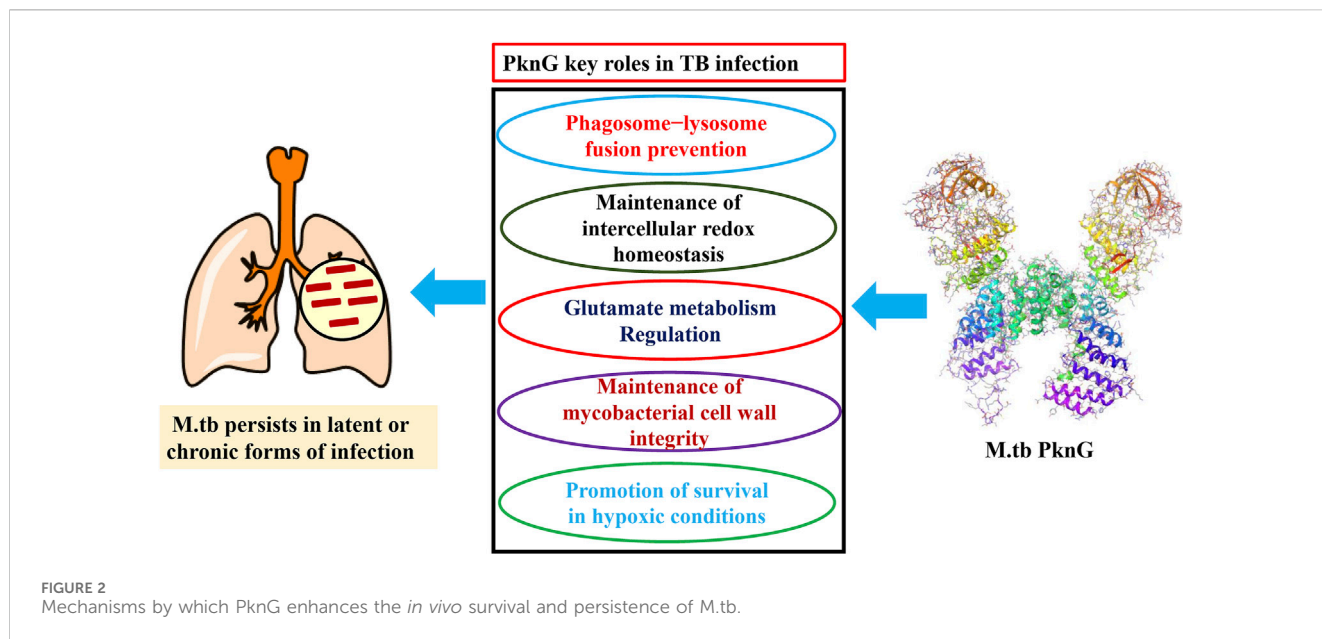
Wizard (Sastry et al., 2013), LigPrep (Schrödinger Release, 2023), Glide (Friesner et al., 2004; Halgren et al., 2024), Prime (Jacobson et al., 2002a; Jacobson et al., 2002b), Qikprop (QikProp, 2023), Jaguar (Bochevarov et al., 2013) and Desmond (Bowers et al., 2006). These tools were accessed utilizing Maestro graphical interface (Maestro, 2023). Additionally, ADMETlab 2.0 (Xiong et al., 2021) an integrated online webserver was used for ADMET properties estimation.

2.1 Molecular docking study

Virtual screening analysis of the NCI library (https://cactus.nci.nih.gov/download/roadmap/) of 460,000 molecules was conducted, using Virtual Screening Workflow (VSW) of Schrödinger suite. The downloaded compounds library were converted to 3D formats and then OPLS4 force field was used for optimization. The structures

were set for docking and the ligands' original chirality's were maintained, using LigPrep module. For generating the possible ionization states, the Epik was used at pH 7.00 ± 2 units. For each ligand one low energy conformer was generated. The 3D crystal structure of M.tb PknG complexed with the reference ligand AX20017 (PDB code: 2PZI), was obtained from the Protein Data Bank (PDB) website (www.rcsb.org). Subsequently, we utilized the multi-step Protein Preparation Wizard (PrepWizard) to refine and optimize the protein structure for further analysis. After removal of all water molecules, only the co-crystallized ligand remained at the enzyme's catalytic site. OPLS4 force field was used to perform optimization and energy minimization. The receptor grid generation tool implanted within the maestro suite was employed to create the grid box around the coordinates of the reference ligand. Prepared ligands were then screened against the refined target protein following multimode receptor docking workflow using Glide module of Schrödinger suite. Initially, Glide high-throughput virtual screening (HTVS) mode was employed for filtering the compounds library, then for further screening the standard precision (SP) mode was used and finally more accurate docking calculations results were obtained utilizing extra precision (XP) mode. A single optimal pose was generated for each input molecule, and their ranking was decided based on their Glide docking score.

2.2 Binding free energy calculations

Estimation of the binding free energies of receptors and docked ligands was done using Prime module. The free binding energy of the protein-ligand complexes was computed using the Prime module, integrated with Schrödinger software. For this purpose, the Post-docking generated Pose Viewer Files (PVFs) of the top Hits**1-7** were used as input files. Free binding energy parameters were then calculated using OPLS4 (Optimized Potentials for Liquid Simulations, version 4) force field along with Variable Dielectric
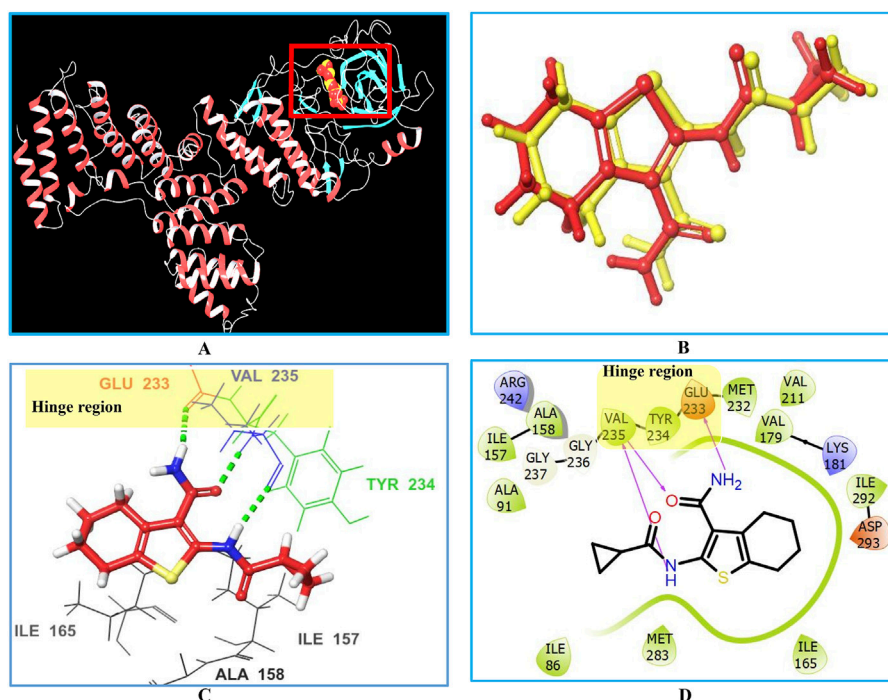
FIGURE 4
Interactions between the co-crystallized ligand (AX20017) and PknG (PDB ID: 2PZI) as the target enzyme. Panel **(A)** displays the 3D crystal structure of the target enzyme complexed with the native AX20017 ligand, Panel **(B)** presents a superposition of the co-crystallized ligand conformation (yellow) and the docked ligand conformation (red), with an RMSD value of 0.28 Å. Panel **(C)** shows the corresponding 3D crystal structure. The interacting amino acid residues at the binding site are represented by their three-letter codes. Hydrogen bond interactions are indicated by dotted green lines in panel **(C)** and solid magenta lines in panel **(D)**.
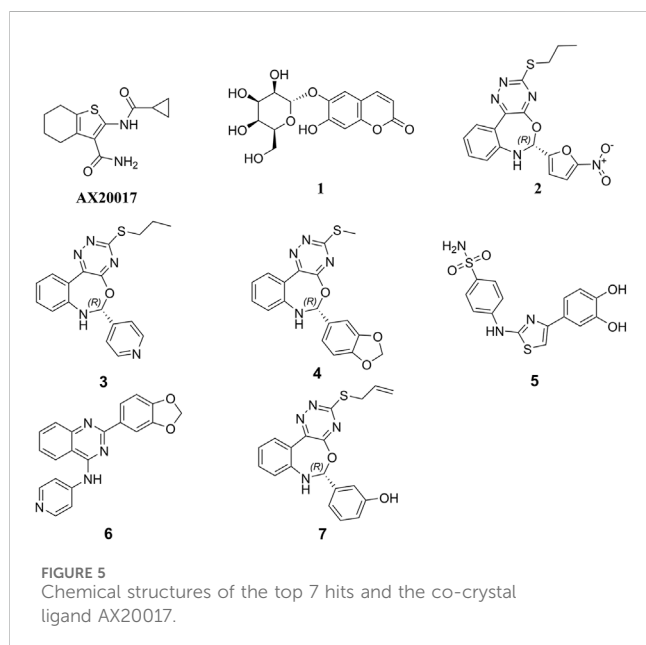
FIGURE 5
Chemical structures of the top 7 hits and the co-crystal ligand AX20017.

Generalized Born (VSGB) 2.0 as solvation model, following the established protocol (Azam et al., 2021). Molecular Mechanics-Generalized Born Surface Area (MM-GBSA) dG binding energy score was employed to rank the ligands based on their relative affinities.

2.3 *In silico* absorption, distribution, metabolism, excretion, and toxicity (ADMET) profiling

In this study, we evaluated the ADMET profiles and drug-likeness characteristics of the top 7 candidates using the Qikprop computational tool within the Schrödinger suite. Furthermore, the free web-based tool ADMETlab 2.0 available at (https://admetmesh.scbdd.com) was employed to predict the toxicity parameters. All of the calculated parameters were evaluated to ensure compliance with their respective standard ranges.

2.4 Quantum computational calculations

Quantum chemical calculations of the co-crystal ligand and Hit **1** electronic molecular properties such as Electron density, Molecular Electrostatic Potential Map (MESP) and energies of both Highest Occupied Molecular Orbital (HOMO) and Lowest Unoccupied Molecular Orbital (LUMO) were calculated using DFT method in the Jaguar module of Schrödinger suite (Khan and Singh, 2023). The values of the E_{LUMO} and E_{HOMO} were subsequently employed to compute the various quantum chemical properties, including the energy gap HOMO-LUMO Gab (HLG), chemical chemicals (softness and hardness), global electrophilicity index and electronegativity, according to equations established in the literature (Kohn and Sham, 1965; Guezane-Lakoud et al., 2023). Electron-

TABLE 1 Docking results and the interaction forces of the top hit molecules.

PubChem ID	Hit	Docking score (kcal/mol)	Interactions	
			H-bond	Pi-cation
673,481	Co-crystallized ligand(AX20017)	−8.14	Val235 and Glu233	-
6,604,620	1	−12.75	Val235; Tyr234; Glu233; Gly237; Ser239 and Arg242	-
285,8302	2	−8.96	Val235 and Arg242	-
285,8937	3	−8.31	Val235	Arg242
2,849,297	4	−8.53	Val235 and Arg242	-
2,928,782	5	−8.76	Ala91; Ile157; Lys181; Val235; Arg242 and Glu280	-
3,234,587	6	−8.86	Val235 and Lys241	-
6,410,292	7	−10.03	Val235 and Ile157	-

deficient surfaces are marked by the blue color, whereas the electron-rich ones are indicated by the red color.

2.5 Molecular dynamics (MD) simulations

MD simulations were achieved using Desmond. The input files of docked conformers of both Hit **1** and the co-crystallized ligand complexes were obtained from docking study. These complexes were immersed in a cubic water box with dimensions of 10 Å × 10 Å × 10 Å, utilizing Simple Point Charge (SPC) as solvation medium. To achieve balance in the net charges, Na^+ counter ions were added to the built systems, and subsequently sodium chloride 0.15 M was also added to attain the system's neutralization. The simulations were conducted in an NPT ensemble, ensuring that the temperature and pressure of the system were maintained at 300 K and 1 bar, respectively. Prior to simulation run, the default relaxation protocol in the Desmond module of Schrodinger suite 2023-1 was then used to minimize and pre-equilibrate the system. The MD simulations extended over a duration of 100 ns, generating 1,000 frames of data captured at every 100 ps interval. The Simulation Interaction Diagram tool in Desmond was used to perform post-simulation trajectory analysis. Critical parameters such as Root Mean Square Deviation (RMSD), Root Mean Square Fluctuation (RMSF), and protein-ligand contacts were computed to assess the stability of the complexes and the nature of their interaction profiles throughout the simulation period.

3 Results and discussion

Despite the existence of several drugs for treatment of TB infection, drawbacks associated with them such as prolonged treatment regimens, adverse effects, poor patient compliance and emergence of drug resistance, dictates the development of novel drugs with optimum therapeutic properties (Rock, 2019; Akinnuwesi et al., 2023; Capela et al., 2023). An *in silico* strategy is considered an attractive approach that could be applied at different drug discovery stages to accelerate the identification of potential anti-TB drug leads (Macalino et al., 2020). In the current work, we report on high-throughput multilevel virtual screening of

460,000 molecules from an NCI database against the ATP binding site of PknG to identify potential hits using molecular docking score and the free binding energy to as filtering parameters. Further, ADMET profiling and quantum computational calculations were performed to better understand their drug utility and to discriminate between hits for further optimization studies.

3.1 Molecular docking study

Initially, the 3D crystal structure of PknG, of M.tb (PDB ID 2PZI) in complex with tetrahydrobenzothiophene (AX20017), was downloaded from the protein data bank (PDB: https://www.rcsb.org/) for structure-based virtual screening. The bound AX20017 (Figure 4A) was docked into the same binding cavity to confirm the validity of the docking protocol and the RMSD between the docked and the experimental co-crystallized poses (Figure 4B) was 0.28 Å which was within the acceptable range (Santiago-Silva et al., 2023). As shown in Figures 4C,D, AX20017 formed three H-bonds with the hinge region residues using its amide side chains, two with Val235 and the other with Glu233. Further, hydrophobic interactions were observed with residues Ile86, Asp87, Ala91, Ile157, Ala158, Ile165, Val179, Tyr234, Met283, and Ile292. These results were found consistent with what has been reported by Arica-Sosa et al. (2022). Following this step, a multilevel docking approach was employed, beginning with docking in Glide High Throughput Virtual Screening mode (Glide-HTVS), followed by Glide Standard Precision mode (Glide-SP), and concluding with Glide Extra Precision mode (Glide-XP). Molecules exhibiting a Glide-XP docking score lower than that of AX20017 (−8.14 kcal/mol) were then selected as top hits Chemical structures of these Hits **1-7** are provided in Figure 5. The analysis of docking results indicated that Hits **1-7** displayed XP docking score within the range of −8.31 to −12.75 kcal/mol (Table 1). Hit **1**, a chromene glycoside, had the highest docking score (−12.75 kcal/mol) followed by the oxazepine derivative **7** which scored −10.03 kcal/mol. The remaining top hits generally exhibited similar docking scores, all of which were higher than that of the reference ligand (Table 1). While Hits **2**, **3**, **4**, and **7** feature the tricyclic triazinobenzoxazepin ring system, Hits **5** and **6** are derivatives of benzene sulphonamide and quinazoline, respectively.
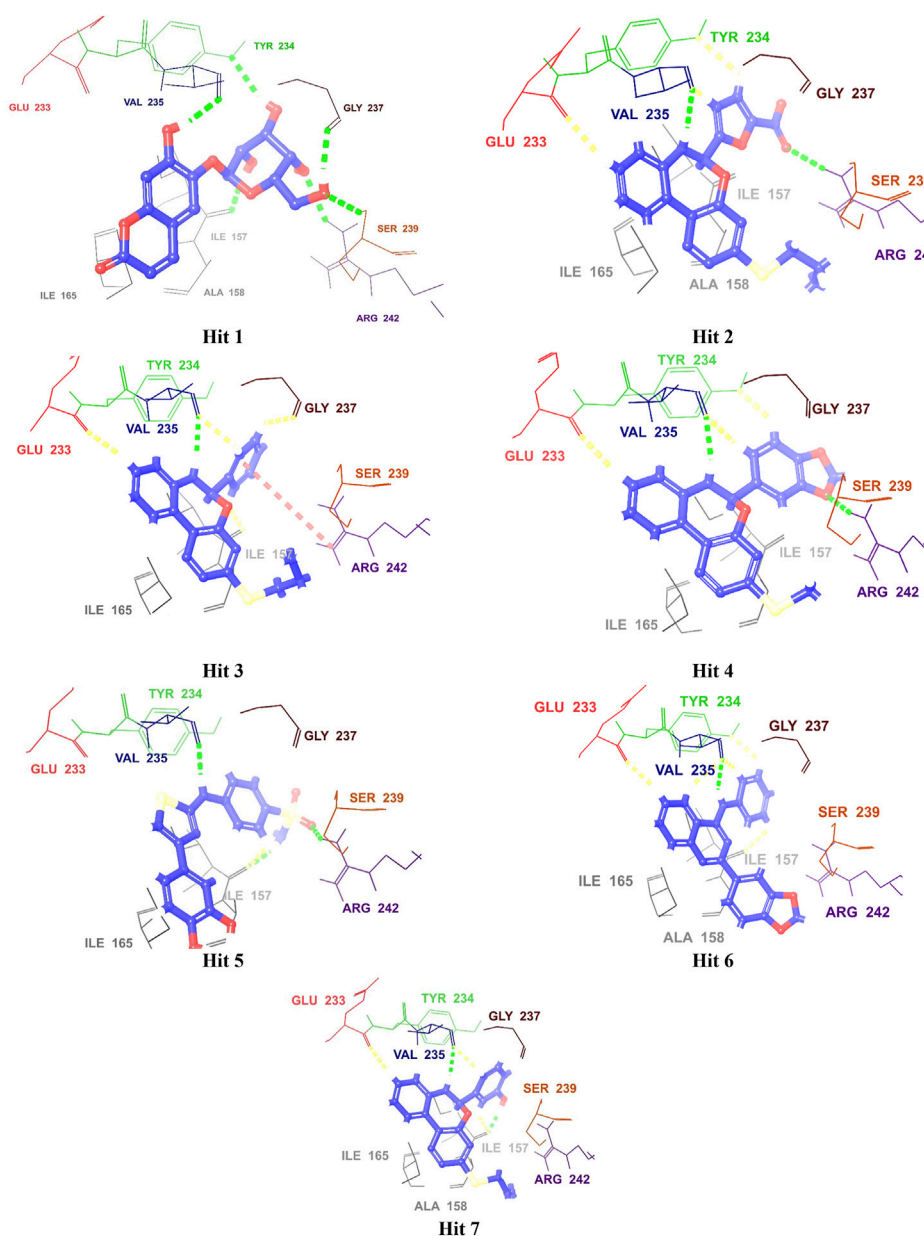
FIGURE 6
3D Interaction diagrams of top identified Hits (1−7) with the M. tb PknG binding site. Hydrogen bonds (green), aromatic-H bonds (yellow), and π-cation interactions (red) shown. Amino acid residues are displayed using three-letter codes.

In addition, Hits **1−7** formed multiple hydrogen bonds with various residues in the catalytic site (Figure 6; Supplementary Figure S1), exhibiting interaction patterns similar to those reported for experimentally validated molecules (Singh et al., 2015; Arica-Sosa et al., 2022).

All hits were positioned precisely within the same binding site as the reference compound AX20017, which validated the robustness of the docking protocol and confirmed the hits' suitability as potential inhibitors. Detailed analysis of interaction patterns revealed that the hits formed key hydrogen bonds with **Val235**, a critical residue located in the hinge region. This interaction was particularly significant because the hinge region played a central role in maintaining the structural integrity and proper folding of the

active site, thereby facilitating effective ligand binding. Hydrogen bonding with Val235 was pivotal for stabilizing the ligand-enzyme complex, as previously reported by Arica-Sosa et al. (2022). This residue, due to its position in the hinge region, mediated essential interactions that anchored the ligand within the binding pocket. Furthermore, similar to AX20017, the hits engaged in hydrophobic interactions and π-π stacking with neighboring residues, which further enhanced the binding affinity. Notably, the spatial positioning and interaction patterns observed in Figures 6, 7 confirmed that the hits not only mimicked the binding mechanism of AX20017 but also exhibited comparable interaction strength, reinforcing their potential as strong inhibitors. These findings underscored the importance of

FIGURE 7
The overlay of the co-crystallized ligand AX20017 (red) and the docked conformations of the top 7 hits (blue) interacting with the 2PZI binding pockets (the hydrophobic and the hinge). The conventional H-bonds are shown in green color, while the aromatic H-bonds are shown in yellow. The most critical residues for proper interaction and for ligand-enzyme complex stability (Glu233 and Val235) are shown in red and blue colors, respectively.

targeting the hinge region to achieve high binding stability and effective inhibition of the enzyme. By exploiting such conserved interactions, these hits provided a promising starting point for further optimization and lead development.

3.2 Binding free energy calculations

To estimate the binding free energy of the enzyme-ligand complexes, MM-GBSA method was utilized. This is one of the most common methods used to estimate the binding free energy of the small molecules to their respective macromolecular targets (Wang et al., 2019). This could be attributed to its relatively high

scoring function accuracy relative to the molecular docking simulation and is thus employed here to improve the results of virtual screening (Genheden and Ryde, 2015). Table 2 displays the binding free energy values for the top 7 hits alongside that of the co-crystal ligand. Hits **1–7** displayed free binding energies ranging from −60.92 to −69.95 kcal/mol, which were lower than that of the co-crystal ligand (−60.23 kcal/mol), pointing to their higher affinity towards the enzyme binding pocket.

Hits **3**, the triazinobenzoxazepin derivative, showed the lowest free binding energy (−69.95 kcal/mol). It is evident that out of the top 7 hits, 4 hits incorporate the triazinobenzoxazepin ring system. Replacement of the nitrofuran moiety attached to the C-2 of benzoxazepine ring in **2** by the pyridine ring in **3** increased the binding affinity. Unsaturation of the C2-C3 of the propyl side chain in **3** (compound **8** shown in Figure 8) resulted in slight reduction in the binding affinity (−68.99 kcal/mol). Inversion of the chirality in Hit **3** (compound **9** shown in Figure 8) increased both the docking score (−5.28 kcal/mol) and the total binding energy (−65.88 kcal/mol) indicating the importance of the R configuration for higher affinity. Substitution of the pyridine ring in compound **8** with the hyroxyphenyl ring afforded Hit **7** with relatively lower binding affinity (−65.81 kcal/mol). Extension of the methyl group in **4** to n-propyl as in **2** and **3** (compound **10** shown in Figure 8) reduced the binding affinity (−58.17 kcal/mol), as did the shortening of the n-propyl in Hit **3** to methyl in compound **11** (Figure 8) (binding energy = −69.47 kcal/mol). Thus, it could reasonably be concluded that, pyridine ring linked to C-2 of the benzoxazepine ring together with the n-propyl chain attached to the triazine ring might be important for optimal affinity.

The overall binding free energy for each hit arose from multiple energy components (Table 2; Figure 9), encompassing Coulombic energy (Coulomb), covalent bonding (Covalent), hydrogen bonding (Hbond), lipophilic interactions (Lipo), π-π packing interactions (Packing), generalized solvent binding (Solv GB), and van der Waals interactions (VdW)Among these terms, the contribution of the VdW energy was more than the others in the total binding energies of the top 7 hits and the co-crystal ligand. Coulomb energy came in the second place after the VdW energy as contributing force of interaction for Hits **1**, **3**, **5** and **6** alongside

TABLE 2 Energy terms contributing to the free energy (Gbind) of Hits 1-7 and the co-crystal ligand AX20017.

Hit	MMGBSA dG bind (kcal/mol)	MMGBSA dG bind coulomb	MMGBSA dG bind Hbond	MMGBSA dG bind lipo	MMGBSA dG bind packing	MMGBSA dG bind vdW	MMGBSA dG bind covalent	MMGBSA dG bind solv GB
Co-crystal ligand	−60.23	−20.65	−1.51	−19.54	0.00	−44.71	0.41	25.76
1	−61.27	−38.16	−3.63	−20.85	0.00	−41.03	7.07	35.32
2	−64.55	−0.221	−1.36	−25.21	−0.04	−52.91	0.41	23.78
3	−69.95	−60.75	−0.52	−27.80	−0.14	−49.80	0.95	68.10
4	−60.92	−6.58	−1.02	−27.54	−0.01	−54.27	1.41	27.09
5	−60.98	−36.32	−4.08	−19.32	−0.13	−43.44	4.07	38.23
6	−69.14	−56.21	−1.08	−22.95	−0.32	−50.44	1.55	60.31
7	−65.81	−9.95	−1.04	−27.40	−0.21	−52.33	1.25	23.86
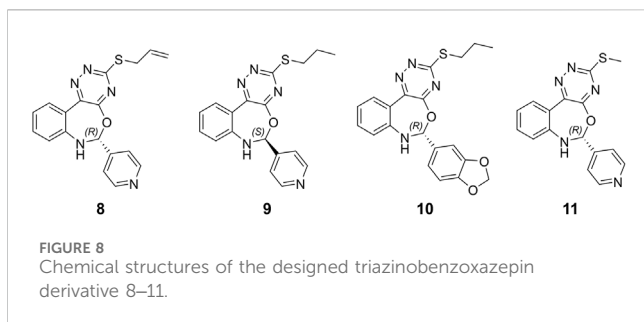
FIGURE 8
Chemical structures of the designed triazinobenzoxazepin derivative 8–11.

FIGURE 9
The major energy components contributing to the free energies (ΔGbind) of the top 7 hits and the co-crystal ligand, including electrostatic (ΔGbind Coulomb), Van der Waals (ΔGbind VDW), lipophilic (ΔGbind Lipo), and hydrogen bonding (ΔGbind Hbond).

the co-crystal ligand. In contrast, for the triazinobenzoxazepin **2**, **4** and **7** the second most contributing force was the lipophilic one. Interestingly, the triazinobenzoxazepin **3** (the hit with the highest affinity), coulomb energy was the principal contributing force of interactions. This could be attributed to the presence of the ionizable positively charged pyridine ring, which interacts via pi-cation forces with Arg242. As for co-crystal ligand, the contributions of H-bonding and the π-π packing forces to the total binding energy of the top 7 hits were very little. Overall, the outcome of this analysis indicates that, Hits **1–7** possessed affinity towards the PknG binding domain higher than that of the co-crystal ligand. Additionally, the decomposed energy terms contributing to the total free binding energies for Hits **1–7** were similar to those of the co-crystal ligand and were therefore considered all for the next ADMET filtering step.

To provide context for our findings, we conducted a comparative analysis with previously reported potent inhibitors of M.tb PknG (Figure 10). Tables 1–3 revealed notable differences in docking scores and binding energies for M.tb PknG inhibitors. Tables 1 and 2 summarized the results for the computationally identified Hits **1–7**, while Table 3 provided data for experimentally validated inhibitors. The docking scores of Hits **1–7** were significantly better than those of the validated inhibitors. For example, Hit **1** achieved a docking score of −12.75 kcal/mol, outperforming AX20017, the co-crystallized ligand in Table 3, which had a docking score of −8.14 kcal/mol. Other hits, such as Hit **7** (−10.03 kcal/mol) and Hit **6** (−8.86 kcal/mol), also showed stronger docking affinities compared to most validated inhibitors, whose scores ranged from −2.43 kcal/mol to −8.14 kcal/mol. In terms of binding energies, the Hits **1–7** in Table 2 demonstrated more favorable values. Hit **3** exhibited the strongest binding energy at −69.95 kcal/mol, followed by Hit **6** (−69.14 kcal/mol) and Hit **7** (−65.81 kcal/mol). In contrast, AX20017, the most potent validated inhibitor in Table 3, had a binding energy of −60.23 kcal/mol. Other inhibitors in Table 3 showed weaker binding energies, ranging from −32.23 kcal/mol to −60.23 kcal/mol. Overall, the results indicated that Hits **1–7** exhibited stronger predicted binding affinities and docking scores compared to the experimentally validated inhibitors. These findings suggest that the computationally identified hits have promising potential as superior candidates for M.tb PknG inhibition, though experimental validation would be necessary to confirm their effectiveness. As shown in Supplementary Figure S2, with the exception of AX20017 and RO9021, the experimentally validated inhibitors displayed less efficient interactions compared to our identified hits (Supplementary Figure S1), particularly in terms of
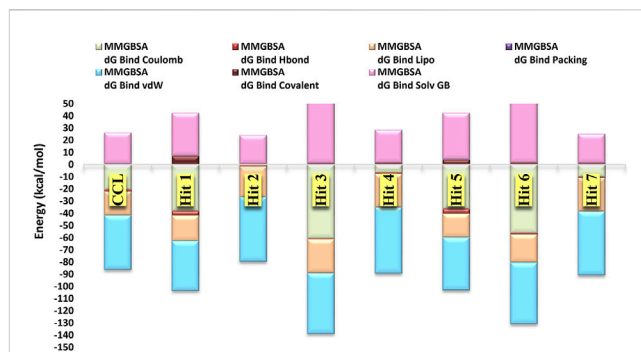
binding to the hinge region. This difference in interaction patterns correlates with the lower binding affinities observed for these inhibitors, as their suboptimal binding to critical residues in the hinge region likely reduces the overall stability and strength of the ligand-enzyme complex.

Compared to the reported PknG inhibitors, the identified hits in this study represent novel classes of PknG inhibitors, marking a significant advancement in tuberculosis drug discovery. To the best of our knowledge, these are the first reported examples of PknG inhibition for the following scaffolds: chromene glycoside, triazinobenzoxazepin derivative, quinzoline, and benzene sulphonamide. These scaffolds are not only structurally unique but also provide a promising basis for the development of new anti-tubercular therapies targeting the PknG enzyme, which is essential for the survival and pathogenicity of M.tb. The chromene glycoside scaffold, while known for its diverse biological activities (Amen et al., 2021), has never been explored for PknG inhibition before. Similarly, the triazinobenzoxazepin derivatives, which have been previously studied for their activity in other therapeutic areas (Stefaniak and Olszewska, 2021), are also reported here for the first time as potential PknG inhibitors. The quinzoline scaffold, traditionally associated with anti-tubercular properties (Kushwaha et al., 2023), has been linked to PknG inhibition in this study for the first time. This discovery is particularly exciting, as quinzoline derivatives have shown promise in other aspects of tuberculosis treatment, and their application as PknG inhibitors may offer an additional, synergistic mechanism of action. Finally, the benzene sulphonamide scaffold, widely known for its antimicrobial properties (Kapısuz et al., 2024), has not previously been explored in the context of PknG inhibition. The identification of this scaffold as a potent PknG inhibitor is a significant milestone and could lead to the development of compounds that specifically target drug-resistant strains of M.tb, a growing concern in the fight against tuberculosis. Collectively, these scaffolds represent a promising foundation for the development of new anti-TB therapies. The discovery of these novel scaffolds as PknG inhibitors could therefore pave the way for more effective treatments, particularly in the context of drug resistance, marking a significant advancement in the search for new tuberculosis therapies. Current anti-TB drugs

FIGURE 10
Chemical structures of the experimentally validated M.tb PknG inhibitors.
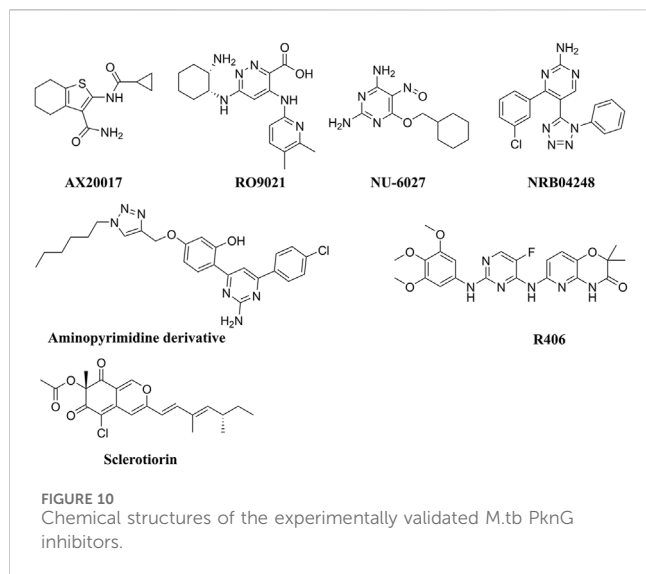
face significant limitations, including lengthy treatment durations, low cure rates ranging from 40% to 50%, and the challenge of being confounded by factors such as poor nutrition and co-infections. Additionally, these drugs often require large dosages and are associated with more side effects due to poor pharmacokinetic properties (Wei et al., 2024). These shortcomings present a critical mechanistic gap in existing treatments. The identified hits in this study address this gap by specifically targeting PknG, offering a novel approach to inhibit M.tb persistence and survival within the host. These hits are unique in that they have the potential to target non-proliferating mycobacteria during the latency stage and prevent the development of Mtb-resistant strains, which could significantly enhance treatment outcomes. Furthermore, these hits have the potential to be used in combination with existing anti-TB drugs, increasing their efficacy, reducing the risk of resistance, and overcoming the limitations of current therapies. By targeting a novel pathway and providing an additional layer of treatment, these inhibitors could not only improve therapeutic efficacy but also shorten treatment durations, offering a crucial solution to address the global TB crisis (Farhat et al., 2024).

However, off-target effects in PknG inhibitors pose a significant challenge in drug development, as these unintended interactions with non-target molecules can lead to adverse biological responses. Such interactions compromise treatment specificity and may cause harmful side effects, limiting the clinical utility and safety of these compounds. Given that PknG is a kinase in M.tb, understanding kinase off-target effects is critical. Numerous studies have shown that off-target kinase inhibition can result in adverse outcomes, highlighting the necessity of comprehensive screening to ensure the selectivity of the identified hits as PknG specific inhibitors and reduce potential therapeutic risks (Green et al., 2023). Our docking analysis of the top identified hits revealed interactions with residues in the PknG binding site that are specific to PknG, such as Ile165, Val179, Gly236, Ile292, Ile87, and Ala92. These residues are absent in the 11 other serine/threonine protein kinases (STPKs) from M.tb and are also absent in human kinases, which aligns with the behavior of the previously reported inhibitor NU-6027 (Kidwai et al., 2019). Furthermore, the frequencies of occurrence for the residues Ile165, Val179, Gly236, and Ile292 in the surrounding PknG binding site are minimal (Scherr et al., 2007). The combination of these residues is not observed in any other human kinase sequences. Additionally, the Ile87 and Ala92 residues, which are located within the amino-terminal peptide stretch, are also unique to the ligand-binding pocket of PknG (Scherr et al., 2007; Kidwai et al., 2019). While these findings suggest that our identified hit may exhibit selectivity, it is important to note that these conclusions are based solely on *in silico* studies and require further experimental validation. Such validation includes conducting comprehensive kinase profiling to identify potential off-target interactions and chemically modifying the inhibitors to enhance selectivity for PknG. Structural modifications can be made to prevent binding to off-target kinases while preserving strong affinity for PknG.

3.3 *In silico* ADMET profiling

In-silico prediction approaches of ADMET properties for potential hits have become an integral component of modern drug discovery process (Vrbanac and Slauter, 2017; Ferreira and Andricopulo, 2019). Owing to their reduced cost compared to the

TABLE 3 Experimentally validated M.tb PknG inhibitors with docking scores, binding free energies, and IC$_{50}$ values.

No.	Name	Docking score (kcal/mol)	Binding energy (kcal/mol)	IC$_{50}$	References
1	AX20017 (Co-crystallized ligand)	−8.14	−60.23	0.2 ± 0.04 μM	Scherr et al. (2007), Arica-Sosa et al. (2022)
2	RO9021	−2.43	−52.48	4.4 ± 1.1 μM	Arica-Sosa et al. (2022)
3	NRB04248	−4.75	−38.17	43% inhibition at 25 μM	Singh et al. (2015)
4	Aminopyrimidine derivative	−4.48	−42.49	43 ± 2.94 at 100 μM	Anand et al. (2012)
5	NU-6027	−4.83	−32.23	at 50 μM selectively inhibits PknG	Kidwai et al. (2019)
6	R406	−5.37	−47.53	83.8% inhibition at 16.1 μM	Kanehiro et al. (2018)
7	Sclerotiorin	−1.68	−24.43	76.5 μM	Chen et al. (2017)

TABLE 4 Quantum chemical reactivity descriptors of Hit 1 and the co-crystal ligand (eV).

Compound	E_{HOMO} (eV)	E_{LUMO} (eV)	HLG	Electron affinity	Ionization potential	Chemical hardness	Chemical softness	Electronegativity	Global electrophilicity index
Co-crystal ligand	−5.67	−1.10	4.57	1.10	5.67	2.28	0.43	3.38	2.50
Hit 1	−6.10	−1.85	4.25	1.85	6.10	2.12	0.47	3.97	3.71

experimental ones, these approaches have attracted the attention of the scientific community (Ntie-Kang, 2013). In this context, *in silico* ADMET prediction of the 7 top-ranked hits was achieved using the QikProp module in Schrödinger software and the publicly accessible webserver ADMETLab 2.0. The predicted descriptors were compared with the limiting ranges. In general, results indicated positive physicochemical and pharmacokinetic properties for the 7 top ranked hits (Supplementary Table S1). The overall ADME-compliance score–drug-likeness parameter (indicated by #stars) of these hits were within the specified limit indicating that they had properties similar to those for 95% of known drugs. In addition they showed no violations to Lipinski (Rule of Five) or Rule of Three. With Hits **1** and **5** showing medium oral absorption (<60%), the rest exhibited high oral absorption rate (>85%) pointing for their potential for oral administration, a favorable criterion for ideal anti-TB drug (Sotgiu et al., 2015). Since TB could involve CNS as a primary site of infection (Rock et al., 2008) anti-TB drug's crossing of the BBB is considered an important feature. To this end, the predicted brain/blood partition coefficient (QP log BB) and the Polar Surface area (PSA) are Qikprop descriptors employed to evaluate the BBB permeability of potential drug candidates (Dighe et al., 2020). The values for these descriptors for the top-ranked hits were within the designated ranges, indicating their high potential for CNS penetration. Further, the efficient distribution of Hits **1–7** in the human body was estimated using apparent Caco-2 (QPPCaco) and MDCK cell (QPPMDCK) permeability parameters (Dighe et al., 2020; Amengor et al., 2022). Excluding the chromene glycoside, Hit **1**, the rest displayed an enhanced permeability in both Caco-2 and MDCK cells (the predicted values fell within the recommended ranges) confirming their potentiality for efficient distribution in the human body following oral administration. Binding of a given drug to the blood plasma proteins is a crucial factor affecting the efficacy of that drug, since it determines its free concentration that would be available to cross the biological membranes and consequently to interact with its target (Hann et al., 2022). Accordingly, the QPlogKhsa parameter was done here for evaluating the binding of Hits **1–7** to the human albumin which is considered the highly abundant plasma protein capable of binding to a variety of drugs (Hann et al., 2022). Hits **1-7** were found to be compliant to this parameter, and thus would be expected to circulate in the blood smoothly from side to side until they reach their site of action. Human Ether-a-go-go Related Gene (HERG) encodes a potassium ion channel that is documented to play a key role in a fatal type of arrhythmia known as torsade *de pointes* (Lamothe et al., 2016). Further, it represents a macromolecular via which several drugs mediate their cardiotoxic effects (Lamothe et al., 2016; Amengor et al., 2022). In this context, the IC_{50} value for blockage of HERG K^+ channels parameter (QPlogHERG) was used in the present study to evaluate the propensity of Hits **1–7** to impose cardiotoxic side effects. All the investigated hits, except Hit **1**, were detected to have the potential to induce HERG-related cardiotoxic effects since their predicted IC_{50} values for blockage of HERG K^+ channels fell outside the specified limit (concern below −5). The number of likely metabolic reactions of a drug candidate is an essential descriptor used to identify whether it could reach its site of action following entering the blood circulation. The computed
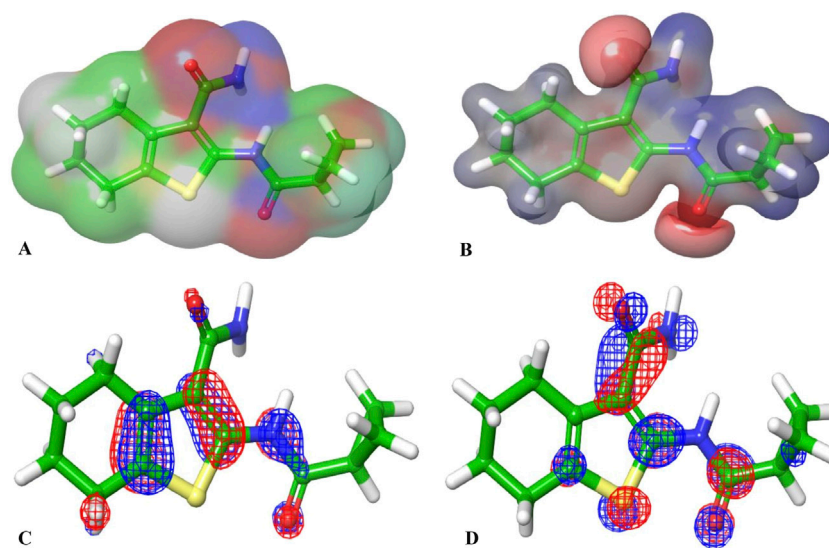
FIGURE 11
(A, B) are the electron density and MESP of the reference ligand; **(C, D)** are the molecular orbital distribution plots of E_{HOMO} and E_{LUMO} of the reference ligand, respectively.

numbers of possible metabolic reactions for Hits **1–7** were between 2–5 which were within the recommended set limit (1–8). Overall, attractive pharmacokinetic profiles. Given the above information, Hits **1–7**, in general, had appropriate ADMET profiles, nevertheless further optimization is required to boost up their therapeutic properties. Based on the obtained favorable ADME profiles for Hits **1–7**, the research was directed to assess their potential toxicity. *In-silico* assessment of potential adverse effects of a drug candidate has now become a routine practice in the pharmaceutical industry, particularly at the earlies stages of the drug discovery program to reduce the drug attrition rate (Liu et al., 2023; Rababi and Nag, 2023). In the same regard, the webserver ADMETLab 2.0 was used to perform toxicity evaluation of Hits **1–7**. As shown in Supplementary Table S2, all of the investigated Hits had the high risk to induce liver injury. Hits **1** and **5** had the low probability to be hepatotoxic (the output values < 0.3), Hit **7** had the borderline low probability to precipitate liver toxicity (the output value < 0.7), the rest had greater potential to be hepatotoxic (the output values > 0.7). It was noticed that the triazinobenzoxazepines **2–4** and **7** showed active remarks in both AMES and respiratory toxicity parameters (output values > 0.7). Estimation of the carcinogenic properties of the investigated hits pointed to the high risk of Hits **2** and **4** to induce cancer. To get an insight on the possible side effects that could emerge upon prolonged and frequent administration of Hits **1–7**, rat oral acute toxicity descriptors (ROA) were determined. It was observed that all of the hits were safe and having less potential to impose acute toxic effects in human. Calculated values for eye corrosion (EC), eye irritation (EI) and skin sensitization (SkinSen) were found to meet the standards for safe drug candidate. In addition, we conducted a comparative study between the most widely used and clinically established first-line anti-TB drug Isoniazid (INH) and Hit **1** to gain a deeper understanding of their pharmacokinetic characteristics and toxicity profiles

(Supplementary Tables S1, S2). The anti-TB drug INH had a smaller molecular weight (137.14) and solvent accessible surface area (SASA: 329.65) compared to Hit **1**, indicating that INH was smaller in size and had different polarity. INH demonstrated superior permeability (QPPCaco: 273.87 nm/sec) and solubility (QPlogS: −1.03) than Hit **1**, suggesting better drug-likeness. Additionally, INH had fewer hydrogen bond acceptors (4.5) and higher human oral absorption (66.7%) compared to Hit 1 (42.33%). Both INH and Hit **1** complied with Lipinski's Rule of Five, although Hit **1** violated Jorgensen's Rule of Three. Regarding toxicity, INH displayed a poorer profile for hepatotoxicity (H-HT: 0.71) and drug-induced liver injury (DILI: 0.70) compared to Hit **1** (0.12 and 0.81, respectively). INH also showed higher mutagenicity (AMES: 0.93) and skin sensitization (SkinSen: 0.98) compared to Hit **1** (0.33 and 0.69). However, Hit **1** exhibited significantly better respiratory toxicity (0.03) than INH (0.99). Both compounds had low recommended daily doses (FDAMDD: 0.06 for INH, 0.0 for Hit **1**), and although INH had a higher eye irritation potential (EI: 1.00), Hit **1** showed a more favorable value (0.23) for this parameter. In summary, while INH demonstrated better pharmacokinetics, Hit **1** exhibited a safer toxicity profile, making it a promising candidate with potential advantages in terms of safety. Thus, the selection of Hit **1** was primarily driven by its superior safety profile, which emerged as the most significant factor distinguishing it from the other top hits. Among the evaluated candidates, Hit **1** demonstrated the lowest predicted toxicity risks, ensuring its suitability for further development. In addition, it exhibited favorable ADMET properties, which further supported its drug-likeness and potential for clinical translation. The prioritization of Hit **1** was also influenced by its balanced physicochemical characteristics, aligning with the criteria for successful drug candidates. This comprehensive evaluation provided strong justification for advancing Hit **1** to more detailed computational studies. These investigations aim to
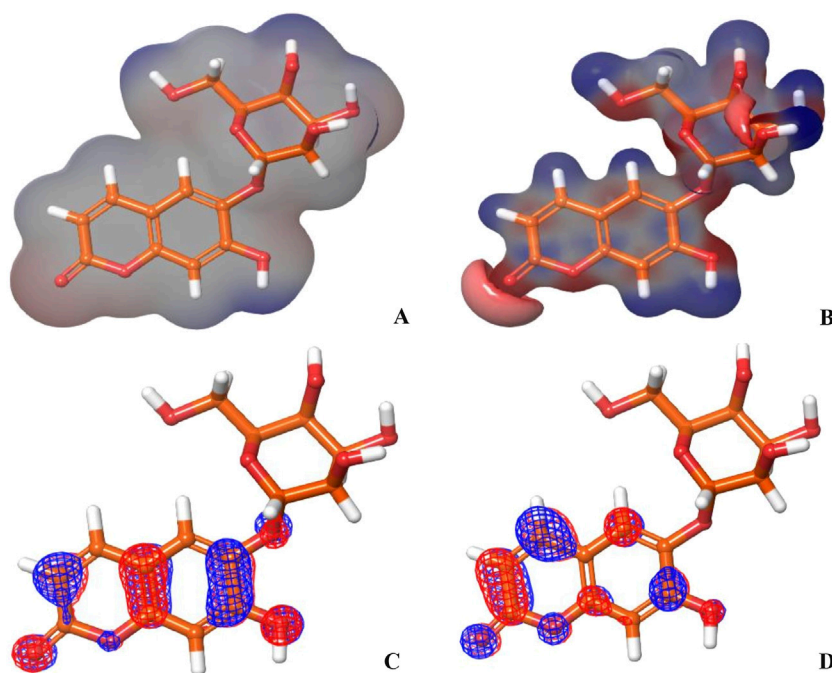
FIGURE 12
(A, B) show the electron density and MESP of Hit 1; **(C, D)** show the molecular orbital distribution plots of E_{HOMO} and E_{LUMO} of Hit 1, respectively.
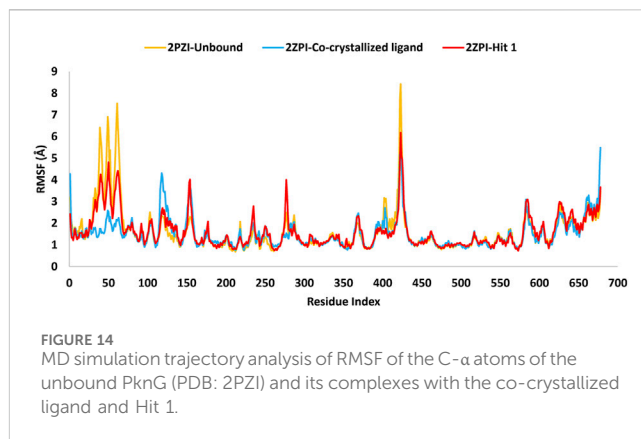
explore its structural and electronic features, laying the groundwork for targeted modifications to enhance its efficacy, selectivity, and overall therapeutic potential.

3.4 Quantum computational calculations

The molecular orbital and electronic features of the investigational hits are commonly computed employing quantum mechanical methods (Zhou et al., 2010). In this study the DFT (density functional theory) analysis of Hit **1** and the co-crystal ligand was performed using Jaguar module of Schrödinger suite. Table 4 illustrates the Frontier Molecular orbitals (FMOs) E_{HOMO} and E_{LUMO}, the HOMO-LUMO Gap (HLG) along with the quantum chemical reactivity descriptors of Hit **1** and the co-crystal ligand. Molecule's electron affinity is directly related to its E_{LUMO}, while its ionization potential is associated with its E_{HOMO} (Ahmad et al., 2023). Hit **1** exhibited E_{HOMO} value similar to that of the co-crystal ligand indicating their similar ability to donate electrons to an acceptor molecule, meanwhile, it displayed more negative E_{LUMO} pointing to its relatively higher electron affinity as compared to the co-crystal ligand. The E_{HOMO} and E_{LUMO} plots of the co-crystal ligand (Figures 11C,D) implies that nearly the entire structural units of the molecule involved in FMOs and are thus could significantly participate in the electron donation/acceptance processes.

On the other hand, the E_{HOMO} and E_{LUMO} plots of Hit **1** (Figures 12C,D) localized exclusively over the chromene ring rather than the sugar moiety, HLG indicates whether the molecule is kinetically and chemically stable or not (Alsehli et al., 2021). Both, the co-crystal ligand and Hit **1** demonstrated similar HLG values (Table 4) implying that they had similar chemical and kinetic stability and

are thus having similar electrons transferring and exchanging liabilities. Likewise, the molecular hardness (η) and softness (σ) of the co-crystal ligand and Hit **1** were similar which further confirmed their intermediate chemical stability since these descriptors are directly related to HLG. It was observed that the computed electronegativity (χ) for the co-crystal ligand and Hit **1** were 3.385 and 3.975 eV, respectively, indicating the comparatively high potential of Hit **1** for electron attraction. Further, the global electrophilicity index (ω) was calculated to evaluate the capacity of Hit **1** and the co-crystal ligand to accept from molecules. As shown in Table 4, the calculated electronegativity ω of Hit **1** and the co-crystal ligand is found to be 2.507 and 3.71, eV, respectively which reflects the strong electrophilic property of the identified Hit relative to that of the reference ligand (Rana et al., 2021; Burkhanova et al., 2022). The electron density and the MESP of the co-crystal ligand and Hit **1** (Figures 11A, B, 12A, B, respectively) were computed to display the electron-rich, electron-deficient and neutral regions of these molecules. In addition it also provide information regarding the molecular size and shape of the tested compounds. The electrostatic potential differences on the regions are depicted in red, yellow, and blue colors which refer to the highly negative, negative and the highly positive molecular regions, respectively. While the positive regions represent the favorable site for nucleophilic attack, the negative regions are the favorable site for electrophilic attacks. As illustrated in Figures 11A, B, 12A, B, the negative surfaces are presented in the electronegative oxygen atoms alongside the C=C bonds, meanwhile the positive ones are localized at the hydrogen atoms. These electrostatic surfaces were shown to play a critical role in helping co-crystal ligand and Hit **1** to interact with diverse forces of interactions to the PknG catalytic site.

FIGURE 13
RMSD plot generated through MD trajectories of the C-α atoms of the unbound PknG (PDB: 2PZI) and its complexes with co-crystallized ligand, along with Hit 1.

FIGURE 14
MD simulation trajectory analysis of RMSF of the C-α atoms of the unbound PknG (PDB: 2PZI) and its complexes with the co-crystallized ligand and Hit 1.
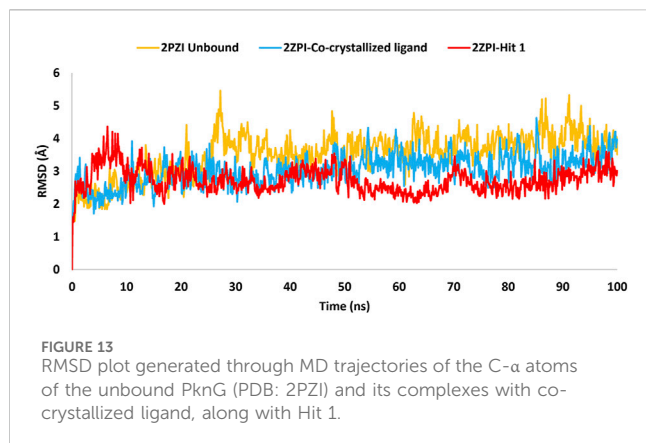
3.5 MD simulation

To assess the strength of binding of the most promising compound, Hit **1,** to PknG binding site, all-atom MD simulation was performed for 100 ns time frame. The docked complexes of Hit 1 and the co-crystallized ligand were used as input files, alongside the unbound PknG for comparison. MD descriptors such as the Root Mean Squire Deviation (C-α RMSD) (Figure 13), Root Mean Squire of Fluctuation (RMSF) (Figure 14) and protein-ligand contacts (Figure 15) were extracted from the 100 ns trajectory simulation run. C-α RMSD calculations used extensively to evaluate the deviation of a protein relative to a reference structure during MD simulation. Low RMSD values ligand-protein complex indicate stability and limited structural changes (Arnittali et al., 2019). The RMSD plot (Figure 13) indicates that Hit **1** complex displayed relatively high fluctuation in the initial frames when compared to the co-crystallized ligand and the unbound protein. This could be attributed to the initial structural adjustments of Hit **1** complex to adopt the real binding mode. Following 10 ns of the MD simulation start, Hit **1** complex stabilization was attained and steady profile was displayed throughout the rest of simulation run. Generally, Hit **1** complex displayed great stability with minimal fluctuations (averaging RMSD 2.73 ± 0.37 Å) (Table 5) when compared to those of the co-crystallized ligand (averaging RMSD 3.03 ± 0.45 Å) and the unbound protein (averaging RMSD 3.52 ± 0.65 Å). This indicates that Hit **1** formed stable complex with PknG binding pocket and it remained tightly bound there for the whole of the simulation course.

The RMSF analysis presented in Table 6 provided insights into the dynamic flexibility of the PknG protein under different conditions. In its unbound state (2PZI), the protein exhibited the highest flexibility, with a maximum RMSF of 8.4 Å, a minimum of 0.68 Å, and an average of 1.61 Å, indicating significant motion within the structure. Binding with the co-crystallized ligand notably reduced the flexibility, reflected by a lower maximum RMSF of 5.4 Å, a minimum of 0.74 Å, and an average of 1.50 Å, suggesting enhanced stabilization of the protein. When bound to Hit **1**, the flexibility of PknG was intermediate, with a maximum RMSF of 6.1 Å, a minimum of 0.72 Å, and an average of 1.60 Å. This implied that Hit **1** provided some level of stabilization to the protein but was less effective compared to the co-crystallized ligand. Overall, the data indicated that while Hit **1** binding reduced the protein's flexibility

FIGURE 15
Binding modes of co-crystallized ligand **(A)**, Hit 1 **(B)** with PknG (PDB: 2PZI) during the simulation run. H-bonds are shown in green, hydrophobic interaction in grey, ionic bonds in deep pink and water bridges in blue.
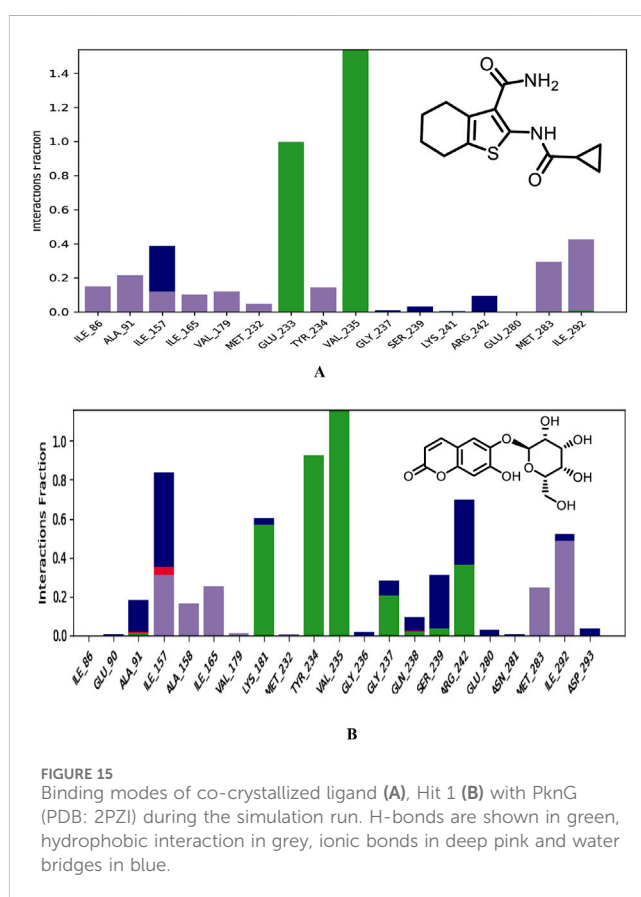
relative to its unbound state, it did not achieve the same level of stabilization as the co-crystallized ligand, highlighting its potential as a stabilizing agent but with scope for further optimization.

Moreover, an analysis of the flexibility of the binding site residues was performed. The RMSF analysis of the PknG binding site residues, revealed that flexibility was similar across the different conditions. In the unbound state (2PZI), the binding site exhibited a maximum RMSF of 1.6 Å, a minimum of 0.68 Å, and an average of 1.04 Å, indicating moderate motion. Binding with the co-crystallized ligand slightly increased the maximum RMSF to 1.67 Å and the minimum to 0.75 Å, while maintaining an average of 1.04 Å, suggesting minimal impact on the stabilization of the binding site

TABLE 5 Detailed analysis of the RMSD values, including minimum, maximum, and average for the Hit 1 complex. This also includes comparative data for the co-crystallized ligand complex and the unbound protein.

PknG RMSD (Å)			
Protein	Maximum	Minimum	Average
2PZI Unbound	5.46	1.41	3.52 ± 0.65
2PZI-Co-crystallized ligand	4.63	1.57	3.03 ± 0.45
2PZI-Hit 1	4.36	1.42	2.73 ± 0.37

TABLE 6 Detailed analysis of the RMSF values, including minimum, maximum, and average for the Hit 1 complex. This also includes comparative data for the co-crystallized ligand complex and the unbound protein.

PknG RMSF (Å)			
Protein	Maximum	Minimum	Average
2PZI Unbound	8.4	0.68	1.61
2PZI-Co-crystallized ligand	5.4	0.74	1.50
2PZI-Hit 1	6.1	0.72	1.60

residues. Binding with Hit **1** resulted in a maximum RMSF of 1.64 Å, a minimum of 0.80 Å, and a slightly higher average of 1.10 Å. These results suggested that both the co-crystallized ligand and Hit **1** influenced the dynamics of the binding site residues to a similar extent, with Hit **1** inducing slightly higher average flexibility. This indicated that Hit **1**'s binding effect was comparable to that of the co-crystallized ligand but required further optimization to achieve greater stabilization.

Near the conserved ATP-binding site, PknG possessed an additional hydrophobic pocket, distinct from most protein kinases due to its low sequence homology (Scherr et al., 2007; Caballero et al., 2018). This distinctiveness was attributed to the presence of a unique N-terminal segment spanning residues 5–60, which contributed significantly to the structural and functional divergence of PknG. The dynamic nature of this N-terminal segment was evident in the RMSF analysis, which revealed marked differences between the bound and unbound states. In the unbound state (2PZI), residues 5–60 exhibited the highest flexibility, with an RMSF range of 1.26–6.9 Å and an average of 3.03 Å, reflecting considerable motion within this region. Binding with the co-crystallized ligand markedly reduced flexibility, with an RMSF range of 1.28–2.5 Å and an average of 1.68 Å, indicating strong stabilization of these residues. In comparison, binding with Hit 1 resulted in intermediate flexibility, with an RMSF range of 1.21–4.8 Å and an average of 2.4 Å. While Hit **1** reduced the flexibility of residues 5–60 compared to the unbound state, it did not provide the same degree of stabilization as the co-crystallized ligand. These findings highlighted the potential of Hit **1** as a stabilizing agent for this region, though further optimization may be required to enhance its effectiveness. The significant reduction in RMSF values upon binding to the co-crystallized ligand or Hit **1** demonstrated that the hydrophobic pocket stabilized through ligand-induced structural adjustments. This stabilization not only

enhanced binding affinity but also underscored the critical role of the N-terminal segment in regulating access to the hydrophobic pocket and optimizing ligand interactions. Notably, 90% of the inhibitors interacted with the unique N-terminal segment of PknG via hydrophobic interactions, further reinforcing the functional importance of this region (Caballero et al., 2018).

Plots for RMSF of amino acid residues are shown at a time function of 100 ns in Figure 14. It is clear that the key residues involved in protein-ligand interactions were of minimal flexibility (<1.5 Å) during the entire trajectory run. These low RMSF values for the interacting residues significantly impacted the stability and the firm binding of Hit **1** to the enzyme catalytic site. Further, relatively high variations were observed for residues Pro99 to Ser133, Arg222, Asn346 and Ala490 to Gly495 for both, the unbound protein and Hit **1** complex. Fortunately, these residues did not play a direct role in interacting with Hit **1**, so their flexibility did not impact the overall stability of Hit **1** complex.

Next, different types of protein-ligand interactions occurring in the simulation time were investigated. Four different types of protein-ligand contacts were identified, specifically: H-bonds, water bridges, ionic interactions, and hydrophobic interactions. As illustrated in Figure 15, the co-crystallized ligand maintained the same interactions with the key residues encountered for XP docking conformer. These interactions included three H-bonds with the hinge region residues, two with Val235 and the other with Glu233. These H-Bonds retained for the entire simulation time frame. Further, hydrophobic interactions were also observed with critical residues Ile86, Ala91, Ile157, Ile165, Val179, Met232, Tyr234, Met283, and Ile292. The hinge region of PknG, comprising Glu233, Tyr234, and Val235, plays a pivotal role in ligand stabilization (Arica-Sosa et al., 2022). In this context, the hydrogen bond formed by Hit **1** with the key residue Val235 in this region remained stable for the majority of the simulation time (93%), compared to 99% stability observed in the co-crystallized ligand complex (Supplementary Figure S3). However, the H-Bond with the crucial residue Glu233 detected for the docked complex lost and was replaced with stable H-Bond with the adjacent residue Tyr234 in the same region. The later bond was also maintained for most of the simulation time (92%). This loss of interaction with Glu233 may impact the overall binding affinity, as Glu233 plays a significant role in stabilizing ligands within the ATP-binding site. However, Hit **1** compensated for this loss by forming a stable interaction with the hinge region residue Tyr234 and the catalytic residue Lys181 (Arica-Sosa et al., 2022), which were present for nearly 92% and 60% of the simulation, respectively. These interactions, which were not observed for the co-crystallized ligand, may contribute to maintaining binding stability and potentially offset the impact of the missing Glu233 interaction. Given that Lys181 is critical for catalytic activity, the interaction with this residue could enhance the functional efficacy of Hit **1**, despite the reduced affinity caused by the absence of Glu233 engagement. Thus, Future optimization of Hit **1** could focus on re-establishing interactions with Glu233 to improve its binding affinity without compromising its interaction with Lys181. In addition, Hit **1** created multiple H-Bonds and Water Bridges with different residues including Lys181, Ile157, Ser239, and Arg242. Some of these bonds lasted for >55% of the timeline, further contributed to stabilization of Hit **1** complex. These additional connections could be attributed to the presence of the sugar

TABLE 7 Maximum, Minimum and Average number of H-Bonds, hydrophobic interactions, and Water-Bridges observed during 100 ns MD simulation of hit 1 and the co-crystallized ligand complexes with PknG (PDB: 2PZ1).

2PZI-complex	Co-crystallized ligand	Hit 1
H-bond contacts		
Average	2.54	3.28
Maximum	4	8
Minimum	1	0
Hydrophobic contacts		
Average	1.61	1.41
Maximum	7	5
Minimum	0	0
Water-bridge contacts		
Average	0.41	1.55
Maximum	4	7
Minimum	0	0

moiety attached to C-6 of the chromone ring in Hit **1** which amplifies its hydrophilicity as compared to the co-crystallized ligand. Regarding hydrophobic interaction, it was observed for Hit **1** with several residues existed in the hydrophobic region of the enzyme binding pocket such as Ile157, Ala158, Ile165, Val179, Met283, and Ile292.

Furthermore, to get detailed insights into the stability and specificity of the PknG-Hit **1** interactions, the number of H-Bonds along with hydrophobic interactions were analyzed and the results are provided in Table 7 and Supplementary Figure S4. Hit **1** demonstrated a relatively high number of H-Bonds during the simulation compared to those made by the co-crystallized ligand (Supplementary Figure S4A), averaging 3.28 and 2.54, respectively. This could justify the better stability of Hit **1** complex compared to that of the co-crystalized ligand, as H-bonds are increasingly regarded as facilitators of protein-ligand binding (Chen et al., 2016). Moreover, Hit **1** established hydrophobic interactions (Supplementary Figure S4B), comparable to those formed by the co-crystallized ligand, with averages 1.47 and 1.61, respectively. Thus, we can reasonably conclude that Hit **1** created a stable and favorable interaction profile with the mycobacterial PknG catalytic site, making it a potential PknG inhibitor for the treatment of tuberculosis. The average water-bridge contacts for the co-crystallized ligand were 0.41, while Hit **1** showed a significantly higher average of 1.55. This suggested that Hit **1** formed more frequent water-mediated interactions with the protein. The maximum number of water-bridge contacts for Hit **1** was 7, compared to 4 for the co-crystallized ligand, indicating that Hit **1** had the potential to establish stronger networks. Both ligands showed a minimum of 0 water bridges, implying the absence of such interactions in some configurations. These findings highlighted the enhanced water-bridge interaction of Hit **1** with the protein. In conclusion, Hit **1** demonstrated a more favorable interaction profile with PknG, evidenced by a higher number of hydrogen bonds and water-bridge contacts, as well as comparable hydrophobic

interactions to the co-crystallized ligand. These factors suggest that Hit **1** formed a more stable and specific complex with the mycobacterial PknG catalytic site. Therefore, Hit **1** presents itself as a promising candidate for further optimization as a PknG inhibitor for tuberculosis treatment.

3.6 Study limitations and future perspective

Various computational approaches, including molecular docking, free energy calculations, ADMETox studies, DFT analysis, and MD simulations, have been employed in this study to identify novel potential inhibitors targeting PknG of *M. tuberculosis*. These inhibitors are expected to suppress the growth and multiplication of drug-resistant *M. tuberculosis* that survive within alveolar macrophages, thereby potentially addressing the challenge of latent tuberculosis. A compound library comprising 460,000 small molecules underwent multimode virtual screening, from which seven compounds (hits 1–7) demonstrated notable binding affinity and robust interactions with essential residues within the catalytic binding pocket of mycobacterial PknG. While all seven hits exhibited acceptable drug-like properties, the chromene glycoside (hit 1) stood out for its lower toxicity. However, strategies to optimize its oral bioavailability are strongly recommended. Additionally, DFT analysis indicated that the mechanical and electronic properties of hit 1 were superior to those of the reference ligand (AX20017). Molecular dynamics (MD) simulations further confirmed the stability of the hit 1-PknG complex, supporting its potential as a lead compound for anti-tuberculosis drug development. Despite these promising computational results, several limitations must be acknowledged. The reliability of computational models depends heavily on the quality of structural data and the assumptions used in the simulations, which, although thorough, may not fully capture the intricate complexities of biological systems *in vivo*. In silico models, while powerful, have inherent limitations in accurately predicting the behavior of compounds within living organisms. These models often fail to account for complex *in vivo* molecular interactions, such as off-target effects and biotransformation pathways, introducing uncertainty regarding the safety and efficacy of the investigated compounds. Molecular docking, a fundamental computational technique, relies on assumptions about the flexibility of proteins and ligands. It typically represents the binding site as static or semi-flexible, potentially overlooking the dynamic nature of proteins that can adopt multiple conformations. Consequently, docking scores, which estimate binding potential, do not always correlate with experimental binding affinity values. To mitigate these issues, MM-GBSA calculations were employed to provide more accurate binding energy estimates by incorporating molecular flexibility and solvent effects. Additionally, MD simulations validated the stability of PknG-inhibitor complexes, offering dynamic insights and reinforcing the potential of the identified hit as effective PknG inhibitors. Nonetheless, this study's structure-based virtual screening was limited to the NCI database, which, despite its extensive coverage, may exclude certain chemical classes with potential PknG inhibitory activity. Future studies should explore additional chemical libraries to identify a broader range of inhibitors. Furthermore, translating computational findings into

actionable drug discovery requires experimental validation. Wet lab investigations, such as enzyme inhibition assays and cell-based activity tests, are essential to confirm the identified hit's activity. Additionally, *in vivo* studies are necessary to evaluate the ADMET profile, therapeutic potential, and overall safety of the identified hit. Structural modifications to the lead candidate, chromene glycoside, or the implementation of various formulation and delivery strategies should also be explored to address its bioavailability limitations while preserving its inhibitory potency.These efforts are crucial to bridging the gap between computational predictions and clinical applications, ensuring the development of effective PknG inhibitors for tuberculosis treatment.

4 Conclusion

In conclusion, this study employed a comprehensive array of computational approaches to identify potential inhibitors targeting PknG of M.tb. Among the seven promising hits identified, chromene glycoside (hit 1) emerged as the most potent candidate due to its strong binding affinity, favorable interactions, and lower toxicity profile. DFT analysis further highlighted its superior electronic properties compared to the reference ligand. Molecular dynamics simulations confirmed the stability of the hit 1-PknG complex, reinforcing its potential as a lead compound. However, optimization of its oral bioavailability remains necessary to enhance its drug-like properties and therapeutic applicability.

Data availability statement

The original contributions presented in the study are included in the article/Supplementary Material, further inquiries can be directed to the corresponding authors.

Author contributions

MA: Conceptualization, Funding acquisition, Supervision, Writing–original draft, Writing–review and editing. TE: Formal Analysis, Methodology, Software, Writing–original draft, Writing–review and editing. MM: Formal Analysis, Investigation, Methodology, Writing–original draft, Writing–review and editing. AE: Investigation, Validation, Writing–original draft. JM: Investigation, Validation, Writing–review and editing. YA:

Formal Analysis, Investigation, Writing–review and editing. SH: Formal Analysis, Investigation, Writing–review and editing. SM: Formal Analysis, Investigation, Writing–original draft. HA: Validation, Writing–review and editing. MJA: Investigation, Validation, Writing–review and editing. MMA: Investigation, Writing–review and editing.

Funding

Conflict of interest

The authors declare that the research was conducted in the absence of any commercial or financial relationships that could be construed as a potential conflict of interest.

Generative AI statement

The author(s) declare that Generative AI was used in the creation of this manuscript. AI used for proofreading and style correction.

Publisher's note

All claims expressed in this article are solely those of the authors and do not necessarily represent those of their affiliated organizations, or those of the publisher, the editors and the reviewers. Any product that may be evaluated in this article, or claim that may be made by its manufacturer, is not guaranteed or endorsed by the publisher.

Supplementary material

The Supplementary Material for this article can be found online at: https://www.frontiersin.org/articles/10.3389/fchem.2025.1531152/full#supplementary-material

References

Ahmad, I., Kuznetsov, A. E., Pirzada, A. S., Alsharif, K. F., Daglia, M., and Khan, H. (2023). Computational pharmacology and computational chemistry of 4-hydroxyisoleucine: physicochemical, pharmacokinetic, and DFT-based approaches. *Front. Chem.* 11, 1145974. doi:10.3389/fchem.2023.1145974

Akinnuwesi, A., Egieyeh, S., and Cloete, R. (2023). State-of-the-art strategies to prioritize *Mycobacterium tuberculosis* drug targets for drug discovery using a subtractive genomics approach. *Front. Drug Discov.* 3. doi:10.3389/fddsv.2023.1254656

Alsehli, M. H., Seth, D.S., El-Gaby, M. S. A., Okasha, R. M., Hagar, M., Afifi, T. H., et al. (2021). DFT and in-silico investigations, along with in-vitro antitumor and antimicrobial assessments of pharmacological molecules. 1570–1794.

Amen, Y., Elsbaey, M., Othman, A., Sallam, M., and Shimizu, K. (2021). Naturally occurring chromone glycosides: sources, bioactivities, and spectroscopic features. *Molecules* 26 (24), 7646. doi:10.3390/molecules26247646

Amengor, C. D. K., Orman, E., Danquah, C. A., Ben, I. O., Biniyam, P. D., and Harley, B. K. (2022). Pyridine-N-Oxide alkaloids from allium stipitatum and their synthetic disulfide analogs as potential drug candidates against Mycobacterium tuberculosis: a molecular docking, QSBAR, and ADMET prediction approach. *Biomed. Res. Int.* 2022, 6261528. doi:10.1155/2022/6261528

Anand, N., Singh, P., Sharma, A., Tiwari, S., Singh, V., Singh, D. K., et al. (2012). Synthesis and evaluation of small libraries of triazolylmethoxy chalcones, flavanones and 2-aminopyrimidines as inhibitors of mycobacterial

FAS-II and PknG. *Bioorg Med. Chem.* 20 (17), 5150–5163. doi:10.1016/j.bmc. 2012.07.009

Arica-Sosa, A., Alcantara, R., Jimenez-Avalos, G., Zimic, M., Milon, P., and Quiliano, M. (2022). Identifying RO9021 as a potential inhibitor of PknG from Mycobacterium tuberculosis: combinative computational and *in vitro* studies. *ACS Omega* 7 (23), 20204–20218. doi:10.1021/acsomega.2c02093

Arnittali, M., Rissanou, A. N., and Harmandaris, V. (2019). Structure of biomolecules through molecular dynamics simulations. *Procedia Comput. Sci.* 156, 69–78. doi:10. 1016/j.procs.2019.08.181

Athar, M., Lone, M. Y., Khedkar, V. M., and Jha, P. C. (2016). Pharmacophore model prediction, 3D-QSAR and molecular docking studies on vinyl sulfones targeting Nrf2-mediated gene transcription intended for anti-Parkinson drug design. *J. Biomol. Struct. Dyn.* 34 (6), 1282–1297. doi:10.1080/07391102.2015.1077343

Azam, F., Eid, E. E. M., and Almutairi, A. (2021). "Targeting SARS-CoV-2 main protease by teicoplanin: a mechanistic insight by docking," in *MM/GBSA and molecular dynamics simulation*. 0022-2860 (Print).

Bagcchi, S. (2023). WHO's global tuberculosis report 2022. *Lancet Microbe* 4 (1), e20. doi:10.1016/s2666-5247(22)00359-7

Bloom, B. R. (2023). A half-century of research on tuberculosis: successes and challenges. *J. Exp. Med.* 220 (9), e20230859. doi:10.1084/jem.20230859

Bochevarov, A. D., Harder, E. D., Hughes, T., Greenwood, J. R., Braden, D. A., Philipp, D. M., et al. (2013). Jaguar: a high-performance quantum chemistry software program with strengths in life and materials sciences. *Int. J. Quantum Chem.* 113, 2110–2142. doi:10.1002/qua.24481

Bowers, K. J., Chow, E., Xu, H., Dror, R. O., Eastwood, M. P., Gregersen, B. A., et al. (2006). "Scalable algorithms for molecular dynamics simulations on commodity clusters," in *Proceedings of the 2006 ACM/IEEE conference on supercomputing*, 84–es.

Burkhanova, T. M., Krysantieva, A. I., Babashkina, M. G., Konyaeva, I. A., Monina, L. N., Goncharenko, A. N., et al. (2022). *In silico* analyses of betulin: DFT studies, corrosion inhibition properties, ADMET prediction, and molecular docking with a series of SARS-CoV-2 and monkeypox proteins. *Struct. Chem.* 34, 1545–1556. doi:10.1007/s11224-022-02079-8

Caballero, J., Morales-Bayuelo, A., and Navarro-Retamal, C. (2018). Mycobacterium tuberculosis serine/threonine protein kinases: structural information for the design of their specific ATP-competitive inhibitors. *J. Comput. Aided Mol. Des.* 32 (12), 1315–1336. doi:10.1007/s10822-018-0173-3

Capela, R., Félix, R., Clariano, M., Nunes, D., Perry, M. d.J., and Lopes, F. (2023). Target identification in anti-tuberculosis drug discovery. *Int. J. Mol. Sci.* 24 (13), 10482. doi:10.3390/ijms241310482

Chen, D., Ma, S., He, L., Yuan, P., She, Z., and Lu, Y. (2017). Sclerotiorin inhibits protein kinase G from *Mycobacterium tuberculosis* and impairs mycobacterial growth in macrophages. *Tuberculosis* 103, 37–43. doi:10.1016/j.tube.2017.01.001

Chen, D., Oezguen, N., Urvil, P., Ferguson, C., Dann, S., and Savidge, T. (2016). Regulation of protein-ligand binding affinity by hydrogen bond pairing. *Sci. Adv.* 2 (3), e1501240. doi:10.1126/sciadv.1501240

Cowley, S., Ko, M., Pick, N., Chow, R., Downing, K. J., Gordhan, B. G., et al. (2004). The *Mycobacterium tuberculosis* protein serine/threonine kinase PknG is linked to cellular glutamate/glutamine levels and is important for growth *in vivo*. *Mol. Microbiol.* 52 (6), 1691–1702. doi:10.1111/j.1365-2958.2004.04085.x

Dartois, V. A., and Rubin, E. J. (2022). Anti-tuberculosis treatment strategies and drug development: challenges and priorities. *Nat. Rev. Microbiol.* 20 (11), 685–701. doi:10. 1038/s41579-022-00731-y

Dighe, S. N., Tippana, M., van Akker, S., and Collet, T. A. (2020). Structure-based scaffold Repurposing toward the discovery of novel cholinesterase inhibitors. *ACS Omega* 5 (48), 30971–30979. doi:10.1021/acsomega.0c03848

Farhat, M., Cox, H., Ghanem, M., Denkinger, C. M., Rodrigues, C., Abd El Aziz, M. S., et al. (2024). Drug-resistant tuberculosis: a persistent global health concern. *Nat. Rev. Microbiol.* 22, 617–635. doi:10.1038/s41579-024-01025-1

Fernandes, G. F. S., Thompson, A. M., Castagnolo, D., Denny, W. A., and Dos Santos, J. L. (2022). Tuberculosis drug discovery: challenges and new horizons. *J. Med. Chem.* 65 (11), 7489–7531. doi:10.1021/acs.jmedchem.2c00227

Ferreira, L. L. G., and Andricopulo, A. D. (2019). ADMET modeling approaches in drug discovery. *Drug Discov. Today* 24 (5), 1157–1165. doi:10.1016/j.drudis.2019.03.015

Forrellad, M. A., Klepp, L. I., Gioffre, A., Sabio y Garcia, J., Morbidoni, H. R., de la Paz Santangelo, M., et al. (2013). Virulence factors of the *Mycobacterium tuberculosis* complex. *Virulence* 4 (1), 3–66. doi:10.4161/viru.22329

Friedrich, M. (2017). Tuberculosis update 2017. *Jama* 318 (23), 2287. doi:10.1001/jama.2017.18477

Friesner, R. A., Banks Jl Fau - Murphy, R. B., Murphy Rb Fau - Halgren, T. A., Halgren Ta Fau - Klicic, J. J., Klicic Jj Fau - Mainz, D. T., Mainz Dt Fau - Repasky, M. P., et al. (2004). Glide: a new approach for rapid, accurate docking and scoring. *Drug Discov. Today. Technol.* 1. 253, 260. doi:10.1016/j.ddtec.2004.11.008

Genheden, S., and Ryde, U. (2015). The MM/PBSA and MM/GBSA methods to estimate ligand-binding affinities. *Expert Opin. Drug Discov.* 10 (5), 449–461. doi:10. 1517/17460441.2015.1032936

Green, J. R., Mahalingaiah, P. K. S., Gopalakrishnan, S. M., Liguori, M. J., Mittelstadt, S. W., Blomme, E. A. G., et al. (2023). Off-target pharmacological activity at various kinases: potential functional and pathological side effects. *J. Pharmacol. Toxicol. Methods* 123, 107468. doi:10.1016/j.vascn.2023.107468

Guezane-Lakoud, S., Ferrah, M., Merabet-Khelassi, M., Touil, N., Toffano, M., and Aribi-Zouioueche, L. (2023). 2-Hydroxymethyl-18-crown-6 as an efficient organocatalyst for alpha-aminophosphonates synthesized under eco-friendly conditions, DFT, molecular docking and ADME/T studies. *J. Biomol. Struct. Dyn.*, 1–17. doi:10.1080/07391102.2023.2213336

Halgren, T. A., Murphy Rb Fau - Friesner, R. A., Friesner Ra Fau - Beard, H. S., Beard Hs Fau - Frye, L. L., Frye Ll Fau - Pollard, W. T., Pollard Wt Fau - Banks, J. L., et al. (2024). "Glide: a new approach for rapid, accurate docking and scoring. 2," in *Enrichment factors in database screening*. 0022-2623 (Print).

Hann, E., Malagu, K., Stott, A., and Vater, H. (2022). "Chapter Three - the importance of plasma protein and tissue binding in a drug discovery program to successfully deliver a preclinical candidate," in *Progress in medicinal chemistry*. Editors D. R. Witty, and B. Cox (Elsevier), 163–214.

Jacobson, M. P., Friesner Ra Fau - Xiang, Z., Xiang Z Fau - Honig, B., and Honig, B. (2002a). On the role of the crystal environment in determining protein side-chain conformations, 320, 597–608. doi:10.1016/s0022-2836(02)00470-9

Jacobson, M. P., Pincus Dl Fau - Rapp, C. S., Rapp Cs Fau - Day, T. J. F., Day Tj Fau - Honig, B., Honig B Fau - Shaw, D. E., Shaw De Fau - Friesner, R. A., et al. (2002b). *A hierarchical approach to all-atom protein loop prediction*, 1097–0134. (Electronic).

Kanehiro, Y., Tomioka, H., Pieters, J., Tatano, Y., Kim, H., Iizasa, H., et al. (2018). Identification of novel mycobacterial inhibitors against mycobacterial protein kinase G. *Front. Microbiol.* 9, 1517. doi:10.3389/fmicb.2018.01517

Kapısuz, Ö., Rudrapal, M., Gül, Ü. D., Rathod, S. S., Işık, M., Durgun, M., et al. (2024). Investigation of antibacterial and antifungal properties of benzene sulfonamide derivatives by experimental and computational studies. *Chem. Phys. Impact* 9, 100712. doi:10.1016/j.chphi.2024.100712

Khan, M. A., and Singh, S. K. (2023). Atom-based 3D-QSAR and DFT analysis of 5-substituted 2-acylaminothiazole derivatives as HIV-1 latency-reversing agents. *J. Biomol. Struct. Dyn.* 41 (14), 6759–6774. doi:10.1080/07391102.2022.2112078

Khan, M. Z., Bhaskar, A., Upadhyay, S., Kumari, P., Rajmani, R. S., Jain, P., et al. (2017). Protein kinase G confers survival advantage to *Mycobacterium tuberculosis* during latency-like conditions. *J. Biol. Chem.* 292 (39), 16093–16108. doi:10.1074/jbc. M117.797563

Khan, M. Z., Kaur, P., and Nandicoori, V. K. (2018). Targeting the messengers: serine/threonine protein kinases as potential targets for antimycobacterial drug development. *IUBMB Life* 70 (9), 889–904. doi:10.1002/iub.1871

Kidwai, S., Bouzeyen, R., Chakraborti, S., Khare, N., Das, S., Priya Gosain, T., et al. (2019). NU-6027 inhibits growth of *Mycobacterium tuberculosis* by targeting protein kinase D and protein kinase G. *Antimicrob. Agents Chemother.* 63 (9), 009966–e1019. doi:10.1128/AAC.00996-19

Kohn, W., and Sham, L. J. (1965). Quantum density oscillations in an inhomogeneous electron gas. *Phys. Rev.* 137 (6A), A1697–A1705. doi:10.1103/PhysRev.137.A1697

Koul, A., Choidas, A., Tyagi, A. K., Drlica, K., Singh, Y., and Ullrich, A. (2001). *Serine/threonine protein kinases PknF and PknG of Mycobacterium tuberculosis: characterization and localization*, 1350–0872. (Print).

Kushwaha, N., Sahu, A., Mishra, J., Soni, A., and Dorwal, D. (2023). An insight on the prospect of quinazoline and quinazolinone derivatives as anti-tubercular agents. *Curr. Org. Synth.* 20 (8), 838–869. doi:10.2174/1570179420666230316094435

Lamothe, S. M., Guo, J., Li, W., Yang, T., and Zhang, S. (2016). The human ether-a-go-go-related gene (hERG) potassium channel represents an unusual target for protease-mediated damage. *J. Biol. Chem.* 291 (39), 20387–20401. doi:10.1074/jbc. M116.743138

Liu, A., Seal, S., Yang, H., and Bender, A. (2023). Using chemical and biological data to predict drug toxicity. *SLAS Discov.* 28 (3), 53–64. doi:10.1016/j.slasd.2022.12.003

Lone, M. Y., Kumar, S. P., Athar, M., and Jha, P. C. (2018). Exploration of *Mycobacterium tuberculosis* structural proteome: an in-silico approach. *J. Theor. Biol.* 439, 14–23. doi:10.1016/j.jtbi.2017.11.021

Macalino, S. J. Y., Billones, J. B., Organo, V. G., and Carrillo, M. C. O. (2020). *In silico* strategies in tuberculosis drug discovery. *Molecules* 25 (3), 665. doi:10.3390/molecules25030665

Maestro, S. (2023). New York, NY: LLC.

Ntie-Kang, F. (2013). *An in silico evaluation of the ADMET profile of the StreptomeDB database*, 2193–1801. (Print).

O'Hare, H. M., Duran, R., Cervenansky, C., Bellinzoni, M., Wehenkel, A. M., Pritsch, O., et al. (2008). Regulation of glutamate metabolism by protein kinases in mycobacteria. *Mol. Microbiol.* 70 (6), 1408–1423. doi:10.1111/j.1365-2958.2008. 06489.x

QikProp, S. (2023). New York, NY: LLC.

Rababi, D., and Nag, A. (2023). Evaluation of therapeutic potentials of selected phytochemicals against Nipah virus, a multi-dimensional *in silico* study. *3 Biotech.* 13 (6), 174. doi:10.1007/s13205-023-03595-y

Rana, K. M., Maowa, J., Alam, A., Dey, S., Hosen, A., Hasan, I., et al. (2021). *In silico* DFT study, molecular docking, and ADMET predictions of cytidine analogs with antimicrobial and anticancer properties. *Silico Pharmacol.* 9 (1), 42. doi:10.1007/s40203-021-00102-0

Rock, J. (2019). Tuberculosis drug discovery in the CRISPR era. *PLoS Pathog.* 15 (9), e1007975. doi:10.1371/journal.ppat.1007975

Rock, R. B., Olin, M., Baker, C. A., Molitor, T. W., and Peterson, P. K. (2008). Central nervous system tuberculosis: pathogenesis and clinical aspects. *Clin. Microbiol. Rev.* 21 (2), 243–261. table of contents. doi:10.1128/CMR.00042-07

Santiago-Silva, K. M., Camargo, P., Felix da Silva Gomes, G., Sotero, A. P., Orsato, A., Perez, C. C., et al. (2023). *In silico* approach identified benzoylguanidines as SARS-CoV-2 main protease (M(pro)) potential inhibitors. *J. Biomol. Struct. Dyn.* 41 (16), 7686–7699. doi:10.1080/07391102.2022.2123396

Sastry, G. M., Adzhigirey M Fau - Day, T., Day T Fau - Annabhimoju, R., Annabhimoju R Fau - Sherman, W., and Sherman, W. (2013). *Protein and ligand preparation: parameters, protocols, and influence on virtual screening enrichments*, 1573–4951. (Electronic)).

Scherr, N., Honnappa, S., Kunz, G., Mueller, P., Jayachandran, R., Winkler, F., et al. (2007). Structural basis for the specific inhibition of protein kinase G, a virulence factor of *Mycobacterium tuberculosis*. *Proc. Natl. Acad. Sci.* 104 (29), 12151–12156. doi:10.1073/pnas.0702842104

Schrödinger Release, S. (2023). New York, NY: LLC.

Simmons, J. D., Stein, C. M., Seshadri, C., Campo, M., Alter, G., Fortune, S., et al. (2018). Immunological mechanisms of human resistance to persistent Mycobacterium tuberculosis infection. *Nat. Rev. Immunol.* 18 (9), 575–589. doi:10.1038/s41577-018-0025-3

Singh, N., Tiwari, S., Srivastava, K. K., and Siddiqi, M. I. (2015). Identification of novel inhibitors of *Mycobacterium tuberculosis* PknG using pharmacophore based virtual screening, docking, molecular dynamics simulation, and their biological evaluation. *J. Chem. Inf. Model* 55 (6), 1120–1129. doi:10.1021/acs.jcim.5b00150

Sotgiu, G., Centis, R., D'Ambrosio, L., and Migliori, G. B. (2015). Tuberculosis treatment and drug regimens. *Cold Spring Harb. Perspect. Med.* 5 (5), a017822. doi:10.1101/cshperspect.a017822

Stefaniak, M., and Olszewska, B. (2021). 1, 5-Benzoxazepines as a unique and potent scaffold for activity drugs: a review. *Arch. Pharm.* 354 (12), 2100224. doi:10.1002/ardp.202100224

Sudarshan, K., and Aidhen, I. S. (2017). Convenient synthesis of 3-glycosylated isocoumarins. *Eur. J. Org. Chem.* 2017 (1), 34–38. doi:10.1002/ejoc.201601264

Sudarshan, K., Yarlagadda, S., and Sengupta, S. (2024). Recent advances in the synthesis of diarylheptanoids. *Chem. Asian J.* 19 (15), e202400380. doi:10.1002/asia.202400380

Swain, S. P., Gupta, S., Das, N., Franca, T. C. C., Goncalves, A. D. S., Ramalho, T. C., et al. (2022). Flavanones: a potential natural inhibitor of the ATP binding site of PknG of *Mycobacterium tuberculosis*. *J. Biomol. Struct. Dyn.* 40 (22), 11885–11899. doi:10.1080/07391102.2021.1965913

Teneva, Y., Simeonova, R., Valcheva, V., and Angelova, V. T. (2023). Recent advances in anti-tuberculosis drug discovery based on hydrazide-hydrazone and thiadiazole derivatives targeting InhA. *Pharm. (Basel)* 16 (4), 484. doi:10.3390/ph16040484

Vrbanac, J., and Slauter, R. (2017). "Chapter 3 - ADME in drug discovery," in *A comprehensive guide to toxicology in nonclinical drug development*. Editor A. S. Faqi Second Edition (Boston: Academic Press), 39–67.

Wang, E., Sun, H.A.-O., Wang, J.A.-O., Wang, Z., Liu, H.A.-O., Zhang, J.A.-O., et al. (2019). *End-point binding free energy calculation with MM/PBSA and MM/GBSA: strategies and applications in drug design*, 1520–6890. (Electronic)).

Wei, X., Yue, L., Zhao, B., Jiang, N., Lei, H., and Zhai, X. (2024). Recent advances and challenges of revolutionizing drug-resistant tuberculosis treatment. *Eur. J. Med. Chem.* 277, 116785. doi:10.1016/j.ejmech.2024.116785

Who, G. (2020). Global tuberculosis report 2020. *Glob. Tuberc. Rep.*, 2020.

Xiong, G., Wu, Z., Yi, J., Fu, L., Yang, Z., Hsieh, C., et al. (2021). ADMETlab 2.0: an integrated online platform for accurate and comprehensive predictions of ADMET properties. *Nucleic Acids Res.* 49 (W1), W5–W14. doi:10.1093/nar/gkab255

Yoshiyama, T., Takaki, A., Aono, A., Mitarai, S., Okumura, M., Ohta, K., et al. (2021). Multidrug resistant tuberculosis with simultaneously acquired drug resistance to bedaquiline and Delamanid. *Clin. Infect. Dis.* 73 (12), 2329–2331. doi:10.1093/cid/ciaa1064

Zhou, T., Huang D Fau - Caflisch, A., and Caflisch, A. (2010). *Quantum mechanical methods for drug design*, 1873–4294. (Electronic)).

Frontiers | Frontiers in Chemistry

Healing and leishmanicidal activity of *Zanthoxylum rhoifolium* Lam.

Juliana Correa-Barbosa[1,2], Heliton Patrick Cordovil Brígido[3,4], Bibiana Franzen Matte[5], Paloma Santos De Campos[5], Marcelo Lazzaron Lamers[5], Daniele Ferreira Sodré[6], Pedro Henrique Costa Nascimento[6], Gleison Gonçalves Ferreira[8], Valdicley Vieira Vale[1], Andrey Moacir do Rosário Marinho[7], José Edson De Sousa Siqueira[7], Márlia Regina Coelho-Ferreira[8], Marta Chagas Monteiro[2,9,10,11] and Maria Fâni Dolabela[1,2]*

[1]Postgraduate Pharmaceutical Innovation Program, Institute of Health Sciences - Federal University of Pará (UFPA) Belém, Brazil, [2]Postgraduate Pharmaceutical Sciences Program, Institute of Health Sciences - Federal University of Pará (UFPA), Belém, Brazil, [3]National Council for Scientific and Technological Development (CNPq), Federal University of Pará, Belém, Brazil, [4]Biotechnology and Biodiversity Postgraduate Program (BIONORTE), Federal University of Pará, Belém, Brazil, [5]Faculty of Dentistry, Institute of Health Sciences - Federal University of Rio Grande do Sul (UFRGS), Porto Alegre, Brazil, [6]Faculty of Pharmacy, Institute of Health Sciences - Federal University of Pará (UFPA), Belém, Brazil, [7]Postgraduate Program in Chemistry, Institute of Exact and Natural Sciences - Federal University of Pará (UFPA), Belém, Brazil, [8]Botany Coordination, Museu Paraense Emílio Goeldi, Ministério da Ciência, Tecnologia, Inovação e Comunicações, Belém, Pará, Brazil, [9]Coordinator of the National Institute of Science, Technology and Innovation INCT-PROBIAM Pharmaceuticals Amazonia, Federal University of Pará, Belém, Brazil, [10]Postgraduate Neuroscience and Cellular Biology Program, Federal University of Pará, Belém, Brazil, [11]Postgraduate Pharmacology and Biochemistry Program, Federal University of Pará, Belém, Brazil

Zanthoxylum rhoifolium is used in folk medicine as an antiparasitic agent. Therefore, this study evaluated the phytochemical aspects and biological activities of *Z. rhoifolium*. For this, the ethanolic extract (EE) was obtained by macerating the peel with ethanol and subjected to acid-base partition to obtain the neutral fractions (FN) and alkaloid fractions (FA). These samples were analyzed using chromatography techniques. From this, a substance was isolated from FN and identified by nuclear magnetic resonance. For biological activity, strains of *Leishmania amazonensis* were used for leishmanicidal activity. For cytotoxicity, cell viability methods were used and finally, the selectivity index (SI) was determined. Cell proliferation assay (SRB method) was also performed, such as a wound healing assay. After analysis, it was inferred that in chromatography, EE, FN and FA presented peaks suggestive of alkaloids, and the alkaloid chelerythrine was isolated from FN. In antiparasitic activity against promastigotes, EE, FN and FA were active. Against amastigotes, the infection inhibition index was dose dependent for EE and FN. In the cytotoxicity test (J774), EE and FN showed moderate cytotoxicity, while FA demonstrated cytotoxicity. In VERO strain, EE and FA showed moderate cytotoxicity, while FN was not cytotoxic. Finally, considering the SI, EE, FN and FA showed high selectivity. Furthermore, EE and FN increased cell proliferation and FN promoted a healing effect. Thus, it is highlighted that the specie *Z. rhoifolium* presented antileishmanial activity and selectivity for the parasite, and its FN presented healing potential.

KEYWORDS

alkaloids, Rutaceae, *Zanthoxylum rhoifolium*, *Leishmania amazonensis*, cytotoxicity

1 Introduction

It is estimated that 350 million people are at risk of contracting leishmaniasis, with approximately 20,000 to 30,000 deaths annually (Paho, 2023). Leishmaniasis is classified according to clinical manifestations, which differ among cutaneous, visceral, and tegumentary manifestations, with the latter being subdivided into mucocutaneous, cutaneous, and diffuse cutaneous manifestations (PAHO, 2023). The species *Leishmania amazonensis*, the causative agent of tegumentary leishmaniasis, can cause wounds that are difficult to heal (Bortoleti et al., 2022). This process involves interactions between cells and various messenger systems, such as cytokines and growth factors, and is divided into 3 phases: inflammatory, proliferative, and remodeling (Ramos et al., 2020).

The treatment of leishmaniases is carried out with pentavalent antimonials (Sb 5+) (Herwaldt, 1999; Rath et al., 2003), amphotericin B, and pentamidines. These drugs are extremely toxic (Mohamed et al., 2023), and there are reports of parasite resistance to these drugs (Domagalska et al., 2023). Most of these drugs are used parenterally, and their treatment is costly. Faced with related problems, the search for therapeutic alternatives has become urgent (Zahra et al., 2023).

Medicinal plants, especially those containing alkaloids, may be promising as leishmanicidal (Veiga et al., 2020; Brígido et al., 2024). *Zanthoxylum rhoifolium* (Rutaceae) is a species that is used as a healing agent and contains alkaloids (Ribeiro et al., 2017; Castillo et al., 2014). An *in vitro* study evaluated the leishmanicidal activity of the ethanolic extract obtained from the bark of *Z. rhoifolium* against macrophages infected with *L. amazonensis* promastigotes, with the best activity occurring at 72h (IC_{50}: 9.57 µg/mL) (Melo-Neto et al., 2016). The hydroalcoholic extract of *Z. rhoifolium* leaves showed moderate activity against strains of *L. amazonensis* (IC_{50}: 143 µg/mL) (Moura-Costa et al., 2012). The hexane fraction showed *in vitro* activity against macrophages infected with *L. amazonensis* promastigotes and was more promising at 72h (IC_{50}: 7.96 µg/mL) (Melo-Neto et al., 2016).

There are still no studies that have evaluated the wound healing activity of this species. However, an *in vivo* study demonstrated that the oil from *Z. bungeanum* seeds increased the proportion of wound healing in a dose-dependent manner and significantly reduced the wound debridement time and the time for complete closure, with the debridement time being shorter than that in the positive control (Li et al., 2017). The authors also revealed a significant increase in the expression of type III collagen protein in wounds (Li et al., 2017). Due to this, the present study describes the antipromastigote and antiamastigote activities and the wound healing potential of ethanolic extracts obtained from *Z. rhoifolium* bark (EE), neutral fractions (FN), and alkaloids (FA). Additionally, the cytotoxicity and possible mechanism of action of the alkaloids isolated from the plant were evaluated.

2 Methods

2.1 Plant material, processing and chemical studies

The bark of the plant species *Zanthoxylum rhoifolium* was collected and identified by researchers from the Museu Paraense Emílio Goeldi, and its voucher specimen was deposited in the João Murça Herbarium of the same museum, with the identification number MG 224385. The bark powder of *Z. rhoifolium* was subjected to exhaustive maceration with ethanol (ratio of 1:10). The ethanolic solution was filtered and concentrated in a rotary evaporator under reduced pressure until a residue was obtained, resulting in the ethanolic extract (EE) of *Z. rhoifolium*. Fractionation of the EE was carried out to obtain the neutral fraction (FN) and alkaloidal fraction (FA) through acid–base partitioning.

Mass spectra of the samples were obtained using MAXIS 3G Bruker Daltonics equipment. A reverse-phase C18 column (250 × 4.6 mm) with a 5 µm particle size was used, with UV detection from 200 to 400 nm, a flow rate of 1.0 mL/min, and a column oven temperature of 40°C. The gradient employed consisted of 0.1% formic acid in acetonitrile and 0.1% formic acid in ultrapure water. Mass spectra were obtained using an electrospray ionization (ESI+) system with a capillary voltage of 4,500 and a cone voltage of 500 eV.

The FN were subjected to preparative thin-layer chromatography (TLC) fractionation (dimensions: 0.75 mm) using silica gel as the stationary phase and a dichloromethane: methanol (95:5) mobile phase. The substance was identified using bidimensional methods (COSY and HMBC) and nuclear magnetic resonance spectroscopy (^{1}H NMR 400 MHz and ^{13}C at 100 MHz).

Chelerythrine: ^{1}H NMR data revealed signals characteristic of alkaloids, with the main signals being a *s* at 2.73 ppm, a *s* at 3.92 ppm, a *s* at 3.93 ppm, and a *s* at 6.05 ppm ^{13}C NMR detected the presence of 17 signals, most of which refer to the carbons of the aromatic rings (105.6; 149.2; 149.8; 101.4; 139.5; 87.7; 126.4; 153.7; 114.7; 120.2; 121.0; 124.9; 132.8 ppm), however, the presence of other signals stands out at 56.7 ppm (OCH_3), 62.1 ppm (OCH_3), 41.1 ppm (CH_3) and 102.8 ppm (CH_2 dioxolo). The other 4 carbons in the structure had their displacements defined by HMBC. HMBC: key correlations between H-12 (7.51 ppm) and C-4a (128.0 ppm) and C-10b (123.9 ppm). H-1 (7.15 ppm) with C-4a (128.0 ppm). H-6 (5.55 ppm) with C-6a (126.41 ppm, J2), with C-7 (148.0 ppm), and with the C-5 of the methyl linked to nitrogen (41.13 ppm). H-9 (7.19 ppm) with C-7 (148.0 ppm) and with C-10a (126.3 ppm). The H of the methyl group linked to nitrogen (C-5) at 2.73 ppm, with C-4b (139.55 ppm) with a two-bond distance (J2) and with C-6 (87.67 ppm) with a two-bond distance (J2). The H of the methoxy group (C-7) at 3.92 ppm, with C-7 (148.0 ppm) showing a two-bond distance (J2). The H of the methoxy group (C-8) at 3.93 ppm, with C-8 (153.68 ppm) showing a two-bond distance (J2). COSY: two couplings, one between hydrogen (H-9) and hydrogen (H-10) and the other between hydrogen (H-11) and hydrogen (H-12) (Supplementary Material).

2.2 Leishmanicidal activity

2.2.1 Antipromastigote

Strains of *Leishmania* (L.) *amazonensis*, which was isolated from a human patient originating from the municipality of Ulianópolis in the state of Pará, were used and were provided by the Evandro Chagas Institute (IEC, Ananindeua/Pará) under registration number MHOM/BR/2009/M26361. The promastigotes were cultivated in Roswell Park Memorial Institute (RPMI) medium.

The test was performed in the logarithmic phase using a suspension of 5×10^6 parasites/100 µL of culture. The samples were tested at doses ranging from 200 to 3,125 µg/mL. As a negative control, culture medium solution and parasite suspension were used. As a positive control, amphotericin B was used. Subsequently, the plate was incubated at 26°C for 24 h. After the incubation period, 10 µL of 3-(4,5-dimethylthiazol-2-yl)-2,5-diphenyltetrazolium bromide (MTT; 5 mg/mL) was added to each well. After 4 h, 10 µL of dimethyl sulfoxide (DMSO) was added, and the optical density (OD) of the samples was measured using a multiplate reader at a wavelength of 490 nm. The percentage of parasites was calculated using the formula adapted from Ngure et al. (2009). Samples were considered very active when the IC_{50} was less than 10 µg/mL (Mota et al., 2015).

2.2.2 Antiamastigote

For the amastigote assay, macrophages of the RAW 264.7 lineage (from the cell bank in Rio de Janeiro) were adhered to circular coverslips (13 mm; 5×10^6 cells) previously inserted into 24-well plates, infected with stationary-phase promastigotes of *L. amazonensis* (2×10^6 parasites), and incubated for 4 h in a 37°C oven with a 5% CO_2 atmosphere (Silva, 2005). After incubation, the contents of each well were aspirated, and medium containing different concentrations (200 µg/mL, 100 µg/mL, and 50 µg/mL) of EE and FN was added. The negative control consisted of infected macrophages with culture medium without the drug. The positive control consisted of amphotericin B, followed by incubation for 24 h in a 37°C oven with 5% CO_2. The tests were performed in triplicate. Subsequently, the coverslips were stained with Giemsa stain. The coverslips were observed under a light microscope with a ×40 objective and immersion (×100), where the number of amastigotes per 100 macrophages on each coverslip was determined. The anti-amastigote activity was evaluated using the equation according to Silva (Silva, 2005).

2.3 Cell viability and selectivity index

For this assay, MTT and the VERO (from the cell bank in Rio de Janeiro) cell line were used, following the methodology described by Mosmann (1983), and were seeded at 8×10^3 cells/mL. After 24 h, the cells were treated with seven decreasing concentrations of EE, FN, and FA (500 µg/mL to 7.812 µg/mL). After 24 h of treatment, 10 µL of MTT (5 mg/mL) was added. After 4 h, 100 µL of dimethyl sulfoxide (DMSO) was added for complete dissolution of the crystals. The absorbances of the wells were read in a microplate scanning spectrophotometer at a wavelength of 490 nm. The values of the 50% cytotoxic concentration (CC_{50}) were calculated using the Galucio (2018) equation. The CC_{50} was determined by linear regression (GraphPad Prism version 6.0 software) and classified as cytotoxic, moderately cytotoxic, or noncytotoxic (Silva-Silva, 2016). The selectivity index was determined by the equation adapted from Reimão (2009). An SI greater than 10 indicates that the compound under study exhibits greater toxicity to the parasite than to the cell line. An SI less than 10 indicates a compound with greater toxicity to the cell line than to the parasite.

2.4 Proliferation and wound healing assays

The SRB method was used in HaCaT (from the cell bank in Rio de Janeiro) cells and primary fibroblasts (UFRGS Ethics Committee CAE#59124916.6.0000.5327) at a concentration of 4,000 cells/well. After 24 h, they were treated with different concentrations of EE, FN, and FA (15–700 µg/mL) and then incubated again for 24 h. Subsequently, the cell monolayers were fixed with 10% (w/v) trichloroacetic acid and stained with SRB dye for 30 min. The dye bound to the protein was dissolved in 10 mM Tris base solution for determination of the optical density (OD) at 560 nm using a microplate reader (adapted from Virchai and Kirtikara, 2006).

For the wound healing assay (cell migration), the HaCaT cell line was used. Cells were seeded in 6-well plates and incubated with complete medium at 37°C and 5% CO_2. When cellular confluence was observed, the monolayer cells were horizontally and vertically scraped with sterile P200 pipette tips to form a cross. Debris was removed by washing with PBS. Cells were treated with EE, FN, or FA at concentrations of 15 or 30 µg/mL. Untreated cells were used as a negative control, and cells treated with solvent (500 µg/mL) were used as a solvent control. The induced scratch representing the wound was photographed at 0h using an inverted phase microscope (Axio Observer Z1, Zeiss, Göttingen, Germany) at ×10 magnification before incubation with treatment. After 12, 24, 36, 48, 60, and 72 h of incubation, new sets of images were taken. To determine the migration rate, the images were analyzed using ImageJ software, and the percentage of the closed area was measured and compared to the value obtained at 0h. An increase in the percentage of closed areas indicated cell migration. Analysis of variance (ANOVA) followed by Tukey's *post hoc* test was performed to verify differences between groups. The calculation used to determine the % wound closure is represented below:

The % of wound closure was greater than 100 = 12h × 100/0 h.

At 12 h, the percentage of wound closure was greater than 0 = 100.

These calculations were carried out individually for 12, 24, 36, 48, 60 and 72h of treatment.

2.5 Molecular docking of the chelerythrine alkaloid

The alkaloid cheleritrina was drawn in MarvinSketch™ and optimized in Avogrado™ to its most stable conformation, applying the MMFF94 force field. The enzymes leishmanolysin (1LML) and trypanothione reductase (TR; 6ER5) were obtained from the public domain RCSB PDB (https://www.rcsb.org/) and optimized using the APBS server (http://server.poissonboltzmann.org/), where charges were added, polar hydrogens were included, and water and cocrystallized solvents were removed from the enzymes.

Molecular docking was performed using the SwissDock server (http://www.swissdock.ch/docking), which utilizes multiobjective scoring constructed from the CHARMM22 force field and the FACTS solvation model, divided into four steps. The server allows the identification of the most favorable clusters through multivariable calculations, which are presented through the discrimination of the binding energy (ΔG) (Haberthür and Cafisch, 2008; Grosdidier et al., 2011). For the enzyme 1LML,
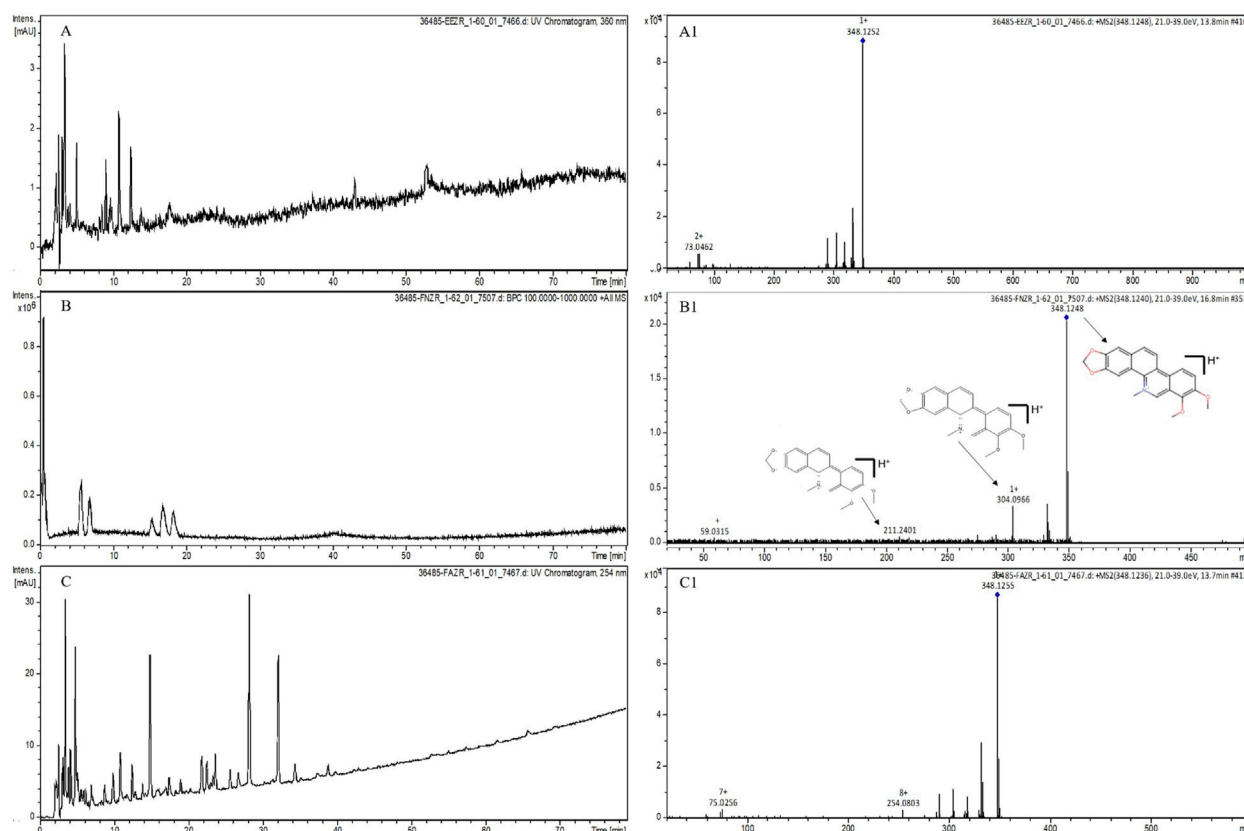
FIGURE 1
Liquid chromatography of EE, FN and FA of *Zanthoxylum rhoifolium* and suggestive mass spectra of the alkaloid chelerythrine. Conditions: system obtained by an HPLC MS C18 column (5 μm, 250 x 4.6 mm); mobile phase composed of 0.1% formic acid in water **(A)** and 0.1% formic acid in acetonitrile **(B)** O min. 80% A and 20% B, 80 min. 20% A and 80% B; flow rate 1.0 mL/min; temp. 40°C ESI+ ionization voltage with capillary at 4500 eV; cone voltage at 500 eV; reading at a wavelength of 360 nm. Legend: **(A)** Ethanol extract (EE) at 360 nm; **(B)** Neutral fraction (FN) in lull-scan mode; **(C)** Alkaloid fraction (FA) at 254 nm; A1: Mass spectrum for a retention time of 13.8 min in EE; 81: Mass spectrum for a retention time of 16.8 min in FN; C1: Mass spectrum for a retention time of 13.7 min in FA.

which does not contain a cocrystallized inhibitor, a grid box with dimensions of 35 × 35 × 35 (xyz) centered on the Zn in the active site (Mercado-Camargo et al., 2020) was created. For the establishment of the RMSD, a consensus was used where Cheleritrina was subjected to 25 distinct anchorings, and these positions were overlapped, as indicated by the standard deviation. For the enzyme 6ER5, the grid box was established by the inhibitor (2-(diethylamino)ethyl 4-((3-(4-nitrophenyl)-3-oxopropyl)amino) benzoate), from which the following coordinates were extracted: X, 5.986600; Y, −31.853867; and Z, 16.029433. Additionally, redocking was established using the same grid box (Turcano et al., 2018). Amphotericin B was used as the standard drug for docking.

3 Results

3.1 Chemical studies

The EE, FN, and FA were subjected to analysis by thin-layer chromatography (TLC) and presented bands suggestive of alkaloids. LC–MS analyses were carried out to identify the possible alkaloids present in EE, FN, and FA. According to the EE chromatograms and mass spectra, the presence of 9 alkaloids (magnoflorine, laurifoline, magnocurarine, isomagnocurarine, avicine, sanguinarine, chelerythrine, nitidine e oxyavicine) is suggested. Despite differences in retention time (tR) compared to that of EE, similar mass spectra were observed in the chromatogram of FN, and the presence of 7 alkaloids (magnoflorine, laurifoline, avicine, sanguinarine, chelerythrine, nitidine e oxyavicine) previously suggested in EE was suggested. Alkaloids similar to those in EE were found in FA. The presence of alkaloids was suggested by mass spectrometry described in the methodology. Among the alkaloids suggested in the samples, chelerythrine, an alkaloid with a mass of 348 g/mol, was notable (Figure 1). The FN underwent fractionation, and all analyses performed by spectroscopic methods confirmed that the isolated substance was a chelerythrine alkaloid (Figure 2), confirming the mass spectrometry findings.

3.2 Leishmanicidal activity and cytotoxicity

The specie demonstrated activity against the promastigote forms of *Leishmania amazonensis*, with IC_{50} values of 1.3 μg/mL, 1.0 μg/

FIGURE 2
Structure of the benzonanthridine alkaloid chelerythrine, which was isolated from the subtraction obtained from the neutral fraction (FN) of *Zanthoxylum rhoifolium*.

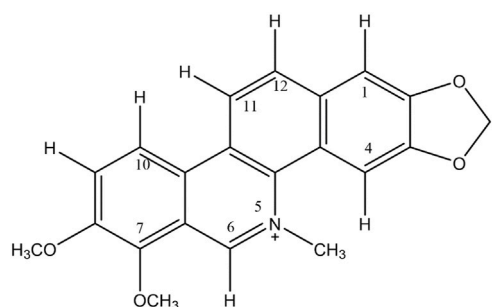TABLE 2 Evaluation of the antiamastigote activity of ethanolic extract (EE) and neutral fraction (FN) in macrophages (RAW 264.7) infected with amastigotes of *Leishmania amazonensis*.

Samples	Inhibition Index (%)/ Concentrations (mg/mL)		
	200	100	50
EE	40 ± 4.3	25.5 ± 2.1	27 ± 7.0
FN	50 ± 5.6	38 ± 1.4	31.7 ± 3.1
	10	5	2.5
Amphotericin B	93 ± 1.5	85 ± 5.0	92.5 ± 2.1

Legend: Ethanolic extract (EE) and Neutral fraction (FN); n = 3.

mL, and 0.9 µg/mL for EE, FN, and FA, respectively (Table 1). Both EE and FA exhibited moderate toxicity to the VERO cell line, while FN showed considerably lower cytotoxic potential (Table 1). Only EE and FN were subjected to investigation of antiamastigote activity, with more significant inhibition indices observed at a concentration of 200 µg/mL, reaching 40% for EE and 50% for FN (Table 2; Figure 3).

3.3 Proliferative and wound healing effects

The proliferative effect of EE, FN, and FA was evaluated on a keratinocyte cell line (HaCaT), where an increase in proliferation was observed at lower concentrations and an inhibitory effect at higher concentrations (Figure 4). Regarding fibroblasts, a similar proliferative effect to that of the control was observed at lower concentrations. However, for the first time pronounced antiproliferative activity was observed, especially at higher concentrations (500 and 700 µg/mL).

The wound healing potential of EE, FN, and FA was evaluated using a HaCaT cell migration model at 2 concentrations (15 and 30 µg/mL) of each sample, which showed increased proliferation in the previous assay. For EE and FN, wound closure was time dependent, with pronounced closure observed after 36 h of treatment with EE (15 µg/mL) and FN (15 and 30 µg/mL) (Figure 5).

3.4 Molecular docking of chelerythrin

The chelerythrine alkaloid exhibited favorable binding to a leishmanolysin (gp63) with an affinity of −10.17 kcal/mol (total energy: −35.007). Its active site includes the amino acids HIS264, GLU265, HIS268, HIS334, and MET345, along with a zinc atom. Chelerythrine formed two bonds with the amino acid HIS265: one hydrogen bond with a distance of 2.86 Å and one electrostatic bond with a distance of 3.48 Å. Additionally, it formed other hydrogen bonds with ALA227 (2.68 Å) and ALA349 (2.71 Å) and hydrophobic interactions with the residues TRP226 (5.98 Å) and VAL223 (5.10 Å). Upon binding to the pocket, chelerythrine established other interactions, such as van der Waals forces, but did not bind to the other residues belonging to the active site, making it impossible to establish the distance of these interactions. Amphotericin B, used as a control drug, primarily interacted with the GLU220 and GLU265 residues, as well as the zinc atom (Table 3; Figure 6).

When analyzing the coupling of chelerythrine with TR, we obtained a binding affinity of −7.35 kcal/mol (total energy: −13.562), where we observed mainly hydrogen and hydrophobic bonds. The majority of bonds are hydrogen bonds, with bonds to residues ARG85, LEU88, LYS211 and MET70, with distances ranging from 2.22 to 3.09 Å, with chelerythrine forming two bonds with each of these residues. Hydrophobic bonds occur with the ARG74, ARG85 and ILE73 residues (Table 3; Figure 6).

TABLE 1 Antipromastigote activity, cytotoxicity and selectivity index of Z. *rhoifolium*.

Samples	Antipromastigote		VERO	SI
	IC$_{50}$ (µg/mL) ±SD	Interpretation	IC$_{50}$ (µg/mL)	
EE	1.3 ± 0.2	MA	330.6 ± 0.8	254
FN	1.0 ± 0.4	MA	831.9 ± 0.6	832
FA	0.9 ± 0.2	MA	111.7 ± 0.8	124
Amphotericin B	0.1 ± 0.0	MA	ND	ND

Legend: IC$_{50}$- Concentration Inhibitory 50%; EE, Ethanol Extract; FN, Neutral Fraction; FA, Alkaloid Fraction; VERO, Normal Cells of African Green Monkey Kidney; ND, Not Determined; MA, Very Active; n = 3.
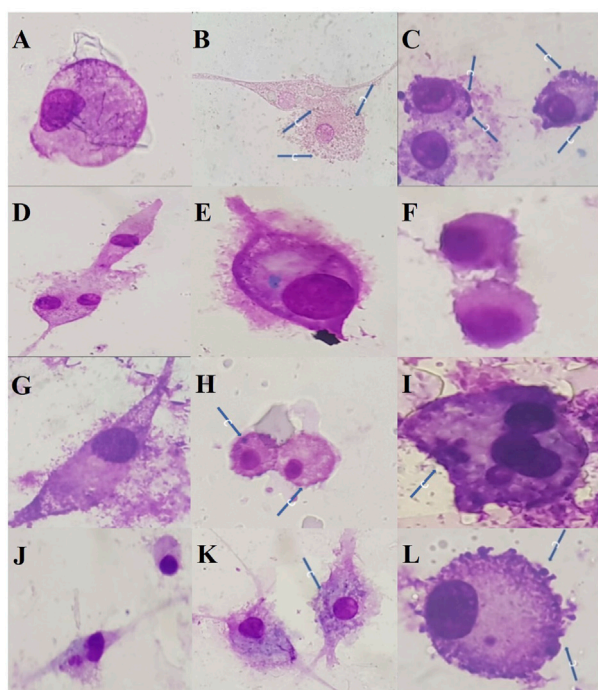
FIGURE 3
Antiamastigote (*L. amazonensis*) activity of the ethanolic extract
(EE) and neutral fraction (FN) obtained from the bark of *Zanthoxylum
rhoifolium*. Legend: Reading in MO, 40X magnification: **(A)**:
Uninfected macrophage control; **(B)**: Solvent control; **(C)**:
Solvent control; **(D)**: Amphotericin B - 10 μg/mL; **(E)**: Amphotericin B -
5 μg/mL; **(F)**: Amphotericin B - 2.5 μg/mL; **(G)**: EE - 200 μg/mL; **(H)**: EE
- 100 μg/mL; **(I)**: EE - 50 μg/mL; **(J)**: FN- 200 μg/mL; **(K)**: FN - 100 μg/
mL; **(L)**: FN - 50 μg/mL. Arrows indicate the presence of amastigotes.

4 Discussion

Chemical studies of EE, FN, and FA have demonstrated the
presence of alkaloids, including those with indolic,
benzophenanthridine, and furoquinoline moieties (Wei et al.,
2021; Azonsivo et al., 2023). Additionally, alkaloids such as
magnoflorine (Zanon, 2010), avicine, characterized by ^{1}H and ^{13}C

NMR analysis (Jullian et al., 2006; Tavares et al., 2014),
chelerythrine, nitidine and oxyavicin were isolated from *Z.
rhoifolium*, with structural elucidation by mass spectrometry and
^{1}H NMR (Jullian et al., 2006; Zanon, 2010). Furthermore, alkaloids
such as laurifoline, magnocurarine and isomagnocurarine were
isolated from other species belonging to this genus (Fan et al.,
2019) together with sanguinarine, identified by spectrometry mass
(Tian et al., 2017).

Studies demonstrate that leishmanicidal activity may be related
to the presence of alkaloids (Correa-Barbosa et al., 2023), as example
stands out the leishmanicidal efficacy of alkaloid β-carboline (Silva-
Silva et al., 2019) and indole alkaloids (Brígido et al., 2020; Veiga
et al., 2020). Additionally, previous research has shown that
alkaloids isolated from *Z. rhoifolium*, such as avicine and
fagaridine, exhibit activity against promastigote forms of *L.
amazonensis*, with IC_{50} values below 13.6 μM in both cases.
Furthermore, alkaloids from other species of the genus
Zanthoxylum, such as the alkaloid γ-fagarine isolated from the
species *Z. tingoassuiba*, demonstrated activity against *L.
amazonensis* promastigotes, with an IC_{50} of 31.3 ± 1.4 μM (Costa
et al., 2018).

However, despite not observing a significant interference of
fractionation in the antipromastigote activity, a reduction in
cytotoxicity was noted, accompanied by an increase in the
selectivity index, mainly related to FN. The chemical variation
among substances, notably alkaloids, present in the samples may
be crucial in explaining the differences observed in cytotoxicity. The
fractionation process seems to play a crucial role in attenuating FN
toxicity, suggesting a selective process that influences the
concentration of less harmful alkaloids. The diversity in the
presence of alkaloids can result in distinct cytotoxic responses, as
each alkaloid possesses unique properties, and variations in their
relative concentrations can directly impact toxicity (Ketema
et al., 2023).

FN showed no toxicity; however, EE and FA exhibited moderate
cytotoxicity to VERO cells, and this moderate cytotoxicity of EE and
FA may be related to the presence of different concentrations of
alkaloids, such as sanguinarine, which is known for its cytotoxic
properties (Croaker et al., 2022). Another relevant hypothesis is that
the presence of a combination of alkaloids in the samples may result
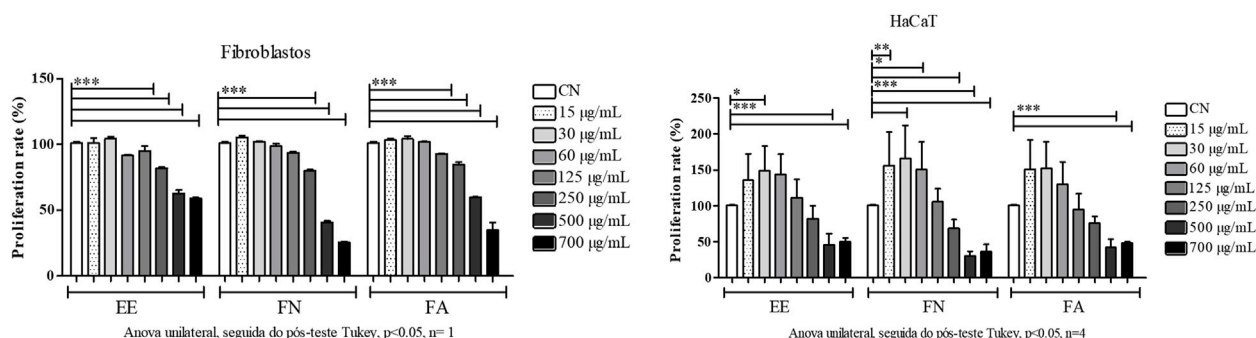
FIGURE 4
Evaluation of the proliferative effect of Z. *rhoifolium* on keratinocytes (HaCaT) and normal primary fibroblasts. Legend: EE, ethanol extract of
Zanthoxylum rhoifolium; FN, neutral fraction of Z rhoifolium; FA, alkaloid fraction of Z. rhoifolium . Analysis of variance and Tukey's post hoc test, p <0.05,
n = 1. Asterisks (*) indicate differences between doses.
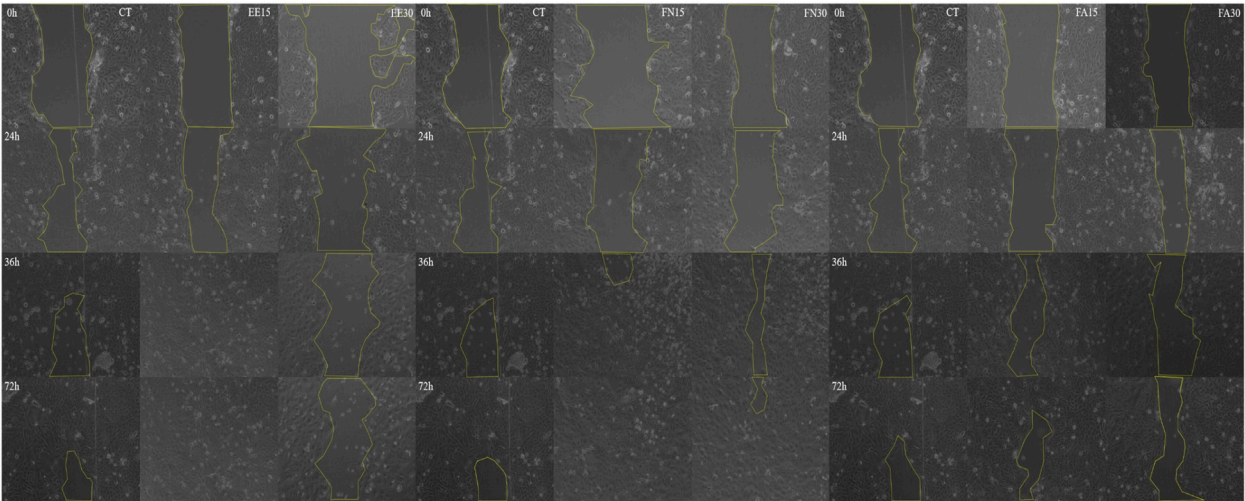
FIGURE 5
Wound healing assay in *Zanthoxylum rhoifolium* HaCaT cells. Wound closure at 0, 24, 48 and 72 hours. Legend: EE, ethanol extract of *Zanthoxylum rhoifolium*; FN, neutral fraction of *Z. rhoifolium*; FA, alkaloid fraction of *Z. rhoifolium*.

TABLE 3 Binding affinity (kcal/mol) between chelerythrin and the enzymes leishmanolysin and TR and the types and distance of the bonds made.

Ligands	Binding energy prediction (Kcal/mol)	Number of H-bridges and/or pi-pi interactions; residue.
1LML		
Chelerythrin	-9.14	4; Ala^{227}, Ala^{349}, Glu^{265}
Amphotericin	-11.02	
6ER5		
Chelerythrin	-7.35	8; Arg^{85}, Leu^{88}, Lys^{211}, Met^{70}
Amphotericin	-10.37	
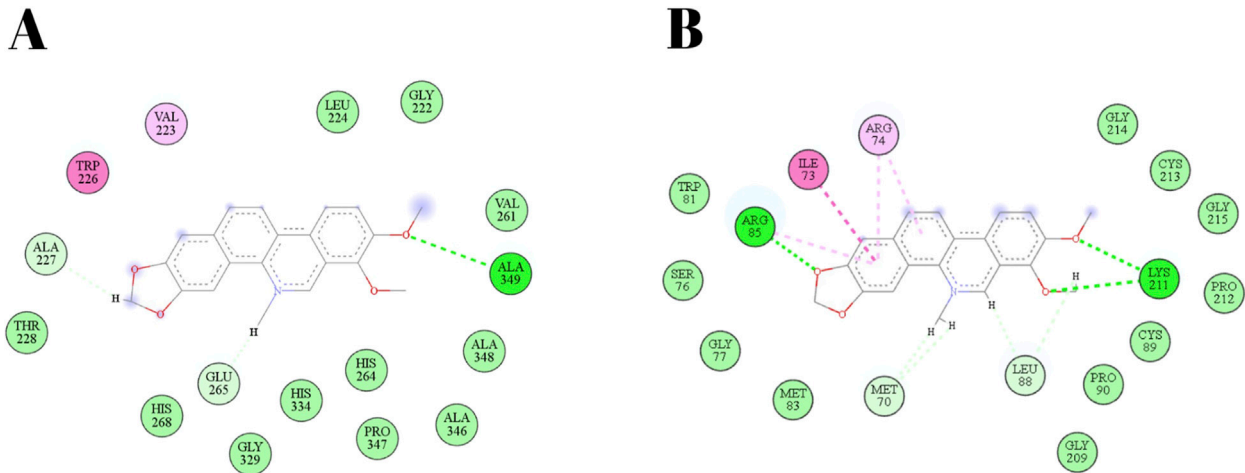
FIGURE 6
2D diagram of the connections made by cheleritrin. Legend: **(A)** -Leishmanolysin (gp63; 1LML) of *L. major*, **(B)** - trypanothione reductase (TR; 6ER5) of *L.infantum*.

in synergistic or antagonistic interactions between these substances. This complexity can influence the total cytotoxic response and explain the differences observed between EE, FA, and FN (Yap et al., 2023). In this regard, the modification of the relative composition of alkaloids in the samples during fractionation is a possible explanation for the alteration in toxicity. The finding that FN has lower cytotoxicity suggests selection during the process, favoring the concentration of alkaloids with noncytotoxic potential.

The antiamastigote effects of EE and FN were tested, and the highest inhibition index was observed at 200 μg/mL. This result is consistent with findings from other studies, where higher concentrations of plant extracts or isolated compounds demonstrated greater efficacy against intracellular parasitic forms (Brigido et al., 2020). The reduction in cytotoxicity and increase in the selectivity index observed for FN, along with its effectiveness against promastigotes and amastigotes, reinforce the promising anti-leishmanial activity of these samples, indicating their potential for application as a source of therapeutic compounds against leishmaniasis.

Given that leishmaniasis causes skin lesions, the proliferative and healing profiles of the most promising samples in this study were examined. Thus, after analyzing the proliferative profile, the results suggested that the higher the tested concentration was, the lower the cell proliferation was compared to that of the control group, indicating that lower concentrations are less cytotoxic. Another study involving cells treated with *Citrullus colocynthis* at concentrations of 100, 50, 25, and 20 μg/mL showed a significant decrease in cell proliferation after 24 h (Yonbawi et al., 2021). However, at lower doses of 10 and 15 μg/mL, it did not reduce the proliferation of HaCaT cells, supporting the presented hypothesis.

An ethnobotanical study conducted in the Brazilian Legal Amazon reported the topical use of decoctions or macerations of the bark or fruits of the species *Z. rhoifolium* for wound healing (Ribeiro et al., 2017), corroborating the findings of the study at lower tested doses. Another study demonstrated that the methanolic extract of *Kigelia africana* showed potential wound healing properties at various concentrations against HaCaT cells, achieving complete wound closure before the control group (Karatay et al., 2023). However, at concentrations of up to 300 μg/mL, it had a low cytotoxic effect, differing from the findings in the present study.

Finally, the observed wound healing activity can be explained by the presence of alkaloids in the samples, as studies have demonstrated the wound healing activity of plants rich in these metabolites, such as *Bowdichia virgilioides* (Barbosa-Filho et al., 2004) and *Solanum xanthocarpum* (Dewangan et al., 2012). However, it is noteworthy that a lesser wound healing effect was observed for FA and at the highest concentration of EE. One hypothesis for the difference in activity could be related to the concentration of these metabolites in each fraction.

Due to the superior activities found in NF, this sample was fractionated until the isolation and identification of the major substance, which was identified as the alkaloid chelerythrine, to which biological activities were attributed. Notably, this metabolite has already shown promising effects when tested alone on strains of *L. amazonensis* amastigotes (Castillo et al., 2014). Thus, to elucidate

the possible molecular interactions involved in the mechanism of action of this alkaloid, an *in silico* study was conducted.

Leishmanolysin (gp63) is a metalloprotease of the M8 family that is mainly expressed on the parasite surface (Mercado-Camargo et al., 2020). Studies infer that gp63 affects the parasite's intracellular survival through the cleavage and/or degradation of fibronectin receptors, which in turn are responsible for a series of functions, including cell adhesion (Maran et al., 1992; Brittingham et al., 1995). Amphotericin B, used as a control drug, mainly interacts with the GLU220 and GLU265 residues and with the zinc atom, and it is known that this drug deregulates the parasite's membrane. Therefore, we can infer that chelerythrine may disrupt a parasite's cell wall, leading to its death (Mercado-Camargo et al., 2020).

Thioredoxin reductase (TR) is a fundamental enzyme in parasite survival because it prevents the effects of hydrogen peroxide produced by macrophages, allowing parasite survival and multiplication within the intracellular environment. TR has become an important target because its unique expression in Trypanosomatidae makes this enzyme a safe target for new drugs (Saravanamuthu et al., 2004; Turcano et al., 2018). Although chelerythrine did not bind to the active sites, there was still favorable binding, necessitating additional studies to elucidate this binding. It is possible that chelerythrine may act allosterically, altering the conformation of the target molecule.

Since the alkaloid chelerythrine exhibits high activity against intracellular amastigote forms of *L. amazonensis*, comparable to amphotericin B in terms of the necessary dose for activity, and shows nonspecific toxicity to macrophages, in a model of cutaneous leishmaniasis, it was able to reduce the parasite load by 29% after 6 weeks of treatment (Castillo et al., 2014). These data support our study, which demonstrated that the alkaloid chelerythrine has high leishmanicidal activity, possibly through deregulation of the parasite's cell wall mediated by inhibition of leishmanolysin (gp63), and contributes to the slight decrease in its survival within macrophages by binding to TR.

5 Conclusion

The present study demonstrated that *Z. rhoifolium* is a species with high antileishmanial activity *in vitro*. Furthermore, the species has shown promise in the healing process, due to its ability to increase the rate of cell proliferation. It is worth mentioning that the fractionation of the extract is extremely important, since FN presented the best selectivity index against *L. amazonensis* and was the most promising sample for healing activity. Finally, the need for safety analyzes and *in vivo* biological activities is inferred to confirm the promising potential of the species.

Data availability statement

The raw data supporting the conclusions of this article will be made available by the authors, without undue reservation.

Author contributions

JC-B: Conceptualization, Data curation, Investigation, Methodology, Project administration, Software, Visualization, Writing–original draft, Writing–review and editing. HB: Investigation, Methodology, Writing–original draft, Writing–review and editing. BM: Investigation, Methodology, Writing–original draft, Writing–review and editing. PC: Investigation, Methodology, Writing–original draft, Writing–review and editing. ML: Investigation, Methodology, Writing–original draft, Writing–review and editing. DS: Investigation, Methodology, Writing–original draft, Writing–review and editing. PN: Investigation, Methodology, Writing–original draft, Writing–review and editing. GF: Investigation, Methodology, Software, Writing–original draft, Writting–review and editing. VV: Investigation, Methodology, Writing–original draft, Writing–review and editing. AM: Investigation, Methodology, Writing–original draft, Writing–review and editing. JS: Investigation, Methodology, Writing–original draft, Writing–review and editing. MC-F: Methodology, Writing–original draft, Writing–review and editing. MM: Methodology, Supervision, Writing–original draft, Writing–review and editing. MD: Conceptualization, Data curation, Formal analysis, Funding acquisition, Methodology, Project administration, Resources, Supervision, Visualization, Writing–original draft, Writing–review and editing.

Funding

Conflict of interest

The authors declare that the research was conducted in the absence of any commercial or financial relationships that could be construed as a potential conflict of interest.

Generative AI statement

The author(s) declare that no Generative AI was used in the creation of this manuscript.

Publisher's note

All claims expressed in this article are solely those of the authors and do not necessarily represent those of their affiliated organizations, or those of the publisher, the editors and the reviewers. Any product that may be evaluated in this article, or claim that may be made by its manufacturer, is not guaranteed or endorsed by the publisher.

Supplementary material

The Supplementary Material for this article can be found online at: https://www.frontiersin.org/articles/10.3389/fchem.2025.1504998/full#supplementary-material

References

Azonsivo, R., Albuquerque, K. C. O. D., Castro, A. L. G., Correa-Barbosa, J., Souza, H. J. R. D., Almada-Vilhena, A. O. D., et al. (2023). Cytotoxicity and Genotoxicity evaluation of *Zanthoxylum rhoifolium* Lam and *in silico* studies of its alkaloids. *Molecules* 28 (14), 5336–5353. doi:10.3390/molecules28145336

Barbosa-Filho, J. M., Almeida, J. R. G. S., Costa, V. C. O., Da-Cunha, E. V. L., Silva, M. S., and Braz-Filho, R. (2004). Bowdichine, a new diaza-adamantane alkaloid from Bowdichia virgilioides. *J. Asian Nat. Prod. Res.* 6 (1), 11–17. doi:10.1080/1028602031000119763

Bortoleti, B. T. S., Detoni, M. B., Gonçalves, M. D., Tomiotto-Pellissier, F., Silva, T. F., Concato, V. M., et al. (2022). Solidagenone *in vivo* leishmanicidal activity acting in tissue repair response, and immunomodulatory capacity in Leishmania amazonensis. *Elsevier* 361 (6), 109969. doi:10.1016/j.cbi.2022.109969

Brígido, H. P. C., Ramos, B. T. C., Paz, M. K. B., Bastos, M. L. C., and Dolabela, M. F. (2020). Antimicrobial activity of Aspidosperma nitidum benth (apocynaceae). *Electron. J. Collect. Health* 12 (10), 41–49. doi:10.25248/reas.e4123.2020

Brígido, H. P. C., Varela, E. L. P., Quadros Gomes, A. R., Neves Cruz, J., Correa-Barbosa, J., Siqueira, J. E. d. S., et al. (2024). Aspidosperma nitidum reduces parasite load and modulates cytokines in BALB/c mice infected with Leishmania (Leishmania) amazonensis. *Front. Chem.* 12, 01. doi:10.3389/fchem.2024.1492770

Brittingham, A., Morrison, C. J., McMaster, W. R., McGwire, B. S., Chang, K. P., and Mosser, D. M. (1995). Role of the Leishmania surface protease gp63 in complement fixation, cell adhesion, and resistance to complement-mediated lysis. *J. Immunol.* 6, 3102–3111. doi:10.4049/jimmunol.155.6.3102

Castillo, D., Sauvain, M., Rivaud, M., and Jullian, V. (2014). *In vitro* and *in vivo* Activity of Benzo[c]phenanthridines against Leishmania amazonensis. *Med. Plant* 80 (11), 902–906. doi:10.1055/s-0034-1382826

Correa-Barbosa, J., Sodré, D. F., Nascimento, P. H. C., and Dolabela, M. F. (2023). Activity of the genus Zanthoxylum against diseases caused by protozoa: a systematic review. *Front. Pharmacol.* 13, 873208. doi:10.3389/fphar.2022.873208

Costa, R. S., Souza-Filho, O. P., Júnior, O. C. S. D., Silva, J. J., Hyaric, M. L., Santos, M. A. V., et al. (2018). *In vitro* antileishmanial and antitrypanosomal activity of compounds isolated from the roots of Zanthoxylum tingoassuiba. *Braz. J. Pharmacogn.* 28 (5), 551–558. doi:10.1016/j.bjp.2018.04.013

Croaker, A., Davis, A., Carroll, A., Liu, L., and Myers, S. P. (2022). Understanding of black salve toxicity by multicompound cytotoxicity assays. *BMC Complement. Med. Ther.* 20 (22), 247–259. doi:10.1186/s12906-022-03721-y

Dewangan, H., Bais, M., Jaiswal, V., and Verma, V. K. (2012). Potential wound healing activity of the ethanolic extract of Solanum xanthocarpum schrad and wendl leaves. *Pak. J. Pharm. Sci.* 25 (1), 189–194. https://applications.emro.who.int/imemrf/Pak_J_Pharm_Sci/Pak_J_Pharm_Sci_2012_25_1_189_194.pdf.

Domagalska, M. A., Barrett, M. P., and Dujardin, J. C. (2023). Drug resistance in Leishmania: does it truly matter? *Trends Parasitol.* 39 (4), 251–259. doi:10.1016/j.pt.2023.01.012

Fan, M., Tian, Y., Chen, G., Sarker, S. D., Nahar, L., Wu, J., et al. (2019). Enrichment and analysis of quaternary alkaloids from *Zanthoxylum simulans* using weak cation exchange solid-phase extraction coupled with LC–MS. *Phytochem. Anal.* 30 (6), 727–734. doi:10.1002/pca.2860

Galucio, N. C. R. (2018). Estudos Fitoquímicos, Citotoxicidade e Genotoxicidade de Eleutherine Plicata Herb. Dissertação (Mestrado em Ciências Farmacêuticas). (Belém – PA) Universidade Federal do Pará, Instituto de Ciências da Saúde.

Grosdidier, A., Zoete, V., and Michielim, O. (2011). Fast docking using the CHARMM force field with EADock DSS. *J. Comput. Chem.* 32 (10), 2149–2159. doi:10.1002/jcc.21797

Haberthür, U., and Cafisch, A. (2008). Facts: Fast analytical continuum treatment of solvation. *J. Comput. Chem.* 29 (5), 701–715. doi:10.1002/jcc.20832

Herwaldt, B. L. (1999). Leishmaniasis. *Lancet* 354 (9185), 1191–1199. doi:10.1016/S0140-6736(98)10178-2

Jullian, V., Bourdy, D., Georges, S., Maurel, S., and Sauvain, M. (2006). Validation of use of a traditional antimalarial remedy from French Guiana, *Zanthoxylum rhoifolium* Lam. *J. Ethnopharmacol.* 106 (3), 348–352. doi:10.1016/j.jep.2006.01.011

Karatay, K. B., Fazilet, Z. B. M., Benedict, L., and Omer, A. (2023). Methanolic extract of Kigelia africana and wound healing: an *in vitro* study. *J. Wound Care* 32 (6), 392–398. doi:10.12968/jowc.2023.32.6.392

Ketema, T., Tadele, M., Gebrie, Z., Makonnen, E., Hailu, A., and Abay, S. M. (2023). *In vitro* anti-leishmanial activities of methanol extract of Brucea antidysenterica J.F. Mill seeds and its solvent fractions. *J. Exp. Pharmacol.* 13 (15), 123–135. doi:10.2147/JEP.S397352

Li, X. Q., Kang, R., Huo, J. C., Xie, Y. H., Wang, S. W., and Cao, W. (2017). Woundhealing activity of Zanthoxylum bungeanum Maxim seed oil on Experimentally Burned Rats. *Pharmacogn. Mag.* 13 (51), 363–371. doi:10.4103/pm.pm_211_16

Maran, R. P. C., Corcostegui, B., and Vilaro, S. (1992). Inmunolocalización de la fibronectina, laminina y macrófagos en membranas vitreorretinianas de la retinopatía diabética proliferativa. *Arq. Bras. Oftalmol.* 55, 134–140. doi:10.5935/0004-2749.19920031

Melo-Neto, B., Leitão, J. M. S. R., Oliveira, L. G. C., Santos, S. E. M., Carneiro, S. M. P., Rodrigues, K. A. F., et al. (2016). Inhibitory effects of *Zanthoxylum rhoifolium* Lam. (Rutaceae) against the infection and infectivity of macrophages by Leishmania amazonensis. *An. Acad. Bras. Ciências* 88 (3), 1851–1861. doi:10.1590/0001-3765201620150131

Mercado-Camargo, J., Cervantes-Ceballos, L., Vivas-Reyes, R., Pedretti, A., Serrano-García, M. L., and Gómez-Estrada, H. (2020). Homology modeling of leishmanolysin (gp63) from Leishmania panamensis and molecular docking of flavonoids. *ACS omega* 5 (24), 14741–14749. doi:10.1021/acsomega.0c01584

Mohamed, A. A. O., Ahmed, A. L., Ahmed, A. A., Mohammed, M. A., Basel, A., Abdel, W., et al. (2023). Alternative Non-drug treatment options of the most Neglected parasitic Disease cutaneous leishmaniasis: a Narrative review. *Trop. Med. Infect. Dis.* 8 (5), 275. doi:10.3390/tropicalmed8050275

Mosmann, T. (1983). Rapid colorimetric assay for cellular growth and survival: application to proliferation and cytotoxicity assays. *J. ofImmunological Methods* 65, 55–63. doi:10.1016/0022-1759(83)90303-4

Mota, E. F., Rosario, D. M., Silva Veiga, A. S., Brasil Do, S., Silveira, F. T., and Dolabela, M. F. (2015). Biological activities of Croton palanostigma Klotzsch. *Pharmacogn. Mag.* 11 (43), 96–606. doi:10.4103/0973-1296.176109

Moura-Costa, G. F., Nocchi, S. R., Ceole, L. F., De Mello, J. C., Nakamura, C. V., Dias Filho, B. P., et al. (2012). Antimicrobial activity of plants used as medicinals on an indigenous reserve in Rio das Cobras, Paraná, Brazil. *J. Ethnopharmacol.* 143 (2), 631–638. doi:10.1016/j.jep.2012.07.016

Ngure, P. K., Tonui, W. K., Ingonga, J., Mutai, C., Kigondu, E., Ng'ang'a, Z., et al. (2009). *In vitro* antileishmanial activity of extracts of Warburgia ugandensis (Canellaceae), a Kenyan medicinal plant. *J. Med. Plants Res.* 3 (2), 61–66. https://www.researchgate.net/publication/254629873_In_vitro_antileishmanial_activity_of_extracts_of_Warburgia_ugandensis_Canellaceae_a_Kenyan_medicinal_plant

Pan American Health Organization (2023). Leishmaniasis: Epidemiological report for the Americas. No.12 (December 2023). *PAHO*, 12, 14.

Pradhan, S., Schwartz, R. A., Patil, A., Grabbe, S., and Goldust, M. (2022). Treatment options for leishmaniasis. *Clin. Exp. Dermatol* 47 (3), 516–521. doi:10.1111/ced.14919

Ramos, T. D., et al. (2020). Combined therapy with adipose tissue-derived mesenchymal stromal cells and meglumine antimoniate controls lesion development and parasite load in murine cutaneous leishmaniasis caused by Leishmania amazonenses. *Stem Cell Res. Ther.* 11, 20–374. doi:10.1186/s13287-020-01889-z

Rath, S., Trivelin, L. A., Imbrunito, T. R., Tomazela, D. M., De Jesús, M. N., Marzal, P. C., et al. (2003). Antimoniais empregados no tratamento da leishmaniose: estado da arte. *Quím. Nova* 26 (4), 550–555. doi:10.1590/S0100-40422003000400018

Reimão, J. Q. (2009). *Estudo da atividade anti-leishmania de compostos de invertebrados marinhos brasileiros. Dissertação (Mestrado em Ciências). São*

Paulo – SP Secretaria do Estado de São Paulo, Programa de Ciências da Coordenadoria de Controle de Doenças.

Ribeiro, R. V., Bieski, I. G. C., Balogun, S. O., and De Oliveira Martins, D. T. (2017). Ethnobotanical study of medicinal plants used by Ribeirinhos in the North Araguaia microregion, Mato Grosso, Brazil. *J. Ethnopharmacol.* 205, 69–102. doi:10.1016/j.jep.2017.04.023

Saravanumuthu, A., Vickers, T. J., Bond, C. S., Perterson, M. R., Hunter, W. N., and Fairlamb, A. H. (2004). Two interacting binding sites for quinacrine derivatives in the active site of trypanothione reductase: a template for drug design. *J. Biol. Chem.* 279 (28), 29493–29500. doi:10.1074/jbc.M403187200

Silva, F. S. (2005). Avaliação *in vitro* da azitromicina nas espécies Leishmania (Leishmania) amazonensis, Leishmania (Leishmania) braziliensis e Leishmania (Leishmania) chagasi. *Portal Reg. BVS.* 12, 43. (Dissertation).

Silva-Silva, J. V. (2016). Estudo farmacognóstico, fitoquímico e atividade leishmanicida de duas espécies de Geissospermum (Apocynaceae). *Portal Reg. BVS* 1, 14. (Dissertation).

Silva-Silva, J. V., Cordovil Brigido, H. P., Oliveira de Albuquerque, K. C., Miranda Carvalho, J., Ferreira Reis, J., Vinhal Faria, L., et al. (2019). Flavopereirine—an alkaloid derived from Geissospermum vellosii—Presents leishmanicidal activity *in vitro*. *Molecules* 24 (9), 785–748. doi:10.3390/molecules24040785

Tavares, L. C., Zanon, G., Weber, A. D., Neto, A. T., Mostardeiro, C. P., Da Cruz, I. B. M., et al. (2014). Structure-activity relationship of benzophenanthridine alkaloids from *Zanthoxylum rhoifolium* having Antimicrobial activity. *PLOS ONE* 9 (5), e97000–e97097. doi:10.1371/journal.pone.0097000

Tian, Y., Zhang, C., and Guo, M. (2017). Comparative study on alkaloids and their anti-proliferative activities from three Zanthoxylum species. *BMC complementary Altern. Med.* 17, 460–516. doi:10.1186/s12906-017-1966-y

Turcano, L., Torrente, E., Missineo, A., Andreini, M., Gramiccia, M., Di Muccio, T., et al. (2018). Identification and binding mode of a novel Leishmania Trypanothione reductase inhibitor from high throughput screening. *Plos Neglected Trop. Dis.* 2, e0006969. doi:10.1371/journal.pntd.0006969

Veiga, A. do S. S. da., Brígido, H. P. C., Percário, S., Marinho, A. M. do R., and Dolabela, M. F. (2020). Antileishmanial potential of alkaloids isolated from plants: an integrative review. *Res. Soc. Dev.* 9 (10), 91–109. doi:10.33448/rsd-v9i10.9334

Virchai, V., and Kirtikara, K. (2006). Sulforhodamine B colorimetric assay for cytotoxicity screening. *Nat. Protoc.* 1 (15), 1112–1116. doi:10.1038/nprot.2006.179

Wei, W.-J., Chen, X. H., Guo, T., Liu, X. Q., Zhao, Y., Wang, L. L., et al. (2021). A review on classification and biological activities of alkaloids from the genus Zanthoxylum species. *Mini Rev. Med. Chem.* 21 (3), 336–361. doi:10.2174/1389557520666200910091905

Yap, V. L., Tan, L. F., Rajagopal, M., Wiart, C., Selvaraja, M., Leong, M. Y., et al. (2023). Evaluation of phytochemicals and antioxidant potential of a new polyherbal formulation TC-16: additive, synergistic or antagonistic? *BMC Complement. Med. Ther.* 28, 93–103. doi:10.1186/s12906-023-03921-0

Yonbawi, A. R., Hossam, M. A., Faris, A. A., Abdulrahman, E. K., and Charles, M. H. (2021). Anti-proliferative, cytotoxic and antioxidant properties of the methanolic extracts of five Saudi Arabian flora with folkloric medicinal use: Aizoon canariense, Citrullus colocynthis, Maerua crassifolia, Rhazya stricta and Tribulus macropterus. *Plants* 10, 10. doi:10.3390/plants10102073

Zahra, A., Mohsen, S., Ali, A. A., Arash, G., and Gholamreza, H. (2023). The novel treatments based on tissue engineering, cell therapy and nanotechnology for cutaneous leishmaniasis. *Int. J. Pharm.* 25, 633–122. doi:10.1016/j.ijpharm.2023.122615

Zanon, G. (2010). "Análise fitoquímica e estudo das atividades antimicrobiana, antioxidante e de inibição da enzima acetilcolinesterase das espécies *Zanthoxylum rhoifolium* e Zanthoxylum hyemale," in *Dissertação mestrado (Programa de Pós-graduação em Química) (Santa Maria – RS)*. Universidade Federal de Santa Maria.

Two-dimensional QSAR-driven virtual screening for potential therapeutics against *Trypanosoma cruzi*

Naseer Maliyakkal[1†], Sunil Kumar[2†], Ratul Bhowmik[3†], Harish Chandra Vishwakarma[2], Prabha Yadav[2] and Bijo Mathew[2]*

[1]Department of Basic Medical Sciences, College of Applied Medical Sciences, King Khalid University, Khamis Mushait, Saudi Arabia, [2]Department of Pharmaceutical Chemistry, Amrita School of Pharmacy, AIMS Health Sciences Campus, Amrita Vishwa Vidyapeetham, Kochi, India, [3]Department of Pharmaceutical Chemistry, School of Pharmaceutical Education and Research, Jamia Hamdard, New Delhi, India

Trypanosoma cruzi is the cause of Chagas disease (CD), a major health issue that affects 6–7 million individuals globally. Once considered a local problem, migration and non-vector transmission have caused it to spread. Efforts to eliminate CD remain challenging due to insufficient awareness, inadequate diagnostic tools, and limited access to healthcare, despite its classification as a neglected tropical disease (NTD) by the WHO. One of the foremost concerns remains the development of safer and more effective anti-Chagas therapies. In our study, we developed a standardized and robust machine learning-driven QSAR (ML-QSAR) model using a dataset of 1,183 *Trypanosoma cruzi* inhibitors curated from the ChEMBL database to speed up the drug discovery process. Following the calculation of molecular descriptors and feature selection approaches, Support Vector Machine (SVM), Artificial Neural Network (ANN), and Random Forest (RF) models were developed and optimized to elucidate and predict the inhibition mechanism of novel inhibitors. The ANN-driven QSAR model utilizing CDK fingerprints exhibited the highest performance, proven by a Pearson correlation coefficient of 0.9874 for the training set and 0.6872 for the test set, demonstrating exceptional prediction accuracy. Twelve possible inhibitors with $pIC_{50} \geq 5$ were further identified through screening of large chemical libraries using the ANN-QSAR model and ADMET-based filtering approaches. Molecular docking studies revealed that F6609-0134 was the best hit molecule. Finally, the stability and high binding affinity of F6609-0134 were further validated by molecular dynamics simulations and free energy analysis, bolstering its continued assessment as a possible treatment option for Chagas disease.

1 Introduction

Chagas disease (CD), caused by the protozoan parasite *Trypanosoma cruzi*, was diagnosed for the first time in humans in 1909 (Abras et al., 2022; Rassi et al., 2010; Rassi et al., 2012). CD has shifted from a regional to a global health concern, spreading beyond vector-borne transmission. *T. cruzi* infection can occur through blood transfusion, organ transplantation, congenital transmission, and laboratory accidents (Carbajal-de-la-Fuente et al., 2022). Among these, congenital transmission is particularly alarming, affecting both endemic regions (with vectors) and non-endemic areas (without vectors), making it a growing public health threat worldwide (Carbajal-de-la-Fuente et al., 2022). CD affects 6–7 million people globally, mainly in Latin America. With migration, CD has spread from rural to urban areas and beyond endemic regions, posing a growing global health challenge. In 2010, WHO classified CD as a neglected tropical disease (NTD) and later included it in the 2021–2030 roadmap for elimination. Managing NTDs remains challenging, especially in non-endemic regions, due to low awareness, limited diagnostic guidelines, and resource redirection during the COVID-19 pandemic (Fraundorfer, 2024; Kiehl et al., 2023). These factors, along with healthcare inaccessibility for vulnerable groups, threaten progress toward 2030 targets. Control efforts focus on vector control and screening, as no vaccine exists. The complex immunology and chronic nature of CD hinder vaccine development, making prevention and early detection crucial in combating the disease (Sarabi Asiabar et al., 2024). The currently approved drugs, Benznidazole and Nifurtimox, are effective but associated with severe toxicity due to their nitro groups, which generate reactive metabolic radicals (Kannigadu and N'Da, 2020; Trovato et al., 2020). This leads to adverse effects such as mutagenicity, genotoxicity, and carcinogenicity, limiting their long-term therapy (Kannigadu and N'Da, 2020). Given these challenges, the search for safer and more selective therapeutic alternatives has gained at this momentum. Since the 1990s, researchers have focused on sterol 14α-demethylase (CYP51) inhibitors, which is a crucial target in the sterol biosynthesis pathway of parasite (Choi et al., 2014; Lepesheva et al., 2011; Patterson and Fairlamb, 2019). These inhibitors offer greater selectivity and potentially reduced toxicity, making them promising candidates for improved CD treatment. However, clinical development of these compounds remains challenging, requiring further optimization to balance efficacy and safety. CYP51, a key enzyme in sterol biosynthesis, is essential for parasite survival, making it a promising drug target. Azoles like posaconazole and ravuconazole inhibit CYP51 by interacting with its heme iron, offering potential for selective treatment (Lepesheva et al., 2007; Parker et al., 2014; Rabelo et al., 2017). Other targets include cruzipain, pyrophosphate enzymes, and trypanothione reductase, though many inhibitors have shown high toxicity. Despite extensive research, benznidazole and nifurtimox remain the only FDA-approved drugs. Recent studies suggest piperazine analogues of fenarimol as safer alternatives, highlighting the need for novel and less toxic therapies (Mazzeti et al., 2021; Salomao et al., 2016; Zobi and Algul, 2025). The new derivatives with amide, sulfonamide, aromatic, carbamate, and carbonate substituents were evaluated for their ability to inhibit *T. cruzi in vitro* and showed very promising results (Keenan et al., 2013; Keenan and Chaplin, 2015).

Despite 2 decades of research, no more effective and less toxic therapeutic alternatives have been identified, and existing drug combinations remain under clinical evaluation (Cheesman et al., 2017; Harrison et al., 2020). Cheminformatics and molecular modelling offer a valuable approach, providing cost-effective solutions compared to traditional drug discovery methods (Baldi, 2010; Bayat Mokhtari et al., 2017; Siddiqui et al., 2025). QSAR is a statistical approach that correlates molecular descriptors with biological activity, aiding in the prediction of compounds with more effectiveness (Naithani and Guleria, 2024; Patel et al., 2014; Winkler, 2002). In this study, we developed a robust 2-dimensional machine learning QSAR model using a dataset of *T. cruzi inhibitors* from the ChEMBL database (https://www.ebi.ac.uk/chembl/) to predict biological activity. The model was trained on multiple molecular descriptors to establish a robust structure-activity relationship, enabling accurate activity predictions for new compounds. To further validate potential candidates, we performed virtual screening using molecular docking to assess binding affinity within the target site. The top-ranked compounds were further subjected to molecular dynamics simulations to evaluate their stability and interactions over time, ensuring their potential effectiveness as novel *T. cruzi* inhibitors.

2 Materials and methods

2.1 Data curation

To construct a machine learning-driven quantitative structural activity relationship model (ML-QSAR), we retrieved a dataset of 1,183 *T. cruzi* inhibitors along with their chemical structures as Simplified Molecular Input Line Entry System (SMILES) and biological data as maximum inhibitory concentration (IC_{50}) values from the ChEMBL database (https://chembl.gitbook.io/chembl-interface-documentation/web-services). The data curation was carried out using chembl web resource client Python module. To ensure a normalized scale for the ML-QSAR model as well as to reduce variability in data analysis, the IC_{50} values were converted to pIC_{50}, i.e., negative logarithm (base 10) of IC_{50}.

2.2 Molecular descriptor calculation and feature selection

We used padelpy (https://github.com/ecrl/padelpy), a Python wrapper of the PaDEL-descriptor software, to calculate 1,024 CDK fingerprints and 780 atom pair 2D fingerprints (Yap, 2011) for the retrieved 1,183 inhibitors. Following the descriptor calculation step, we further implemented variance threshold scores and Pearson correlation analysis-based selection (correlation coefficient >0.9) to eliminate the constant and highly correlated features, respectively, from both the fingerprint datasets.

2.3 ML-QSAR model development and evaluation

We used an 80:20 split ratio for generating the training and test datasets for both fingerprints. We implemented Support Vector Machine (SVM), Artificial Neural Network (ANN), and Random

Forest (RF) ML algorithms to develop individual QSAR models for each of the fingerprint datasets using the scikit-learn (https://scikit-learn.org/stable/) Python programming library (Breiman, 2001; Goel et al., 2023; Utkin, 2019). For the SVM model, we implemented the radial basis function (RBF) kernel to capture the non-linear relationships between the molecular fingerprints and biological activity. Additionally, the model was optimized for C (regularization) and gamma (kernel coefficient) parameters. In case of the ANN-driven QSAR model, we implemented a feedforward neural network (FNN) with one hidden layer. We also tuned the number of neurons, activation function (ReLU), and optimizer (Adam) for the ANN model. For the RF-driven QSAR model, an ensemble of decision trees was used along with a feature bagging technique to enhance the predictive power of the model. Additionally, we also optimized the number of estimators (trees), the depth of trees, and the minimum samples per split.

Following the development of the initial model, we further performed principal component analysis (PCA) to assess the distribution of compounds and detect potential outliers in both training and test datasets. PCA was applied to transform the high-dimensional descriptor space into principal components, retaining maximum variance in a low-dimensional space. The first two principal components were further visualized using a scatter plot to inspect cluster formation as well as to detect points deviating from the main distribution. Molecules falling outside the main data clusters were detected as outliers and were removed from further modeling.

Following outlier detection and removal, we further trained the model using grid-based hypertuning and cross-validation metrics using SVM, ANN, and RF algorithms. To determine the best-performing models, we computed a diverse set of statistical metrics for each model: root mean squared error (RMSE), mean squared error (MSE), mean absolute error (MAE), Pearson Correlation coefficient, and 10-fold cross-validation metrics. The model with the lowest RMSE, MSE, and MAE values while retaining a high Pearson Correlation Coefficient was selected as the optimal QSAR model for predicting the inhibition mechanism.

2.4 Feature elucidation of the ML-QSAR model for rational drug-design

To further enhance the interpretability of the ML-QSAR models for both the fingerprints, we further implemented different feature importance analysis techniques like Variance Importance in Projection Analysis (VIP), Correlation Matrix Analysis, and Shapley Additive Explanations (SHAP) (https://shap.readthedocs.io/en/latest/) analysis (Nohara et al., 2022). For the VIP plot analysis, we computed the Partial Least Squares Regression (PLSR) method to rank descriptors based on their contribution to the model (Cao et al., 2017). For Correlation Matrix analysis, a pairwise correlation matrix was generated to identify the positively and negatively correlated molecular fingerprints for both models. For SHAP analysis, we individually computed SHAP values for each fingerprint to interpret how each molecular fingerprint influenced the pIC_{50} values across the datasets. Additionally, we also did cluster analysis for both highly active ($pIC_{50} \geq 7$) and weak inactive molecules ($pIC_{50} \leq 4$) using Tanimoto Coefficient-based similarity analysis (https://github.com/MunibaFaiza/tanimoto_similarities).

This clustering approach helped in identifying shared molecular features among compounds demonstrating strong or weak inhibition activity. To further enhance the interpretability of the clustering approach, we employed a WordCloud (https://pypi.org/project/wordcloud/) approach to visualize the most frequently occurring molecular features among the two groups.

2.5 Machine learning-driven chemical library screening

To further pave the path for the discovery of novel and more effective drug candidates, we implemented a two-dimensional multiplex modeling to screen large chemical libraries. We curated an Antiprotozoal Screening Compound Library of 8,200 molecules from the Life Chemicals database (https://lifechemicals.com/screening-libraries/targeted-and-focused-screening-libraries/antiprotozoal-library). We then implemented the first layer of virtual screening approach, i.e., pharmacokinetic and toxicophore analysis of the molecule library through the ChemBioServer 2.0 (https://chembioserver.vi-seem.eu/). We initially screened the molecules through Lipinski's Rule of Five, Veber's Rule, and Ghose's Filter using the ChemBioServer 2.0. Following this, we again used the ChemBioServer 2.0 to utilize the toxiphore analysis approach to screen out the toxic molecules (Karatzas et al., 2020). The screened molecules were then subjected to the second layer of virtual screening, i.e., activity prediction and screening using our previously developed ML-QSAR for both the molecular feature datasets, i.e., CDK and atom 2D pair fingerprints.

2.6 Molecular docking

On the aforementioned conformations, molecular docking studies were performed to investigate residue interactions and binding energy scores of lead molecules from chemical library screening. For the current investigation, the drug target, cruzain enzyme from *T. cruzi* (PDB ID: 1ME3) (Huang et al., 2003) was retrieved from the protein data bank (https://www.rcsb.org/) with a superior resolution of 1.2 Å, bearing a co-crystallized ligand. Missing residues were restored with the glide after the existing ligands were removed and hydrogen atoms were added. The co-crystallized ligand has been redocked to the active site of the 1ME3 to ascertain the docking parameters. Molecular docking employed a three-step approach that comprised protein energy reduction using the Protein Preparation Wizard (PPW) tool, optimization, and pre-processing to create protein crystal structures. LigPrep was utilized to create the ligands, guaranteeing accurate assignment of atom types and protonation states at pH 7.4 ± 1.0. Hydrogen atoms were added, and the structures underwent bond ordering. Then, using the Receptor grid generating tool (Kumar et al., 2024; Rampogu et al., 2018), a grid was created at the binding pocket coordinates (x, y, z) and aligned with a co-crystallized ligand.

2.7 Molecular dynamics simulation (MDS)

The "Desmond V 7.2 package" (Schrodinger 2022-4) has been used to conduct MDS to examine how the solvent system affects the
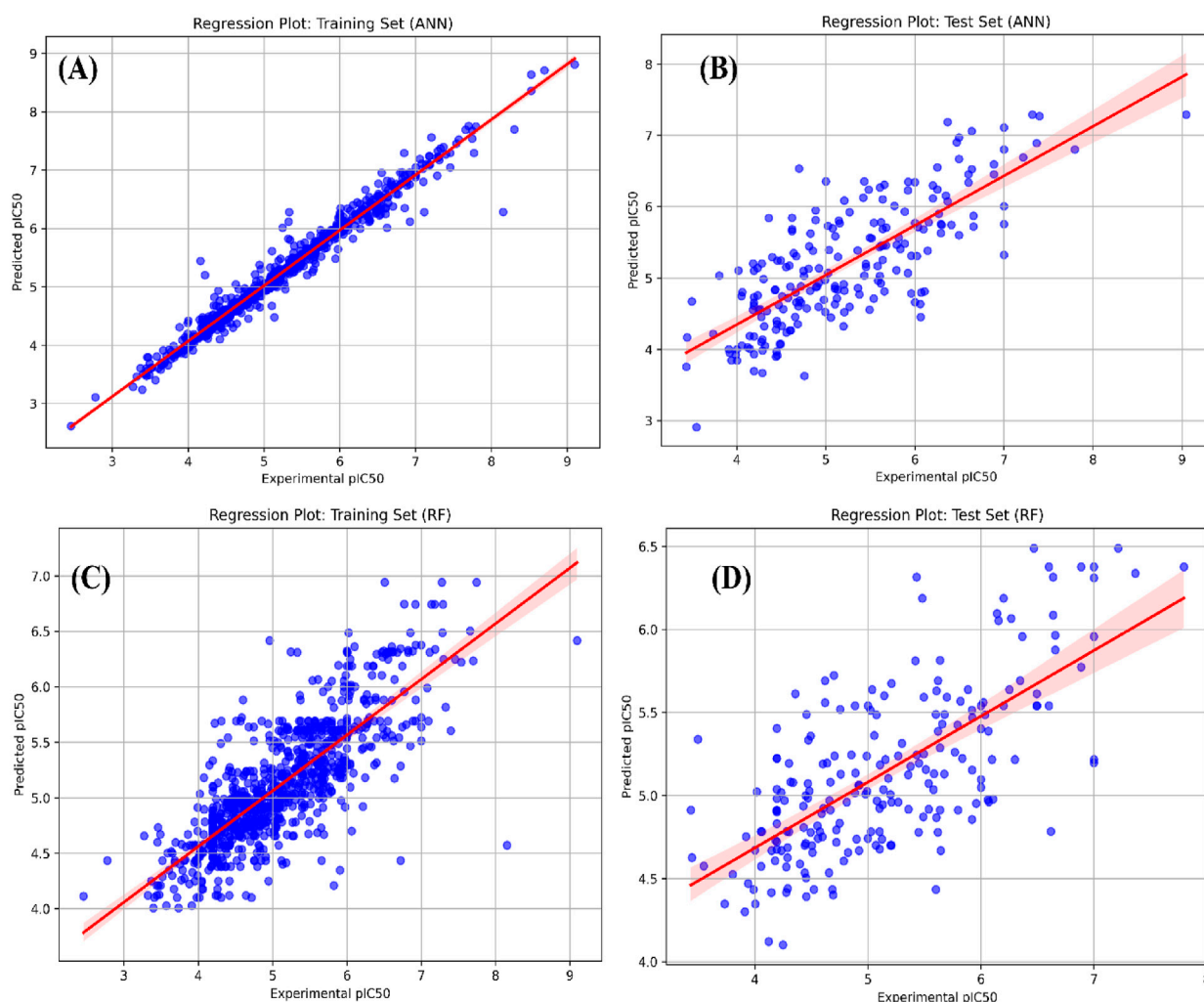
FIGURE 1
(A,B) represent regression plots for the training and test datasets for the best CDK fingerprint-driven ANN-QSAR model, respectively; **(C,D)** represent regression plots for the training and test datasets for the best atom 2D pair fingerprint-driven RF-QSAR model.

TABLE 1 Statistical metrics of all the generated CDK fingerprint-driven QSAR models. Best model is in bold.

Algorithm	Train RMSE	Test RMSE	CV RMSE	Train MSE	Test MSE	Train MAE	Test MAE	Train pearson	Test pearson
Initial models									
RF	0.2659	0.5986	0.6908	0.0707	0.3583	0.1943	0.4607	0.9656	0.7630
SVM	0.4449	0.5887	0.6682	0.1980	0.3465	0.2755	0.4493	0.8845	0.7735
ANN	0.1512	0.7272	0.8266	0.0229	0.5288	0.0868	0.5614	0.9875	0.6872
Final models (hypertuned and outliers removed)									
RF	0.3413	0.5692	0.6824	0.1165	0.3240	0.2518	0.4417	0.9441	0.7985
SVM	0.4827	0.6345	0.7237	0.2330	0.4026	0.3029	0.4835	0.8641	0.7415
ANN (best model)	**0.1675**	**0.6168**	**0.7870**	**0.0280**	**0.3804**	**0.0915**	**0.4842**	**0.9846**	**0.7683**

structure of the protein-ligand complex. The simulations were done on a Dell Inc. Precision 7,820 Tower running Ubuntu 22.04.1 LTS 64-bit and outfitted with an Intel Xeon (R) Silver 4210R processor and an NVIDIA Corporation GP104GL (RTX A 4000) graphics

processing unit. The docked complex's MDS (F6609-0134-1ME3) was performed using the OPLS4 force field. For MDS, the complex is positioned in the middle of an orthorhombic cubic box. After adding SPC water molecules and buffers, the protein atom and the edge of

TABLE 2 Statistical metrics of all the generated atom 2D pair fingerprint-driven QSAR models. Best model is bold.

Algorithm	Train RMSE	Test RMSE	CV RMSE	Train MSE	Test MSE	Train MAE	Test MAE	Train pearson	Test pearson
Model (default parameters)									
RF (best model)	**0.4763**	**0.6249**	**0.7472**	**0.2269**	**0.3905**	**0.3335**	**0.4990**	**0.8609**	**0.7381**
SVM	0.6141	0.6925	0.7331	0.3771	0.4795	0.4222	0.5514	0.7549	0.6655
ANN	0.4851	0.7449	0.8031	0.2354	0.5548	0.3392	0.5731	0.8595	0.6319
Model (hypertuned)									
RF	0.4846	0.6237	0.7415	0.2348	0.3891	0.3446	0.5007	0.8561	0.7397
SVM	0.7839	0.8239	0.8147	0.6145	0.6788	0.5964	0.6568	0.5404	0.4691
ANN	0.4639	0.6992	0.8298	0.2152	0.4888	0.3047	0.5444	0.8671	0.6698
Model (hypertuned and outliers removed)									
RF	0.5438	0.6383	0.7162	0.2958	0.4074	0.4112	0.5185	0.7929	0.6925
SVM	0.6314	0.6979	0.7286	0.3987	0.4870	0.4554	0.5593	0.6877	0.6008
ANN	0.5910	0.7095	0.7697	0.3493	0.5034	0.4489	0.5630	0.7479	0.6044

(A)   **(B)**
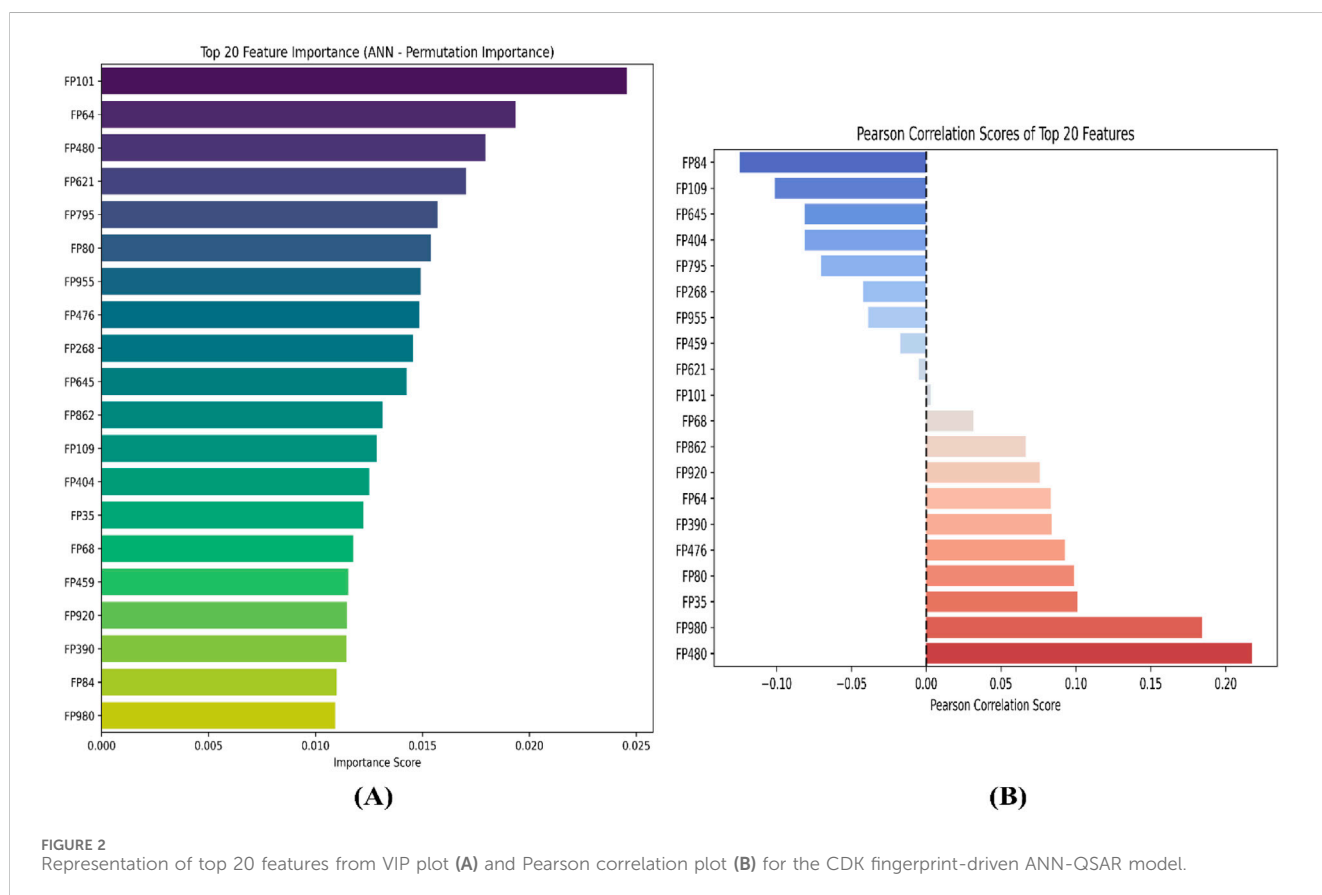
FIGURE 2
Representation of top 20 features from VIP plot **(A)** and Pearson correlation plot **(B)** for the CDK fingerprint-driven ANN-QSAR model.

the box are separated by 10 Å using the NPT ensemble. Together with counterions like Na+ and Cl-injected to randomly neutralize the system, the boundary condition box volume has also been calculated depending on the complex type. To assess domain correlations, a study of the protein-ligand interaction, root mean square deviation (RMSD), and root mean square fluctuation (RMSF) was conducted over all Cα atoms during the 200 ns MD simulation (da Costa et al., 2022; Maliyakkal et al., 2024).

3 Results and discussion

3.1 ML-QSAR model development

Following the removal of constant features and highly correlated features using variance threshold and correlation-based feature elimination approaches, we retained 533 molecular features for the CDK fingerprint Dataset, and 25 molecular features for the

FIGURE 3
Representation of top features from SHAP analysis **(A)** and outlier analysis through PCA plot **(B)** for the CDK fingerprint-driven ANN-QSAR model.
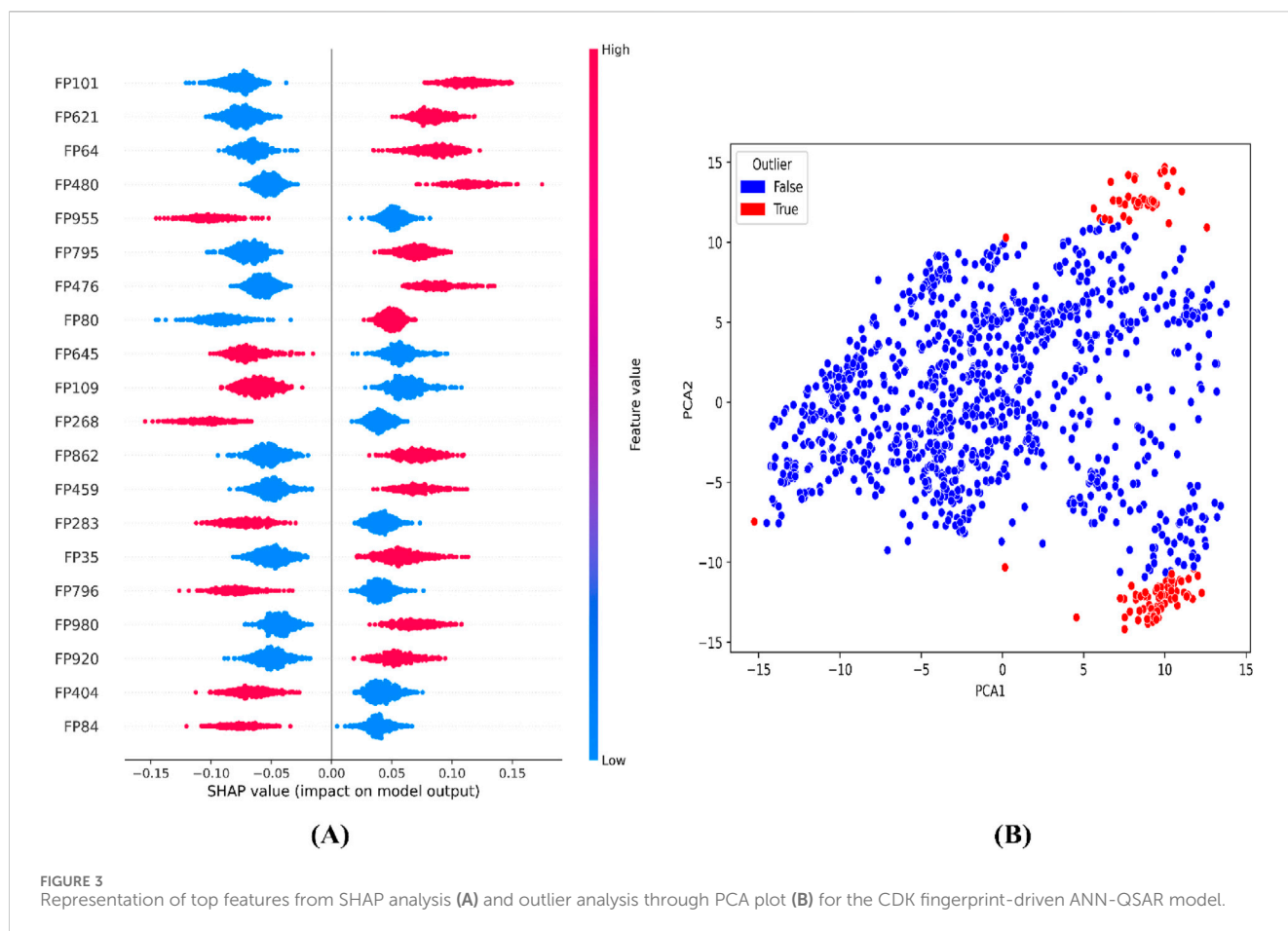
atom pair 2D fingerprint dataset. Following this, we followed an 80: 20 split for both fingerprint datasets before model development, individually for the two fingerprint datasets. The split resulted in 946 molecules in the training set and 237 molecules in the test set. We further implemented SVM, ANN, and RF-based ML algorithms using the generated training and test datasets to develop individual ML-QSARs for two different molecular features, i.e., CDK and atom 2D pair fingerprint datasets.

For the CDK fingerprint model, the ANN-driven QSAR model was found to show the best statistics and model accuracy for the initial run. The model demonstrated a Pearson correlation coefficient of 0.9874 and 0.6872, RMSE of 0.1511 and 0.7271, MSE of 0.0228 and 0.5287, and MAE of 0.0086 and 0.5614, for training and test datasets, respectively. Following the initial model run, we further implemented PCA analysis to detect the outliers in the datasets. The PCA-based clustering revealed that 119 molecules from both the training and test datasets deviated significantly from the main cluster and were classified as outliers. These molecules were removed from both the training and test datasets before final model deployment. Following outlier removal, we optimized hyperparameters for all 3 ML algorithms using randomized search cross-validation. For the RF model, we set the n_estimators between 100 and 700, the max_depth range between 10 and 30, and the min_sample_split range between 2 and 6. For the SVM model, we optimized the C value between 1 and 100, the gamma value range between 0.01 and 0.0001, the epsilon value between 0.01 and 0.2, and kernel type as "rbf," "poly," "sigmoid." Lastly, for

the RF model, we optimized hidden layer size to [(128,64), (256,128,64), (512,256,128)], set activation functions to "relu" and "tanh", and solver to "adam" and "sdg." For the RF model, the learning rates and maximum iterations were kept in the range of 0.001–0.1 and 1,000–2,000, respectively. Even after hyperparameter optimization, the ANN model demonstrated the best performance for the CDK fingerprints by demonstrating a Pearson correlation coefficient of 0.9845 and 0.7683, RMSE of 0.1674 and 0.6167, MSE of 0.028 and 0.3804, and MAE of 0.0915 and 0.4842, for the training and test datasets, respectively. Additionally, it demonstrated a 10-fold cross-validation of 0.7870. Overall, it was evident that the hypertuned CDK fingerprint-driven ANN-QSAR shows the best accuracy and robustness among all the trained models (Figure 1; Table 1).

For the atom 2D fingerprint model, the RF-driven QSAR model was found to show the best statistics and model accuracy for the initial run. The model demonstrated a Pearson correlation coefficient of 0.86088 and 0.73814, RMSE of 0.47631 and 0.62489, MSE of 0.22687 and 0.39084, and MAE of 0.33354 and 0.49899, for the training and test datasets, respectively. Additionally, the 10-fold cross-validation for the initial run of the RF-QSAR model was performed. Following the initial model run, we further implemented PCA analysis to detect the outliers in the datasets. The PCA-based clustering revealed that 118 molecules from both the training and test datasets deviated significantly from the main cluster and were classified as outliers. These compounds were removed from both the training and test datasets before final
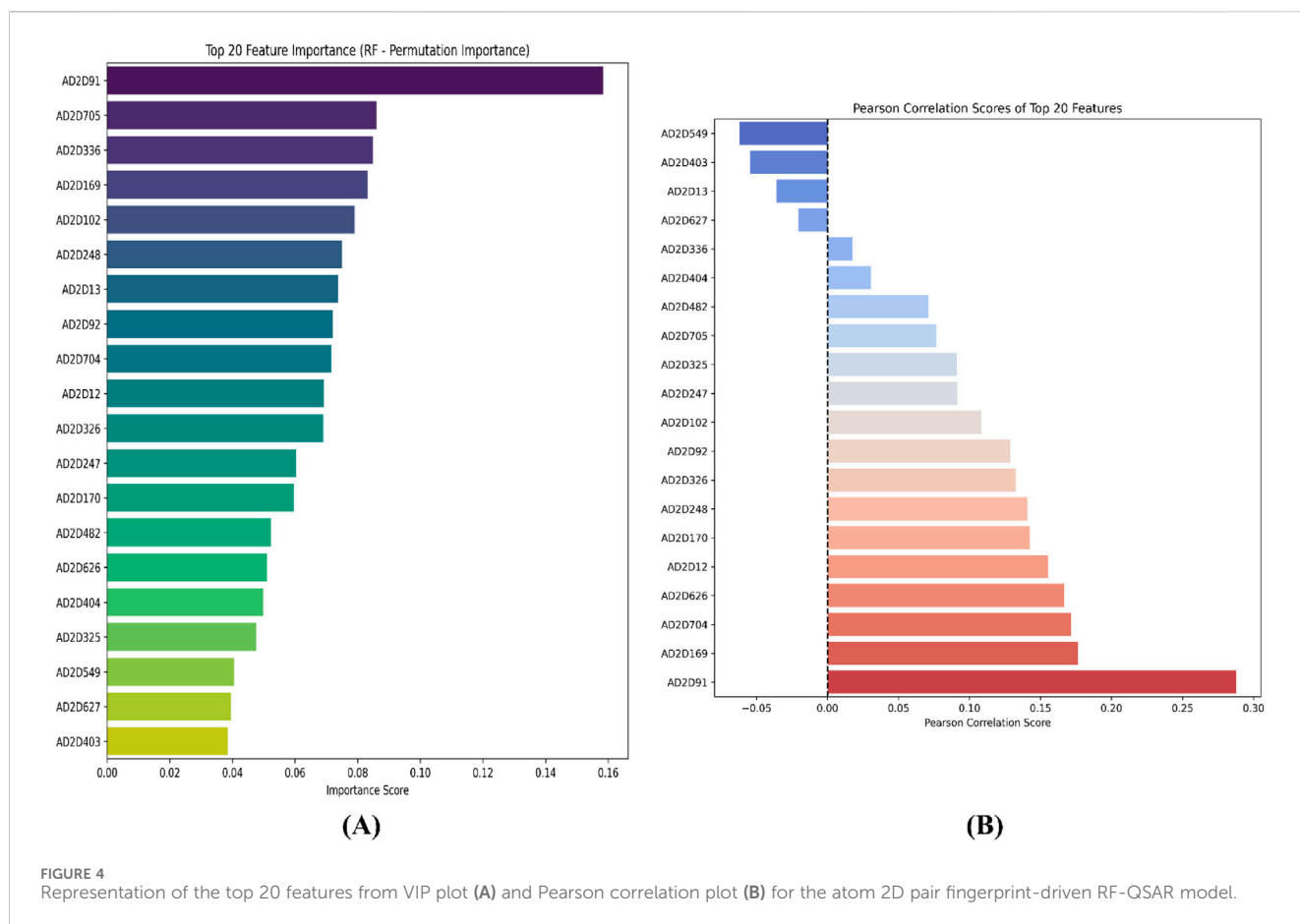
FIGURE 4
Representation of the top 20 features from VIP plot **(A)** and Pearson correlation plot **(B)** for the atom 2D pair fingerprint-driven RF-QSAR model.

model deployment. Following outlier removal, we optimized hyperparameters for all 3 ML algorithms using randomized search cross-validation. We kept the same hyperparameters for the 3 ML algorithms that we implemented previously for the CDK fingerprint-based QSAR models. Even after hyperparameter optimization, the RF model demonstrated the best performance for atom 2D pair fingerprints by demonstrating a Pearson correlation coefficient of 0.79293 and 0.69248, RMSE of 0.5438 and 0.63825, MSE of 0.2957 and 0.4073, and MAE of 0.4111 and 0.5184, for training and test datasets, respectively. Additionally, it demonstrated a 10-fold cross-validation of 0.7161. Since there was a reduction in the statistical robustness of the outlier-driven hypertuned model, we implemented the same hyperparameter optimization on the original dataset without outlier removal. We observed that even though the RF algorithm performed better than the outlier-driven hypertuned RF model, it still demonstrated low accuracy and robustness as compared to the initial RF-QSAR model with default parameters. Thereby, we concluded that the initial RF-QSAR model without outlier analysis demonstrated the best performance for the atom 2D pair fingerprint dataset (Figure 1; Table 2).

3.2 Feature elucidation of the ML-QSAR model for rational drug-design

To further interpret the top 20 significant features ML-QSAR model for rational design of novel and more efficient inhibitors, we implemented VIP plot, correlation matrix, and SHAP analysis. For the CDK fingerprint-driven ANN QSAR, we observed that fingerprints, like FP101, FP64, FP480, FP980, and FP35, demonstrated high variance threshold scores in VIP plot analysis, suggesting that the presence of these features in the inhibitor molecule might lead to an increase in biological activity (pIC$_{50}$ value). We also observed that fingerprints, FP84, FP109, and FP645, showed low variance threshold scores in the VIP plot, thereby suggesting they might have a negative relationship with biological activity. However, to build a suggestive narrative as to whether these fingerprints in the VIP plot are positively or negatively correlated, we further investigated them through a Pearson correlation matrix and SHAP analysis. Through Pearson correlation matrix analysis, we observed that FP480, FP980, and FP35 demonstrated positive correlation scores towards biological activity, whereas FP84, FP109, and FP645 demonstrated negative correlation scores towards biological activity. Furthermore, from SHAP analysis, it was evident that fingerprints FP480, FP980, and FP64 demonstrated high feature value, thereby suggesting that their presence would lead to an increased pIC$_{50}$ value, whereas on the other hand fingerprints FP84, FP109, and FP645, demonstrated negative SHAP values, suggesting the fact that their presence would lead to a decrease in pIC$_{50}$ value. Additionally, we did a molecular feature-driven Tanimoto clustering analysis of the high-activity and low-activity molecules of the QSAR dataset. The cluster analysis of the high activity molecules further validated the presence of fingerprints such as FP480, FP64, FP980, and FP35, which were already visualized by
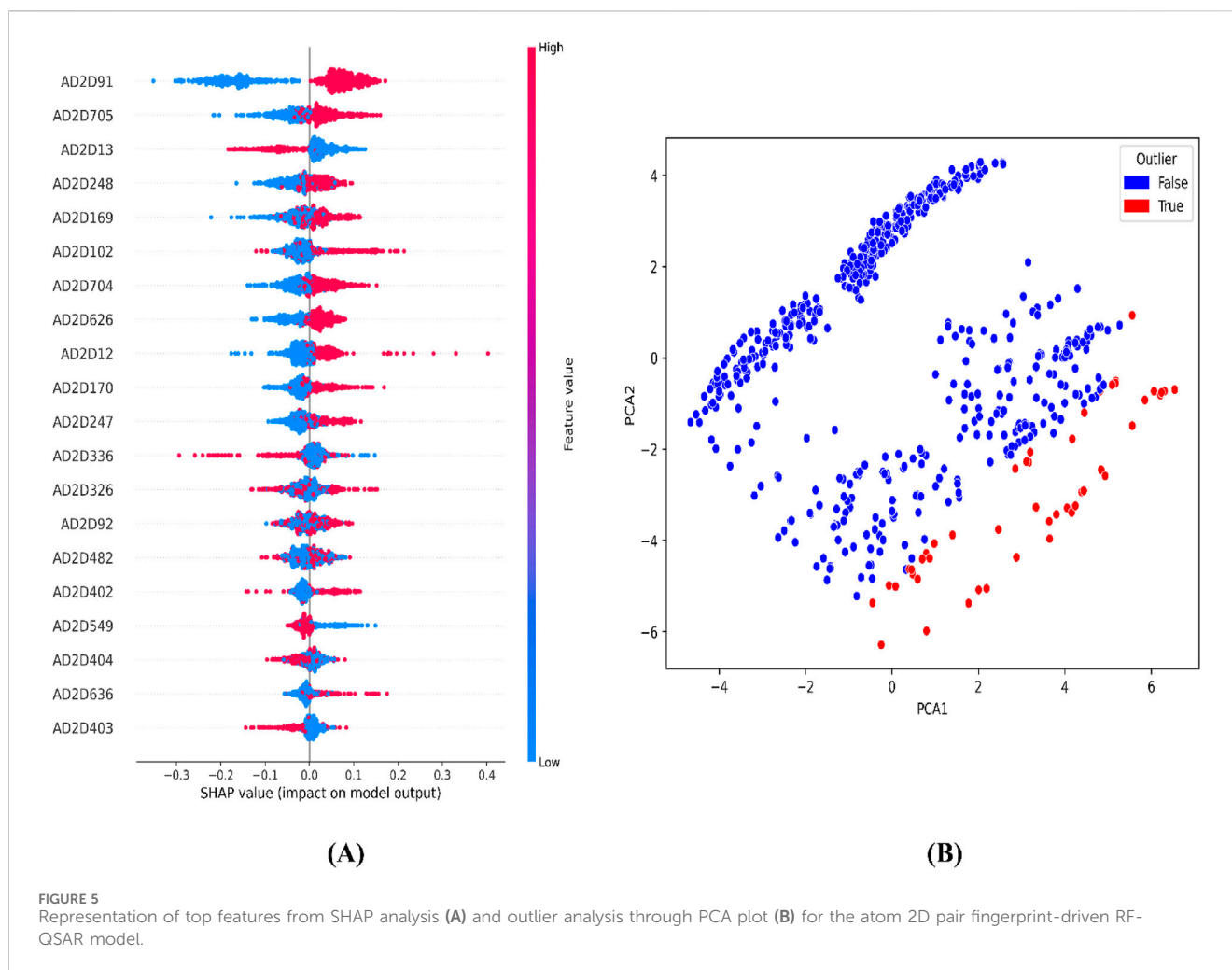
FIGURE 5
Representation of top features from SHAP analysis **(A)** and outlier analysis through PCA plot **(B)** for the atom 2D pair fingerprint-driven RF-QSAR model.

Pearson correlation and SHAP analysis plots as positively correlated features. Furthermore, the cluster analysis of the low activity molecules of the QSAR dataset further validated the presence of fingerprints such as FP84, FP109, and FP645, which were already labelled as negatively correlated by the Pearson correlation matrix and SHAP analysis (Figures 2, 3, 6).

For the atom 2D pair fingerprint-driven RF-QSAR model, it was evident that features AD2D91 (presence of N-N at topological distance 2), AD2D705 (presence of C-O at topological distance 10), AD2D336 (presence of O-O at topological distance 5), AD2D169 (presence of N-N at topological distance 3), AD2D102 (presence of O-O at topological distance 2), AD2D248 (presence of N-O at topological distance 4), and AD2D13 (presence of N-N at topological distance 1), demonstrated high variance threshold scores through the VIP plot analysis. We also observed that molecular features like, AD2D92 (presence of N-O at topological distance 2), AD2D704 (presence of C-N at topological distance 10), AD2D12 (presence of C-X at topological distance 1), AD2D247 (presence of N-N at topological distance 4), AD2D326 (presence of N-O at topological distance 5), AD2D170 (presence of N-O at topological distance 3), AD2D482 (presence of N-O at topological distance 7), AD2D626 (presence of C-N at topological distance 9), AD2D404 (presence of N-O at topological distance 6), AD2D325 (presence of N-N at

topological distance 5), AD2D549 (presence of C-O at topological distance 8), AD2D627 (presence of C-O at topological distance 9), and AD2D403 (presence of N-N at topological distance 6) demonstrated moderate to low variance threshold score through VIP plot analysis. To further investigate the nature of the correlation of the VIP plot-derived features, we conducted a Pearson correlation matrix and SHAP analysis. Through the Pearson correlation matrix analysis, it was evident that fingerprints AD2D91, AD2D169, AD2D704, AD2D626, and AD2D12 demonstrated positive correlation with high biological activity, whereas fingerprints AD2D170, AD2D248, AD2D326, AD2D92, AD2D102, AD2D325, and AD2D705 demonstrated moderately positive correlation with biological activity. Additionally, the Pearson correlation matrix also demonstrated that fingerprints, AD2D549, AD2D403, AD2D13, AD2D627, AD2D336, AD2D404, and AD2D482 showed negative correlation with biological activity. For SHAP analysis, it was observed that AD2D91, AD2D169, AD2D170, and AD2D12 demonstrated higher SHAP values, suggesting their positive impact on biological activity, whereas AD2D13, AD2D248, AD2D336, and AD2D705 showcased negative SHAP values, thereby demonstrating their negative impact on biological activity. We also did a molecular feature-driven Tanimoto clustering analysis of the high-activity and low-activity molecules of the QSAR dataset. We observed that positively

FIGURE 6
Representation of top features through Tanimoto similarity-driven cluster analysis of highly active **(A)** and low active molecules **(B)** from the CDK fingerprint dataset; highly active **(C)** and low active **(D)** molecules from the atom 2D pair fingerprint dataset.
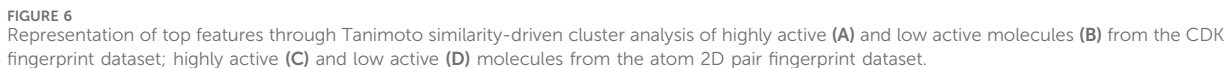
TABLE 3 Top 12 hit molecules bioactivity prediction scores using our previously developed ML-QSAR models.

Name	Predicted_pIC$_{50}$_a2d_fp	Predicted_pIC$_{50}$_cdk_fp	Predicted_pIC$_{50}$_cumulative
F2207-0115	4.9917	6.9805	5.9861
F2207-0102	5.2784	6.6665	5.9725
F6548-1609	5.1616	6.6195	5.8906
F6548-3996	5.3880	6.1246	5.7563
F6609-0134	5.9258	5.5255	5.7256
F6619-3684	5.9071	5.4719	5.6895
F2014-0155	5.5000	5.8509	5.6754
F6609-0164	5.5789	5.7068	5.6428
F3222-1452	4.9646	6.2789	5.6217
F0507-2033	6.8440	4.313	5.5785
F1872-0526	4.5384	6.6049	5.5716
F0676-0414	6.8440	4.2031	5.5236

TABLE 4 Docking score of 1ME3 with lead molecules from virtual screening, and native ligand. Best docking score is in bold.

Compound	Docking score (kcal/mol)	Compound	Docking score (kcal/mol)
F2207-0115	−5.052	F6609-0164	−4.842
F2207-0102	−4.368	F3222-1452	−5.252
F6548-1609	−3.843	F0507-2033	−5.389
F6548-3996	−4.236	F1872-0526	−4.864
F6609-0134	**−6.352**	F0676-0414	−5.479
F6619-3684	−3.868	Co-ligand	−6.023
F2014-0155	−4.94		

correlated features such as AD2D549, AD2D102, AD2D336, AD2D92, AD2D248, AD2D404, AD2D704, AD2D170, AD2D403, AD2D626, AD2D12, and AD2D326 from the Pearson correlation matrix and SHAP analysis were also found to be present in the cluster analysis of highly active molecules of the dataset. On the other hand, molecular features like AD2D480, which were labelled to be negatively correlated to biological activity in both SHAP and Pearson correlation matrix analysis, were found to be significantly present in cluster analysis of low activity molecules of the QSAR dataset (Figures 4–6).

3.3 Machine learning-driven chemical library screening

We initially screened the Antiprotozoal Screening Compound Library of 8,200 molecules from the Life Chemicals database using the combination of Lipinski's Rule of Five, Veber's Rule, and Ghose's Filter through the ChemBioServer 2.0. A total of 133 molecules that passed through this filtration step were further subjected to toxiphore analysis. A total of 93 out of 133 molecules were found to pass the toxicophore analysis study. Following this, we further predicted the biological activity (pIC_{50} value) of the 93 molecules using our previously developed CDK fingerprint-driven RF-QSAR and atom 2 days pair fingerprint-driven ANN-QSAR model. We then calculated the cumulative of the predicted biological activities for each molecule from both models to identify the most promising inhibitor. To streamline the drug discovery process further, we identified 12 molecules with $pIC_{50} \geq 5$ (Table 3).

3.4 Molecular docking

Molecular docking studies were conducted to have a better understanding of the lead compound's binding processes. Lead compounds found by virtual screening coupled with the 1ME3 protein, and the docking procedure was confirmed using native ligands. We also did a comparative docking analysis with the native ligand P10 (PubChem CID: 5289091). P10 molecule has already been experimentally tested as an active against *T. cruzi* (BioAssay AID: 977610; BioAssay AID: 1811). In the previous study on the 3D crystal structure of 1ME3, inhibitors were found to form a strong hydrogen bond with His159, part of the canonical catalytic

triad (Cys25, His159, Asn175). The P2-position phenylalanine fits into the hydrophobic S2 pocket formed by Leu67, Ala133, and Leu157, with Glu205 rotating to accommodate the side chain. The inhibitor backbone is stabilized by hydrogen bonds with Gly66 and Asp158, along with key water-mediated interactions. Additionally, the nitrogen atom of inhibitors shows potential interaction with the hydroxyl group of Ser61. The compounds mentioned in Table 4 have docking scores (XP mode) for 1ME3 ranging from −3.843 to −6.352 kcal/mol. With a docking score of −6.352 kcal/mol, F6609-0134 had the highest binding affinity of all of them, whereas the co-ligand received a value of −6.023 kcal/mol (Table 4). F6609-0134 established a hydrogen connection with Leu157, more precisely with the NH atom of the pyrimidine ring, according to an analysis of the 2-D and 3-D interaction map. Hydrophobic interactions were also noted with Asp158, Gly160, Glu205, Leu67, Met68, Cys25, Trp26, Thr59, Ser61, and Ser64 (Figure 7). Furthermore, the lead chemical demonstrated hydrogen bonding with significant residues, as previously reported in the literature and discussed above regarding the binding pocket (Durrant et al., 2010; Rampogu et al., 2018; Rogers et al., 2012; Wiggers et al., 2013; Huang et al., 2003). The discovered hits may be promising lead candidates for the therapy of Chagas disease, as the lead compound had lower binding energies and higher docking scores than the reference compounds.

3.5 Molecular dynamics

To investigate the flexibility and stability of the docked complex of F6609-0134 at the binding site of the 1ME3 protein in biological situations, MD simulations were performed. We also performed a comparative MD analysis of our hit molecule against P10 molecules (co-crystallized native ligand). MD trajectories were used to calculate protein-ligand interactions as well as RMSD and RMSF. Figure 8 shows a number of analyses of the MD trajectory data for the F6609-0134-1ME3 complex.

3.5.1 Root mean square deviation

According to RMSD Figure 8, the Cα atoms of the protein in connection with F6609-0134 and co-ligand had RMSD values ranging from 0.83 to 1.80 Å and 0.74 to 1.52 Å, respectively. This suggests that the ligand-protein complex remained stable throughout the simulation. Except for a slight variation observed between 120 and 130 ns, the protein's RMSD remained constant
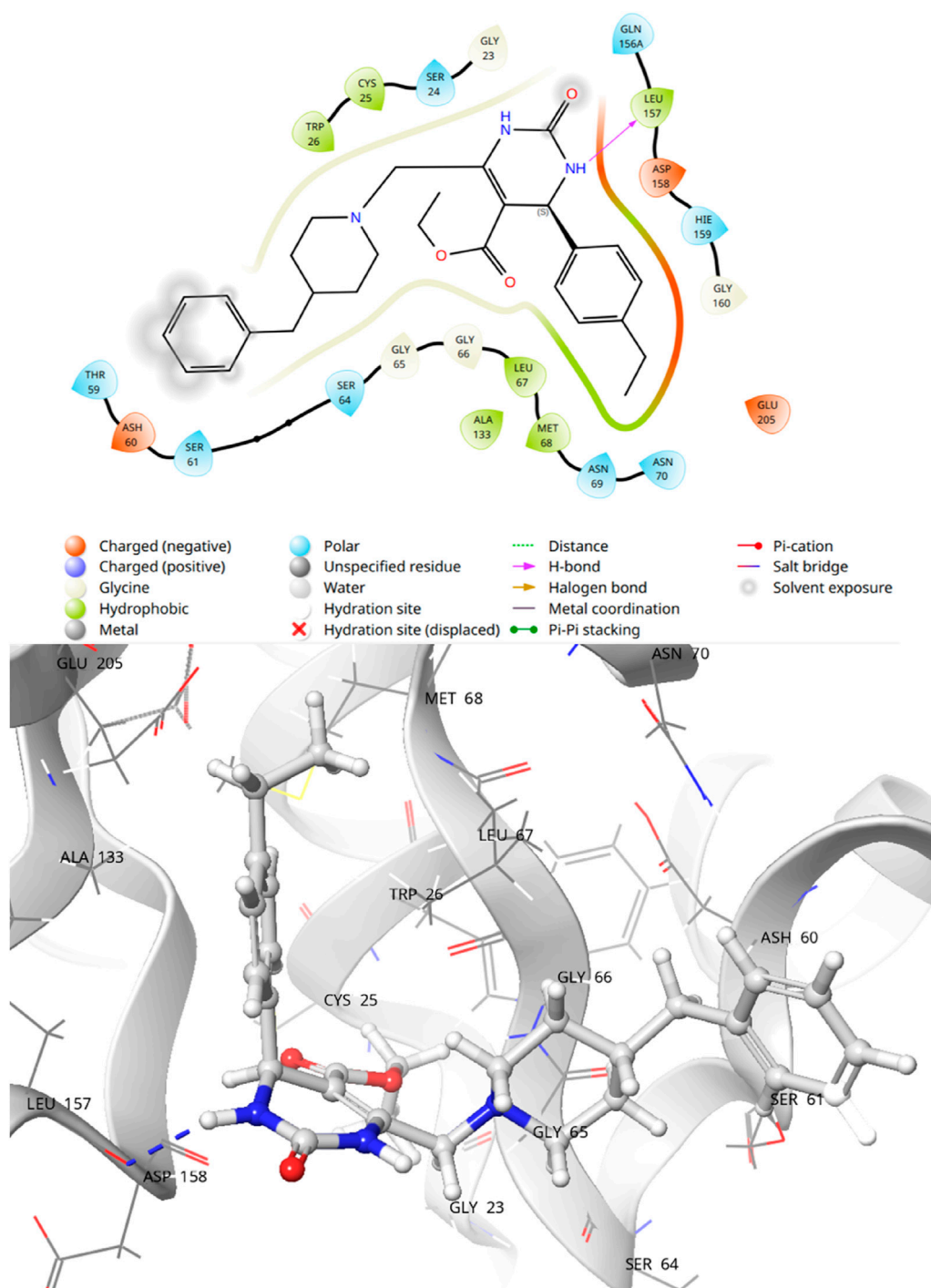
FIGURE 7
2-D and 3D interaction of Lead compound F6609-0134 with binding pocket of 1ME3.

throughout the simulation, and the co-ligands did not differ all that much. Based on the complex's predicted trajectory, the RMSD values of its Cα atoms demonstrated the stability of the protein-ligand complex in a dynamic environment. A higher RMSD value indicates unfolding for protein Cα atoms, whereas a smaller value indicates compactness. The modest change in the backbone RMSD further supported the equilibration of the protein-ligand combination. The difference between the highest and lowest

RMSD values represented the backbone deviation. In summary, the total RMSD of the F6609-0134-1ME3 complex remains consistent and dependable in a fluctuating environment.

3.5.2 Root mean square fluctuation

The flexibility of the protein system was measured during the simulation using the RMSF of each amino acid residue. The RMSF plot showed that differences in N-terminal residues were more
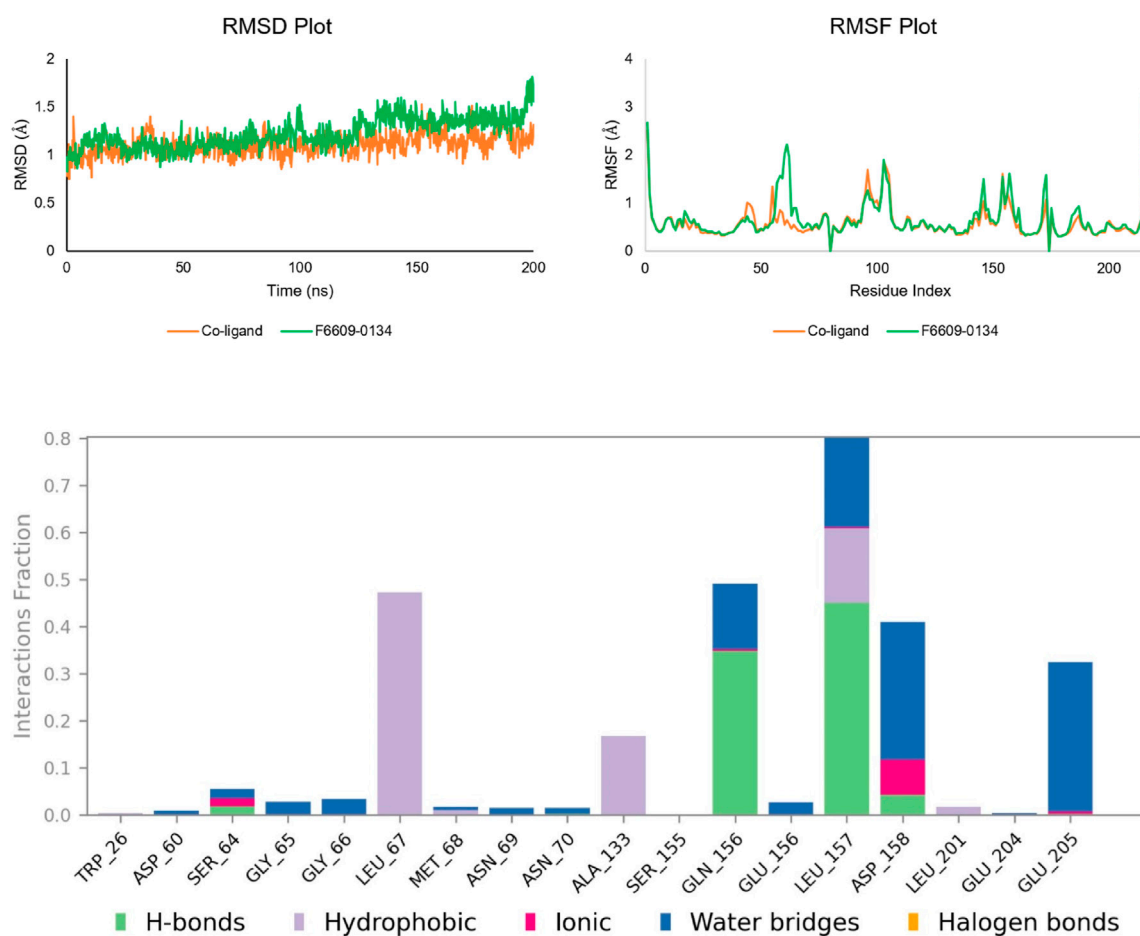
FIGURE 8
Analysis of the inhibitor-ligand complex using MD simulation: RMSD plot (co-crystallized ligand RMSD is shown in orange, and RMSD of F6609-0134 is shown in green); RMSF plot (co-crystallized ligand RMSF is shown in orange, and RMSF of F6609-0134 is shown in green); and analysis of protein-ligand contacts of the MD trajectory of the F6609-0134-1ME3 complex.

TABLE 5 Amino acid contacts with the ligand and their RMSF value.

Compound	Amino acids that come into contact with ligands and their RMSF (Å)
F6609-0134	Trp26 (0.44 Å), Asp60 (2.02 Å), Ser64 (0.89 Å), Gly65 (0.89 Å), Gly66 (0.63 Å), Leu67 (0.57 Å), Met68 (0.48 Å), Asn69 (0.50 Å), Asn70 (0.57 Å), Ala133 (0.43 Å), Ser155 (1.61 Å), Glu156 (1.18 Å), Gln156 (0.76 Å), Leu157 (0.62 Å), Asp158 (0.9 Å), Leu201 (0.48 Å), Glu204 (0.56 Å), and Glu205 (0.48 Å)
Co-ligand	Gln19 (0.46 Å), Cys25 (0.37 Å), Trp26 (0.39 Å), Thr59 (0.81 Å), Asp60 (0.55 Å), Ser61 (0.65 Å), Cys63 (0.47 Å), Ser64 (0.54 Å), Gly65 (0.48 Å), Gly66 (0.42 Å), Leu67 (0.42 Å), Met68 (0.38 Å), Asn70 (0.44 Å), Ala133 (0.39 Å), Ala136 (0.46 Å), Leu157 (0.49 Å), Asp158 (0.55 Å), His159 (0.36 Å), and Trp177 (0.49 Å)

noticeable. During the simulation, it was discovered that the co-ligand and compound F6609-0134 interacted with amino acids 19 and 18, respectively, of 1ME3. With a few exceptions (Figure 8; Table 5), all of these interacting residues had RMSF values smaller than 1 Å. Certain amino acid residues in the protein-ligand complex are essential for the stability of dynamic processes. The RMSF parameter, which is derived from the MD simulation trajectories, measures the deviation of individual amino acids from the reference or native structure. The RMSF visualization facilitates comprehension of the remaining vibrations in the F6609-0134-1ME3 complex. This finding suggests a solid binding of the lead medication with minor conformational changes within the binding pocket of the target protein, since the main chain and active site residues only slightly varied.

3.5.3 Protein ligand contact analysis

The most prevalent contact types, as determined by MD simulations, were hydrophobic, hydrogen bonding, and polar (water-mediated hydrogen bonding). According to a protein-ligand contact research, Leu67, Ala133, Glu156, Leu157, Asp158, and Glu205 strongly contacted F6609-0134. The simulation results show that compound F6609-0134, Leu167, Gln156, Leu157, Asp157, and Glu205 can stabilize 1ME3 protein because the particular contact is sustained for over 40% of the simulation time

FIGURE 9
Secondary structure element (SSE) distribution plotted against residue index for 1ME3. The SSE composition across each trajectory frame throughout the simulation for 1ME3.

FIGURE 10
PCA of F6609-0134-1ME3 protein-ligand complex.

TABLE 6 Free binding energies of the molecule F6609-0134 shown through MM-GBSA.*

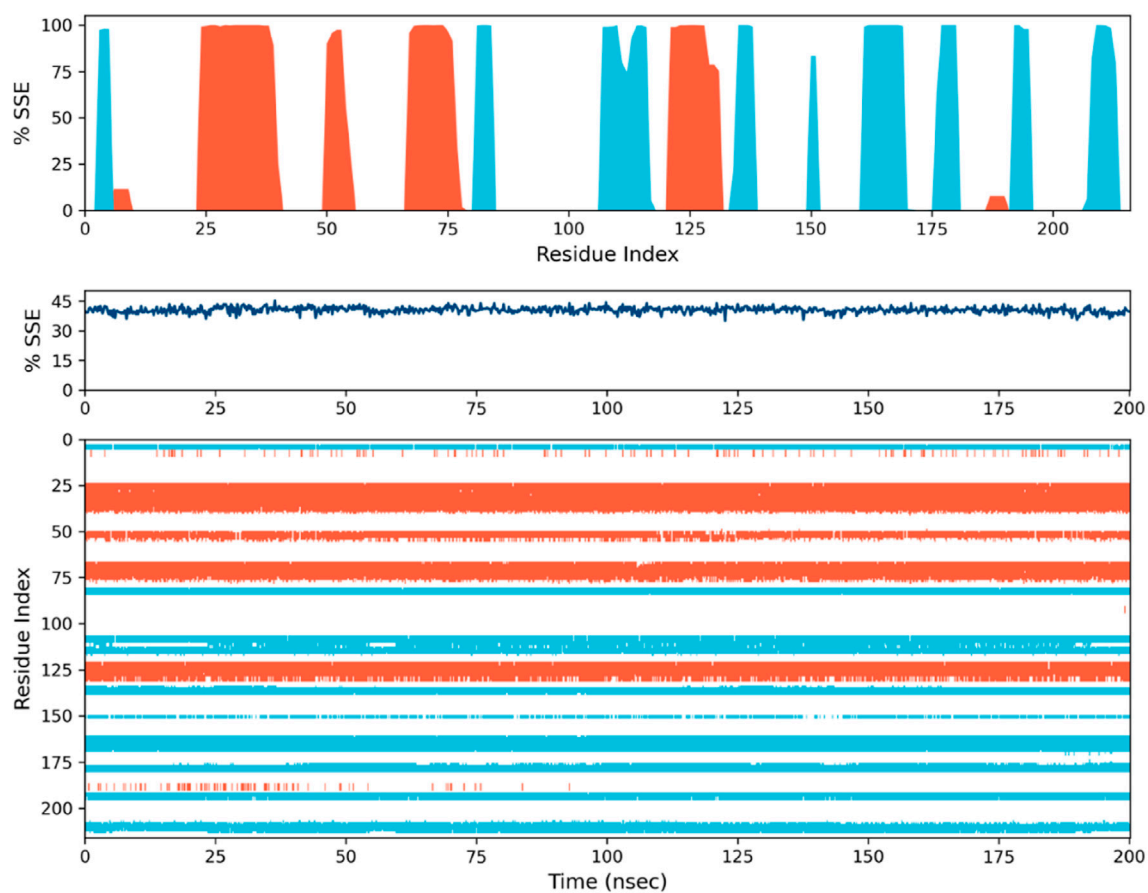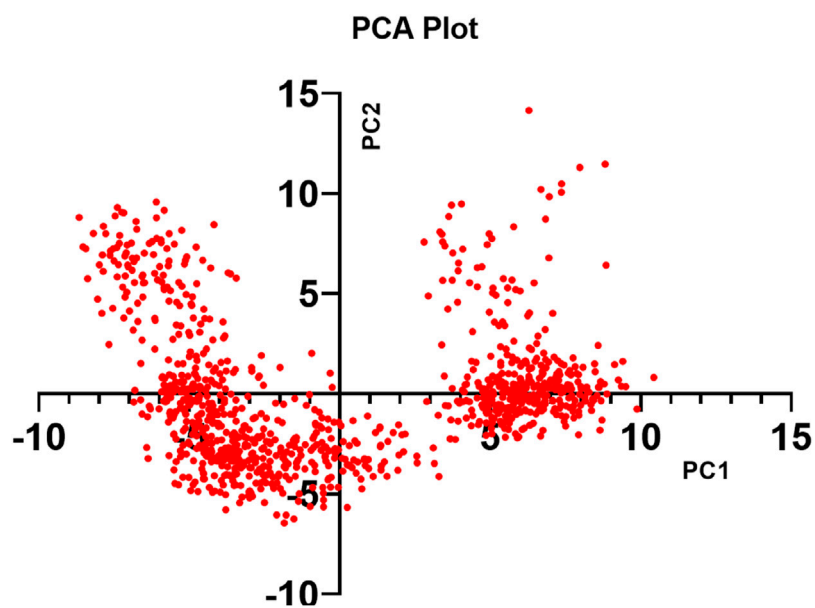| MD snapshot (ns)	ΔG bind	ΔG bind H-bond	ΔG bind lipo	ΔG bind vdW
0	−42.53	−0.44	−19.28	−41.31
20	−44.91	−0.32	−12.51	−44.77
40	−48.29	−0.65	−11.28	−43.58
60	−36.16	−0.09	−14.18	−43.65
80	−43.75	−0.28	−16.17	−44.75
100	−31.46	−1.30	−12.02	−27.83
120	−38.84	−1.05	−14.46	−34.12
140	−40.92	−0.10	−19.65	−41.10
160	−42.44	−0.86	−17.16	−39.31
180	−35.11	−1.33	−13.02	−37.02
200	−33.87	−1.00	−13.20	−31.12
Average	**−39.84**	**−0.67**	**−14.81**	**−38.96**

*kcal/mol.

(Figure 8). Comparing the ligand's 2-D interaction during docking (Figure 9) with the subsequent simulation reveals similar interactions. The Figure 7 simulation result for compound F6609-0134 indicates that it forms a hydrogen bond with amino acid Leu157, which may indicate that it can stabilize the binding pocket of 1ME3.

3.5.4 Protein secondary structure elements

The comparative analysis of secondary structure elements (SSE) in the 1ME3 protein highlights notable differences in structural organization and stability over a 200 ns molecular dynamics (MD) simulation. The SSE histogram plots reveal that 1ME3 consistently exhibits prominent α-helices (in red) and β-strands (in blue) across its residue indices. This continuous and broader distribution of secondary structures reflects a well-organized and stable protein conformation. As shown in Figure 9, 1ME3 maintains an overall SSE content of 40.54%, comprising 19.45% α-helices and 21.09% β-strands. These values indicate a slightly more ordered and stable secondary structure. Furthermore, the SSE timeline plots (Figure 9) confirm that 1ME3 preserves its secondary structure throughout the simulation, with minimal structural deviations. Overall, the data suggest that the 1ME3 protein retains its structural integrity and demonstrates marginally enhanced conformational stability, as evidenced by higher SSE content and reduced fluctuations during the MD simulation.

3.5.5 Principal component analysis (PCA)

Throughout the simulation, the PCA method was used to examine the protein's conformational distribution and large-scale collective motions within the protein-ligand complex. Using the Desmond script (trj_essential_dynamics.py), Essential Dynamics (ED) analysis calculated the primary components of Cα atoms to anticipate the dynamic behavior of the protein. Except for PC1 and PC2 negative modes, phase-space projection along PC1 showed a consistent conformational distribution. RMSD, RMSF, and PCA values derived from MD

simulation trajectories verified the stability of the F6609–0134–1ME3 complex in dynamic states (Figure 10).

3.5.6 Molecular mechanics/generalized born surface area (MM-GBSA)

The free binding energy of the ideal molecule, F6609-0134, which exhibited the highest docking score and predicted activity, was analyzed based on its molecular dynamics (MD) simulation frames. Over a 0–200 ns MD trajectory, the total average binding energies were calculated as follows: ΔG Bind (−39.84 kcal/mol), ΔG Bind H-bond (−0.67 kcal/mol), ΔG Bind Lipo (−14.81 kcal/mol), and ΔG Bind vdW (−38.96 kcal/mol). Analysis of these values, as presented in Table 6, indicates that ΔG Bind and ΔG Bind vdW contributed most significantly to the overall binding energy, emphasizing the role of van der Waals interactions in molecular stability.

Stable van der Waals contacts with important amino acid residues were found by analyzing the ΔG Bind vdW values for F6609-0134 interactions with the protein complex. It was discovered that the binding energies derived from MM-GBSA computations based on MD simulation trajectories and docking investigations were consistent. Interestingly, the molecule's low free binding energy suggested that it had a high affinity for the receptor. These results support F6609-0134's potential as a promising inhibitor by indicating that it interacts strongly with 1ME3.

4 Conclusion

Trypanosoma cruzi causes Chagas disease, a neglected tropical illness that continues to pose a serious threat to world health because of the lack of effective treatments and medication resistance. The potential of machine learning-driven QSAR modeling to speed up the drug discovery process for Chagas disease is demonstrated in this work. The model exhibiting the highest predictive accuracy among those assessed was the ANN-based QSAR model utilizing CDK fingerprints. The stability and high binding affinity of F6609-0134 were confirmed

using molecular docking studies and molecular dynamics simulations, which further substantiated its selection as a possible lead molecule. According to these findings, F6609-0134 is a promising therapeutic option for *Trypanosoma cruzi* that needs more experimental support. The molecule should be manufactured or purchased commercially to enhance its potential as an anti-Chagas agent, and thorough *in vitro* tests aimed at *T. cruzi* should be used to evaluate its effectiveness. In the end, these follow-up investigations will promote its development as a treatment candidate for Chagas disease by confirming its trypanocidal efficacy and offering crucial information on cytotoxicity, selectivity, and mechanism of action.

Data availability statement

The datasets used in this study were curated from ChEMBL (https://www.ebi.ac.uk/chembl/), which is an open-source data repository. The code for generating the ML-assisted QSAR model can be found at: https://github.com/RatulChemoinformatics/QSAR-Models.

Author contributions

NM: Writing – review and editing, Writing – original draft. SK: Methodology, Supervision, Data curation, Conceptualization, Writing – review and editing, Visualization, Writing – original draft, Validation, Formal Analysis. RB: Writing – original draft, Data curation, Methodology, Writing – review and editing, Formal Analysis. HV: Writing – original draft. PY: Writing – original draft. BM: Writing – review and editing, Conceptualization, Writing – original draft, Supervision.

Conflict of interest

The authors declare that the research was conducted in the absence of any commercial or financial relationships that could be construed as a potential conflict of interest.

Generative AI statement

The author(s) declare that no Generative AI was used in the creation of this manuscript.

Publisher's note

All claims expressed in this article are solely those of the authors and do not necessarily represent those of their affiliated organizations, or those of the publisher, the editors and the reviewers. Any product that may be evaluated in this article, or claim that may be made by its manufacturer, is not guaranteed or endorsed by the publisher.

References

Abras, A., Ballart, C., Fernández-Arévalo, A., Pinazo, M.-J., Gascón, J., Muñoz, C., et al. (2022). Worldwide control and management of Chagas disease in a new era of globalization: a close look at congenital *Trypanosoma cruzi* infection. *Clin. Microbiol. Rev.* 35 (2), e0015221. doi:10.1128/cmr.00152-21

Baldi, A. (2010). Computational approaches for drug design and discovery: an overview. *Syst. Rev. Pharm.* 1 (1), 99. doi:10.4103/0975-8453.59519

Bayat Mokhtari, R., Homayouni, T. S., Baluch, N., Morgatskaya, E., Kumar, S., Das, B., et al. (2017). Combination therapy in combating cancer. *Oncotarget* 8 (23), 38022–38043. doi:10.18632/oncotarget.16723

Breiman, L. (2001). Random forests. *Mach. Learn.* 45 (1), 5–32. doi:10.1023/A:1010933404324

Cao, D., Deng, Z., Zhu, M., Yao, Z., Dong, J., and Zhao, R. (2017). Ensemble partial least squares regression for descriptor selection, outlier detection, applicability domain assessment, and ensemble modeling in QSAR/QSPR modeling. *J. Chemom.* 31 (11). doi:10.1002/cem.2922

Carbajal-de-la-Fuente, A. L., Sánchez-Casaccia, P., Piccinali, R. V., Provecho, Y., Salvá, L., Meli, S., et al. (2022). Urban vectors of Chagas disease in the American continent: a systematic review of epidemiological surveys. *PLoS Neglected Trop. Dis.* 16 (12), e0011003. doi:10.1371/journal.pntd.0011003

Cheesman, M. J., Ilanko, A., Blonk, B., and Cock, I. E. (2017). Developing new antimicrobial therapies: are synergistic combinations of plant extracts/compounds with conventional antibiotics the solution? *Pharmacogn. Rev.* 11 (22), 57–72. doi:10.4103/phrev.phrev_21_17

Choi, J. Y., Podust, L. M., and Roush, W. R. (2014). Drug strategies targeting CYP51 in neglected tropical diseases. *Chem. Rev.* 114 (22), 11242–11271. doi:10.1021/cr5003134

da Costa, A. P. L., Silva, J. R. A., and de Molfetta, F. A. (2022). Computational discovery of sulfonamide derivatives as potential inhibitors of the cruzain enzyme from *T. cruzi* by molecular docking, molecular dynamics and MM/GBSA approaches. *Mol. Simul.* 48 (18), 1678–1687. doi:10.1080/08927022.2022.2120625

Durrant, J. D., Keränen, H., Wilson, B. A., and McCammon, J. A. (2010). Computational identification of uncharacterized cruzain binding sites. *PLoS Neglected Trop. Dis.* 4 (5), e676. doi:10.1371/journal.pntd.0000676

Fraundorfer, M. (2024). "Neglected tropical diseases," in *South American policy regionalism* (Brazil: Routledge), 223–247. doi:10.4324/9781003519577-14

Goel, A., Goel, A. K., and Kumar, A. (2023). The role of artificial neural network and machine learning in utilizing spatial information. *Spatial Inf. Res.* 31 (3), 275–285. doi:10.1007/s41324-022-00494-x

Harrison, J. R., Sarkar, S., Hampton, S., Riley, J., Stojanovski, L., Sahlberg, C., et al. (2020). Discovery and optimization of a compound series active against *Trypanosoma cruzi*, the causative agent of Chagas disease. *J. Med. Chem.* 63 (6), 3066–3089. doi:10.1021/acs.jmedchem.9b01852

Huang, L., Brinen, L. S., and Ellman, J. A. (2003). Crystal structures of reversible ketone-based inhibitors of the cysteine protease cruzain. *Bioorg. Med. Chem.* 11 (1), 21–29. doi:10.1016/s0968-0896(02)00427-3

Kannigadu, C., and N'Da, D. D. (2020). Recent advances in the synthesis and development of nitroaromatics as anti-infective drugs. *Curr. Pharm. Des.* 26 (36), 4658–4674. doi:10.2174/1381612826666200331091853

Karatzas, E., Zamora, J. E., Athanasiadis, E., Dellis, D., Cournia, Z., and Spyrou, G. M. (2020). ChemBioServer 2.0: an advanced web server for filtering, clustering and networking of chemical compounds facilitating both drug discovery and repurposing. *Bioinforma. Oxf. Engl.* 36 (8), 2602–2604. doi:10.1093/bioinformatics/btz976

Keenan, M., Alexander, P. W., Diao, H., Best, W. M., Khong, A., Kerfoot, M., et al. (2013). Design, structure-activity relationship and *in vivo* efficacy of piperazine analogues of fenarimol as inhibitors of Trypanosoma cruzi. *Bioorg. and Med. Chem.* 21 (7), 1756–1763. doi:10.1016/j.bmc.2013.01.050

Keenan, M., and Chaplin, J. H. (2015). A new era for chagas disease drug discovery? *Prog. Med. Chem.* 54, 185–230. doi:10.1016/bs.pmch.2014.12.001

Kiehl, W. M., Hodo, C. L., Hamer, G. L., Hamer, S. A., and Wilkerson, G. K. (2023). Exclusion of horizontal and vertical transmission as major sources of *Trypanosoma cruzi* infections in a breeding colony of rhesus macaques (Macaca mulatta). *Comp. Med.* 73 (3), 229–241. doi:10.30802/AALAS-CM-23-000005

Kumar, S., Oh, J. M., Prabhakaran, P., Awasti, A., Kim, H., and Mathew, B. (2024). Isatin-tethered halogen-containing acylhydrazone derivatives as monoamine oxidase inhibitor with neuroprotective effect. *Sci. Rep.* 14 (1), 1264. doi:10.1038/s41598-024-51728-x

Lepesheva, G. I., Ott, R. D., Hargrove, T. Y., Kleshchenko, Y. Y., Schuster, I., Nes, W. D., et al. (2007). Sterol 14α-demethylase as a potential target for antitrypanosomal therapy: enzyme inhibition and parasite cell growth. *Chem. Biol.* 14 (11), 1283–1293. doi:10.1016/j.chembiol.2007.10.011

Lepesheva, G. I., Villalta, F., and Waterman, M. R. (2011). Targeting *Trypanosoma cruzi* sterol 14α-demethylase (CYP51). *Adv. Parasitol.* 75, 65–87. doi:10.1016/B978-0-12-385863-4.00004-6

Maliyakkal, N., Oh, J. M., Kumar, S., Gahori, P., Tengli, A., Beeran, A. A., et al. (2024). Synthesis, biochemistry, and *in silico* investigations of isatin-based hydrazone derivatives as monoamine oxidase inhibitors. *Appl. Biol. Chem.* 67 (1), 63. doi:10.1186/s13765-024-00917-3

Mazzeti, A. L., Capelari-Oliveira, P., Bahia, M. T., and Mosqueira, V. C. F. (2021). Review on experimental treatment strategies against *Trypanosoma cruzi*. *J. Exp. Pharmacol.* 13, 409–432. doi:10.2147/JEP.S267378

Naithani, U., and Guleria, V. (2024). Integrative computational approaches for discovery and evaluation of lead compound for drug design. *Front. Drug Discov.* 4. doi:10.3389/fddsv.2024.1362456

Nohara, Y., Matsumoto, K., Soejima, H., and Nakashima, N. (2022). Explanation of machine learning models using shapley additive explanation and application for real data in hospital. *Comput. Methods Programs Biomed.* 214, 106584. doi:10.1016/j.cmpb.2021.106584

Parker, J. E., Warrilow, A. G. S., Price, C. L., Mullins, J. G. L., Kelly, D. E., and Kelly, S. L. (2014). Resistance to antifungals that target CYP51. *J. Chem. Biol.* 7 (4), 143–161. doi:10.1007/s12154-014-0121-1

Patel, H. M., Noolvi, M. N., Sharma, P., Jaiswal, V., Bansal, S., Lohan, S., et al. (2014). Quantitative structure–activity relationship (QSAR) studies as strategic approach in drug discovery. *Med. Chem. Res.* 23 (12), 4991–5007. doi:10.1007/s00044-014-1072-3

Patterson, S., and Fairlamb, A. H. (2019). Current and future prospects of nitro-compounds as drugs for trypanosomiasis and leishmaniasis. *Curr. Med. Chem.* 26 (23), 4454–4475. doi:10.2174/0929867325666180426164352

Rabelo, V. W., Santos, T. F., Terra, L., Santana, M. V., Castro, H. C., Rodrigues, C. R., et al. (2017). Targeting CYP51 for drug design by the contributions of molecular modeling. *Fundam. Clin. Pharmacol.* 31 (1), 37–53. doi:10.1111/fcp.12230

Rampogu, S., Lee, G., Baek, A., Son, M., Park, C., Zeb, A., et al. (2018). Discovery of non-peptidic compounds against chagas disease applying pharmacophore guided molecular modelling approaches. *Mol. Basel Switz.* 23 (12), 3054. doi:10.3390/molecules23123054

Rassi, A., Rassi, A., and Marcondes de Rezende, J. (2012). American trypanosomiasis (Chagas disease). *Infect. Dis. Clin. N. Am.* 26 (2), 275–291. doi:10.1016/j.idc.2012.03.002

Rassi, A., Rassi, A., and Marin-Neto, J. A. (2010). Chagas disease. *Lancet London Engl.* 375 (9723), 1388–1402. doi:10.1016/S0140-6736(10)60061-X

Rogers, K. E., Keränen, H., Durrant, J. D., Ratnam, J., Doak, A., Arkin, M. R., et al. (2012). Novel cruzain inhibitors for the treatment of Chagas' disease. *Chem. Biol. Drug Des.* 80 (3), 398–405. doi:10.1111/j.1747-0285.2012.01416.x

Salomao, K., Menna-Barreto, R. F. S., and de Castro, S. L. (2016). Stairway to heaven or hell? Perspectives and limitations of chagas disease chemotherapy. *Curr. Top. Med. Chem.* 16 (20), 2266–2289. doi:10.2174/1568026616666160413125049

Sarabi Asiabar, A., Jabbari, A., Rezapour, A., Jabbari Khanbebin, M., Atafimanesh, P., Mazaheri, E., et al. (2024). Policy and executive barriers in preventing and eradicating neglected tropical diseases: a systematic review. *Int. J. Prev. Med.* 15, 49. doi:10.4103/ijpvm.ijpvm_251_23

Siddiqui, B., Yadav, C. S., Akil, M., Faiyyaz, M., Khan, A. R., Ahmad, N., et al. (2025). Artificial intelligence in computer-aided drug design (CADD) tools for the finding of potent biologically active Small molecules: traditional to modern approach. *Comb. Chem. High Throughput Screen.* 28. doi:10.2174/0113862073334062241015043343

Trovato, M., Sartorius, R., D'Apice, L., Manco, R., and De Berardinis, P. (2020). Viral emerging diseases: challenges in developing vaccination strategies. *Front. Immunol.* 11, 2130. doi:10.3389/fimmu.2020.02130

Utkin, V. (2019). An imprecise extension of SVM-based machine learning models. *Neurocomputing* 331, 18–32. doi:10.1016/j.neucom.2018.11.053

Wiggers, H. J., Rocha, J. R., Fernandes, W. B., Sesti-Costa, R., Carneiro, Z. A., Cheleski, J., et al. (2013). Non-peptidic cruzain inhibitors with trypanocidal activity discovered by virtual screening and *in vitro* assay. *PLoS Neglected Trop. Dis.* 7 (8), e2370. doi:10.1371/journal.pntd.0002370

Winkler, D. A. (2002). The role of quantitative structure--activity relationships (QSAR) in biomolecular discovery. *Briefings Bioinforma.* 3 (1), 73–86. doi:10.1093/bib/3.1.73

Yap, C. W. (2011). PaDEL-descriptor: an open source software to calculate molecular descriptors and fingerprints. *J. Comput. Chem.* 32 (7), 1466–1474. doi:10.1002/jcc.21707

Zobi, C., and Algul, O. (2025). The significance of mono- and dual-effective agents in the development of new antifungal strategies. *Chem. Biol. Drug Des.* 105 (1), e70045. doi:10.1111/cbdd.70045

Ruta montana L. from Morocco: comprehensive phytochemical analysis and exploration of its antioxidant, antimicrobial, anti-inflammatory and analgesic properties

Mohamed El Ouardi[1,2], Aziz Drioiche[1,3]*, Imane Tagnaout[2], Aicha Benouahi[1,2], Omkulthom AL kamaly[4], Abdelaaty Abdelaziz Shahat[5], El Makhoukhi Fadoua[1,2], Handaq Nadia[2], Sevser Sahpaz[6], Touriya Zair[2]* and Mohamed Alaoui Belghiti[1]

[1]Laboratory of Spectroscopy, Molecular Modelling, Materials, Nanomaterial, Water and Environment, CERNE2D, Faculty of Science, Mohammed V, University in Rabat, Rabat, Morocco, [2]Research Team of Chemistry of Bioactive Molecules and the Environment, Laboratory of Innovative Materials and Biotechnology of Natural Resources, Faculty of Sciences, Moulay Ismaïl University, Meknes, Morocco, [3]Higher Institute of Nursing Professions and Health Techniques of Fez, Regional Health Directorate Fez-Meknes, EL Ghassani Hospital, Fez, Morocco, [4]Department of Pharmaceutical Sciences, College of Pharmacy, Princess Nourah bint Abdulrahman University, Riyadh, Saudi Arabia, [5]Pharmacognosy Department, College of Pharmacy, King Saud University, Riyadh, Saudi Arabia, [6]University Lille, University of Liège, University of Picardie Jules Verne, JUNIA, UMRT 1158 BioEcoAgro, Specialized Metabolites of Plant Origin, Lille, France

Ruta montana L., a medicinal plant native to Morocco's Middle Atlas region, has been traditionally used for its therapeutic properties. This study aims to investigate its phytochemical composition and evaluate its biological and pharmacological activities, with a focus on its essential oil (EO) and phenolic extracts. The essential oil was extracted via hydrodistillation and analyzed using GC-MS to determine its chemical composition. Aqueous, hydro-ethanolic, and hydro-methanolic extracts were prepared and analyzed for their polyphenol, flavonoid, and tannin content using spectrophotometric methods and HPLC/UV ESI-MS. Antimicrobial activity was assessed using minimum inhibitory concentration (MIC) assays, while antioxidant potential was evaluated using the DPPH radical scavenging method. Analgesic and anti-inflammatory effects were tested using abdominal writhing and edema inhibition models, respectively. Subacute toxicity was assessed by monitoring organ weights and biochemical parameters in treated animals. The EO was predominantly composed of 2-undecanone (81.16%) and decyl propanoate (9.33%). Phenolic extracts were rich in rosmarinic acid 3'-glucoside, p-coumaroylquinic acid, quercitrin, ferulic acid, and embelin. The EO exhibited strong antimicrobial activity (MIC = 2.34–37.5 mg/mL), particularly against *Aspergillus niger*, and significant analgesic effects (44.55% reduction in abdominal writhing at 0.2 mL), outperforming the aqueous extract (23.37%). Phenolic extracts demonstrated notable antioxidant activity (IC_{50} = 117.24 μg/mL in DPPH), while the EO showed moderate antioxidant potential (IC_{50} = 29.42 μg/mL; BHT = 1.62 μg/mL). Anti-inflammatory assays revealed that both the EO (71% inhibition at 0.2 mL) and

aqueous extract (79% inhibition at 300 mg/kg) were comparable to indomethacin. Subacute toxicity tests indicated no significant organ weight changes, although slight increases in hepatic AST (91.33 U/L) and creatinine (2.36 mg/L) were observed at higher doses. These findings highlight *R. montana's* potential as a natural source of antioxidant, antimicrobial, and anti-inflammatory agents. The EO, in particular, shows promise as a therapeutic alternative. However, further studies are needed to evaluate its long-term safety and efficacy. *R. montana* demonstrates significant pharmacological potential, particularly its essential oil, which warrants further investigation for therapeutic applications.

1 Introduction

The discovery of antibiotics was the miracle of the 20th century, significantly reducing mortality associated with infectious diseases and improving the health and wellbeing of humanity. Today, however, this effectiveness is being challenged due to the excessive use of antibiotics aimed at addressing numerous human illnesses. Alas, this misuse has extended to other fields such as agriculture and livestock farming, thereby contributing to the residual contamination of food and, subsequently, the natural evolution of antibiotic resistance in pathogenic microbial strains (Okaiyeto et al., 2024). As a result, it has become increasingly difficult to treat infections that were once curable, leading to situations of therapeutic impasse (Touat et al., 2019). The phenomenon of antibiotic resistance has now become entrenched in our daily lives and represents a global concern. To address this issue, extensive research has been conducted in recent years to develop new antimicrobial agents of natural origin and, consequently, produce safe food products (Lucera et al., 2012; Mendonca et al., 2018; Lucera et al., 2012).

On the other hand, interest in natural antioxidants continues to grow among consumers, healthcare professionals, and food scientists, owing to their ability to protect food from oxidative deterioration and shield the body from the harmful effects of oxidative stress (García-Caparrós et al., 2021). Consequently, several natural antioxidants have been isolated for use as pharmaceutical and nutraceutical products, as well as food preservatives (Gutiérrez-del-Río et al., 2018; Lourenço et al., 2019; Fernandes et al., 2020; Teixeira et al., 2022). This popular trend has spurred numerous scientific studies aimed at exploring the chemical composition and biological properties of extracts and essential oils (EOs) derived from novel plant sources. In this context, certain species of *Ruta* (Rutaceae) have been investigated for their chemical components and pharmacological activities. Species of the Rutaceae family are renowned for their economic importance, including their citrus fruits and cultivated essential oils (Groppo et al., 2022).

The genus *Ruta* comprises around sixty species, some of which are found in the Mediterranean region (Hammiche and Azzouz, 2013). Among these, *Ruta montana* is widely distributed geographically, particularly in Morocco, Algeria, Tunisia, Portugal, Greece, and Turkey (Mohammedi et al., 2019). It is a semi-shrub with evergreen foliage, ranging from 40 to 60 cm in height, highly branched, and woody at the base. Its leaves are fine and triangular in shape, while its small yellow flowers feature two

whorls of stamens and are bisexual. Its fruits are capsules with four rounded lobes. The essential oil (EO) contained in large pockets housing secretory glands gives *R. montana* a pungent odor. *R. montana* is commonly referred to as "fidjel" in Arabic and "aourmi" in Berber (Bellakhdar, 1997).

In traditional Moroccan medicine, decoctions and infusions of mountain rue are used for the treatment of diabetes (Tahraoui et al., 2007). An ethnobotanical study conducted among herbalists revealed that *R. montana* L. has a high usage value in southwestern Morocco, with an index of 7 (El-Ghazouani et al., 2021). Its decoction is frequently used for treating oral and dental diseases, as well as for gum rinsing, by the population of the Middle Atlas (Najem et al., 2020). Another ethnobotanical study cited the use of infusions and decoctions of *R. montana* flowers for treating bronchial congestion and asthma in the central Middle Atlas region of Morocco (Najem et al., 2021). Bencheikh et al. (2021) reported the use of decoctions of this plant in the traditional treatment of kidney diseases. This species is also used in Algeria to treat digestive disorders (Adli et al., 2021), alleviate toothaches and joint pain, and facilitate difficult childbirths (Hammiche and Azzouz, 2013; Miara et al., 2019; Adli et al., 2021). Benkhaira et al. (2022) documented the use of *R. montana* for treating diabetic, digestive, respiratory, neurological, and gynecological ailments in North Africa.

On a scientific level, several *in vitro* and *in vivo* studies have demonstrated the various biological potentials of *R. montana*, including antibacterial properties (Zellagui et al., 2012; Mohammedi et al., 2019; Benali et al., 2020b), antifungal properties (Drioiche et al., 2020a; Slougui et al., 2023; Bouhenna et al., 2024), antioxidant properties (Kambouche et al., 2008; Benali et al., 2020a), antihypertensive effects (El-Ouady and Eddouks, 2021), antidiabetic activity (Farid et al., 2017), anti-acetylcholinesterase activity (Khadhri et al., 2017), anticancer properties (Kara Ali et al., 2016), antifertility effects (Merghem et al., 2017), as well as insecticidal and larvicidal properties (Boutoumi et al., 2009; Bouzeraa et al., 2019; Bouabida and Dris, 2022). Despite the numerous therapeutic benefits of *R. montana*, it can easily become toxic if improperly dosed. An ethnobotanical study conducted in northern Morocco cited this plant as toxic, causing digestive and neurological disorders (Kharchoufa et al., 2021). Previous studies have highlighted the richness of *R. montana* in various phytochemical compounds, including alkaloids, coumarins, flavonoids, tannins, and volatile compounds (Daoudi et al., 2016; Bouhenna et al., 2024).

Although *R. montana* has been the subject of several research studies regarding its chemical composition and biological activities, relevant data on Mountain Rue collected from Morocco are often

FIGURE 1
R. montana L. (El Ouardi Mohamed and Touriya Zair, 2024).

TABLE 1 List of tested bacterial and fungal strains used for antimicrobial tests.

		Strains	Abbreviations
Bacteria	Gram-negative bacilli	*Enterobacter cloacae*	*E. cloacae*
		Klebsiella pneumoniae	*K. pneumoniae*
		Escherichia coli	*E. coli sauvage*
	Gram-positive cocci	*Staphylococcus aureus*	*S. aureus*
		Staphylococcus epidermidis	*S.epidermidis*
Fungi	Yeasts	*Candida albicans*	*C.albicans*
		Candida dubliniensis	*C. dubliniensis*
		Candida tropicalis	*C. tropicalis*
		Candida parapsilosis	*C. parapsilosis*
	Molds	*Aspergillus niger*	*A.niger*

scattered and fragmented. Furthermore, few scientific studies have investigated its phenolic profile, and many pharmacological activities, such as anti-inflammatory and analgesic properties, remain unexplored. Therefore, the aim of this work is to determine the chemical composition of the essential oil (EO) and the phenolic profile of *R. montana* extracts, as well as to evaluate their antioxidant and antimicrobial effects. Additionally, it seeks to examine, for the first time, the anti-inflammatory and analgesic activities, as well as to assess the subacute toxicity of the extracts and the EO.

2 Materials and methods

2.1 Plant material

The aerial parts of *R. montana* were collected in June 2024 from wild populations in the Boulemane region, specifically in the Municipality of Guigou (Figure 1). The harvesting site, the harvested plant part, and its source are detailed in Supplementary Table S1. Botanical identification was carried out through a meticulous morphological analysis of the specimens, comparing them with herbarium material and consulting botanical literature. After the plant was identified by a botanist, represented by Professor Amina Bari from the Biology Department of the Faculty of Sciences (FSDM) at USMBA in Fez, the samples were deposited in the herbarium of the Biology Department under the reference number LRM00252024. After harvesting, the collected plant material was dried to preserve it. The aerial parts were spread out in a single layer and dried at room temperature (protected from direct sunlight) in dry, clean, and well-ventilated areas to minimize the degradation of bioactive substances. The drying process was conducted at a temperature of 25°C for 2 weeks, until the material was completely dehydrated. Each sample of dried plant material was then transferred into a labeled paper bag and stored in a cool, dark place at room temperature for future analysis.

2.2 Microbiological materials

In this study, the antimicrobial activity of the EO and extracts from the flowering tops of *R. montana* was evaluated against five bacterial strains and five fungal strains. These microorganisms are contaminants and pathogens widely identified in various human pathologies (Table 1). All strains were successively revitalized in Mueller-Hinton and Sabouraud broths, subcultured, and stored in a 20% glycerol stock at −80°C.

2.3 Animal material

In this study, male and female Swiss albino mice (weighing between 30 and 35 g) as well as Wistar rats (weighing between 200 and 250 g) were used as animal models. The animals were initially weighed and then housed individually in polypropylene plastic cages in a controlled temperature environment, with a 12-h light/dark cycle and unlimited access to food and water. All experimental procedures and protocols were meticulously conducted in strict adherence to ethical guidelines and regulations to ensure animal welfare, with the study being reviewed and approved by the Institutional Animal Care and Use Committee (IACUC) of the Faculty of Sciences Dhar El Mehraz, Sidi Mohamed Ben Abdallah University, Fès, Morocco, under reference #04/2019/LBEAS, in accordance with institutional ethical standards and the European Economic Community (EEC) Directive 86/609/EEC (Council Directive 86/609/EEC of 24 November, 1986).

2.4 Quality control of plant material

2.4.1 Moisture content determination

The procedure used to determine the moisture content complies with the AFNOR standard (AFNOR Editions, 1985; Saidi et al., 2023). A quantity of 5 g of plant sample was weighed in crucibles that had been previously dried and tared. The crucibles containing the plant material were then placed in an oven at a temperature between 103°C and 105°C for 24 h. After this period, they were

cooled in a desiccator and weighed. The moisture content was calculated using the following Formula 1:

$$TH\% = \left(\frac{m_0 - m_1}{m_0}\right) \times 100 \qquad (1)$$

where:

m$_0$: Initial mass of the plant material (in grams)

m$_1$: Mass after drying (in grams)

The result is expressed as a percentage of dry matter.

2.4.2 Determination of pH

The method involves mixing 2 g of ground sample with 10 mL of warm distilled water. After stirring, the cooled mixture is filtered. The pH meter electrode is then immersed in a volume of the filtrate to record the pH value (Saidi et al., 2023).

2.4.3 Determination of titrable acidity

Titrable acidity corresponds to the sum of free mineral and organic acids. The principle of this method is based on an acid-base titration using a NaOH solution. A quantity of 2 g of the ground plant sample was added to 100 mL of boiling distilled water. After 15 min of stirring, the mixture was filtered and then titrated with a NaOH solution (N = 0.01), in the presence of a few drops of phenolphthalein, until a color change was observed, resulting in a persistent pink color lasting approximately 30 s. The recorded titration volume is converted into citric acid equivalent by multiplying it by a factor obtained from the following calculation (Equation 2) (AFNOR Editions, 1985; Saidi et al., 2023).

$$Titratable\ acidity\ (\%) = Dilution\ factor* $$
$$\frac{weight\ of\ acid\ equiv.*NaOH\ normality*titration\ vol.(mL)}{sample\ weight\ (g)}$$

$$(2)$$

2.4.4 Mineral matter (ash) and organic matter content

The ash content corresponds to the mineral matter remaining after the destruction of organic matter by incineration at high temperatures in a furnace. A quantity of 5 g of ground sample is placed in a muffle furnace at a temperature of 550°C until the complete destruction of all carbonaceous particles and the attainment of whitish ash of constant weight (AFNOR Editions, 1972). The organic matter content was calculated using the following Formula 3 (Saidi et al., 2023):

$$MO\% = \left(\frac{M_1 - M_2}{PE}\right) \times 100 \qquad (3)$$

where:MO%: Organic matter content.M$_1$: Weight of the crucible and the sample before incineration.M$_2$: Weight of the crucible and the sample after incineration.PE: Test portion.

The ash content was calculated as follows (Equation 4):

$$Ash\% = 100 - MO\% \qquad (4)$$

2.4.5 Heavy metal analysis: inductively coupled plasma atomic emission spectrometry (ICP-AES)

The analysis of heavy metals in *R. montana* seeds was performed using the Inductively Coupled Plasma Atomic Emission

Spectrometry technique, following the standardized mineralization protocol (AFNOR, 1999). This method first involves preparing the sample in liquid form by mixing 0.1 g of plant powder with 3 mL of aqua regia, prepared from 1 mL of nitric acid HNO$_3$ (99%) and 2 mLof hydrochloric acid HCl (37%). The mixture is placed in a reflux setup at 200°C for 2 h to ensure the complete dissolution of residual metal particles. After cooling and decantation, the supernatant is collected, filtered through a 0.45 μm membrane, and adjusted to 15 mL with distilled water. The concentrations of heavy metals, including arsenic (As), cadmium (Cd), chromium (Cr), iron (Fe), lead (Pb), antimony (Sb), and titanium (Ti), were determined using the inductively coupled plasma atomic emission spectrometer ICP-AES (Ultima 2 Jobin Yvon) at the Technical Support Unit for Scientific Research (UATRS) laboratory at the CNRST in Rabat (Skujins, 1998; Ailli et al., 2023).

2.4.6 Phytochemical screening

This qualitative analysis aims to identify the primary and secondary metabolites present in the flowering tops of *R. montana*. The tests rely on visual observations of color changes, precipitate formation, and complex formation, while other tests involved examining samples under UV light. The detection of chemical compound groups was carried out according to the protocols described in previous studies, including those by Bekro et al. (2007), Bruneton (2009), Dohou et al. (2003), Mezzoug et al. (2007), Mogode (2005), and N'Guessan et al. (2009).

2.5 Extraction and quality control of essential oils

2.5.1 Extraction and determination of essential oil yields

The flowering tops of *R. montana* were hydrodistilled to extract essential oils (EOs). A 2-L flask containing 100 g of the plant material was immersed in 1 L of water and placed in a Clevenger apparatus equipped with a spherical condenser. After 3 h of boiling, the essential oils were distilled off continuously and collected. All of the experiments were carried out in triplets. The essential oils isolated were separated from the aqueous phase under reduced pressure using a graduated cylinder's separator in hydrodistillation. The oils were dried; using anhydrous sodium sulfate (Na$_2$SO$_4$), to obtain the completely dried samples. The diluted essential oils were used for Gas chromatography-mass spectrometry (GC-MS) analysis with hexane as a solvent. This dilution made it easier to distinguish and identify volatiles during analysis. Dry essential oils were kept at −4°C in tightly capped amber glass vials after dilution, to preserve their chemical composition until analysis. The yield of EO (%EO) extraction was expressed as the volume of essential oil per mass of plant material (V/M) according to the following Formula 5 (Akrout et al., 2001). The use of hexane as a solvent for GC-MS analysis was chosen due to its high volatility and low interference with the detection of essential oil constituents.

$$EO\% = \left[\frac{V}{M_0 - (M_0 \times \%MC)} \times 10^4\right] \mp Ecart - type \qquad (5)$$

where:

MC (%): Moisture content of the plant material (percentage of humidity or water content).

M_0: Mass of the distilled plant material.

V: Volume of essential oil collected (in ml).

2.5.2 Analysis and identification of the chemical composition of essential oils

The chromatographic analysis of essential oils was performed using a Thermo Electron gas chromatograph (Trace GC Ultra) coupled with a mass spectrometer (Thermo Electron Trace MS system; Polaris Q MS). Fragmentation was carried out by electron impact at an intensity of 70 eV. The chromatograph was equipped with a DB-5 column (5% phenyl-methyl-siloxane) measuring 30 m × 0.25 mm with a film thickness of 0.25 μm. The system included a flame ionization detector (FID) powered by a hydrogen/air gas mixture. The column temperature was programmed to increase at a rate of 4°C/min from 50°C to 200°C, maintaining this temperature for 5 min. The injection mode was split (split ratio: 1/70, flow rate: mL/min), and nitrogen was used as the carrier gas at a flow rate of 1 mL/min. The identification of the chemical composition of essential oils was achieved by comparing their calculated Kovats indices (KI) with those provided by Adams and known reference products in the literature (Davies, 1990; Goodner, 2008; Jennings, 2012). This was further complemented by comparing the indices and mass spectra with various references (Adams, 2007; Linstrom and Mallard, 2001). A cut-off match factor of 80% was used to ensure accurate identification of compounds. Additionally, peak deconvolution was performed using the AMDIS software to resolve overlapping peaks and improve identification accuracy.

2.6 Extraction of phenolic compounds

Phenolic compounds are considered multifunctional agents in medicinal chemistry, pharmaceutical development, and various synthetic processes (Rappoport, 2004; Makarem et al., 2019; 2023; Klika et al., 2021). Thus, studying the phenol content in plant extracts can reveal their biological profile (Alara et al., 2021).

In this section, the extraction of phenolic compounds was carried out using decoction and solid-liquid extraction with the aid of a Soxhlet apparatus. The decoction process was performed by adding 30 g of plant powder to 600 mL of distilled water. The resulting mixture was heated and brought to a boil under stirring for 1 h at 80°C. Subsequently, the decanted mixture was filtered under low pressure, and the decoction extract was recovered in powdered form in a glass vial. After drying the extract in an oven at 70°C, the decoction extract was stored in a tinted glass bottle, protected from light. As for the second extraction method, the Soxhlet apparatus was employed. In this process, 30 g of plant powder were placed in a cartridge and brought into contact with extraction solvents, specifically ethanol (70/30) and methanol (70/30) solutions. The extracts were concentrated using a rotary evaporator after several extraction cycles. The extracts were coded in accordance with Supplementary Table S2, which outlines the codification of R. montana extracts.

2.7 Determination of phenolic compounds

The quantification of total phenols in various extracts was performed using the Folin-Ciocalteu method, as described by Singleton and Rossi (1965). The absorbance was recorded using a UV mini-1240 spectrophotometer set at 760 nm and compared to a blank. A calibration curve was established using gallic acid as a positive control. The results were expressed in milligram gallic acid equivalent per gram of extract (mg GAE/g). Each test was performed in triplicate.

2.8 Quantification of flavonoids

The quantification of flavonoids was performed using the method established by Djeridane et al. (2006). The flavonoid content was calculated based on a calibration curve using quercetin as the standard. The results are expressed in milligrams of quercetin equivalent per gram of extract (mg QE/g). Each test was conducted in triplicate.

2.9 Determination of condensed tannins

The quantification of condensed tannins was carried out using the vanillin method, as described by Price et al. (1978). In this technique, a vanillin/methanol solution (4% w/v) was mixed with varying quantities of (+)-catechin solution (2 mg/mL) and manually agitated. Each concentration was then placed in a test tube containing 1.5 mL of hydrochloric acid. The reaction mixture was left at room temperature for 20 min. Absorbance was measured at 499 nm using a UV-visible spectrophotometer, with reference to a blank. The condensed tannin content in our samples was calculated using the calibration curve of catechin as the standard ($Y = 0.7421X + 0.0318$; $R^2 = 0.998$). The tannin content is expressed in milligrams of catechin equivalent per gram of extract (mg CE/g).

2.10 HPLC/UV ESI-MS analysis of the three extracts of R. montana

The analysis of phenolic compounds in the three extracts of R. montana was conducted using high-performance liquid chromatography coupled with Q Exactive Plus mass spectrometry, employing electrospray as the molecular ionization method (HPLC/UV-ESI-MS). The analysis was performed on an UltiMate 3000 HPLC system (Thermo Fisher Scientific, Sunnyvale, CA, United States) equipped with an autosampler. The autosampler was set to maintain the samples at 5°C. The HPLC system utilized a reversed-phase C18 column with a column temperature of 40°C (Lichro CART, Lichrospher, Merck, Darmstadt, Germany, 250 × 4 mm, ID 5 μm). The mobile phase consisted of solvent A: 0.1% formic acid in water (v/v) and solvent B: 0.1% formic acid in acetonitrile (v/v), with degassing performed ultrasonically. At 20, 25, 26, and 30 min, the gradient composition transitioned from 2% B to 30%, 95%, 2%, and 2% B, respectively. The flow rate was 1 mL/min, and the injection volume was 20 μL. Broadband collision-induced dissociation (bbCID) detection was carried out on a Maxis

Impact HD (Bruker Daltonik, Bremen, Germany) following negative electrospray ionization. A diode array detector L-2455 (Merck-Hitachi, Darmstadt, Germany) was also employed for UV detection, with scanning in the range of 190–600 nm and acquisition at three wavelengths: 280, 320, and 360 nm. The parameters used included a capillary voltage of 3,000 V, a drying gas temperature of 200°C, a dry gas flow rate of 8 L/min, a nebulizer gas pressure of 2 bars, and an offset plate voltage of 500 V. Nitrogen was used both as the nebulizing gas and the desolvation gas. The m/z range for MS data acquisition was 100 to 1,500. Data collection and analysis were performed using the Thermo Scientific Chromeleon 7.2 Chromatography Data System (CDS). By examining the mass spectra of the eluted molecules, the eluted compounds were investigated.

2.11 Antioxidant activity

2.11.1 Free radical scavenging activity by DPPH• assay

The antiradical effect of the essential oils (EOs) and extracts of *R. montana* was evaluated using the 2,2-diphenyl-1-picrylhydrazyl (DPPH) radical, following the method described by Liu et al. (2009). In test tubes containing absolute ethanol, different concentrations of *R. montana* extract or EO were prepared to reach a total volume of 200 μL. Subsequently, 2.8 mL of an ethanolic DPPH° solution (24 μg/mL, equivalent to a molar concentration of 6.12×10^{-5} M) were added to the mixture and incubated for 30 min in the dark. Absorbance was measured at 515 nm using a UV-Vis spectrophotometer. All tests were performed in triplicate. The concentration range used for the extracts was crucial to determine the IC_{50} value, which represents the concentration required to inhibit 50% of the DPPH radicals. This range was systematically varied to ensure accurate calculation of the IC_{50}. The reference standard used was butylated hydroxytoluene (BHT) at various concentrations. The results were expressed as the percentage of DPPH• reduction (*PI*%) and calculated using the following Formula 6:

$$PI\% = \frac{A_0 - A}{A_0} \times 100 \tag{6}$$

where:

PI%: Percentage of antioxidant activity.

A_0: Absorbance of the solution containing only the DPPH• radical solution (negative control).

A: Absorbance of the test samples in the presence of DPPH•.

The half-maximal inhibitory concentration (IC_{50}) of the DPPH• radicals, either for BHT or our extracts, was determined from the graph plotting the variation of antioxidant activity as a function of concentration.

2.11.2 Ferric reducing antioxidant power (FRAP) method

The reducing power of the phenolic extracts from *R. montana* to reduce ferric iron (Fe^{3+}) present in the potassium ferricyanide complex to ferrous iron (Fe^{2+}) was determined using the method described by Oyaizu (1986). The assay involves mixing 1 mL of the

plant extract with 2.5 mL of phosphate buffer (0.2 M, pH 6.6) and 2.5 mLof a 1% potassium ferricyanide ($K_3Fe(CN)_6$) solution. The resulting mixture is incubated in a water bath at 50°C for 20 min. Subsequently, 2.5 mL of 10% trichloroacetic acid is added to stop the reaction. The mixture is then centrifuged at 3,000 rpm for 10 min. Finally, 2.5 mL of the supernatant from each concentration is mixed with 2.5 mL of distilled water and 0.5 mL of a 0.1% aqueous $FeCl_3$ solution. The absorbance of the reaction medium is measured at 700 nm against a blank prepared similarly, replacing the aqueous extract with distilled water to calibrate the instrument (UV-Vis spectrophotometer). The positive control is represented by a solution of a standard antioxidant, BHA (butylated hydroxyanisole), whose absorbance was measured under the same conditions as the samples. All tests were performed in triplicate. The graph plotting the variation of reducing power as a function of the concentration of BHT or our extracts was used to determine the concentration corresponding to an absorbance of 0.5 (EC_{50}).

2.11.3 Total antioxidant capacity

The phosphomolybdenum assay, as described by Khiya et al. (2021), was used to evaluate the total antioxidant capacity of *R. montana* extracts. This assay is based on the reduction of molybdenum Mo^{6+} (VI) to molybdenum Mo^{5+} (V) in the presence of the extracts, resulting in the formation of a green phosphate/Mo^{5+} (V) complex at acidic pH, with maximum absorbance at 695 nm. In a test tube, 3 mL of the reagent solution (0.6 M sulfuric acid, 28 mM sodium phosphate, and 4 mM ammonium molybdate) was added to a volume of the extract. The tubes were shaken and incubated at 95°C for 90 min, then allowed to return to room temperature. After cooling, the absorbance of the solutions was measured at 695 nm. Ascorbic acid was used as the standard. The results are expressed in milligram equivalents of ascorbic acid per gram of extract (mg AAE/g).

2.12 Antimicrobial activity

The Minimum Inhibitory Concentration (MIC) was determined using 96-well microplates and the reference microdilution method (Balouiri et al., 2016). MIC is defined as the lowest concentration of essential oil required to completely inhibit the visible growth of the tested microorganism during incubation. A series of dilutions were prepared from a stock solution of the essential oil dissolved in 10% DMSO, resulting in concentrations ranging from 5 to 0.93×10^{-2} mg/mL for each essential oil. These dilutions were prepared in a final volume of 100 μL in Sabouraud broth for fungi and Mueller-Hinton medium for bacteria. Subsequently, 100 μL of microbial inoculum was added to each dilution step, with a final concentration of 10^6 CFU/mL for bacteria or 10^4 CFU/mL for fungi. Ten microliters of resazurin were added to each well to measure bacterial growth after a 24-h incubation at 37°C. The color change from purple to pink after a second incubation at 37°C for 2 h indicated microbial growth. The MIC value was determined as the lowest concentration that prevented the color change of resazurin. Growth and sterility controls were included in the 11th and 12th wells, respectively. This test was performed twice for the essential oil. For comparison, 250 mg of terbinafine, a standard antifungal agent

used in the study, was ground and dissolved in 2 mL of 10% DMSO. The Minimum Bactericidal Concentration (MBC) and Minimum Fungicidal Concentration (MFC) were determined by transferring 10 μL from wells showing no visible growth onto Mueller-Hinton agar (for bacteria) or Sabouraud broth (for fungi) and incubating for 24 h at 37°C. The lowest concentration of the sample that resulted in a 99.99% reduction in CFU/mL compared to the control was designated as the MBC or MFC. Additionally, the MBC/MIC or MFC/MIC ratio was calculated for each extract to evaluate its antimicrobial potency. If the ratio was less than 4, the essential oil was considered bactericidal/fungicidal, while a ratio greater than 4 indicated a bacteriostatic/fungistatic effect (Bissel et al., 2014). The biological assays were conducted in accordance with globally recognized standardized protocols, following the guidelines of the CLSI (Clinical and Laboratory Standards Institute) for antimicrobial testing.

2.13 Anti-inflammatory activity

The anti-inflammatory potential of each extract was evaluated based on Winter et al.'s method (1962) (Winter et al., 1962), with certain modifications. This experiment was repeated twice. Carrageenan at a concentration of 1% was dissolved in saline solution and used as the edema-inducing agent. A total of 35 rats were randomly allocated into 7 groups, each consisting of 5 rats. The difference in footpad circumferences before and after carrageenan injection (Sigma-Aldrich, Ref. 3B-C1804, Barcelona, Spain) was measured in millimeters (mm) at 3, 4, 5, and 6 h using calipers (Küpeli and Yesilada, 2007). The inhibitory activity of each treatment was calculated using the following Formula 7:

$$Percent\ inhibition = 100 \left[1 - \left(\frac{a - x}{b - y} \right) \right] \quad (7)$$

where:
   a: Mean paw volume after carrageenan administration.
   x: Mean paw volume before the injection.b: Mean paw volume of control rats after the injection.
   y: Mean paw volume of control rats before the injection.
   This formula quantifies the anti-inflammatory effect by comparing the changes in paw volume between treated and control groups over time.

2.14 Antinociceptive activity

The antinociceptive effect of each extract was assessed by counting the number of writhes induced in mice following the intraperitoneal injection of a 0.7% acetic acid solution (10 mL/kg). The tested extracts were administered orally to the mice 1 h prior to the acetic acid injection. The number of writhes was recorded for 30 min after the acetic acid injection (Hernández-Pérez and Rabanal, 2002). This experiment was repeated twice. The percentage inhibition (PI%) of the writhes was calculated using the following Formula 8:

$$PI\,(\%) = \frac{(NC - NT)}{NC} * 100 \quad (8)$$

where:
   NC: Number of writhes in the negative control group.
   NT: Number of writhes in the tested groups.
   This formula quantifies the antinociceptive effect by comparing the writhes in treated groups to those in the control group, providing a measure of the extract's ability to reduce pain-induced behavior.

2.15 Statistical analysis

The results were expressed as mean values ± standard error of the mean (SEM) to ensure accurate representation of data variability. Statistical analyses were performed using one-way analysis of variance (ANOVA), followed by Tukey's *post hoc* test to determine significant differences between groups. All analyses were conducted using GraphPad Prism 9 (version 9.5.1, San Diego, CA, United States), a widely recognized statistical software for biological and pharmacological research. A significance threshold of $p < 0.05$ was applied to establish statistical relevance, ensuring that only robust and meaningful differences were considered in the interpretation of the results. Correlations between phenolic compound content and antioxidant activities were examined using R software (version 4.4.2).

3 Results and discussion

3.1 Quality control of plant material

3.1.1 Determination of moisture content, pH, acidity, ash, and organic matter

The results of the quality control analysis for the flowering tops of *R. montana* are presented in Table 2.

The moisture content, defined as the amount of water contained within plant cells, is a crucial parameter that influences the quality, shelf life, and therapeutic efficacy of plant material, as well as its susceptibility to microbial contamination. In this study, the moisture content of the powdered flowering tops of *R. montana*, determined using the oven-drying method, was approximately 12.141%, a value slightly above 10%, which is optimal for medium-term storage of the powder during this study. The pH of the plant extract was slightly acidic (5.11), classifying *R. montana* among acidophilic plants that do not tolerate limestone, a characteristic that enhances its capacity for iron absorption, as confirmed by ICP analysis results. Titratable acidity, a parameter ensuring the conformity of the consumed product to specific requirements such as appearance, texture, and taste, was measured at 2.38 ± 0.251 for the studied plant. Additionally, the ash or mineral content, an important indicator of the quality and purity of the plant extract, was found to be 11.77% for the flowering tops of *R. montana*, a value comparable to those reported for *R. graveolens* leaves (11.8%) (Dhale et al., 2010) and *R. angustifolia* leaves (10.75%) (Wahyuni et al., 2023). These findings collectively underscore the quality and specific characteristics of *R. montana*, supporting its potential suitability for therapeutic applications.

TABLE 2 Analysis and quality control of flowering tops of *R. montana*.

Moisture content (%)	pH	Acidity	Ash	Organic matter
12.14 ± 0.01	5.11 ± 0.01	2.38 ± 0.25	11.77 ± 0.21	88.23 ± 0.21

TABLE 3 Concentration of heavy metals (mg/L) (ICP).

Species	Chromium (Cr)	Antimony (Sb)	Arsenic (As)	Lead (Pb)	Cadmium (Cd)	Iron (Fe)	Copper (Cu)	Titanium (Ti)
R. montana	0.0021	0.0020	0.0078	0.0300	<0.001	0.8909	0.0074	<0.001
Maximum limits (FAO/WHO)	2	1	1	3	0.3	20	—	—

TABLE 4 Essential Oil yield of *R. montana*.

R. montana	Yield (%)	Color	Odor
Flowering tops	2.07 ± 0.25	Yellow	Aromatic

TABLE 5 Physicochemical properties of *R. montana* EO.

Properties	EO
Density (g/mL)	0.97 ± 0.01
Brix Degree	56.00 ± 0.05
Acid Value	1.12 ± 0.05
Iodine Value	13.00 ± 1.19
Peroxide Value	13.24 ± 0.98

3.1.2 Assessment of heavy metal

The presence of certain heavy metals in the environment, which can be absorbed by plants, poses a potential toxicity risk, making the determination of heavy metal content an essential test to ensure the safety and quality of plant materials. In this study, we evaluated the concentrations of eight heavy metals—chromium (Cr), antimony (Sb), arsenic (As), lead (Pb), cadmium (Cd), iron (Fe), copper (Cu), and titanium (Ti)—using Atomic Emission Spectrometry. As shown in Table 3, the flowering tops of *R. montana* exhibited a high iron content of 0.8909 mg/L, while copper was detected at a moderately low concentration of approximately 0.0074 mg/L. Notably, the concentrations of all other detected heavy metals fell within the permissible ranges established by FAO/WHO regulatory standards. These findings indicate that the studied plant can be safely consumed directly, used as an ingredient in food processing, or repackaged as needed without posing a risk to human health.

3.2 Essential oil yield

The hydrodistillation extraction of the flowering tops of *R. montana* yielded an average of 2.07% (v/w) of a yellowish essential oil with a strong aromatic odor (Table 4). This EO yield is higher than those reported in Algeria by Slougui et al. (2023) (0.67%). However, it is lower than those noted in Morocco by Barbouchi et al. (2021) (2.24% ± 0.02%) and in Algeria by Zeraib et al. (2021) (2.5%). Variations in essential oil yields arise from several factors, including the plant's geographical location, climatic conditions, harvesting period, and the extraction method used. These differences in yield could be attributed to the specific characteristics of the plant material and the extraction conditions employed in each study.

3.3 Quality control of essential oil

Physicochemical properties such as acid value, peroxide value, and iodine value are among the key methods for verifying and controlling

the quality of the essential oil extracted from the flowering tops of *R. montana*. These parameters are determined according to specific protocols. The results are presented in Table 5 and summarized below.

The essential oil extracted from the studied plant recorded a density of 0.97. The AFNOR standard (2005) recommends a density between 0.906 and 0.990, suggesting that the essential oil extracted from the flowering tops of *R. montana* meets the standards for a very high-quality essential oil.

The acid value refers to the content of free fatty acids present in the EO. Indeed, fresh essential oils contain very little free acid (Fauconnier, 2006). Moreover, an essential oil is considered well-preserved if its acid value is less than 2. In this study, the EO extracted from the flowering tops of *R. montana* recorded an acid value of 1.12. Therefore, we conclude that the studied EO is well-preserved against any factors promoting degradation. Among the physicochemical parameters determined in this study is the iodine value, which measures the degree of unsaturation of the EO and directly affects its stability. In this work, the EO extracted from the flowering tops of *R. montana*. recorded an iodine value of 13 g/100 g of oil. As for the peroxide value, it is a crucial indicator of the quality and stability of the EO, reflecting its level of oxidation. The analyzed EO showed a peroxide value of 13.24 ± 0.98 mEq/kg. By comparing our results with the commercial standards, CODEX STAN 210-1999, we observe that the studied EO complies with the standards, allowing us to classify it as of good quality.

3.4 Chemical composition of the essential oil

The chromatogram of the essential oil (EO) of *R. montana* reveals a highly prominent main peak, clearly distinguishable from

TABLE 6 Chemical composition of the essential oil of *R. montana*.

N°	RT (min)	Compound	KI (Adams)	Area (%)	Mass	Formula
1	11.34	o-Cymene	1026	0.03	134	$C_{10}H_{14}$
2	12.51	γ-Terpinene	1059	0.06	136	$C_{10}H_{16}$
3	14.08	2-Nonanone	1090	0.52	142	$C_9H_{18}O$
4	14.62	trans-Thujone	1114	0.92	152	$C_{10}H_{16}O$
5	16.08	iso-3-Thujanol	1138	0.04	152	$C_{10}H_{16}O$
6	16.22	Camphor	1146	0.04	152	$C_{10}H_{16}O$
7	17.28	Borneol	1169	0.07	154	$C_{10}H_{18}O$
8	17.38	Terpinen-4-ol	1177	0.05	154	$C_{10}H_{20}O$
9	17.67	2-Decanone	1192	1.21	156	$C_{10}H_{16}O$
10	19.47	Pulegone	1237	1.86	152	$C_{10}H_{16}O$
11	20.59	(5Z)-Octenol propanoate	1298	0.25	184	$C_{11}H_{20}O_2$
12	21.31	2-Undecanone	1294	81.16	170	$C_{11}H_{22}O$
13	21.56	n-Undecanol	1370	0.80	172	$C_{11}H_{24}O$
14	22.08	Thymol	1290	0.03	150	$C_{10}H_{14}O$
15	22.31	Carvacrol	1299	0.11	150	$C_{10}H_{14}O$
16	23.40	2-Dodecanone	1389	1.99	184	$C_{12}H_{34}O$
17	24.70	Valeric acid,α-methylbenzyl ester	1400	0.04	206	$C_{13}H_{18}O_2$
18	24.82	(E)-Caryophyllene	1419	0.24	204	$C_{15}H_{24}$
19	25.28	Decyl propanoate	1501	9.33	214	$C_{13}H_{26}O_2$
20	26.68	Dauca-4(11),8-diene	1531	0.02	204	$C_{15}H_{24}$
21	27.05	α-trans-Bergamotene	1434	0.17	204	$C_{15}H_{24}$
22	27.30	Phenyl ethyl 2-methylbutanoate	1487	0.12	206	$C_{13}H_{18}O_2$
23	27.42	2-Tridecanone	1496	0.88	198	$C_{13}H_{26}O$
24	31.74	Caryophylla-4(12),8(13)-dien-5β-ol	1640	0.04	220	$C_{15}H_{24}O$
25	36.67	6,10,14-Trimethylpentadecan-2-one	1800	0.02	268	$C_{18}H_{36}O$
		Hydrocarbon Monoterpenes				0.09
		Oxygenated Monoterpenes				3.12
		Hydrocarbon Sesquiterpenes				0.43
		Oxygenated Sesquiterpenes				0.06
		Others				96.3
		Total				100

other less intense peaks (Supplementary Figure S1). This peak, detected at a retention time (RT) of 21.40 min, was identified as corresponding to the major compound 2-undecanone. Furthermore, the use of peak deconvolution enabled the effective separation of co-eluting compounds, thus ensuring a more accurate and detailed representation of the essential oil's chemical profile.

Based on chromatographic data and mass spectra, the chemical analysis identified 25 components, which together make up the entire composition of the essential oil (Table 6). The five most significant compounds, accounting for 95.55% of the total, are 2-undecanone (81.16%), decyl propanoate (9.33%), 2-dodecanone (1.99%), pulegone (1.86%), and 2-decanone (1.21%). It appears that the essential oil under study lacks monoterpenes (3.21%) and sesquiterpenes (0.49%), but contains other chemical classes (96.3%). These classes are primarily composed of aliphatic ketones (88.6%), followed by esters (9.74%). Meanwhile, alcohols (1.14%) and hydrocarbons (0.52%) are nearly absent (Figure 2).

The chemical composition described in this study shows similarities with the profile of *R. montana* from Morocco, particularly in terms of the dominance of 2-undecanone: 85.76%

FIGURE 2
Distribution of the main chemical families of the EO of
R. montana.
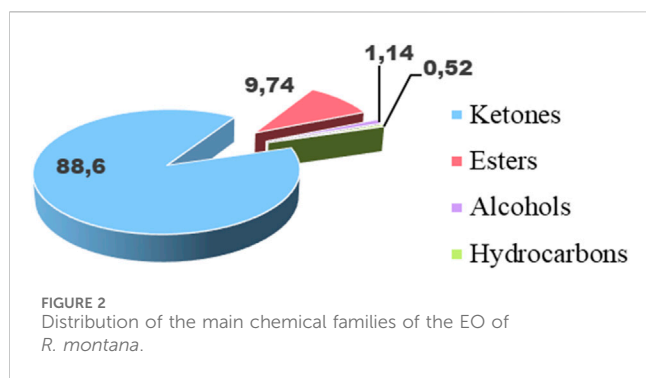
reported by Flouchi et al. (2024), and 63.97% by Benali et al. (2020b). In Algeria, comparative studies on the essential oils of *R. montana* collected from different regions have shown slight variations in the major components. Mohammedi et al. (2019), emphasized the impact of climatic conditions on the chemical composition of the essential oil, with its main components being 2-undecanone (27.2%–81.7%), 2-nonanone (1.9%–39.5%), and 2-nonanyl acetate (trace–24.8%). Zellagui et al. (2012) found that the major components of the first essential oil were 2-undecanone (60.1%), 2-nonanone (8.6%), monoethylhexyl phthalate (6.4%), and decanone (6.2%), while the second essential oil had 2-undecanone (90.4%), 2-nonanone (4%), and decanone (1.4%).

It is equally important to highlight the influence of the developmental stage and the condition of the plants (whether fresh or dried) on the composition of EO. In this context, the fresh aerial parts collected in eastern Algeria are primarily composed of undecan-2-one (37.74%), resorcinol (27.66%), and 2-acetoxytetradecane (9.19%) (Djarri et al., 2013), whereas these compounds were not identified in other Algerian samples. In Tunisia, Hammami et al. (2015) found that the EO extracted from dried leaves was predominantly composed of 1-butene (38.33%), methylcyclopropane (15.47%), 2-butene (22.56%), and caryophyllene oxide (8.18%). Conversely, in the same country, Yosra et al. (2019) reported a chemical profile of EO extracted from dried leaves that was dominated by the same major compounds found in Moroccan and Algerian samples, particularly 2-undecanone (86.77%), followed by 2-decanone (4.91%) and 2-nonanone (23.62%).

It is important to highlight that the abundance of 2-undecanone in the EO of *Ruta* species has made it a relevant chemotaxonomic marker for this genus (Bennaoum et al., 2017). Thus, 2-undecanone appears to be an indispensable compound in the EO of *R. montana*, given its presence in all the EOs of the species from Morocco, Algeria, and Tunisia, regardless of the region or the plant's growth conditions. The variation in cultivation environments is mainly reflected in the differing percentages of this compound depending on the regions.

3.5 Phytochemical screening

The results of the phytochemical screening on the plant powder of the flowering tops of *R. montana* are illustrated in Table 7.

This qualitative analysis revealed the diversity of primary and secondary metabolites in *R. montana*. The plant is particularly rich in lipids and proteins, and moderately rich in reducing sugars and glycogens. Regarding secondary metabolites, the various extracts showed a moderate presence of alkaloids, flavones, and both gallic and condensed tannins. A positive reaction was also observed for saponosides, sterols, and triterpenes, whereas mucilages showed a negative reaction. The richness of this plant's extracts in secondary metabolites explains its use in traditional medicine to treat numerous diseases. The results of this study align with those of Drioiche et al. (2020a), who found that the aerial parts of Moroccan *R. montana* L. contained alkaloids, mucilages, triterpenes, sterols, flavonoids, leucoanthocyanins, and tannins. Similarly, Drioueche et al. (2021) discovered that the polar extract of the aerial parts of mountain rue from Algeria contained alkaloids, flavonoids, tannins, and coumarins.

3.6 HPLC/UV ESI-MS analysis of *R. montana* extracts

The chromatographic profile, shown in Figure 3, displays the peaks of phenolic and non-phenolic compounds derived from the decoction and hydroethanolic and hydromethanolic extracts of the flowering tops of *R. montana*, along with their retention times and relative abundances. The HPLC/UV-ESI-MS technique was used to evaluate the decoction, hydromethanolic, and hydroethanolic extracts of *R. montana*. By analyzing the mass spectra in parallel with the chromatogram, a total of 35 molecules were identified and are listed in Table 8. The chromatographic profile highlights the diverse richness of the analyzed extracts in various molecules.

The distribution of chemical classes in the extracts of *R. montana*, as presented in Figure 4, reveals that phenolic compounds predominate across all extracts, with the highest proportion observed in the hydromethanolic extract (36.05%), followed by the decoction (32.33%) and the hydroethanolic extract (31.91%). Phenolic acids are most abundant in the decoction (36.67%), demonstrating the efficiency of water as a solvent for their extraction, whereas flavonoids are better extracted using mixed solvents such as hydromethanolic and hydroethanolic solutions (37.02% and 38.33%, respectively). Coumarins, although present in smaller quantities, are slightly more concentrated in the hydromethanolic extract (0.65%), while compounds classified as "others" are primarily found in the decoction (2.50%). These findings highlight the influence of solvents on the extraction process, with mixed solvents favoring flavonoids and water being more suitable for phenolic acids. From a biological perspective, the phenolic acids and flavonoids, owing to their antioxidant and anti-inflammatory properties, offer promising prospects for therapeutic and nutraceutical applications.

The primary compounds identified in the extracts include rosmarinic acid 3′-glucoside, which is present in significant quantities in all extracts, reaching up to 23.8% in the hydroethanolic extract. p-Coumaroylquinic acid is also highly abundant, with a concentration of 18.4% in the hydroethanolic extract. Ferulic acid stands out due to its dominance in the hydroethanolic extract, where it reaches 8.44%. Embelin is notably present in all extracts, with a maximum concentration of

TABLE 7 Results of phytochemical tests conducted on extracts of *R. montana*.

Chemical families		R. montana
Polysaccharides		++
Reducing Sugars		++
Lipids		+++
Proteins	Biuret reaction	+++
	Xanthoproteic reaction	+
Tannins	Catechic	++
	Gallic	++
Flavonoids	Free Flavonoids	++ (flavones)
	Anthocyanins	++
	Leucoanthocyanins	+
Alkaloids	Dragendorff	++
	Mayer	++
Sterols and Triterpenes		++
Saponosides		++
Mucilages		–

Classification: (–): Absence of the desired compound in the reaction; +: Low presence of the tested compound; ++: Presence of the compound, with relatively high concentration; +++: Presence of the compound with high concentration.

6.25%. Quercitrin, a major flavonoid, accounts for up to 15.5% in these extracts. Additionally, we recorded a content of Rhamnetin 3-rhamnoside in the hydromethanolic extract with a concentration of 6.27%. Furthermore, certain specific compounds, such as (+)-Gallocatechin, are detected exclusively in the hydroethanolic extract. Figure 5, which presents the chemical structures of the main identified compounds, complements this analysis by providing precise structural details.

The analysis of compounds by mass spectrometry in negative ion mode (ESI-MS) allows for the exploration of their specific fragmentation patterns, thereby providing valuable insights into their molecular structure. The ESI-MS spectrum of Rosmarinic acid 3′-glucoside displays a molecular ion $[M–H]^-$ at m/z 521, fragmenting through the loss of a glucose residue (162 u) to m/z 365, followed by the loss of a rosmarinic acid fragment to reach m/z 197. The p-Coumaroylquinic acid, with a $[M–H]^-$ ion at m/z 337, suggests the loss of coumaroyl or quinic acid fragments. The fragmentation of Ferulic acid generates fragments at m/z 175 and 147, corresponding to the loss of a water molecule (18 u) and a methoxy group (28 u), respectively. Quercitrin exhibits a $[M–H]^-$ ion at m/z 447, with a typical flavonoid fragmentation involving the loss of a rhamnose residue (162 u) to form the aglycone quercetin (m/z 285), followed by an aromatic cleavage at m/z 151. Regarding Embelin, the $[M–H]^-$ ion at m/z 293 loses a bulky fragment (109 u) to reach m/z 184. (+)-Gallocatechin fragments into m/z 275 (loss of 30 u, corresponding to a water molecule), then into m/z 125 through cleavage of the flavonoid ring. Finally, Rhamnetin 3-rhamnoside presents a $[M–H]^-$ ion at m/z 461, fragmenting through the loss of a rhamnose residue (146 u) to form the aglycone rhamnetin (m/z

315), followed by an aromatic cleavage at m/z 151. These results highlight common fragmentation mechanisms, including the loss of carbohydrate residues, specific functional groups, and cleavages at aromatic rings or side chains, enabling precise characterization of the studied molecules.

In the literature, the phenolic profile of *R. montana* has been scarcely studied. Khadhri et al. (2017) reported the abundant presence of flavonoid-type polyphenols in the decoction, as well as phenolic acids in the decoction of *R. montana* originating from Tunisia. Szewczyk et al. (2023) noted the existence of catechin in the methanolic extract of *R. montana* L. cultivated *in vitro*. Toker and collaborators (Toker et al., 1998) determined the rutin content in the methanolic extract of the aerial parts of *R. montana* L. from Turkey, using the HPLC method, to be 6.79 μg/mL.

Moreover, a study conducted by Pacifico et al. (2016) demonstrated that the hydroalcoholic extract of *R. graveolens* leaves collected in Italy contains rutin, isorhamnetin-3-O-rutinoside, 4-O-p-coumaroylquinic acid, and 4-O-feruloylquinic acid. Additionally, this study highlighted the variation in the chemical composition of this species depending on the harvest season.

All the major compounds quantified in the three extracts of *R. montana* possess therapeutic properties. For example, rosmarinic acid glucoside exhibits significant anticancer, anti-angiogenic, antioxidant, anti-inflammatory, and antimicrobial properties (Budzianowski et al., 2023). In turn, p-coumaroylquinic acid is distinguished by its numerous biological activities, including antioxidant, anticancer, antimicrobial, antiviral, anti-inflammatory, antiplatelet aggregation, anxiolytic, antipyretic, analgesic, and antiarthritic effects (Pei et al., 2016). Additionally, quercitrin demonstrates potential antioxidant, anti-inflammatory, antiviral, and anticancer properties, as well as the ability to alleviate certain cardiovascular diseases (Ulusoy and Sanlier, 2020). Ferulic acid is also recognized for its antioxidant, anticancer, anti-inflammatory, hepatoprotective, antimicrobial, and antiviral effects (Pyrzynska, 2024). Similarly, rhamnetin possesses various pharmacological properties, including antioxidant, anticancer, anti-inflammatory, antiviral, and antibacterial activities (Medeiros et al., 2022). Finally, embelin exhibits antimicrobial, antioxidant, analgesic, anti-inflammatory, anxiolytic, antifertility, antimalarial, and anticancer properties (Basha et al., 2022).

3.7 Extraction yield, total polyphenol, flavonoid, and catechic tannin content

Figure 6 presents the average extraction yields, as well as the polyphenol, flavonoid, and catechin tannin contents of *R. montana*, based on the extraction methods employed.

The extraction yields depend on both the solvent and the extraction method. We observe that aqueous methanol yielded the highest extraction yield (17.91%), followed by aqueous ethanol (17.39%). In contrast, decoction recorded the lowest extraction yield (16.16%). Regarding the quantification of polyphenols, flavonoids, and condensed tannins, their contents are expressed in mg GAE/g of extract, mg QE/g of extract, and mg CE/g of extract, respectively. It appears that the flowering tops of *R. montana* L. are rich in these molecules. Indeed, aqueous methanol
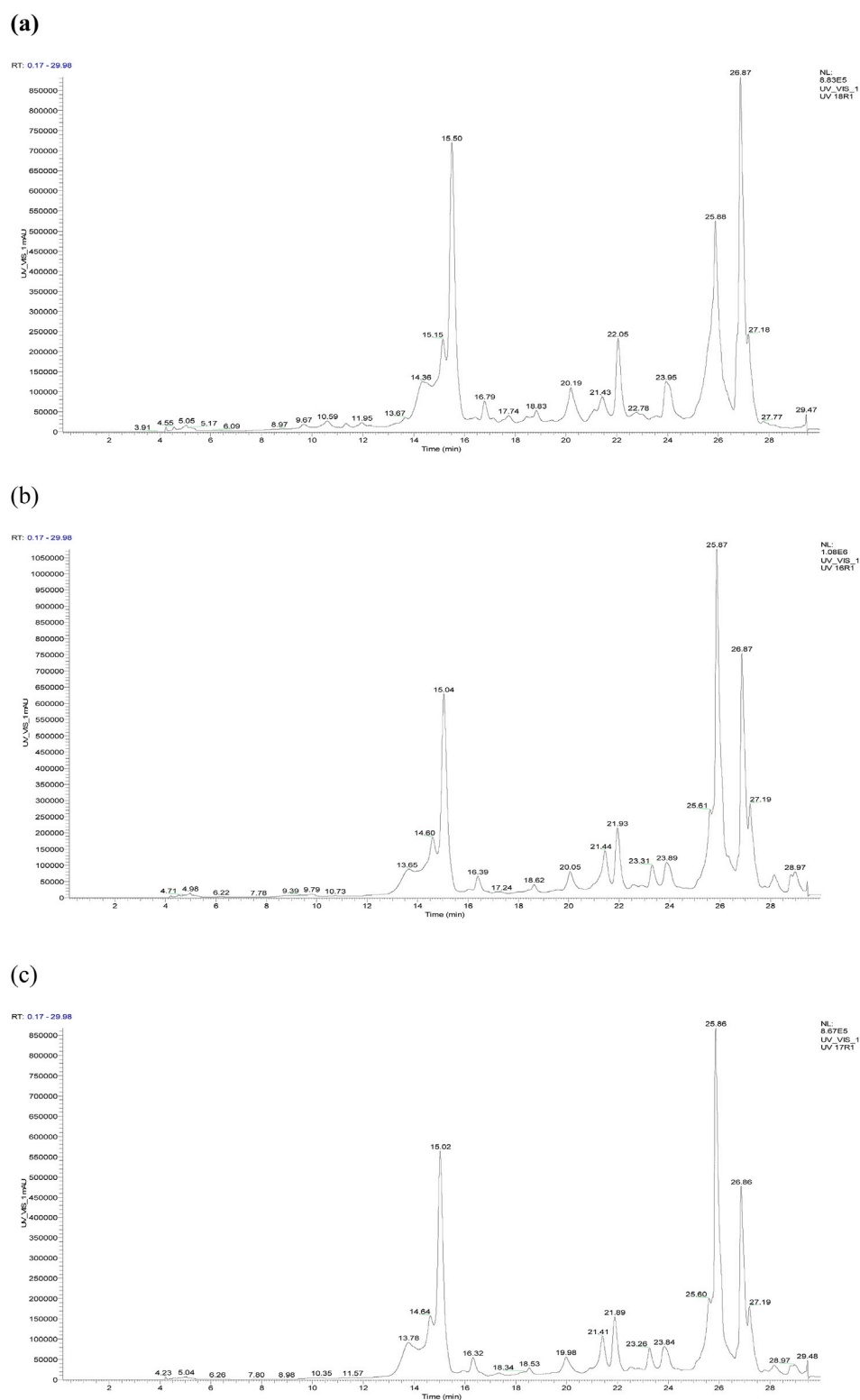
FIGURE 3
HPLC chromatogram of *R. montana* compounds of aqueous extract **(a)**, hydroethanolic extract **(b)**, and hydromethanolic extract **(c)**.

is the most effective extractor of polyphenols and flavonoids for R. montana L., with average values of 67.32 mg GAE/g of extract and 26.14 mg QE/g of extract, respectively. This is followed by aqueous ethanol, which shows contents of approximately 55.26 mg GAE/g of

extract and 21.39 mg QE/g of extract, respectively. However, the decoction recorded the lowest polyphenol and flavonoid contents, amounting to 40.35 mg GAE/g of extract and 9.92 mg QE/g of extract, respectively.

TABLE 8 List of compounds identified in the extracts of the flowering tops of *R. montana* by HPLC/UV-ESI-MS.

| N°	RT (min)	Molecules	Classes	Nominal masses	[M−H]⁻ (m/z)	Fragment ions (m/z)	E (1)	E (2)	E (3)
1	4,23	2,5-Dihydro-2-furancarboxylic acid	Others	114	113	113-97-69	0.11	0.05	0.1
2	5,05	Salicylic acid	Phenolic compound	138	137	139-277	0.23	0.03	0.1
3	8,97	Caffeic acid	Phenolic acid	180	179	135-107	0	0	0.35
4	9,67	Ferulic acid derivative	Phenolic acid	222	221	149-117	0.25	0.36	0.73
8	9,8	Luteolin	Flavonoid	286	285	175-151-133	0	0.17	0
5	10,59	Vanillic acid	Phenolic acid	168	167	167-123	0.1	0.06	0.98
6	11,34	Formononetin	Flavonoid	268	267	251-223	0	0	0.41
6	11,57	Propyl gallate	Phenolic compound	212	211	211-137-107	0.84	0.03	0
7	11,95	Umbelliferone	Coumarin	162	161	161-133	0.65	0.1	0.55
8	12,27	Protocatechuic acid	Phenolic acid	154	153	153-109	0.11	0.01	0.35
9	13,65	Gallic acid	Phenolic acid	170	169	125-107	0.23	0.13	1.37
10	14,36	Embelin	Phenolic compound	294	293	293-184	6.25	4.01	6.12
11	14,6	Ferulic acid	Phenolic acid	194	193	193-175-147	6.1	8.44	6.49
12	15,5	p-Coumaroylquinic acid	Phenolic acid	338	337	337-435	15.5	18.4	15.08
13	16,43	Harpagide	Others (Iridoid)	364	363	363-195-179	0	0	0.98
14	16,79	3-Feruloylquinic acid	Phenolic acid	368	367	367-191-173	1.72	1.08	1.46
15	17,13	Chrysin	Flavonoid	254	253	253-143-107	0	0	0.54
13	17,34	Methyl rosmarinate	Phenolic compound	374	373	373-179-135	0.69	0	0
16	17,74	1-Caffeoyl-beta-D-glucose	Phenolic compound	342	341	341-177-135	0.81	0.7	1.3
14	18,34	Amentoflavone	Flavonoid	538	537	355-179-151	0.74	0.35	0
17	18,45	Oleuroside	Phenolic compound	540	539	539-301-123	0	0	0.9
18	18,83	Stigmasterol	Others (Steroid)	412	411	411-227-119	0	0	1.42
16	19,22	Vanillic acid glucoside	Phenolic compound	330	329	329-169-151	0.42	0	0
19	19,44	Quercetin 3-rutinoside-7-rhamnoside	Flavonoid	756	755	755-467-301-179	3.44	3.5	0.66
17	19,51	Catechin-4-ol 3-O-β-D-galactopyranoside	Flavonoid	468	467	467-303-171	0.4	0	0
20	20,19	Valoneic acid dilactone	Phenolic compound	470	469	469-307-179	2.77	1.82	3.88
20	20,93	Quercetin 3-(6″-malonyl-glucoside)	Flavonoid	550	549	549-505	0.73	0	0
21	21,12	Alyssonoside	Flavonoid	770	769	769-463	0	0	1.18
22	21,43	Rutin	Flavonoid	610	609	609-301-255	4.09	4.31	2.37
23	22,05	Chlorogenic Acid	Phenolic acid	354	353	707 [2M−H]−, 191, 179, 135	1.32	0.51	4.75

(Continued on following page)

TABLE 8 (*Continued*) List of compounds identified in the extracts of the flowering tops of *R. montana* by HPLC/UV-ESI-MS.

N°	RT (min)	Molecules	Classes	Nominal masses	[M-H]⁻ (m/z)	Fragment ions (m/z)	E (1)	E (2)	E (3)
24	22,78	Quercetin-3-O-pentosyl-pentoside	Flavonoid	566	565	565-303-151	0.23	0	1.24
24	22,81	Quercetin-3′-glucoside	Flavonoid	464	463	463-447-301	0.74	0	0
24	22,89	Myricetin glucuronide	Flavonoid	494	493	493-317	0	0.1	0
25	22,98	Gallic acid 4-O-(6-galloylglucoside)	Phenolic acid	484	483	483-331-169	0	0.13	0.77
25	23,26	Oleuropeic acid 8-O-glucoside	Phenolic compound	346	345	345-171-143	2.14	0	0
25	23,31	Betonyoside A	Phenolic compound	654	653	653-491-271	0	1.52	0
26	23,55	Rhamnetin 3-rutinoside	Flavonoid	624	623	632-301-169	3.31	2.62	0.97
27	23,95	3,4-Di-O-galloylquinic acid	Phenolic acid	496	495	495-341-169	0	0.21	4.19
27	24,36	Cyanidin 3-arabinoside	Flavonoid	454	453	453-303-179	0.5	0	0
29	25,6	Rhamnetin 3-rhamnoside	Flavonoid	462	461	461-315-151	6.27	3.75	0.27
30	25,87	Rosmarinic acid 3′-glucoside	Phenolic compound	522	521	521-365-197	21.9	23.8	20.03
31	26,87	Quercitrin	Flavonoid	448	447	447-285-151	10.46	15.5	15.42
32	27,18	Salvigenin	Flavonoid	328	327	327-297-167	0	0	3.89
31	27,19	(+)-Gallocatechin	Flavonoid	306	305	305-275-125	0	5.3	0
33	27,41	Taxifolin	Flavonoid	304	303	303-273-125	4.82	1.33	0.25
32	27,77	7-Methoxyflavone	Flavonoid	252	251	251-221-181	1.29	0.33	0
34	29,54	Syringetin-3-O-hexoside	Flavonoid	508	507	507-345	0	1.07	0.11
35	30,55	Caffeoyl-feruloyltartaric acid	Phenolic acid	488	487	487-457-375	0.71	0.23	0.15

FIGURE 4
Distribution of different classes of compounds in the analyzed samples.
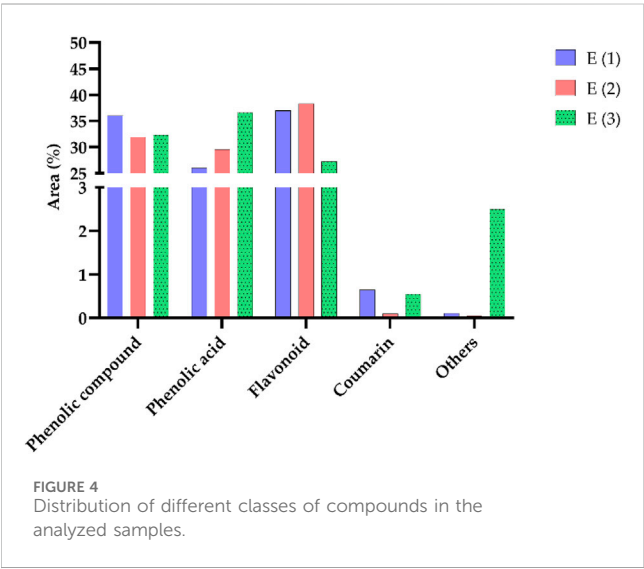
Unlike polyphenols and flavonoids, the condensed tannins of *R. montana* were more soluble in aqueous ethanol (58.27 mg CE/g of extract) than in the decoction (58.27 mg CE/g of extract) and aqueous methanol (39.47 mg CE/g of extract).

The contents of Mountain Rue extracts found in this study are significantly higher than those reported by Szewczyk et al. (2023), where the polyphenol and condensed tannin contents of the methanolic extract prepared from *in vitro* cultivated biomass were 41.61 mg GAE/g of extract and 10.97 mg CE/g of extract, respectively. Similarly, Drioiche et al. (2020a) reported that the polyphenol and flavonoid contents of the hydro-methanolic extract from the aerial parts of Moroccan *R. montana* L. were 33.684 mg GAE/g of extract and 0.843 mg QE/g of extract, respectively. Merghem and Dahamna (2020) noted that the ethyl acetate extract of *R. montana* L. from Algeria contained the highest quantities of polyphenols, tannins, and flavonoids, with values of 257.1 µg gallic acid equivalent/mg of extract, 251 tannic acid equivalent/mg of extract, 117.4 µg quercetin equivalent/mg of extract, and 139.5 µg rutin equivalent/mg of extract, respectively. Our results are lower than those reported by Benali et al. (2020a), where the highest phenolic compound and flavonoid contents were found in the methanolic extract of *R. montana* collected from northeastern Morocco, with values of 117.70 mg GAE/g of extract and 77.00 mg RE/g of extract.

The variation in polyphenol and flavonoid levels among the analyzed extracts can be explained by the difference in the solubility of phenolic compounds, which is influenced by the extraction temperature as well as the structure of these compounds.
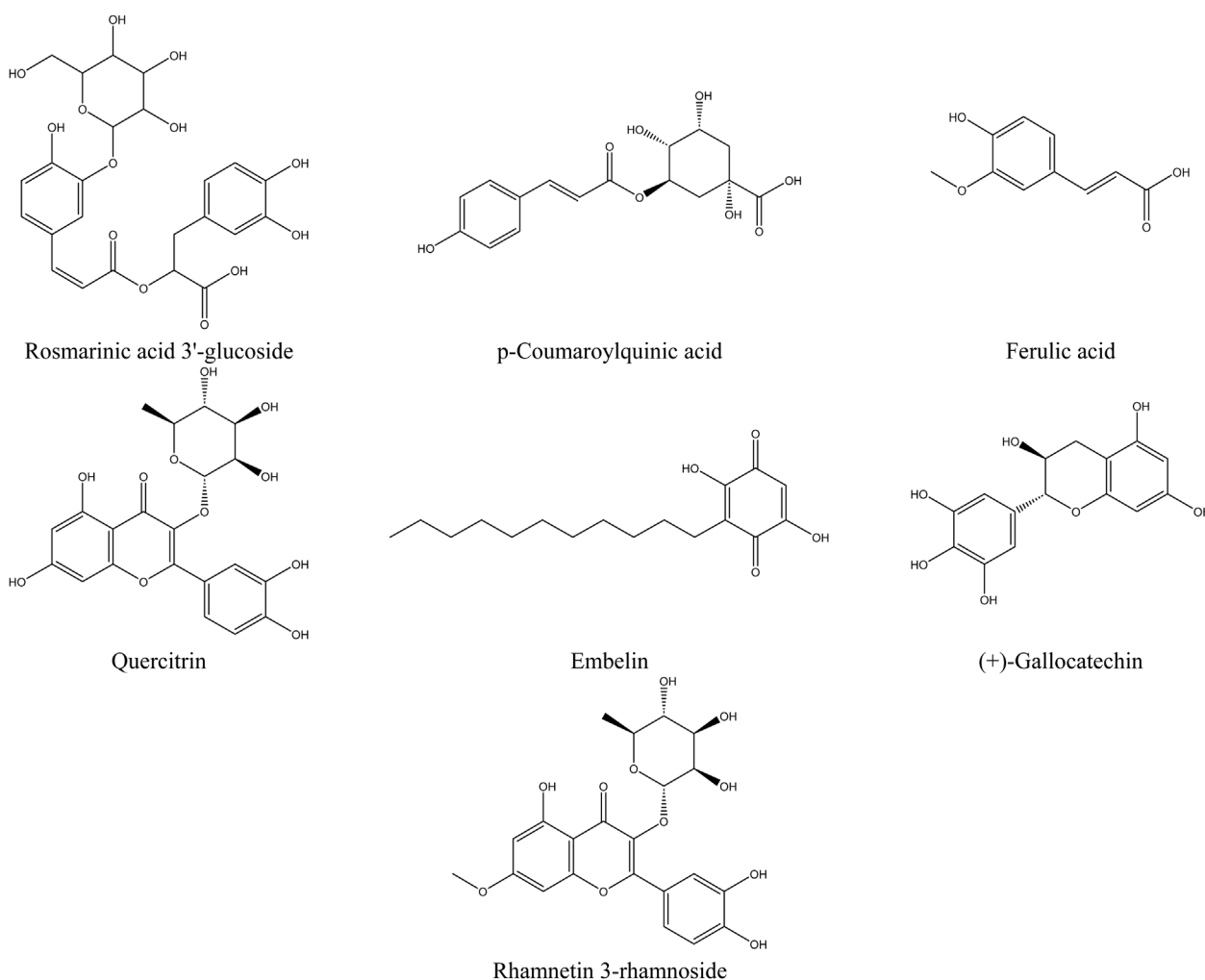
FIGURE 5
Structure of the main compounds identified in the extracts of the flowering tops of *R. montana*.

Additionally, the choice of extraction method can also have a significant impact on the extraction and quantification of polyphenols, flavonoids, and condensed tannins (Alara et al., 2021; Lama-Muñoz and Contreras, 2022; El Mannoubi, 2023).

3.8 Antioxidant activity of the EO and phenolic extracts

3.8.1 Antioxidant activity of the EO

The results reveal that the inhibition of DPPH radicals varies depending on the concentration of the EO from *R. montana*. According to the IC_{50} values presented in Figure 7, the standard antioxidant butylated hydroxytoluene (BHT) exhibits a significantly greater antioxidant capacity compared to the EO of *R. montana*. Indeed, the latter shows a weak ability to reduce DPPH free radicals, with an IC_{50} value 18.16 times higher than that of BHT.

The antioxidant potential of the EO of *R. montana* has already been examined by various researchers. In Morocco, Benali et al. (2020b) indicated that the EO from the aerial parts of mountain rue collected in Taza, Morocco, which

contains components such as 2-undecanone (63.97%), camphor (3.82%), and cyclopropanecarboxylic acid (3.66%), exhibits a remarkable ability to reduce free radicals (IC_{50} = 244.62 μg/mL). Meanwhile, the reducing power of this EO, expressed in terms of micrograms of ascorbic acid equivalent per gram of EO, was 1.39 μg/g. In the same country, Drioiche et al. (2020a) found through the DPPH method that the EO of the aerial parts of *R. montana* collected in Boulemane, Morocco, with 2-undecanone (82.62%), 2-undecanol (2.87%), and 2-undecanol acetate (2.13%) as its main compounds, has an IC50 (548.5 μg/mL) 10.28 times higher than that of ascorbic acid (53.35 μg/mL). In Algeria, Mohammedi et al. (2019) confirmed through the DPPH method the significant antioxidant capacity of all EOs isolated from *R. montana* collected in seven different regions. In particular, EO samples 6 and 7 exhibited strong DPPH inhibition activity with IC_{50} values of 49.6 and 50.2 μg/L, respectively. Moreover, these values were not influenced by the cultivation site. These researchers attributed the remarkable antioxidant activity of EOs 6 and 7 to their high content of 2-undecanone, which was 81.7% and 78.6%, respectively (Mohammedi et al., 2019). However, the study by Slougui et al. (2023) reported the inactivity of the EO extracted
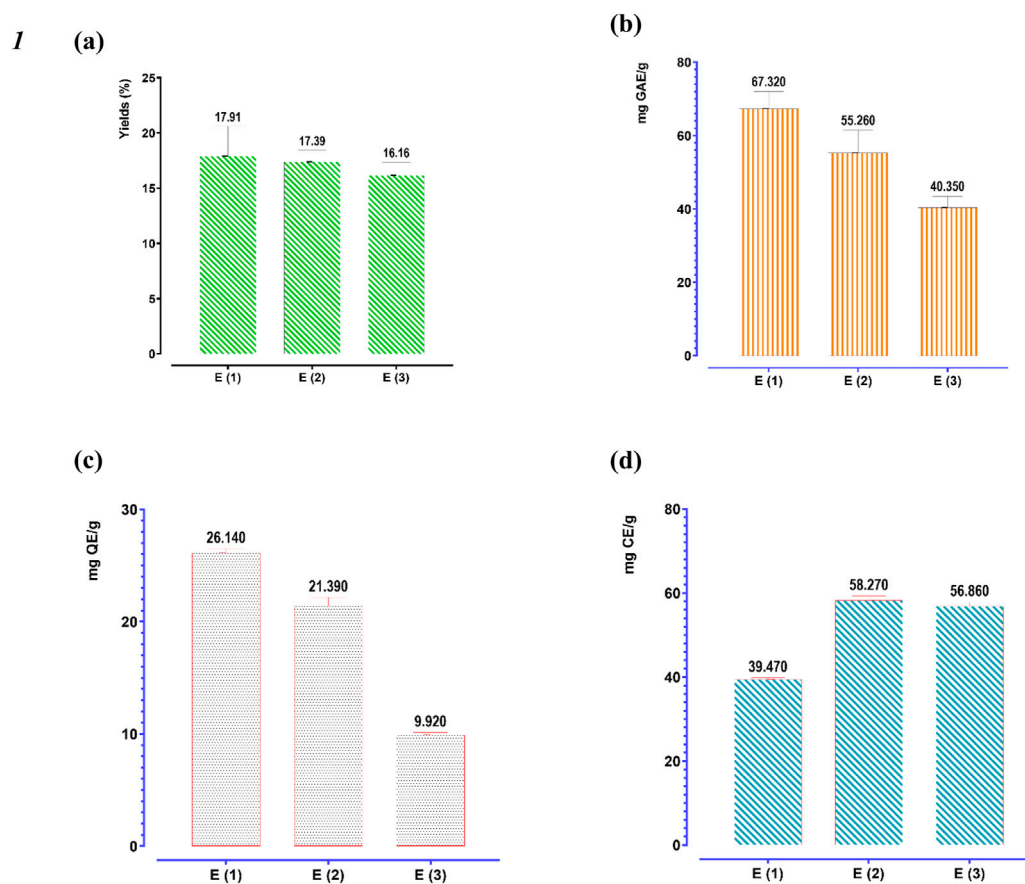
FIGURE 6
Extraction yield **(a)**, phenolic content **(b)**, flavonoid **(c)**, and condensed tannins contents **(d)** of three extracts of *R. montana*. The means display a significant difference ($p < 0.001$).
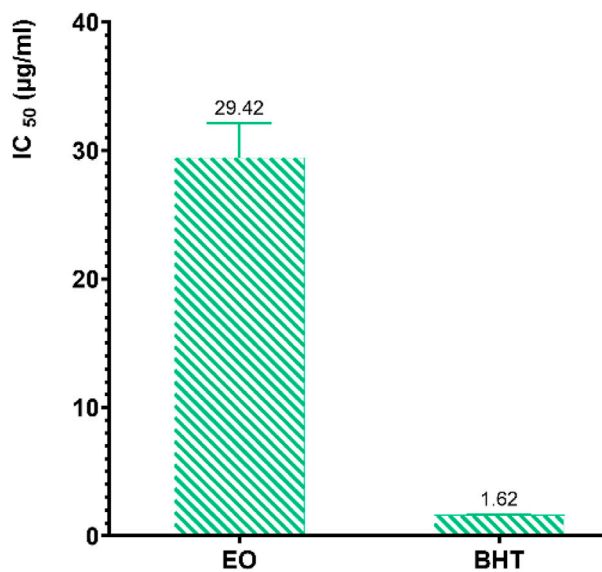
FIGURE 7
IC$_{50}$ values of *R. montana* and the standard antioxidant BHT using the DPPH method.

from the aerial parts of Algerian *R. montana* using the DPPH, CUPRAC, ABTS, and FRAP methods, with its main compounds being 2-nonanone (24.93%) and 2-undecanone (22.62%).

The antioxidant activity of EOs generally arises from the complex interaction between the various chemical components present in the EOs, which can act either antagonistically or synergistically. It should also be noted that EOs are composed of a complicated mixture of different classes of compounds, including aliphatic alcohols, monoterpenes, sesquiterpenes, ketones, aldehydes, and acids. For this reason, it is often difficult to fully understand the interactions and identify the compounds responsible for the antioxidant activity.

In the literature, the EOs of the *Ruta* genus have demonstrated promising antioxidant potential through various mechanisms, depending on the concentration. Moreover, the EOs of *Ruta* species are generally characterized by a mixture of ketones, which can represent up to 84% of the EO (Bertrand et al., 2003; Kambouche et al., 2008). However, significant disparities exist between species, both in terms of the concentration of these compounds and the presence of other compounds in high concentrations. This can be attributed to the fact that the composition of EOs isolated from *Ruta* species is strongly influenced by a combination of intrinsic and extrinsic factors, such as genetic and environmental factors. In this context, a study by Jaradat et al. (2017) highlighted the influence of

the collection region of *R. chalepensis* leaves on the antioxidant activity of its EO. These researchers found using the DPPH method that the EO of *R. chalepensis* from Jerusalem exhibited the highest antioxidant power (IC_{50} = 6.9 µg/mL), followed by those from Hebron (IC_{50} = 7.8 µg/mL) and Jenin (IC_{50} = 19.9 µg/mL). Another study revealed the influence of vegetative stages, flowering, and different organs of *R. chalepensis* on the chelating activity of its EOs. EOs extracted from the stems and flowers of *R. chalepensis* harvested during the flowering stage exhibited higher chelating power than those from the leaves (Krayni et al., 2015). Recently, a study evaluated the antioxidant power of the EO extracted from the aerial parts of Saudi *R. chalepensis* using three *in vitro* methods. The authors observed powerful concentration-dependent antioxidant activity using DPPH, nitric oxide scavenging, and ferric ion reducing power (FRAP) methods, with IC_{50} values of 40.26%, 36.88%, and 19.09%, respectively (Aati et al., 2023). The EO extracted from the aerial parts of *R. graveolens* from Romania, containing 2-undecanone (76.19%) and 2-nonanone (7.83%), was capable of reducing the stable DPPH free radical with an IC_{50} value of 0.25 mg/mL (Jianu et al., 2021). In summary, these studies highlight the antioxidant effects of EOs from *Ruta* species, indicating their potential for commercial use as natural antioxidants.

3.8.2 Antioxidant activity of extracts

The antioxidant activity of the decoction and the hydromethanolic and hydroethanolic extracts of *R. montana* was determined using three methods: DPPH radical scavenging, ferric ion reducing power, and total antioxidant capacity. By varying the concentrations of the extracts (mg/mL), we were able to determine the IC_{50} (the concentration of extract required to reduce 50% of the DPPH free radical levels) and the EC_{50} (the effective concentration at which the absorbance equals 0.5) for the FRAP method.

According to the results presented in Figure 8, the IC_{50} and EC_{50} values for ascorbic acid and the EC_{50} of BHA, used as reference molecules in the DPPH and FRAP methods, are significantly lower than those of the extracts, indicating a high antioxidant activity of the standards.

The estimation of the antioxidant capacity of the three extracts showed considerable variability depending on the nature of the solvent used for extraction. Indeed, the hydromethanolic extract, which exhibited high levels of polyphenols and flavonoids, stands out from the other extracts through the three methods with significantly higher radical scavenging power, ferric ion reducing power, and Mo(VI) molybdate reducing power. Its strong antioxidant activity is reflected in a total antioxidant capacity of 403.32 mg EAA/g of extract, with IC_{50} values of 117.24 and 142.35 µg/mL for the DPPH and FRAP methods, respectively. It is followed by the hydroethanolic extract, which displays moderate antioxidant power with a total antioxidant capacity of 334.56 mg EAA/g of extract, with IC_{50} and EC_{50} values of 120.35 and 144.81 µg/mL for the DPPH and FRAP methods, respectively. The decoction, on the other hand, showed the weakest antioxidant powers, with a total antioxidant capacity of 188.62 mg EAA/g of extract, with IC_{50} and EC_{50} values of 178.83 µg/mL and 221.88 µg/mL for the DPPH and FRAP methods, respectively.

The difference in antioxidant activity observed between the *R. montana* extracts is specifically attributed to the levels of polyphenols, flavonoids, and other aromatic compounds present.

In our study, referring to the results of phenolic compound assays, we found that the three extracts analyzed contain high levels of phenolic compounds, with the hydromethanolic extract recording the highest content of polyphenols and flavonoids. This is followed by the hydroethanolic extract and the decoction, which is frequently used in traditional medicine.
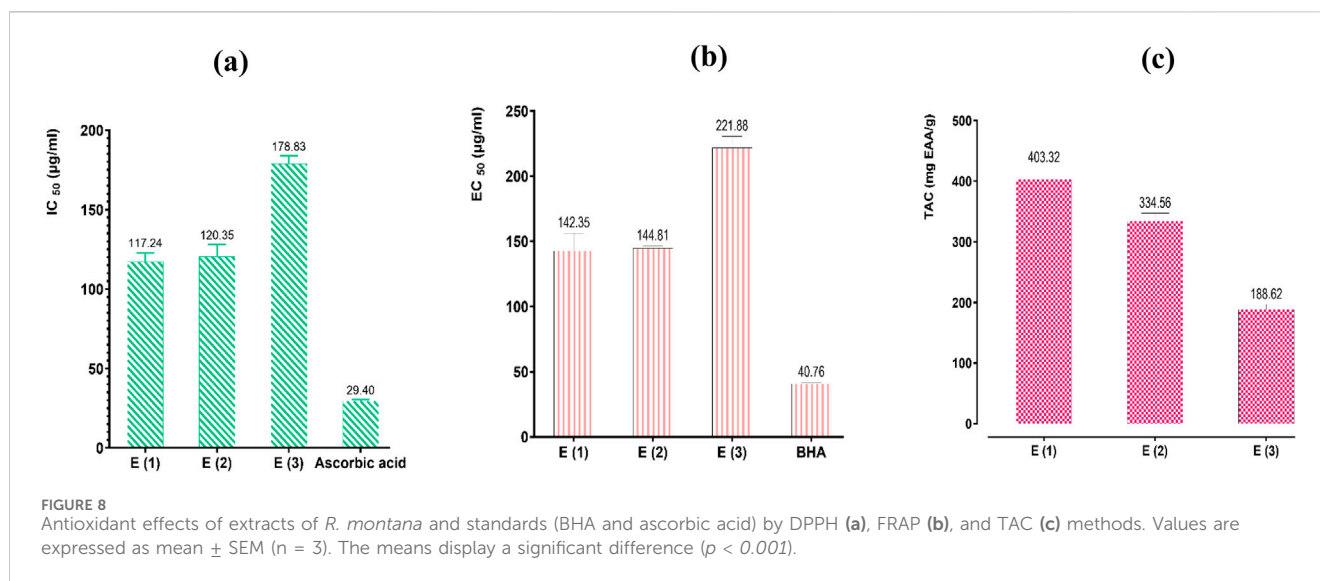
Furthermore, the results of chromatographic analyses performed using HPLC-MS on the decoction and the hydroethanolic and hydromethanolic extracts from the flowering tops of *R. montana*. revealed great diversity in their chemical profiles. This diversity is clearly illustrated by the presence of several chemical families such as phenolic acids, flavonoids, and benzoquinones. In the hydromethanolic extract, the main constituent is rosmarinic acid glucoside (21.9%), followed by p-coumaroylquinic acid (15.5%), quercitrin (15.5%), rhamnetin 3-rhamnoside (6.27%), embelin (6.25%), and ferulic acid (6.1%). In the hydroethanolic extract, the dominant compound is rosmarinic acid glucoside (23.8%), followed by p-coumaroylquinic acid (18.4%), quercitrin (15.5%), ferulic acid (8.44%), and gallocatechin (5.3%). In the decoction, the major component is rhamnetin 3-rhamnoside (20.03%), followed by rosmarinic acid glucoside (15.42%), quercitrin (15.42%), p-coumaroylquinic acid (15.08%), 4-di-O-galloylquinic acid (8.94%), ferulic acid (6.49%), and embelin (6.12%).

Similar results are reported by Benali et al. (2020a), where the methanolic extract of *R. montana* L. collected from Taza (Northeast Morocco) exhibited superior antioxidant activity compared to the ethanolic extract. These researchers found, using the DPPH and Reducing power methods (TAC), that the IC_{50} values for the methanolic extract were 10.66 µg/mL and 66.66 mg AAE/g of extract, respectively, while for the ethanolic extract, the IC_{50} values were 13.00 ± 1.73 µg/mL and 36.33 mg AAE/g of extract, respectively. Merghem and Dahamna (2020) confirmed the antioxidant potential of the aerial parts of *R. montana* using the DPPH free radical scavenging and ferrous ion chelation tests. In this study, the aqueous extract (IC_{50} = 83 µg/mL) and the methanolic extract (IC_{50} = 67 µg/mL) exhibited remarkable radical scavenging power, surpassing those of quercetin (IC_{50} = 3.491 mg/mL) and rutin (IC_{50} = 4.179 mg/mL), which were used as reference antioxidants.

Also, through the ferrous ion chelation test, the methanolic extract (IC_{50} = 21 µg/mL) and aqueous extract (IC_{50} = 5 µg/mL) exhibited significant activity. Slougui et al. (2023) reported the antioxidant effect of the ethyl acetate extract of the aerial parts of *R. montana* L. from Algeria using the FRAP and DPPH methods, noting IC_{50} values of 84.01 and 135.40 µg/mL, respectively. Another study found, using the DPPH method, that the antioxidant potential of the hydromethanolic extract obtained by Soxhlet from the aerial parts of *R. montana*. from Morocco was superior to that of the methanolic macerate, with IC_{50} values of 1097.2 µg/mL and 1332.8 µg/mL, respectively (Drioiche et al., 2020a).

3.9 Correlation between phenolic content and antioxidant activities of *R. montana* extracts

The results obtained previously demonstrate the relationship between phenolic compounds and the antioxidant activity of

FIGURE 8
Antioxidant effects of extracts of *R. montana* and standards (BHA and ascorbic acid) by DPPH **(a)**, FRAP **(b)**, and TAC **(c)** methods. Values are expressed as mean ± SEM (n = 3). The means display a significant difference (*p < 0.001*).

the three *R. montana* extracts. This is illustrated in this context (Table 9).

The linear correlation coefficients range from −0.700 to 0.9997. The antioxidant capacity of the extracts appears to be influenced primarily by the total polyphenol and flavonoid contents. These compounds showed high coefficients in comparison to condensed tannins (0.913 ≤ r ≤ 0.9995). In contrast, a negative correlation was observed between condensed tannins and the three antioxidant activities, namely the DPPH method (r = −0.5), the FRAP method (r = −0.478), and total antioxidant capacity (r = −0.7). This result leads us to suggest that condensed tannins do not influence the antioxidant activity of *R. montana* L. extracts. Similar results have linked the group of condensed tannins to phenolic compounds (r = −0.795) and flavonoids (r = −0.678).

On the other hand, we observe a very strong correlation between the IC_{50} and EC_{50} values from the DPPH and FRAP tests (r = 0.9997), between the IC_{50} values of DPPH and TCA (r = 0.969), and between the EC_{50} values of FRAP and TCA (r = 0.962). This indicates that the antioxidant activities demonstrated by these three tests are likely provided by the same active molecules.

3.10 Antimicrobial activity of *R. montana* extracts and essential oil

Tables 10, 11 present the minimum inhibitory concentrations (MIC), minimum fungicidal concentrations (MFC), and minimum bactericidal concentrations (MBC) expressed in mg/mL for the extracts and EO of *R. montana* against the tested microorganisms.

According to the results of the antifungal activity illustrated in Table 10, the hydromethanolic extract and the EO of *R. montana* tested against the four *Candida* strains and *Aspergillus niger* revealed promising antifungal activity, while the decoction and hydroethanolic extract showed moderate activity.

For the three extracts, the MIC and MFC values ranged from 3.13 to 50 mg/mL and varied between different fungi; in some cases, they were equal, indicating a fungicidal action. *Aspergillus niger* was

TABLE 9 Linear correlation coefficients (r) between polyphenol content (PC), flavonoid content (FC), condensed tannin content (CT), and the antioxidant activity of *R. montana* extracts.

	PC	FC	CT	DPPH	FRAP	TCA
PC	1	0.985	−0.795	0.923	0.913	0.990
FC	0.985	1	−0.678	0.976	0.970	0.9995
CT	−0.795	−0.678	1	−0.500	−0.478	−0.700
DPPH	0.923	0.976	−0.500	1	0.9997	0.969
FRAP	0.913	0.970	−0.478	0.9997	1	0.962
TCA	0.990	0.9995	−0.700	0.969	0.962	1

the most sensitive, with MIC and MFC values of 12.5, 6.25, and 3.13 mg/mL for the decoction, hydromethanolic extract, and hydroethanolic extract, respectively. However, against the *Candida* yeasts, the decoction and hydroethanolic extract exhibited moderate action, with MIC and MFC values of 50 mg/mL, except for *Candida albicans* and *Candida tropicalis*, where the activity of both extracts was null.

The hydromethanolic extract also exhibited both fungistatic and fungicidal powers against *Candida* yeasts at the same concentration of 50 mg/mL, except for *C. tropicalis*, for which the MIC and MFC were 25 mg/mL.

The essential oil EO, on the other hand, demonstrated a stronger fungicidal effect on the yeasts than the tested extracts. The MIC and MFC values ranged from 2.34 to 37.75 mg/mL. The minimum fungicidal concentration of 4.69 mg/mL was achieved against *A. niger*. The highest MFC of 37.5 mg/mL was recorded against *Candida parapsilosis*. *Candida tropicalis* was inhibited and destroyed at the same concentration of 9.38 mg/mL, while *C. albicans* and *Candida dubliniensis* showed MFC values of 18.75 mg/mL.

For the antibacterial activity, the results obtained from Table 11 show that the extracts and the EO of *R. montana* exhibit activity against bacterial strains. Furthermore, the determination of the MIC of the extracts and EO revealed variable levels of action. Among the

TABLE 10 MIC and MBC (mg/mL) of the extracts of *R. montana*, and MIC (μg/mL) of antibiotics against the microbial strains studied.

Bacterial strains	E (1)			E (2)			E (3)			EO			Antibiotics *			
	CMI	CMB	CMB/CMI	CMI	CMB	CMB/CMI	CMI	CMB	CMB/CMI	CMI	CMB	CMB/CMI	Gentamycin	Amoxicillin–Clavulanate	Vancomycin	Trimethoprim-Sulfamethoxazole
E. cloacae	25	25	1	25	25	1	50	50	1	50	50	1	>4	>8/2		>4/76
K.pneumoniae	>100	>100	—	50	50	1	>100	>100	—	50	50	1	≤1	≤2/2		≤1/19
E. coli	>100	>100	—	>100	>100	—	>100	>100	—	50	50	1	2	8/2		≤1/19
S. aureus	25	25	1	25	25	1	>100	>100	—	100	100	1	<0.5		2	<10
S. epidermidis	25	50	2	50	50	1	50	50	1	100	100	1	2		>8	>4/76

*: The minimum inhibitory concentration (MIC) of the antibiotics was measured using the BD, Phoenix™ identification and anti-biogram device.

three extracts tested, the aqueous ethanolic extract was more active compared to the aqueous methanolic extract and the decoction. The latter was found to be inactive against all the tested bacteria, except for *E. cloacae* and *S. epidermidis*, for which the MIC and MBC were 50 mg/mL.

The methanolic and aqueous ethanolic extracts exhibited both bacteriostatic and bactericidal actions at a concentration of 25 mg/mL against *E. cloacae* and *S. aureus*. Additionally, both extracts showed bactericidal activity at 50 mg/mL against *S. epidermidis*. Moreover, the hydroethanolic extract demonstrated bactericidal activity at 50 mg/mL against the *Klebsiella pneumoniae* strain, while the aqueous methanolic extract was inactive.

Thus, the three extracts tested did not exhibit any effect on wild *Escherichia coli*. In contrast, the essential oil inhibited and destroyed the strains *Enter. cloacae*, *Kleb. pneumoniae*, and wild *E. coli* at a concentration of 50 mg/mL. *S. aureus* and *S. epidermidis* appeared less sensitive, showing higher MIC and MBC values of 100 mg/mL.

The variation in sensitivity of the tested microorganisms to the extracts of *R. montana* could be explained by the distinct composition of secondary metabolites in these extracts. On the other hand, it may be due to the absence of strongly antimicrobial molecules or the low potency of the antibacterial compounds present in the extracts.

The results of the antimicrobial activity of the EO of *R. montana* obtained are consistent with those of Drioiche et al. (2020b). These authors described the antibacterial activity of the EO from *R. montana* from Morocco, primarily containing 2-undecanone (82.62%), as moderate against *Staphylococcus epidermidis*, *K. pneumoniae* spp. pneumoniae, *E. coli*, *Enterobacter cloacae*, and *Staphylococcus aureus* STAIML/MRS/mecA/HLMUP/BLACT. However, the same study revealed a significant antifungal potential of this EO against eight yeasts (*C. albicans*, *C. tropicalis*, *Candida glabrata*, *C. dubliniensis*, *Candida* sp., *Rhodotorula rubra*, *Trichosporon* sp., *Cryptococcus neoformans*), three molds (*A. niger*, *Fusarium* sp., *Penicillium* sp.), and one dermatophyte (*Trichophyton mentagrophytes*), with MFC values of 1.8 mg/mL for yeasts, 0.9 mg/mL for molds, and 0.45 mg/mL for dermatophytes, respectively.

Benali et al. (2020a) reported the moderate antimicrobial action of the EO of *R. montana* from Morocco, predominantly composed of 2-undecanone (63.97%), against eight microbial strains, including *Bacillus subtilis*, *S. aureus*, *E. coli*, *Pseudomonas aeruginosa*, and *C. albicans*, with inhibition zone diameters ranging from 9.2 ± 0.5 mm to 18 mm. Flouchi et al. (2024) also revealed the modest antibacterial activity of the Moroccan *R. montana* EO, which contained 2-undecanone (85.76%), 2-nonanone (3.95%), 2-decanone (3.67%), and 2-dodecanone (1.94%), with MIC values ranging from 4% (v/v) for *Pantoea* to 8% (v/v) for *S. aureus*, *P. aeruginosa*, *E. coli*, *Pantoea* spp., *K. pneumoniae*, *Escherichia hermannii*, *Stenotrophomonas maltophilia*, except for *K. pneumoniae*, where no inhibition was detected.

Another study evaluated the antimicrobial activity of the EO of *R. montana* isolated from the aerial parts collected in Algeria on eight microbial strains (*S. aureus*, *B. subtilis*, *Enterococcus faecium*, *E. coli*, *Klebsiella pneumonia*, and *P. aeruginosa*) and two yeasts (*C. albicans* and *Saccharomyces cerevisiae*) using the agar disc diffusion method. The authors described the antimicrobial activity of this plant as moderate (inhibition zone diameters ≤ 18 mm) (Mohammedi et al., 2019).

TABLE 11 MIC and MFC of the extracts of *R. montana*, and MIC (µg/mL) of antifungals against the Fungal strains studied.

Fungal strains	E (1)			E (2)			E (3)			EO			Antifungals#
	CMI	CMF	CMF/CMI	CMI	CMF	CMF/CMI	CMI	CMF	CMF/CMI	CMI	CMF	CMF/CMI	Terbinafine
C. albicans	50	50	1	50	50	1	>50	>50	—	9.38	18.75	2	12.500
C. dubliniensis	50	50	1	50	50	1	50	50	1	18.75	18.75	1	3.125
C. tropicalis	25	25	1	>50	>50	—	50	50	1	9.38	9.38	1	12.500
C. parapsilosis	50	50	1	50	50	1	50	50	1	18.75	37.5	2	6.250
Aspergillus niger	6.25	6.25	1	3.13	3.13	1	12.5	12.5	1	2.34	4.69	2	3.125

#: The MIC, of terbinafine was calculated on a microplate.

Another study compared, using the agar disc diffusion method, the antibacterial activity of *R. montana* EO alone and in combination with five conventional antibiotics (gentamicin, amoxicillin, cefazolin, tetracycline, and amoxicillin/clavulanic acid against three pathogenic bacteria (*S. aureus*, *P. aeruginosa*, and *E. coli*). The results showed that the EO of *R. montana* from Algeria, whose main compounds are 2-undecanone (63.39%), 2-nonanone (5.65%), 2-acetoxytetradecane (4.94%), 2-decanone (4.47%), and 2-dodecanone (3.35%), had no or very weak antibacterial activity against *E. coli* and *S. aureus*, with MIC values ranging from 125 to 250 mg/mL. However, the combination of *R. montana* EO with antibiotics, particularly with amoxicillin and cefazolin, induced significant synergistic effects against all the bacterial strains tested. The inhibition zones for amoxicillin and cefazolin were 19.7–34 mm and 21.5–41 mm, respectively (Zeraib et al., 2021).

Generally, the antimicrobial power of EOs is related to their chemical composition. Some previous studies have reported the moderate antimicrobial activity of EOs from the *Ruta* genus (Coimbra et al., 2020; Nahar et al., 2021). In our study, the modest antimicrobial activity of *R. montana* L. EO could be attributed to the high percentage of aliphatic ketones, which represent 88.6% of the total chemical compounds, with the main compound being 2-undecanone (81.16%). Indeed, the antibacterial activity of this compound is known to be limited against bacterial strains (Gibka et al., 2009; Kunicka-Styczyńska and Gibka, 2010). On the other hand, this low activity could also be due to the multi-resistance of the strains.

3.11 Anti-inflammatory activity of *R. montana* extracts and essential oil

This experiment was conducted to determine the ability of the aqueous extract and the EO to reduce inflammation following carrageenan injections to induce inflammatory pain. Starting from the third hour after the carrageenan injection, doses of the aqueous extract and EO of R. montana (100 and 300 mg/kg, 0.1 and 0.2 mL) showed a significant suppression ($p < 0.001$) of paw edema compared to the negative control group (Table 12).

However, only the highest concentrations of the aqueous extract and the essential oil (EO) significantly reduced the edema induced by the subplantar injection of carrageenan ($p < 0.001$ at 6 h). Indeed, the dose of 300 mg/kg of the aqueous extract and the volume of

0.2 mL of the EO provided the greatest protection against paw volume increases, with suppression values of 79% and 71%, respectively, at the sixth hour. In contrast, the doses of 100 mg/kg of the aqueous extract and the volume of 0.2 mL of the EO showed lower protection compared to the 300 mg/kg dose of the aqueous extract and 0.1 mL of the EO, with suppression values of 28% and 23%, respectively. This indicates that the effectiveness of the anti-inflammatory effects of the aqueous extract and EO of *R. montana* is dose-dependent, and injections at these higher doses are more effective as anti-inflammatory treatments.

When comparing the groups that received indomethacin at a dose of 10 mg/kg, a protective effect of 90% was observed. Although the anti-inflammatory effect of the aqueous extract at a dose of 300 mg/kg and the EO at a dose of 0.2 mL was lower than that of indomethacin (10 mg/kg), both showed comparable anti-inflammatory effects throughout the observation period. Furthermore, after 3 h, the EO and aqueous extract of *R. montana*, as well as the standard medication, showed significant anti-inflammatory efficacy. This could be attributed to the time required for both substances to reach their site of action.

Carrageenan is a phlogistic agent known for its classic biphasic effect. Its administration triggers an inflammatory process, characterized by pain, heat, redness, and especially by swelling of the rat's hind paw, i.e., edema. The first phase is vascular and lasts between 90 and 180 min. It is characterized by the release of several mediators such as histamine and serotonin. In contrast, the second swelling phase, known as the cellular phase, extends from 270 to 360 min. It is mediated by the release of substances such as prostaglandins and cytokines (TNF-α and IL-1β) (Di Rosa et al., 1971), during which various cells, including neutrophils and monocytes, infiltrate the inflammatory site (Chen et al., 2018).

There is limited scientific information regarding the anti-inflammatory activity of *R. montana* L. Previous studies have described the anti-inflammatory effects of certain *Ruta* species. For example, the methanolic extract of *R. graveolens* leaves collected in India (400 mg/kg) showed a significant inhibitory effect on edema formation after carrageenan injection, with an inhibition percentage of 47.19% after 5 h, which is lower than our results (Kataki et al., 2014). Another group of researchers found that, in an acute model induced by carrageenan, the anti-inflammatory activity of the alkaloid fraction of Indian *R. graveolens* at a dose of 10 mg/kg exhibited superior anti-inflammatory activity (83%) compared to polyphenols (64%) and the standard drug used,

TABLE 12 Anti-edematous Effect of the Aqueous Extract E (3) and EO of the Flowering Tops of *R. montana* and Indomethacin (*$p < 0.05$; **$p < 0.01$; and ***$p < 0.001$).

Diameter (cm) and % of inhibition						
Treatment	Dose (mg/kg)	0 h	3 h	4 h	5 h	6 h
Control (NaCl 0.9%)	—	2.36 ± 0.14	2.93 ± 0.08**	2.90 ± 0.05**	2.83 ± 0.03**	2.73 ± 0.03*
Control (corn oil)	—	2.36 ± 0.04	2.83 ± 0.03***	2.83 ± 0.04***	2.73 ± 0.03**	2.63 ± 0.03**
Indomethacine	10	2.33 ± 0.03	2.53 ± 0.03** 65%	2.47 ± 0.01* 75%	2.41 ± 0.01 83%	2.37 ± 0.03 90%
Aqueous extract E (3)	100	2.16 ± 0.03	2.66 ± 0.03*** 13%	2.61 ± 0.03*** 17%	2.53 ± 0.01*** 22%	2.43 ± 0.03*** 28%
	300	2.23 ± 0.03	2.60 ± 0.05** 36%	2.50 ± 0.05* 50%	2.40 ± 0.05 64%	2.31 ± 0.04 79%
EO	0.1 mL	2.20 ± 0.05	2.65 ± 0.02*** 5%	2.56 ± 0.04*** 24%	2.48 ± 0.04** 25%	2.41 ± 0.04* 23%
	0.2 mL	2.30 ± 0.05	2.70 ± 0.02*** 15%	2.58 ± 0.03** 59%	2.48 ± 0.04* 62%	2.38 ± 0.04 71%

diclofenac (70%) (Ratheesh et al., 2009). Another study suggested that the anti-inflammatory activity observed in the ethanolic extract of *R. chalepensis* could be attributed to the presence of flavonoids (Iauk et al., 2004).

Flavonoids, due to their structure, can exert effective anti-inflammatory activity by inhibiting the secretion of factors responsible for inflammation, such as histamine, prostaglandins, serotonin, and lipoxygenases (Oubihi et al., 2020; Abou Baker, 2022; Al-Khayri et al., 2022). Another study revealed that, in the presence of polyphenols, the production of prostaglandins, which are responsible for the onset of inflammation, is reduced (Yahfoufi et al., 2018). HPLC chromatographic analysis of plant extracts showed the presence of the following phenolic compounds: rhamnetin 3-rhamnoside, rosmarinic acid glucoside, quercitrin, p-coumaroylquinic acid, 4-di-O-galloylquinic acid, ferulic acid, and embelin (6.12%). The anti-inflammatory activity of these compounds, such as phenolic acids (Liu et al., 2023), flavonoids (Shahidi and Yeo, 2018), and benzoquinones (Martínez and Bermejo Benito, 2005; Basha et al., 2022), has already been demonstrated in previous studies.

Regarding the EO of *R. montana*, no previous studies have investigated its anti-inflammatory effect. However, prior research has reported the anti-inflammatory activity of EOs from certain *Ruta* species. The EO of *R. chalepensis* from Algeria, composed of 2-undecanone (35.51%), 1-decanol-2-methyl (8.62%), and 2-dodecanone (6.86%), significantly reduced carrageenan-induced edema. The researchers suggested that the anti-inflammatory effect of this essential oil results from the inhibition of inflammation mediators such as serotonin, prostaglandins, and histamine (Boudjema et al., 2018). For the EO of *R. graveolens*, Nonnenmacher et al. (2016) (Nonnenmacher et al., 2016) found that its oral administration at a dose of 100 mg/kg was effective in reducing the edema index and inflammatory process in mice.

The anti-inflammatory effect of the EO of *R. montana* observed in this study is primarily associated with its chemical composition. An *in vivo* study demonstrated that the EO of *Houttuynia cordata* Thunb., of which 2-undecanone is the major component, possesses anti-inflammatory activity. The study showed that 2-undecanone

inhibits the formation of ear edema induced by xylene in a dose-dependent manner. Furthermore, its inhibition percentage of ear swelling is similar to that of aspirin at a dose of 8 mg/20 g, reaching 28% (Chen et al., 2014). Another study by Chen et al. (2014) also confirmed the ability of 2-undecanone to reduce xylene-induced ear edema. Li et al. (2011) reported that 2-undecanone inhibits, in a dose-dependent manner, the induction of TNF-α, NO, and H2O2 production by lipopolysaccharides. Therefore, the anti-inflammatory activity of the EO of *R. montana* observed in this study can be attributed to its predominant component, 2-undecanone (81.16%).

3.12 Antinociceptive activity of *R. montana*

The abdominal writhing test induced by acetic acid, widely used for its high sensitivity, allows the detection of substances with analgesic effects. In this study, this experimental model is used to determine the analgesic effect of the aqueous extract and essential oil of *R. montana*. Table 13 illustrates the analgesic activity in mice treated with the essential oil and aqueous extract of *R. montana* as well as the reference analgesic, Tramadol (10 mg/kg).

The large number of abdominal writhings observed after the injection of acetic acid in the presence of distilled water reveals the algogenic effect of this chemical compound. All tested doses of the aqueous extract and essential oil of *R. montana* significantly reduced ($p < 0.001$) the abdominal writhings induced by acetic acid in rats compared to the negative control groups. A preliminary analysis of the results allowed us to conclude that the aqueous extract and essential oil of this plant exert an analgesic effect, the intensity of which varies depending on the dose administered. The aqueous extract (100 and 300 mg/kg), administered orally 1 h before the injection of the stimulus, significantly ($p < 0.001$) and progressively reduced the writhings of rats exposed to acetic acid (11.621%–23.371%). The analgesic activity of *R. montana* essential oil was found to be superior to that of the aqueous extract. Indeed, the maximal inhibition was achieved with a volume of 0.2 mL (44.554%), which remained lower than that of Tramadol

TABLE 13 Antinociceptive effect of the aqueous extract and EO of *R. montana* flowering tops and tramadol.

Treatment	Dose	Number of writhes	Writhes inhibition (%)
Negative control (NaCl)		68.67 ± 2.028	
Negative control (Corn oil)		71.67 ± 2.186	
Tramadol	10 mg//kg	15.67 ± 1.764	77.032%
R. montana			
Aqueous extract E (3)	100 mg/kg	60.67 ± 1.453	11.621%
	300 mg/kg	52.67 ± 2.404	23.371%
EO	0.1 mL	41.00 ± 1.732	42.820%
	0.2 mL	39.67 ± 0.882	44.554%

(77.032%). We also observed that a 0.1 mL volume of the essential oil of this plant produced an analgesic effect close (42.820%) to that of 0.2 mL of the EO.

The abdominal writhings induced by acetic acid result from the activation of local peritoneal receptors (Ouédraogo et al., 2012), as well as the release of mediators such as prostaglandins (PGE2α, PGF2α) and cytokines (TNF-α, IL-1β, IL-8) (Bentley et al., 1983; Negus et al., 2006). The analgesic effect expressed by the aqueous extract and essential oil of *R. montana* L. indicates the presence of compounds capable of inhibiting the release of these chemical mediators.

In the literature, there is limited scientific data regarding the analgesic properties of *Ruta* species. The hexane extract of *R. graveolens*, using the acute tail immersion model, revealed a high analgesic effect of 62.1% (Micael et al., 2015). Similarly, the methanolic leaf extract of this species (100 mg/kg) significantly reduced by 54% the number of writhings induced by acetic acid (Loonat and Amabeoku, 2014). These researchers attributed this effect to the secondary metabolites present, such as flavonoids, tannins, saponins, and triterpenoid steroids.

Moreover, previous studies have demonstrated the analgesic effects of tannins, phenolic acids, and flavonoids (Sengupta et al., 2012; Ferraz et al., 2020; Zouhri et al., 2023). Therefore, the effect of our extract could be attributed to its richness in bioactive compounds, primarily phenolic acids and flavonoids.

Regarding essential oils, previous work suggests that their analgesic effects are due to their main constituents and a possible synergy between these chemical components. Their antinociceptive activity relies on peripheral (anti-inflammatory) and/or central mechanisms (Sarmento-Neto et al., 2016).

3.13 Subacute toxicity of the essential oil and aqueous extract of *R. montana*

R. montana, a plant native to the Mediterranean region, has a long history of medicinal use and is known for its various pharmaceutical activities due to the presence of bioactive compounds. This species contains a significant amount of alkaloids and furocoumarins (Milesi, 2001). Furthermore, ethnobotanical studies have reported cases of poisoning by *R. montana*, manifested by respiratory diseases, skin toxicity,

digestive disturbances, and neurological issues (Mitra et al., 2020; Belhaj et al., 2021). In this context, we investigated the subacute toxicity of the essential oil and aqueous extract at doses previously tested for their anti-inflammatory and analgesic activities. The variation in the relative organ weights, as well as biochemical analyses, highlighted the consequences of oral treatments with the essential oil (at 0.1 and 0.2 mL) and the aqueous extract of *R. montana* L. (at 100 and 300 mg/kg) on renal and hepatic functions.

3.13.1 Relative organ weight

The weight of the organs is an important indicator of physiological and pathological states in animals. Table 14 presents the effect of the aqueous extract and essential oil of *R. montana* L. on the relative weight (%) of several organs (kidneys, livers, and spleens) in rats exposed to different doses, compared to the control groups.

The essential oil and aqueous extract, administered at the tested doses to male mice on a daily basis, caused no fatalities or toxic symptoms in the rats. They behaved normally throughout the study and survived until the end of the experiment (28 days). Furthermore, no visible changes in the internal organs were detected macroscopically in any of the rats. The relative organ weight of the livers, kidneys, and spleens of all the tested groups at all tested doses remained within the normal range of the control group.

3.13.2 Study of serum biochemical parameters

The results of the biochemical parameters related to renal and hepatic functions are summarized in Table 15.

Many researchers use the liver and kidneys of rats to assess the safety or toxicity of drugs and plant-derived substances (Satyapal et al., 2008). Urea and creatinine are among the main markers of renal function (Treacy et al., 2019). In this study, the biochemical parameters used to evaluate renal function are presented in Figure 9. The daily oral administration of essential oil and aqueous extract of *R. montana* L. did not significantly alter the mean serum levels of uric acid in the experimental rats compared to those of the control rats. These mean values ranged between 0.20 mg/dL and 0.24 mg/dL in the control group and between 0.24 mg/dL and 0.26 mg/dL in the experimental group.

In contrast, creatinine levels slightly increased in a non-significant manner in rats treated with the aqueous extract

TABLE 14 The relative mass of the organs of the control and treated rats under the conditions of subacute toxicity by aqueous extracts E (3) and EO of *R. montana*.

Organs	Control NaCl	Control corn oil	E (3) 100 mg/kg	E (3) 300 mg/kg	EO 0.1 mL	EO 0.2 mL
Liver	4.242 ± 0.089	4.137 ± 0.086	$3{,}475 \pm 0{,}269^{ns}$	$3{,}701 \pm 0{,}206^{ns}$	$4{,}641 \pm 0.075^{ns}$	$4{,}591 \pm 0{,}241^{ns}$
Kidney	0.787 ± 0.019	0.768 ± 0.034	0.708 ± 0.146	0.670 ± 0.122	0.751 ± 0.028	0.669 ± 0.025
Spleen	0.296 ± 0.005	0.313 ± 0.029	0.301 ± 0.057	0.271 ± 0.052	0.356 ± 0.008	0.306 ± 0.018

TABLE 15 Biochemical parameters of rats treated orally with aqueous extract E (3) and essential oil (EO) from *R. montana* for 28 days.

Treatment	Dose	UREA	CREA	ALT	AST
Control (NaCl)	----	0.20 ± 0.01	1.61 ± 0.19	55.33 ± 2.02	82.67 ± 4.63
Control (corn oi)	----	0.24 ± 0.01	2.08 ± 0.16	58.33 ± 4.63	81.00 ± 6.50
Aqueous extract E (3)	100 mg/kg	0.25 ± 0.02	2.36 ± 0.21	49.00 ± 2.64	85.33 ± 2.02
	300 mg/kg	0.25 ± 0.01	1.94 ± 0.26	46.33 ± 3.48	91.33 ± 4.63
EO	0.1 mL	0.26 ± 0.00	1.49 ± 0.12	46.33 ± 2.40	81.33 ± 4.63
	0.2 mL	0.24 ± 0.01	1.50 ± 0.13	47.33 ± 0.88	89.33 ± 0.66
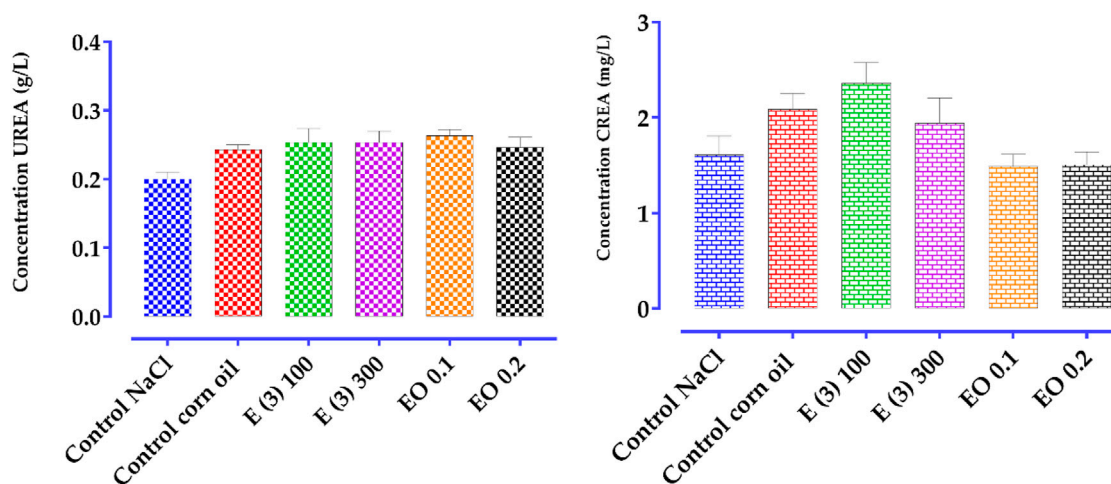
FIGURE 9
Effect of *R. montana* aqueous extract E (3) and EO on creatinine and urea levels in rats. Values are expressed as mean ± SEM (n = 6). The means display a significant difference (*p < 0.01*).

compared to the control group. These mean values ranged from 1.61 mg/dL to 2.08 mg/dL in the control group, and from 2.36 mg/dL to 1.94 mg/dL, respectively, for the doses of 100 and 300 mg/kg in the experimental group. A slight decrease in creatinine levels was observed in the group of rats treated with 0.1 and 0.3 mL of the essential oil. These results suggest that the essential oil of *R. montana* does not have a negative effect but appears to have a protective effect on the kidneys.

For liver function, the liver is one of the organs where a large number of compounds derived from plants are accumulated and detoxified (Guan and He, 2015). The analysis of transaminase levels is a good indicator of the toxic effects of medicinal plants on the liver (Adeneye et al., 2006; Amang et al., 2020). In this regard, the potential hepatotoxicity of the extract and essential oil of *R. montana* was evaluated by measuring the enzymatic activities of aminotransferases (ALT and AST). AST (aspartate aminotransferase) is an enzyme known for its rapid response to acute liver damage (within 24 h), with an increase that can reach up to ten times (Whitehead et al., 1999; Al-Busafi and Hilzenrat, 2013). While ALT (alanine aminotransferase) is a highly specific
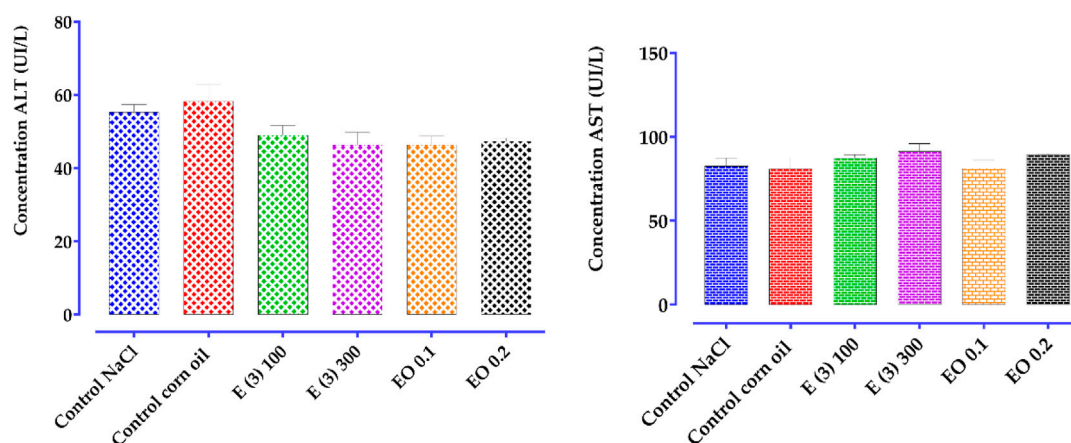
FIGURE 10
Effect of administration of total aqueous extract E (3) and EO of *R. montana* on some biochemical parameters for the evaluation of hepatic function (AST, ALT) in rats. Values are expressed as mean $\pm$ SEM (n = 6). The means display a significant difference ($p < 0.01$).

indicator of liver cell damage (Ozer et al., 2008; Adewale et al., 2016). The results of the biochemical parameters analyzed for liver function (ALT and AST) are presented in Figure 10. A slight, non-significant decrease in ALT levels was observed in the rat groups treated with the aqueous extract and essential oil compared to the control group.

For AST, a non-significant increase was detected in the group of rats treated with 100 and 300 mg/kg of the aqueous extract compared to the control group. These mean values ranged from 82.67 UI/L to 81.00 UI/L in the control group, and from 85.33 UI/L to 91.33 UI/L in the experimental group. Similarly, the essential oil at a dose of 0.2 mL induced a non-significant increase in AST levels (89.33 UI/L), while the 0.1 mL dose did not alter the AST levels (81.33 UI/L).

Based on these results, it is reasonable to assume that repeated administration of the aqueous extract at doses of 100 and 300 mg/kg, as well as the essential oil at a dose of 0.2 mL for 28 days, may induce toxicity in vital organs such as the heart and kidneys. In contrast, the essential oil at a dose of 0.1 mL appears to have hepatoprotective and nephroprotective effects.

4 Conclusion

This study provided a detailed chemical characterization and a comprehensive evaluation of the biological properties of *Ruta montana L.* from Morocco, highlighting its therapeutic potential. The essential oil, predominantly composed of 2-undecanone (81.16%) and decyl propanoate (9.33%), exhibited significant antimicrobial activity, particularly against *Candida albicans*, *Candida tropicalis*, and *Aspergillus niger*.

The phenolic extracts, enriched with compounds such as rosmarinic acid 3′-glucoside and quercitrin, demonstrated notable antioxidant capacity. Furthermore, anti-inflammatory and analgesic assays revealed dose-dependent efficacy, with the essential oil showing effects comparable to standard treatments like indomethacin. Notably, analgesic tests indicated a marked reduction in pain induced by acetic acid when using the essential oil.

From a toxicological perspective, the essential oil and extracts were found to be relatively safe at controlled doses, although slight increases in AST and creatinine levels at higher concentrations warrant further investigation.

R. montana presents promising prospects for the development of natural antimicrobial agents, antioxidant supplements, and treatments for inflammation and pain. Further clinical studies, long-term safety evaluations, and exploration of interactions with other bioactive compounds are essential to fully harness its pharmaceutical and nutraceutical potential.

Data availability statement

The raw data supporting the conclusions of this article will be made available by the authors, without undue reservation.

Ethics statement

The animal study was approved by the study was approved by an animal ethics committee. It was reviewed and approved by the Institutional Animal Care and Use Committee (IACUC) of the Faculty of Sciences Dhar El Mehraz, Sidi Mohamed Ben Abdallah University, Fès, Morocco, under reference #04/2019/LBEAS. The study was conducted in accordance with the local legislation and institutional requirements.

Author contributions

ME: Writing – review and editing, Conceptualization, Software, Writing – original draft, Methodology, Investigation. AD: Methodology, Software, Conceptualization, Writing – review and editing, Writing – original draft. IT: Investigation, Writing – original draft. AB: Investigation, Writing – original draft. OA: Formal Analysis, Writing – original draft, Funding acquisition, Methodology. AS: Methodology, Formal Analysis, Writing – original draft, Funding

acquisition. EF: Visualization, Validation, Writing – original draft, Data curation. HN: Writing – original draft, Formal Analysis. SS: Writing – original draft, Data curation. TZ: Methodology, Visualization, Supervision, Project administration, Validation, Writing – original draft. MB: Supervision, Formal Analysis, Investigation, Writing – original draft.

Conflict of interest

The authors declare that the research was conducted in the absence of any commercial or financial relationships that could be construed as a potential conflict of interest.

Generative AI statement

The author(s) declare that no Generative AI was used in the creation of this manuscript.

Publisher's note

All claims expressed in this article are solely those of the authors and do not necessarily represent those of their affiliated organizations, or those of the publisher, the editors and the reviewers. Any product that may be evaluated in this article, or claim that may be made by its manufacturer, is not guaranteed or endorsed by the publisher.

Supplementary material

The Supplementary Material for this article can be found online at: https://www.frontiersin.org/articles/10.3389/fchem.2025.1614984/full#supplementary-material

References

Aati, H. Y., Attia, H., Babtin, R., Al-Qahtani, N., and Wanner, J. (2023). Headspace solid phase micro-extraction of volatile constituents produced from Saudi ruta chalepensis and molecular docking study of potential antioxidant activity. *Molecules* 28, 1891. doi:10.3390/molecules28041891

Abou Baker, D. H. (2022). An ethnopharmacological review on the therapeutical properties of flavonoids and their mechanisms of actions: a comprehensive review based on up to date knowledge. *Toxicol. Rep.* 9, 445–469. doi:10.1016/j.toxrep.2022.03.011

Adams, R. P. (2007). "Identification of essential oil components by gas chromatography/mass spectroscopy," in *Salt Lake allured pub corp*.

Adeneye, A. A., Ajagbonna, O. P., Adeleke, T. I., and Bello, S. O. (2006). Preliminary toxicity and phytochemical studies of the stem bark aqueous extract of Musanga cecropioides in rats. *J. Ethnopharmacol.* 105, 374–379. doi:10.1016/j.jep.2005.11.027

Adewale, O. B., Onasanya, A., Anadozie, S. O., Abu, M. F., Akintan, I. A., Ogbole, C. J., et al. (2016). Evaluation of acute and subacute toxicity of aqueous extract of Crassocephalum rubens leaves in rats. *J. Ethnopharmacol.* 188, 153–158. doi:10.1016/j.jep.2016.05.003

Adli, B., Touati, M., Yabrir, B. B., Bezini, E., Hachi, M., Yousfi, I., et al. (2021). Consensus level and knowledge of spontaneous medicinal plants used in Algerian central steppe region (djelfa). *Agric. Conspec. Sci.* 86, 139–152.

Ailli, A., Handaq, N., Touijer, H., Gourich, A. A., Drioiche, A., Zibouh, K., et al. (2023). Phytochemistry and biological activities of essential oils from six aromatic medicinal plants with cosmetic properties. *Antibiotics* 12, 721. doi:10.3390/antibiotics12040721

AFNOR Editions (1972). *NF V05-113: Fruits, vegetables and derived products—mineralization of organic matter—method by incineration*. Paris: AFNOR.

AFNOR Editions (1985). *NF V03-402: Spices and herbs. Determination of water content. Entrainment method/Spices and aromatics. Determination of water content. Entrainment method.* Paris: AFNOR.

Akrout, A., Chemli, R., Chreïf, I., and Hammami, M. (2001). Analysis of the essential oil of Artemisia campestris L. *Flavour Fragr. J.* 16, 337–339. doi:10.1002/ffj.1006

Alara, O. R., Abdurahman, N. H., and Ukaegbu, C. I. (2021). Extraction of phenolic compounds: a review. *Curr. Res. Food Sci.* 4, 200–214. doi:10.1016/j.crfs.2021.03.011

Al-Busafi, S. A., and Hilzenrat, N. (2013). Mild hypertransaminasemia in primary Care. *ISRN Hepatol.* 2013, 1–6. doi:10.1155/2013/256426

Al-Khayri, J. M., Sahana, G. R., Nagella, P., Joseph, B. V., Alessa, F. M., and Al-MssallemM, Q. (2022). Flavonoids as potential anti-inflammatory molecules: a review. *Molecules* 27, 2901–2924. doi:10.3390/molecules27092901

Amang, A. P., Kodji, E., Mezui, C., Baane, M. P., Siwe, G. T., Kuissu, T. M., et al. (2020). Hepatoprotective effects of aqueous extract of opilia celtidifolia (opiliaceae) leaves against ethanol-induced liver damage in rats. *Evid. Based Complement. Altern. Med.* 2020, 6297475. doi:10.1155/2020/6297475

Balouiri, M., Sadiki, M., and Ibnsouda, S. K. (2016). Methods for *in vitro* evaluating antimicrobial activity: a review. *J. Pharm. Anal.* 6, 71–79. doi:10.1016/j.jpha.2015.11.005

Barbouchi, M., Benzidia, B., and Choukrad, M. (2021). Chemical variability in essential oils isolated from roots, stems, leaves and flowers of three Ruta species growing in Morocco. *J. King Saud. Univ. - Sci.* 33, 101634. doi:10.1016/j.jksus.2021.101634

Basha, N. J., Basavarajaiah, S. M., Baskaran, S., and Kumar, P. (2022). A comprehensive insight on the biological potential of embelin and its derivatives. *Nat. Prod. Res.* 36, 3054–3068. doi:10.1080/14786419.2021.1955361

Bekro, Y.-A., Mamyrbekova Békro, J. A., Boua, B. B., Fézan, H. T. B., and Ehile, E. E. (2007). Étude ethnobotanique et screening phytochimique de Caesalpinia benthamiana (Baill.) Herend. et Zarucchi (Caesalpiniaceae). *Sci. Nat.* 4, 217–225. doi:10.4314/scinat.v4i2.42146

Belhaj, S., Chaachouay, N., and Zidane, L. (2021). Ethnobotanical and toxicology study of medicinal plants used for the treatment of diabetes in the High Atlas Central of Morocco. *J. Pharm. Pharmacogn. Res.* 9, 619–662. doi:10.56499/jppres21.1014_9.5.619

Bellakhdar, J. (1997). Contribution à l'étude de la pharmacopée traditionnelle au Maroc: la situation actuelle, les produits, les sources du savoir (enquête ethnopharmacologique de terrain réalisée de 1969 à 1992). *Univ. Paul. Verlaine - Metz.* Available online at: https://hal.univ-lorraine.fr/tel-01752084 (Accessed March 11, 2025).

Benali, T., Chtibi, H., El Yamani, M., Marmouzi, I., Khabbach, A., El Achbani, H., et al. (2020a). Effect of extraction solvent on total phenol content, total flavonoids content, antioxidant and antimicrobial activities against phytopathogenic and foodborne pathogens bacteria of Ruta Montana extracts. *Moroc. J. Chem.* 8, 552–559. doi:10.48317/IMIST.PRSM/morjchem-v8i2.18788

Benali, T., Habbadi, K., Khabbach, A., Marmouzi, I., Zengin, G., Bouyahya, A., et al. (2020b). GC-MS analysis, antioxidant and antimicrobial activities of achillea odorata subsp. pectinata and ruta Montana essential oils and their potential use as food preservatives. *Foods* 9, 668. doi:10.3390/foods9050668

Bencheikh, N., Elbouzidi, A., Kharchoufa, L., Ouassou, H., Merrouni, I. A., Mechchate, H., et al. (2021). Inventory of medicinal plants used traditionally to manage kidney diseases in north-eastern Morocco: ethnobotanical fieldwork and pharmacological evidence. *Plants* 10, 1966. doi:10.3390/plants10091966

Benkhaira, N., Koraichi, S. I., and Fikri-Benbrahim, K. (2022). Ruta Montana (L.) L.: an insight into its medicinal value, phytochemistry, biological properties, and toxicity. *J. HerbMed Pharmacol.* 11, 305–319. doi:10.34172/jhp.2022.36

Bennaoum, Z., Benhassaini, H., Falconieri, D., Piras, A., and Porcedda, S. (2017). Chemical variability in essential oils from Ruta species among seasons, and its taxonomic and ecological significance. *Nat. Prod. Res.* 31, 2329–2334. doi:10.1080/14786419.2017.1303692

Bentley, G. A., Newton, S. H., and Starr, J. (1983). Studies on the antinociceptive action of α-agonist drugs and their interactions with opioid mechanisms. *Br. J. Pharmacol.* 79, 125–134. doi:10.1111/J.1476-5381.1983.TB10504.X

Bertrand, C., Fabre, N., Moulis, C., and Bessiere, J. M. (2003). Composition of the essentials oil of ruta corsica DC. *J. Essent. Oil Res.* 15, 98–99. doi:10.1080/10412905.2003.9712079

Bissel, S. J., Winkler, C. C., DelTondo, J., Wang, G., Williams, K., and Wiley, C. A. (2014). Coxsackievirus B4 myocarditis and meningoencephalitis in newborn twins. *Neuropathology* 34, 429–437. doi:10.1111/neup.12121

Bouabida, H., and Dris, D. (2022). Phytochemical constituents and larvicidal activity of Ruta graveolens, Ruta Montana and Artemisia absinthium hydro-methanolic extract against mosquito vectors of avian plasmodium (Culiseta longiareolata). *South Afr. J. Bot.* 151, 504–511. doi:10.1016/J.SAJB.2022.05.017

Boudjema, K., Mouhouche, Guerdouba, A., and Hali, L. (2018). Composition, physicochemical analysis, antimicrobial and anti-inflammatory activities of the essential oils obtained from Ruta chalepensis. L growing wild in northen of Algeria. *J. Chem. Soc. Pak* 40, 1054–1062.

Bouhenna, M. M., Bendif, H., Segueni, N., Khalfa, H., Djadoudi, A., Tahraoui, S., et al. (2024). Phytochemical profiling, LC-MS analyses, cytotoxicity, antioxidant, and antimicrobial activities of ruta Montana: an ethnomedicinally important plant in Algeria. *Curr. Bioact. Compd.* 20 (10), 90–99. doi:10.2174/1573407219666230606140634

Boutoumi, H., Moulay, S., and Khodja, M. (2009). Essential oil from ruta Montana L. (Rutaceae) chemical composition, insecticidal and larvicidal activities. *J. Essent. Oil-Bear. Plants* 12, 714–721. doi:10.1080/0972060X.2009.10643780

Bouzeraa, H., Bessila-Bouzeraa, M., and Labed, N. (2019). Repellent and fumigant toxic potential of three essential oils against Ephestia kuehniella. *Biosyst. Divers.* 27, 349–353. doi:10.15421/011946

Bruneton, J. (2009). *Pharmacognosie, phytochimie, plantes médicinales.* 4E Edn. Paris, France: LAVOISIER.

Budzianowski, J., Romaniuk-Drapała, A., Kikowska, M., Budzianowska, A., Thiem, B., Lisiak, N., et al. (2023). Rosmarinic acid 4′-O-β-glucoside – a compound with prospective medicinal and cosmetological applications - its isolation from callus and root cultures of Eryngium species and biological activity. *Ind. Crops Prod.* 193, 116138. doi:10.1016/j.indcrop.2022.116138

Chen, J., Wang, W., Shi, C., Wan, J., Deng, L., and Fang, J. (2014). Determination of four volatile compounds with anti-inflammatory biological activity in Houttuynia chordata Thunb. By gas chromatography and gas chromatography-mass spectrometry. *Anal. Lett.* 47, 730–741. doi:10.1080/00032719.2013.858260

Chen, L., Deng, H., Cui, H., Fang, J., Zuo, Z., Deng, J., et al. (2018). Inflammatory responses and inflammation-associated diseases in organs. *Oncotarget* 9, 7204–7218. doi:10.18632/oncotarget.23208

Coimbra, A. T., Ferreira, S., and Duarte, A. P. (2020). Genus Ruta: a natural source of high value products with biological and pharmacological properties. *J. Ethnopharmacol.* 260, 113076. doi:10.1016/j.jep.2020.113076

Council Directive 86/609/EEC of 24 November, (1986). On the approximation of laws, regulations and administrative provisions of the Member States regarding the protection of animals used for experimental and other scientific purposes. Publications Office of the European Union, 358, 1–28.

Daoudi, A., Hrouk, H., Belaidi, R., Slimani, I., Ibijbijen, J., and Nassiri, L. (2016). Valorisation de Ruta montana et Ruta chalepensis: Etude ethnobotanique, Screening phytochimique et pouvoir antibactérien. *J. Mater. Environ. Sci.* 7, 926–935.

Davies, N. W. (1990). Gas chromatographic retention indices of monoterpenes and sesquiterpenes on methyl silicon and Carbowax 20M phases. *J. Chromatogr. A* 503, 1–24. doi:10.1016/S0021-9673(01)81487-4

Dhale, D. A., Markandeya, S. K., and Niturkar, Y. D. (2010). Standardization of homoeopathic drug ruta graveolens L. *J. Phytol.* 2, 1–7.

Di Rosa, M., Giroud, J. P., and Willoughby, D. A. (1971). Studies of the mediators of the acute inflammatory response induced in rats in different sites by carrageenan and turpentine. *J. Pathol.* 104, 15–29. doi:10.1002/PATH.1711040103

Djarri, L., Ferhat, M., Chelghoum, A., Laggoune, S., Semra, Z., Smati, F., et al. (2013). Composition and antibacterial activity of the essential oil of Ruta chalepensis subsp. Angustifolia from Algeria. *Pharm. Lett.* 5, 252–255.

Djeridane, A., Yousfi, M., Nadjemi, B., Boutassouna, D., Stocker, P., and Vidal, N. (2006). Antioxidant activity of some algerian medicinal plants extracts

containing phenolic compounds. *Food Chem.* 97, 654–660. doi:10.1016/j.foodchem.2005.04.028

Dohou, N., Yamni, K., Tahrouch, S., Idrissi Hassani, L. M., Badoc, A., and Gmira, N. (2003). Screening phytochimique d'une endémique ibéro-marocaine, Thymelaea lythroides. *Bull. Société Pharm. Bordx.* 142, 61–78.

Drioiche, A., Amine, S., boutahiri, S., Saidi, S., Ailli, A., Rhafouri, R., et al. (2020a). Antioxidant and antimicrobial activity of essential oils and phenolic extracts from the aerial parts of ruta Montana L. Of the Middle Atlas mountains-Morocco. *J. Essent. Oil-Bear. Plants* 23, 902–917. doi:10.1080/0972060X.2020.1829995

Drioiche, A., Benhlima, N., Kharchouf, S., El-makhoukhi, F., Mehanned, S., Aaziz, H., et al. (2020b). Research team on the chemistry of bioactive molecules and environment Moulay Ismaïl. *Univ. Fac. Sci* 16, 1–14. doi:10.21010/ajtcam.v16n2.1

Drioueche, A., Boutoumi, H., and Lettreuch, H. (2021). Antimicrobial activity of xanthotoxin isolated from ruta Montana L. Extract and effect of harvesting time on its content production. *J. Mater Env. Sci.* 12, 974–983.

El-Ghazouani, F., El-Ouahmani, N., Teixidor-Toneu, I., Yacoubi, B., and Zekhnini, A. (2021). A survey of medicinal plants used in traditional medicine by women and herbalists from the city of Agadir, southwest of Morocco. *Eur. J. Integr. Med.* 42, 101284. doi:10.1016/j.eujim.2021.101284

El Mannoubi, I. (2023). Impact of different solvents on extraction yield, phenolic composition, *in vitro* antioxidant and antibacterial activities of deseeded Opuntia stricta fruit. *J. Umm Al-Qura Univ. Appl. Sci.* 9, 176–184. doi:10.1007/s43994-023-00031-y

El-Ouady, F., and Eddouks, M. (2021). Ruta Montana evokes antihypertensive activity through an increase of prostaglandins release in L-NAME-induced hypertensive rats. *Endocr. Metab. Immune Disord. Drug Targets* 21, 305–314. doi:10.2174/1871530320666200628025430

Farid, O., Hebi, M., Ajebli, M., Hidani, A.E., and Eddouks, M. (2017). Antidiabetic effect of Ruta Montana L. in streptozotocin-induced diabetic rats. *J. Basic Clin. Physiol. Pharmacol.* 28, 275–282. doi:10.1515/jbcpp-2016-0030

Fauconnier, M.-L. (2006). Huile essentielle d'Ylang-ylang: sa fiche qualité et son suivi de distillation.

Fernandes, F. A., Carocho, M., Heleno, S. A., Rodrigues, P., Dias, M. I., Pinela, J., et al. (2020). Effect of natural preservatives on the nutritional profile, chemical composition, bioactivity and stability of a nutraceutical preparation of aloe arborescens. *Antioxidants* 9, 281. doi:10.3390/antiox9040281

Ferraz, C. R., Carvalho, T. T., Manchope, M. F., Artero, N. A., Rasquel-Oliveira, F. S., Fattori, V., et al. (2020). Therapeutic potential of flavonoids in pain and inflammation: mechanisms of action, pre-clinical and clinical data, and pharmaceutical development. *Molecules* 25, 762. doi:10.3390/molecules25030762

Flouchi, R., Chraibi, M., Elmniai, A., Fahsi, K., Touzani, I., Farah, A., et al. (2024). Phytochemistry and antimicrobial activity of Moroccan Origanum compactum and Ruta Montana essential oils against nosocomial bacteria. *J. HerbMed Pharmacol.* 13, 324–332. doi:10.34172/jhp.2024.49412

García-Caparrós, P., De Filippis, L., Gul, A., Hasanuzzaman, M., Ozturk, M., Altay, V., et al. (2021). Oxidative stress and antioxidant metabolism under adverse environmental conditions: a review. *Bot. Rev.* 87, 421–466. doi:10.1007/s12229-020-09231-1

Gibka, J., Kunicka-Styczyñska, A., and Gliñski, M. (2009). Antimicrobial activity of undecan-2-one, undecan-2-ol and their derivatives. *J. Essent. Oil-Bear. Plants* 12, 605–614. doi:10.1080/0972060X.2009.10643763

Goodner, K. L. (2008). Practical retention index models of OV-101, DB-1, DB-5, and DB-Wax for flavor and fragrance compounds. *LWT - Food Sci. Technol.* 41, 951–958. doi:10.1016/j.lwt.2007.07.007

Groppo, M., Afonso, L. F., and Pirani, J. R. (2022). A review of systematics studies in the Citrus family (Rutaceae, Sapindales), with emphasis on American groups. *Braz. J. Bot.* 45, 181–200. doi:10.1007/s40415-021-00784-y

Guan, Y. S., and He, Q. (2015). Plants consumption and liver health. *Evid. Based Complement. Altern. Med.* 2015, 1–10. doi:10.1155/2015/824185

Gutiérrez-del-Río, I., Fernández, J., and Lombó, F. (2018). Plant nutraceuticals as antimicrobial agents in food preservation: terpenoids, polyphenols and thiols. *Int. J. Antimicrob. Agents* 52, 309–315. doi:10.1016/J.IJANTIMICAG.2018.04.024

Hammami, I., Smaoui, S., Hsouna, A. B., Hamdi, N., and Triki, M. A. (2015). Ruta Montana L. leaf essential oil and extracts: characterization of bioactive compounds and suppression of crown gall disease. *EXCLI J.* 14, 83–94. doi:10.17179/excli2014-655

Hammiche, V., and Azzouz, M. (2013). Les rues: ethnobotanique, phytopharmacologie et toxicité. *Phytothérapie* 11, 22–30. doi:10.1007/s10298-013-0751-9

Hernández-Pérez, M., and Rabanal, R. M. (2002). Evaluation of the antinflammatory and analgesic activity of *Sideritis canariensis* var. *pannosa* in mice. *J. Ethnopharmacol.* 81, 43–47. doi:10.1016/S0378-8741(02)00033-8

Iauk, L., Mangano, K., Rapisarda, A., Ragusa, S., Maiolino, L., Musumeci, R., et al. (2004). Protection against murine endotoxemia by treatment with Ruta Chalepensis L., a plant with anti-inflammatory properties. *J. Ethnopharmacol.* 90, 267–272. doi:10.1016/J.JEP.2003.10.004

Jaradat, N., Adwan, L., K'aibni, S., Zaid, A. N., Shtaya, M. J. Y., Shraim, N., et al. (2017). Variability of chemical compositions and antimicrobial and antioxidant activities of ruta chalepensis leaf essential oils from three palestinian regions. *Biomed. Res. Int.* 2017, 2672689–9. doi:10.1155/2017/2672689

Jennings, W. (2012). *Qualitative analysis of flavor and fragrance volatiles by glass capillary gas chromatography*. Elsevier.

Jianu, C., Goleţ, I., Stoin, D., Cocan, I., Bujancă, G., Mişcă, C., et al. (2021). Chemical profile of ruta graveolens, evaluation of the antioxidant and antibacterial potential of its essential oil, and molecular docking simulations. *Appl. Sci. Switz.* 11, 11753. doi:10.3390/app112411753

Kambouche, N., Merah, B., Bellahouel, S., Bouayed, J., Dicko, A., Derdour, A., et al. (2008). Chemical composition and antioxidant potential of Ruta Montana L. essential oil from Algeria. *J. Med. Food* 11, 593–595. doi:10.1089/jmf.2007.0515

Kara Ali, W., Ihoual, S., and Abidli, N. (2016). Antioxidant and MDR reversal activity in resistant human ovarian cancer cells of methanolic extract from Ruta Montana located in the North of Algeria. *Pharma Chem.* 8, 215–223.

Kataki, M. S., Kakoti, B. B., Bhuyan, B., Rajkumari, A., and Rajak, P. (2014). Garden rue inhibits the arachidonic acid pathway, scavenges free radicals, and elevates FRAP: role in inflammation. *Chin. J. Nat. Med.* 12, 172–179. doi:10.1016/S1875-5364(14)60029-7

Khadhri, A., Bouali, I., Belkhir, S., Mokded, R., Smiti, S., Falé, P., et al. (2017). *In vitro* digestion, antioxidant and antiacetylcholinesterase activities of two species of ruta: ruta chalepensis and ruta Montana. *Pharm. Biol.* 55, 101–107. doi:10.1080/13880209.2016.1230634

Kharchoufa, L., Bouhrim, M., Bencheikh, N., Addi, M., Hano, C., Mechchate, H., et al. (2021). Potential toxicity of medicinal plants inventoried in northeastern Morocco: an ethnobotanical approach. *Plants* 10, 1108. doi:10.3390/plants10061108

Khiya, Z., Oualcadi, Y., Gamar, A., Berrekhis, F., Zair, T., and Hilali, F. E. L. (2021). Correlation of total polyphenolic content with antioxidant activity of hydromethanolic extract and their fractions of the salvia officinalis leaves from different regions of Morocco. *J. Chem.* 2021, 1–11. doi:10.1155/2021/8585313

Klika, K. D., Pieve, C. D., Kopka, K., Smith, G., and Makarem, A. (2021). Synthesis and application of a thiol-reactive HBED-type chelator for development of easy-to-produce Ga-radiopharmaceutical kits and imaging probes. *Org. Biomol. Chem.* 19, 1722–1726. doi:10.1039/D0OB02513E

Krayni, H., Fakhfakh, N., Aloui, L., Zouari, N., Kossentini, M., and Zouari, S. (2015). Chemical composition and chelating activity of Ruta chalepensis L. (Rutaceae) essential oil as influenced by phenological stages and plant organs. *J. Essent. Oil Res.* 27, 514–520. doi:10.1080/10412905.2015.1023906

Kunicka-Styczyńska, A., and Gibka, J. (2010). Antimicrobial activity of undecan-x-ones (x = 2-4). *Pol. J. Microbiol.* 59, 301–306. doi:10.33073/pjm-2010-045

Küpeli, E., and Yesilada, E. (2007). Flavonoids with anti-inflammatory and antinociceptive activity from *Cistus laurifolius* L. leaves through bioassay-guided procedures. *J. Ethnopharmacol.* 112, 524–530. doi:10.1016/j.jep.2007.04.011

Lama-Muñoz, A., and Contreras, M. D. M. (2022). Extraction systems and analytical techniques for food phenolic compounds: a review. *Foods* 11, 3671. doi:10.3390/foods11223671

Li, W., Niu, X., Zhou, P., Li, M., and He, L. (2011). A combined peritoneal macrophage/cell membrane chromatography and offline GC-MS method for screening anti-inflammatory components from Chinese traditional medicine Houttuynia cordata Thunb. *Chromatographia* 73, 673–680. doi:10.1007/s10337-011-1926-5

Linstrom, P. J., and Mallard, W. G. (2001). The NIST chemistry webBook: a chemical data resource on the internet. *J. Chem. Eng. Data* 46, 1059–1063. doi:10.1021/je000236i

Liu, M. H., Otsuka, N., Noyori, K., Shiota, S., Ogawa, W., Kuroda, T., et al. (2009). Synergistic effect of kaempferol glycosides purified from Laurus nobilis and fluoroquinolones on methicillin-resistant *Staphylococcus aureus*. *Biol. Pharm. Bull.* 32, 489–492. doi:10.1248/bpb.32.489

Liu, W., Cui, X., Zhong, Y., Ma, R., Liu, B., and Xia, Y. (2023). Phenolic metabolites as therapeutic in inflammation and neoplasms: molecular pathways explaining their efficacy. *Pharmacol. Res.* 193, 106812. doi:10.1016/j.phrs.2023.106812

Loonat, F., and Amabeoku, G. J. (2014). Antinociceptive, anti-inflammatory and antipyretic activities of the leaf methanol extract of ruta graveolens l. (rutaceae) in mice and rats. *Afr. J. Tradit. Complement. Altern. Med.* 11, 173–181. doi:10.4314/ajtcam.v11i3.25

Lourenço, S. C., Moldão-Martins, M., and Alves, V. D. (2019). Antioxidants of natural plant origins: from sources to food industry applications. *Molecules* 24, 4132. doi:10.3390/molecules24224132

Lucera, A., Costa, C., Conte, A., Nobile, M. A. D., Hayashi, M. A. F., Meyer, R. L., et al. (2012). Food applications of natural antimicrobial compounds. *Front. Microbiol.* 3, 287. doi:10.3389/fmicb.2012.00287

Makarem, A., Gheibi, M., Mirsafaei, R., and Eftekhari, M. (2023). Hydrothermally synthesized tannic acid-copper(I) complex-based nanoparticles for efficient decontamination of lead ions from aqueous solutions. *J. Mol. Liq.* 388, 122743. doi:10.1016/j.molliq.2023.122743

Makarem, A., Sarvestani, M. K., Klika, K. D., and Kopka, K. (2019). A multifunctional HBED-type chelator with dual conjugation capabilities for radiopharmaceutical development. *Synlett* 30, 1795–1798. doi:10.1055/s-0039-1690194

Martínez, M. J. A., and Bermejo Benito, P. (2005). Biological activity of quinones. *Stud. Nat. Prod. Chem.* 30, 303–366. doi:10.1016/S1572-5995(05)80036-5

Medeiros, D. L., Lima, E. T. G., Silva, J. C., Medeiros, M. A., and Pinheiro, E. B. F. (2022). Rhamnetin: a review of its pharmacology and toxicity. *J. Pharm. Pharmacol.* 74, 793–799. doi:10.1093/jpp/rgab163

Mendonca, A., Jackson-Davis, A., Moutiq, R., and Thomas-Popo, E. (2018). "Use of natural antimicrobials of plant origin to improve the microbiological safety of foods," in *Food and feed safety systems and analysis* (Academic Press), 249–272.

Merghem, M., and Dahamna, S. (2020). *In-Vitro* antioxidant activity and total phenolic content of ruta Montana L. Extracts. *J. Drug Deliv. Ther.* 10, 69–75. doi:10.22270/jddt.v10i2.3919

Merghem, M., Dahamna, S., Samira, K., and Khennouf, S. (2017). Effect of chronic oral administration of ruta Montana l. Areal part extract on fertility potential in albino rats. *Annu. Res. Rev. Biol.* 21, 1–8. doi:10.9734/ARRB/2017/38608

Mezzoug, N., Elhadri, A., Dallouh, A., Amkiss, S., Skali, N. S., Abrini, J., et al. (2007). Investigation of the mutagenic and antimutagenic effects of Origanum compactum essential oil and some of its constituents. *Mutat. Res. Toxicol. Environ. Mutagen.* 629, 100–110. doi:10.1016/J.MRGENTOX.2007.01.011

Miara, M. D., Bendif, H., Rebbas, K., Rabah, B., Hammou, M. A., and Maggi, F. (2019). Medicinal plants and their traditional uses in the highland region of Bordj Bou Arreridj (Northeast Algeria). *J. Herb. Med.* 16, 100262. doi:10.1016/J.HERMED.2019.100262

Micael, R. C., Tahira, S. M., Fatima, M. M. M., and Jan, C. D. (2015). Analgesic activity of Ruta graveolens L. (Rue) extracts. *Afr. J. Pharm. Pharmacol.* 9, 1–5. doi:10.5897/ajpp2014.4152

Milesi, S. (2001). *Etude de la production de furocoumarines par la Rue officinale (Ruta graveolens L.): Cultures de plantes au champ et cultures* in vitro. Nancy, France: Institut National Polytechnique de Lorraine.

Mitra, A., Chatterjee, S., Voronina, A. V., Walther, C., and Gupta, D. K. (2020). "Lead toxicity in plants: a review," in *Lead in plants and the environment*. Editors D. K. Gupta, S. Chatterjee, and C. Walther (Germany: Springer International Publishing Ag), 99–116.

Mogode, D. J. (2005). Etude phytochimique et pharmacologique de Cassia nigricans Vahl (Caesalpiniaceae) utilisé dans le traitement des dermatoses au Tchad.

Mohammedi, H., Mecherara-Idjeri, S., and Hassani, A. (2019). Variability in essential oil composition, antioxidant and antimicrobial activities of Ruta Montana L. collected from different geographical regions in Algeria. *J. Essent. Oil Res.* 32, 88–101. doi:10.1080/10412905.2019.1660238

Nahar, L., El-Seedi, H. R., Khalifa, S. A. M., Mohammadhosseini, M., and Sarker, S. D. (2021). Ruta essential oils: composition and bioactivities. *Molecules* 26, 4766. doi:10.3390/molecules26164766

Najem, M., Harouak, H., Ibijbijen, J., and Nassiri, L. (2020). Oral disorders and ethnobotanical treatments: a field study in the central Middle Atlas (Morocco). *Heliyon* 6, e04707. doi:10.1016/j.heliyon.2020.e04707

Najem, M., Ibijbijen, J., and Nassiri, L. (2021). Ethnobotanical treatment of respiratory diseases in the central Middle Atlas (Morocco): qualitative and quantitative approach. *Eur. J. Integr. Med.* 46, 101358. doi:10.1016/j.eujim.2021.101358

Negus, S. S., Vanderah, T. W., Brandt, M. R., Bilsky, E. J., Becerra, L., and Borsook, D. (2006). Preclinical assessment of candidate analgesic drugs: recent advances and future challenges. *J. Pharmacol. Exp. Ther.* 319, 507–514. doi:10.1124/jpet.106.106377

N'Guessan, K., Kadja, B., Zirihi, G., Traoré, D., and Aké-Assi, L. (2009). Screening phytochimique de quelque plantes médicinales ivoiriennes utilisées en pays Krobou (Agboville, Côte-d'Ivoire). *Sci. Nat.* 6. doi:10.4314/scinat.v6i1.48575

Nonnenmacher, J. L., Mikulski, B. S., and Roman, S. S. (2016). Anti-inflammatory activity of the essential oil and hydroalcoholic extract of Ruta graveolens l. (Rue) on ear edema in mice. *Perspectiva* 41, 125–134.

Okaiyeto, S. A., Sutar, P. P., Chen, C., Ni, J.-B., Wang, J., Mujumdar, A. S., et al. (2024). Antibiotic resistant bacteria in food systems: current status, resistance mechanisms, and mitigation strategies. *Agric. Commun.* 2, 100027. doi:10.1016/j.agrcom.2024.100027

Oubihi, A., Hosni, H., Nounah, I., Ettouil, A., Harhar, H., Alaoui, K., et al. (2020). Phenolic content, antioxidant activity, anti-inflammatory potential, and acute toxicity study of thymus leptobotrys murb. Extracts. *Biochem. Res. Int.* 2020, 1–7. doi:10.1155/2020/8823209

Ouédraogo, N., Lompo, M., Sawadogo, R. W., Tibiri, A., Hay, A. E., Koudou, J., et al. (2012). Étude des activités anti-inflammatoire, analgésique et antipyrétique des décoctés aqueux des feuilles et des racines de Pterocarpus erinaceus Poir. (Fabaceae). *Phytothérapie* 10, 286–292. doi:10.1007/s10298-012-0732-z

Oyaizu, M. (1986). Studies on products of browning reaction. Antioxidative activities of products of browning reaction prepared from glucosamine. *Jpn. J. Nutr. Diet.* 44, 307–315. doi:10.5264/EIYOGAKUZASHI.44.307

Ozer, J., Ratner, M., Shaw, M., Bailey, W., and Schomaker, S. (2008). The current state of serum biomarkers of hepatotoxicity. *Toxicology* 245, 194–205. doi:10.1016/J.TOX.2007.11.021

Pacifico, S., Piccolella, S., Galasso, S., Fiorentino, A., Kretschmer, N., Pan, S.-P., et al. (2016). Influence of harvest season on chemical composition and bioactivity of wild rue plant hydroalcoholic extracts. *Food Chem. Toxicol.* 90, 102–111. doi:10.1016/j.fct.2016.02.009

Pei, K., Ou, J., Huang, J., and Ou, S. (2016). p-Coumaric acid and its conjugates: dietary sources, pharmacokinetic properties and biological activities. *J. Sci. Food Agric.* 96, 2952–2962. doi:10.1002/jsfa.7578

Price, M. L., Scoyoc, S. V., and Butler, L. G. (1978). A critical evaluation of the vanillin reaction as an assay for tannin in sorghum grain. *J. Agric. Food Chem.* 26, 1214–1218. doi:10.1021/jf60219a031

Pyrzynska, K. (2024). Ferulic acid—a brief review of its extraction, bioavailability and biological activity. *Separations* 11, 204. doi:10.3390/separations11070204

Rappoport, Z. (2004). *The chemistry of phenols.* John Wiley and Sons.

Ratheesh, M., Shyni, G. L., Sindhu, G., and Helen, A. (2009). Protective effects of isolated polyphenolic and alkaloid fractions of ruta graveolens L. on acute and chronic models of inflammation. *Inflammation* 33, 18–24. doi:10.1007/s10753-009-9154-y

Saidi, S., Remok, F., Handaq, N., Drioiche, A., Gourich, A. A., Menyiy, N. E., et al. (2023). Phytochemical profile, antioxidant, antimicrobial, and antidiabetic activities of Ajuga iva (L.). *Life* 13, 1165. doi:10.3390/life13051165

Sarmento-Neto, J. F., Do Nascimento, L. G., Felipe, C. F. B., and De Sousa, D. P. (2016). Analgesic potential of essential oils. *Molecules* 21, 20–29. doi:10.3390/molecules21010020

Satyapal, U. S., Kadam, V. J., and Ghosh, R. (2008). Hepatoprotective activity of livobond a polyherbal formulation against CCl4 induced hepatotoxicity in rats. *Int. J. Pharmacol.* 4 (6), 472–476. doi:10.3923/ijp.2008.472.476

Sengupta, R., Sheorey, S. D., and Hinge, M. A. (2012). Analgesic and anti-inflammatory plants: an updated review. *Int. J. Pharm. Sci. Rev. Res.* 12, 114–119.

Shahidi, F., and Yeo, J. D. (2018). Bioactivities of phenolics by focusing on suppression of chronic diseases: a review. *Int. J. Mol. Sci.* 19, 1573–16. doi:10.3390/ijms19061573

Singleton, V. L., and Rossi, J. A. (1965). Colorimetry of total phenolics with phosphomolybdic-phosphotungstic acid reagents. *Am. J. Enol. Vitic.* 16, 144–158. doi:10.5344/AJEV.1965.16.3.144

Skujins, S. (1998). Handbook for ICP-aes (Varian-Vista). A short guide to vista series ICP-aes operation. *Varian Int. Ag. Zug Switz.* Version 1.0.

Slougui, N., Rabhi, N. L., Achouri, R., and Bensouici, C. (2023). Evaluation of the antioxidant, antifungal and anticholinesterase activity of the extracts of ruta Montana L., harvested from souk-ahras (North-East of Algeria) and composition of its extracts by GC-MS. *Trop. J. Nat. Prod. Res.* 7, 3452–3461. doi:10.26538/tjnpr/v7i7.25

Szewczyk, A., Marino, A., Taviano, M. F., Cambria, L., Davì, F., Trepa, M., et al. (2023). Studies on the accumulation of secondary metabolites and evaluation of biological activity of *in vitro* cultures of ruta Montana L. In temporary immersion bioreactors. *Int. J. Mol. Sci.* 24, 7045–18. doi:10.3390/ijms24087045

Tahraoui, A., El-Hilaly, J., Israili, Z. H., and Lyoussi, B. (2007). Ethnopharmacological survey of plants used in the traditional treatment of hypertension and diabetes in south-eastern Morocco (Errachidia province). *J. Ethnopharmacol.* 110, 105–117. doi:10.1016/j.jep.2006.09.011

Teixeira, B. F., Aranha, J. B., and Vieira, T. M. F. de S. (2022). Replacing synthetic antioxidants in food emulsions with microparticles from green acerola. *Future Foods* 5, 100130. doi:10.1016/J.FUFO.2022.100130

Toker, G., Turkoz, S., and Erdemoglu, N. (1998). High performance liquid chromatographic analysis of rutin in some Turkish plants II. *J. Chem. Soc. Pak.* 20, 240–243.

Touat, M., Opatowski, M., Brun-Buisson, C., Cosker, K., Guillemot, D., Salomon, J., et al. (2019). A payer perspective of the hospital inpatient additional Care costs of antimicrobial resistance in France: a matched case–control study. *Appl. Health Econ. Health Policy* 17, 381–389. doi:10.1007/s40258-018-0451-1

Treacy, O., Brown, N. N., and Dimeski, G. (2019). Biochemical evaluation of kidney disease. *Transl. Androl. Urol.* 8 (4), S214–S223. doi:10.21037/tau.2018.10.02

Ulusoy, H. G., and Sanlier, N. (2020). A minireview of quercetin: from its metabolism to possible mechanisms of its biological activities. *Crit. Rev. Food Sci. Nutr.* 60, 3290–3303. doi:10.1080/10408398.2019.1683810

Wahyuni, T. S., Khoiriyah, N., Tumewu, L., Ekasari, W., Fuad, A., and Widyawaruyanti, A. (2023). Microscopic and physicochemical evaluation of Ruta angustifolia leaves. *J. Public Health Afr.* 14, 7–129. doi:10.4081/jphia.2023.2520

Whitehead, M. W., Hawkes, N. D., Hainsworth, I., and Kingham, J. G. C. (1999). A prospective study of the causes of notably raised aspartate aminotransferase of liver origin. *Gut* 45, 129–133. doi:10.1136/gut.45.1.129

Winter, C. A., Risley, E. A., and Nuss, G. W. (1962). Carrageenin-induced edema in hind paw of the rat as an assay for antiinflammatory drugs. *Proc. Soc. Exp. Biol. Med.* 111, 544–547. doi:10.3181/00379727-111-27849

Yahfoufi, N., Alsadi, N., Jambi, M., and Matar, C. (2018). The immunomodulatory and anti-inflammatory role of polyphenols. *Nutrients* 10, 1618–1623. doi:10.3390/nu10111618

Yosra, B., Manef, A., and Sameh, A. (2019). Biological study from ruta plants extracts growing in Tunisia. *Iran. J. Chem. Chem. Eng.* 38, 85–89.

Zellagui, A., Belkassam, A., Belaidi, A., and Gherraf, N. (2012). Environmental impact on the chemical composition and yield of essential oils of Algerian Ruta Montana (Clus.) L and their antioxidant and antibacterial activities. *Adv. Environ. Biol.* 6, 2684–2688.

Zeraib, A., Boudjedjou, L., Suici, N., Benmeddour, T., Rahal, K., and Fercha, A. (2021). Synergistic effects of ruta Montana (Clus.) l. essential oil and antibiotics against some pathogenic bacteria. *J. Phytol.* 13, 101–107. doi:10.25081/jp.2021.v13.7088

Zouhri, A., Bouddine, T., Menyiy, N. E., Kachkoul, R., El-mernissi, Y., Siddique, F., et al. (2023). Ionomic analysis, polyphenols characterization, analgesic, antiinflammatory and antioxidant capacities of Cistus laurifolius leaves: *in vitro*, *in vivo*, and *in silico* investigations. *Sci. Rep.* 13, 22890–17. doi:10.1038/s41598-023-50031-5

Frontiers in
Chemistry

Explores all fields of chemical science across the periodic table

Advances our understanding of how atoms, ions, and molecules come together and come apart. It explores the role of chemistry in our everyday lives - from electronic devices to health and wellbeing.

Discover the latest Research Topics

See more →

frontiers | Research Topics